January 2009
SLAC-R-913

UNIVERSITA' DEGLI STUDI DI MILANO

Facoltà di Scienze Matematiche, Fisiche e Naturali

Corso di Laurea Magistrale in Fisica

Measurements of Time-Dependent $\mathbb{CP}$-Asymmetry Parameters in B Meson Decays to $\eta'\mathrm{K}^0$ and of Branching Fractions of $\mathrm{SU}(3)$ Related Modes with *BABAR* Experiment at SLAC

Relatore: Prof. Fernando PALOMBO
Correlatore: Dott. Alfio LAZZARO

Tesi di Laurea di:
Pietro BIASSONI
Matricola 716592
Codici PACS: 13.25.Hw,
12.15.Hh, 11.30.Er
SLAC-R-913

Anno Accademico 2007-2008

SLAC National Accelerator Laboratory, Menlo Park, Ca 94025
Work supported in part by US Department of Energy contract DE-AC02-76SF00515

There are three kinds of lies:
lies, damned lies, and statistics.

Benjamin Disraeli

Contents

Introduction

In October 1957, C. N. Yang and T .D. Lee won the Nobel Prize *”for their penetrating investigation of the so-called parity laws which has led to important discoveries regarding the elementary particles”*, expressed one year before [1]. On 15^{th} January 1956, C. S. Wu had produced a paper [2] reporting some experimental results which confirmed Lee and Yang’s predictions and that deeply influenced the assignation of the mentioned Nobel Prize. C. S. Wu never won a Nobel Prize. The woman who discovered the parity violation was victim herself of an evident parity violation.

The search for symmetries conservation always played a central role in elementary particle physics research. During the 40s and in the beginning of 50s, many experiments concerning parity conservation in strong and electromagnetic interactions led to the conclusion that this was a good symmetry for the theory, and this conservation was assumed for weak interaction, too. The discovery of strange particles [3] and the consequent research in this new field of physics pointed out the so called $\theta - \tau$ *puzzle*. This consist on two particles with the same mass and decay time that were observed to decay into two different states with opposite parity [4]. This experimental observation led Lee and Yang to critically survey that there was no evidence of parity conservation in weak interactions, and, one year later, experiments confirmed this guess. However, the CP symmetry was supposed to be conserved. Seven years later, J. H. Christensen, J. W. Cronin, V. L. Fitch, and R. Turlay performed an experiment with a kaon beam, produced by the interaction of a 30 GeV proton beam on fixed target, at Brookheaven National Laboratory. This experiment showed that CP was violated in K meson decays [5]. This discovery came as a breakthrough in the world of particle physics and met many resistances before being accepted. Ten years later, Kobayashi and Maskawa, generalizing the quark mixing matrix introduced by N. Cabibbo [6], proposed a model which could explain the mechanism of CP violation in K meson system [7]. This model predicted the presence of three families of quarks, but experimental results had evidence of three kinds of quarks only, divided into two families. The $charm$ quark was discovered one year later [8], while the $bottom$ and the top quarks (which belong to the third family) in 1977 [9] and in 1994 [10], respectively. After 30 years of researches, in 1999 the evidence of direct CP violation in the K meson system was found [11].

The actual knowledge about CKM scenario and the constraints on New Physics (NP) effects has been deeply influenced by the study of decays of B meson, a particle quite similar to K meson, with a quark b instead of s. Such studies were performed at asymmetric beam energy B factories by *BABAR* and Belle Collaborations. The two experiments reached their original goal with the measurement of CP parameter in the $b \to c\bar{c}s$ [12] decays and , more recently, with the observation of the direct CP violation in $B^0 \to K^+\pi^-$ [13]. Many other goals were reached far beyond the ones planned during the experiments proposal, the most important being the evidence of $D^0 - \bar{D}^0$ mixing [14], the observation of a charged charmonium-like resonance [15] and the observation of the ground state of the bottomium [16]. Due to the great amount of their datasets, B factories offer also the possibility of high-precision probes of the Standard Model (SM) and look for NP. NP's effects can result in differences of CP violation parameters between loop (penguin) dominated $b \to s$ transitions and tree dominated (NP free) $b \to c\bar{c}s$ ones [17] . In fact, if a new heavy particle can occur in the loop, we can measure deviations from SM contributions, which are dominating in tree diagrams. Unfortunately, these penguin decays are Cabibbo suppressed and have branching fractions of order 10^{-4} or smaller. Yet, the great amount of B meson produced at B factories allows us to have very precise measurement of these decay modes.

This thesis work describes the updated measurement of CP violation parameters in penguin dominated decay $B^0 \to \eta' K^0$ using the final *BABAR* dataset. The CP-asymmetry violation in $B^0 {\to} \eta' K^0$ mode was first observed in 2006 by *BABAR*, with a great contribution of Milan group [18]. This measurement contributed to the results presented at *International Conference on High Energy Physics (ICHEP) 2008*, that took place in Philadelphia, USA. They are included into a paper already submitted to *Physical Review D* [19]. The candidate was the primary editor of the analysis document and co-author of the journal draft.

Due to the presence of suppressed contribution from other amplitudes in the loop diagram which determine $B^0 \to \eta' K^0$ decay, deviations from expected SM-CP violation parameters can occur. Many approaches were followed in order to calculate an upper bound to the possible amount of these deviations; the use of $SU(3)$ symmetries leads to some relations between this bound and branching fractions of the B meson decays into some final states such as $\eta\eta$, $\eta\phi$, and $\eta'\phi$ [20, 21, 22, 23].
In addiction, there is an important issue related to the branching fractions of $\eta^{(\prime)}K$ (charged and neutral) modes. Since the discover of $B \to \eta' K$ in 1997 [24], with a high branching fraction (higher than expected), it was found that the corresponding mode with η is suppressed. A possible explanation of this was proposed by Lipkin in 1991 [25], using

arguments concerning the $\eta - \eta'$ mixing angle and the parity of K meson.

This thesis work describes the measurements of branching fractions (or determination on their upper limits) for $\eta\eta$, $\eta'\eta'$, ηK^0_S, $\eta^{(\prime)}\omega$ and $\eta^{(\prime)}\phi$, too. Some of these branching fractions are involved in the calculation of the above mentioned bound and can give some information about the relative magnitude of decays which differ only for the presence of η instead of η'. Results of this analysis were submitted and presented during *Flavor Physics and CP Violation (FPCP) 2008* Conference, that took place in Taipei, Taiwan. They will be soon included into a paper to be submitted to *Physical Review D*. The candidate was co-author of the analysis document and primary editor of the *conference contribution*.

All our analyses are based on multivariate analysis techniques, with the use of an unbinned extended maximum likelihood fit to extract signal yields and CP parameters. In order to perform these fits Milan group have developed a flexible program in C++ language, called `MiFit`[1].

All the results presented in this thesis have been reviewed and approved by the *BABAR* Collaboration.

The candidate defended the scientific validity of both analyses during two distinct plenary *Collaboration Wide Talks*.

This thesis is structured in seven chapters. In the first we give an outlook of neutral meson mixing and CP violation phenomenology in the K and B meson systems and we explain the origin of CP violation in SM. In the second chapter we present a more detailed theoretical treatment of decays modes measured into this thesis work. In the third chapter we will describe the *BABAR* detector and its reconstruction software. In chapter four we will describe data analysis techniques used in our measurements. In chapter five we will explain how our events are reconstructed and selected. Chapter six and seven will contain results of our analyses for CP parameters and branching fractions measurements, respectively.

I would like to thank Professor Fernando Palombo, Dr. Alfio Lazzaro and all other members of *BABAR* Milan group for their support and help in my thesis work.

---

[1] `MiFit` was mainly developed by Dr. Alfio Lazzaro, with many contributors including the candidate.

Chapter 1

Origin and Phenomenology of CP Violation

1.1 Introduction

Discrete symmetries always played a central role in the development of theoretical understanding of particle physics phenomenology. The discovery of parity violation [2] and CP violation [5] led to important improvement of the theory which is at present known as the Standard Model (SM)[1]. Actually CP violation is well understood in SM as an effect of the quark mixing matrix [7], named Cabibbo-Kobayashi-Maskawa (CKM) matrix, and is experimentally confirmed both in K meson system [5, 11] and in B meson system [12, 13]. CP violation is also one of the tree conditions used by Sakharov [26] in order to explain the matter-antimatter asymmetry in the universe. In addiction to this, New Physics (NP) effects can be undercovered looking at discrepancies between measured CP violation parameters and SM predictions.

In this chapter we give an overview of neutral mesons mixing and CP violation phenomenology. We then discuss the origin of CP violation in the SM and techniques used in order to determine the magnitude and phases of the Cabibbo-Kobayashi-Maskawa (CKM) matrix.

1.2 Discrete Symmetries

The set of operators on the Hilbert space of state functions on the quantum field contains both discrete and continuous transformations that preserve the Minkowski interval $t^2 - \vec{x}^2$. The set of continuous transformations that preserve this interval are the Lorentz transfor-

---

[1] Historically this model grew up as a continuous improvement of Fermi's theory of β decay, including, step by step, all the new evidences that experiments provided.

mations, composed by space rotations, translations, Lorentz boosts and their products. The three independent discrete transformations that also preserve $t^2 - \vec{x}^2$ are the charge conjugation operator (C), the parity operator (P), and the time-reversal operator (T). These form a complete set of discrete Minkowski-interval-preserving transformations of the Hilbert space. Although one can build other transformation in the SM which have this property [27, 28, 29], all can be reduced to a proper combination of C, P, T, and the group of continuous Lorentz and gauge rotations. We describe below the action of discrete transformations on a Dirac, 1/2 spin, field. A more detailed treatment of such transformations can be found elsewhere [30, 31].

Parity

The parity operator $\mathcal{P}$ reverses the signs of the 3 spatial elements of a four-vector: $(t, \vec{x}) \to (t, -\vec{x})$ and $(E, \vec{p}) \to (E, -\vec{p})$. This transformation reverses the momentum of a particle but leaves its spin unchanged:

Consider the action of parity on the particle and antiparticle annihilation operators of the Dirac field $a^s_{\vec{p}}$ and $b^s_{\vec{p}}$. Parity should transform the states $a^s_{\vec{p}}|0\rangle$ and $b^s_{\vec{p}}|0\rangle$ to $a^s_{-\vec{p}}|0\rangle$ and $b^s_{-\vec{p}}|0\rangle$. This implies

$$\mathcal{P}a^s_{\vec{p}}\mathcal{P}^{-1} = \eta_a a^s_{\overrightarrow{-p}} \qquad \text{and} \qquad \mathcal{P}a^s_{\vec{p}}\mathcal{P}^{-1} = \eta_b b^s_{\overrightarrow{-p}} \tag{1.1}$$

where η_a and η_b are phases. Since $\mathcal{P}^2 = \mathbf{1} \Rightarrow \eta_a, \eta_b$ must equal ± 1 (the parity group, as with the other two discrete operators, is idempotent, *i.e.* $\mathcal{P}^{-1} = \mathcal{P}$, so the equation above could just as easily have been written $\mathcal{P}a^s_{\vec{p}}\mathcal{P}$, etc.). To find the matrix representation of $\mathcal{P}$ and the phases η_a and η_b, consider the action of $\mathcal{P}$ on $\phi(x)$. Decomposing ϕ into eigenstates of spin and momentum gives:

$$\mathcal{P}\phi(x)\mathcal{P}^{-1} = \frac{1}{\sqrt{2E_{\vec{p}}}} \int \frac{d^3p}{(2\pi)^3} \sum_s \left(\eta_a a^s_{\overrightarrow{-p}} u^s(p) e^{-ipx} + \eta_b^* b^{s\dagger}_{\overrightarrow{-p}} v^s(p) e^{ipx} \right) \tag{1.2}$$

The key is to change variables to (not surprisingly) $p' = (p^0, \overrightarrow{-p}) \Rightarrow p \cdot x = p' \cdot (t, -\vec{x})$ and $p' \cdot \sigma$ (where σ is the four-vector of 2×2 Pauli matrices) $= p \cdot \sigma^\dagger \gamma^0$ (where γ^0 is the 0^{th} Dirac matrix) $= p \cdot \bar{\sigma}$, where

$$\bar{\sigma} \equiv \sigma^\dagger \gamma^0 \tag{1.3}$$

Thus the four-spinors $u(p)$ and $v(p)$ can be written as:

$$\begin{aligned} u(p) &= \begin{pmatrix} \sqrt{p\cdot\sigma}\varsigma \\ \sqrt{p\cdot\bar{\sigma}}\varsigma \end{pmatrix} = \begin{pmatrix} \sqrt{p'\cdot\bar{\sigma}}\varsigma \\ \sqrt{p'\cdot\sigma}\varsigma \end{pmatrix} = \gamma^0 u(p') \\ v(p) &= \begin{pmatrix} \sqrt{p\cdot\sigma}\varsigma \\ -\sqrt{p\cdot\bar{\sigma}}\varsigma \end{pmatrix} = \begin{pmatrix} \sqrt{p'\cdot\bar{\sigma}}\varsigma \\ -\sqrt{p'\cdot\sigma}\varsigma \end{pmatrix} = -\gamma^0 v(p') \end{aligned} \tag{1.4}$$

where ς is a generic two-component spinor. Thus (1.2) can be written as:

$$\begin{aligned} \mathcal{P}\phi(x)\mathcal{P}^{-1} = \frac{1}{\sqrt{2E_{\vec{p}'}}}\int\frac{d^3p'}{(2\pi)^3}\sum_s \quad &\Big(\eta_a a^s_{\vec{p}'}\gamma^0 u^s(p')e^{-ip'\cdot(t,-\vec{x})} \\ &- \eta_b^* b^{s\dagger}_{\vec{p}'}\gamma^0 v^s(p')e^{ip'\cdot(t,-\vec{x})}\Big) \end{aligned} \tag{1.5}$$

But,

$$\begin{aligned} \phi(t,-\vec{x}) = \frac{1}{\sqrt{2E_{\vec{p}'}}}\int\frac{d^3p'}{(2\pi)^3}\sum_s \quad &\Big(a^s_{\vec{p}'} u^s(p')e^{-ip'\cdot(t,-\vec{x})} \\ &+ b^{s\dagger}_{\vec{p}'} v^s(p')e^{ip'\cdot(t,-\vec{x})}\Big) \end{aligned} \tag{1.6}$$

$\Rightarrow \eta_a = 1$, $\eta_b = -1$, and

$$\mathcal{P}\phi(t,\vec{x})\mathcal{P}^{-1} = \gamma^0\phi(t,-\vec{x}) \tag{1.7}$$

Time Reversal

The time reversal operator reverses momentum and spin and also flips the sign of the time component of a state. Therefore we want the transformation of the Dirac particle and antiparticle annihilation operators to be:

$$\mathcal{T}a^s_{\vec{p}}\mathcal{T}^{-1} = \eta'_a a^{-s}_{-\vec{p}} \qquad \text{and} \qquad \mathcal{T}b^s_{\vec{p}}\mathcal{T}^{-1} = \eta'_b b^{-s}_{-\vec{p}} \tag{1.8}$$

We can start to compute the transformation of the fermion field ϕ:

$$\mathcal{T}\phi(t,\vec{x})\mathcal{T}^{-1} = \frac{1}{\sqrt{2E_{\vec{p}}}}\int\frac{d^3p}{(2\pi)^3}\sum_s \mathcal{T}\left(a^s_{\vec{p}}u^s(p)e^{-ipx} + b^{s\dagger}_{\vec{p}}v^s(p)e^{ipx}\right)\mathcal{T}^{-1} \tag{1.9}$$

However, if $\mathcal{T}$ were to only act on the operators a and b, the situation would be the same as with parity and the spatial coordinates would flip sign instead of time (also the operators would reverse spin but not the spinors, which would be an unphysical nonlinearity). $\mathcal{T}$ therefore must act on more than just the operators.

The solution is to let $\mathcal{T}$ act on complex numbers in addition to operators. Let

$$\mathcal{T}z = z^*\mathcal{T} \quad \forall z \in \mathcal{C} \tag{1.10}$$

Thus (1.9) becomes

$$\frac{1}{\sqrt{2E_{\vec{p}}}}\int\frac{d^3p}{(2\pi)^3}\sum_s\Big(\eta_a'^* a^{-s}_{-\vec{p}}(u^s(p))^* e^{ipx} + \eta_b'^* b^{-s\dagger}_{-\vec{p}}(v^s(p))^* e^{-ipx}\Big) \tag{1.11}$$

We need to find a constant matrix $\mathcal{M}$ such that $\mathcal{M}u^{-s}(p') = (u^s(p))^*$ (and similarly for $v^s(p)$) — then we can change variables to p' and $(-t,\vec{x})$ so that we can obtain an answer for the action of the transformation in terms of $\phi(-t,\vec{x})$.

We can see that:

$$\begin{aligned}(u^s(p))^* = \begin{pmatrix}\sqrt{p\cdot\sigma^*}\varsigma^{s*}\\ \sqrt{p\cdot\bar{\sigma}^*}\varsigma^{s*}\end{pmatrix} = \begin{pmatrix}\sigma^2 & 0\\ 0 & \sigma^2\end{pmatrix}\begin{pmatrix}\sigma^2 & 0\\ 0 & \sigma^2\end{pmatrix}\begin{pmatrix}\sqrt{p\cdot\sigma^*}\varsigma^{s*}\\ \sqrt{p\cdot\bar{\sigma}^*}\varsigma^{s*}\end{pmatrix} = \\ -\gamma^1\gamma^3\begin{pmatrix}-i\sigma^2\sqrt{p\cdot\sigma^*}\varsigma^{s*}\\ -i\sigma^2\sqrt{p\cdot\bar{\sigma}^*}\varsigma^{s*}\end{pmatrix}\end{aligned} \tag{1.12}$$

and we can then use the identity

$$\sigma^2\sqrt{p\cdot\sigma^*} = \sqrt{p'\cdot\sigma}\,\sigma^2 \tag{1.13}$$

and the fact that

$$-i\sigma^2\varsigma^{s*} = \begin{pmatrix}0 & 1\\ -1 & 0\end{pmatrix}\begin{pmatrix}\varsigma^{1*}\\ \varsigma^{2*}\end{pmatrix} = \begin{pmatrix}\varsigma^{2*}\\ -\varsigma^{1*}\end{pmatrix} = \varsigma^{-s} \tag{1.14}$$

to obtain for (1.13):

$$-\gamma^1\gamma^3\begin{pmatrix}\sqrt{p'\cdot\sigma}(-i\sigma^2\varsigma^{s*})\\ \sqrt{p'\cdot\bar{\sigma}}(-i\sigma^2\varsigma^{s*})\end{pmatrix} = -\gamma^1\gamma^3\begin{pmatrix}\sqrt{p'\cdot\sigma}\varsigma^{-s}\\ \sqrt{p'\cdot\bar{\sigma}}\varsigma^{-s}\end{pmatrix} = -\gamma^1\gamma^3 u^{-s}(p') \tag{1.15}$$

and similarly for $(v^s(p))^*$. Thus (1.15) becomes

$$-\gamma^1\gamma^3 \frac{1}{\sqrt{2E_{\vec{p}'}}} \int \frac{d^3p'}{(2\pi)^3} \sum_s \Big(\eta_a'^* a_{\vec{p}'}^{-s} u^s(p') e^{-ip'\cdot(-t,\vec{x})} + \eta_b'^* b_{\vec{p}'}^{-s\dagger} v^s(p') e^{ip'\cdot(-t,\vec{x})} \Big) \Rightarrow$$

$$\mathcal{T}\phi(t,\vec{x})\mathcal{T}^{-1} = -\gamma^1\gamma^3\phi(-t,\vec{x}) \tag{1.16}$$

Charge Conjugation

The charge conjugation operator is defined to be the transformation of a particle into its antiparticle without changing momentum or spin. Thus,

$$\mathcal{C}a_{\vec{p}}^s\mathcal{C}^{-1} = \eta_a'' b_{\vec{p}}^s \qquad \text{and} \qquad \mathcal{C}b_{\vec{p}}^s\mathcal{C}^{-1} = \eta_b'' a_{\vec{p}}^s \tag{1.17}$$

so the transformation of the Dirac field is

$$\mathcal{C}\phi(x)\mathcal{C}^{-1} = \frac{1}{\sqrt{2E_{\vec{p}}}} \int \frac{d^3p}{(2\pi)^3} \sum_s \Big(b_{\vec{p}}^s u^s(p) e^{-ipx} + a_{\vec{p}}^{s\dagger} v^s(p) e^{ipx} \Big) \tag{1.18}$$

We want to find what this is in terms of $\bar{\phi} = \phi^\dagger\gamma^0$, so we need a relation between $u^s(p)$ and $v^{s*}(p)$, and between $v^s(p)$ and $u^{s*}(p)$:

$$u^{s*}(p) = \begin{pmatrix} \sqrt{p\cdot\sigma^*}\varsigma^{s*} \\ \sqrt{p\cdot\bar{\sigma}^*}\varsigma^{s*} \end{pmatrix} = \begin{pmatrix} \sqrt{p\cdot\sigma^*}\varsigma^{s*} \\ \sqrt{p\cdot\bar{\sigma}^*}\varsigma^{s*} \end{pmatrix} = \begin{pmatrix} i\sqrt{p\cdot\sigma^*}\sigma^2\varsigma^{-s} \\ i\sqrt{p\cdot\bar{\sigma}^*}\sigma^2\varsigma^{-s} \end{pmatrix} \tag{1.19}$$

However, from the identity (1.13) we can see that:

$$\begin{aligned} \sqrt{p\cdot\sigma^*}\sigma^2 &= \sigma^2\sqrt{p\cdot\bar{\sigma}} \qquad \text{and} \\ \sqrt{p\cdot\bar{\sigma}^*}\sigma^2 &= \sigma^2\sqrt{p\cdot\sigma} \end{aligned} \tag{1.20}$$

Thus,

$$u^{s*}(p) = \begin{pmatrix} i\sigma^2\sqrt{p\cdot\bar{\sigma}}\varsigma^{-s} \\ i\sigma^2\sqrt{p\cdot\sigma}\varsigma^{-s} \end{pmatrix} = \begin{pmatrix} 0 & -i\sigma^2 \\ i\sigma^2 & 0 \end{pmatrix} \begin{pmatrix} \sqrt{p\cdot\sigma}\varsigma^{-s} \\ -\sqrt{p\cdot\bar{\sigma}}\varsigma^{-s} \end{pmatrix} = -i\gamma^2 v^s(p). \tag{1.21}$$

Similarly, $v^{s*}(p) = -i\gamma^2 u^s(p)$, so (1.18) becomes:

$$\begin{aligned}\mathcal{C}\phi(x)\mathcal{C}^{-1} &= \frac{1}{\sqrt{2E_{\vec{p}}}}\int\frac{d^3p}{(2\pi)^3}\sum_s\left(i\gamma^2 b^s_{\vec{p}}v^{s*}(p)e^{-ipx}+i\gamma^2 a^{s\dagger}_{\vec{p}}u^{s*}(p)e^{ipx}\right)\\ &= i\gamma^2\phi^*(x)=i(\bar{\phi}\gamma^0\gamma^2)^T \qquad (1.22)\end{aligned}$$

CPT

The combination $\mathcal{CPT}$ operator has a rather special property: it is guaranteed to be a fundamental symmetry of nature[2], with only the basic assumptions of Lorentz invariance, locality, and the spin-statistics relation.[3]

1.2.1 *CP*

One can easily be convinced that, if we restrict our attention to scalars, pseudoscalars, vectors, and the derivative operator, a Lagrangian formed from only such quantities must remain CP-invariant. Thus a massless spin 1/2 field with real coupling constants cannot violate CP. This is in fact true for quantum fields of any spin. Charge conjugation ensures that the fields themselves transform to their Hermitian conjugates (we have seen this above for the special case of spin 1/2). However, particle masses and coupling constants do not transform under CP (as complex numbers such as these are only transformed by, of the discrete operators, $\mathcal{T}$, as previously seen). If any of these quantities is not purely real, it will suffer a phase shift relative to the quantities that are transformed by CP, thus potentially violating CP symmetry.

Such phase differences must be robust against gauge modifications in order to manifest themselves as CP violation. If simple redefinitions of the phases of any of the fields can remove overall phases in each field coupling, the theory remains CP-conserving.

1.2.2 Mixing of Neutral Mesons

The four pairs of conjugate neutral mesons that decay weakly, K^0, D^0, B^0, and B^0_s, can each mix with their respective antiparticle. The ability to mix requires that the two particles only differ by quantum numbers that are not conserved under weak interaction (*i.e.* flavor) and implies that the flavor eigenstates may not be equivalent to the mass eigenstates. The observed presence of mixing (into conjugate flavor-specific decays) implies

---

[2] From another point of view, we can say that our theory was developed following the hypothesis that CPT is a good symmetry for nature. An eventual discovery of CPT violation will led to deeply reconsider the basic ingredients of the quantum field theory.

[3] Note that the spin-statistics relation itself is implied from Lorentz invariance, positive energies, positive norms, and causality.

that the mass and flavor eigenstates are in fact different. Lack of CP symmetry implies a third set of eigenstates, CP eigenstates, which can differ from the mass and flavor eigenstates, as will be seen below.

Consider a weakly-decaying neutral meson X^0 (which could be any of K^0, D^0, B^0 or B_s^0). An arbitrary linear combination of the flavor eigenstates

$$a|X^0\rangle + b|\bar{X}^0\rangle \tag{1.23}$$

mixes according to the time-dependent Schrödinger equation

$$i\frac{\partial}{\partial t}\begin{pmatrix} a \\ b \end{pmatrix} = \mathcal{H}\begin{pmatrix} a \\ b \end{pmatrix}, \tag{1.24}$$

where

$$\mathcal{H} = M - i\frac{\Gamma}{2} \equiv \begin{pmatrix} m_{11} & m_{12} \\ m_{21} & m_{22} \end{pmatrix} - \frac{i}{2}\begin{pmatrix} \gamma_{11} & \gamma_{12} \\ \gamma_{21} & \gamma_{22} \end{pmatrix} \tag{1.25}$$

The m and γ parts represent the mixing and decay parts, respectively, of the time dependence. Each of the off-diagonal elements can be complex: the angle in the complex plane of m_{12} represents the phase of the mixing, and γ_{12} represents the (complex) coupling to common decay modes of X^0 and $\bar{X}^0$ (for example, $B^0/\bar{B}^0 \to J/\psi K_S^0$ or $\pi^+\pi^-$). We can see that CPT invariance guarantees that $m_{11} = m_{22}$ and $\gamma_{11} = \gamma_{22}$, and that $m_{21} = m_{12}^*$ and $\gamma_{21} = \gamma_{12}^*$. Thus, setting m_{11} and m_{22} to m and γ_{11} and γ_{22} to γ, we have:

$$i\frac{\partial}{\partial t}\begin{pmatrix} \alpha \\ \beta \end{pmatrix} = \begin{pmatrix} m - \frac{1}{2}i\gamma & m_{12} - \frac{1}{2}i\gamma_{12} \\ m_{12}^* - \frac{1}{2}i\gamma_{12}^* & m - \frac{1}{2}i\gamma \end{pmatrix}\begin{pmatrix} \alpha \\ \beta \end{pmatrix} \tag{1.26}$$

The mass eigenstates are the eigenvectors of the Hamiltonian:

$$\begin{aligned} |X_L\rangle &= p|X^0\rangle + q|\bar{X}^0\rangle \\ |X_H\rangle &= p|X^0\rangle - q|\bar{X}^0\rangle \end{aligned} \tag{1.27}$$

where $|X_L\rangle$ and $|X_H\rangle$ are the lighter and heavier mass eigenstates, and the coefficients p and q satisfy the relations

$$|q|^2 + |p|^2 = 1. \tag{1.28}$$

$$q = \sqrt{\frac{m_{12}^* - \frac{1}{2}i\gamma_{12}^*}{m_{12} - \frac{1}{2}i\gamma_{12}}}\,p \tag{1.29}$$

The eigenvalues λ_L e λ_H of (1.25) are:

$$\lambda_L = m_L - i\frac{\Gamma_L}{2}, \quad \lambda_H = m_H - i\frac{\Gamma_H}{2}, \tag{1.30}$$

where m_L and m_H are the masses of the eigenstates $|X_L\rangle$ and $|X_H\rangle$, respectively, and Γ_L and Γ_H their decay parts. Requiring the CPT invariance ($\mathcal{H}_{11} = \mathcal{H}_{22}$ and $\mathcal{H}_{21} = \mathcal{H}^*_{12}$) and defining the mass difference $\Delta m = m_H - m_L$ and amplitude difference $\Delta\Gamma = \Gamma_H - \Gamma_L$, we obtain:

$$(\Delta m)^2 - \frac{1}{4}(\Delta\Gamma)^2 = 4(|m_{12}|^2 - \frac{1}{4}|\gamma_{12}|^2), \quad \Delta m\Delta\Gamma = 4\mathrm{Re}(m_{12}\gamma^*_{12}), \tag{1.31}$$

$$\frac{q}{p} = \sqrt{\frac{m^*_{12} - \frac{1}{2}i\gamma^*_{12}}{m_{12} - \frac{1}{2}i\gamma_{12}}} = -\frac{\Delta m - \frac{i}{2}\Delta\Gamma}{2(m_{12} - \frac{i}{2}\gamma_{12})}. \tag{1.32}$$

1.2.3 The Neutral K System

Mixing between the two neutral K weak eigenstates K^0 and $\bar{K}^0$ was first predicted in 1955 by Gell-Mann and Pais [32]. The two physical states, $|K_1\rangle = \frac{1}{\sqrt{2}}(K^0 + \bar{K}^0)$ and $|K_2\rangle = \frac{1}{\sqrt{2}}(K^0 - \bar{K}^0)$, would thus be *CP* eigenstates with eigenvalues $+1$ and -1. The dominant decay of neutral K mesons is $\pi^+\pi^-$, due to helicity constraints and the fact the 3-body phase space is strongly suppressed at these mass scales (due to the well-known $(\Delta m)^5$ scaling rule). However, $\pi^+\pi^-$ is itself a *CP* eigenstate with eigenvalue $+1$. Thus, if *CP* were exactly conserved, *only the $|K_1\rangle$ physical state could decay into it.*

The limited phase space to decays other than $\pi^+\pi^-$ forces the lifetime of the eigenstate with opposite *CP*, K_2, to be far larger (3 orders of magnitude) than the lifetime of the K_1. Thus the nomenclature K^0_S and K^0_L (for short and long lifetimes) is used. The lifetime difference is very convenient since it allows for simple experimental separation of the two physical states. Another interpretation of this great difference in lifetimes can be understood considering that K^0 and $\overline{K^0}$ have many common decay channels, so $\Gamma_{12} \approx \Gamma_0$. This fact implies that $\Gamma_S \approx \Gamma_0 + \Gamma_{12}$ and $\Gamma_L \approx \Gamma_0 - \Gamma_{12}$ which leads to $\tau_S << \tau_L$, as said before.

In 1964, Fitch and Cronin made the discovery that K^0_L can decay into $\pi^+\pi^-$ with a branching fraction of 2×10^{-3} [5]. Since *CP* is thus not strictly conserved, the general formalism detailed in the previous subsection must be used. Thus we have

$$\begin{aligned} |K_S\rangle &= p|K^0\rangle + q|\bar{K}^0\rangle \\ |K_L\rangle &= p|K^0\rangle - q|\bar{K}^0\rangle \end{aligned} \tag{1.33}$$

where p and q are commonly parametrized as:

$$p = \frac{1+\epsilon}{\sqrt{2(1+|\epsilon|^2)}}; \qquad q = \frac{1-\epsilon}{\sqrt{2(1+|\epsilon|^2)}} \tag{1.34}$$

The real part of ϵ is a measure of CP violation purely in mixing whereas the imaginary part is a measure of CP violation in the interference between mixing and decay (see the following section). The former is the simplest one to be measured experimentally and was the effect seen in the original 1964 discovery. Since, in the K system, $\Delta\Gamma$ is of the same order as Δm, these effects are of similar magnitude, quite unlike the neutral B system, where the latter is far more prevalent.

1.2.4 The Neutral B System

The B^0 meson can mix with its respective antiparticle via a pair of box diagrams shown in fig. 1.1. In 1987 this mixing was observed, with contributions from experiments at both proton-antiproton and electron-positron colliders. Some indication for $B^0 - \overline{B}^0$ mixing, contributed by both $B_d = (\bar{b}d)$ and $B_s = (\bar{b}s)$, was found by UA-1 at the $Sp\bar{p}S$ collider [33]; clear convincing evidence was first obtained by the ARGUS Collaboration at DORIS [34], at the $\Upsilon(4S)$ resonance energy, where only B_d is produced.

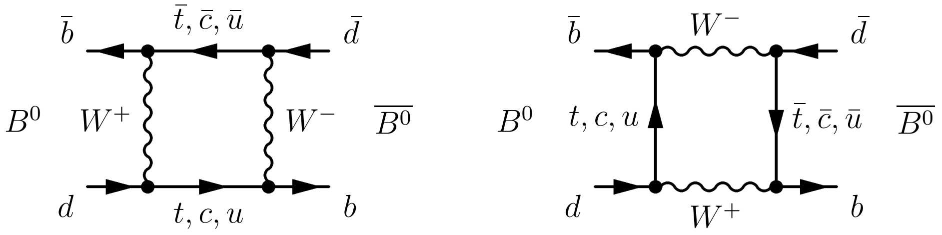

Figure 1.1: Feynman diagrams mixing $B^0 - \overline{B}^0$.

For neutral B mesons, in contrast with the neutral K system, the lifetime difference $\Delta\Gamma$ between the two mass eigenstates is *small* compared with the mixing frequency due to the difference in masses Δm. This difference in behavior of the K and B is due to the larger mass of the B meson and thus far greater phase space for flavor-specific decays in the B system, which dominates the partial width (in contrast to the K system). The resulting lack of decay suppression of either eigenstate implies nearly equivalent lifetimes.

Due to this simplification in formalism, the time evolution of neutral B mesons which are initially created (at time $t = 0$) as pure flavor eigenstates can be written as:

$$|{B^0}_{phys}(t)\rangle = f_+(t)|B^0\rangle + (q/p)f_-(t)|\overline{B}^0\rangle \tag{1.35}$$

$$|{\overline{B}^0}_{phys}(t)\rangle = f_+(t)|B^0\rangle + (q/p)f_-(t)|\overline{B}^0\rangle \tag{1.36}$$

where

$$f_+(t) = e^{-imt}e^{-\Gamma t/2}\cos(\Delta mt/2) \tag{1.37}$$

$$f_-(t) = e^{-imt}e^{-\Gamma t/2}i\sin(\Delta mt/2), \tag{1.38}$$

with $m = (m_H+m_L)/2$, $\Gamma = (\Gamma_H+\Gamma_L)/2$. This approximation holds up to the condition that

$$\Delta\Gamma \ll \Delta m \tag{1.39}$$

Since $\Delta\Gamma = \mathcal{O}(10^{-3})\Delta m$ in the B system, corrections to it are not considered in CP asymmetry measurements with the current statistics.

1.3 Three Types of CP Violation

Three types of CP violation can potentially be observed at B physics experiments:[4]

1) CP violation in decay (often referred to as direct CP violation): this occurs when multiple amplitudes with different weak phases as well as different strong phases contribute to a given final state, the result is visible as differing magnitude of the amplitude to a decay versus its CP conjugate.

2) CP violation purely in mixing: this occurs when the mass eigenstates of a neutral meson are different from the CP eigenstates.

3) CP violation in the interference between decays of mixed and unmixed mesons: this occurs for decays which are common to a neutral meson and its antiparticle.

1.3.1 CP Violation in Decay (Direct CP Violation)

Direct CP violation manifests itself as a difference in the magnitude of the amplitude to a given decay as compared with its CP conjugate, thus resulting in differing rates to the two elements of the CP conjugate pair (see fig. 1.2). It can occur for both neutral and charged decays.[5] Amplitudes from B^0 and $\overline{B}^0$ to a final state and its CP conjugate may be written as

$$A_f = \sum_i A_i e^{i(\phi_i+\delta_i)} \qquad \text{and} \qquad \bar{A}_{\bar{f}} = \eta_f \sum_i A_i e^{i(-\phi_i+\delta_i)} \tag{1.40}$$

---

[4] There can be other manifestations of CP violation, *e.g.* CP violation in interaction, however observable CP violation at B-factories can all be classified into the 3 categories.

[5] For charged decays, it is the *only* potential manifestation of CP violation.

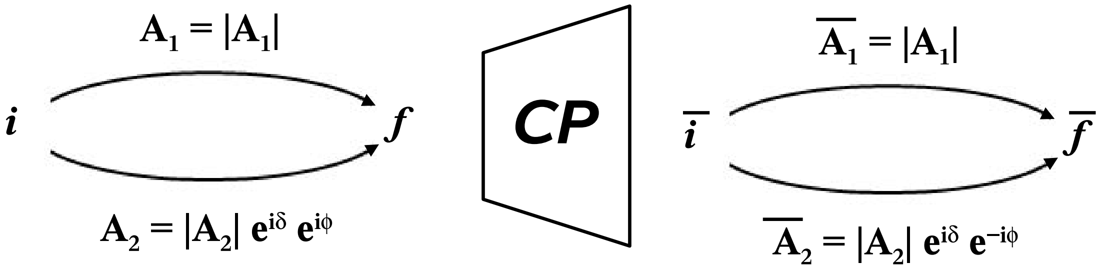

Figure 1.2: Effect of the "CP mirror" on interfering decay amplitudes for the transition between an initial state i and a final state f. The direct CP asymmetry is due to the interference between two amplitudes A_1 and A_2 with a relative CP-conservating phase δ and a CP-violating phase ϕ.

where η_f is the CP eigenvalue (multiplied by a convention-dependent phase) if f is a CP eigenstate, ϕ are the weak phases, and δ are the strong phases. CP violation can only occur when the different weak phase contributions also have different strong phases (otherwise a simple rotation can remove the strong phase and thus the ratio would clearly have unit magnitude). It can also only occur when weak phases are nontrivial, *i.e.* when exists a relative phase between them (that is therefore irreducible by a rotation of the Lagrangian). Only when both different weak phases *and* different strong phases are present can one have the condition:

$$|\bar{A}_{\bar{f}}/A_f| \neq 1 \tag{1.41}$$

This is CP violation in decay. CP violation in decay has been observed in the kaon system and recently in the B system too. Since the strong phases that enter into measurements of CP violation in decay involve hadronic uncertainties, the relation of such measurements to CKM factors (see next section) cannot be calculated from first principles, but the strong phases may themselves be measured if the CKM factors are known from other measurements. These strong phase measurements can then be used as inputs to other measurements which have equivalent strong phases (thus allowing the extraction of other parameters), and thus measurements of CP violation in decay can (indirectly) provide a useful handle on fundamental quantities.

1.3.2 CP Violation Purely in Mixing

From sec. 1.2.2, we recall that the mass eigenstates of the neutral meson system are the eigenvectors of the Hamiltonian

$$|X_L\rangle = p|X^0\rangle + q|\bar{X}^0\rangle$$
$$|X_H\rangle = p|X^0\rangle - q|\bar{X}^0\rangle \tag{1.42}$$

where

$$q = \sqrt{\frac{m_{12}^* - \frac{1}{2}i\gamma_{12}^*}{m_{12} - \frac{1}{2}i\gamma_{12}}}p \tag{1.43}$$

If q and p have different magnitudes, the CP conjugates of the mass eigenstates clearly will differ from the mass eigenstates themselves by more than a trivial phase. Thus the mass eigenstates will not be CP eigenstates and CP violation will be manifest. CP violation from

$$|q/p| \neq 1 \tag{1.44}$$

is purely an effect of mixing and is independent of decay mode. Thus it may be referred to as CP violation purely in mixing.

In neutral B decays, as discussed in sec. 1.2.4, this effect is expected to be very small. Since

$$\Delta m = \mathcal{O}(10^3)\Delta\Gamma \tag{1.45}$$

this implies that

$$|m_{12}| \gg |\gamma_{12}| \tag{1.46}$$

and thus the factor in eq. 1.32 simplifies to a near-phase. CP violation purely in mixing should thus only enter the neutral B system at the 10^{-3} level. An asymmetry in the measurements of the overall rate to flavor tagged B^0 vs. $\overline{B}^0$would be a signature of CP violation purely in mixing. With greater statistics, evidence for this may be seen; at present, experimental limits exist. It has been clearly observed, however, in the neutral kaon system (where it is the prevalent effect); the discovery of CP violation in 1964 was a detection of CP violation purely in mixing.

1.3.3 CP Violation in Interference Between Decays of Mixed and Unmixed Mesons

Final states which may be reached from either B^0 or $\overline{B}^0$ decays can exhibit a third type of CP violation, which results from the interference between the decays of mixed and of unmixed neutral B mesons which both decay to the final state (see fig. 1.3).

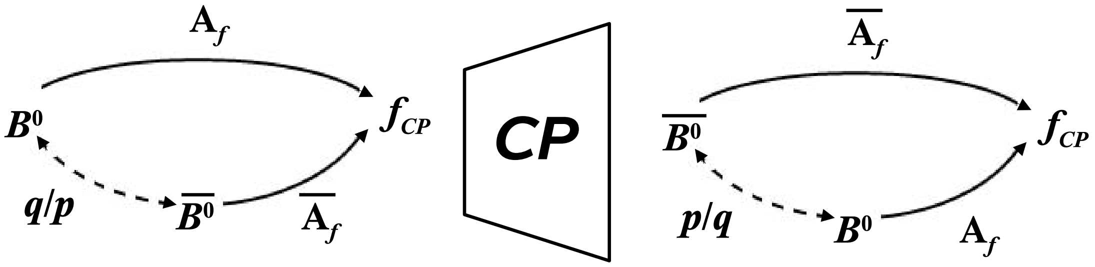

Figure 1.3: Effect of the "CP mirror" on B^0 decay to a CP eigenstate f_{CP}. The CP asymmetry is due to the interference between mixing, described by parameters p and q, and the decay amplitudes A_f and $\bar{A}_f$.

Let's consider the CP-violating asymmetry in rates between B^0 and $\overline{B}^0$ as a function of time:

$$a_{CP}(t) = \frac{\Gamma(B^0_{phys}(t) \to f) - \Gamma(\bar{B}^0_{phys}(t) \to f)}{\Gamma(B^0_{phys}(t) \to f) + \Gamma(\bar{B}^0_{phys}(t) \to f)} \tag{1.47}$$

To calculate each of the time-dependent rates $\Gamma(t)$, one can form the inner product of eq. 1.35–1.36 with the final state f and then take the magnitude squared of the resulting amplitudes:

$$\begin{aligned}
&\Gamma(B^0(t)\to f) \propto \\
&|\langle f|\mathcal{H}|B^0(t)\rangle|^2 = \ e^{-\Gamma t} \ \Bigg\{\cos^2\left(\frac{\Delta m t}{2}\right)|\langle f|\mathcal{H}|B^0\rangle|^2 \\
&\qquad + \sin^2\left(\frac{\Delta m t}{2}\right)\left|\frac{q}{p}\right|^2 |\langle f|\mathcal{H}|\overline{B}^0\rangle|^2 \\
&\qquad - \frac{i}{2}\left|\frac{q}{p}\right| e^{-2i\phi_M}\sin(\Delta m t)\langle f|\mathcal{H}|B^0\rangle\langle f|\mathcal{H}|\overline{B}^0\rangle^* \\
&\qquad + \frac{i}{2}\left|\frac{q}{p}\right| e^{2i\phi_M}\sin(\Delta m t)\langle f|\mathcal{H}|B^0\rangle^*\langle f|\mathcal{H}|\overline{B}^0\rangle\Bigg\}
\end{aligned} \tag{1.48a}$$

$$\begin{aligned}\Gamma(\overline{B}^0(t)\to f) \propto & \\ |\langle f|\mathcal{H}|\overline{B}^0(t)\rangle|^2 = \; & e^{-\Gamma t} \left\{\cos^2\left(\frac{\Delta m t}{2}\right)|\langle f|\mathcal{H}|\overline{B}^0\rangle|^2\right. \\ & + \sin^2\left(\frac{\Delta m t}{2}\right)\left|\frac{p}{q}\right|^2 |\langle f|\mathcal{H}|B^0\rangle|^2 \\ & + \frac{i}{2}\left|\frac{p}{q}\right| e^{-2i\phi_M}\sin(\Delta m t)\langle f|\mathcal{H}|B^0\rangle\langle f|\mathcal{H}|\overline{B}^0\rangle^* \\ & \left. - \frac{i}{2}\left|\frac{p}{q}\right| e^{2i\phi_M}\sin(\Delta m t)\langle f|\mathcal{H}|B^0\rangle^*\langle f|\mathcal{H}|\overline{B}^0\rangle\right\}\end{aligned} \tag{1.48b}$$

where $2\phi_M$ is the phase of q/p. Since, as shown above, for the B system $|q/p| \approx 1$, we can thus write

$$\langle f|\mathcal{H}|\overline{B}^0(t)\rangle = \eta e^{-2i\phi_D}|\lambda|\langle f|\mathcal{H}|B^0(t)\rangle \tag{1.49}$$

where ϕ_D is the phase of the decay, η is the *CP* eigenvalue of f, and

$$\lambda = \frac{q}{p}\frac{\langle f|\mathcal{H}|\overline{B}^0\rangle}{\langle f|\mathcal{H}|B^0\rangle} = |\lambda|e^{-2i(\phi_M+\phi_D)}, \tag{1.50}$$

the expressions simplify greatly:

$$|\langle f|\mathcal{H}|B^0(t)\rangle|^2 = A^2 e^{-\Gamma t}\{1 - \mathrm{C}\cos(\Delta m t) - \mathrm{S}\sin(\Delta m t)\} \quad \text{and} \tag{1.51}$$

$$|\langle f|\mathcal{H}|\overline{B}^0(t)\rangle|^2 = A^2 e^{-\Gamma t}\{1 + \mathrm{C}\cos(\Delta m t) + \mathrm{S}\sin(\Delta m t)\} \tag{1.52}$$

where $A^2 = |\langle f|\mathcal{H}|B^0\rangle|^2$ and

$$\mathrm{C} = \frac{1-|\lambda|^2}{1+|\lambda|^2} \qquad \text{and} \qquad \mathrm{S} = \eta\frac{-2\sin(2(\phi_M+\phi_D))}{1+|\lambda|^2} \tag{1.53}$$

Thus the time-dependent asymmetry

$$a_{CP}(t) = \frac{\Gamma(B^0_{phys}(t)\to f) - \Gamma(\bar{B}^0_{phys}(t)\to f)}{\Gamma(B^0_{phys}(t)\to f) + \Gamma(\bar{B}^0_{phys}(t)\to f)} = \mathrm{C}\cos(\Delta m t) + \mathrm{S}\sin(\Delta m t) \tag{1.54}$$

In the absence of *CP* violation, S and C must both go to zero, since they occur only when weak phases do not cancel. C is nonzero only when the ratio of the amplitude norms differs from unity, which is the signature of direct *CP* violation (see sec. 1.3.1). S, however, represents a distinct type of *CP* violation that can occur even in the absence of *CP* violation purely in decay or in mixing. It results from the interference of the decays of mixed mesons with those of unmixed mesons; if the mixing contains a phase that is not canceled by the decay itself, this observable time-dependent asymmetry above will result. Unlike CP violation in decay, no nontrivial strong phases are required.

As will be shown in the next section, CP violation in interference between decays of mixed and unmixed mesons is a large effect in the Standard Model picture of the neutral B system. Since this is a measurement of an asymmetry rather than an absolute rate, many experimental and model-dependent uncertainties (such as reconstruction efficiency) that would otherwise contribute to experimental error, instead cancel out in the ratio. Thus it provides an excellent mechanism for precision measurements of CP violation and the study of the Standard Model picture of CPV.

1.4 CP Violation in the Standard Model

CP violation find a clear collocation within the context of the Standard Model $\mathrm{SU}(2) \times \mathrm{U}(1)$ electroweak symmetry. The relation between CP violation and such a model was introduced by Kobayashi and Maskawa in 1973 via the postulation of a third family of quarks; at that time there was evidence of only 3 quarks and charm was discovered one year later. The b-quark was then first observed in 1977. The prediction of additional quarks did not occur entirely without precedent, however. Theoretical interpretation of quark mixing via the weak interaction has closely followed experimental result, and the development of the 3 x 3 CKM matrix and its CP violating phase was a steady and piecewise process.

1.4.1 The CKM Matrix

The observed suppression of flavor-changing neutral current decays is interpreted as the quark sector being separated into families, such as the leptonic sector. However, lepton flavor is conserved[6], whereas quark generation is manifestly violated (*e. g.* in weak decays of strange particles). However, strangeness-changing decays have an additional suppression compared with strangeness-conserving weak decays. This suppression, named “Cabibbo suppression”, is accounted considering that quark mass eigenstates differ from the (weak) interaction eigenstates. Thus a mixing matrix describing transitions between quark generations is needed.

Such a matrix must be unitary since quark number, and so baryonic number, is manifestly conserved. With 2 generations, a unitary matrix can be described by a single

---

[6] Conservation of lepton flavor is due to the absence of neutrino masses in the SM. Recent observations [35] seems to indicate that neutrino can oscillate thus allowing lepton flavor violation.

parameter θ_C:

$$\begin{pmatrix} d_{mass} \\ s_{mass} \end{pmatrix} = \begin{pmatrix} \cos\theta_C & \sin\theta_C \\ -\sin\theta_C & \cos\theta_C \end{pmatrix} \begin{pmatrix} d \\ s \end{pmatrix} \tag{1.55}$$

where d_{mass} and s_{mass} are the mass eigenstates and d and s the (weak) flavor eigenstates. The Cabibbo quark-mixing angle θ_C, was introduced in 1963 [6] to explain the small weak-interaction decay rates for particles carrying strangeness. When CP violation was discovered in 1964 by the observation of the CP-odd decay $K^0_L{\to}\pi^+\pi^-$ [5], the intimate relation between the dynamical rules of quark-flavor mixing and the phenomenon of CP violation was not perceived. In 1970, Glashow, Iliopoulos and Maiani (GIM) [36] used the unitary quark-mixing ansatz to postulate the existence of a fourth quark with quantum number charm to explain the observed suppression of strangeness-changing neutral currents (*e. g.*, $K^0_L{\to}\mu^+\mu^-$). This mechanism leads to the absence of tree-level Flavor-Changing Neutral Currents (FCNC) in the SM. The same matrix 1.55 (experimentally) holds for the (u, c) quark pair. The Cabbibo angle θ_C is thus a full description of 2-generation mixing.

At present, our understanding of CP violation is deeply connected to quark-flavor mixing, thanks to ideas pointed out in 1973 by Kobayashi and Maskawa. Assuming the existence of at least three generations of quarks, there are enough physical degrees of freedom left in the quark-flavor mixing matrix to allow for a nonzero phase [7]. The subsequent discovery of bottom and top quarks, and even a third lepton generation, as well as the observation of direct CP violation in the kaon system seem to confirm the KM scenario.

Considering the SM of electroweak interaction with massive fermions allowed by spontaneous symmetry breaking via the Higgs mechanism, for three quarks families the part of the Lagrangian which describe the mass interaction[7] is

$$\mathcal{L}_Y = -Y^d_{ij}\,\overline{Q^I_{Li}}\,\phi\,d^I_{Rj} - Y^u_{ij}\,\overline{Q^I_{Li}}\,\varepsilon\,\phi^* u^I_{Rj} + \text{h.c.}, \tag{1.56}$$

where $Y^{u,d}$ are 3×3 complex matrices which are in principle non-diagonal, ϕ is the Higgs field, i and j are generation labels, and ε is the 2×2 antisymmetric tensor. The Q^I_L are left-handed quark doublets, and d^I_R and u^I_R are right-handed down- and up-type quark singlets, respectively, in the weak-eigenstate basis. In unitary gauge, ϕ acquires a vacuum expectation value, $\langle\phi\rangle = (0, v/\sqrt{2})$, eq. (1.56) so that Dirac mass terms for quarks with 3×3 mass matrices

$$M^{u,d} = \frac{vY^{u,d}}{\sqrt{2}} \tag{1.57}$$

---

[7] Commonly named Yukawa lagrangian, from the name of the physicist who first proposed such kind of interaction to explain strong interaction.

To move from the basis of the flavor eigenstates to the basis of the mass eigenstates, one performs the transformation

$$U_L^{u(d)} M^{u(d)} U_R^{u(d)\dagger} = \mathrm{diag}\Big(m_{u(d)}, m_{c(s)}, m_{t(b)}\Big)\,, \tag{1.58}$$

where $U_L^{u,d}$ and $U_R^{u,d}$ are unitary matrices and the masses m_q are real. The quark mass matrices are diagonalized by different transformations for the left-handed up- and down-quarks, which are part of the same $\mathrm{SU}(2)_L$ doublet,

$$Q_L^I = u_{Li}^I \quad d_{Li}^I = (U_L^{u\dagger})_{ij} u_{Lj} \quad (U_L^u U_L^{d\dagger})_{jk}\, d_{Lk}. \tag{1.59}$$

By convention, we pulled out $(U_L^{u\dagger})_{ij}$, so that the “misalignment” between the two transformations operates on the down-type quark mass eigenstates. Thus the charged-current weak interaction is modified by the product of the diagonalizing matrices of the up- and down-type quark mass matrices, the so-called Cabibbo-Kobayashi-Maskawa matrix,

$$V = U_L^u U_L^{d\dagger} = \begin{pmatrix} V_{ud} & V_{us} & V_{ub} \\ V_{cd} & V_{cs} & V_{cb} \\ V_{td} & V_{ts} & V_{tb} \end{pmatrix}. \tag{1.60}$$

However, the neutral-current part of the Lagrangian in the mass eigenstate basis remains unchanged, *i. e.* there are no flavor-changing neutral currents at tree level.

Being the product of unitary matrices, V itself is unitary, $VV^\dagger = \mathrm{I}$. This requirement and the freedom to arbitrarily choose the global phases of the quark fields reduce the initial nine unknown complex elements of V to three real numbers and one phase, where the latter accounts for CP violation. Because these four numbers effectively govern the rates of all tree- and loop-level electroweak transitions (see sec. 1.4.3 for a description of these transitions) that involve the charged current, it is a compelling exercise to overconstrain V. If inconsistencies among different measurements occur, it would reveal the existence of physics beyond the SM.

1.4.2 Unitarity Conditions and the Unitarity Triangle

Unitarity of the CKM matrix V requires that

$$V^\dagger V = VV^\dagger = \mathrm{I} \quad \Rightarrow \quad \sum_{\mathrm{j}} V_{ji}^*\, V_{jk} = \sum_j V_{ij}\, V_{kj}^* = \delta_{ik} \tag{1.61}$$

This results in 9 independent equations, 3 of which (for the diagonal of the product unit matrix) equal one and 6 of which equal zero. The equations for the off-diagonal elements, each containing a sum of 3 complex numbers which equals 0, will each describe a triangle in the complex plane:

$$V_{cd}V_{ud}^* + V_{cs}V_{us}^* + V_{cb}V_{ub}^* = 0 \tag{1.62a}$$

$$V_{cd}V_{td}^* + V_{cs}V_{ts}^* + V_{cb}V_{tb}^* = 0 \tag{1.62b}$$

$$V_{ud}V_{td}^* + V_{us}V_{ts}^* + V_{ub}V_{tb}^* = 0 \tag{1.62c}$$

$$V_{us}^*V_{ud} + V_{cs}^*V_{cd} + V_{ts}^*V_{td} = 0 \tag{1.62d}$$

$$V_{ub}^*V_{us} + V_{cb}^*V_{cs} + V_{tb}^*V_{ts} = 0 \tag{1.62e}$$

$$V_{ub}^*V_{ud} + V_{cb}^*V_{cd} + V_{tb}^*V_{td} = 0 \tag{1.62f}$$

The differences between these 6 triangles are purely empirical. There is no theoretical motivation at present for the fact that 4 of them are nearly degenerate and only 2 describe triangles that have each of their sides being the same order of magnitude in length. It is empirically the case that only eq. 1.62c and 1.62f above describe triangles which are not nearly degenerate. The triangle corresponding to the last equation, 1.62f, is the one that is used to pictorially represent the irreducible CP violating phase and is referred to as the Unitarity Triangle (UT).

The number of free parameters of V can be greatly reduced by very general considerations. Unitarity and the freedom to arbitrarily choose the global phase of a quark field, reduce the original $2n_g^2$ unknowns (where $n_g = 3$ is the number of generations) to $(n_g-1)^2$ unknowns. Among these $n_g(n_g-1)/2$ are rotation angles and $(n_g-1)(n_g-2)/2$ phases describe CP violation. Three generations allow for only a single CP-violating phase, in total four independent parameters.

Many parametrization exist for the CKM matrix. Chau and Keung [37] proposed the "standard parametrization" of V. It is obtained by the product of three (complex) rotation matrices, where the rotations are characterized by the Euler angles θ_{12}, θ_{13} and θ_{23}, which are the mixing angles between the generations, and one overall phase δ,

$$V = \begin{pmatrix} c_{12}c_{13} & s_{12}c_{13} & s_{13}e^{-i\delta} \\ -s_{12}c_{23} - c_{12}s_{23}s_{13}e^{i\delta} & c_{12}c_{23} - s_{12}s_{23}s_{13}e^{i\delta} & s_{23}c_{13} \\ s_{12}s_{23} - c_{12}c_{23}s_{13}e^{i\delta} & -c_{12}s_{23} - s_{12}c_{23}s_{13}e^{i\delta} & c_{23}c_{13} \end{pmatrix}, \tag{1.63}$$

where $c_{ij} = \cos\theta_{ij}$ and $s_{ij} = \sin\theta_{ij}$ for $i < j = 1, 2, 3$. This parametrization satisfies exactly the unitarity relation[8].

Following the observation of a hierarchy between the mixing angles, $s_{13} \ll s_{23} \ll$

---

[8] In quark sector the commonly used parametrization is the Wolfestein one described below. The "standard parametrization" is, indeed, the most used to parametrize the Pontecorvo-Maki-Nagasawa-Sakata matrix which describe flavor mixing in lepton sector.

$s_{12} \ll 1$, Wolfenstein [38] proposed an expansion of the CKM matrix in terms of the four parameters λ, A, ρ and η ($\lambda \simeq |V_{us}| \approx 0.23$ being the expansion parameter, that is the Cabibbo parameter $\lambda \equiv \sin\theta_C$), which is widely used in the contemporary literature. We use the definitions to *all orders* [39]

$$\begin{aligned} s_{12} &\equiv \lambda\,, \\ s_{23} &\equiv A\lambda^2\,, \\ s_{13}e^{-i\delta} &\equiv A\lambda^3(\rho - i\eta)\,. \end{aligned} \tag{1.64}$$

Inserting the above definitions into eq. (1.63), we have the expressions for all CKM elements. We can truncate at third order in λ:

$$V = \begin{pmatrix} 1-\frac{\lambda^2}{2} & \lambda & A\lambda^3(\rho - i\eta) \\ -\lambda & 1-\frac{\lambda^2}{2} & A\lambda^2 \\ A\lambda^3(1-\rho-i\eta) & -A\lambda^2 & 1 \end{pmatrix} + \mathcal{O}(\lambda^4) \tag{1.65}$$

with (λ, A, ρ, η) as the 4 real parameters describing the CKM matrix, the latter 3 being of order 1. It's useful to point out that this parametrization is *not* unitary, but it has the great advantage to underline the different orders of magnitude of the CKM elements.

Unitary triangle obtained by eq. 1.62f can be rotated and scaled choosing a conventional phase in a way that $V_{cb}^* V_{cd}$ is real, and so aligning related side to real axis, and dividing length of all sides for $|V_{cd}V_{cb}^*|$ so length is normalized to 1. The triangle (show in fig. 1.4) have two fixed vertexes at (0,0) and at (1,0) and coordinates of the remaining vertices will depends by (ρ,η) corresponding to Wolfenstein's parameters. Lengths of sides become:

$$R_u \equiv \left|\frac{V_{ub}^* V_{ud}}{V_{cb}^* V_{cd}}\right| = \sqrt{\rho^2 + \eta^2}, \qquad R_t \equiv \left|\frac{V_{tb}^* V_{td}}{V_{cb}^* V_{cd}}\right| = \sqrt{(1-\rho)^2 + \eta^2}. \tag{1.66}$$

The three angles of out unitary triangle, denoted with α, β and γ, are:

$$\alpha \equiv \arg\left[-\frac{V_{td}V_{tb}^*}{V_{ud}V_{ub}^*}\right], \quad \beta \equiv \arg\left[-\frac{V_{cd}V_{cb}^*}{V_{td}V_{tb}^*}\right], \quad \gamma \equiv \arg\left[-\frac{V_{ud}V_{ub}^*}{V_{cd}V_{cb}^*}\right]. \tag{1.67}$$

These quantities are physical observables and can be measured from CP asymmetries in B meson decays. Consistency among different experimental values gives a solid probe of the SM.

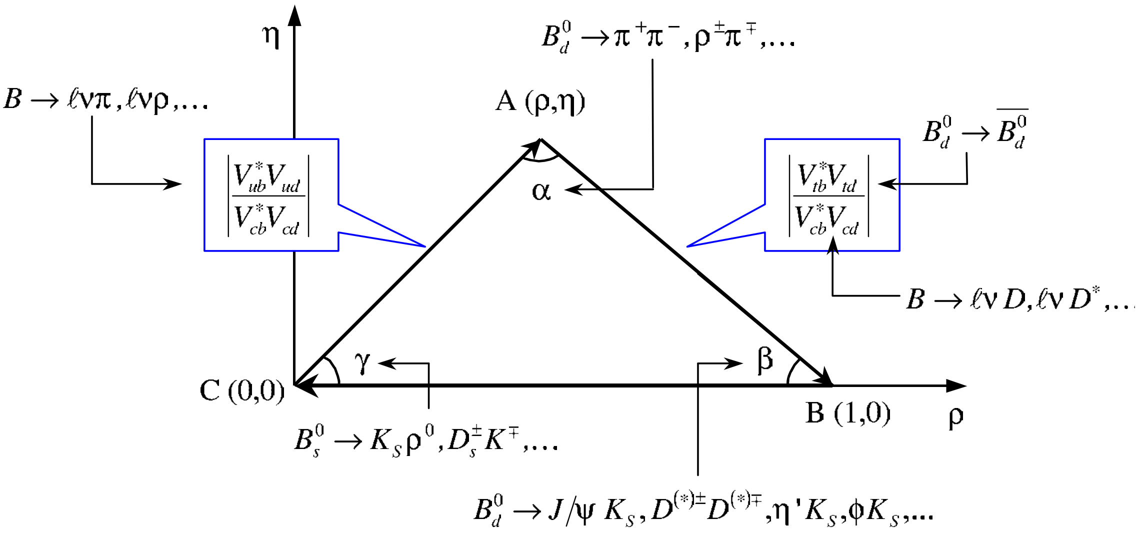

Figure 1.4: Unitary triangle and main decays used to measure the sides and the angles.

1.4.3 Tree and Penguin Processes

Both weak and strong phases difference are an important element in CP asymmetries, so we need to distinguish which diagrams give a contribution to total amplitude with different phases. Decay amplitudes of mesons composed by an heavy quark and a light quark are usually divided in two classes: the so called *tree* and *loop* (also known as *penguin*). Neglecting long distance strong interactions, final state interactions or hadron-hadron interactions, which can in principle occur and that complicates the theoretical treatment of such decays, this split is easily explained through different weak diagrams.

In the penguin diagrams a W boson is emitted and reabsorbed in the same line of emitter quark (fig. 1.5), while all other diagrams are tree, *i. e.* they have no loop in the diagram (fig. 1.6).

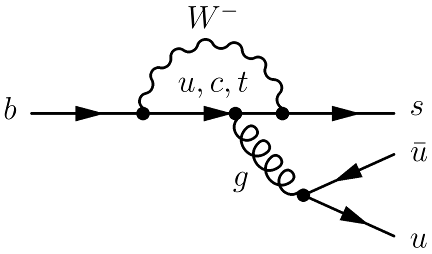

Figure 1.5: Penguin diagram for $b \to sg^*$ process.

Tree diagrams are further split in *spectator* (light quark of the starting meson is disconnected in the weak diagram), *exchange* (W boson is swapped between starting meson quarks) and *annihilation* (starting meson quarks are annihilated to make W). However, this separation between different kinds of tree diagram is not crucial concerning CP vio-

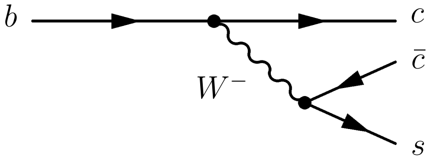

Figure 1.6: Tree diagram for $b{\to}cW^-$ process.

lation because two kinds of tree diagrams, that contribute to a specific decay amplitude, have the same CKM matrix element and so the same weak phase. Differently from tree diagram, in $b \to q$ process with $q = \{d, s\}$, penguin terms contribute with different combinations of CKM elements $V^*_{ib}V_{iq}$ depending by the quark within loop $i = \{u, c, t\}$. So the differences of weak phase, which contribute to the CP-asymmetries, arise from different penguin and tree contributions; therefore it becomes important to know intensities and weak phases related to both kinds of diagram.

Penguin diagrams exhibit the presence of strong interactions, too. The quark in the loop emits a gluon to compensate for mass difference between initial and final quark. Gluon can produce a quark-antiquark pair or be reabsorbed and re-issued from other gluons that can be found in this kind of process. Differences of strong phase of these processes are the base for the direct CP asymmetry.

Due to the fact that FCNC transitions are forbidden at tree level in SM, $b{\to}s$ and $b{\to}d$ transitions can only occur via loop diagrams. If in the loop, the SM particles are replaced with yet-undiscovered particles, rates and kinematic distributions of FCNC decays can significantly deviate from the SM predictions. Therefore the FCNC decays are a sensitive probe of the New Physics.

1.4.4 Extraction of CKM Matrix Elements

With the remarkable exception of the UT angles, the experimental observables presently used to constrain (ρ, η) vertex depend on hadronic matrix elements. QCD is well established as the theory of strong interaction, and it has been tested to high precision in the perturbative regime where the coupling constant α_S is small. However, presently it is difficult to obtain quantitative predictions in the low-energy regime, except for a few special cases. In this section we recall briefly a few general techniques to evaluate the matrix elements relevant to quark-flavor physics. These methods give controllable systematic errors, that is the uncertainties can be incrementally improved in a well-defined way, expanding in small parameters order by order. Most of the model-independent theoretical tools utilize that some quark masses are smaller while others are greater than Λ_{QCD} (here Λ_{QCD} denotes a typical hadronic scale, of order 500 MeV).

Effective Hamiltonians for Weak Decays

All flavor-changing interactions (except that of the top quark) are due to tree and loop diagrams involving heavy virtual particles: W bosons in the SM, or not-yet-discovered particles in its extensions. These particles propagate over much shorter distances than $1/m_b$, so their interactions can be described by local operators. In principle, there is an infinite number of such operators. The contributions of the higher dimensional ones are however suppressed by increasing powers of m_b/m_W, so it is sufficient to consider the first contributions. The effective weak Hamiltonian can be written as $H_W = \sum C_i(\mu)\, O_i(\mu)$, where O_i are the lowest dimensional operators contributing to a certain process and C_i are their Wilson coefficients, with perturbatively calculable scale dependencies. The simplest examples where this methods is applied are the semileptonic decays (like $b{\to}c\ell\bar{\nu}$) while semileptonic decays involving a $\bar{\ell}\ell$ pair and nonleptonic decays presents more theoretical difficulties. For more details please refer to [40].

Chiral Symmetry

The u, d and s-quark masses are small compared with $\Lambda_{\rm QCD}$, so it is useful to consider the $m_q{\to}0$ limit ($q = u, d, s$) and treat corrections perturbatively. This is known as the chiral limit, because the Lagrangian for the light quarks has a $\rm SU(3)_L \times SU(3)_R$ chiral symmetry, under which the left- and right-handed quarks transform differently. This symmetry is spontaneously broken to $\rm SU(3)_V$ by the vacuum expectation value of the quark families. Chiral symmetry relates different hadronic matrix elements to one another, and has various applications in flavor physics.

Because the u and d-quark masses are small, the $\rm SU(2)$ isospin symmetry between the u and d is usually a very good approximation. The corrections to the chiral limit are suppressed by $(m_d - m_u)/\Lambda_{\chi\rm SB}$, where $\Lambda_{\chi\rm SB} \approx 1\rm GeV$ is the chiral symmetry breaking scale, and are usually not larger than a few percent at the amplitude level. There are also explicit violations of chiral symmetry, for example, due to weak or electromagnetic interactions. The full $\rm SU(3)$ symmetry is broken by $m_s/\Lambda_{\chi\rm SB}$, and is known to have typically $20 - 30\%$ corrections.

Some of the most prominent cases of isospin symmetry in the context of the CKM matrix include relations between amplitudes involving charged and neutral pions, the determination of $|V_{ud}|$, and the extraction of the UT angle α from $B{\to}\pi\pi$ decays. Similarly, $\rm SU(3)$ symmetry and chiral perturbation theory are key ingredients in determining $|V_{us}|$. $\rm SU(3)$ has also been used as a bound on the SM-induced deviations of the time-dependent CP asymmetries from $\sin 2\alpha$ or $\sin 2\beta$ in the penguin-dominated modes (see chapter 2).

Heavy-Quark Symmetry and Heavy-Quark Effective Theory

In mesons composed of an heavy quark and a light antiquark the energy scale of strong interactions is small compared with the heavy-quark mass. The heavy quark acts as a static point-like color source with fixed four-velocity, which cannot be altered by the soft gluons responsible for confinement. Hence the configuration of the light degrees of freedom becomes independent of the spin and flavor (mass) of the heavy quark, which, for N_f heavy-quark flavors, results in a $\mathrm{SU(2N_f)}$ heavy-quark spin-flavor symmetry [41].

Heavy-quark spin-flavor symmetry has many important implications for the spectroscopy and strong decays of B and D mesons (for details see [42]). It is especially predictive for exclusive $B \rightarrow D^{(*)} \ell \overline{\nu}$ semileptonic decays, which are relevant for the determination of $|V_{cb}|$.

Deviations from the heavy-quark limit can be included using the heavy-quark effective theory (HQET) [43], which provides a systematic expansion in powers of $\alpha_S(m_Q)$ and $\Lambda_{\mathrm{QCD}}/m_Q$ ($Q = b, c$). The former type of corrections is calculable perturbatively, whereas the latter ones can be parametrized by a minimal set of hadronic matrix elements that can be extracted from data and/or estimated using nonperturbative techniques.

Factorization and Soft-Collinear Effective Theory

In the decay $B \rightarrow M_1 M_2$, if the meson M_1 that inherits the spectator quark from the B is heavy and M_2 is light then “color transparency” can justify factorization [44, 45]. Traditionally, naive factorization refers to the hypothesis that matrix elements of the four-quark operators can be estimated by grouping the quark fields into a pair that can mediate $B \rightarrow M_1$ transition and into another pair that describes vacuum$\rightarrow M_2$ transition.

These ideas are the base of the recent development of the Soft Collinear Effective Theory (SCET) [46]. SCET is designed to describe the interactions of energetic and low invariant-mass partons in the $Q \gg \Lambda_{\mathrm{QCD}}$ limit. It introduces distinct fields for the relevant degrees of freedom, and a power-counting parameter λ. There are two distinct theories, $\mathrm{SCET_I}$ in which $\lambda = \sqrt{\Lambda_{\mathrm{QCD}}/Q}$ and $\mathrm{SCET_{II}}$ in which $\lambda = \Lambda_{\mathrm{QCD}}/Q$. They are appropriate for final states with invariant mass $Q\lambda$, like jets and inclusive $B \rightarrow X_s \gamma$, $X_u \ell \overline{\nu}$, $X_s \ell^+ \ell^-$ decays ($m_X^2 \sim \Lambda_{\mathrm{QCD}} Q$) for $\mathrm{SCET_I}$, and exclusive hadronic final states ($m^2 \sim \Lambda_{\mathrm{QCD}}^2$) for $\mathrm{SCET_{II}}$.

1.4.5 Magnitudes of CKM Matrix Elements

We report in this section the measurements techniques and results for the magnitude of CKM elements. More information can be found in [47][9].

$|V_{ud}|$

$|V_{ud}|$ is studied via superallowed $0^+ \rightarrow 0^+$ nuclear β decays:

$$|V_{ud}| = 0.97418 \pm 0.00027. \tag{1.68}$$

$|V_{us}|$

$|V_{us}|$ is extracted from semileptonic kaon decays:

$$|V_{us}| = 0.2255 \pm 0.0019. \tag{1.69}$$

$|V_{cd}|$

The most precise measurement of $|V_{cd}|$ is based on neutrino and antineutrino interactions. The difference of the ratio of double-muon to single-muon production by neutrino and antineutrino beams is proportional to the charm cross section off valence d-quarks, which allows to obtain:

$$|V_{cd}| = 0.230 \pm 0.011. \tag{1.70}$$

$|V_{cs}|$

The direct determination of $|V_{cs}|$ is possible from semileptonic D or leptonic D_s decays, relying on the calculations of the hadronic matrix elements. We obtain

$$|V_{cs}| = 1.04 \pm 0.06 \tag{1.71}$$

where the error is dominated by theoretical error on the form factor.

$|V_{cb}|$

This matrix element can be determined from exclusive and inclusive semileptonic decays of B mesons to charm:

$$|V_{cb}| = (41.2 \pm 1.1) \times 10^{-3}. \tag{1.72}$$

---

[9] In the following averages referred as [47] are updated to the measurements prior to $15\,^{th}$ Jaunary 2008; the ones referred as [48] are updated to Winter 2008 conferences (late April); the ones referred as [49] are updated to ICHEP 2008 conference (8^{th} August 2008).

$|V_{ub}|$

The determination of $|V_{ub}|$ has been obtained combining measurements from inclusive and exclusive $B{\rightarrow}X_u\ell\bar{\nu}$ decays:

$$|V_{ub}| = (3.93 \pm 0.36) \times 10^{-3}, \tag{1.73}$$

which is dominated by the inclusive measurement. This measurement is somewhat above the range favored by the measurement of the $\sin 2\beta$ discussed below.

$|V_{td}|$ and $|V_{ts}|$

The CKM elements $|V_{td}|$ and $V_{ts}|$ cannot be measured from tree-level decays of the top quark, so one has to rely on determinations from $B-\overline{B}$ oscillations mediated by box diagrams or loop-mediated rare K and B decays. Theoretical uncertainties in hadronic effects limit the accuracy of the current determinations. These can be reduced by taking ratios of processes that are equal in the flavor $\mathrm{SU}(3)$ limit to determine $|V_{td}/V_{ts}|$. For these last measurements a new theoretically clean and significantly improved constraint is provided by the measurements of the mass difference of the two neutral B_s meson by CDF Collaboration, $\Delta m_s = (17.77 \pm 0.10 \pm 0.07)$ ps^{-1} [50].

$$\begin{aligned} |V_{td}| &= (8.1 \pm 0.6) \times 10^{-3} && (1.74)\\ |V_{ts}| &= (38.7 \pm 2.3) \times 10^{-3} && (1.75)\\ |V_{td}/V_{ts}| &= 0.209 \pm 0.001 \pm 0.006 && (1.76)\\ & && (1.77) \end{aligned}$$

$|V_{tb}|$

The direct determination of $|V_{tb}|$ from top decays uses the ratio of branching fractions $R = \mathcal{B}(t{\rightarrow}Wb)/\mathcal{B}(t{\rightarrow}Wq) = |V_{tb}|^2$, where $q = b, s, d$. The measurements give a 95% CL lower limit

$$|V_{tb}| > 0.74. \tag{1.78}$$

A tentative extraction of $|V_{tb}|$ constraining from precision electroweak data gives

$$|V_{tb}| = 0.77^{+0.18}_{0.24} \tag{1.79}$$

where the results is dominated by the the constraint on top loop contribution to $\Gamma{\rightarrow}b\bar{b}$.

1.4.6 Unitarity Triangle Angle Measurements

The UT angles α, β and γ (defined in eq. 1.67) are all accessible from the B sector, albeit with different sensitivity and purity. Whereas the measurements of β (the leading experimental observable here is $\sin 2\beta$) and γ, through B decays in charmonium and open charm, respectively, are theoretically clean, the measurement of α in charmless B decays relies on theoretical assumptions. Because the measurements of α and γ involve interference with transitions governed by the small CKM matrix element V_{ub}, they require larger data samples than when measuring $\sin 2\beta$. The $\sin 2\beta$ can be also measured in penguin dominated modes with $b \rightarrow s$ transitions (see chapter 2), where, also in this case, due to the small branching fractions of the modes involved, a larger data sample than in charmonium final states is required.

The experimental techniques to measure the UT angles also change radically from one to another. The measurements of α and β require $B^0\overline{B}^0$ mixing and therefore use neutral B mesons, whereas the measurements of γ use interference between $b \rightarrow u$ and $b \rightarrow c$ decay amplitudes, and can be performed using both neutral and charged B decays.

Concerning the CP violation in B^0 mixing, which has been searched for with both flavor-specific and inclusive B^0 decays in samples where the initial flavor state is tagged, the current world average is $|q/p| = 1.0025 \pm 0.0019$ [48], whereas the deviation from unity is expected to be $|q/p| - 1 \approx 0.0003$ [51]. For this reason we will neglect it in the following.

In the following sections we will briefly report techniques and measurements of the UT angles. More information can be found in ref. [47].

β from B Decays to Charmonium Final States

In $b \rightarrow c\bar{c}s$ quark-level decays, the time-dependent CP violation parameters measured from the interference between decays with and without mixing are S and C defined in eq. 1.53. In the SM, with a very good approximation, we expect for these decays $S = -\eta_{CP} \sin 2\beta$ and $C = 0$ for the transition $B^0 \rightarrow f$, where $\eta_{CP} = \pm 1$ is the CP eigenvalue of f and 2β is the phase difference between the $B^0 \rightarrow f$ and $B^0 \rightarrow \overline{B}^0 \rightarrow f$ decay paths. The $b \rightarrow sq\bar{q}$ penguin amplitudes have dominantly the same weak phase as the $b \rightarrow c\bar{c}s$ tree amplitude. Since only λ^2-suppressed penguin amplitudes introduce a new CP-violation phase, amplitudes with a single weak phase dominate these decays.

The theoretically cleanest case is $B \rightarrow J/\psi K^0_{S,L}$, but several other charmonium modes have been measured by BABAR and Belle: $J/\psi K^0_S$, $\psi(2S)K^0_S$, $\chi_{c1}K^0_S$ and $\eta_c K^0_S$ modes with $\eta_{CP} = -1$, as well as $J/\psi K^0_L$, which has $\eta_{CP} = +1$. In the latest result from Belle, only $J/\psi K_S^0$ and $J/\psi K_L^0$ are used. The world average reads [48]

$$\sin 2\beta = 0.681 \pm 0.025. \tag{1.80}$$

This measurement has a four-fold ambiguity in β, which can be resolved by a global CKM fit mentioned below. Experimentally, the two-fold ambiguity $\beta \rightarrow \pi/2 - \beta$ (but not $\beta \rightarrow \pi + \beta$) can be resolved by a time-dependent angular analysis of $B^0 \rightarrow J/\psi K^{*0}(892)$ [52] or a time-dependent Dalitz plot analysis of $B^0 \rightarrow \overline{D}^0 h^0$ ($h^0 = \pi^0, \eta, \omega$) with $\overline{D}^0 \rightarrow K_S^0 \pi^+ \pi^-$ [53]. The latter gives the better sensitivity and disfavors the solutions with $\cos 2\beta < 0$ at the 98.3% CL, consistent with the global CKM fit result. In fact from the result 1.80 we obtain for the angle β within $[0, \pi]$ the solutions $(21.5 \pm 0.7)^\circ$ and $(68.5 \pm 0.7)^\circ$, where the first number is compatible with the result from the global CKM fit without the measurement of β, $(27.31^{+0.73}_{-2.10})^\circ$ and $\sin 2\beta_{\mathrm{CKM}} = 0.815\,^{+0.015}_{-0.045}$ [49].

In $b \rightarrow c\bar{c}d$ quark-level decays, such as $B^0 \rightarrow J/\psi \pi^0$ or $B^0 \rightarrow D^{(*)} D^{(*)}$, unknown contributions from (not CKM suppressed) penguin-type diagrams, carrying a different weak phase than the tree-level diagram, compromises the clean extraction of $\sin 2\beta$. Consequently, they are not included in the $\sin 2\beta$ average.

The β angle can be also measured using $b \rightarrow s\bar{q}q$ penguin dominated decays. These decays have the same CKM phase as the $b \rightarrow c\bar{c}s$ tree level decays, up to corrections suppressed by λ^2, since $V_{tb}^* V_{ts} = -V_{cb}^* V_{cs}[1 + \mathcal{O}(\lambda^2)]$. If new physics contributes to the $b \rightarrow s$ loop diagrams and has a different weak phase, it would give rise to $S \neq -\eta_{CP} \sin 2\beta$ and possibly $C \neq 0$. Therefore, the main interest in these modes is not simply to measure $\sin 2\beta$, but to search for the new physics. The $B^0 \rightarrow \eta' K^0$ is one of these modes. Details of the measurements of CP violation time-dependent for these modes are given in chapter 2

As expected in the SM, no direct CP violation has been observed in all these modes.

α from Charmless B Decays

Unlike the measurement of β for which $B^0 \rightarrow J/\psi K^0$ is considered the “golden mode”, because amplitudes with weak phases different from the dominant tree phase are doubly CKM suppressed, the measurement of α involves final states that receive contributions from multiple weak phases. Since α is the angle between $V_{tb}^* V_{td}$ and $V_{ub}^* V_{ud}$, only time-dependent CP asymmetries in $b \rightarrow u\bar{u}d$ dominated tree modes can directly measure $\sin 2\alpha$, in contrast to $\sin 2\beta$, where several different transitions can be used. Since $b \rightarrow u\bar{u}d$ penguin amplitudes have a different CKM phase than $b \rightarrow u\bar{u}d$ tree amplitudes, and their magnitudes are the same order in λ, penguin contributions can be large and complicateα

determination. This complication makes the extraction of the CKM couplings from the experimental observables considerably more difficult, although richer. For the measurement of α, the most sensitive decays are $B^0 \to \pi^+\pi^-$, $\rho^\pm\pi^\mp$, $\rho^+\rho^-$ and $\rho^0\rho^0$. The extraction of α in the presence of unknown penguin amplitudes requires an isospin analysis [54] for $\pi\pi$, $\rho\rho$, and a Dalitz-plot analysis [55] for $\rho^\pm\pi^\mp$. The goal is to estimate the penguin contribution (*penguin pollution*) with respect to tree contribution. Relying on flavor symmetries, in particular $\mathrm{SU}(2)$, does not represent a severe theoretical limitation. However, it certainly creates uncertainties which are model-dependent from flavor-symmetry breaking so that — neglecting statistical considerations — the measurement of α is not so clean as the measurements of $\sin 2\beta$ and γ. A new promising mode to extract α is the $B^0 \to a_1^\pm \pi^\mp$ [56]. Differently from $\rho^\pm\pi^\mp$, here a Dalitz plot analysis is not easy because of the four bodies in the final state. Furthermore, the a_1 meson has a large width which is not well known [47]. Anyway, it is possible to perform an analysis using a quasi-two-body approximation, using $\mathrm{SU}(3)$ symmetry to estimate the penguin pollution [57].

Combining the three measurements of the modes $\pi\pi$, $\rho^\pm\pi^\mp$, and $\rho\rho$ from *BABAR* and Belle experiments, α is constrained as [49]:

$$\alpha = \left(88.3\,^{+5.7}_{-4.8}\right)^\circ . \tag{1.81}$$

This measurement is in agreement with the expectation $\alpha_{\mathrm{CKM}} = (102.1\,^{+2.9}_{-5.8})^\circ$ from the global CKM fit (where the direct α measurement has been excluded from the fit) [49]. The results are shown in the fig. 1.7. A different statistical approach gives similar constraint from the combination of these measurements [58].

γ from B Decays to Open Charm

By virtue of eq. 1.67, γ does not dependent on CKM elements involving the top quark, so it can be measured in tree level B decays. This is an important distinction from the measurements of α and β, and implies that the direct measurements of γ are unlikely to be affected by physics beyond the SM.

The golden methods to determine γ at the B-factories utilize the measurement of direct CP violation in $B^+ \to DK^+$ decays, where the neutral D meson can be both D^0 and $\overline{D}^0$ (and where D^0 also stands for D^{*0}). The D^0 corresponds to the leading $\overline{b} \to \overline{c}$ transition, whereas the $\overline{D}^0$ is produced by a CKM- and color-suppressed $\overline{b} \to \overline{u}$ transition. If the final state is chosen so that both D^0 and $\overline{D}^0$ can contribute, the two amplitudes interfere, and the resulting observables are sensitive to the UT angle γ, the relative weak phase between the two B decay amplitudes.

In order to measure γ, the most used experimental methods are: reconstruction of the

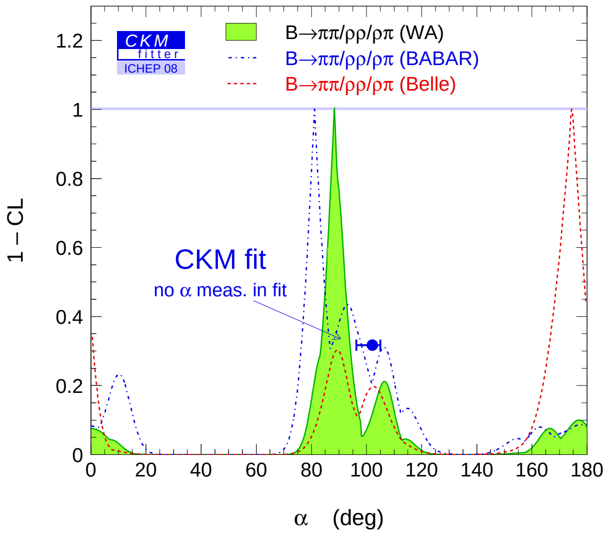

Figure 1.7: Constraints on α from the modes $\pi\pi$ (World Average), $\rho^{\pm}\pi^{\mp}$ (*BABAR*), $\rho\rho$ (WA), compared to the prediction from the CKM fit (not including these measurements) [49].

neutral D in a CP eigenstate (GLW) [59], reconstruction in other final states common to D^0 and $\overline{D}^0$ such as $K^{\mp}\pi^{\pm}$ (ADS) [60] or reconstruction in the self-conjugate three-body final state $K^0_S\pi^+\pi^-$ (GGSZ) [61]. For this last method, the analysis can be optimized by studying the Dalitz plot dependence of the interferences. The best present determination of γ comes from this method. All variations are sensitive to the same B decay parameters and can therefore be treated in a combined fit to extract γ.

Combining the GLW, ADS, and Dalitz analyses [49], γ is constrained as

$$\gamma = \left(67^{+32}_{-25}\right)^{\circ}\,. \tag{1.82}$$

The likelihood function of γ is not Gaussian, and the 95% CL range is $31^{\circ} < \gamma < 117^{\circ}$. This measurement is in agreement with the expectation $\gamma_{\mathrm{CKM}} = (67.4\,^{+3.3}_{-5.6})^{\circ}$ from the global CKM fit (where the direct γ measurement has been excluded from the fit) [49]. The results are shown in the fig. 1.8. Similar results are found in [58].

There is another way to measure γ. Similar to the decay $B^0 \to \rho^{\pm}\pi^{\mp}$, which is not a CP eigenstate but sensitive to α because both final states can be reached by both neutral B flavors, interference between decays with and without mixing can occur in $B^0 \to D^{(*)\pm}\pi^{\mp}(\rho^{\pm})$. A time-dependent analysis of these decays is sensitive to $\sin(2\beta+\gamma)$, because the CKM-favored $\overline{b}\to\overline{c}$ decay amplitude interferes with the CKM-suppressed $b\to u$ decay amplitude with a relative weak-phase shift γ. In these $\overline{b}\to\overline{c}(u\overline{d}),\ \overline{u}(c\overline{d})$ quark-

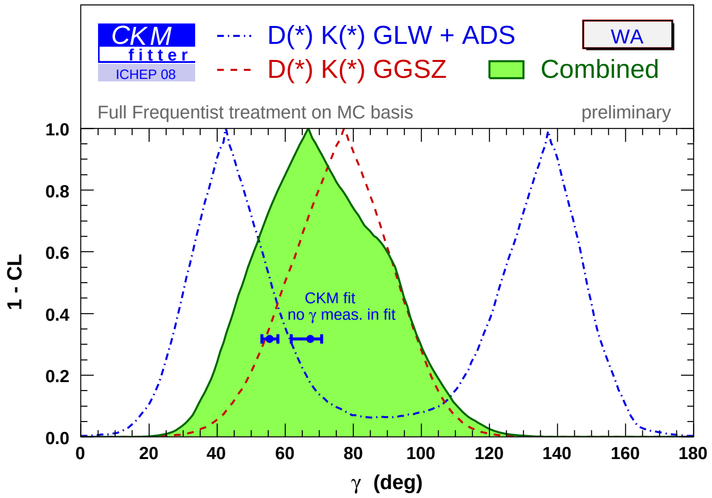

Figure 1.8: Constraints on γ from World Average $D^{(*)}K^{(*)}$ decays (GLW+ADS) and Dalitz analyses (GGSZ) compared to the prediction from the global CKM fit (not including these measurements) [49].

level transitions no penguin contributions are possible, because all quarks in the final state are different. Hence there is no direct CP violation. Combining the $D^{\pm}\pi^{\mp}$, $D^{*\pm}\pi^{\mp}$, and $D^{\pm}\rho^{\mp}$ measurements [62] gives $\sin(2\beta+\gamma) = 0.8^{+0.18}_{-0.24}$, consistent with the previously discussed results for β and γ. The $2\beta+\gamma$ measurements help to exclude large values of γ.

1.4.7 The Global CKM Fit

Using the independently measured CKM elements mentioned in the previous sections, the unitarity of the CKM matrix can be checked. We obtain $|V_{ud}|^2+|V_{us}|^2+|V_{ub}|^2 = 0.9999 \pm 0.0020$ (first row), $|V_{cd}|^2+|V_{cs}|^2+|V_{cb}|^2 = 1.07 \pm 0.06$ (second row), and $|V_{ud}|^2+|V_{cd}|^2+|V_{td}|^2 = 1.001 \pm 0.011$ (first column), respectively. These provide strong tests of the unitarity of the CKM matrix. The sum of the three angles of the unitarity triangle, $\alpha+\beta+\gamma = (176.8\,^{+32.5}_{-25.5})^{\circ}$, is also consistent with the SM expectation.

The CKM matrix elements can be most precisely determined by a global fit to relevant experimental measurements and their SM predictions, which depend on the parameters of the theory, and imposes the SM constraints (*i. e.*, three generation unitarity). Some of the parameters of the theory, such as quark masses or matrix elements, are experimentally or theoretically constrained, whereas others are unknown. These unknowns contain the four Wolfenstein parameters (defined in eq. 1.64), but also, for instance, hadronic quantities that occur in the determination of the UT angles α and γ. There are several approaches to combining the experimental data and to consider the free parameters of the theory. CKM-fitter [49] use frequentist statistics, while UTfit [58] uses a Bayesian approach. These approaches provide similar results.

The constraints implied by the unitarity of the three generation CKM matrix significantly reduce the allowed range of some of the CKM elements. The fit for the Wolfenstein parameters, as obtained in ref. [49], gives

$$\begin{aligned} \lambda &= 0.22521^{+0.00083}_{-0.00082} & \qquad A &= 0.798^{+0.023}_{-0.017}, \\ \rho &= 0.141^{+0.035}_{-0.021}, & \qquad \eta &= 0.307^{+0.012}_{-0.011} \end{aligned}$$

Once the Wolfenstein parameters are fitted, determining fully consistent confidence levels for all related observables is straightforward. The results of the fit are shown in the ρ, η plane in fig. 1.9. The outer contour of the combined fit corresponds to 95% CL exclusion. Also shown are the 95% CL regions for the individual constraints entering the fit (the constraint from $B^+ \to \tau^+ \nu_\tau$ is not shown, although it is included in the fit). This global CKM fit contains all relevant information collected by the experiments. From the new physics perspective, it is interesting to confront the measurements according to their sensitivity to new physics contributions. Fig. 1.10 shows on the left plot the constraints that originate from mainly tree-level processes, together with their combined fit. The right plot shows the constraints from loop-induced processes. To fix the length scale of the UT and the constraints on λ and A from the tree-level determinations of the CKM elements $|V_{ud}|$, $|V_{us}|$ and $|V_{cb}|$ are used. If γ is extracted from the measurement of α using β from mixing-induced CP violation as input, it is effectively a tree-level quantity, because the isospin analysis isolates the $\Delta I = 3/2$ component in the decay amplitude, which is assumed to be standard [49]. Consequently, the constraint for γ that enters the tree-level plot is the average of the direct measurement of γ via open-charm processes, and the value obtained from $\pi - \alpha - \beta$, from which new physics in mixing cancels. This provides the first determination of ρ, η from (effectively) tree-level processes. Good agreement is observed between the tree-level and loop-induced constrained fits.

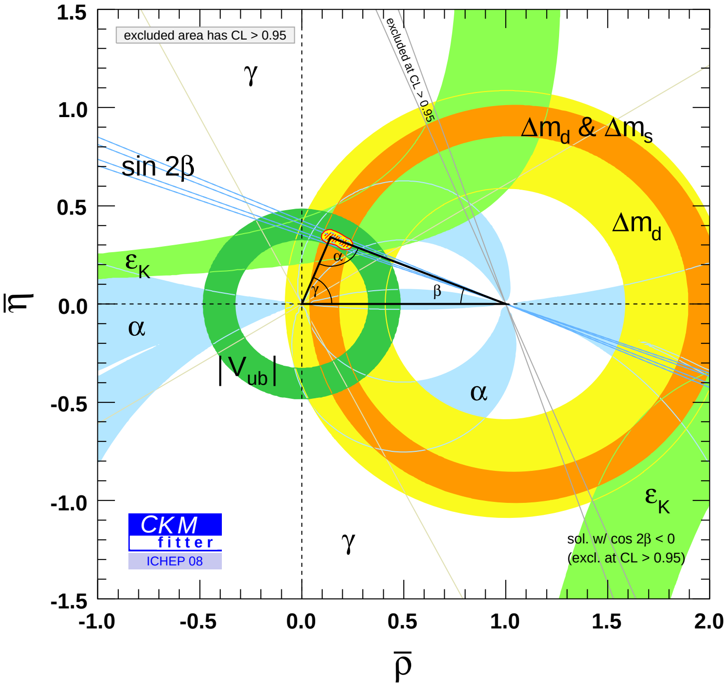

Figure 1.9: Confidence levels in the ρ, η plane for the global CKM fit. The shaded areas indicate 95% CL allowed regions [49].

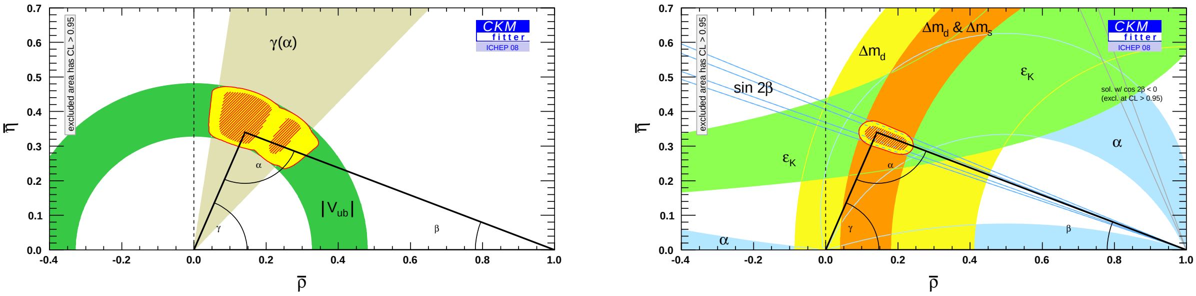

Figure 1.10: Confidence levels in the ρ, η plane for global CKM fits using only tree-level (left) and loop-induced (right) inputs. The shaded areas indicate 95% CL allowed regions [49].

Chapter 2

Rare B Meson Decays Involving $b{\to}s$ Transitions

2.1 Introduction

The goal of this chapter is to explain the scientific interest of our measurements and to give some more specific theoretical introduction to the decays studied into this thesis work. We introduce the importance of CP violation measurement in $b{\to}s$ transitions and more specifically the determination of $\sin 2\beta$ in $B{\to}\eta' K$. Then we discuss the so called *tree pollution* in such a measurement, which arise from contributions from other suppressed loop diagrams, and we introduce some techniques used to estimate the deviation $|S_{\eta' K^0} - \sin 2\beta|$ (ΔS). Finally we will report some consideration about the so called $\eta - \eta'$ *puzzle* which involves decays which differ from each other because the exchange of η with η' meson. Our interest in this chapter is to outline the theoretical issues related to our studies, not to give an exhaustive treatment of them. Interested readers can find such treatments is referenced papers.

2.2 CP Asymmetries in Loop-Dominated $b{\to}s$ Modes

The FCNC $b{\to}s$ transition is mediated by penguin diagrams (see fig. 1.5). It can have any up-type quark in the loop, so its amplitude can be written as

$$\begin{aligned} A_{b\to s} &= m_t V_{tb} V_{ts}^* + m_c V_{cb} V_{cs}^* + m_u V_{ub} V_{us}^* \\ &= (m_c - m_t) V_{cb} V_{cs}^* + (m_u - m_t) V_{ub} V_{us}^* = \mathcal{O}(\lambda^2) + \mathcal{O}(\lambda^4)\,, \end{aligned} \tag{2.1}$$

where the unitarity of the CKM matrix is used. In the SM, the amplitude is dominated by the first, $V_{cb}V_{cs}^*$, term, which has the same weak phase as the amplitude in $B^0{\to}J/\psi K^0$

decay. We expect $||\bar{A}/A| - 1| = \mathcal{O}(\lambda^2)$, and the time-dependent CP asymmetry parameters are given to a similar accuracy by $S_{b \to sq\overline{q}} \approx -\eta_{CP} \sin 2\beta$ and $C_{b \to sq\overline{q}} \approx 0$.

Owing to the large mass scale of the virtual particles that can occur in the loops, additional diagrams from physics beyond the SM, with heavy particles in the loops, may contribute. The measurement of CP violation in these channels and the comparison with the B-to-charmonium reference value is therefore a sensitive probe for physics beyond the SM. A discrepancy between $S_{b \to sq\overline{q}}$ and $\sin 2\beta$ can provide an indication of new physics. If the SM and new physics contributions are both significant, the deviations of the CP asymmetries from $\sin 2\beta$ become mode dependent, because they depend on the relative size and phase of the contributing amplitudes, which are determined by the quantum numbers of the new physics and by strong interactions.

Contributions of the second, CKM-suppressed, term to the $b \to sq\overline{q}$ transition in eq. 2.1 are, anyway, very important to bound because they can produce deviations of $S_{b \to sq\overline{q}}$ from $\sin 2\beta$. This term has a different weak phase than the dominant first term, so its impact on $S_{b \to sq\overline{q}}$ depends on both its magnitude and relative strong phase. Naive factorization suggests that for $q = s$ the λ^2 suppression of the second term is likely to hold because it would require an enhancement of rescattering effects to upset this. However, for $q = u$, there is a color-suppressed $b \to u$ tree diagram, which has a different weak (and possibly strong) phase than the leading λ^2 penguin amplitude. For $q = d$, any light neutral meson formed from $d\overline{d}$ also has a $u\overline{u}$ component, and there is “tree pollution” again. B^0decays to $\pi^0 K^0_S$ and ωK^0_S belong to this last category. Decays to $\eta' K$ and $f_0(980)K$ have significant $s\overline{s}$ components, which may reduce the tree pollution. Neglecting rescattering, the three-body final state $K^0\overline{K}^0K^0$ (reconstructed as $K^0_S K^0_S K^0_S$) has no tree pollution (pure-penguin mode), whereas $B^0 \to K^+K^-K^0$ (excluding ϕK^0, which is a pure-penguin mode) does.

As a consequence, only an effective $S = -\eta_{CP} \sin 2\beta_{\text{eff}}$ is determined. Recently QCD factorization (QCDF) [22, 63, 64] and SCET [65] was used to calculate the deviations $\Delta S = \sin 2\beta_{\text{eff}} - \sin 2\beta$ in some of the two-body penguin modes. It was found that the deviations are the smallest ($\lesssim 0.05$) for ϕK^0 and $\eta' K^0$. The SM shifts enhance $-\eta_f S_f$ (except for ρK^0_S) using [63, 64], while suppress $S_{\eta' K_S}$ using [65]. SU(3) flavor symmetry has also been used to bound the SM-induced deviations ΔS [20, 21, 66]. Owing to the lack of information on strong phases and the weak experimental bounds on some $b \to dq\overline{q}$ mediated rates, the resulting bounds tend to be weak. An exception is $\pi^0 K^0_S$, where SU(3) relates the relevant amplitudes to $\pi^0\pi^0$ and K^+K^- [21]. The theoretical understanding of factorization in three-body decays does not yet allow accurate bounds on ΔS to be computed.

Using present measurements [48][1], the s-penguin average is 0.68 ± 0.03, which is 0.1σ

---

[1] In this chapter results referenced as [48] are updated as after Lepton-Photon 2007 (August 2007).

from charmonium $\sin 2\beta$. Anyway excluding from this average the results for $B\to f_0(980)K^0_S$ from $B\to\pi^+\pi^-K^0_S$ analysis, which suffers highly asymmetric errors and have a deep impact on the final average, and keeping the *BABAR* measurement for $B\to f_0(980)K^0_S$ with $f_0(980)\to K^+K^-$, the s-penguin average is 0.56 ± 0.05, which is 2.2σ from charmonium $\sin 2\beta$.

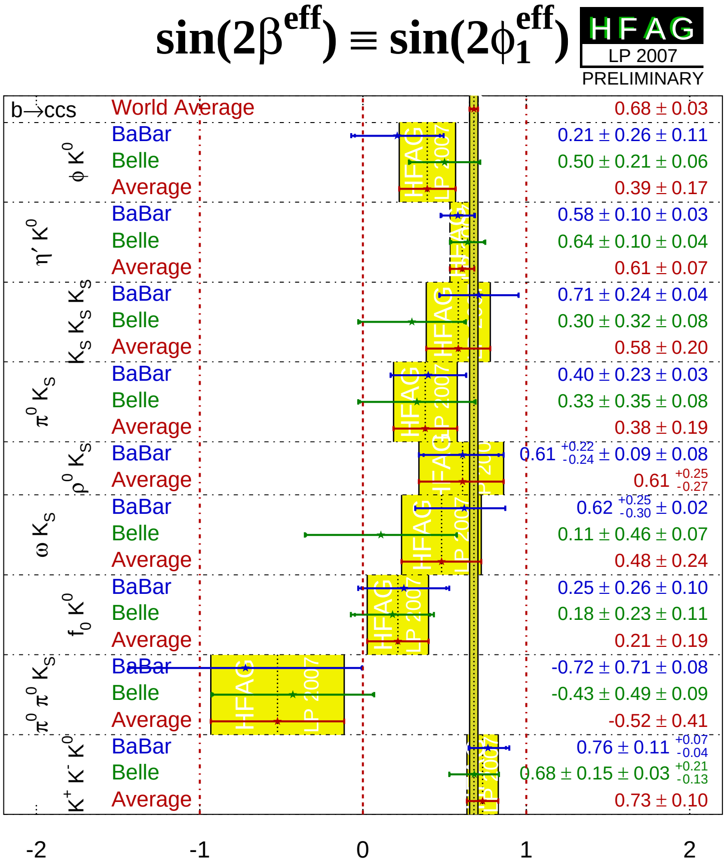

Figure 2.1: Comparison of world average $\sin 2\beta_{(\mathrm{eff})}$ results from penguin-dominated decays, and the charmonium reference value [48]. This results doesn't include $B\to f_0(980)K^0_S$ from $B\to\pi^+\pi^-K^0_S$ analysis, which suffers large asymmetric errors.

As expected in the SM, no direct CP violation has been observed in all these modes, *i. e.* C is consistent with zero. A compilation of the results for C in s-penguin dominated modes is shown in fig. 2.2.

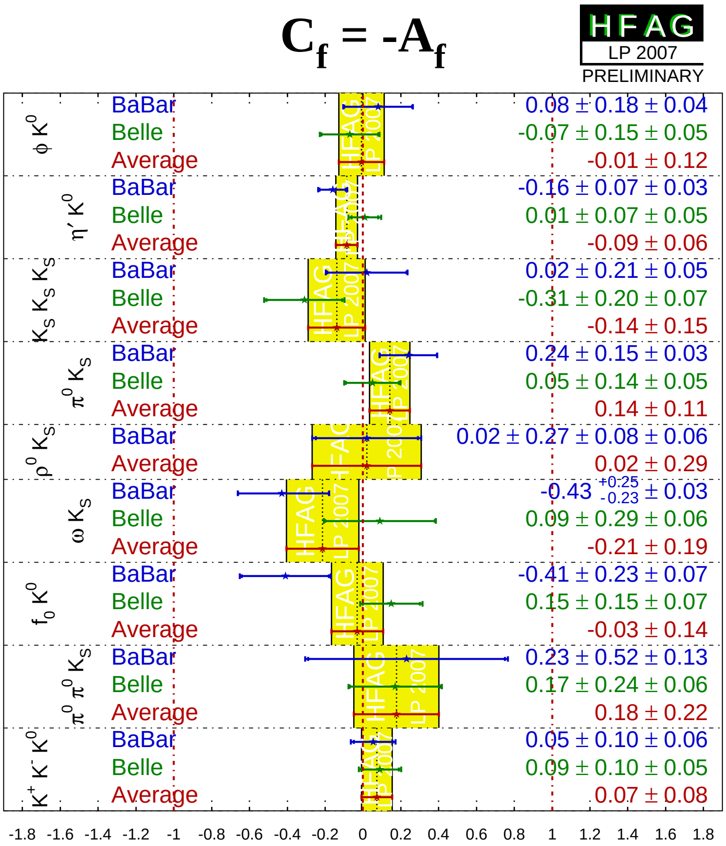

Figure 2.2: Comparison of world average C results from penguin-dominated decays, and the charmonium reference value [48]. This results doesn't include $B\to f_0(980)K^0_S$ from $B\to\pi^+\pi^-K^0_S$ analysis, which suffers large asymmetric errors.

A 2D comparisons plot of averages for C and $\eta_{CP}S$ in the different $b\to s$ modes is shown in fig. 2.3.

2.3 Theoretical Overview on $B\to\eta' K$ Decay Mode

Decays of B^0 mesons to $\eta' K^0$ proceed mostly via a single penguin (loop) amplitude with the same weak phase [17] present in B^0 meson decays through a Cabibbo-Kobayashi-Maskawa (CKM) favored $b\to c\bar{c}s$. However CKM-suppressed amplitudes and multiple particles in the loop introduce other weak phases whose contribution is not negligible [20, 21, 22, 23].

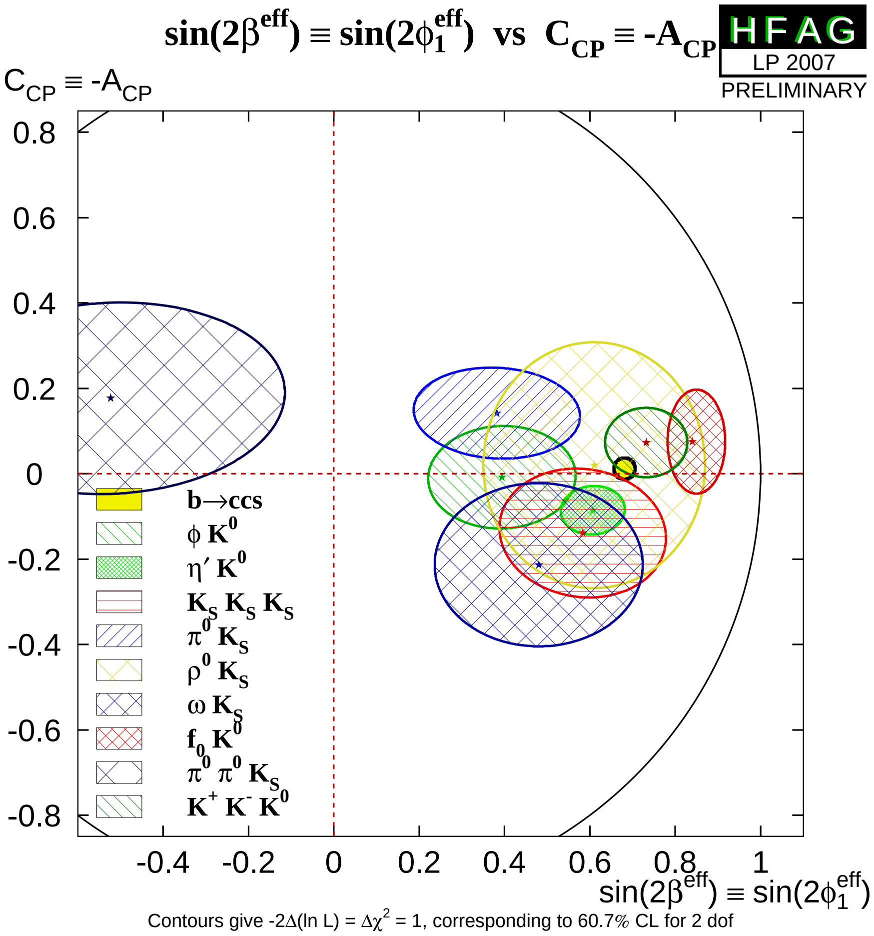

Figure 2.3: 2D comparisons of averages in the different $b \rightarrow s$ modes [48]. This plot (and the averages) assume no correlations between the S and C measurements in each mode.

Figure 2.4 shows the $B^0 - \overline{B}^0$ mixing diagram (a), together with some possible decay amplitudes for $B^0 \rightarrow \eta' K^0$. All the diagrams (b-d), together with electroweak counterparts and other variants, contribute, in principle, to the decay and are CKM suppressed. However the tree (fig. 2.4b) is also Cabibbo (and for the neutral mode color) suppressed, and is expected to be small [17, 22]. The observed branching fraction is larger than at least initially expected [67], spawning a variety of conjectures by way of explanation. Some possible explanations of this fact are reported in sec. 2.4. Both penguin amplitudes have, like the golden mode $J/\Psi K$, vanishing weak phases. Thus a time-dependent asymmetry measurement should, in the absence of new physics, yield an alternative measurement of $\sin 2\beta$. That is, with the usual additional assumption that CP is conserved in the mixing itself, the predictions for our asymmetry measurements are $-\eta_{CP} S = \sin 2\beta$ and $C = 0$.

Additional higher-order amplitudes with different weak phases would lead to devia-

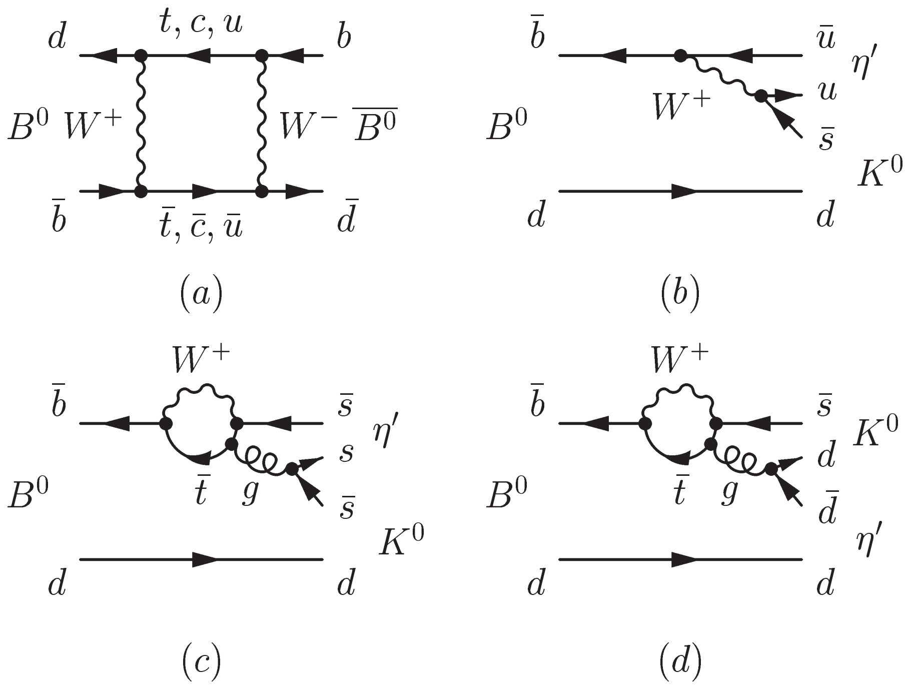

Figure 2.4: Feynman diagrams describing (a) $B^0 - \overline{B}^0$ mixing; the decay $B^0 \to \eta' K^0$ via (b) color-suppressed tree, (c, d) internal gluonic penguin. For the charged mode the corresponding tree diagram is external, not color suppressed.

tions of $-\eta_{CP}S$ from $\sin 2\beta$ For the $B^0\to\eta' K^0$ mode, so the time-dependent asymmetry measurement for this decay provides an approximate measurement of $\sin 2\beta$. Theoretical bounds for the small deviation $\Delta S = (-\eta_{CP}S) - \sin 2\beta$ have been calculated with an SU(3) analysis [20, 21, 68], which uses the branching fractions of the π^0, η, and η' two-body combinations from B^0 decays. Such bounds were improved by last measurements [48], like our measurement of $B^0\to\eta\eta$ mode reported in this thesis work. QCD factorization calculations [22] conclude that ΔS is smaller than what found in these SU(3) based upper bounds. A deviation ΔS superior to this limit can be considered an effect of phases coming from new physics [23].

The relevant theoretical formalism with all details for the calculation of these bounds can be found in [20, 21].

Constraints on CP asymmetries in $\eta' K^0$ can be written in terms of rates of other SU(3) related processes in different superpositions, depending on the level of approximation chosen. In one of these combinations amplitudes of isoscalar pairs including π^0, η and η' mesons in final state are involved:

$$\begin{aligned}
&\frac{1}{4\sqrt{3}}A(\pi^0\pi^0) - \frac{1}{3}A(\pi^0\eta) + \frac{5}{6\sqrt{2}}A(\pi^0\eta') \\
&+\frac{2}{3\sqrt{3}}A(\eta\eta) - \frac{11}{12\sqrt{3}}A(\eta'\eta') - \frac{5}{3\sqrt{3}}A(\eta\eta')
\end{aligned} \tag{2.2}$$

Another combination is based on the assumption that a single SU(3) amplitudes dominates decays into a singlet and an octet pseudoscalar [21]. It involves four decay processes:

$$\frac{1}{3\sqrt{3}}A(\pi^0\pi^0) + \frac{1}{3\sqrt{6}}A(K^+K^-) - \frac{2}{3}A(\pi^0\eta) - \frac{2}{\sqrt{3}}A(\eta\eta') \tag{2.3}$$

Another combination, valid in the approximation of no exchange and no penguin annihilation contributions [21], involves only three strangeness-conserving amplitudes:

$$-\frac{5}{6}A(\pi^0\eta) + \frac{1}{3\sqrt{2}}A(\pi^0\eta') - \frac{\sqrt{3}}{2}A(\eta\eta') \tag{2.4}$$

Some of the modes studied in this thesis work are also involved in the calculation of constraints on CP asymmetries parameters in ϕK^0 can be written in terms of rates of other SU(3) related processes in different superpositions, depending on the level of approximation chosen. In one of these combinations amplitudes of pairs including π^0, η, η', ω, ϕ, ρ^0,K^0_S and K^{*0} mesons in final state are involved:

$$\begin{aligned}
&\frac{1}{2}[A(\overline{K^{*0}}K^0 - A(K^{*0}\overline{K^0}))] + \frac{1}{2}\sqrt{\frac{3}{2}}[cA(\phi\eta) - sA(\phi\eta')] \\
&+\frac{\sqrt{3}}{4}[cA(\omega\eta) - sA(\omega\eta')] - \frac{\sqrt{3}}{4}[cA(\rho^0\eta) - sA(\rho^0\eta')] \\
&+\frac{1}{4}A(\rho^0\pi^0) - \frac{1}{4}A(\omega\pi^0) - \frac{1}{2\sqrt{2}}A(\phi\pi^0)
\end{aligned} \tag{2.5}$$

Where c and s are cosine and sine of $\eta - \eta'$ mixing angle. Anyway we don't calculate this bound in this thesis work.

Existing upper bounds on $|\Delta S|$ are calculated using measurements up to year 2006 [66]. Better bounds should be estimated using the results of this thesis work. For the combination in formula 2.2, actual bound is:

$$\Delta S = 0.15$$

For the combination in formula 2.4, actual bound is:

$$\Delta S = 0.08$$

These bounds are affected by a theoretical error (due to approximations and flavor SU(3) considerations) of order 20 or 30%. We have to note however that such bounds are certainly overestimated because all amplitudes in the combinations 2.2, 2.3, and 2.4 carry different strong phases and we should not expect that they all add up coherently (which is what is done in our calculation of ΔS).

The bounds for ΔS have been calculated in other different theoretical approaches as QCD factorization [22, 64], QCD factorization with modeled rescattering [69], Soft Collinear Effective Theory (SCET) [65]. These models estimate $|\Delta S|$ to be of the order 0.01, and with uncertainties give bounds $|\Delta S| \lesssim 0.05$.

2.4 The $\eta - \eta'$ Puzzle

Since the first measurement [24], $\eta' K$ branching fraction was found to be higher than expected [67], while it was found that the corresponding ηK branching fraction was suppressed.[2] Many conjectures were proposed in order to give an explanation of this fact, we report the most important of them in next sections. Some of such conjectures (the one based on some peculiarity of η' meson) reported here are actually ruled out by experimental data. We think however that they give an interesting view of the complexity of the problem and so we decided to include them into this work[3].

2.4.1 SU(3) Interference

In the framework of SU(3) flavor symmetry [70] we have one singlet and one octet neutral meson

$$\begin{aligned} \eta_1 &\equiv (s\overline{s} + u\overline{u} + d\overline{d})/\sqrt{3} \\ \eta_8 &\equiv (2s\overline{s} - u\overline{u} - d\overline{d})/\sqrt{6} \end{aligned} \tag{2.6}$$

which combine in

$$\begin{aligned} \eta &= \eta_8 \cos\theta - \eta_1 \sin\theta \\ \eta' &= \eta_8 \sin\theta + \eta_1 \cos\theta \end{aligned} \tag{2.7}$$

---

[2] The same evidence, with the role of η and η' reverted, was found in $\eta(')K^*$.

[3] One should be aware that all these model were developed before the high luminosity B factory era, just after the first measurement of $\mathcal{B}(B \to \eta' K)$. This is also an interesting example on how the scientific method works: many theories are developed to explain a single phenomenon, they stimulate interest on measuring particular quantities and such measurements confirm or rule out the various theoretical hypotheses.

where $\theta \approx 20^\circ$, so that a good representation of the physical states can be expressed as

$$\begin{aligned} \eta &\equiv \frac{(s\bar{s} - u\bar{u} - d\bar{d})}{\sqrt{3}} \\ \eta' &\equiv \frac{(2s\bar{s} + u\bar{u} + d\bar{d})}{\sqrt{6}} \end{aligned} \tag{2.8}$$

We now work in the spectator quark assumption, with the light quark of the B meson not taking part into the interaction. It can be shown that decays $B \rightarrow M_8 M_8$, where M_8 are mesons belonging to the SU(3) octet, receive many contributions from different amplitudes. The amplitudes which are not suppressed by kinematics factors can be grouped into three categories: tree (t), tree color-suppressed (c) and penguin (p). All (suppressed) contribution from electroweak diagrams with the exchange of Z or γ doesn't alter SU(3) invariance as far as all the amplitudes have the same change in strangeness (ΔS) between initial and final states. So such electroweak diagrams can be properly grouped into the above mentioned categories. If we now consider final states containing one or two M_1 mesons, belonging to the singlet, more contributions from the exchange of two or more quark in the penguin loop can take place (see fig 2.4.1), we denote these contributions as p_1.

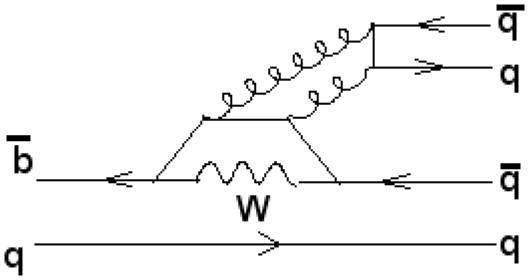

Figure 2.5: Graph contributing to $B \rightarrow M_8 M_1$ and $B \rightarrow M_1 M_1$ involving a two or more gluons exchange in the loop.

One can then compute the contributions from different amplitudes, assuming that SU(3) symmetry in not broken. In tab. 2.4.1 we show results of this calculation [70].

We have to remember that $B \rightarrow \eta(')K$ decay is penguin dominated, so $|p| > |t|$ and $|p| > |c|$. In addiction to this, the fact that p_1 is a higher-order contribution with respect to p lead to the assumption $|p_1| < |p|$, letting p being the main contributor to the decay amplitude. So from tab. 2.4.1 one can convince that $B \rightarrow \eta K$ should be suppressed with

Final	Coefficient of			
state	t	c	p	p_1
$\eta_8 K^+$	$-1/\sqrt{6}$	$-1/\sqrt{6}$	$1/\sqrt{6}$	0
$\eta_1 K^+$	$1/\sqrt{3}$	$1/\sqrt{3}$	$2/\sqrt{3}$	$\sqrt{3}$
ηK^+	$-1/\sqrt{3}$	$-1/\sqrt{3}$	0	$-1/\sqrt{3}$
$\eta' K^+$	$1/\sqrt{6}$	$1/\sqrt{6}$	$3/\sqrt{6}$	$2\sqrt{2/3}$

Table 2.1: Decomposition of $B^+ \to MM$ amplitudes in terms of independent amplitudes t, c, p, p_1 [70]

respect to $B \to \eta' K$.

Some other calculations [25], which rely on the interference between different amplitudes and on the assuption of SU(3) symmetry, predict that $\mathcal{B}(B \to \eta K)$ should be suppressed by a factor between $1/8$ and $1/34$.

2.4.2 Non-Spectator Quark Contribution

Another possible contribution can arise including in the interaction involving the light quark, so leaving the spectator quark framework [71]. In particular a diagram involving the fusion of the gluon from hadronic penguin and a soft gluon emitted by the light quark (see fig. 2.4.2) was found to enhance $B \to \eta' K$ branching ratio.

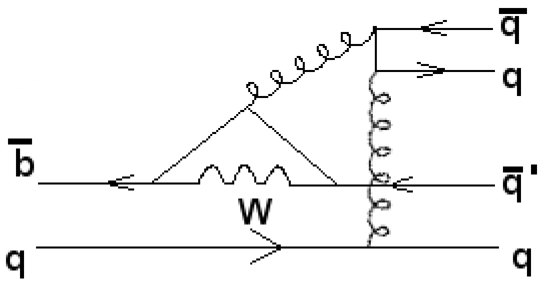

Figure 2.6: Graph representing the fusion of the gluon from hadronic penguin and a gluon emitted by the light quark.

The main source of uncertainty in this picture is the relevant form factor to be used in the Hamiltonian to describe the coupling of η' with gluons. This form factor is usually extracted from $J/\Psi \to \eta' \gamma$ decay, but suffer uncertainties due to the running of the coupling constant α_S which is implicitly contained into it. This model predicts $\mathcal{B}(B \to \eta' K) = 70 \times 10^{-6}$ and $\mathcal{B}(B \to \eta' K^*) = 34 \times 10^{-6}$, the latter one is in contrast with current measurements [48].

2.4.3 Charm Content of η' Meson

Another picture which relies on the fat that η' seems to be a quite special meson[4] is related to the presence of non-valence charm quarks in such a meson [72]. This presence would allow some Cabibbo favored $b \to c\bar{c}s$ amplitudes in the decay of $B \to \eta' X$. The $c\bar{c}$ states is then transformed in a “light” $q\bar{q}$ state (with $q = u, d, s$) via strong interaction. This model relies on the peculiarity of the η' meson and, due to the fact that in this picture η' is considered a strongly bounded state, on calculations based on non-perturbative QCD, which suffer high uncertainties from the theoretical point of view. Anyway, the prediction $\mathcal{B}(B \to \eta' K^*) \approx 2\mathcal{B}(B \to \eta' K)$ [70] and the fact that this enhancement should appear also in other $B \to \eta'$ transitions seems to rule out this model.

2.4.4 QCD Factorization

Results obtained from QCD factorization fit well experimental results both in the case of $B \to \eta' K$ and in many case of $B \to P_1 P_2$, P_1 and P_2 being some pseudoscalar meson. We don’t give any treatment of this approach because it’s great complexity, interested reader can refer to [67]. More recently, some NLO QCD factorization calculation were performed [22] and confirmed the goodness of previous predictions.

---

[4] For example, it’s mass is far larger than other components of the pseudoscalar octet

Chapter 3

The BABAR Experiment

3.1 Overview — B-Factories

Exploring CP violation in the B system and its potential impact on the Standard Model, baryogenesis, and cosmology, requires copious production of B mesons, accurate measurement of the B time of flight and flavor, and reasonably low background in the reconstruction. There are several potential options for experiments which can fulfill these criteria:

1. Hadron colliders ($\overset{(-)}{pp}$): The cross section for $B\overline{B}$ production at TeV hadron colliders is very high compared with e^+e^- B factories, approximately 100 μb vs. 1.2 nb. This large advantage does compete with several disadvantages, however. Hadronic collisions have far more background, making reconstruction of final states which do not contain a J/ψ very challenging. Purely hadronic final states with non-negligible background in e^+e^- colliders at the $\Upsilon(4S)$, such as $\pi^0\pi^0$, may be extremely difficult at a hadronic collider and it is not clear that it will be possible to reconstruct such decays. Nevertheless, these experiments do have a statistical advantage and also have the potential for observing CP violation in the B_s system, which is beyond the reach of $\Upsilon(4S)$ experiments. LHC-b at CERN is a new experiment which will start operations as soon as LCH collider will deliver the beam.

2. Fixed target proton beam experiments: Fixed-target experiments also offer the potential of a higher rate of B production, but have even greater levels of backgrounds, superimposed interactions, and boost which compresses all tracks in a small solid angle. A significant effort was undertaken at DESY to build, using an innovative design, such an experiment called HERA-B at DESY. Unfortunately, this experiment gave no significant scientific results.

3. e^+e^- colliders at the Z-pole: The Z-pole presents a relatively clean environment

for B-physics with a relatively large cross section ($\sim$ 6 nb). However, the luminosities achieved at this energy are low, the only two colliders in the world which can reach it, LEP and SLD, are both dismantled, and the cost of building new experiments at this energy prevents this from being a viable option.

4. Symmetric and asymmetric e^+e^- B-factories: The $\Upsilon(4S)$ resonance provides a very clean environment for B reconstruction, with a very favorable ratio of $b\bar{b}$ production from e^+ and e^- beams compared to lighter quark pairs ($\sigma(b\bar{b})/\sigma(q\bar{q}\,) \simeq 0.28$). Asymmetric e^+ and e^- beams provide a boost to the B meson pair that is produced, allowing for reconstruction of B flavor as a function of time of flight through the separation of the B vertexes in the lab frame, Δz. The concept of asymmetric B-factories was first proposed in 1987 by Pier Oddone [73]. He proposed that the best way to produce and study B particles would be to construct an asymmetric collider that could create a separation in space between the decay products of individual B and $\overline{B}$ mesons. In fact, unlike symmetric beams, the B particles are carried downstream in the direction of the higher energy beam and this forward boost enables the decay products to separate, allowing to observe the distances between their points of decay. This condition is required to measure the time-dependent CP asymmetries (see sec. 3.3). Statistical limitations, of which luminosity is the critical factor, are the dominant source of error for time-dependent CP asymmetries. Two asymmetric B-factories have been built and are currently producing physics: PEP-II/*BABAR* [74] and KEK-B/Belle[1] [75]. Previously, the symmetric B-factory CLEO (at the CESR ring at Cornell) was able to produce precision B physics results, however the symmetric design and the limited statistics precluded measurement of time-dependent CP-violating asymmetries.

The *BABAR* and Belle experiments are very similar, with the following important differences: the KEK-B/Belle B factory has a nonzero beam crossing angle (4.2 mr) at the interaction point (IP), whereas the PEP-II/*BABAR* B factory has a more traditional collinear IP. The KEK design potentially allows a greater number of beam bunches to be stored in the ring, due to absence of parasitic crossings at ± 1m, as are present in the PEP-II design. However KEK-B is a highly non-traditional design; concerns over higher-order mode resonances at the IP led the PEP-II B factory to use a collinear crossing. So far, both KEK-B and PEP-II have performed well. PEP-II ceased its operations on 7th April 2008, having integrated 553.5fb^{-1}, far beyond first expectations. KEK-B has integrated, at the time of writing, more than 857.0 fb^{-1}.

---

[1] KEK-B/Belle experiment is located at Tsukuba, Japan

The particle identification method also differs between *BABAR* and Belle: as will be described in section 3.4.3, *BABAR* uses quartz bars to internally reflect Čerenkov light to a backward-mounted detector (the DIRC), whereas Belle uses an aerogel Čerenkov detector. In addition, *BABAR* has a 5-layer silicon vertex detector (SVT, see sec. 3.4.1) that can perform standalone tracking, whereas Belle uses a 3-layer silicon vertex detector. In fig. 3.1 we show the cartoon of *BABAR* detector, where we indicate each subdetector. The longitudinal section is shown in fig 3.2.

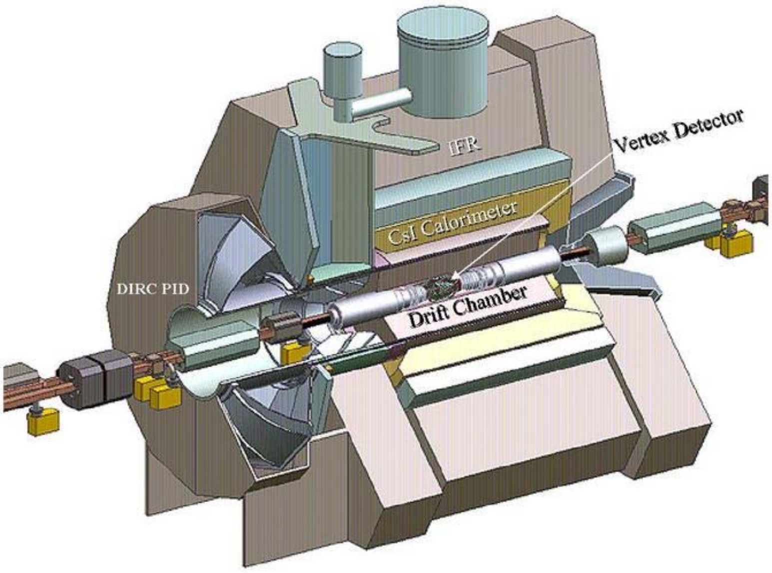

Figure 3.1: *BABAR* detector where each subdetector is indicated.

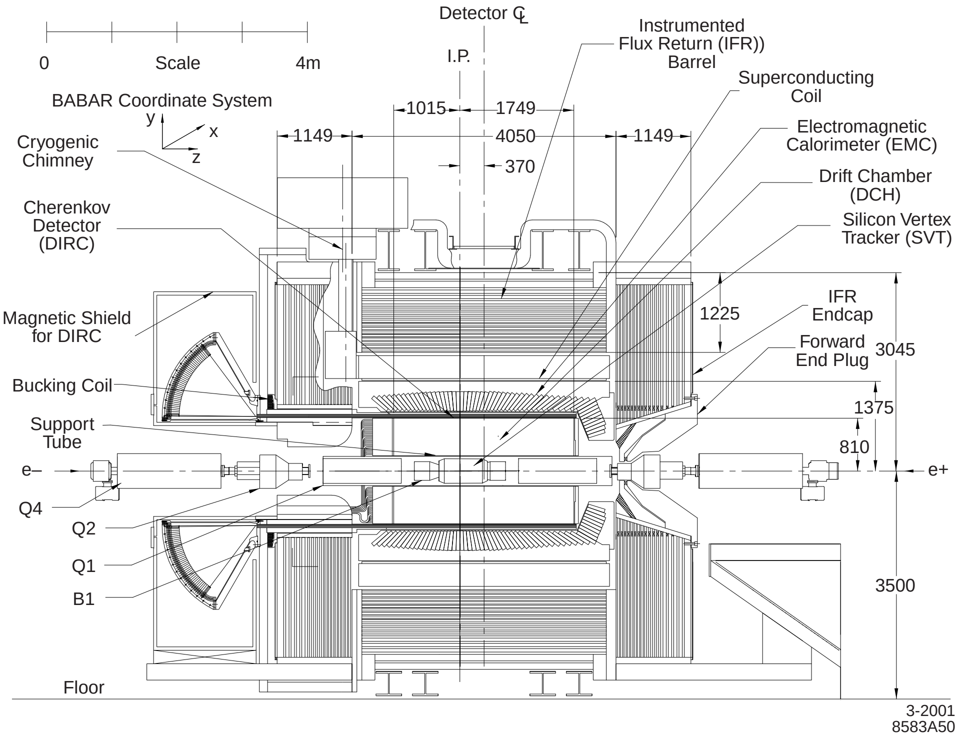

Figure 3.2: *BABAR* detector longitudinal section.

3.2 The PEP-II Asymmetric Collider

The design of PEP-II is shown in fig. 3.3. The 9.0 GeV electrons and 3.1 GeV positrons are injected in PEP-II from the SLAC linac via bypass lines in the linac gallery. They collide in the single interaction point of PEP-II, where *BABAR* is situated. The collisions take place inside a beryllium beam-pipe, with a diameter of 2.5 cm. The beam parameters are listed in table 3.1. PEP-II surpassed design goals both in instantaneous and in average integrated luminosity.

The energy in the center-of-mass system (CMS) is $\sqrt{s} = 10.58~\mathrm{GeV}$, which corresponds to $\Upsilon(4S)$ resonance. With this configuration, the CMS moves in laboratory frame with a relativist boost of $\beta\gamma = 0.56$, which gives an average separation between the two B (coming from $\Upsilon(4S)$ decay) vertexes of $\beta\gamma c\tau = 270\,\mu$m. The cross sections of production of fermionic pairs at CMS energy are shown in table 3.2.

PEP-II data operations started in 1999 and ceased on 7^{th} April 2008. Most of the data were taken at the $\Upsilon(4S)$ resonance (on-peak). However approximately 10% were taken at 40 MeV below the resonance peak (off-peak), where there is not $\Upsilon(4S)$ resonance production, to allow studies of non-resonant background in data (see fig. 3.4). In the last period of operation PEP-II also ran at $\Upsilon(3S)$ and $\Upsilon(2S)$ resonance energy, collecting the two largest world datasets ever recorded at those resonances. A scan over $\Upsilon(4S)$ region was also performed. The total integrated luminosity during the duration of the experiment was 432.89 fb^{-1} at $\Upsilon(4S)$ resonance, 30.23 fb^{-1} at $\Upsilon(3S)$ resonance, 14.45 fb^{-1} at $\Upsilon(2S)$ resonance and 53.85 fb^{-1} at off-peak energy. A plot of PEP-II integrated luminosity, *BABAR* recorded integrated luminosity as a function of time and integrated luminosity per day is shown in fig. 3.5. During data taking, PEP-II integrated 553.48 fb^{-1}, while *BABAR* recorded 531.43 fb^{-1}(which corresponds to an efficiency of 96.0%). It is important to note that the data has been collected in six different periods plus some dedicated runs at $\Upsilon(3S)$ and $\Upsilon(2S)$ energies, so the final dataset at $\Upsilon(4S)$ energy corresponds to run 1 to run 6 [2].

---

[2] The distinction between the runs is merely related to the different temporal period in which data taking occurred.

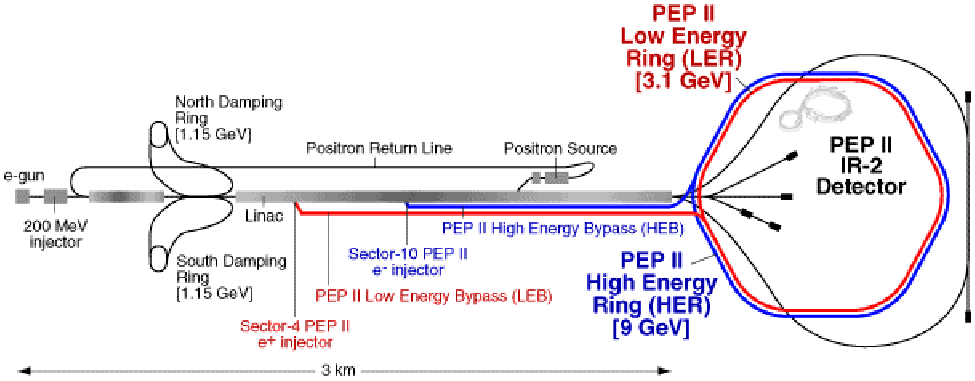

Figure 3.3: The PEP-II asymmetric storage ring and the SLAC linear accelerator. The SLAC linac is the injector for PEP-II. The single interaction point of PEP-II is at Interaction Region 2, where *BABAR* is situated.

Parameters	Design	Typical
Energy HER/LER (GeV)	9.0/3.1	9.0/3.1
Current HER/LER (A)	0.75/2.15	1.88/2.90
# of bunches	1658	1732
σ_{Lx} (μm)	110	120
σ_{Ly} (μm)	3.3	4.1
σ_{Lz} (mm)	9	1.75
Luminosity ($10^{33}\,\mathrm{cm}^{-2}\mathrm{s}^{-1}$)	3	11-12
Luminosity (pb^{-1}/d)	135	891

Table 3.1: PEP-II beam parameters. Values are given for the design and for colliding beam operation at time of writing. HER and LER refer to the high energy e^- and low energy e^+ ring, respectively. σ_{Lx}, σ_{Ly}, and σ_{Lz} refer to the R.M.S. horizontal, vertical, and longitudinal bunch size at the IP.

$e^+e^-\to$	Cross Section (nb)
$b\bar{b}$ ($\sigma_{b\bar{b}}$)	1.05
$c\bar{c}$ ($\sigma_{c\bar{c}}$)	1.30
$s\bar{s}$ ($\sigma_{s\bar{s}}$)	0.35
$u\bar{u}$ ($\sigma_{u\bar{u}}$)	1.39
$d\bar{d}$ ($\sigma_{d\bar{d}}$)	0.35
$\tau^+\tau^-$ (σ_τ)	0.94
$\mu^+\mu^-$ (σ_μ)	1.16
e^+e^- (σ_e)	~40

Table 3.2: Cross sections σ of production of fermionic pairs at $\Upsilon(4S)$ mass energy in nb $= 10^{-33}$cm^2.

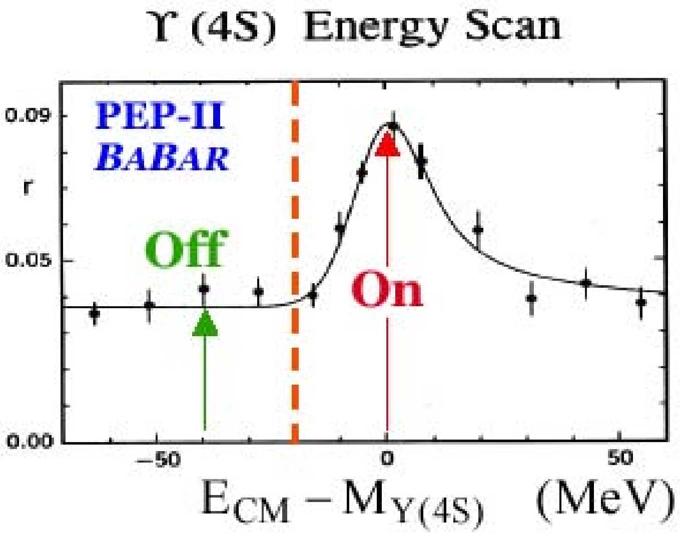

Figure 3.4: Plot of the cross section as function of $\Upsilon(4S)$ resonance mass and PEP-II CMS energy. We show the two regions corresponding to on-peak and off-peak energies.

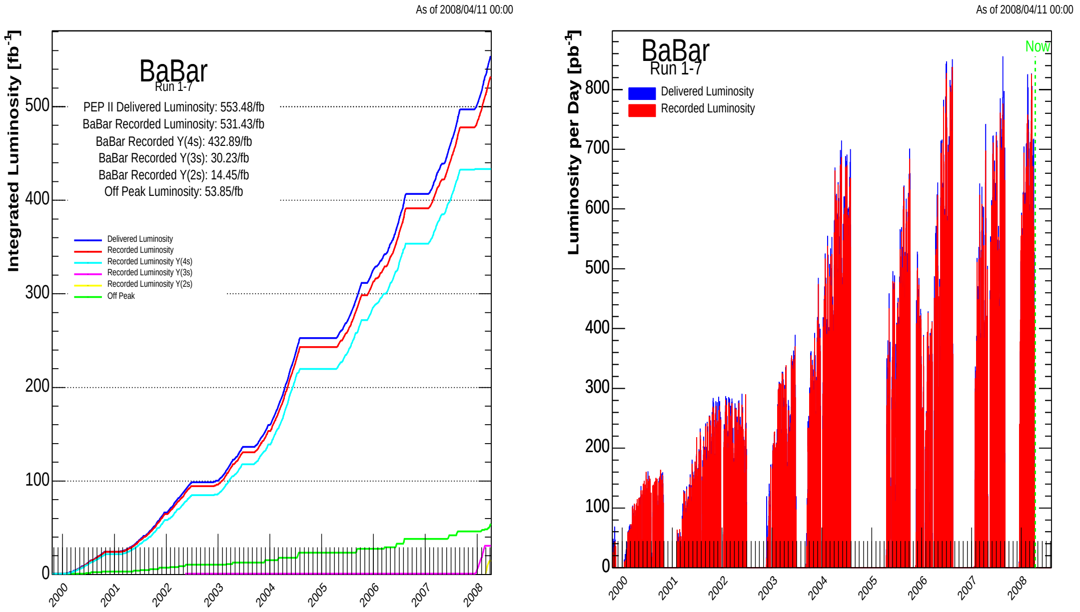

Figure 3.5: Left: PEP-II -*BABAR* integrated luminosity since startup. Right: PEP-II -*BABAR* integrated luminosity per day.

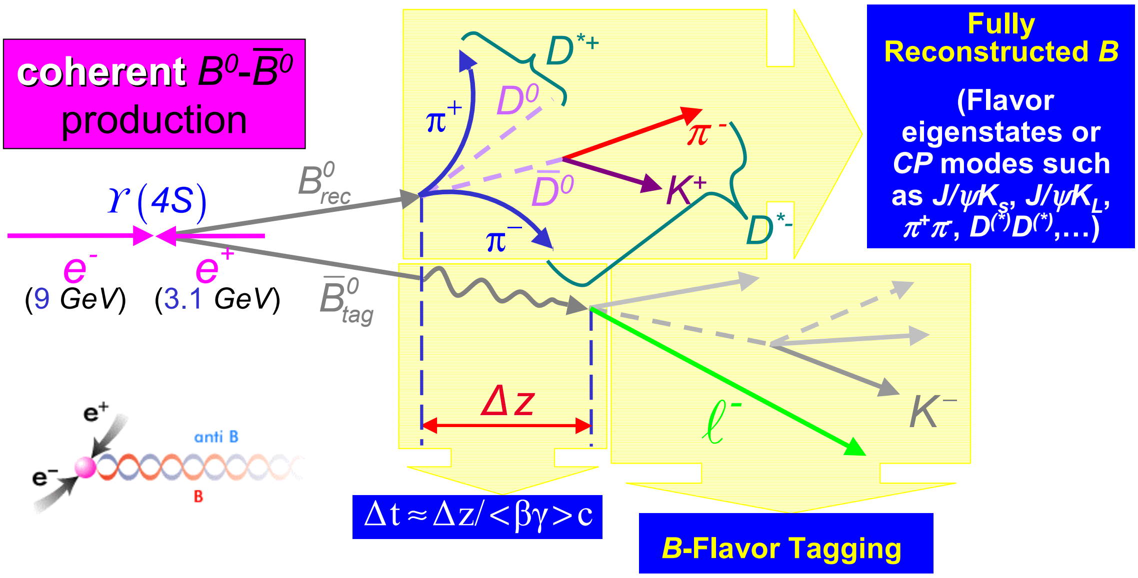

Figure 3.6: Experimental reconstruction technique used for measuring time-dependent CP-violating asymmetries at an $\Upsilon(4S)$ asymmetric collider. A coherent $B\overline{B}$ pair is produced from the $\Upsilon(4S)$ decay, which allows determination of reconstructed neutral B flavor as a function of decay time.

3.3 Overview of Experimental Technique at the $\Upsilon(4S)$

In order to measure time-dependent CP-violating asymmetries at the $\Upsilon(4S)$, one must (of course) first reconstruct a neutral B decay mode that can exhibit CP violation, such as $B^0 \rightarrow D^{*+}D^{*-}$. However, that is merely the first step. Due to the fact that the decay rate is different for B^0 and $\overline{B}^0$ (see eq. 1.51 and 1.52), the determination of the flavor of the signal B (B_{CP}), at the time of decay, is crucial. This goal is achieved from the knowledge of the proper oscillation time of the B_d system and from the determination of the flavor of the other B coming from the $\Upsilon(4S)$ resonance (B_{tag}). This flavor tagging is performed using a specific algorithm (see sec. 3.3.1). After both the event reconstruction and the flavor tagging are completed, the difference in vertex z-position[3] between the reconstructed B vertex and the tag side B vertex must be determined. Due to the asymmetry of the machine, this difference, Δz, is (very nearly) proportional to the decay time difference Δt between the two B decays. Δt is the time measurement over which the CP-violating asymmetry can occur, and it is input in eq. 1.51–1.52. Figure 3.6 gives an overview of this reconstruction method.

---

[3] The z-axis in *BABAR* is along the direction of the beam line, with electrons (and the center-of-mass boost) pointing toward $+z$ in the lab frame.

3.3.1 The Flavor Tagging Algorithm

As said above, a key ingredient in the measurement of the time-dependent CP asymmetries is to determine whether when $B_{\rm tag}$ decays (at $\Delta t = 0$) the meson decaying to a CP final state was a B^0 or a $\overline{B}^0$. This "*flavor tagging*" is achieved with the analysis of the decay products of the recoiling meson $B_{\rm tag}$. All reconstructed charged tracks that are not part of the fully reconstructed B_{CP} candidate are assigned to $B_{\rm tag}$. A set of loose track criteria is applied to these in order to reject ghost tracks. The overwhelming majority of $B_{\rm tag}$ decays to a final state that is flavor-specific, *i. e.* only accessible from either a B^0 or a $\overline{B}^0$, but not from both.

An example is the semileptonic decay $B^0 \to D^{*-}\ell^+\nu_\ell$ (or $\overline{B}^0 \to D^{*+}\ell^-\bar{\nu}_\ell$) with an appreciable branching fraction of 5.16% [47]. Here the charge of the lepton unambiguously identifies the decay from a B^0 or a $\overline{B}^0$. The subsequent decays of $D^{*+} \to D^0\pi^+$ and $D^0 \to K^-X^+$ give a soft pion and a kaon in the final state whose charges also uniquely identify the flavor of $B_{\rm tag}$. Another example is the self-tagging decay $B^0 \to D^{*-}\pi^+$. This decay gives an energetic π^+ and a low-momentum π^- in the final state, and the $B_{\rm tag}$ flavor can be inferred from the charges of both.

The purpose of the flavor tagging algorithm is to determine the flavor of $B_{\rm tag}$ with the highest possible efficiency $\epsilon_{\rm tag}$ and lowest possible probability w of assigning a wrong flavor to $B_{\rm tag}$. In the presence of a finite mistag probability w and a difference of mistag probability for $B_{\rm tag}$ tagged as B^0or $\overline{B}^0$, $\Delta w = w_{B^0} - w_{\overline{B}^0}$, the CP asymmetry (eq. 1.54) is reduced by a dilution factor $D = (1 - 2w)$:

$$f(\Delta t) = \frac{e^{-|\Delta t|/\tau}}{4\tau}\left[1 \mp \Delta w \pm (1-2w)\left[S\sin(\Delta m \Delta t) - C\cos(\Delta m \Delta t)\right]\right] \tag{3.1}$$

The figure of merit for the performance of the tagging algorithm is the effective tagging efficiency (or "tagging power")

$$Q = \epsilon_{\rm tag}(1-2w)^2, \tag{3.2}$$

which is related to the statistical uncertainty σ in the coefficients S and C through

$$\sigma \propto \frac{1}{\sqrt{Q}} \tag{3.3}$$

The *BABAR* tagging algorithm is a modular, multivariate flavor-tagging algorithm that analyses charged tracks on the tag side to assign a flavor and associated probability w to $B_{\rm tag}$. The algorithm currently used is called "`Tag04`" [76].

The flavor of $B_{\rm tag}$ is determined from a combination of nine different tag signatures, such as the properties of charged leptons, kaons, and pions. For each of these signatures, properties such as charge, momentum and decay angles are used as input to a Neural Network (NN) or “sub-tagger”. These sub-taggers are combined in a single Neural Network, or “Committee of Networks” [77, 78], trained to assign the correct flavor to $B_{\rm tag}$. Based on the output of this Neural Network and on the sub-taggers that contributed to it, each event is assigned to one of six mutually exclusive tag categories.

This modular approach, that keeps track of the underlying physics of each event, allows for detailed study of systematics. In particular it allows to separate semi-leptonic B decays, assigned to the `Lepton` tag category, from other decays. These `Lepton` tags do not only have a low w, but have more precisely reconstructed $B_{\rm tag}$ vertexes, are less sensitive to the bias from the charm on the tag side and are immune from the intrinsic mis-tag associated with Doubly Cabibbo Suppressed Decays [79].

The `Tag04` NN output is mapped to values between -1 and 1. The output value NN corresponds approximately [77] to the probability p of correct assignment through

$$p = (1 + |NN|)/2. \tag{3.4}$$

The NN value is used for the final classification in the six hierarchical and mutually exclusive tag categories: `Lepton`, `Kaon I`, `Kaon II`, `Kaon-Pion`, `Pion` or `Other`. The events where the information is not enough to have a clear identification are classified as `Untagged` and are unsuitable for the measurement of CP asymmetries. The name given to each category indicates the dominant physics processes (or subtagger) contributing to the flavor identification.

Since the tagging is mostly independent of the reconstructed B decay mode, the tagging parameters $\epsilon_{\rm tag}$, w, and Δw can be taken from a fit to samples of fully reconstructed B events (so called BReco) which have definite flavor (such as $B^0 \to D^{*-}\pi^+$ or $D^{*-}\rho^+$) (see sec. 3.3.2 for a description of this fit). The overall efficiency of tagging is 74.4% and the fraction of tagged events with an incorrect tag is 15.1%. The tagging power Q is 31.2%.

3.3.2 BReco Fits

In order to obtain the signal fraction, mistag fractions and mistag differences, and the parameters of signal Δt resolution model, we use the high statistic modes $B^0 \to D^{(*)-}\left(\pi^+\,\rho^+\,a_1^+\right)$ (BReco samples). The BReco modes are self-tagging fully reconstructed B decays, fits to these samples are performed, which provides the data for the fits. Fits are performed both on real data and on MC events. This is due to the fact that some differences exist between these two categories of events. So, in order to handle properly possible bias contributions to the fit result, MC BReco parameters are used while performing toys experiments, while BReco parameters (obtained from data) while fitting the real data sample.

In our fits we fix the values of Δm_d and the B lifetimes to the PDG values [98]: $\Delta m_d = 0.507 \pm 0.005$ ps^{-1}, $\tau_{B^\pm} = 1.638 \pm 0.011$ ps, and $\tau_{B^0} = 1.530 \pm 0.009$ ps.

In order to tag the flavor of the "tag" side of the event, we use the `Tag04` tagger with seven tagging categories. We split several quantities according to these tagging categories: signal fraction, mistag fractions and mistag differences, tag efficiency differences, background yields, and core offset of the signal Δt resolution function.

We use the m_{ES} distribution to discriminate between signal and background events. As signal PDF we use a double Gaussian obtained from fit on MC signal events, while for background we use an Argus function. We find the Argus shape parameter separately for each tagging category, and leave them floating in the fit. We fit the Δt for both signal and background using the B mixing physics model convoluted with a resolution model. The B mixing physics model uses as parameters six quantities: lifetime, Δm_d, mistag fraction, mistag difference, tag and reconstruction efficiency differences. We have four components for Δt:

- **signal**
  The lifetime and Δm_d are fixed to their PDG values for neutral B. We use a triple Gaussian as resolution model (core, tail and outlier), where the core and tail biases and resolutions are scaled to $\sigma_{\Delta t}$ (with the tail scale factor fixed at 3.0), and the outlier Gaussian has mean value fixed at zero and width fixed at 8 ps. The signal efficiency, mistag fraction, mistag difference, tag efficiency difference for each tagging category are listed in tab. 3.3 for real data and tab. 3.4 for MC events. The signal resolution parameters are given in tab. 3.5 for real data and tab. 3.6 for MC events. In case of fit on MC Breco sample, only signal component is used into te fit.

- **peaking background**
  The lifetime is fixed to the PDG value for charged B and Δm_d is fixed to zero. The mistag differences are fixed at zero. We fix the fraction of peaking background to signal component at 1.5%. The resolution model, tag and reconstruction efficiency differences are the same of the signal component.

- **lifetime background**
  The mistag differences, Δm_d and tag and reconstruction efficiency differences are fixed to zero. The mistag fractions and the background lifetime are listed in tab. 3.7. We use a double Gaussian resolution model (core and outlier) where the core bias

and resolution are scaled to $\sigma_{\Delta t}$ and the outlier Gaussian again has a fixed mean and width. The background resolution parameters are shown in tab. 3.8.

- **prompt background** (*i. e.* zero lifetime)
  The lifetime, mistag differences, Δm_d and tag and reconstruction efficiency differences are fixed to zero. The resolution model is the same as the lifetime background component. The fraction of prompt background and background mistag fractions are listed in tab. 3.7.

Table 3.3: BReco signal tagging fractions (f), mistag fractions ($\langle w \rangle$), mistag differences (Δw), and tag efficiency differences (μ) for each tagging category determined from fit to the neutral BReco sample.

Category	f_{sig}	$\langle w \rangle$	Δw	μ
`NoTag`	0.2563 ± 0.0019	0.5	0	0
`Lepton`	0.0896 ± 0.0007	0.0282 ± 0.0027	$+0.0027 \pm 0.0052$	-0.0030 ± 0.0094
`KaonI`	0.1082 ± 0.0007	0.0530 ± 0.0033	-0.0010 ± 0.0061	-0.0008 ± 0.0092
`KaonII`	0.1719 ± 0.0009	0.1447 ± 0.0033	$+0.0038 \pm 0.0056$	$+0.0056 \pm 0.0080$
`KopPI`	0.1367 ± 0.0008	0.2326 ± 0.0042	-0.0068 ± 0.0067	$+0.0018 \pm 0.0089$
`Pions`	0.1418 ± 0.0008	0.3253 ± 0.0044	$+0.0508 \pm 0.0067$	-0.0250 ± 0.0089
`Other`	0.0954 ± 0.0007	0.4152 ± 0.0054	$+0.0508 \pm 0.0081$	$+0.0176 \pm 0.0102$

Table 3.4: MC BReco signal tagging fractions (f), mistag fractions ($\langle w \rangle$), mistag differences (Δw), and tag efficiency differences (μ) for each tagging category determined from fit to the neutral BReco sample.

Category	f_{sig}	$\langle w \rangle$	Δw	μ
`NoTag`	0.2563 ± 0.0019	0.5	0	0
`Lepton`	0.0896 ± 0.0007	0.0284 ± 0.0005	-0.0013 ± 0.0011	-0.0039 ± 0.0021
`KaonI`	0.1082 ± 0.0007	0.0600 ± 0.0006	$+0.0030 \pm 0.0012$	-0.0057 ± 0.0021
`KaonII`	0.1719 ± 0.0009	0.1590 ± 0.0007	-0.0022 ± 0.0011	$+0.0051 \pm 0.0019$
`KopPI`	0.1367 ± 0.0008	0.2540 ± 0.0008	-0.0148 ± 0.0013	$+0.0117 \pm 0.0021$
`Pions`	0.1418 ± 0.0008	0.3481 ± 0.0009	$+0.0656 \pm 0.0013$	-0.0167 ± 0.0021
`Other`	0.0954 ± 0.0007	0.4203 ± 0.0011	$+0.0479 \pm 0.0016$	$+0.0053 \pm 0.0024$

3.3.3 Tag Vertex Reconstruction

In order to determine the decay vertex of $B_{\rm tag}$, we perform a geometrical fit using its daughters. Some requirements are applied to reduce ghost tracks. Each track must be

Table 3.5: Summary of BReco signal resolution function parameters.

Parameter	B^0
Scale `Lepton` (core)	1.0291 ± 0.0420
Scale `Not Lepton` (core)	1.0930 ± 0.0210
$\delta(\Delta t)$ `Lepton` (core)	-0.0618 ± 0.0268
$\delta(\Delta t)$ `No Lepton` (core)	-0.1906 ± 0.0125
f (core)	0.8820 ± 0.0080
Scale (tail)	3.0 (fixed)
$\delta(\Delta t)$ (tail)	-1.0347 ± 0.1089
f (outlier)	0.0031 ± 0.0005
Scale (outlier)	8.0 (fixed)
$\delta(\Delta t)$ (outlier) (ps)	0.0 (fixed)

Table 3.6: Summary of MC BReco signal resolution function parameters.

Parameter	B^0
Scale `Lepton` (core)	1.0084 ± 0.0088
Scale `Not Lepton` (core)	1.0973 ± 0.0043
$\delta(\Delta t)$ `Lepton` (core)	-0.0482 ± 0.0056
$\delta(\Delta t)$ `No Lepton` (core)	-0.2366 ± 0.0025
f (core)	0.8963 ± 0.0018
Scale (tail)	3.0 (fixed)
$\delta(\Delta t)$ (tail)	-1.2652 ± 0.0292
f (outlier)	0.0041 ± 0.0001
Scale (outlier)	8.0 (fixed)
$\delta(\Delta t)$ (outlier) (ps)	0.0 (fixed)

Table 3.7: Fit results for BReco prompt background and lifetime mistag fractions and the fraction of prompt background for the neutral BReco sample. The fit background lifetime is 1.306 ± 0.018 ps. † indicates quantities which are in common for all the non-leptonic tag categories.

Category	f_P	$\langle w_L \rangle$	$\langle w_P \rangle$
`Lepton`	0.2114 ± 0.0289	0.3173 ± 0.0178	-0.0403 ± 0.080
`KaonI`	$0.6648 \pm 0.0067^{\dagger}$	0.2919 ± 0.01165	0.1594 ± 0.0063
`KaonII`	$0.6648 \pm 0.0067^{\dagger}$	0.3284 ± 0.0089	0.2412 ± 0.0049
`KopPI`	$0.6648 \pm 0.0067^{\dagger}$	0.4067 ± 0.0111	0.3164 ± 0.0058
`Pions`	$0.6648 \pm 0.0067^{\dagger}$	0.4344 ± 0.0109	0.4560 ± 0.0068
`Other`	$0.6648 \pm 0.0067^{\dagger}$	0.4787 ± 0.0129	0.4321 ± 0.0059

Table 3.8: Summary of BReco background resolution function parameters.

Parameter	B^0
Scale (core)	1.3636 ± 0.0068
$\delta(\Delta t)$ (core)	-0.0424 ± 0.0051
f (core)	0.9889 ± 0.0007
Scale (outlier)	8.0 (fixed)
$\delta(\Delta t)$ (outlier) (ps)	0.0 (fixed)

successfully fit and its momentum is required to be below 10 GeV/c. Furthermore the distance of closest approach (DOCA) to the beam spot (luminous region) must be less than 4 cm along the beam axis and less than 0.4 cm in the transverse direction.

To improve the vertex resolution, K_S^0 or Λ^0 candidates are used as input to the vertex fit in place of their daughters. Furthermore, track pairs that are consistent with photon conversions ($\gamma \to e^+e^-$) are excluded from the fit.

The remaining candidates are used in a geometrical fit to a common vertex, taking into account the beam energies, the beam spot position and the flight direction of B_{CP} candidate. To reduce contributions from charm decay products that bias the determination of the vertex position, tracks with a vertex χ^2 contribution greater than 6 are removed and the fit is repeated until no track fails the χ^2 requirement.

In all but 1.3% of events, a tag side vertex is successfully fit from an average 3.5 tracks. The resolution in $\Delta z = z_{CP} - z_{\rm tag}$ is approximately $190\ \mu$m, corresponding to a resolution in Δt of 1.1 ps, when excluding less than 1% of misreconstructed “outlier” vertexes. It is dominated by the precision in the tag side vertex position $z_{\rm tag}$, and is slightly biased towards negative values due to the presence of charmed particles on the tag side. Figure 3.7 briefly describes the Δt measurement and resolution function. CP violation manifests itself as a difference in Δt distribution 3.1, depending on whether the flavor tag is B^0 or $\overline{B}^0$. This decay time distribution is convolved by the error of Δt (*i. e.* the resolution function). Vertex resolution is mostly independent from the reconstructed B decay mode and small differences are reflected in the assigned Δt errors. So parameters of the Δt resolution function can be taken from fit to the BReco sample, as well as the tagging parameters (see sec. 3.3.2 for a description of this fit).

3.4 The *BABAR* Detector

In the following subsection (sec. 3.4.1-3.4.7) we give a brief description of different subsystem that compose *BABAR* detector, techniques used to reject uninteresting events at

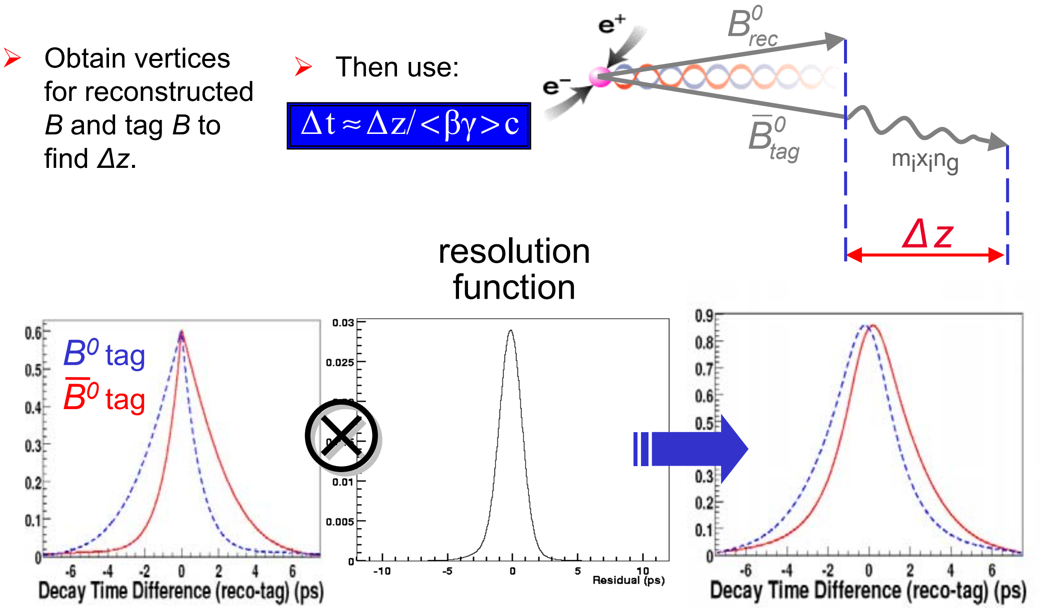

Figure 3.7: Δt measurement and resolution function. The difference in reconstructed z-position of the tag and reconstructed B decay vertexes is used to determine the time difference Δt.

data taking stage and those used to reconstruct tracks and neutral particles using different information from each subsystem. A more detailed description of the *BABAR* detector can be found elsewhere [80].

3.4.1 The Silicon Vertex Tracker (SVT)

The SVT contains 5 layers of silicon, double sided with conductive strip sensors. Strips on the opposite sides of each layer are orthogonal: ϕ strips run parallel to the beam axis and z strips run transverse to the beam direction. An image of fully assembled SVT is shown fig. 3.8.

Together, the SVT and the central tracking drift chamber (DCH) form the charged particle tracking system (see also section 3.4.7). Precise and efficient measurement of track 4-momentum is necessary for full reconstruction of B meson decays, which tend to have multiple charged decay products. In addition, good vertex (and Δz) resolution and accurate extrapolation to the outer subdetectors is essential for reconstruction and background subtraction. Thus, accurate charged particle tracking and vertexing is required.

The 5 layers and relatively long radial separation between SVT detector layers provide both standalone track pattern recognition and refinement of drift chamber tracks via addition of SVT hits. The necessity of precise measurements close to the interaction point for Δz measurement and for background rejection using vertex quality, and for efficient

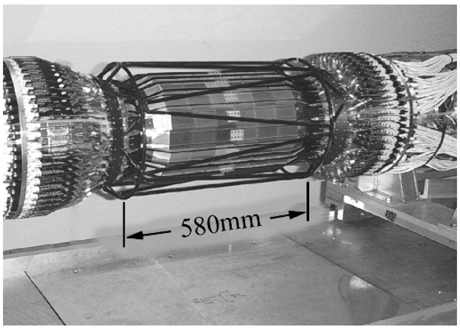

Figure 3.8: Fully assembled SVT. The silicon sensors of the outer layer are visible, as is the carbon-fiber space frame (black structure) that surrounds the silicon.

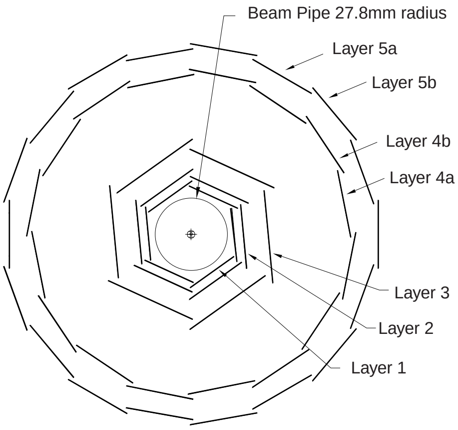

Figure 3.9: Transverse section of the SVT.

reconstruction of low momentum tracks (such as slow pions from D^* decays), drive the requirements for the SVT.

The SVT silicon is composed of n-type substrate with p^+ and n^+ strips on opposite sides. The bias voltage ranges from 25-35 V. The layers of the SVT are divided radially into modules, shown as line segments in fig. 3.9. The modules in the inner 3 layers are straight along the z-axis, while those in layers 4 and 5 are arch-shaped, as shown in fig. 3.10. The arch design was chosen to minimize the amount of silicon as well as increase the angle of incidence of tracks originating at the IP which cross the arch “lampshades” near the edges of acceptance. The total active silicon area is 0.96 m^2. The parameters of the layout of the SVT are shown in table 3.9.

The strip pitch (width) varies from 50 to 210 μm depending on the layer (inner layers are more closely bonded). The strips are AC-coupled to the electronic readout. Only approximately half the strips are read out; most have an unconnected “floating strip” between each pair of active strips (to reduce cost of readout electronics without adversely impacting performance). Digitization is performed by an ATOM (“A Time-Over-Threshold Machine”) chip at the end of each set of 128 strips, which amplifies, digitizes, and buffers the signal from each channel. The ATOM chip compares the charge accumulated on each strip with an (adjustable) threshold of 0.95 fC, and records the time in clock intervals (30 MHz for the SVT) for which each strip is over threshold. This information is then delivered to a computer farm for further processing upon an accept signal from the Level 1 Trigger (see sec. 3.4.6).

A variety of monitoring checks and calibrations were performed on the SVT to maintain data quality. Perhaps the most important of these from an avoidance-of-equipment-

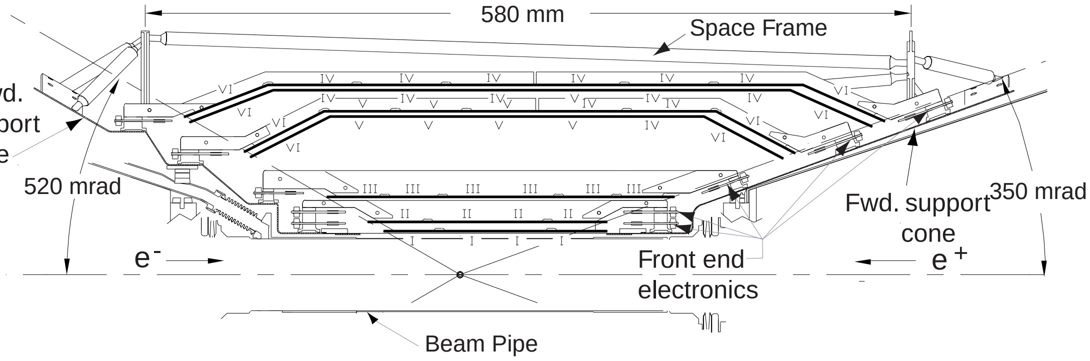

Figure 3.10: Longitudinal section of the SVT.

damage perspective was radiation protection. Twelve silicon PIN diodes surrounded the support cones and monitor both instantaneous radiation and accumulated dose. The beam was automatically aborted if radiation levels was above 1 Rad/s threshold. During its operations, SVT was well below the operational limit of 4 MRad integrated dose. The silicon PIN diodes had a temperature-dependent leakage current that increases with absorbed radiation dose. Due to absorbed doses of over 2 MRad, the leakage current in some diodes was much higher than the current induced by the radiation. The temperature was monitored very precisely but it was a challenge to correct for the temperature dependence of the leakage current, and the annealing and reverse-annealing effects due to radiation damage. During the 2002 summer shutdown a system of two diamond sensors was installed inside the SVT. These diamond sensors, grown by chemical vapor deposition (CVD), had no significant leakage current and was much more radiation hard than silicon PIN diodes. With a bias voltage of 500V applied across a 500-μm-thick polycrystalline CVD diamond sensor, the size of the signal due to a minimum-ionizing particle was more than 50% of that for a signal from a 300-μm-thick silicon sensor. The two diamond sensors improved (rather than replace) the primary existing silicon PIN-diode radiation sensors.

For data quality calibration, channel gains and noise must be individually calibrated; these calibrations were performed online via an integrated pulse generator and calibration electronics. The offline reconstruction had the responsibility for calibration of the alignment of each SVT module. Alignment is critical for accuracy of vertexing and of tracking reconstruction, and was calibrated in two steps. The local SVT alignment used dimuon and cosmic ray events to calibrate the relative position of each of the 340 wafers. The global alignment then determined the overall position and rotation of the SVT with respect to the DCH.

Quantity	Layer 1	Layer 2	Layer 3	Layer 4a	Layer 4b	Layer 5a	Layer 5b
Radius (mm)	32	40	54	124	127	140	144
Wafers/Module	4	4	6	7	7	8	8
Modules/Layer	6	6	6	8	8	9	9
ICs/Readout	7	7	10	5		5	
Length Strip, b/f :							
ϕ (mm)	82	88	127	230/189	230/203	270/257	270/270
z (mm)	40	48	70	104	104	104	104
z Ganging % (f/b):				34/67	48/67	88/98	98/98
Readout pitch (μm):							
ϕ	50	55	55	80–100		80–100	
z	100	100	100	210		210	
Floating Strips:							
ϕ	—	—	—	1		1	
z	1	1	1	1		1	
Intrinsic Resolution (μm):							
ϕ	10	10	10	10–12		10–12	
z	12	12	12	25		25	

Table 3.9: Parameters of the SVT layout.

The SVT performed according to design essentially since its inception. A combined hardware and software hit-finding efficiency greater than 95% was observed, excluding the 4 (out of 208) readout sections which were defective. Single hit resolution for tracks originating from the IP averages 20 μm in both z and ϕ for hits on the inner 3 layers and 40 μm in z and 20 in ϕ for hits in the outer 2 layers. Before the summer 2002 shutdown there were 9 readout sections out of 208 that were not used in the *BABAR* Data Acquisition (DAQ). During the shutdown SVT was recabled and there was the possibility to inspect closely all the modules with problems. This allowed us to fix 5 of the 9 problems. The 4 sections that did never work did not have significantly impact on performances.

3.4.2 The Drift Chamber (DCH)

The DCH contains 40 layers of gold-coated tungsten-rhenium sense wires and gold-coated aluminum field wires in a mixture of 80% helium and 20% isobutane gas. There are a total of 7,104 sense wires and 21,664 field wires, with one electronic channel for each wire. Wires are tensioned (30 grams for sense wires, 155 grams for field wires) and pass through the aluminum endplates via feedthroughs made from Celenex insulating

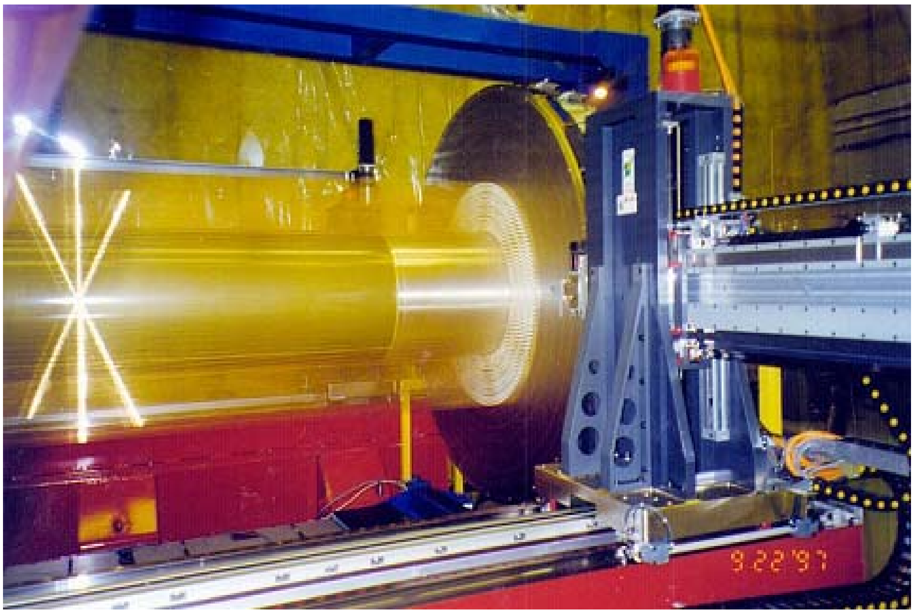

Figure 3.11: DCH wire stringing at TRIUMF (September 1997).

plastic around a copper wire jacket. The layers are grouped by four into 10 superlayers, with the wires in each superlayer oriented as either axial (directly parallel to the z-axis) or “stereo” (at a small angle in ϕ with respect to the z-axis, in order to obtain longitudinal position information). 6 of the 10 superlayers are stereo, and the other 4 are axial.[4] An image of assembled DCH is shown fig. 3.11. The DCH is asymmetric in z about the interaction point, as shown in fig. 3.12, to accommodate the forward boost of the center of mass of physics events.

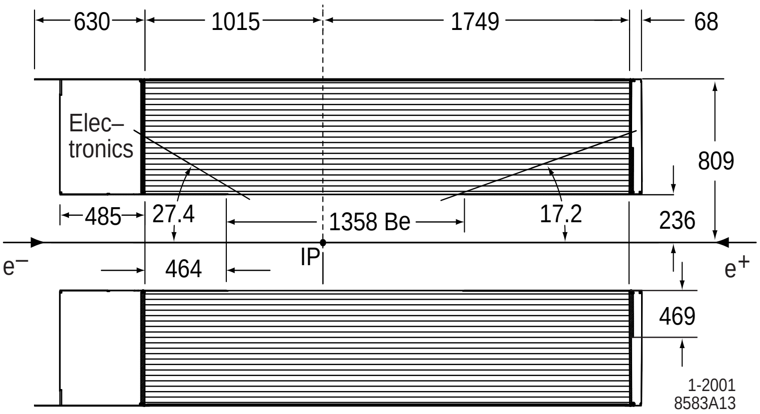

Figure 3.12: Longitudinal section of the drift chamber.

---

[4] The arrangement is, from inner to outer, AUVAUVAUVA (A = axial, U = u stereo ($+\phi$), V = v stereo ($-\phi$)).

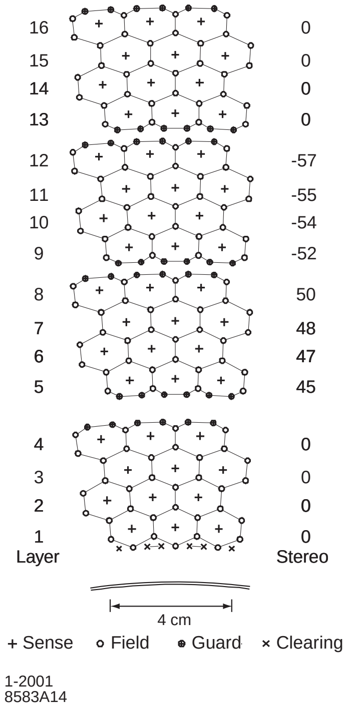

Figure 3.13: DCH cell pattern (for a section of the inner 16 [of 40] layers).

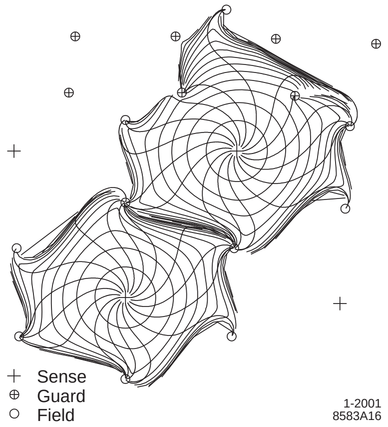

Figure 3.14: DCH cell drift isochrones for cells in layers 3 and 4 (axial). Isochrones are at 100 ns intervals.

The endplates are made of 24 mm thick aluminum, except for the outer 33.1 cm of the forward endplate, which is reduced to 12 cm to minimize the amount of material in front of the forward calorimeter endcap. The inner cylinder is fabricated in beryllium (to minimize the multiple scattering for the section of inner cylinder within the tracking fiducial volume) and aluminum (for the rest). The outer cylinder is 1.6 mm carbon fiber on 6 mm thick honeycomb Nomex core. The total thickness of the DCH is 1.08% X_0.

The cells are arranged in a hexagonal pattern, each with a sense wire at the center and field wires at the corners, as shown in fig. 3.13. Cells on a superlayer boundary have a slightly different arrangement, with two guard wires taking the place of a single field wire. The nominal operating voltage is 1930 V. Isochrones and drift paths, calculated using the GARFIELD simulation, are shown in fig. 3.14.

The DCH electronics are designed to provide accurate measurements of signal time and integrated charge (as well as providing information to the Level 1 Trigger, see sec. 3.4.6). Service boards plug directly onto the wire feedthroughs on the rear endplate. These boards distribute the high voltages as well as pass signal and ground to the front-end electronics assemblies. The front-end assemblies (FEAs) plug into the service boards and amplify, digitize, and buffer (for 12.9 μs) the signals. The digital data is sent, upon receipt of a level 1 trigger accept signal, via 59.5 MHz serial link to a data I/O module which transmits the signal to the external electronics via fiber-optic cable. Extraction of hit time and integrated charge from the digital waveform takes place in the readout modules (ROMs) in external electronics.

Online calibrations of channel gain and threshold were performed daily via internal pulse generation. The data were monitored online to check for FEA or other electronics failure or for miscalibrated output. Monitoring and control of high voltage, radiation protection (using silicon PIN diodes similar to the SVT, as well as RadFETs for integrated dose measurement), the gas system, and temperature were performed, similar to other subsystems, via a slow control system based on EPICS.

Offline calibrations of the time-to-distance relation within cells, as well as of the deposited charge used for particle identification via $\mathrm{d}E/\mathrm{d}x$ measurement, were performed. The time-to-distance relation was determined from two-prong events (Bhabha scattering events and dimuons) and was fit to a sixth-order Chebychev polynomial for each cell layer, with separate fits to right and left sides of wires (to account for $E \times B$ asymmetries). A correction for time-to-distance variations as a function of track entrance angle to the cell was determined via simulation (not calibration) and added to the calibrated entrance-angle-averaged relation. The design goal for the average drift distance resolution was 140 μm. An average resolution of 110 μm was achieved. The drift distance resolution as a function of drift distance could be seen from the offline monitoring plot shown in fig. 3.15 (left side).

The energy loss per unit length of tracks, $\mathrm{d}E/\mathrm{d}x$, contains particle type information due to the dependence of $\mathrm{d}E/\mathrm{d}x$ on particle velocity (Bethe-Bloch relation), and is derived from measurements of integrated charge deposited in each cell along the track path. An overall multiplicative correction to the charge measurements due to gas pressure and temperature variations was performed once per run; additional calibrations due to variations with track entrance angle in ϕ and in θ were performed only when high-voltage settings were changed. Particle identification using the drift chamber provides significant information up to high momenta, as can be seen in fig. 3.15 (right side).

Cell-by-cell channel efficiency was also monitored; typical efficiency was 90-95%.

3.4.3 The Čerenkov Detector (DIRC)

BABAR has stringent requirements for $\pi - K$ separation over a large momentum range. At the lower end of the range, primarily at momenta < 1 GeV, flavor tagging using kaons from cascade decays is an efficient way of determining B flavor. At the high end of the range, reconstructing $B^0 \rightarrow \pi^+\pi^-$ and $B^0 \rightarrow K^+\pi^-$ requires separation at momenta up to 4.2 GeV in the lab frame. At intermediate energies, $\pi - K$ is necessary to reduce background in charmless decays such as $B^+ \rightarrow \eta' K^+$. The particle identification device

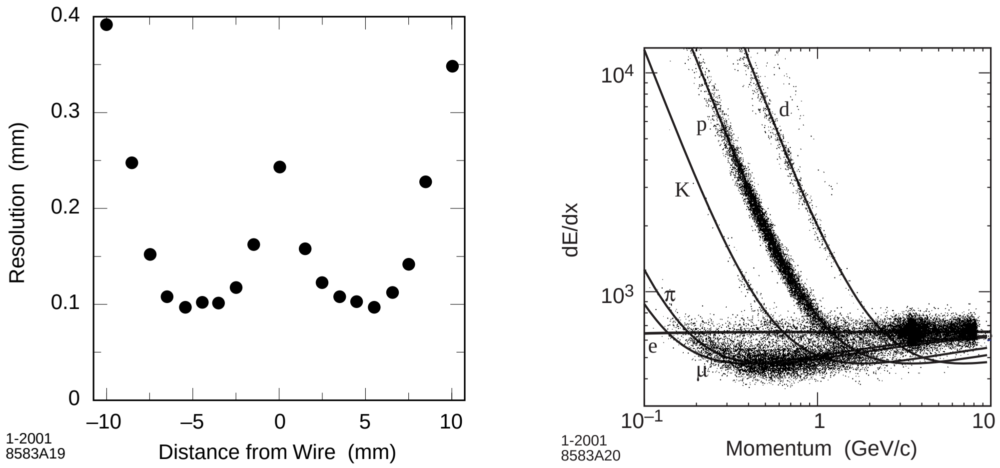

Figure 3.15: DCH drift distance resolution as a function of the drift distance in the cell (left); DCH particle identification as a function of momentum using $\mathrm{d}E/\mathrm{d}x$ (right).

must exhibit sufficient $\pi - K$ separation throughout this wide range of momentum with a minimum of material in order to avoid adversely impacting calorimeter resolution.

The DIRC (Detector of Internally Reflected Čerenkov light) principle uses internal reflection within quartz bars to propagate Čerenkov light to readout phototubes while preserving the Čerenkov angle. This requires extremely flat surfaces in order to avoid the dispersion of the reflected angles. Fused, synthetic silica quartz is used due to the excellent optical surface it allows through polishing, as well as other favorable properties such as long attenuation length, low chromatic dispersion, small radiation length, and radiation hardness. Schematic views of DIRC are shown in figs. 3.16 and 3.17. Figure 3.18 shows how the light is internally reflected down to a wedge to reflect photons into a water-filled “standoff box”. The standoff box (SOB) is enclosed by an array of 10752 photomultiplier tubes (PMTs), which are each 29 mm in diameter. The Čerenkov light from a particle passing through the DIRC forms a ring (essentially a conic section) imaged on the phototubes. The opening angle of this conic section contains information on particle type via the typical relation $\cos\theta_c = 1/(n\beta)$, with β being the particle velocity normalized to the speed of light, and n being the mean index of refraction ($= 1.473$ for fused silica).

Both efficiency and the timing of the electronics are critical for DIRC performance. Timing is critical for two reasons: first of all, for background hit rejection, resolving ambiguities, and separation of hits from differing tracks within an event; secondarily, timing gives information on the photon propagation angles, allowing an independent measurement of the Čerenkov angle. The intrinsic timing resolution of the PMTs is limited to 1.5 ns by transit time spread. Data from the phototubes are read out to front-end electronics, which performs the amplification, digitization, and buffering. Reduction of data from out-of-time or noisy PMTs was performed in in the external electronics and reduces the

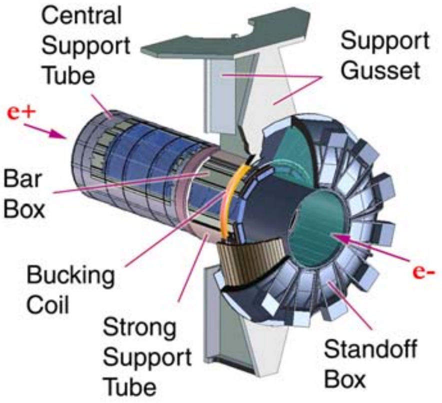

Figure 3.16: View of DIRC mechanical structure.

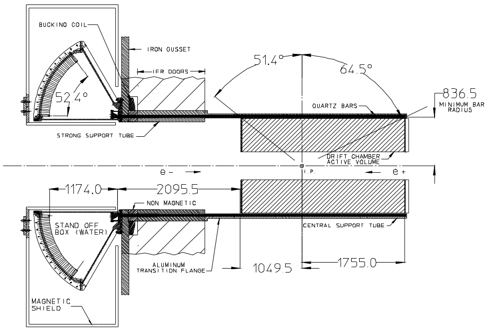

Figure 3.17: Longitudinal section of the DIRC. Length units are mm.

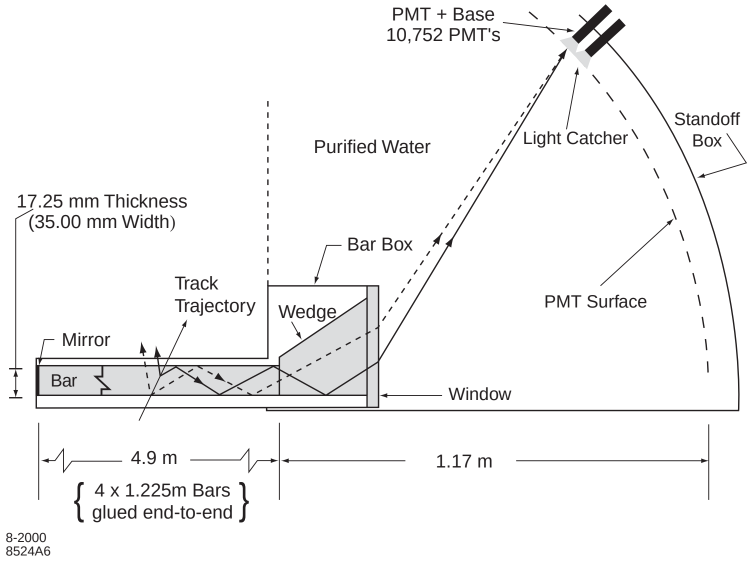

Figure 3.18: DIRC schematic showing the principle behind Particle IDentification (PID) measurements. The Čerenkov angle is preserved through specular internal reflection.

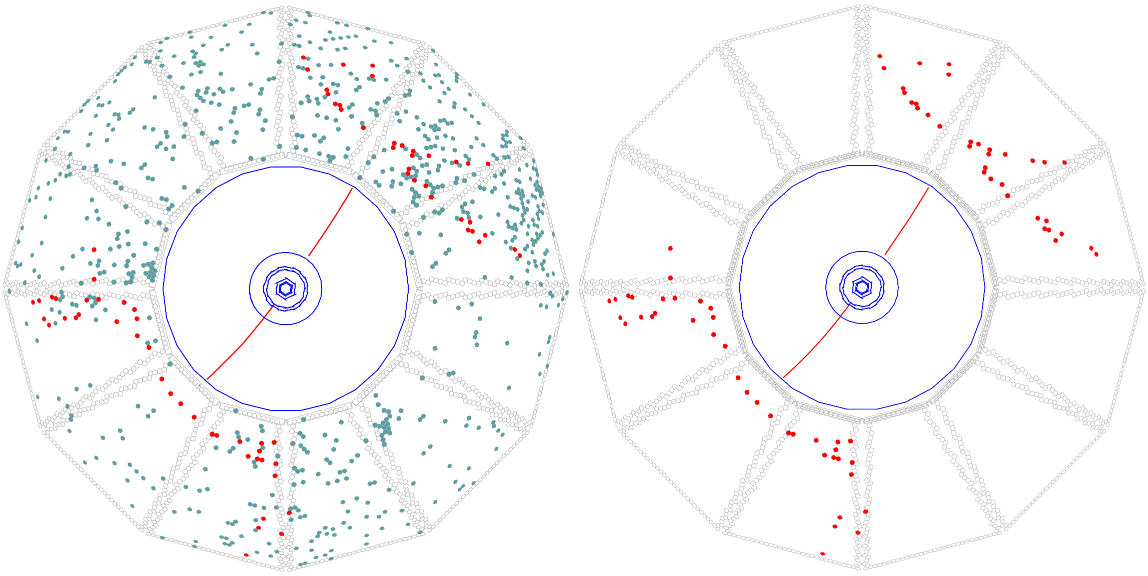

Figure 3.19: Display of an $e^+e^- \rightarrow \mu^+\mu^-$ event reconstructed in *BABAR* with two different time cuts. On the left, all DIRC PMTs with signals within the ±300 ns trigger window are shown. On the right, only those PMTs with signals within 8 ns of the expected Čerenkov photon arrival time are displayed.

data volume by 50% using rough timing cuts. Online calibration of PMT efficiency, timing response, and electronics delays used a light pulser system which generated precise 1 ns flashes from blue LEDs inside the SOB. In fig. 3.19 we show the effect of applying PMTs timing requirements to the DIRC output in a dimuon event.

The DIRC performed well throughout *BABAR*'s operational lifetime: 99.7% of PMTs were operating with design performance. The measured time resolution was 1.7 ns, very close to the intrinsic resolution of the PMTs. The Čerenkov angle resolution for dimuon events was 2.5 mrad, close to the design goal of 2.2 mrad. This resulted in $\pi - K$ separation at 3 GeV of 4.2σ. The distributions of the Čerenkov angle, as function of the momentum, for a sample of π and a sample of K are shown in fig. 3.20. The mean kaon selection efficiency and pion misidentification for a "loose" selection were 96.2% and 2.1% respectively, as can be seen in fig. 3.21. This results in dramatic background rejection with little signal loss , as may be seen in fig. 3.22 in the case of charm reconstruction.

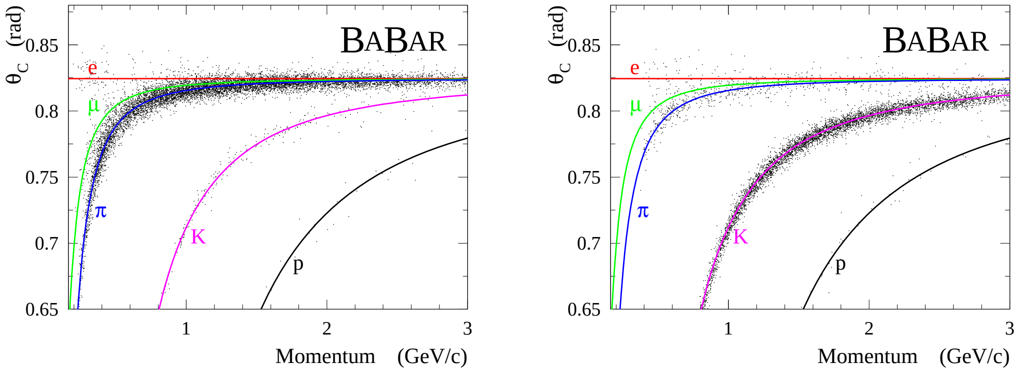

Figure 3.20: Čerenkov angle distributions, as function of the momentum, for a sample of π (left) and a sample of K (right). The samples come from the reconstruction of decay $D^{*+} \rightarrow D^0\,(\rightarrow K^-\pi^+)\,\pi^+$.

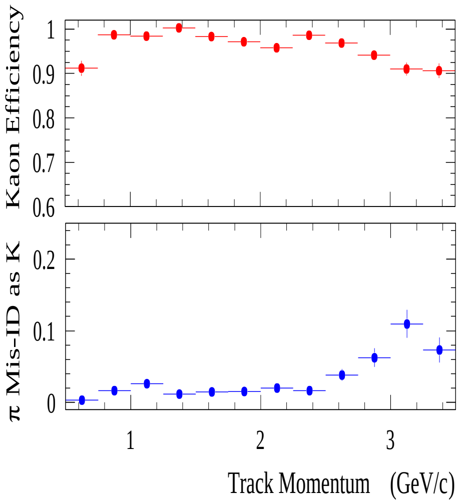

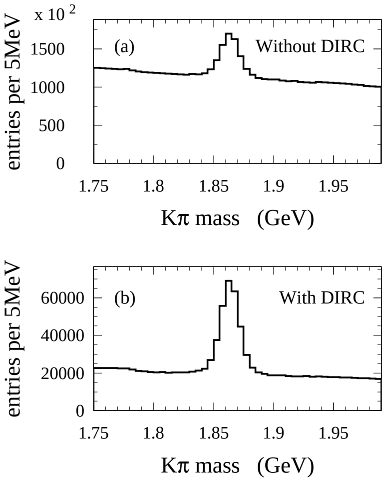

Figure 3.21: Kaon selection efficiency (top) and pion misidentification probabilities (bottom) as a function of momentum.

Figure 3.22: Inclusive $K\pi$ invariant mass spectrum (a) without and (b) with the use of the DIRC for kaon identification.

3.4.4 The Electromagnetic Calorimeter (EMC)

The design parameters for the *BABAR* EMC are driven by the requirements of precisely measuring energies over a spectrum from 20 MeV up to 9 GeV in a 1.5 T magnetic field and a high radiation environment. At the high end of the spectrum, measurements of QED processes such as Bhabha and two-photon scattering, as well as (at slightly lower energies) photons from the critical physics processes $B^0 \to \pi^0\pi^0$ and $B^0 \to K^*\gamma$ decays, present the motivating incentive. The need for efficient detection of photons from high multiplicity B decays containing π^0's determines the requirement for the low end of the spectrum. *BABAR* uses a thallium-doped cesium iodide (CsI(Tl)) crystal calorimeter in order to achieve the necessary energy and angular resolution to meet these physics requirements.

The EMC contains a cylindrical barrel and a conical endcap containing a total of 6580 CsI(Tl) crystals. The crystals have nearly square front and rear faces with a trapezoidal longitudinal cross-section. They range in length from 29.6 to 32.4 cm with a typical front face dimension of 4.7 x 4.7 cm. A diagram can be seen in fig. 3.23. The crystals are mounted in thin (300 μm) carbon-fiber composite housings which are mounted on an aluminum strong-back (see fig. 3.24). Although light incident on the crystal boundary is internally reflected, the small part that is emitted is reflected back with a coating of white reflective TYVEK on the outer surface. Surrounding that are thin layers of aluminum and mylar to act as RF shielding and electrical insulation respectively. On the rear face of the crystal, two 1 cm^2 silicon PIN diodes with quantum efficiency of 85% for CsI(Tl) scintillation light are mounted via transparent polystyrene substrate.

Each diode is connected to a low-noise preamplifier which shapes and amplifies the signal by a factor between 1 and 32. The signal is then transmitted to mini-crates at the

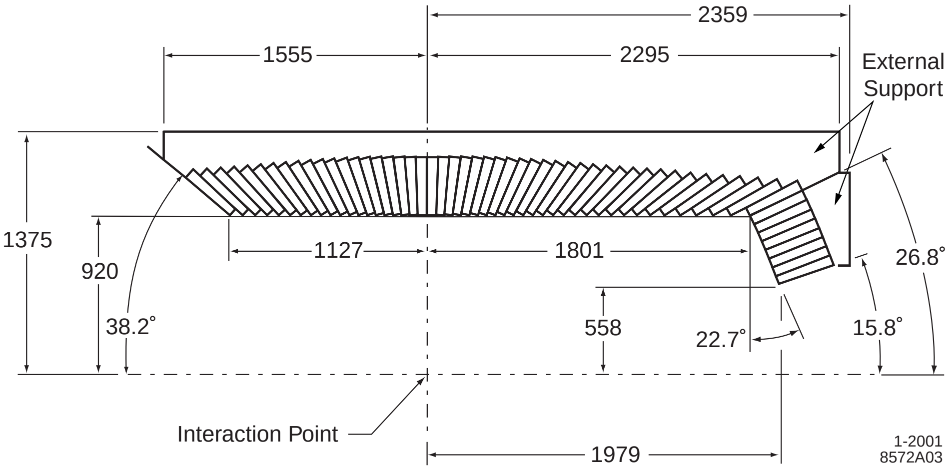

Figure 3.23: Longitudinal section of the EMC. Length units are mm.

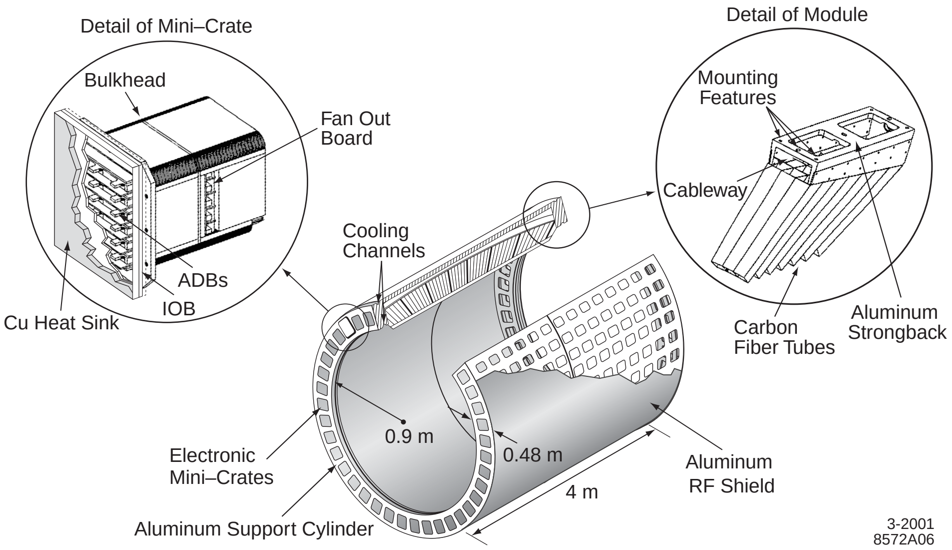

Figure 3.24: The EMC barrel support structure, modules, and mini-crates.

end of the barrel (see fig. 3.24) where a digitization CARE ("custom auto-range encoding") chip provides an additional variable amplification factor. Unlike other subsystems (except for the Intrumented Flux Return), the EMC does not buffer the data on front-end electronics; rather it outputs the full digital datastream to the read-out modules in external electronics, which perform, on receipt of a level 1 accept signal, a parabolic fit to the digitally filtered datastream to derive energy and time measurements.

A variety of online calibrations and checks were performed, including a neutron source which produced a monoenergetic 6.13 MeV calibration signal and a xenon flash light pulser system. Offline energy calibrations were necessary for higher energy corrections. The relation between polar angle and energy of Bhabha and radiative Bhabha scattering events was used to calibrate the 0.8-9 GeV range. The middle range was covered by π^0 calibration, which constrained the mass of a sample of π^0's to the known value, extracting correction coefficients.

The clustering pattern recognition used a seed crystal algorithm to establish energy clusters. Local energy maxima within a cluster were used (if there are more than 1) to separate the cluster into bumps. Charged particle tracks were associated with bumps using a χ^2 consistency cut. In a typical hadronic event, 15.8 clusters were detected, of which 10.2 were not associated to a track.

Energy resolution, using $\chi_{c1}{\rightarrow}J/\psi\gamma$ and Bhabha scattering events, was found to be

$$\frac{\sigma_E}{E} = \frac{(2.32 \pm 0.30)\%}{\sqrt[4]{E(\mathrm{GeV})}} \oplus (1.85 \pm 0.12)\% \tag{3.5}$$

and angular resolution, using π^0 and η decays, was found to be

$$\left(\frac{3.87 \pm 0.07}{\sqrt{E(\mathrm{GeV})}} + 0.00 \pm 0.04\right) \text{mrad}. \tag{3.6}$$

As can be seen in fig. 3.25, the reconstructed π^0 average width was 6.9 MeV. The EMC allowed a good separation between electrons and charged hadrons using the ratio of shower energy to track momentum (E/p) and other variables which describe the shower shape. These last variables were also used to discriminate K_L^0 mesons from photons.

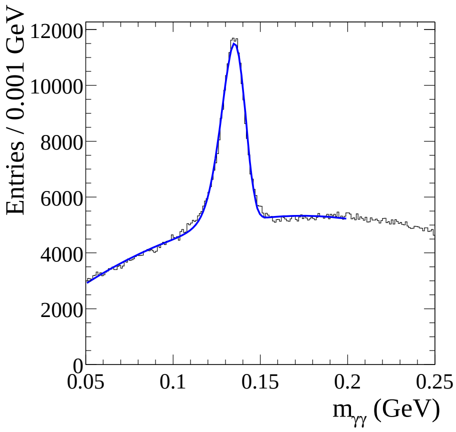

Figure 3.25: Two photon invariant mass, using photons between 30 and 300 MeV.

3.4.5 The Instrumented Flux Return (IFR)

Detection of neutral hadrons (primarily K_L^0's) and muons is necessary for several *BABAR* analyses and analysis techniques. Muons provide a very clean B flavor tag, extremely useful for increased efficiency in tagging the opposite-side B for time-dependent CP violation measurements. Muons are also necessary for reconstructing $J/\psi \rightarrow \mu^+\mu^-$, as well as for measuring semileptonic branching fractions, required for extracting magnitudes of CKM elements. K_L^0 reconstruction is critical for the $B^0 \rightarrow J/\psi K_L^0$ and $B^0 \rightarrow \eta' K_L^0$ channels. Initially, *BABAR* used an Instrumented Flux Return (IFR) composed of layers of resistive plate chambers (RPCs) and steel plates in order to provide enough material to separate pions and kaons from muons and to efficiently detect the presence and position of both μ and K_L^0 over a large solid angle. Due to some inefficiencies of some RPCs, during Summer 2004 shutdown a part of the RPCs of the barrel region (see fig. 3.26) has been replaced with plastic Limited Streamer Tubes (LSTs).

As shown in fig. 3.26, the IFR consists of layers of planar RPCs/LSTs in a barrel and endcap [5] (red lines) as well as 2 layers of cylindrical RPCs (green lines) between the EMC and the magnet. Between the RPC/LST layers are steel plates of thickness varying between 2 cm (inner plates) to 10 cm (outer plates). The total mass of the IFR is 870 metric tons.

Planar RPCs contain a 2 mm Bakelite gap with $\sim$ 8 kV across it. Ionizing particles which cross the gap create streamers of ions and electrons in the gas mixture (which is typically 56.7% Argon, 38.8% Freon, and 4.5% isobutane) which in turn creates signals via capacitive coupling on the “x-strips” and “y-strips” on opposite sides of the RPC. Strip width varies between 16 mm and 38.5 mm. The 2 mm gap is kept constant using polycarbonate spacers spread at 10 cm intervals and glued to the Bakelite. The Bakelite surface is smoothed with an application of linseed oil. Cylindrical RPCs are composed of a special thin and flexible plastic, rather than Bakelite, and have no linseed oil or other surface treatment. They are laminated to cylindrical fiberglass boards.

A “standard” LST configuration consists of a silver plated wire 100 μm in diameter, located at the center of a cell with 9x9 mm^2 section. A plastic (PVC) extruded structure, or “profile”, contains 8 of such cells, open on one side, as shown in fig. 3.27. The profile is coated with a resistive layer of graphite, having a typical surface resistivity between 0.2 and 1 MΩ/square. The profiles, coated with graphite and strung with wires, are inserted in plastic tubes (“sleeves”) of matching dimensions for gas containment. The signals for the measurement of one coordinate can be read directly from the wires, but it has become customary instead to read both coordinates with strip planes, thereby avoiding the complications of feedthroughs and DC-blocking capacitors. For such tubes the operating

---

[5] In the endcap regions there are only RPCs.

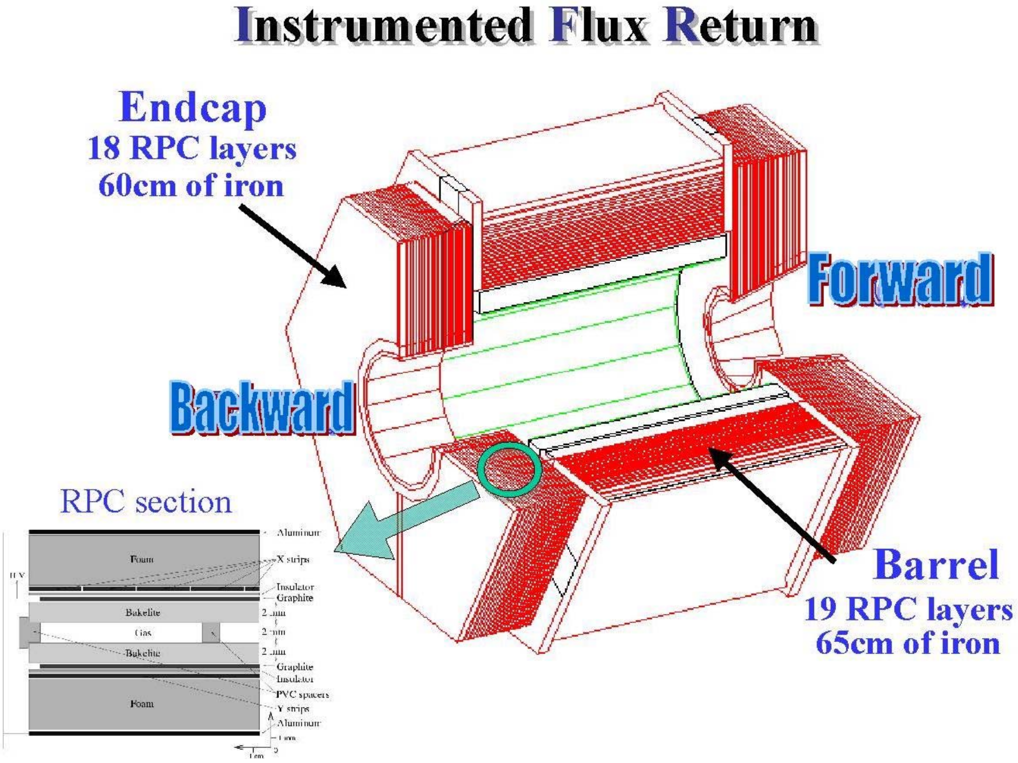

Figure 3.26: The instrumented flux return modules, structure, and RPCs/LSTs.

voltage is typically 4.7 kV; the efficiency plateaus are at least 200 V wide; the signals on the wire are of the order of 200/300 mV (into 50 Ω), typically 50 ns at the base, sometimes with an afterpulse. The gas mixtures are strongly quenching: the original one (25% Ar, 75% n-pentane) being explosive has been replaced in accelerator use by a non-flammable one based on CO_2. The LST geometrical efficiency is limited by the ratio of active versus total volume in the cell. The effect is mitigated by the fact that most tracks do not impinge perpendicularly. If the gap between iron slabs is wide enough, the inefficiency can be greatly reduced by using larger cells or, alternatively, a double-layer geometry.

The RPC strips are connected to front-end cards (FECs) containing the amplification and digitization electronics, which are primarily sandwiched between the iron plates. FECs shape the signal and perform a comparison with an adjustable threshold. For LST, instead of recycling the existing FECs, it was decided to build new FECs. These FECs have a different input section but with the same interface to the existing IFR-FIFO boards, which is used for the readout of the LST's and are well integrated in the DAQ. The data format is the same as in the RPC system. This choice allowed us to use the present DAQ software and electronics also with the LST system. Compared to the RPC FECs, two new functions are provided: front-end amplification and a settable threshold.

Similar to the EMC, the IFR does not buffer its data on the detector, so the full digital

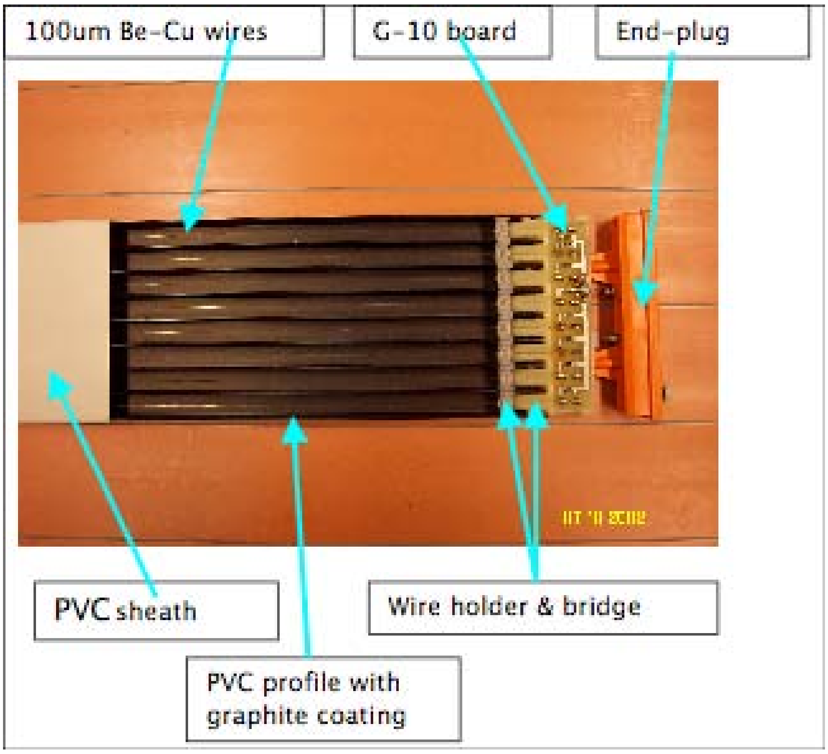

Figure 3.27: Photo of a standard LST, partially inserted in the sleeves.

datastream is output to front-end crates (located beside the detector) which contain TDC timing as well as buffering and calibration electronics. Data is read out to the ROMs on receipt of a level 1 accept signal. Online calibration was performed using test pulse generators integrated in the front-end crates. Offline efficiency calibration was also necessary for muon ID (in order to determine the expected hits for the muon hypothesis), and this was done using cosmic rays.

Reconstruction of clusters proceeded via two methods: a standalone method where groups of hits along 1 dimension within a module were joined to form one-dimensional clusters, which were then combined with opposite-side hits to form two-dimensional clusters, and then with other modules to form 3D clusters; and a “swimmer” method, where charged tracks were propagated to the IFR — 1D clusters within 12 cm of the expected path were combined to form 2D or 3D clusters. Clusters which were not matched to a charged track were considered as neutral clusters. Muon identification used variables such as number of expected vs. actual interaction lengths transverse and the χ^2 match to the charged track.

3.4.6 The Trigger

The *BABAR* trigger needs to provide high efficiency that is well-understood and stable for physics events. Since the events which pass the trigger must be fully reconstructed in the offline event reconstruction, the output rate must be no higher than 120 Hz to satisfy computing limitations of the offline processing farm. Since events with either a DCH track or a $> 100\ \mathrm{MeV}$ EMC cluster occur at 20 kHz, the trigger is responsible for scaling this rate down by a factor of > 150 while accepting over 99% of B events, over 95% of hadronic continuum, and over 90% of $\tau^+\tau^-$ events. Taking a look at tab. 3.2, one can easily convince that the most that the trigger cut are Bhabha and dimuon events. It also must be flexible enough to deal with changing background conditions, as this can happen at any given time at *BABAR*, without impact on physics or increase in online dead time (which must be $< 1\%$). The *BABAR* trigger is implemented in two levels, a Level 1 hardware trigger (called L1), and a Level 3 software trigger (called L3); a Level 2 trigger is used in some other high energy particle physics experiments, but was not needed for *BABAR*.

The L1 Trigger consists of four subsystems: the Drift Chamber Trigger (DCT) a trigger for charged particles, the Calorimeter Trigger (EMT) for neutral particles, an IFR Trigger used for calibration and works as cosmic trigger (IFT), and global electronics for producing the final L1 accept signal (GLT stands for Global Level Trigger). A scheme of the L1 Trigger is shown in fig. 3.28. The DCT is further subdivided azimuthally into track segment finders (TSF), a binary link tracker for producing tracks from the segments (BLT), and a p_t discriminator (PTD). The 24 TSF modules sample each DCH cell in axial layers for signals every 269 ns (64 clock ticks of the PEP-II-*BABAR* 4.2 ns clock interval). The DCT and EMT receive information from the DCH and EMC detectors, respectively, process it, and send condensed data to the Global Trigger.

The axial DCH cells are arranged into 1776 “pivot groups” (see fig. 3.29) and segments are constructed from hits within a pivot group. The cells in a pivot group are numbered 0 through 7, as shown in fig. 3.29 (cell 4 is the pivot cell). Note that if the pivot group template (the black circles in the figure) were to move one cell to the right, a new pivot cell (cell 4a) and a new pivot group would be defined. In the first version, only axial layers were used to avoid the complication of accounting for stereo layer within hardware electronics. Since 2004, the DCT Trigger has been upgraded with a new system which performs 3D tracking using stereo wire information from the DCH to obtain ~ 4 cm resolution in track z (along the beamline) coordinates of tracks to improve background rejection. Each cell contributes a 2 bit quantity (containing very rough information on the time, as well as the presence, of a hit on that cell) per sample, thus each pivot group outputs 16 bits. The TSF look-up table then determines if a given 16-bit quantity corre-

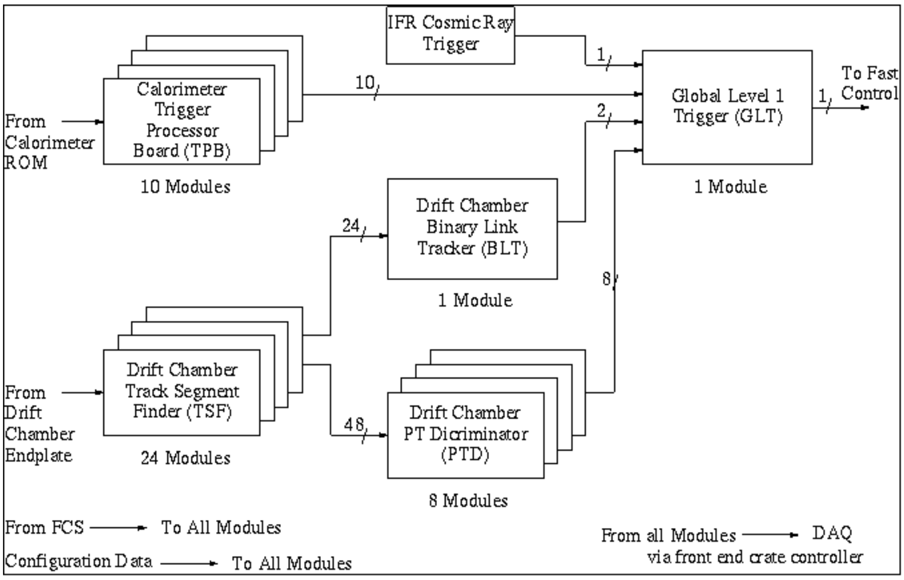

Figure 3.28: Trigger L1 scheme.

sponds to a valid segment or not. The binary link tracker (BLT) receives this information and determines whether segments lie in a road defined by “supercells,” which are sectors of a superlayer covering to 1/32 of the DCH in ϕ. Patterns of segment-containing supercells that appear to correspond to tracks (according to the BLT look-up table) are output to the L1 global Trigger. In parallel with the BLT, the p_t discriminator (PTD) checks TSF segments in axial superlayers to see if they are consistent with a track having a greater p_t than a configurable minimum cutoff value. This information is also output to the GLT.

The L1 Calorimeter Trigger (EMT) divides the EMC into 280 “towers” of 24 crystals each (22 for the endcap). All crystal energies within a tower which are above a 20 MeV threshold are summed and supplied to the EMT Trigger processor boards (TPBs). The TPBs digitally filter the energy deposition (to smooth the output waveform of noise) and compare neighboring towers to look for clusters which span more than one tower. Trigger line “primitives” (bytes corresponding to trigger type and information) are output to the GLT corresponding to the energy and placement of found clusters.

The GLT attempts to match the angular locations of calorimeter towers and drift chamber tracks, and flexibly generates L1 Triggers and sends them on to the Fast Control and Timing system (FCTS), based on the results of the processing. The GLT also uses the IFT information to independently trigger on cosmic ray and mu-pair events. The L1 trigger rates are typically 2.5 kHz at a luminosity of $L = 8 \times 10^{33}$cm^{-2}s^{-1}. The various stages of the L1 system operate at 4 MHz to 15 MHz intervals with a total L1 Trigger latency of $\sim 11\mu$s. The combined L1 Trigger efficiency is $> 99.9\%$ for generic $B\overline{B}$ events, 99% for continuum, and 94.5% for $\tau^+\tau^-$ events.

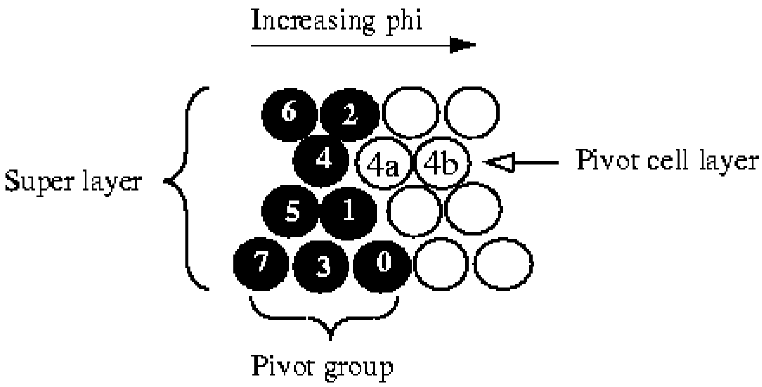

Figure 3.29: Showing the definitions of pivot cell and pivot group. Numbers indicate the cell number within a pivot group; the pivot cell is number 4. 4a and 4b indicate adjacent pivot cells.

The L3 Trigger analyzes the event data from the DCH and EMC sub-systems in conjunction with the L1 Trigger information to further reduce background events. An event display reconstruction from L3 Trigger is shown in fig. 3.30. The L3 DCH algorithm fits L1 tracks to helices and is able to determine the z_0 of tracks, which is important information for rejecting background. The dominant source of events accepted by L1 is beam-gas or beam-wall interaction background, as well as cosmic rays, which can be separated from physics events using the point of closest approach of tracks to the interaction point (IP). L3 Trigger also performs Bhabha veto, selection of various calibration events and critical general online monitoring tasks. The L3 operates on an online farm which consists of 28 Dell 1650 (dual Pentium-III 1.4 GHz) computers with fast algorithms processing at $\sim$4 ms per event. The L1 Triggers are reduced by typically a factor of ~ 20 after the L3 filtering, before logging to the data storage system.

3.4.7 Track Reconstruction

Complete reconstruction of B decays (in addition to other major *BABAR* analysis techniques, such as tagging) requires precise and efficient charged particle tracking. As will be seen later, separation of B decays from combinatorial background requires precise determination of mass and energy, which in turn requires precision measurement of track momentum. Data from the SVT and DCH is combined to satisfy the stringent charged particle tracking requirements of *BABAR*.

Charged tracks are parametrized by the 5 variables $d_0, \phi_0, \omega, z_0, \tan\lambda$ and their error matrix. The parameters are defined as: d_0 is the distance of the track to the z-axis at the track's point of closest approach to the z-axis, z_0 is the distance along the z-axis

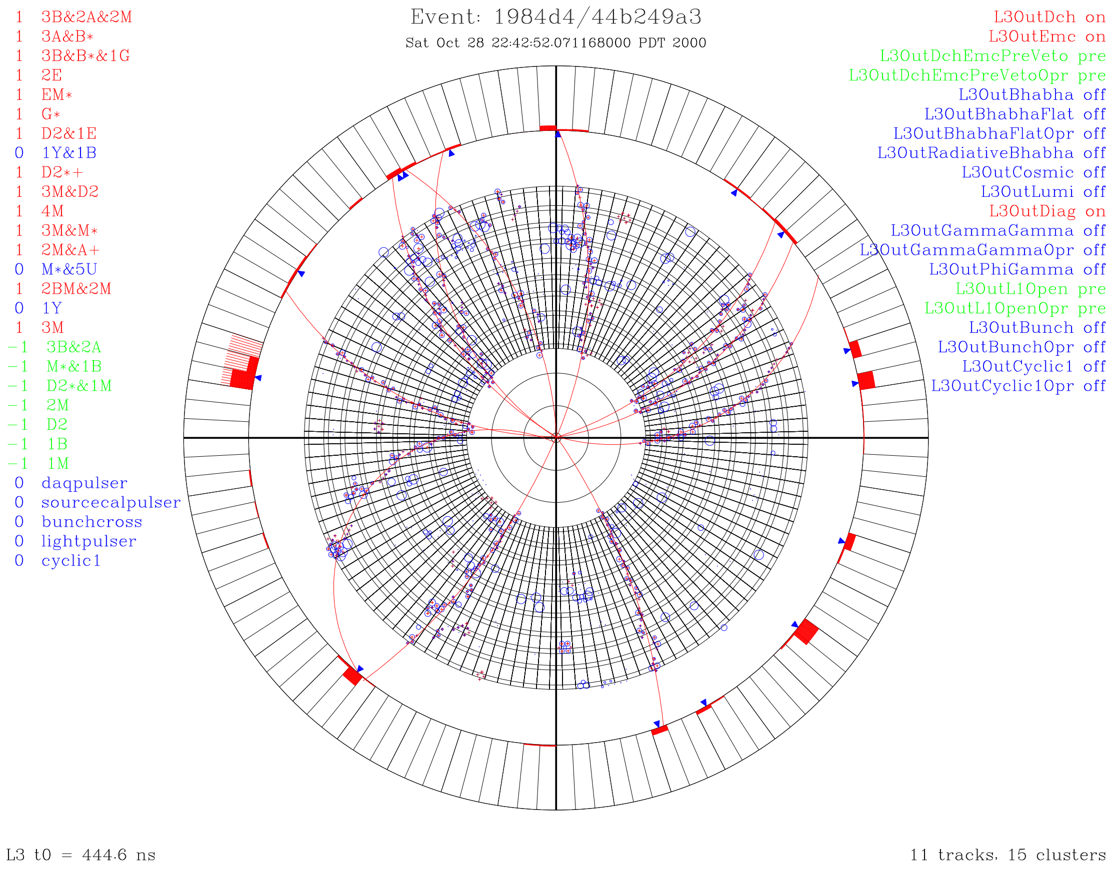

Figure 3.30: A L3 Trigger event display for a multihadron event.

of that point to the origin, ϕ_0 is the azimuthal angle of the track at that point, λ is the dip angle with respect to the transverse plane, and ω is the curvature of the track and is proportional to $1/p_t$. After tracks are recognized by the pattern recognition algorithms, these 5 variables are fitted, and error matrices are extracted.

Offline track reconstruction begins with tracking and event time information from the L3 trigger. L3 trigger provides both tracks and an estimate of the time at which the interaction occurred (with a resolution of approximately 5 ns), referred to as the t_0.[6] Reconstruction continues by building track segments of 4 hits on four layers within a superlayer and using a linear fit to estimate and improve the L3 t_0 to a precision of about 3 ns. Next, the level 3 DCH tracks are refitted using the more precise offline time-to-distance calibration and placed on the list of reconstructed tracks. The t_0 value is refined further (to 3 ns resolution) by finding the best t_0 fit to the tracks themselves. Following that, two additional DCH track pattern recognition algorithms are run which select tracks with hits not used in L3 tracks. The t_0 is improved again (to < 2 ns resolution) using these

---

[6] The e^+e^- interaction time is referred to as the “bunch t_0,” often shortened to “t_0.”

extra tracks. The DCH tracks are then fit using a Kalman filter algorithm. DCH tracks are then extrapolated into the SVT via a hit-adding algorithm, and then two standalone SVT track pattern recognition algorithms add any remaining SVT tracks. Finally, SVT tracks are extrapolated into the DCH to pick up any remaining DCH hits. This sequence will be discussed in detail in the following subsections.

t_0 Reconstruction

Reconstruction of the event interaction time, or t_0, is necessary for both fitting DCH tracks (since the DCH time-to-distance relation is necessary for position information of a track within a given cell, a time must be provided as input) and for rejecting out-of-time hits within the SVT to reduce background. t_0 reconstruction takes place in several steps, iterated with track pattern recognition since the two are interdependent, during offline reconstruction.

The initial measurement of the event time is provided by the L1 Trigger in hardware electronics. The L1 trigger looks for track segments in the DCH and clusters in the EMC, and sends an accept that includes all data in each subsystem latency buffer to be read out. The trigger timing is tuned such that this buffer typically starts about 450 ns before the event, with a resolution of about 50 ns. That estimate, with an error of approximately 50 ns, forms the first event t_0 estimate. The L3 Trigger uses the level 1 DCH segments and a fast, rudimentary time-to-distance function to fit tracks. The fit produces an event time measurement that is accurate to approximately 5 ns. This estimate is then given to offline reconstruction as input.

Offline t_0 reconstruction begins with the DCH segment-based t_0 finder. Four consecutive hits on adjacent layers within a superlayer form a DCH segment. A t_0 value is fitted for each segment such that the corresponding isochrone on each cell is tangent to a line segment passing through the superlayer. This requires a 3×3 matrix inversion corresponding to the two parameters of the line segment in addition to the t_0. The event t_0 estimate must then be obtained by combining these fitted segment t_0s. There are several different segment cell patterns corresponding to different angles of the track through the superlayer, and segments are weighted according to type (highly-angled segments give lower-quality information than radial ones, since they tend to be from lower-momentum tracks). The segment t_0's are sorted according to time and the weighted average is taken of the middle third of this list. Using only the middle third provides robustness against out-of-time background segments. The weighted average segment t_0 is used as input to the Level 3 track converter, which then outputs a list of tracks to the event.

The tracks are then used to provide a more precise estimate of the t_0 using the DCH track-based t_0 finder. The DCH track-based t_0 finder takes a list of tracks as input and finds the best fit t_0 from the list of tracks. For each track, an average of the time residuals from each hit, weighted by the error on the residual taken from the time-to-distance resolution function, is calculated. This average is then added to the prior t_0 estimate in order to obtain the best-fit t_0 from that track, along with its associated error. The weighted average of these track t_0s is then taken, with the track t_0 with the largest χ^2 from the initial average dropped from the final average (for robustness against the occasional background track). This forms the track-based event t_0.

The track-based t_0 is calculated once after both the offline L3 track converter and the first DCH pattern recognition algorithm have run, and again after the two additional DCH pattern recognition algorithms have run. The final DCH t_0 is used for all final track fits and is provided to the DRC for background rejection, after which the DRC is able to refine the t_0 further.

Track Fitting

BABAR tracks are exact helices but for 3 effects: multiple scattering, energy loss in material, and inhomogeneities in the magnetic field. Although these effects are fairly small in *BABAR* due to the small amount of material in the tracking volume and the $< 5\%$ inhomogeneities in the field, they nevertheless are important for the level of precision needed for accurate Δz and vertex fit quality. Thus a Kalman filter is used to propagate tracks accounting for each of those three effects and create a piecewise helix trajectory. For initial fits (and for input to the Kalman algorithm), a simple helix fit will suffice. Track fitting is done using both helix fits (for initial fitting) and a piecewise-helix Kalman fit algorithm (for the final fit). The DCH and SVT standalone track fitters (and DCH-specific hit-adder) use a helix fit for the initial fit which is replaced by a Kalman fit later in reconstruction, whereas the DCH $\rightarrow$ SVT and SVT $\rightarrow$ DCH hit-adders are integrated with the Kalman fitter to perform a piecewise helix fit as the hits are added.

The helix fit algorithm performs a least-squares fit to a list of hits. It assumes the weight matrix is diagonal, *i. e.* that the hits are uncorrelated. The fit iterates and removes the hit with largest “pull” (residual divided by error) on each iteration if it lies more than 3 sigma from the fit. Removed hits which return to within 3 sigma after an iteration are added back. Convergence occurs either when the change in total χ^2 is less than 0.01 or if the fit reaches 12 iterations. If the latter occurs before the former the fit is considered failed.

The Kalman fit takes into account the effects of material and inhomogeneous magnetic field to create a piecewise helix fit. The parameters of a track can be transformed into “weight space” where:

$$\gamma \equiv C^{-1}, \quad \beta \equiv \gamma P \tag{3.7}$$

where P is the vector of 5 track parameters (taken as input from a preliminary helix fit) and C is the corresponding covariance matrix. The effect of adding a hit on these parameters is:

$$\gamma_H \equiv L^T w^2 L, \quad \beta_H \equiv L^T w(LR - r) \tag{3.8}$$

where r is the residual of the hit, R is the hit position, and $L \equiv \frac{\delta r}{\delta P}|_R$. These act as additive corrections to the weights:

$$\gamma_{new} = \gamma_{old} + \gamma_H, \quad \beta_{new} = \beta_{old} + \beta_H \tag{3.9}$$

These are the Kalman filter equations.

Performing the fit in weight space also allows for simple equations describing magnetic field inhomogeneities, energy loss, and multiple scattering. The materials and magnetic field map are kept in the *BABAR* conditions database (the database used for storage of detector calibration constants) allowing for their use directly in the fit. Both an inwards and an outwards fit are done, with the final weights β and γ being the sum of the inner and outer fits (this is referred to as “smoothing”). A resolution of $\sigma(p_t)/p_t = 0.13\% \times p_t + 0.45\%$ is obtained.

In early 2007 *BABAR* Collaboration developed a great improvement to the tracking software, named `TrkFixup`. After the effort of reprocessing the whole dataset, the final gain in efficiency is as high as 50% in modes with a great number of charged tracks. `TrkFixup` consists of two main parts. `TrkFixupSequence` contains modules designed to work on the reconstructed track objects (`TrkRecoTrk`), each addressing a particular problem or issue with the tracks found in reconstruction. They achieve better performance than `BtaCandidate`-level equivalent algorithms by making use of the full Kalman fit and the individual hits information available, which weren’t used previously due to the fact that the software was designed when the real performances of the detector were unknown. `TrkFixupSequence` starts by assembling basic information about the event such as finding the primary and secondary vertexes. The `TrkListSplit` module then pre-selects tracks which have characteristics suggestive of the problems or features which the subsequent `TrkFixup` modules are designed to address. Pre-selected tracks are placed on the *Work* list, which is the input to all subsequent modules. All tracks not pre-selected are placed on the *Good* list, and are subsequently ignored. `TrkListSplit` also *promotes* all the tracks on the *Work* list to have a full Kalman fit, using all the hit information stored to rebuild essentially the same `TrkRecoTrk` object as was present in reconstruction. This enables the subsequent modules access to the full reconstruction information. So the effect of `TrkFixup` is to perform specific operation on tracks that are “difficult” to be reconstructed, in order to reject ghost tracks and keep real track with a higher performance with respect to previous software. Among the various operations that were improved with `TrkFixup`, the most important are:

- Determination of primary and secondary decay vertex;
- Improvement of resolution of tracks by adding previously unused hits
- Rejection of *ghost pairs*, *i.e.* two reconstructed tracks which correspond to only one real track.
- Rejection of tracks generated by interaction with the detector material
- Decay-in-flight identification

3.5 *BABAR* Software

In this chapter we will present *BABAR* framework and software tools used during this thesis work. This section includes a presentation of the simulation and the reconstruction programs used in *BABAR* collaboration.

The *BABAR* software system includes two parts: *online* system (data acquisition, checking and monitoring) and *offline* system (reconstruction, simulation and data analysis). It is implemented on PC with commercial Unix operative systems (SunOS e OSF/1) and Linux.

3.5.1 Programming Choices

The software used in the *BABAR* experiment is developed using *Object Oriented* programming [81] implemented on Unix machines.

There is a big choice of object oriented programming languages; among all possibilities, the *BABAR* collaboration has chosen the C++ [82] for its specific demands, like large availability for compilers, distributed with free open-source licenses, compatibility with different platforms, efficiency of the code and tools for development and debugging, and large availability of libraries.

Object Oriented Programming

The main feature of object oriented coding can be simplified through an analogy with real world: utilization of an object is not linked to knowledge, for an user, of its internal operation. For example, driving a car do not need to know how engine is made and how it works, but this (substantial) difference doesn't influence our driving. This is an example of separation between *what* an object offers in functionality terms and *how* it realizes this functionality; the way to interface with an user should be constant in the time, but system can be modified, expanded and optimized. This feature is fundamental in complex software system codes, as what used in *BABAR*.

In C++, the tool that allows us to use object oriented programming is the *class*, data type defined by programmer; it is composed by a public interface that gives us functions to operate on contained data, and a hidden, private, structure that typically includes both internal representation of data and utility functions to operate on themselves. This way to hide the effective implementation is called *encapsulation* and it's typical for object oriented programming. So, classes can be thought as boxes that speak each other with messages: we can operate on data for a class (that is most the interesting thing for an user) only through some function in public interface; these functions are called *methods*. Such a way to operate can give us some advantages because we can shield data from illegal operations and verify finished operations (*e. g.*, verification on variation interval of a quantity, as in data input stage). Furthermore, it allows a re-utilization of the code (*e. g.*, a set of classes to operate on vectors and matrices with usual addition and product operations) and it reduces the development and software debugging times.

Another object oriented feature is *objects hierarchy*, which we can illustrate with a real world example: it's possible to define some abstract data types with certain base properties; in fact we are able to think to abstract objects, like a particle, and to derive from these other objects with more definite properties, "boson or fermion?". Continuing in this hierarchy, we can specify more detailed properties, "if fermion: lepton or quark?" and reach up for more internal levels maintaining base class properties, leaving them as before or modifying parts of them. This feature is called *heredity* and we can have single heredity (if it is derived by only one more base class) or multiple heredity (if derived by more classes).

The third concept of object oriented language is the *polymorphism*, which is strictly linked to heredity. This is the language ability to use some specific objects (derived by more basis classes) as generic class objects. For example, it would be possible to have a list with all particles with a fixed momentum, independently if they are bosons or leptons, and to use them in a uniform way (for a fixed particles class definition). This propriety is typical of the containers, like lists of objects.

3.5.2 Code Organization

The *BABAR* software is accessible to all registered users through NFS system file (*Networked File System*) or AFS (*Andrew File System*), mounted on every UNIX workstation at SLAC. The scheme is replied in all computing labs in the countries that collaborate to the experiment: USA, France, England, Italy and Germany.

BABAR Framework

The *BABAR* software is organized like a framework for the reconstruction of events recorded by the detector. To figure out what programming inside a framework means, it's possible to compare it with reality: in every home we find water, electricity, telephones, etc. and these services are supplied without worrying about how they are realized. The full set of the services is the framework.

In software engineering, a framework supplies base services, like I/O, graphic management, data scheme management. The obvious advantage is: low-level function problems have already been solved and generally in a very efficient way with few faults. So, the user can only work in his specific domain; by this way, a re-use of the code is favored (a well written code can be re-used to solve similar problems even if not identical).

Package

The *BABAR* framework is completely modular, and his base element is the *package*, defined as a set of classes planned to solve certain specific common problems (for example a selectors package, where his classes are planned to assign a specific identity to a candidate particle). In every package we can find classes with same tasks, that differ for chosen approach or chosen operative technique.

Many dozens of packages are available, to cover a large spectrum of possibilities and requests coming from events reconstruction and analysis.

Release

We define *release* the set of all packages, each defined in his specific version. If packages are updated with new classes, releases are updated with new packages. Particularly, we can distinguish releases in two kinds: testing releases for code implementation and testing and stable releases used for official analyses.

Module

The *BABAR* framework base unity is defined as *module* and it can be either a class of a package or an user defined class based on other package classes. The modules hold code that draws data for every event, runs specific algorithms and it can eventually give back results that can be used in next phases.

An executable analysis program is formed by one or more compiled and linked modules; each of them can be enabled or disabled during execution if it is useful or not in data processing. Framework functionality management is left to TCL (*Tool Command Language*) language that has two features: it can interpret commands, so it can be an interface among user and framework, and it can be used as a scripting language to check exactly the operations for every module, in a similar way with a Unix shell. It can be used on many platforms.

Modules can be added in a *sequence* in which they are executed in the right order. Modules and sequences can be combined in a *path*, a completed sequence which begins with an input module and ends with an output module. The presence of particular filter modules can allow that a path will be finished before exiting and so a processed event won't reach output module. Multiple paths can be specified and each of them can be enabled or disabled.

3.5.3 Online System

The *BABAR* Online software comprehends detector check and monitoring systems, processes related to data flow, data acquisition and storage in database, and the run checking programs. These tasks are solved by main Online system components: *Data Flow*, *Run Control*, *Online Event Processing* (OEP) and *Prompt Reconstruction*. There is another component, *Detector Control*, but it is not joined to events acquisition: it checks software and hardware detector components (*e. g.*, for example DCH high tension system).

Online Data Flow (ODF)

The data acquisition system is composed by a software and a hardware component; the former is called *Data Flow*, the latter is called *Platform*. Often, we refer to both as *BABAR Data Flow*.

Data Flow has the task of joining all data coming from front-end electronics, processing them in a preliminary way (so called *feature-extraction*) and delivering them to OEP.

Main Platform elements are: checking masters that give the trigger interface, the distribute clock, and the command system; the read-out modules (ROM); particular modules that catch data from front-end electronics and execute feature-extraction; and the *bulk data fabric* which transports data inside-outside the platform. Every platform needs a clock and an external trigger system; it has 32 input lines for the trigger that produce L1 trigger acceptance signal (L1 accept). Then this signal is propagated to all the platforms. A platform can manage electronics for more than one sub-detector. By this way, the sub-detectors can't be independent if they are on a same platform, unless they are on different platforms. To maximize resources, such platforms are *partitioned*, so operations related to different sub-detectors are performed in parallel. Data Flow platform has been drawn considering rigorous conditions due to experiment for dimensions and events frequency. Components are organized in a hierarchy that permits to execute operations with a high-grade of parallelism.

Online Event Processing (OEP)

OEP receives completed events from Data Flow's Event Builder, executes L3 trigger algorithms, checks data quality through so called *Fast Monitoring* processes and develops other tasks as supporting functions to calibration activities. Furthermore, OEP provides avaliable events for the reconstruction to *Prompt Reconstruction*.

Work done by OEP is distributed among knots of a farm composed by Unix machines. On every machine are solved identical processes in parallel.

Prompt Reconstruction

The tasks of Prompt Reconstruction are to reconstruct, in short time, all events that passed L3 trigger filter and to furnish calibration constraints and information on data quality. This allowed us to diagnose immediately detector problems in such a way that they can be solved without losing integrated luminosity. In particular, this function was important in the preliminary phases of the experiment. Many calibration constraints, like pedestals and electronics component gain, were evaluated through special runs. Others, like DCH time-distance relationship and relative corrections of alignment between chamber and vertex detector, needed a large number of reconstructed events. Prompt Reconstruction receives these quantities from a previous (but recent) calibration, stored in the dataset, and applies them to current data. Generated constraints per every reconstructed events block are storage in the Condition Database to be read again during the following reconstruction block.

The Prompt Reconstruction results were monitored by *Prompt Monitoring* that checks, for example, DCH performances, data quality, and reconstruction and calibration algorithms of reconstruction. Unlike Fast Monitoring, Prompt Monitoring analyzed reconstructed events and has a large number of information on tracks.

3.5.4 Monte Carlo Simulation

Completed simulation of the detector is formed by three parts: events generation, particles tracing through the detector, and detector reply simulation.

Generators

Simulation process starts with event generation, using one of the available different generators: generator of $B\overline{B}$ events with the corresponding decay channels; generator of $q\bar{q}$, with $q = u, d, s, c$, background events; generator of e^+e^- diffusion events; and other backgrounds linked with accelerator operation. Furthermore, energies of beams and the interaction point position smearing are simulated. For each beam is used a Gaussian with width 5.5 MeV for the high energy beam, and 3.1 MeV for the low energy beam. Smearing for interaction point is 160 μm and 6 μm in the x and y coordinates, respectively, and it is simulated with a Gaussian distribution for each coordinate. The z beam position is modeled on a flat distribution 1 cm long.

Most important events generator for $B\overline{B}$ is EvtGen. This generator furnishes a scheme in which specific decay channels can be implemented as modules. Such modules, called EvtGen *patterns,* can solve different functions, *e. g.* they can evaluate decay amplitudes. EvtGen introduces the $B - \overline{B}$ mixing, generating $\Upsilon(4S)$ decays in a user defined proportion of $B^0\overline{B}^0$, $\overline{B}^0\overline{B}^0$ and B^0B^0 final states with correct Δt distributions. The CP asymmetries are generated with modules which modify the B mesons lifetime distributions.

Generic patterns to simulate two-body decays to combinations of scalar, vector and tensor mesons are available. There are also generic patterns to simulate three-body decays or radiative decays. Decay features (branching ratio, numbers of sons and patterns) are inserted in an ASCII file called `DECAY.DEC`.

Generator manages only exclusive final states; for quarks to hadrons fragmentation we use Jetset7.4, which is used for $q\bar{q}$ background generation and weak baryons decays. Jetset7.4 decay table has been updated to latest measurements.

BOGUS

BOGUS simulator (BABAR *Object-oriented Geant4-based Unified Simulation*), using Geant4 [83] package developed by CERN, provides an unified simulation, since it permits either a complete simulation or a faster simulation.

Geant4 includes tools to simulate detector geometry, charged and neutral tracks revelation through the detector, interactions and decays of every kind of particle, magnetic field and detector reply.

BOGUS is composed by several packages, one for each subdetector. Each one contains standard routines recalled in different simulation phases. Geometries of each subdetector are re-created starting from parameters hold in a format ASCII data bank, where materials, dimensions, positions, and orientations of every enabled and disabled subdetector are specified.

Monte Carlo tracks hits are called in the *BABAR* terminology *GHits*. These contain all needed information to obtain detector reply simulation in a second phase. Monte Carlo truth information and *GHits* are stored for next analyses.

Detector Reply

Tracks hits digitalizing happens in another process called *SimApp*. This process takes *GHit* input information and produces digitalized data as output in the same format of those produced by real detector. At the end of such a process, Monte Carlo data are processed by same code of real data. This code is organized like a subsystems packages set. These packages contain routines to give simulated data sample as most similar as data coming from detector. Another function of SimApp packages code is to add background hits: rather than simulate background in the detector, it is preferred to catch a random trigger sample and mix (using correct luminosity factors) them with Monte Carlo simulated events.

3.5.5 *BABAR* Database

The original *BABAR* Event Store used two data-storage formats: *Objectivity* database and *Kanga* (“Kind ANd Gentler Analysis”) datasets. In a second stage, *BABAR*’s data storage has changed to a completely new system. The new model is called *CM2* (“Computing Model 2”).

The Objectivity database was a large object-oriented database with several levels of detail stored for each event. It could be used for almost any analysis or detector study. The Objectivity database had four levels of detail: *raw*, *reco*, *micro* and *nano* (or "tag"). *Raw* and *reco* were very big databases that kept virtually all of the details for every event. The original idea was to keep *raw* and *reco* information for jobs like detector studies. They were infrequently used, and only a small part of the information was ever accessed. *Micro* was a smaller and more user-friendly database, where the information were more useful for physics analyses, rather than detector studies, or more refined analysis tasks. *Nano* ("tag") contained even less details, and was used only to skim data for few given key characteristics in order to save the loading time of the whole event information for each event (a time-consuming process).

The Kanga datasets stored only the micro level information in ROOT-type files (architecture for object oriented data analysis developed by CERN) [84]. This is the level of detail required for most physics analysis jobs, avoiding the complication of interacting with the full Objectivity database.

The idea was to have Objectivity as the main database, and use Kanga files at remote sites.

The new CM2 Event Store has just one database, the *Mini*. The *Mini* database is basically an extended version of the *micro*, however with the additional capability to store information written into "skims" by users (“user data”), *i. e.* user-defined composite candidate lists and user-calculated quantities. The *Mini* contains all of the information from the old *Micro* database, plus a small part of *Raw* and *Reco*.

The new data storage format is more like *Kanga* than anything else, so we may refer to the CM2 Mini database as "CM2 Kanga," "new Kanga" or (since old-kanga is obsolete) just "Kanga". In the tab. 3.10 we summarize the differences between the old Objectivity/Kanga system and the new CM2/Mini system.

	Old Objectivity/Kanga	**New CM2/Mini/Kanga**
Level of detail	Objectivity: high detail Old Kanga: low detail	Mini: intermediate detail
Portability	Objectivity: central Old Kanga: portable	Mini: central, but easily skimmed to make portable collections
User data	Objectivity: None (central database) Old Kanga: Lots (small, user-defined collections)	Mini: some user data in central database

Table 3.10: Differences between the old system database and CM2.

3.5.6 Reconstruction Software

We already gave prominence to packages as base element of *BABAR* software; in the following sections we will describe the main *packages* used for analyses presented in this thesis work.

`Beta` Package

`Beta` is a data analysis program developed for *BABAR*, and it is the base interface for data reconstruction. `Beta` main task is to furnish a solid and simple basement to write detailed physical analysis programs; to do that it gives the needed tools for particles identification, B flavor tagging, vertexes reconstruction, etc.

All the `Beta` structure, and so the reconstruction mechanism, is based on four fundamental concepts:

- *Candidate*. A candidate is the representation that `Beta` gives to the particle that could be existed in the considered event. There are many kinds of candidates, like charged tracks, reconstructed by SVT and DCH, which can be, for example, pions or kaons, or calorimeter neutral clusters, which can be photons. The important thing is that all candidates have same interface (they are `BtaCandidate` objects) and they can be used in a general way.

- *Operator*. An operator acts on one or more candidates, combining them in new candidates (for example, defining a mother particle by two charged tracks) or extracting information as mass, energy, charge etc. by them.
- *Selector*. A selector is a particular structure that creates candidates with certain features starting by available candidates lists. For example a selector for π^0 selection can seek, in a list of photons, pairs of photons with invariant mass close to nominal π^0 mass and combine them with a right operator in π^0 candidates. Selectors can be generic or destined to a specific physical analysis, and they can be used in different analyses (for different decay channels) without modifying anything.

  The selector commonly used in order to produce particle lists are contained into `SimpleComposition`. This package contains selectors that describe a fixed decay reaction, for example $\pi^0 \rightarrow \gamma\gamma$, starting by `BtaCandidate` existing lists. Candidates obtained are tree-like decay. For these trees we can impose kinetics and geometrical constraints and cuts, like masses, energies, momenta, and composite candidate reconstruction probability cuts. So, composite candidates are decay trees that combine tracks, neutral clusters, PID and fitting. By this way, using all the information given by detector, `SimpleComposition` is the package for the reconstruction of every kind of composite particle.
- *Combiner*. It creates a connection between two candidates. For example, reconstructed candidates can be combined to respective Monte Carlo generated candidates.

For every *BABAR* event, reconstructed `BtaCandidate` objects are gathered in lists. Each list has a different identity hypothesis and different selection criteria. In tab. 3.11 are listed some default lists available in the Micro database level.

Name of the list	Description
`ChargedTracks`	Candidates with charge not equal to zero. Pion mass hypothesis is assigned.
`CalorNeutral`	Candidates are single bumps not associated to any tracks. Photon mass hypothesis is assigned.
`CalorClusterNeutral`	Candidates that correspond to multi-bump neutral or single bumps not associated to any cluster related to a track.
`NeutralHad`	Candidates that correspond neutral clusters in hadronic calorimeter not associated to any tracks.
`GoodTracksVeryLoose`	`ChargedTracks` list candidate with: • Min Transverse Momentum: 0.0 GeV • Max Momentum: 10 GeV • DCH min # hit: 0 • Max DOCA in xy plane: 1.5 cm • Max z DOCA: 2.5 cm • V^0 (K_S^0, Λ and γ conversion) tracks removed
`GoodTracksLoose`	Same cuts as `GoodTracksVeryLoose` with: • Max Transverse Momentum: 0.050 GeV/c
`GoodPhotonLoose`	`CalorNeutral` list candidate with: • Min energy: 0.030 GeV • Min # of crystals: 0 • Max “lateral momentum”: 0.8 Gev

Table 3.11: Main available lists in Micro database.

Chapter 4

Statistical Data Analysis Techniques

4.1 Introduction

In this chapter we will discuss about some data analysis techniques that are used into our analyses. All these techniques belong to the ”multivariate” analysis techniques because they take advantage from using more than one variable at the same time. A comprehensive introduction to statistical data analysis can be found elsewhere [85], for more details on multivariate analysis techniques please refer to [86]. In the following sections we will introduce signal-background discrimination, maximum likelihood (ML) fit technique and tests used to verify the correctness of our analysis technique. Finally we will describe the software used to perform the analyses.

4.2 Signal-Background Discrimination

In general we consider an ”event” $\mathbf{x}$ belonging to the space of events Ω of dimension n as a vector of n x_i random variables. $\mathbf{x}$ is distributed according $f(\mathbf{x}, \theta)$, the probability density function (PDF) of $\mathbf{x}$, where some of the θ_i parameters of the function can eventually be unknown *a priori*. If we have to distinguish between many hypotheses $H_0,\ H_1, ...$, each of such hypotheses will imply a given PDF $f_i(\mathbf{x}|H_i)$. In order to investigate the agreement of the observed data with a given hypothesis we have to construct a test statistic $\mathbf{t}(\mathbf{x})$. Then for each hypothesis a PDF $g_i(\mathbf{t}|H_i)$ is defined. The test statistic $\mathbf{t}$ is allowed to have as many dimension as $\mathbf{x}$ has, but the advantage of constructing a test statistic with dimension $m < n$ is to preserve discrimination between hypotheses and reduce the amount of data to be stored. Once we have got the test statistic PDF $g_i(\mathbf{t}|H_i)$, we can define a *critical region* for t (and its complementary, the *acceptance region*). If the value of the test statistic evaluated for a certain event $\mathbf{x_A}$ belong to the *critical region,* we state that $\mathbf{x_A} \notin H_0$. The critical region has to be chosen in order to maximize some figure of merit (FOM), in order to achieve the better discrimination between various hypoteses. We usually restrict to the case with only two hypotheses: the null one (”signal”) and another one (”background”).

Neyman-Person lemma states that given an efficiency ϵ for the null hypothesis, defined as

$$\epsilon = \frac{\text{events in acceptance region}}{\text{total events}}$$

the maximum signal purity is achieved in the region

$$\frac{g(\mathbf{t}|H_0)}{g(\mathbf{t}|H_1)} > c(\epsilon)$$

where c is some number determined according to ϵ, a proof of this can be found in [87]. Note that a test based on the (multidimensional) Neyman-Person acceptance region is equivalent to the one-dimensional statistic given by

$$r = \frac{g(\mathbf{t}|H_0)}{g(\mathbf{t}|H_1)} \tag{4.1}$$

which is called *likelihood ratio* for the hypotheses H_0 and H_1. Anyway the likelihood ratio test statistic is quite unpractical in the common use because it relies on the knowledge of the exact (multidimensional) functional forms for $g(\mathbf{t}|H_i)$ and also implies great computational effort.

Simpler test statistics can be used following simple assumption on the form of the test statistics. In addiction to the possibility of choosing a critical region where apply a cut, PDFs $g(\mathbf{t}|H_i)$ of the test statistics can eventually be used into the ML fit described in section 4.3. In the following subsections we describe the most commonly used test statistics.

4.2.1 Cut Selection

The simplest test statistics one can imagine is

$$\mathbf{t} = \mathbf{x}$$

which is at the origin of the simple cut analysis technique. The optimization relies on choosing the best set of $\mathbf{t_{cut}}$ cut values which maximize a predetermined FOM, usually the statistical significance

$$SS = \frac{S}{\sqrt{S+B}} \tag{4.2}$$

where S and B are respectively the number of signal and background events after the cuts. In order to maximize the set of $\mathbf{t_{cut}}$ an algorithm called ”bump hunting” is usually used[1]. The principle of the operations performed by such an algorithm is illustrated in fig. 4.1, for a 2–dimensional optimization. Anyway, such an algorithm can be applied to any n-dimensional problem. The algorithm starts with a box containing both all signal events (red points) and all background events (blue circles). Then the box is shrunk, moving one side per time, and at each step a fraction α of the events are *peeled* off; α is called *peel parameter* and the new box is chosen between all possible boxes according to the predetermined FOM. The process stops when the current box contain a minimum number of points, chosen by the user. After the shrinking process is terminated, the algorithm try to enlarge the box, if this enanche the FOM; this second process is called *pasting*.

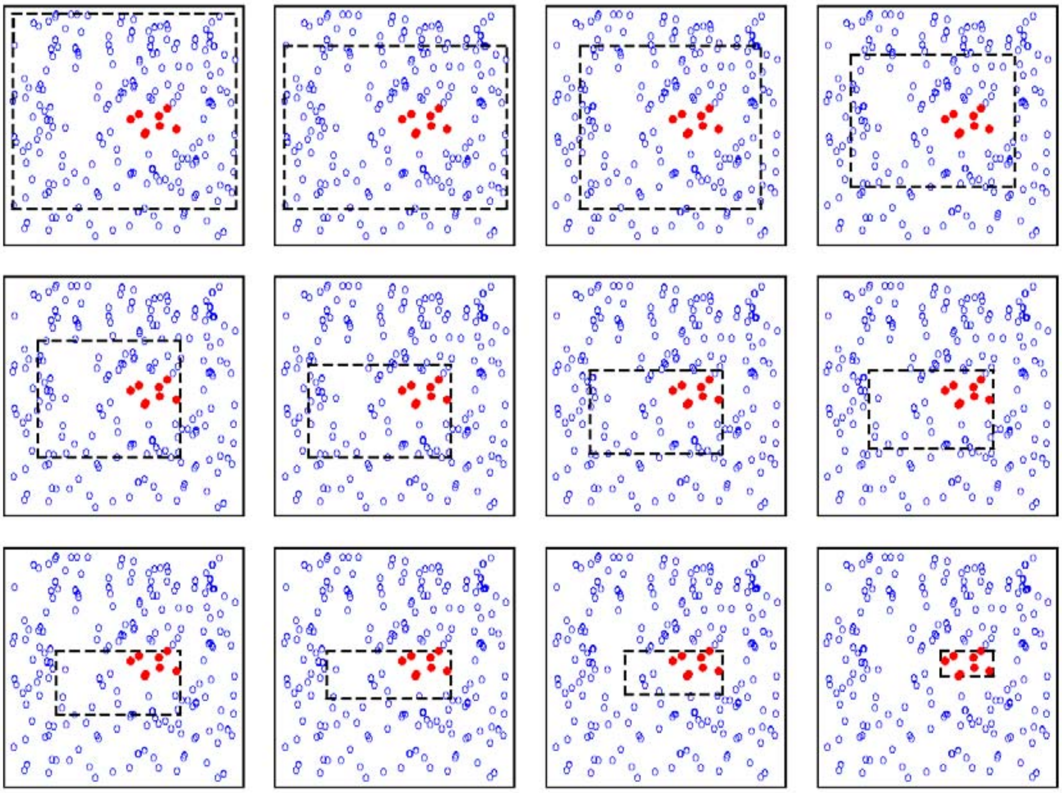

Figure 4.1: Schematic representation of the operation performed by a ”Bump Hunting” algorithm. Red points represents signal events, blue circles background ones. The black box represents acceptance region. The box is shrunk down at each step, removing a fraction α of the events, in order to maximize the chosen FOM.

---

[1] Many implementations of such an algorithm exist. In our analysis we use the Bump Hunter algorithm implemented in `StatPatternRecognition` package [88]

4.2.2 Fisher Discriminant

Another simple *ansatz* for the test statistic is a linear combination of the variables

$$t(\mathbf{x}) = \sum_{i=1}^{n} a_i x_i = \mathbf{a}^{\mathbf{T}}\mathbf{x} \tag{4.3}$$

where $\mathbf{a}^{\mathbf{T}}$ is the transposed of the coefficients vector. The goal of the minimization is to choose the a_i values that maximize the separation between $g(t|H_0)$ and $g(t|H_1)$. A possible approach, proposed by Fisher [89], is based on the following considerations. The data have the mean values and covariance matrix

$$\begin{aligned} (\mu_k)_i &= \int x_i f(\mathbf{x}|H_k) \mathrm{dx}_i ... \mathrm{dx}_n \qquad (4.4) \\ (V_k)_{ij} &= \int (x - \mu_k)_i (x - \mu_k)_j f(\mathbf{x}|H_k) \mathrm{dx}_i ... \mathrm{dx}_n \end{aligned}$$

here i and j refers to the components of $\mathbf{x}$ and $k = 0, 1$ refers to the two different hypotheses H_0 and H_1. By the same way at each hypothesis corresponds different mean and covariance matrix for t distribution

$$\begin{aligned} \tau_k &= \int t\, g(\mathbf{x}|H_k) \Delta t = \mathbf{a}^{\mathbf{T}} \mu_{\mathbf{k}} \qquad (4.5) \\ \Sigma_k^2 &= \int (t - \tau_k)^2\, g(\mathbf{x}|H_k) \Delta t = \mathbf{a}^{\mathbf{T}} V_k \mathbf{a} \end{aligned}$$

To increase the separation we should clearly try to maximize $|\tau_0 - \tau_1|$ and at the same time we want to have $g(t|H_0)$ and $g(t|H_1)$ as slight as possible, this being controlled by Σ_0^2 and Σ_1^2. A possible measure of separation that takes into account both these requests is

$$J(\mathbf{a}) = \frac{(\tau_0 - \tau_1)^2}{\Sigma_0^2 + \Sigma_1^2} \tag{4.6}$$

the numerator can be expressed as

$$\begin{aligned} (\tau_0 - \tau_1)^2 &= \sum_{i,j=1}^{n} a_i a_j (\mu_0 - \mu_1)_i (\mu_0 - \mu_1)_j \\ &= \sum_{i,j=1}^{n} a_i a_j B_{ij} = \mathbf{a}^{\mathbf{T}} B \mathbf{a} \qquad (4.7) \end{aligned}$$

where matrix B defined as

$$B_{ij} = (\mu_0 - \mu_1)_i (\mu_0 - \mu_1)_j \tag{4.8}$$

represents the separation ”between” the two classes corresponding to H_0 and H_1. Similarly the denominator of eq. 4.6 becomes

$$\Sigma_0^2 + \Sigma_1^2 = \sum_{i,j=1}^{n} a_i a_j (V_0 + V_1)_{ij} = \mathbf{a}^{\mathbf{T}} W \mathbf{a} \tag{4.9}$$

here $W_{ij} = (V_0 + V_1)_{ij}$ represents the sum of covariance matrices ”within” the two classes. Then eq. 4.6 can be expressed as

$$J(\mathbf{a}) = \frac{\mathbf{a}^{\mathbf{T}} B \mathbf{a}}{\mathbf{a}^{\mathbf{T}} W \mathbf{a}} \tag{4.10}$$

The minimization of this functions gives

$$\mathbf{a} \propto W^{-1}(\mu_0 - \mu_1) \tag{4.11}$$

so coefficients are determined up to an arbitrary scale factor. Usually this scale factor is absorbed into an offset so that the Fisher discriminant $\mathcal{F}$ is defined as

$$\mathcal{F}(\mathbf{x}) = a_0 + \sum_{i=1}^{n} a_i x_i \tag{4.12}$$

Using the Fisher discriminant is equivalent to apply a rotation plus a traslation in the $n-$dimensions variables space, or to choose a cut hyperplane which has a certain orientation and isn’t simply defined as $x_i = 0,\ i \in [1, n]$; a graphic representation of this concept in 2-dimensions variable space is shown in fig. 4.2 One can prove that if the PDFs of the variables $f(\mathbf{x}|H_0)$ and $f(\mathbf{x}|H_1)$ are multigaussians with the same covariance matrix $V_0 = V_1 = V$ the Fisher discriminant perform as well as likelihood ratio. In particular we can observe that this is always true in case of uncorrelated variables, while if using correlated variables, one should be aware that the correlations are similar on signal and background events.

4.2.3 Decision Trees

The cut analysis method described in section 4.2.1 finds an acceptance region which is an hyper-rectangle in n dimensions. An obvious generalization is to try to divide the whole space in more regions (hyper-rectangles) that can be assigned to acceptance or rejection region. Such an idea is implemented in the so called tree-based methods; applying a succession of binary cuts on a training sample, a tree-based classifier reach this goal and can then be used to test if an independent event falls in a signal (acceptance) or background (rejection) region. The main issue in using tree-based methods is the high variance of

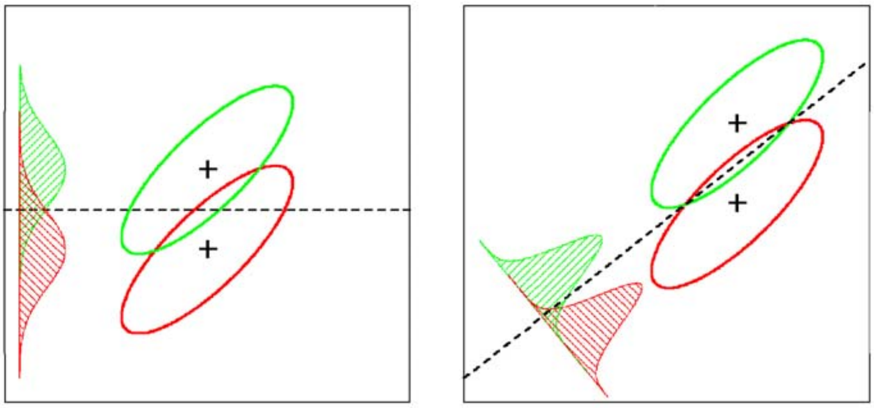

Figure 4.2: Example of the effect of using a Fisher discriminant, in green signal and in red background. In the left figure we can see that distributions doesn't have a good separation, so the power of the cut is limited. In the right figure using a variable obtained by a rotation plus a translation in the variable space, the separation between the variables improves.

this method, *i.e.* the possibility of having very different results with a small change in the training sample; this problem is solved using the *boosting* and *bagging* algorithms described below. Like all complex classifiers, decision trees also suffer from *overtraining*, *i.e.* training on a specific sample, the algorithm can incur in an adaptation to very particular features of *that* sample and will overperform on it. This gives an artificious high performance on the training sample and possible low performance on other independent samples. There are many implementation both commercial and open-source of decision trees available[2], in the following paragraphs we discuss widely used techniques for training trees and avoiding overtraining.

Training a Decision Tree

We consider a training sample of n elements $\mathbf{x}$, the training starts with the root node, where an initial splitting criterion for the full training sample is determined. The split results in two subsets of training events, each of them goes through the same algorithm in order to determine the next splitting iteration. This procedure is repeated until the whole tree is built. At each node, the split is determined by finding the variable and corresponding cut value that provides the best separation between signal and background. The node splitting is stopped once it has reached the minimum number of events. The end (*leaf*) nodes are classified as signal or background according to the class the majority of events belongs to.

A variety of separation criteria can be configured to assess the performance of a vari-

---

[2] For our studies we use TMVA [90] package which is now included into ROOT [84] distribution.

able and a specific cut requirement. Because a cut that selects predominantly background is as valuable as one that selects signal, the criteria are symmetric with respect to the event classes. All separation criteria have a maximum where the samples are fully mixed, *i.e.*, at purity $p = 0.5$, and fall off to zero when the sample consists of one event class only. Tests have revealed no significant performance disparity between the following separation criteria:

- *Gini Index*, defined by $p \cdot (1 - p)$.
- *Cross entropy*, defined by $-p \cdot \ln(p) - (1 - p) \cdot \ln(1 - p)$.
- *Misclassification error*, defined by $1 - \max(p, 1 - p)$.

The splitting criterion being always a cut on a single variable, the training procedure selects the variable and cut value that optimizes the increase in the separation index between the parent node and the sum of the indexes of the two daughter nodes, weighted by their relative fraction of events. The cut values are optimized numerically, in figure 4.3 we show the shape of the above mentioned measures for a two class problem; the fact that *Gini Index* and *Cross entropy* are smooth functions of p, let them to be more amenable for numerical minimization.

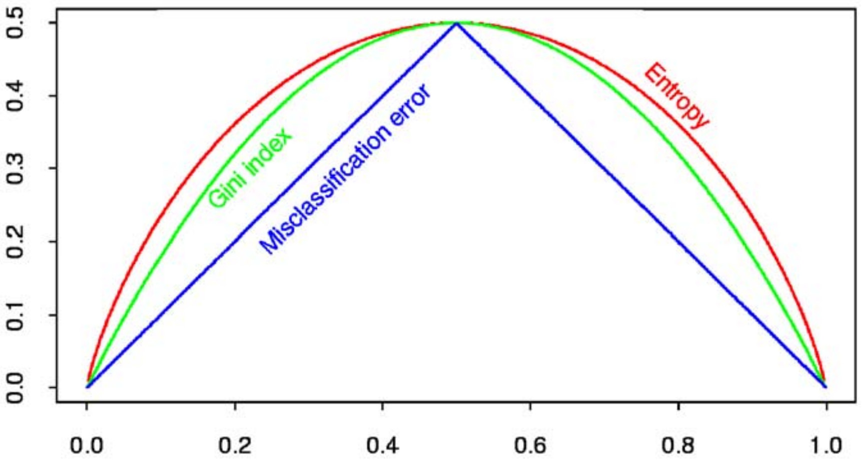

Figure 4.3: Node impurity measures, as function of purity of background events: misclassification error (blue), Gini index (green), entropy (red). Entropy has been scaled in order to pass through $(0.5, 0.5)$.

The choice of the maximum dimension of a tree should take into account two considerations: a very large tree might overfit the data, while a small tree might not capture the important structure. Tree size is a tuning parameter governing the model's complexity and is usually expressed as the minimum number of events in a node, when this minimum number is reached the node is not split anymore and is marked as *leaf* node. The preferred strategy is to grow a large size tree T_0 choosing a small value for this minimum and then prune the tree using *cost-complexity pruning,* that we now describe.

We define a subtree $T \subset T_0$ to be any tree that can be obtained by collapsing any number of internal (not leaf) nodes of T_0. We index with m the leaf nodes, with node m representing a certain region R_m in the variable space. Let $|T|$ denote the number of such regions, so letting

$$\begin{aligned} \hat{c}_m &= \frac{1}{N_m} \sum_{\mathbf{x_i} \in R_m} y_i \\ Q_m(T) &= \frac{1}{N_m} \sum_{\mathbf{x_i} \in R_m} (y_i - \hat{c}_m)^2 \end{aligned} \tag{4.13}$$

where N_m is the total number of events $\mathbf{x_i}$ in the region R_m, we define the *cost-complexity* criterion

$$C_\alpha(T) = \sum_{m=1}^{|T|} N_m Q_m(T) + \alpha|T| \tag{4.14}$$

The idea is to find for each α, the subtree $T_\alpha \subseteq T_0$ to minimize $C_\alpha(T)$. The tuning parameter $\alpha > 0$ governs the tradeoff between tree size and its goodness of fit to the data. Large values of α result in smaller trees T_α, and conversely for smaller values of α. As the notation suggests $\alpha = 0$ correspond to the full tree.

For each α one can show that there is a unique smallest T_α that minimize $C_\alpha(T)$. In figure 4.4 we show the architecture of a pruned decision tree used as *anti-spam* filer.

Boosting and Bagging

Boosting is a general procedure whose application is not limited to decision trees. The same classifier is trained several times using a successively boosted (reweighted) training event sample. The final classifier is then derived from the combination of all the individual classifiers. By this way we define a *forest* of decision tree; an event will then be processed by all the trees in the forest and the final output will be a proper average of results of each tree. The most popular boosting algorithm is the so-called AdaBoost [91] (adaptive boost), where events that were misclassified during the training of a tree get a higher event weight in the training of the following trees. Starting with the original event weights when training the first decision tree, the subsequent tree is trained using a modified event sample where the weights of previously misclassified events are multiplied by a common boost weight β. The boost weight is derived from the misclassification rate w of the previous

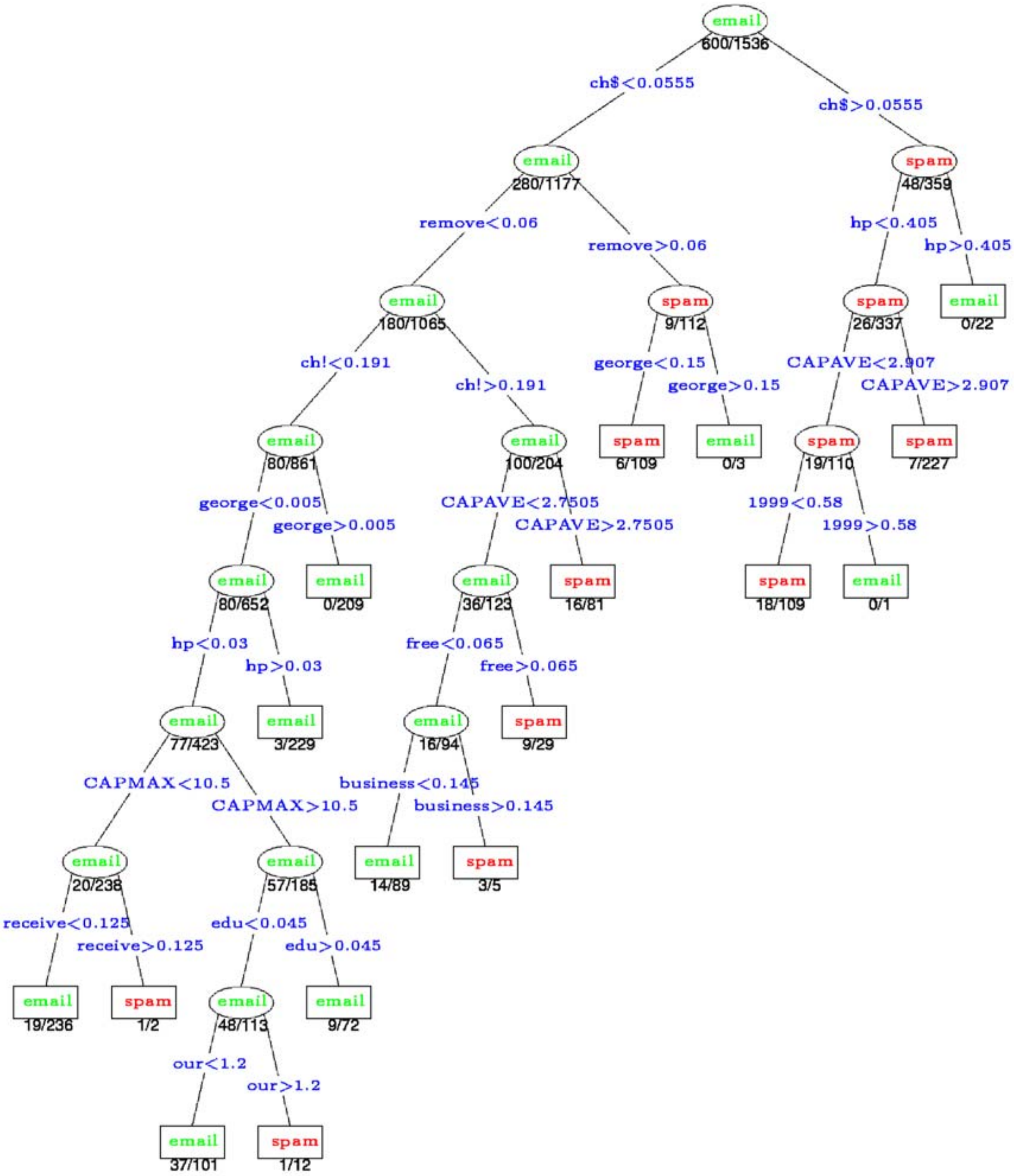

Figure 4.4: Example of a decision tree structure. This tree was trained in order to act as anti-spam filter.

tree,

$$\beta = \frac{1-w}{w}$$

The entire event sample is then renormalized to keep the total number of events (sum of weights) in a tree constant. Letting the result $T(\mathbf{x})$ of an individual tree be $T(\mathbf{x}) = +1$ for signal and $T(\mathbf{x}) = -1$ for background, the resulting event classification $BDT(\mathbf{x})$ for the boosted classifier is then given by

$$BDT(\mathbf{x}) = \sum_{i \in forest} \ln(\beta_i) \cdot T_i(\mathbf{x}) \tag{4.15}$$

where the sum is over all trees in the forest. Small (large) values for $BDT(\mathbf{x})$ indicate a background-like (signal-like) event.

Bagging is a resampling technique, the result of such a technique is usually called *random forest*. The resampling is done with replacement, which means that the same event is allowed to be (randomly) picked several times from the parent sample. This is equivalent to regarding the training sample as being a representation of the PDF of the parent event ensemble. If one draws an event out of this ensemble, it is more likely to draw an event from a region that is high populated. If a selected event is kept in the original sample (that is when the same event can be selected several times), the parent sample remains unchanged so that the randomly extracted samples will have the same parent distribution, albeit statistically fluctuated. Training several decision trees with different resampled training data and combining them into a forest results in an averaged classifier that, just as for boosting, is more stable with respect to statistical fluctuations in the training sample. Technically the resampling is implemented by applying random weights to each event of the parent sample. Therefore the result of the classifier is given by eq. 4.15, yet.

4.2.4 Artificial Neural Networks

A more complex estimator that is able to manage also with highly correlated variables, or variables which have a very poor discrimination power is the *Artificial Neural Network* (ANN).The ANN is composed by some nodes called *neurons*, which are arranged in different layers and connected each other.

Network Architecture

While in principle a neural network with n neurons can have n^2 directional connections, the complexity can be reduced by organizing the neurons in layers and only allowing directional connections from one layer to the immediate next one[3]. This kind of neural network is termed *multilayer perceptron*. The first layer of a multilayer perceptron is the input layer, the last one the output layer, and all others are hidden layers. For a classification problem with n_{var} input variables and 2 output classes the input layer consists of n_{var} neurons that hold the input values, x_1 , ..., x_{nvar} , and one neuron in the output layer that holds the output variable, the neural net estimator y_{ANN}.

Each directional connection between the output of one neuron and the input of another has an associated weight. The output value of each neuron is multiplied with the weight to be used as input value for the next neuron. Each neuron as a *neuron response function* ρ, which maps the neuron input i_1 , ..., i_n onto the neuron output. Often it can be separated into a $\mathcal{R}^n \rightarrow \mathcal{R}$ synapsis function κ, and a $\mathcal{R} \rightarrow \mathcal{R}$ neuron activation function α, so that $\rho = \alpha \circ \kappa$. The functions κ and α can have the following forms:

$$\kappa \ : \ (y_1^{(l)}, ..., y_n^{(l)} | w_{0j}^{(l)}, ..., w_{nj}^{(l)}) \rightarrow \begin{cases} w_{0j}^{(l)} + \sum_{i=1}^{n} y_i^{(l)} w_{ij}^{(l)} & Sum \\ w_{0j}^{(l)} + \sum_{i=1}^{n} \left(y_i^{(l)} w_{ij}^{(l)} \right)^2 & Sum\ of\ Squares \\ w_{0j}^{(l)} + \sum_{i=1}^{n} \left| y_i^{(l)} w_{ij}^{(l)} \right| & Sum\ of\ Absolutes \end{cases} \tag{4.16}$$

$$\alpha \ : \ x \rightarrow \begin{cases} x & Linear \\ \frac{1}{1+e^{-kx}} & Sigmoid \\ \frac{e^x - e^{-x}}{e^x + e^{-x}} & Tanh \\ e^{-x^2/2} & Radial \end{cases} \tag{4.17}$$

where $y_i^{(l)}$ is the output of the i^{th} neuron in the l^{th} layer and $w_{ij}^{(l)}$ is the weight of the connection between the i^{th} neuron in the l^{th} layer and the j^{th} neuron in the $(l+1)^{th}$ layer.

When building a network one should keep in mind the theorem by Weierstrass, accertaining that for a multilayer perceptron a single hidden layer is sufficient to approximate a given continuous correlation function to any precision, given an arbitrary large number of neurons in the hidden layer. If the available computing power and the size of the training data sample are sufficient, one can thus raise the number of neurons in the hidden layer until the optimal performance is reached. It is possible that the same performance can be reached with a network with more than one hidden layer and a potentially much smaller total number of hidden neurons. This would lead to a shorter training time and a more robust network.

---

[3] See for example fig. 5.19.

Neural Network Training

The most common algorithm for adjusting the weights that optimize the classification performance of a neural network is the so-called back propagation. It belongs to the family of supervised learning methods, where the desired output for every input event is known. The output of a network (here for simplicity assumed to have a single hidden layer with a $\tanh$ activation function, and a linear activation function in the output layer) is given by

$$y_{ANN} = \sum_{j=1}^{n_h} y_j^{(2)} w_{j1}^{(2)} = \sum_{j=1}^{n_h} \tanh\left(\sum_{i=1}^{n_{var}} x_i w_{ij}^{(1)}\right) \cdot w_{j1}^{(2)} \tag{4.18}$$

where n_{var} and n_h are the number of neurons in the input layer and in the hidden layer, respectively, $w_{ij}^{(1)}$ is the weight between input-layer neuron i and hidden-layer neuron j, and $w_{j1}^{(2)}$ is the weight between the hidden-layer neuron j and the output neuron. Simple summation was used in eq. 4.18 as synapsis function κ. During the learning process the network is supplied with N training events $x_a = (x_1, ..., x_{nvar})a$, $a = 1, ..., N$. For each training event a the neural network output $y_{ANN,a}$ is computed and compared to the desired output $y_a \in \{1, 0\}$ (1 for signal events and 0 for background events). An *error function* E, measuring the agreement of the network response with the desired one, is defined by

$$E(\mathbf{x_1}, ..., \mathbf{x_N}|\mathbf{w}) = \sum_{a=1}^{N} E_a(\mathbf{x_a}|\mathbf{w}) = \sum_{a=1}^{N} \frac{1}{2}(y_{ANN,a} - \hat{y}_a)^2 \tag{4.19}$$

where $\mathbf{w}$ denotes the ensemble of adjustable weights in the network. The set of weights that minimizes the error function can be found using the method of steepest or gradient descent, provided that the neuron response function is differentiable with respect to the input weights. Starting from a random set of weights $\mathbf{w}(\rho)$ the weights are updated by moving a small distance in w-space into the direction $-\nabla_{\mathbf{w}} E$ where E decreases most rapidly

$$\mathbf{w}^{(\rho+1)} = \mathbf{w}^{(\rho)} - \eta \nabla_{\mathbf{w}} E \tag{4.20}$$

where η is a positive number called *learning rate*, which is responsible to avoid serious overtraining of the network.

The weights connected with the output layer are updated by

$$\Delta w_{j1}^{(2)} = -\eta \sum_{a=1}^{N} \frac{\partial E_a}{\partial w_{j1}^{(2)}} = -\eta \sum_{a=1}^{N} (y_{ANN,a} - \hat{y}_a) y_{j,a}^{(2)} \tag{4.21}$$

and the weights connected with the hidden layers are updated by

$$\Delta w_{ij}^{(1)} = -\eta \sum_{a=1}^{N} \frac{\partial E_a}{\partial w_{ij}^{(1)}} = -\eta \sum_{a=1}^{N} (y_{ANN,a} - \hat{y}_a) y_{j,a}^{(2)} (1 - y_{j,a}^{(2)}) w_{j1}^{(2)} x_{i,a} \tag{4.22}$$

where we have used $\tanh' x = \tanh x(1 - \tanh x)$.

This method of training the network is denoted *bulk learning*, since the sum of errors of all training events is used to update the weights. An alternative choice is the so-called *online learning*, where the update of the weights occurs at each event. The weight updates are obtained from eq. 4.21 and 4.22 by removing the event summations. In this case it is important to use a well randomized training sample[4].

4.3 Maximum Likelihood Technique

In this section we will describe the analysis technique based on unbinned maximum likelihood fit (ML fit), chosen by *BABAR* collaboration as the official one. This kind of analysis allows high efficiency and the possibility to take in account errors with a better precisions than cut and count analysis and to consider correlations between variables.

We consider a random variable x (or a multidimensional random vector $\hat{x} = (x_1, \dots, x_n)$) distributed with a distribution function $f(x;\theta)$. We suppose the expression $f(x;\theta)$ well-known, but at least a parameter θ (or parameters $\hat{\theta} = (\theta_1, \dots, \theta_n)$) is unknown. So, $f(x;\theta)$ expression represents, after normalizing it, hypothesized PDF for x variable. Then, we suppose to perform an experiment where a measurement has been repeated N times, supplying $x_1, \dots, x_N$ values. The probability of x_i included between the interval $[x_i, x_i + \mathrm{dx}_i]$ for every i is

$$P(\theta) = \prod_{i=1}^{N} f(x_i;\theta)\mathrm{dx}_i. \tag{4.23}$$

If the hypothesized expression $f(x;\theta)$ for PDF and the parameter θ are correct, this probability will have a large value for measured data. Vice versa, a parameter value very different from the real one gives us a small probability for our measurements. The maximum likelihood method is a technique to estimate the parameter value for a finite data sample. Since dx_i does not depend on any parameters, the same considerations done for

---

[4] Online learning is the learning method implemented in TMVA package, used in this thesis work.

$P(\theta)$ can be extended to the function $\mathcal{L}$, defined as:

$$\mathcal{L}(\theta) = \prod_{i=1}^{N} f(x_i; \theta) \tag{4.24}$$

called *likelihood function*. In order to estimate the parameter value we have to maximize this function (*i. e. maximum likelihood*). We should underline that x_i are measured and the $f(x;\theta)$ function is well-known, so $\mathcal{L}$ only depends on parameters we want to fit. The evaluation of maximum for likelihood $\mathcal{L}$ as function of the unknown parameter, or equivalently the minimum of $-\ln(\mathcal{L})$ [5], can be performed numerically.

It is often the case that the number of observations N in the sample is itself a Poisson random variable with a mean value n. So, the result of the experiment can be defined as the number N and the N values $x_1, \ldots, x_N$. The likelihood function is then given by the product of the Poisson probability to find N and the function 4.24 for the N values of x,

$$\mathcal{L}(n, \theta) = \frac{e^{-n}}{N!} \prod_{i=1}^{N} n f(x_i; \theta). \tag{4.25}$$

This function is called *extended likelihood function*. It differs from the usual likelihood function, only because the sample size N is considered as a result of the experiment. In this case we have to maximize $\mathcal{L}(n, \theta)$ as function of n value and θ parameter (*i. e. extended maximum likelihood*).

Let's now consider, as example, how this method can be applied in order to extract component yields form a sample composed by signal and background events. Each event is fully described by h observable quantities $\hat{x} = (x_1, \ldots, x_h)$ (*e. g.* mass, energy, angular helicity). Let's suppose that parameters we have to evaluate are the number of events $n_1, \ldots, n_s$, each one corresponding to a particular kind of events (like signal, continuum background, non-continuum background). To distinguish events of each specie between them, we determine the distributions for each observable quantity that present a high discriminant power between those species. We fit these distributions with corresponding PDFs, indexed with $f_j^1, \ldots, f_j^h$, with $j = 1, \ldots, s$. So, we have a PDF for each observable quantity and for each specie, which means h PDFs for each specie and $h \times s$ PDFs in total. If the observable quantities are independent (otherwise we should consider correlation terms), we can define the total PDF for event i with observable quantities

---

[5] So called negative log-likelihood (NLL). In some case it is usefulle to minimize the function $\chi^2 = -2\ln(\mathcal{L})$.

$\hat{x}^i = (x_1^i, \ldots, x_h^i)$ and the specie j as

$$\mathcal{P}_j^i = \prod_{l=1}^{h} f_j^l(x_l^i) \tag{4.26}$$

and the extended likelihood function becomes:

$$\mathcal{L} = \frac{e^{-\sum_{j=1}^{s} n_j}}{N!} \prod_{i=1}^{N} \sum_{j=1}^{s} n_j \mathcal{P}_j^i. \tag{4.27}$$

The yields we want to measure are then obtained as the set of $n_1, \ldots, n_s$ that maximizes 4.27.

4.4 Validation Techniques

In this section we expose many techniques that are used in order to check that the maximum likelihood fit results are correct and unbiased.

4.4.1 Toy Experiments

Toy experiments are a widely used technique that estimates the fit bias, due to correlations or inappropriate fit strategy. Toy experiments consist on generating many data samples, that reproduce the known or expected composition of the real data sample, and fitting on these to study the fit behavior. Samples are generated drawing events from PDFs or extracting them at random from MC events. MC events are generated taking into account correlation between the variables, while drawing events from PDFs neglect such correlation. We expect that the distribution of the results of the fits should be a Gaussian distribution with central value as used in the generation of the events.

Toy experiments are usually divided into *pure* toys and *MC embedded* toys, according to the fact that the whole sample or only a part of it is generated. *Pure* toys usually undercover problems with the fit strategy (*i.e.* bad PDFs shape, wrong choice of some variables), while *MC embedded* ones, can take into account correlations between variables that are neglected in the likelihood function 4.25. Usually correlations decrease the discrimination power of the likelihood function, so not considering them can lead to bias in the final results. Toy experiments are so used in order to determine the fit bias: one performs many toy experiments (*e.g.* 500) and then fit the results with a Gaussian shape. The bias is taken as the difference between the value used for the generation and the mean of the Gaussian. It can be taken into account as systematic effect or used as correction to the fit result.

4.4.2 Projections

If we want to project a variable x, we should to emphasize the signal in the data sample with respect to the background. For this reason we apply a cut on the function

$$R = \frac{calP_s}{calP_s + \sum \mathcal{P}_b}$$

, where $\mathcal{P}_s$ and $\mathcal{P}_b$ are the probability of the signal and the background, evaluated without using x. First of all, we optimize the cut value on R, using a sample of signal and background events generated according to $\mathcal{P}_s$ and $\mathcal{P}_b$. After that, we apply the cut to the data and then show the distribution of the variable x and the shapes of $\mathcal{P}_s$ and $\mathcal{P}_b$, rescaled taking into account the cut efficiency.

4.4.3 $sPlots$

The $sPlot$ consists on an event-weighting technique where we use the covariance matrix and PDFs from the ML fit to determine a probability for each event [92].

Let's consider a variable x that can be expressed as a function of the variables y used into the fit. From the knowledge of the PDFs f_i and the yields N_i, for all events we can naively define the weight

$$\mathcal{P}_n(y_e) = \frac{N_n f_n(y_e)}{\sum_{k=1}^{N_s} N_k f_k(y_e)} \tag{4.28}$$

which can be used to build the x-distribution $\tilde{M}_n$ defined by

$$N_m \tilde{M}_n(\overline{x})\delta x \equiv \sum_{e \subset \delta x} \mathcal{P}_n(y_e) \tag{4.29}$$

where the sum $\sum_{e\subset\delta x}$ runs over the $N_{\delta x}$ events for which x_e (i.e. the value taken by the variable x for event e) lies in the x-bin centered on x and of total width δx. In other words, $N_m \tilde{M}_n(\overline{x})\delta x$ is the x-distribution obtained by histogramming events, using the weight of eq. 4.28. This procedure reproduces, on average, the true distribution $\mathrm{M}_n(x)$. In effect, on average, we can replace the sum in eq. 4.29 by the integral

$$\left\langle \sum_{e\subset\delta x} \right\rangle \rightarrow \int \mathrm{dy} \sum_{j=1}^{N_s} N_j f_j(y) \delta(x(y) - \overline{x})\delta x \tag{4.30}$$

then identifying the umber of events N_i as determined by the fit to be the expected number of events, we obtain

$$\begin{aligned}
\langle N_m \tilde{M}_n(\overline{x}) \rangle &= \int \mathrm{dy} \sum_{j=1}^{N_s} N_j f_j(y) \delta(x(y) - \overline{x}) \mathcal{P}_n(y) \\
&= \int \mathrm{dy} \sum_{j=1}^{N_s} N_j f_j(y) \delta(x(y) - \overline{x}) \times \frac{N_n f_n(y_e)}{\sum_{k=1}^{N_s} N_k f_k(y_e)} \\
&= N_n \int \mathrm{dy} \delta(x(y) - \overline{x}) f_n(y) = N_n \mathbf{M}_n(\overline{x})
\end{aligned} \tag{4.31}$$

Therefore, the sum over events of the naive weight $\mathcal{P}_n$ provides a direct estimate of the x-distribution of events of the n^{th} species. Plots obtained that way are referred to as $inPlots$: they provide a correct means to reconstruct $\mathbf{M}_n(x)$ only insofar as the variable considered is in the set of discriminating variables y. These $inPlots$ suffer from a major drawback: x being correlated to y, the PDFs of x enter implicitly in the definition of the naive weight, and as a result, the $\tilde{M}_n$ distributions cannot be used easily to assess the quality of the fit, because these distributions are biased in a way difficult to grasp, when the PDFs $f_i(y)$ are not accurate.

Let's now consider a truly control variable x , *i.e.* x does not belong to y. More precisely, the two sets of variables x and y are assumed to be uncorrelated: hence, the total PDFs $f_i(x, y)$ all factorize into products $\mathbf{M}_i(x) f_i(y)$. In this case eq. 4.31 becomes

$$\begin{aligned}
\langle N_m \tilde{M}_n(\overline{x}) \rangle &= \iint \mathrm{dxdy} \sum_{j=1}^{N_s} N_j \mathbf{M}_j(x) f_j(y) \delta(x(y) - \overline{x}) \mathcal{P}_n(y) \\
&= \int \mathrm{dy} \sum_{j=1}^{N_s} \mathbf{M}_j(\overline{x}) N_j f_j(y) \frac{N_n f_n(y_e)}{\sum_{k=1}^{N_s} N_k f_k(y_e)} \\
&= N_n \sum_{j=1}^{N_s} \mathbf{M}_j(\overline{x}) \left(N_j \int \mathrm{dy} \frac{f_n(y) f_j(y)}{\sum_{k=1}^{N_s} N_k f_k(y_e)} \right) \\
&\neq N_n \mathbf{M}_n(\overline{x})
\end{aligned} \tag{4.32}$$

So, due to the presence of the correction term

$$N_j \int \mathrm{dy} \frac{f_n(y) f_j(y)}{\sum_{k=1}^{N_s} N_k f_k(y_e)} \tag{4.33}$$

the naif weight 4.28 is inappropriate to obtain $\mathbf{M}_n(x)$. However, this correction term is related to the second derivative of the negative likelihood function $-\mathcal{L}$

$$\mathbf{V}_{nj}^{-1} = \frac{\partial^2(-\mathcal{L})}{\partial N_n \partial N_j} = \sum_{e=1}^{N} \frac{f_n(y_e) f_j(y_e)}{\left(\sum_{k=1}^{N_s} N_k f_k(y_e)\right)^2} \tag{4.34}$$

using eq. 4.30 we obtain

$$\begin{aligned}
\langle \mathbf{V}_{nj}^{-1} \rangle &= \iint \text{dxdy} \sum_{l=1}^{N_s} N_l \mathbf{M}_l(x) f_l(y) \frac{f_n(y) f_j(y)}{\left(\sum_{k=1}^{N_s} N_k f_k(y_e)\right)^2} \\
&= \int \text{dy} \sum_{l=1}^{N_s} N_l f_l(y) \frac{f_n(y) f_j(y)}{\left(\sum_{k=1}^{N_s} N_k f_k(y_e)\right)^2} \times \int \text{dx} \mathbf{M}_l(x) \\
&= \int \text{dy} \frac{f_n(y) f_j(y)}{\sum_{k=1}^{N_s} N_k f_k(y_e)}
\end{aligned} \tag{4.35}$$

Therefore eq. 4.32 can be written as

$$\langle \tilde{M}_n(\overline{x}) \rangle = \sum_{j=1}^{N_s} \mathbf{M}_j(\overline{x}) N_j \langle \mathbf{V}_{nj}^{-1} \rangle \tag{4.36}$$

Inverting this matrix equation, we recover the x-distribution of interest

$$N_n \mathbf{M}_n(\overline{x}) = \sum_{j=1}^{N_s} \langle \mathbf{V}_{nj} \rangle \langle \tilde{M}_j(\overline{x}) \rangle \tag{4.37}$$

Hence, when x does not belong to the set y, the appropriate weight is the covariance-weighted quantity (thereafter called $sWeight$) defined by

$${}_s\mathcal{P}_n(y_e) = \frac{\sum_{j=1}^{N_s} \mathbf{V}_{nj} f_j(y_e)}{\sum_{k=1}^{N_s} N_k f_k(y_e)} \tag{4.38}$$

To obtain $sPlot$ distribution for x we fit our data removing x from the likelihood function $\mathcal{L}$, then we calculate the x-distribution according to the formula

$$N_{n\,s}\tilde{M}_n(\overline{x}) \delta x = \sum_{e \subset \delta x} {}_s\mathcal{P}_n(y_e) \tag{4.39}$$

which reproduce, on average the true distribution

$$\langle N_{n\,s}\tilde{M}_n(x) \rangle = N_n \mathbf{M}_n(x)$$

Finally we plot the original PDF for the x variable, which is now unknown to the fit used to obtain the $sPlot$, over the histogram. If the control variable x exhibits significant correlation with the discriminating variable y, the $sPlots$ obtained with eq. 4.39 cannot be easily compared with the pure x-distribution.

4.5 Analysis Software

In this section we report an essential description of the software used for data analysis. A more detailed description of this software is referred in the text.

4.5.1 ROOT

BABAR software uses ROOT, an object oriented framework dedicated to scientific data analysis [84]. The project was born at CERN in the middle of ’90s to furnish tools for data analysis that would offer a better stability with respect to FORTRAN traditional tools. At the same time, people need a programming that allow them to manage quickly big projects, realized by huge and mixed groups, using advanced software programming techniques: object oriented programming was chosen because, in the 90s, it stood out as optimal choice to realize complex projects.

ROOT framework has been developing using a liberal and informal style where it is necessary an interaction between developers and users, roles very similar and often superimposed: this allows to maintain a continuous evolving project. ROOT architecture is really portable: released version for more common commercial Unix versions (SunOS/-Solaris, IBM AIX, HP-UX, SGI IRIX, Compaq/DEC OSF1), Linux, Windows, Cygwin, and MacOs are available. Furthermore the availability of the source code gives adaption to specific necessities of operative system possible.

The ROOT basic structure is formed by a hierarchy of over 300 classes, divided in 14 categories and organized as a tree with one common root, where a large part of classes inherits from common class `TObject`. Among categories we find:

- *container classes* that implement a series of complex data structures as vectors, lists, sets and maps used very often in ROOT;
- *histogram classes* and *minimization* procedure that offer advanced functionality for statistical data analysis as histograms in one, two or three dimensions, profiles, fitting, minimization and evaluation of mathematical formulas;
- *tree classes* and *ntuple* that extend potentialities of PAW[6] n-tuples, 2D and 3D

---

[6] Framework for statistical analysis developed in FORTRAN [93].

graphical classes and classes for both graphical and textual interface for the user;

- *operative system interface* that represents the only link with Operative System and favors framework portability;
- *classes for the documentation* that allows a careful and complete documentation generation during project development.

ROOT is based on C/C++ interpreter called CINT [94]; his goal is to process programs (*script*) which do not need high performance but allowing a quick development. CINT supports about 95% of ANSI C code and about 85% of C++.

4.5.2 RooFit

RooFit package is formed by a set of classes constructed on ROOT framework dedicated to unbinned maximum likelihood fit, and uses a natural and intuitive notation, that not needs a direct knowledge of ROOT programming [95].

RooFit is composed by two packages: RooFitModels and RooFitCore. The former contains all the classes for the PDFs definition and complex models (as sum or product of PDFs). The latter puts at everybody disposal a set of classes to define fitting models and fitting methods; it extends ROOT graphical functions allowing to project fitting models as function of several parameters; it allows data and both discrete and continuous variables management. The most important classes are:

- `RooRealVar`: this object is featured with a value, a minimum and maximum limit, an error, a name, an unit of measurement, a description and other attributes
- `RooArgList` and `RooArgSet`: these object permit to list `RooRealVar` and to share this list between different classes.
- `RooCategory`: this object is really similar to `RooRealVar`, but permit to manage discrete variables
- `RooDataSet`: it permits to organize the data as a matrix, in which single variables are represented in columns while single events in rows.
- `RooAbsPdf`: is the main class for defining PDFs, and all specific-PDF classes (for example Gaussian shape) inherits from it. This classes offers many common methods to handle with PDFs, such as random generator based on *accept–reject* technique, `fitTo()` method that use the Minuit algorithm [96], minimization of the likelihood function in several steps (`MIGRAD, MINOS, HESSE`), graphical interfaces. Furthermore we can compose single PDFs through sum (`RooAddPdf`),

product (`RooProdPdf`), and convolution (`RooConvPdf`). A particular constructor of `RooAddPdf` class permits to declare the extended likelihood functions.

4.5.3 *Selector*

The variables determined for each event during the events reconstruction are saved in ROOT files contained in particular structures called *tree*. These files represent the output of the events reconstruction process. During this stage loose cuts are applied on the variables to effect a first discrimination between signal and background (*preliminary* cuts). This permits to reduce files dimension.

After the reconstruction, we can optimize the values of the cuts (obviously using tighter cuts). To do that, it is necessary a program that allows us to read values of the variables, held in the trees, and to apply the new cuts. Then, the new survived events are saved in ROOT files for later analysis (ML fit). ROOT realizes that with a solid and flexible method, using the so called *selector*. This procedure is based on the realization of an user's personalized class (*i .e.* depending on the analysis to realize) that is derived from the `TSelector` class. The following methods are implemented in it:

- `TSelector::Begin`: This function is called before to read the values of the first event stored in the trees. It is possible to furnish a configuration parameter that permits to effect several kind of operations for a fixed selector, like saving events for the ML fit, to perform cut and count analysis, to draw variables distributions. Configuration parameter is an alphanumeric string: reading of this parameter and the identification of the operation requested is performed in this function `Begin`.

- `TSelector::Process`: This function is called for every single event. It contains the definition of the cuts to be applied on variables' values. After each cut we have a counter that allows us to determine the number of the events that pass it. If the variable values of an event pass all the cuts, the event is counted in all the counters and saved. Vice versa, if a determined cut is not respected, the event is rejected and the counting operation is interrupted in the last passed cut.

- `TSelector::Terminate`: This function is called at the end of variables reading of all the events. It performs the conclusive operations, *i. e.* closing the output file, drawing histograms, showing at screen the number of the events after all the cuts.

Cause different analyses differ essentially for the variables and for the cut values, from the description above, we can guess that the method which is more specific for each analysis is `Process`. For all the other methods is possible to realize a template which we can refer to.

4.5.4 `MiFit`

In order to perform maximum likelihood (ML) fits we use a program, called `MiFit`, which was developed by *BABAR* Milan group[7]. This program is developed in C++, and we use the ROOT and RooFit classes in a standalone executable code. `MiFit` code is composed by many classes that are involved in performing specific operations, this modularity of the code allows to modify and improve it even without a global knowledge of the whole program.

The main goal of `MiFit` is to provide a very simple interface to perform several operations used in the different analyses. It is not requested any skills about ROOT and RooFit, in fact any configuration of the program is given using intuitive configuration text files: `mipdf.cfg` and `mifit.cfg`. The former is used when we make the PDF fits of the variables, while the latter for any other function of the program. The structure of the two files is very similar. However, we have decided to consider the operation of PDF fit as different from the other ones and therefore we use two different files. `MiFit` can perform a great variety of operations:

- Fit PDFs to data and return PDFs parameters values.
- Fits to data in order to extract yields and other floating parameters. The fitter can apply or not (on user's choice) MC/data corrections and blinding procedure[8]. After the fit is possible to perform a scan of the negative-log-likelihood function or to determine the level curves at given distance (in standard deviations) from the minimum (*contour plots*).
- Perform *pure* and *MC embedded* toy experiments.
- Perform likelihood cut optimization, projections, $sPlots$.
- Perform, with an automatic procedure, fits where fixed PDFs parameters are moved of $\pm 1\sigma$ in order to study systematic effects due to PDFs shapes parametrization.

---

[7] Mainly by Dr. Alfio Lazzaro, with many contributors including the candidate.

[8] The blinding procedure is usually used in the first stages of the analisys, when selection criteria should be optimized. It's goal is to avoiding to change them in order to force the analysis to converge on a specific results. Blinding is based on converting a string (called *blinding string*) into a number in a way that the user can't reproduce easily, this number is then added to the result. Eventually the blinding procedure can also result in multiplying the result by -1. Errors are unaffected by the blinding procedure. This procedure is implemented in RooFit.

A complete description of `MiFit` usage can be found elsewhere [97].

Currently a new version of `MiFit` which use High Performance Computing (HPC) techniques and intensive parallelization is being developing[9] and is currently able to run over up to 40 CPUs at the same time.

---

[9] By Dr. Alfio Lazzaro. Who writes performed many tests in order to check the correctness of physical results obtained by this new program.

Chapter 5

Events Reconstruction and Selection

5.1 Introduction

The neutral B modes studied in this thesis work are reconstructed in the final states ηK^0_S, $\eta\phi$, $\eta\eta$, $\eta\omega$, $\eta' K^0_S$, $\eta' K^0_L$, $\eta'\phi$, $\eta'\omega$, $\eta'\eta'$. For the charged B modes, we consider the final state $\eta' K^{\pm}$. Then, the B daughter resonances are reconstructed in:

- $\eta\to\gamma\gamma$ ($\eta_{\gamma\gamma}$), $\eta\to\pi^+\pi^-\pi^0$ ($\eta_{3\pi}$);
- $\pi^0\to\gamma\gamma$;
- $K^0_S\to\pi^+\pi^-$ (K^0_{S+-}), $K^0_S\to\pi^0\pi^0$ (K^0_{S00});
- $\phi\to K^+K^-$;
- $\omega\to\pi^+\pi^-\pi^0$;
- $\eta'\to\rho^0\gamma$ ($\eta'_{\rho\gamma}$), $\eta'\to\eta\pi^+\pi^-$ ($\eta'_{\eta\pi\pi}$);
- $\rho^0\to\pi^+\pi^-$.

The K^0_L meson candidates are identified either as an unassociated cluster of energy in the EMC or as a cluster of hits in the IFR. We use the information from the tracking system, the EMC and the DIRC to identify charged pions and kaons in the final state. The photon candidates are identified in the EMC.

In the first part of this chapter, we will describe the methods used to identify particles inside *BABAR* and to verify the detector reply. Furthermore, we will describe the resonances and B mesons reconstruction.

In the following parts, we will introduce the common discriminant variables used into the ML fit and we will show specific selection cuts and their optimization.

5.2 Particles Reconstruction and Identification

The charged tracks reconstruction is described in section 3.4.7. Once that the tracks are reconstructed, their identification is realized using particular selectors. They take all information for each track and give the probability that a track is a specific kind of particle. The information are combined using a likelihood or a boosted decision tree technique. We have selectors for kaons, pions, electrons, muons, and protons identification.

Each selector has different levels for the identification: very tight, tight, loose, and very loose. While very tight has the lowest efficiency and misidentification rate, the very loose has the highest ones. It is possible to use the selectors as veto for the charged tracks selection, *e. g.* we want select pions among the reconstructed charged tracks and for this reason we apply veto for kaons, protons, electrons, and muons using their respective selectors. In the analyses described into this thesis work we do not use the muon selector.

It is important to note that the selectors for the charged tracks are verified using specific data sample, so called control sample, with high signal purity and statistics. In general a control sample is used for several goals:

- study of the reply for the subdetectors,
- evaluate the performance of the algorithms for the particles identifications,
- estimate systematic uncertainties.

Pure samples of a particle are selected using only kinematical information.

A pure pions sample is selected using $K^0_S \to \pi^+\pi^-$ decay channel and applying tight cuts on several variables such as: angle between K^0_s candidate direction and the directions of his daughters, distance of the vertex from interaction point and mass of reconstructed K^0_s candidate. Invariant mass distribution of $\pi^-\pi^+$ pairs is shown in fig. 5.1: purity of the sample is greater than 99%.

K mesons control sample with a very high purity is obtained from the decay $D^{*+} \to \pi^+ D^0$, $D^0 \to \pi^+ K^-$ and its charge conjugation. In fig. 5.2 we show the distribution of the mass difference between $K\pi\pi$ and $K\pi$, $0.139 < \Delta M < 0.162\ \mathrm{GeV}/c^2$. With a tight cut on this variable, the combinatorial background is equal to 13% for a kaons sample with 90% of purity.

Electrons are separated from charged hadrons through energy, lateral momentum of the shower and tracks momentum information. To obtain a better precision, we have to check that energy loss $\mathrm{d}E/\mathrm{d}x$ in DCH and the Čerenkov angle of DIRC are consistent with electron hypothesis. One of the most important variables for electrons-hadrons discrimination is the ratio between the energy left in the calorimeter and track momentum (E/p). Figure 5.3 shows efficiency for the electrons identification and probability of a

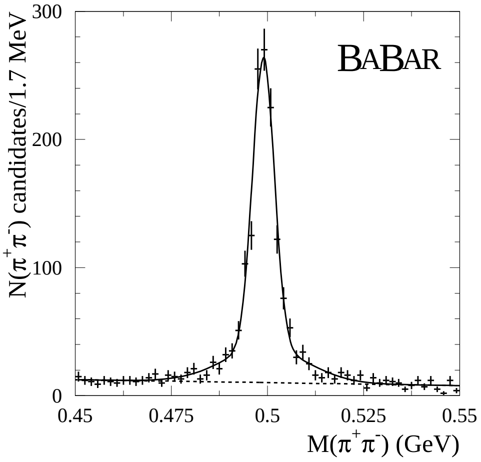

Figure 5.1: Mass distribution for K_S^0 candidates used to select pions control sample.

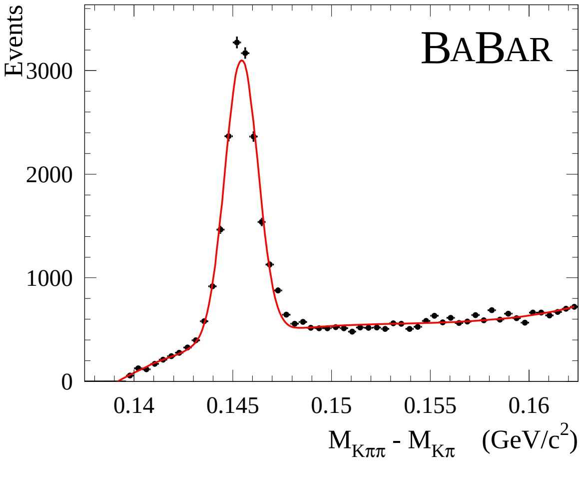

Figure 5.2: Distribution of mass difference for D^* and D^0 candidates, used to select kaons control samples.

misidentification of pions; both of them are function of the momentum and the polar angle, measured in the lab frame. Efficiency for electrons identification has been studied using electrons coming from radiative Bhabha and events $\gamma\gamma \rightarrow 4e$. Probability of misidentification of pions is measured using τ three body decays and charged pions coming from K_S^0 decay.

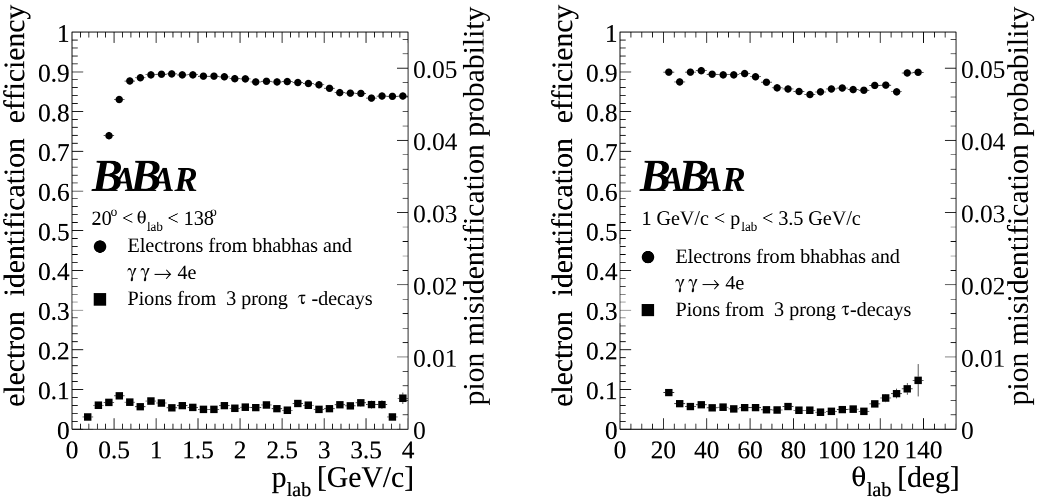

Figure 5.3: Efficiency of the electrons identification and probability of a incorrect pions identification vs momentum (left) and polar angle (right).

Photons are identified in the electro-magnetic calorimeter. Usually an EMC electro-magnetic shower is distributed on many adjacent crystals forming a *cluster* of a certain left energy. We can distinguish two kind of energy deposit: single *cluster* with a single energy maximum and *merged cluster* where we have more local energy maxima, called *bumps*. The reconstruction and the identification algorithm efficiently identify the *clusters*, distinguish them from *bumps* and determine if they are generated by a neutral or charged track. A *cluster* has at least one crystal with energy greater than 10 MeV and the adjacent crystals are considered part of a *cluster* if their energy exceeds the 1 MeV threshold. To establish the local energy maxima inside a *cluster* it's requested that candidate crystal would have an energy, $E_{LocalMax}$, greater than every adjacent crystal. Furthermore the condition $0.5(N - 2.5) > \frac{E_{NMax}}{E_{LocalMax}}$, where E_{NMax} is the maximum energy for N adjacent crystals with energy greater than 2 MeV, have to be verified. All the clusters are divided in many *bumps* in the same number of local maxima. The energy of every crystal is associated with each *bump* with a simultaneous adjustment, starting from the shape of electro-magnetic shower, the centers and energies of the *bumps*. Then all the reconstructed charged tracks in the tracking volume are extrapolated until the EMC entrance and for every track-bump pairs the association probability is evaluated. All the *bumps* with a low probability are considered photons candidates. A little percentage of these candidates is rejected if the shape is not compatible with the one expected for an electro-magnetic shower. Control samples used to check this algorithm consist on $\pi^0 \rightarrow \gamma\gamma$ and $\eta \rightarrow \gamma\gamma$. We assume their origin to be the primary interaction point. The spectrum of the invariant mass for the $\gamma\gamma$ pairs is shown in fig. 5.4 for different E_γ and $E_{\gamma\gamma}$ ranges; it's possible to distinguish peaks for π^0 and η. The mass resolution for π^0 is 6.9 MeV in the multi-hadronic events while 6.5 MeV for $\tau\tau$ events. The detector segmentation and the spatial resolution allow to reconstruct π^0 with the EMC photons separation until 5 cm without a significant worsening in the mass resolution. The little fraction of high energy π^0 in which we cannot separate the photons (named *merged pions*), about 10% in the 4-6 GeV region, are distinguished through single photons with the help of the cluster shape.

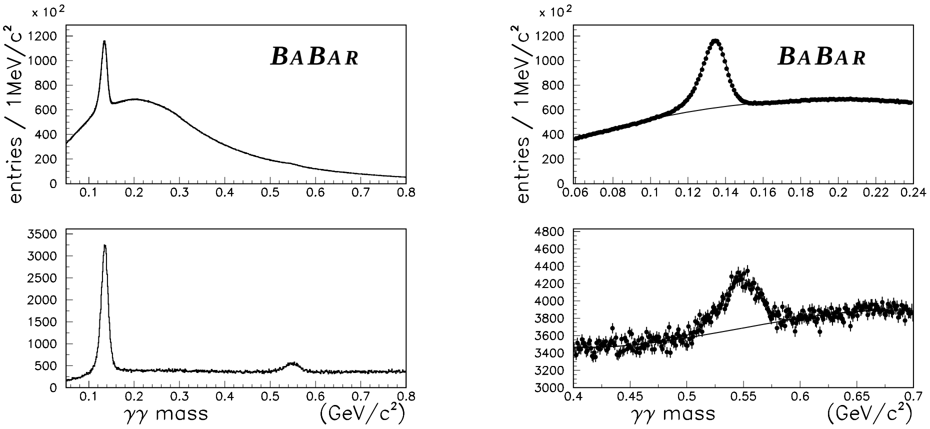

Figure 5.4: Mass spectrum for $\gamma\gamma$ pairs in the hadronic events in the π^0 and η regions. $E_\gamma > 30\mathrm{MeV}$, $E_{\gamma\gamma} > 300\mathrm{MeV}$ (left), $E_\gamma > 100\mathrm{MeV}$, $E_{\gamma\gamma} > 1\mathrm{GeV}$(right).

5.3 Events Reconstruction

In this section, we describe how daughter resonances and the B meson are reconstructed. All event selections use the *BABAR*'s `Beta` user package. Some charged tracks and electromagnetic showers, identified by the detector, are combined in order to form particle candidates, using tools from the `SimpleComposition` package.

Cuts described in the sec. 5.3.1 – 5.3.2 are applied at reconstruction level (preliminary cuts). Tighter cuts are described in sec. 5.5.

5.3.1 Daughter Resonance Reconstruction

π^0

Two photons with energy greater than 0.030 GeV are combined to form a π^0 candidate using the standard tool `pi0LooseMass`. We make a cut on mass between 0.10 and 0.16 GeV/c^2 and on energy in the LAB frame greater then 0.20 GeV.

ρ^0

Two charged tracks taken from `GoodTracksVeryLoose` list with pion mass hypothesis are combined to form a ρ^0 candidate using the standard tool `rho0Default`. ρ^0 candidate mass is required to be between 0.469 and 1.00 GeV/c^2 around its nominal value.

ω

Two charged tracks taken from `GoodTracksVeryLoose` list with pion mass hypothesis are combined with one π^0 to form a ω. The ω candidate mass is required to be 0.050 GeV/c^2 around nominal PDG [98] value.

$\eta_{\gamma\gamma}$

The η meson is reconstructed in $\eta \rightarrow \gamma\gamma$ ($\eta_{\gamma\gamma}$) decay channel by using the standard tool `etaggDefault`. We combine two photons with energy greater than 0.050 GeV in order to form our candidate. We make a cut on mass between 0.470 and 0.620 GeV/c^2 an on momentum in the LAB frame greater then 0.20 GeV/c.

$\eta_{3\pi}$

The η meson is reconstructed in $\eta \rightarrow \pi^+\pi^-\pi^0$ ($\eta_{3\pi}$) decay channel by combining two charged tracks from `GoodTracksLoose`, with all the charged particles considered as pions, with one π^0 candidate. We make a cut on mass between 0.515 and 0.575 GeV/c^2.

$\eta'_{\rho\gamma}$

The η' meson is reconstructed in $\eta' \rightarrow \rho^0\gamma$ ($\eta'_{\rho\gamma}$) decay channel by using the `etaPrgDefault`. Photons with an energy > 100 MeV are combined with a candidate ρ^0. We make a cut on mass between 0.90 and 1.01 GeV/c^2.

$\boldsymbol{\eta'_{\eta(\gamma\gamma)\pi\pi}}$

The η' mesons is reconstructed in $\eta' \to \eta_{\gamma\gamma}\pi\pi$ ($\eta'_{\eta(\gamma\gamma)\pi\pi}$) decay channel, with $\eta \to \gamma\gamma$. For charged tracks we use `GoodTracksLoose` list with all pion mass hypothesis. We apply a mass cut between 0.90 and 1.01 GeV/c^2.

$\boldsymbol{\eta'_{\eta(3\pi)\pi\pi}}$

The η' mesons is reconstructed in $\eta' \to \eta_{3\pi}\pi\pi$ ($\eta'_{\eta(3\pi)\pi\pi}$) decay channel, with $\eta \to \pi^+\pi^-\pi^0$. For charged tracks we use `GoodTracksLoose` list with all pion mass hypothesis. We make a cut on mass between 0.90 and 1.01 GeV/c^2.

$\boldsymbol{\phi}$

One charged track taken from `GoodTracksVeryLoose` and one taken from `GoodTracksLoose` list with kaon mass hypothesis are combined to form a ϕ candidate using the standard tool `phiDefault`. The ϕ candidate mass is required to be 0.030 GeV/c^2 around nominal PDG [98] value.

$\boldsymbol{K^0_{s+-}}$

The K^0_S mesons are reconstructed in $K^0_S \to \pi^+\pi^-$ decay channel combining oppositely charged tracks from `ChargedTracks` list, with all the charged particles considered as pions. We use `TreeFitter` algorithm to calculate the decay vertex constraining the K^0_S production point to lie in the beam spot region[1]. We apply a cut of $0.45 - 0.55$ GeV/c^2 on the K^0_S mass.

$\boldsymbol{K^0_{s00}}$

The K^0_S mesons are reconstructed in $K^0_S \to \pi^0\pi^0$ decay channel combining two π^0 candidates. We use `WalkFit` algorithm in order to extract the K^0_S decay vertex, constraining the K^0_S production point to lie in the beam spot region. Essentially in a first step the decay vertex is chosen in the nominal beam spot, so the angles between photons are underestimated, this leading to too low invariant masses for π^0 mesons. Anyway this allow the determination of the K^0_S momentum direction. After that, the K^0_S decay vertex is fitted in different positions along this direction, requiring a π^0 mass constraint. We apply a cut of $0.34 - 0.61$ GeV/c^2 on the K^0_S mass.

---

[1] See sec. 5.3.2 for a description of the `TreeFitter` algorithm and the beam spot constraint.

K_L^0

The K_L^0 selection is similar to what done in the analyses $B^0 \rightarrow J/\psi K_L^0$ [99] and $B^0 \rightarrow \phi K_L^0$ [100]. The `klong` list are described below for candidates reconstructed in the EMC or in the IFR. About 60% of the K_L^0 are detected in the EMC while 40% are detected in the IFR.

We cannot measure the magnitude of K_L^0 meson momentum ($|p_{K_L^0}|$) with the detector. So we measure the direction of K_L^0 momentum, taken from the η' vertex to the centroid of the EMC or IFR candidate, then, from the η' four-momentum and fixing the mass of B candidates and K_L^0 candidates to PDG values [98], we can extract $|p_{K_L^0}|$.
It's simple to verify that considering the decay $B \rightarrow X K_L^0$, and letting p_x being the X momentum, E_x the X energy, and θ_k the angle between X and K_L^0, $|p_{K_L^0}|$ satisfies

$$\left(E_x^2 - |p_x|^2 \cos^2\theta_k\right) \left|p_{K_L^0}\right|^2 - 2d|p_x||p_{K_L^0}| \cos\theta_k + E_x^2 m_k^2 - d^2 = 0 \qquad (5.1)$$

where

$$d = \frac{m_B^2 - m_x^2 - m_{K_L^0}^2}{2}$$

If 5.1 has two positives solutions, we take the smaller one.

K_L^0 selection from EMC

In order to create a list for K_L^0 reconstructed in the EMC, we apply the following selection criteria to `CalorClusterNeutral`:

- The centroid of the cluster has $\cos\theta < 0.935$, where θ is the polar angle of the cluster center of gravity (cog).
- The cluster energy is at least 200 MeV and smaller than 2 GeV.
- The `CalorClusterNeutral` list includes candidates with a track-shower match probability of less than 0.1%.
- We require that the bump associated to the K_L^0 don't form a $\gamma\gamma$ invariant mass between 100 MeV/c^2 and 150 MeV/c^2 together with another cluster, for events with at least 30 MeV of energy (the requirement is not applied if the Zernike moment[2] $|Z_{20}|$ is less then 0.8).
- We reject two-bump clusters if the cluster energy is larger than 1 GeV and they are consistent with a merged π^0 ($M(\text{2bumps}) > 110\ \text{MeV}/c^2$).

---

[2] See sec. 5.5.2 for a detailed definition of this variable.

K_L^0 selection from IFR

The list for K_L^0 candidates detected in the IFR is obtained applying the following cuts to `NeutralHadrons` list

- At least two planar IFR layers.
- The cluster center of gravity (cog) must have $-0.75 < \cos\theta < 0.93$.
- For any track with a momentum larger than 0.75 GeV/c, the relative position between the cluster centroid in the IFR (θ_{K_L}, ϕ_{K_L}) and the position of the charged tracks in the EMC ($\theta_{track}, \phi_{track}$) must not satisfy $|\theta_{K_L} - \theta_{track}| < 350$ mrad; as well as $-750 < (\phi_{K_L} - \phi_{track}) < 300$ mrad for positively charged tracks and $-300 < (\phi_{K_L} - \phi_{track}) < 750$ mrad for negatively charged tracks.
- If the K_L^0 is revealed into the endcap, first layer must be less or equal to 13.

5.3.2 B Candidates Reconstruction

B candidates are reconstructed combining their daughter candidates. In particular, in case of daughter resonances with reconstructed multiple decays, we consider the cases shown in tab. 5.1. We combine the B daughters and determine the B decays vertex using a particular algorithm, `TreeFitter`, which performs the vertex fit of the B candidates with a global decay chain fit based on a Kalman filter, which was described in sec. 3.4.7. For this fit we apply geometrical and kinematical (on the momentum) constraints. We consider also a ”beamspot” constraint, which forces the B to originate from the interaction point, taking the error in that point into account. The beamspot is calculated event by event and his errors are the size of the interaction point, which is about 10 μm in y, 200 μm in x and 8 mm in z. In the reconstruction of modes with K_L^0 we use also a B mass constraint [98]. As additional preliminary cuts we apply a cut between 4.99 and 5.59 GeV on the energy of the B candidate in CMS frame and a cut on B mass between 4.7 and 5.7 GeV/c^2. Other cuts for the analysis will be described in detail in sec 5.5.

5.4 Discriminating Variables

In this section we describe the discriminating variables used to separate signal from background events. We will consider both kinematical and topological variables.

Background events arise primarily from random combinations of particles in continuum $e^+e^- \to q\bar{q}$ events ($q = u, d, s, c$). For some of the decay chains we must also consider crossfeed from B-meson decays by modes other than the signal.

Main Decay	Daughter Resonances Sub-Decays	Labels
$B^0 \to \eta K^0_S$	$\eta_{\gamma\gamma}$, $\eta_{3\pi}$, K^0_{S+-}	$B^0 \to \eta_{\gamma\gamma} K^0_S$
		$B^0 \to \eta_{3\pi} K^0_S$
$B^0 \to \eta\eta$	$\eta_{\gamma\gamma}$, $\eta_{3\pi}$	$B^0 \to \eta_{\gamma\gamma}\eta_{\gamma\gamma}$
		$B^0 \to \eta_{\gamma\gamma}\eta_{3\pi}$
		$B^0 \to \eta_{3\pi}\eta_{3\pi}$
$B^0 \to \eta\omega$	$\eta_{\gamma\gamma}$, $\eta_{3\pi}$	$B^0 \to \eta_{\gamma\gamma}\omega$
		$B^0 \to \eta_{3\pi}\omega$
$B^0 \to \eta\phi$	$\eta_{\gamma\gamma}$, $\eta_{3\pi}$	$B^0 \to \eta_{\gamma\gamma}\phi$
		$B^0 \to \eta_{3\pi}\phi$
$B^0 \to \eta' K^0_S$	$\eta_{\gamma\gamma}$, $\eta_{3\pi}$,$\eta'_{\rho\gamma}$, $\eta'_{\eta\pi\pi}$, K^0_{S+-}	$B^0 \to \eta'_{\eta(\gamma\gamma)\pi\pi} K^0_S$
		$B^0 \to \eta'_{\eta(3\pi)\pi\pi} K^0_S$
		$B^0 \to \eta'_{\rho\gamma} K^0_S$
	$\eta_{\gamma\gamma}$,$\eta'_{\rho\gamma}$, $\eta'_{\eta\pi\pi}$, K^0_{S00}	$B^0 \to \eta'_{\eta(\gamma\gamma)\pi\pi} K^0_{S00}$
		$B^0 \to \eta'_{\rho\gamma} K^0_{S00}$
$B^0 \to \eta' K^0_L$	$\eta_{\gamma\gamma}$, $\eta_{3\pi}$, $\eta'_{\eta\pi\pi}$	$B^0 \to \eta'_{\eta(\gamma\gamma)\pi\pi} K^0_L$
		$B^0 \to \eta'_{\eta(3\pi)\pi\pi} K^0_L$
$B^0 \to \eta'\eta'$	$\eta_{\gamma\gamma}$, $\eta'_{\rho\gamma}$, $\eta'_{\eta\pi\pi}$	$B^0 \to \eta'_{\eta(\gamma\gamma)\pi\pi}\eta'_{\eta(\gamma\gamma)\pi\pi}$
		$B^0 \to \eta'_{\rho\gamma}\eta'_{\eta(\gamma\gamma)\pi\pi}$
$B^0 \to \eta'\omega$	$\eta_{\gamma\gamma}$, $\eta'_{\rho\gamma}$, $\eta'_{\eta\pi\pi}$	$B^0 \to \eta'_{\eta(\gamma\gamma)\pi\pi}\omega$
		$B^0 \to \eta'_{\rho\gamma}\omega$
$B^0 \to \eta'\phi$	$\eta_{\gamma\gamma}$, $\eta'_{\rho\gamma}$, $\eta'_{\eta\pi\pi}$	$B^0 \to \eta'_{\eta(\gamma\gamma)\pi\pi}\phi$
		$B^0 \to \eta'_{\rho\gamma}\phi$
$B^+ \to \eta' K^+$	$\eta_{\gamma\gamma}$, $\eta_{3\pi}$,$\eta'_{\rho\gamma}$, $\eta'_{\eta\pi\pi}$	$B^+ \to \eta'_{\eta(\gamma\gamma)\pi\pi} K^+$
		$B^+ \to \eta'_{\eta(3\pi)\pi\pi} K^+$
		$B^+ \to \eta'_{\rho\gamma} K^+$

Table 5.1: B decay modes and their subdecays studied in this thesis work. In the right column we show the labels used to indicate these modes, reconstructed in their specific subdecays, in the following chapters.

At $\Upsilon(4S)$ resonance energy, we have a number of $e^+e^- \to q\bar{q}$ events about three times with respect to $B\overline{B}$ events. The $q\bar{q}$ continuum background can be studied using collected data under the resonance (off-peak data), while for the study of $B\overline{B}$ background simulated Monte Carlo data are used.

Topological variables describe the spatial structure of the events and furnish a separation between $B\overline{B}$ events and the continuum background ones; kinematical variables allow us to discriminate signal from non-continuum background and further from the continuum one.

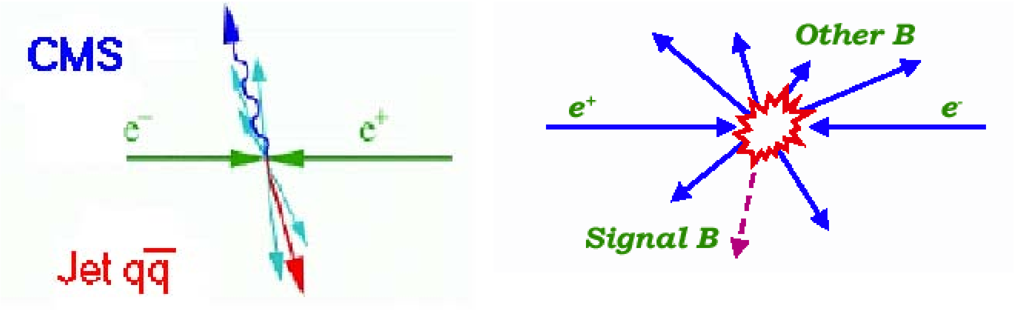

Figure 5.5: Schematic topological representations of $e^+e^-\to q\bar{q}$ (left) and $e^+e^-\to\Upsilon(4S)\to B\overline{B}$ (right) events.

5.4.1 Topological Variables: θ_{T} and $\mathcal{F}$

From the kinematical study of $e^+e^-\to q\bar{q}$ we deduce that background and signal events have a different geometry. Since beam energy in the center of mass (CM) is equal to $10.580\ \mathrm{GeV}$, $u\bar{u}$, $d\bar{d}$, $s\bar{s}$, $c\bar{c}$ ($udsc$) pairs have a great kinetical energy that lead to a back-to-back geometry of the event. In the case of $e^+e^-\to\Upsilon(4S)\to B\overline{B}$ the kinetical energy for B mesons is low, so, the event will be much more isotropic. This fact is illustrated in fig. 5.5.

These different spatial distributions of the particles in the final states allow us to define some topological variables used for background suppression. In particular, in our analyses we use:

- the cosine of angle between the thrust axis of the B candidate and the thrust axis of the other-B in the event, $\cos\theta_{\mathrm{T}}$;
- The the cosine of the angle between the B direction and the beam axis.
- The cosine of the angle between the thrust axis of the B candidate and the beam axis.
- The Legendre polynomials L_0 and L_2.

These variables are described in the next sections. All these variables, but the first, are combined using a Fisher discriminant in order to increase their discriminating power.

The θ_{T} Angle

The thrust axis is defined as the versor $\vec{n}$ which maximizes the value of variable T, the thrust, defined as:

$$T = \max_{|\vec{n}|=1} \frac{\sum_i |\vec{n}\cdot\vec{p}_i|}{\sum_i |\vec{p}_i|}. \tag{5.2}$$

where p_i are the particles momenta. We consider $\theta_{\rm T}$, which is the angle between the thrust axis of the B candidate and the thrust axis of the rest of the event (the particles not belonging to the reconstructed B candidate), calculated in CMS frame. For the thrust axis determination we use the information from neutral and charged particles of the event. The $|\cos\theta_{\rm T}|$ variable has a nearly flat distribution for $B\overline{B}$ events while it is sharply peaked at 1 for continuum background events (fig. 5.6), due to the different topology of $B\overline{B}$ and $q\overline{q}$ events as explained above. So this variable gives a strong discrimination power between signal and background events. Usually the cut $|\cos\theta_T| < 0.9$ is applied, but in some cases of high continuum background contribution we use a tighter cut value.

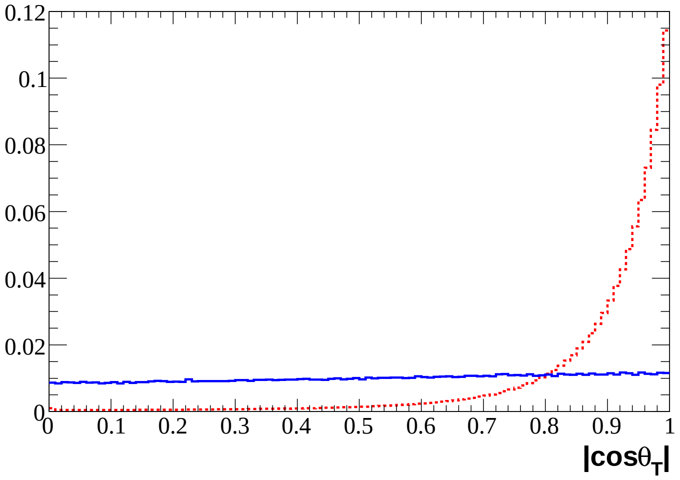

Figure 5.6: Comparison of $|\cos\theta_T|$ variable calculated for $B\overline{B}$ MC signal events (blue solid line) and off-peak data (red dashed line).

$\mathcal{F}$ Fisher Discriminant

A detailed description of the Fisher Discriminant ($\mathcal{F}$) as a test statistic used to discriminate between two hypotheses can be found in sec. 4.2.2.

Due to the fact that many variables related to the event shape have a little discriminating power, we decide to combine them using such a technique. Many tests were also performed using different classifiers (Neural Networks, Decision Trees), but without significant increase in signal-background separation.

We use 5 variables as input to $\mathcal{F}$:

- $|\cos\boldsymbol{\theta}_{\boldsymbol{B}-\mathbf{Beam}}|$

  The $\cos\theta_{B-\rm Beam}$ variable is the cosine of the angle between the B direction and the beam axis, calculated in CM frame. This is essentially the decay angle of the $\Upsilon(4S)$ meson. For the $\Upsilon(4S)\rightarrow B\overline{B}$ system, $\cos\theta_{B-\rm Beam}$ variable has a $\sin^2$ distribution. Since there is not B meson in the continuum background, the distribution of $\cos\theta_{B-\mathrm{Beam}}$ for these events is expected to be flat.

- **$|\cos\boldsymbol{\theta}_{\mathbf{T-Beam}}|$**
  The $\cos\theta_{\mathrm{T-Beam}}$ variable is the cosine of the angle between the thrust axis of the B candidate and the beam axis, calculated in CM frame. The distribution for this variable is flat for signal events. For background events the $\cos\theta_{\mathrm{T-Beam}}$ variable follows a $(1+\cos^2)$ distribution.

- **$\boldsymbol{L_0}$ and $\boldsymbol{L_2}$**
  L_0 and L_2 are the monomials with L_n defined as:

$$L_n = \sum_{i \in ROE} p_i \times |\cos(\theta_i)|^n \tag{5.3}$$

  where the sum is over the list of the rest of event (all tracks and neutrals which do not belong to the B candidate), p_i is the momentum of particle i, and θ_i is the angle between the direction of particle i and the thrust axis of the B candidate.

- **$|\boldsymbol{Tag}04|$**
  The continuous output of the Tag04 tagging algorithm [76], a description of the *BABAR* tagging algorithm is given is sec. 3.3.1.

All these variables are shown in fig. 5.7 for MC signal events and off-peak data events. We consider all candidates per event. The idea is to have as more information as possible to describe also the combinatorial background. Due to the fact that the Fisher Discriminant (Fisher) use topological information, variation of its shape between different decay modes is a second order effect. So we can train the Fisher on a specific decay mode and then use it safely to any other mode. The Fisher is trained using the multivariate analysis tool TMVA [90]. We train our Fisher using $\eta'_{\rho\gamma}\omega$ mode, since this modes have the highest available statistics for background events. For $B\to\eta' K$ analysis it is, indeed, trained on $\eta'_{\rho\gamma}K^+$ mode. We use 4000 MC signal events as signal sample and 4000 off-peak events as background sample for the training. Other 4000 events for each sample are used for the validation. We show in fig. 5.8 the correlations between the variables used in the Fisher. Our Fisher discriminant has the following form:

$$\begin{aligned}\mathcal{F} &= (0.178\cdot L_0 - 0.598\cdot L_2 - 0.382\cdot|\cos\theta_{TB}| - 0.302\cdot|\cos\theta_{BB}| \\ &\qquad +0.385\cdot|\mathrm{Tag}_{04}|) - 0.452 \qquad (\eta'_{\rho\gamma}K^+ \text{ mode}) \qquad (5.4)\\ \mathcal{F} &= (0.405\cdot L_0 - 0.858\cdot L_2 - 0.219\cdot|\cos\theta_{TB}| - 1.95\cdot|\cos\theta_{BB}| \\ &\qquad +0.756\cdot|\mathrm{Tag}_{04}|) - 0.134 \qquad (\eta'_{\rho\gamma}\omega \text{ mode}) \qquad (5.5)\end{aligned}$$

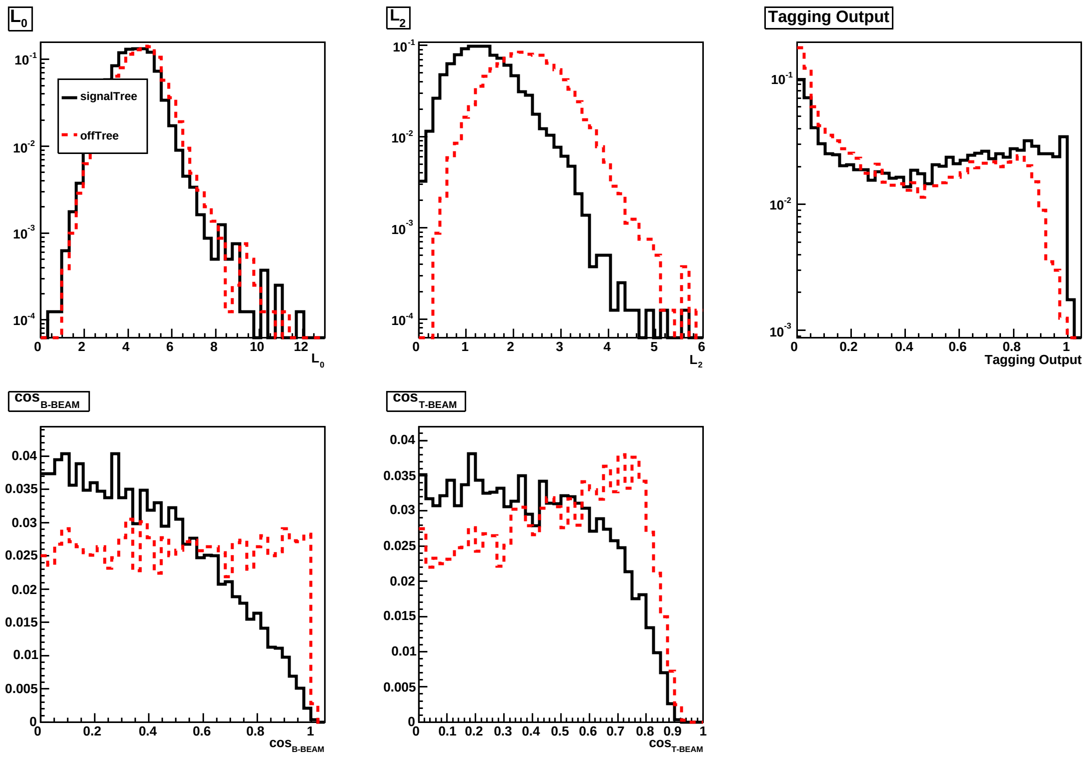

Figure 5.7: Shape variables ($\eta'_{\rho\gamma}K^+$ mode): black solid line refers to MC signal events, red dashed line to off-peak background events.

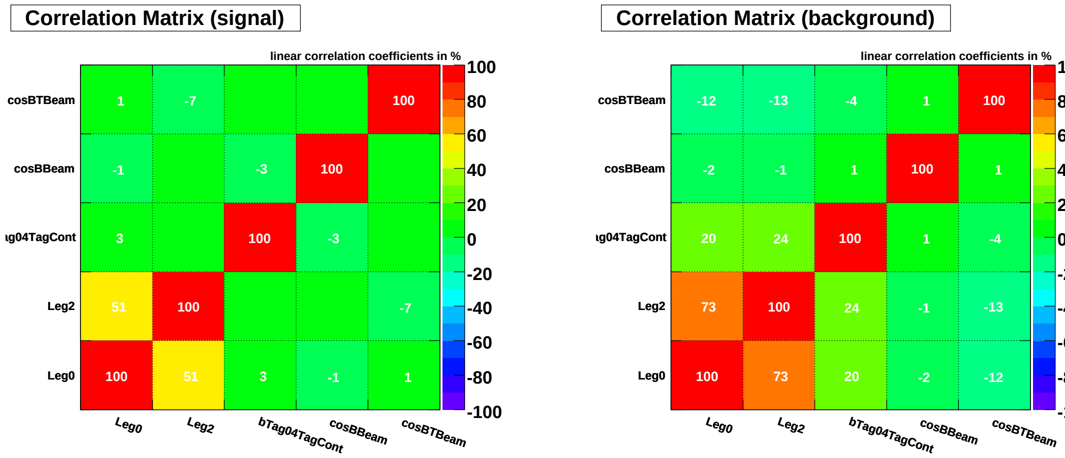

Correlation Matrix (signal)

	Leg0	Leg2	bTag04TagCont	cosBBeam	cosBTBeam
cosBTBeam	1	-7			100
cosBBeam	-1		-3	100	
ıg04TagCont	3		100	-3	
Leg2	51	100			-7
Leg0	100	51	3	-1	1

Correlation Matrix (background)

	Leg0	Leg2	bTag04TagCont	cosBBeam	cosBTBeam
cosBTBeam	-12	-13	-4	1	100
cosBBeam	-2	-1	1	100	1
ıg04TagCont	20	24	100	1	-4
Leg2	73	100	24	-1	-13
Leg0	100	73	20	-2	-12

Figure 5.8: Correlations between shape variables used in the Fisher discriminant ($\eta'_{\rho\gamma}K^+$ mode). Where no value is shown in the cell, the correlation is equal to zero

where the coefficients are chosen in order to maximize signal-background separation and to have signal and background distributions with average in $+1$ and -1, respectively.

It was noticed that $\mathcal{F}$ defined in eq. 5.5 is correlated with the tagging category; the amount of such a correlation is about 18.5% for continuum background and 1.8% for signal in $\eta'_{\rho\gamma}K^+$. Since in our measurements the reconstructed data samples are dominated by continuum background events, the correlation in continuum is most important to remove. We therefore apply a category by category correction, determined on the off-peak sample, in order to reduce the first order correlation between the shape of the Fisher distribution and the tagging category. For each tagging category, we shift the value of $\mathcal{F}$ so that the distribution for all category has the same average. We define the new Fisher variable $\mathcal{F}'$ [3] as

$$\mathcal{F}' = \mathcal{F} + \delta(\mathrm{Cat}_{\mathrm{Tag04}}), \tag{5.6}$$

$\delta(\mathrm{Cat}_{\mathrm{Tag04}})$ for each tagging category are listed in tab. 5.2. The effect of this correction

bTag04 Category	δ
0	$+0.1111$
63	$+0.04666$
64	$+0.03514$
65	-0.03818
66	-0.00116
67	$+0.0855$
68	$+0.13764$

Table 5.2: Magnitude of the category-by-category correction applied to $\mathcal{F}$ in order to reduce the correlation between $\mathcal{F}$ and the tagging category in the background sample.

is to reduce background correlation to 0.5% and increase signal correlation to 25% (they were 18.5% and 1.8%,respectively). Due to the fact that we don't use any information about the tagging category in the ML fit for the BF analysis (but the Fisher itself), this correction is applied only in the TD analysis.

We show in fig. 5.9 the output of Fisher discriminant $\mathcal{F}'$ for the $\eta'_{\rho\gamma}K^+$ data sample.

5.4.2 Kinematical Variables: m_{ES} and ΔE

In this experiment the momentum of the initial e^+e^- state is known within an uncertainty of few MeV. For a final state with two particles we can determine four kinematic variables from conservation of energy and momentum. These may be taken as polar and azimuthal angles of the line of flight of the two particles, and two energy, momentum, or mass variables, such as the masses of the two particles. In practice, since we fully reconstruct one B meson candidate, we make the assumption that it is one of two final-state particles of equal mass. We compute two largely uncorrelated variables that test consistency with this constraint, and with the known value [98] of the B-meson mass. In our analyses, the

---

[3] In the following chapters we will use the simple $\mathcal{F}$ notation to indicate $\mathcal{F}'$.

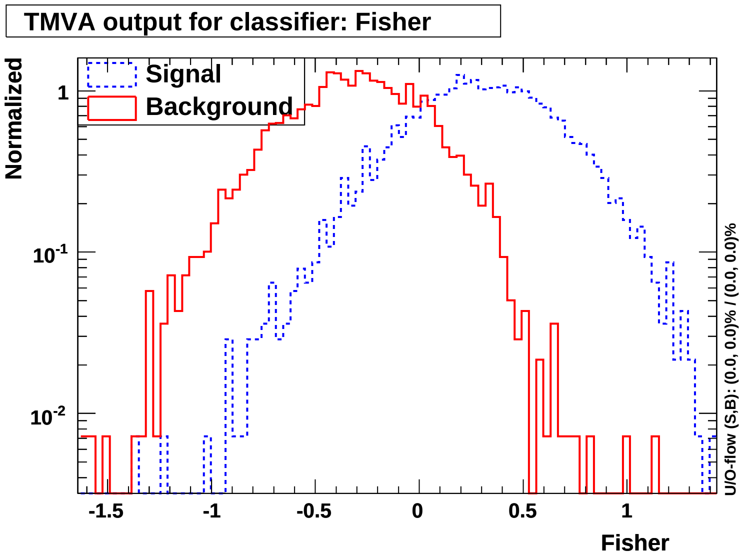

Figure 5.9: Fisher output distributions for signal and background in $\eta'_{\rho\gamma}K^+$: blue dashed line refers to MC signal events, red solid line to off-peak background events.

B candidates are kinematically characterized by ΔE and $m_{\rm ES}$. These two variables are defined in order to minimize the correlation between themselves.

The invariant ΔE is defined as:

$$\Delta E = \frac{2q_{\Upsilon(4S)}q_B - s}{2\sqrt{s}} \tag{5.7}$$

where $q_{\Upsilon(4S)}$ and q_B are four-momenta of the $\Upsilon(4S)$ and the B candidate. We require $|\Delta E| < 0.2$ GeV($-0.01 < \Delta E < 0.08$ GeV for $B^0 \to \eta' K^0_L$ analysis). In the fig. 5.10 we can see that ΔE is essentially a Gaussian distribution for signal events while it is a linear polynomial for continuum background. In $B^0 \to \eta' K^0_L$ mode, where we apply a B mass constraint to reconstruct the events, the background shape of ΔE is described by an Inverse Argus function [101], defined as:

$$F(x) = C\,x(1-x)^{-2}e^{\xi' x} \tag{5.8}$$

where C is a normalization factor, $x \equiv \Delta E - (\Delta E)_{min}$, with $(\Delta E)_{min}$ is fixed to -0.01, and ξ' is a shape parameter. This distribution is shown in fig. 5.10, too.

The $m_{\rm ES}$ is the beam-energy substituted mass, computed in the LAB frame and independent of mass hypotheses assigned to B candidate daughters:

$$m_{\rm ES} = \sqrt{\frac{(s/2 + \vec{p}_{\Upsilon(4S)} \cdot \vec{p}_B)^2}{E^2_{\Upsilon(4S)}} - \vec{p}_B^{\,2}} \tag{5.9}$$

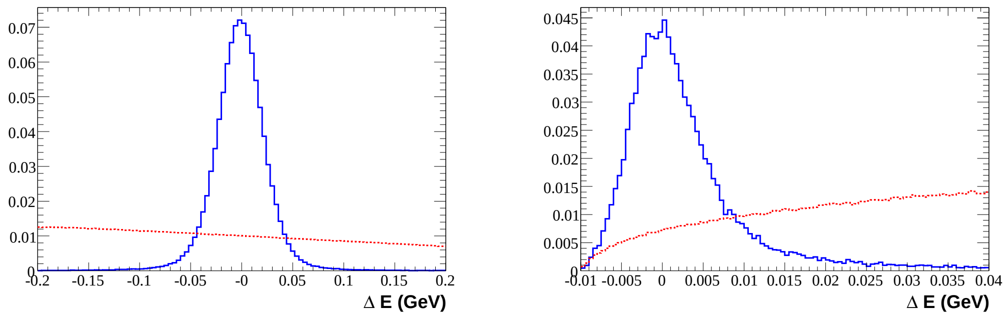

Figure 5.10: Comparison of ΔE distributions for modes without K_L^0 meson (left) and $B^0 \to \eta' K_L^0$ mode (right). Blue solid line represents $B\overline{B}$ MC signal events, while red dashed line off-peak data.

where $s \equiv (q_{\Upsilon(4S)})^2$ is the square of the CM energy, $p_{\Upsilon(4S)}$ and p_B are three-momenta of the $\Upsilon(4S)$ and the B candidate in the LAB frame and $E_{\Upsilon(4S)} \equiv q^0_{\Upsilon(4S)}$ is the energy of the $\Upsilon(4S)$ in the LAB frame. We require $5.25 < m_{\rm ES} < 5.2893\ {\rm GeV}/c^2$. Because of reconstruction technique used in K_L^0 analysis, there is a strong correlation between ΔE and $m_{\rm ES}$ in $B^0 \to \eta' K_L^0$ modes. For this reason in this analysis we don't use $m_{\rm ES}$ variable. The comparison between $m_{\rm ES}$ distributions for signal and background is shown in fig. 5.11; essentially the signal is described by a Gaussian distribution while the continuum background by an Argus function [101], defined as:

$$F(x) = C\,x\sqrt{1-x^2}\;\; e^{-\xi(1-x^2)} \tag{5.10}$$

where C is a normalization factor,$x \equiv 2m_{\rm ES}/\sqrt{s}$, and ξ is a shape parameter.

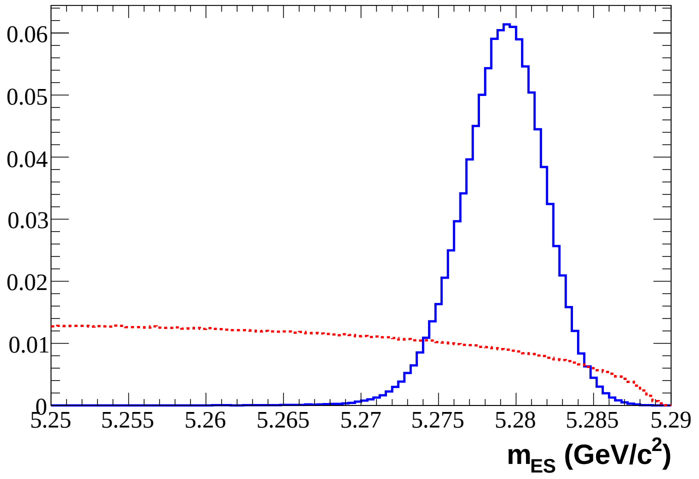

Figure 5.11: $m_{\rm ES}$ variable distributions for $B\overline{B}$ MC signal events (blue solid line) and off-peak data (red dashed line).

The selection cuts for ΔE and $m_{\rm ES}$ are in general quite loose to allow a high efficiency and to provide a sufficient number of events in the sidebands in order to characterize well the backgrounds.

5.5 Event Selection

After the cuts applied at reconstruction time (called preliminary cuts), described in sec. 5.3, some tighter cuts are applied to produce the input to maximum likelihood fit. First, we will describe some preliminary cuts that were omitted in sec. 5.3. Then, we will show the optimization procedure for some specific cuts. Finally, we will list all the cuts used to produce the input sample to maximum likelihood fits. Efficiencies of these cuts are given in sec. 6.5.1 and 7.4.1, for TD and BF analysis, respectively.

5.5.1 Preliminary Cuts

We show here some preliminary cuts applied at reconstruction time and not mentioned in sec. 5.3.

- Charged particles from: `GoodTracksLoose` list for $\eta_{3\pi}$, $\eta'_{\eta\pi\pi}$; `GoodTracksVeryLoose` list for ρ^0 and ω; a kaon from `GoodTracksLoose` list and a kaon from `GoodTracksVeryLoose` list for ϕ; `ChargedTracks` list for K^0_S.
- A minimum number of charged tracks in the event (from `ChargedTracks` list) $\geq \max[3, N_{\text{tracks in the B decay mode}} + 1]$. This cut allows to reduce strongly the background from $e^+e^- \to \tau^+\tau^-$.
- $E_\gamma > 0.030$ GeV for π^0; $E_\gamma > 0.050$ GeV for $\eta_{\gamma\gamma}$; $E_\gamma > 0.100$ GeV for $\eta'_{\rho\gamma}$.
- $|\cos\theta_{\rm T}| < 0.9$ ($|\cos\theta_{\rm T}| < 0.8$ for $\eta_{\gamma\gamma}\omega$ and $\eta'_{\rho\gamma}\omega$).
- $5.25 < m_{\rm ES} < 5.29\ {\rm GeV}/c^2$ (this cut doesn't apply for modes with K^0_L).
- $|\Delta E| < 0.2$ GeV; $-0.15 < \Delta E < 0.20$ GeV for ηK^0_S modes (the asymmetric negative cut value allows suppression of most of the $B\overline{B}$ background); $-0.01 < \Delta E < 0.08$ GeV for $\eta' K^0_L$ modes.
- $P(\chi^2) > 0$ B vertex fit cut to reject events with high χ^2 values.
- energy of π^0 in the LAB frame greater than 0.200 GeV;
- momentum of $\eta_{\gamma\gamma}$ in the LAB frame greater than 0.200 ${\rm GeV}/c$;
- Preliminary cuts on the daughter resonances, as described in section 5.3.1.

5.5.2 Background Suppression for $B^0 \to \eta' K_L^0$ Modes

For $B^0 \to \eta' K_L^0$ modes, we consider specific cuts in order to suppress the background from fake K_L^0. We consider here two variables:

- Missing Momentum P_{miss}^{pro}. We calculate the K_L^0 missing momentum P_{miss} from all tracks (`GoodTrackLoose`) and EMC clusters (`CalorClusterNeutral`) excluding the K_L^0 candidate. Then we project it onto the axis of the K_L^0 candidate in the transverse plane to the beam direction and we subtract from this projection the transverse momentum of the K_L^0 candidate. By this way we obtain the transverse missing projected momentum P_{miss}^{pro}. We show in fig. 5.12 the comparison between the distribution of P_{miss}^{pro} for off-peak data and MC signal events.

- $\cos\theta_{P_{miss}}$, defined as the cosine of the polar angle of missing momentum with respect to the beam direction in the laboratory frame. The variable distribution is shown in fig. 5.12.

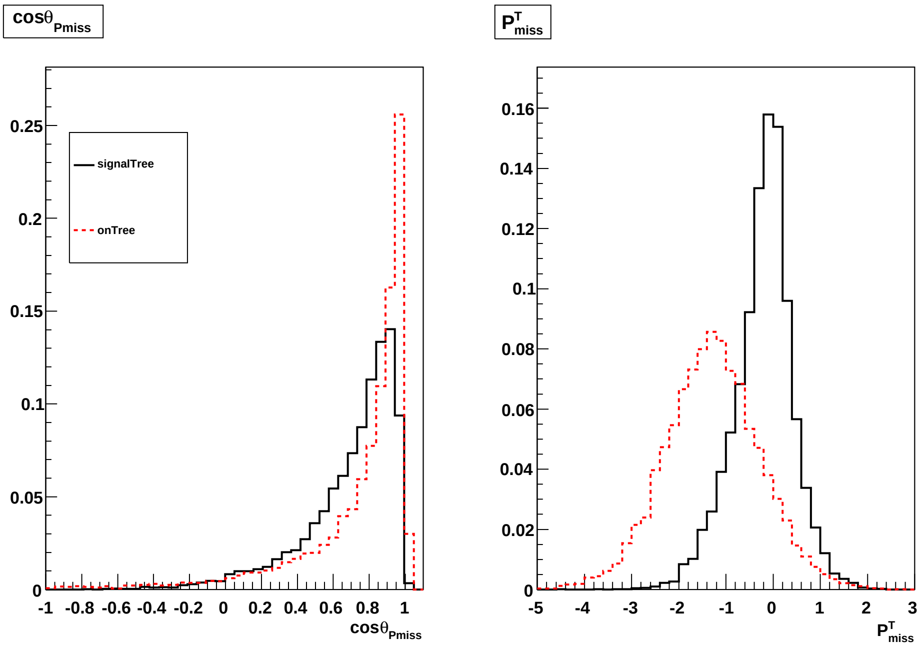

Figure 5.12: $\cos\theta_{P_{miss}}$ and P_{miss}^{pro}: comparison between MC signal events (red dashed line) and sideband ($0.05 < \Delta E < 0.08$ GeV) on-peak data (blue solid line) for the $\eta'_{\eta(\gamma\gamma)\pi\pi} K_L^0$ mode.

We optimize the cuts on these variables using a Bump Hunter algorithm, described in sec. 4.2.1, implemented in `StatPatternRecognition` tool [88]. We use 5000 signal MC as signal events and 5000 sideband on-peak events (requiring $0.05 < \Delta E < 0.08$ GeV) as background. An equal number of independent events is used as validation sample. Events for this optimization are taken from

$\eta'_{\eta(\gamma\gamma)\pi\pi}K^0_L$ mode because it has larger statistics than $\eta'_{\eta(3\pi)\pi\pi}K^0_L$. The algorithm is used with peel parameter is 0.05, maximizing the signal statistical significance ($S/\sqrt{S+B}$, where S and B are the number of signal and background events, respectively, after the cuts). We round the cut on P^{pro}_{miss} to the first decimal in order to increase signal efficiency. We find the following results:

- P^{pro}_{miss} greater than -0.80 GeV$/c$.
- $\cos\theta_{P_{miss}}$ smaller than 0.958.

Another variables used to suppress background due to fake K^0_L is an Artificial Neural Network described below.

Artificial Neural Network

The main source of background in K^0_L reconstruction is photon misidentification in the EMC. Anyway there are many variables, that describes the electromagnetic shower in the EMC, which can help in γ/K^0_L separation. We studied many classifiers and many classifiers architectures to use these (correlated) EMC variables to suppress the background from fake K^0_L in EMC. EMC variables used for our classifiers are:

- *Number of crystals* in the bump.
- *Total Energy* of the bump.
- *Second moment*, defined as:

  $$\mu_2 = \frac{\sum E_i \cdot r_i^2}{\sum E_i},$$

  where E_i is the energy of crystal i and r_i is the distance of crystal i to the cluster center.
- *Lateral moment* , defined as:

  $$\mu_{LAT} = \frac{\sum_{i=2,n} E_i \cdot r_i^2}{(\sum_{i=2,n} E_i \cdot r_i^2) + 25(E_0 + E_1)},$$

  where E_0 refers to the most energetic crystal and E_n to the least energetic one.
- *S1/S9:* The energy of the most energetic crystal (S1) divided by the energy sum of the 3x3 crystal block (S9) with the most energetic crystal in its center.
- *S9/S25:* The energy sum of the 3x3 crystal block (S9) with the most energetic crystal in its center, divided by the energy sum of the 5x5 crystal block (S25) with the most energetic crystal in its center.

– *Zernike moments* $|Z_{20}|$, $|Z_{42}|$ of the spatial energy distribution of the EMC cluster expressed as a series of Zernike polynomials

$$\zeta' : E(x,y) = \sum_{n,m} Z_{n,m} \cdot \zeta'_{n,m}(r,\phi)$$

In fig. 5.13 and 5.14 you can find input variable distributions comparison for signal, on-peak sideband ($0.05 < \Delta E < 0.08$ GeV) and off-peak data. In fig. 5.15 you can find correlation matrix coefficients for input variables.

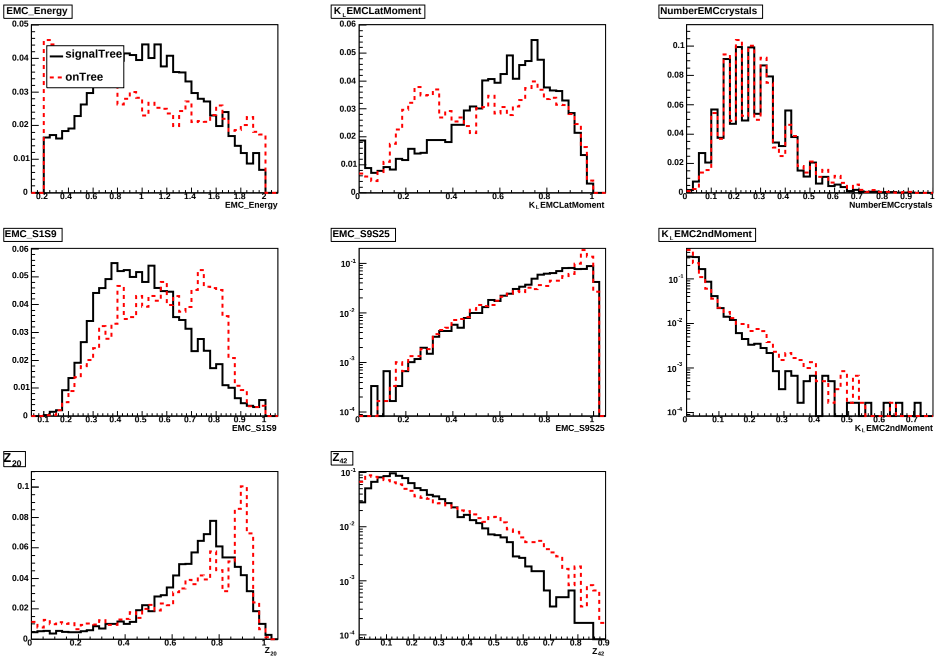

Figure 5.13: ANN input variables comparison between signal MC (continuum black line) and on-peak sideband ($0.05 < \Delta E < 0.08$ GeV) data (dashed red line) using $\eta'_{\eta(\gamma\gamma)\pi\pi}K^0_L$ mode.

We use TMVA [90] to train, test and evaluate our classifiers, using $\eta'_{\eta(\gamma\gamma)\pi\pi}K^0_L$ events. The training configuration is the following: 3000 events for both signal and background samples as training samples and independent 3000 events for both signal and background for validation. We use on-peak sideband (requiring $0.05 < \Delta E < 0.08$ GeV) events as background and MC signal events as signal.

We find TMVA Artificial Neural Network and Boosted Decision Tree to be most performing methods. In fig. 5.16 we show various ROC curves (signal efficiency vs background rejection) for different input variables for ANN and BDT. It's easy to see that adding EMC total energy as input variables improve a lot the discriminating power of the classifiers. We perform further tests to investigate if a different choice of classifier parameters would improve discriminating power. Results of these tests are shown in fig. 5.17 and 5.18.

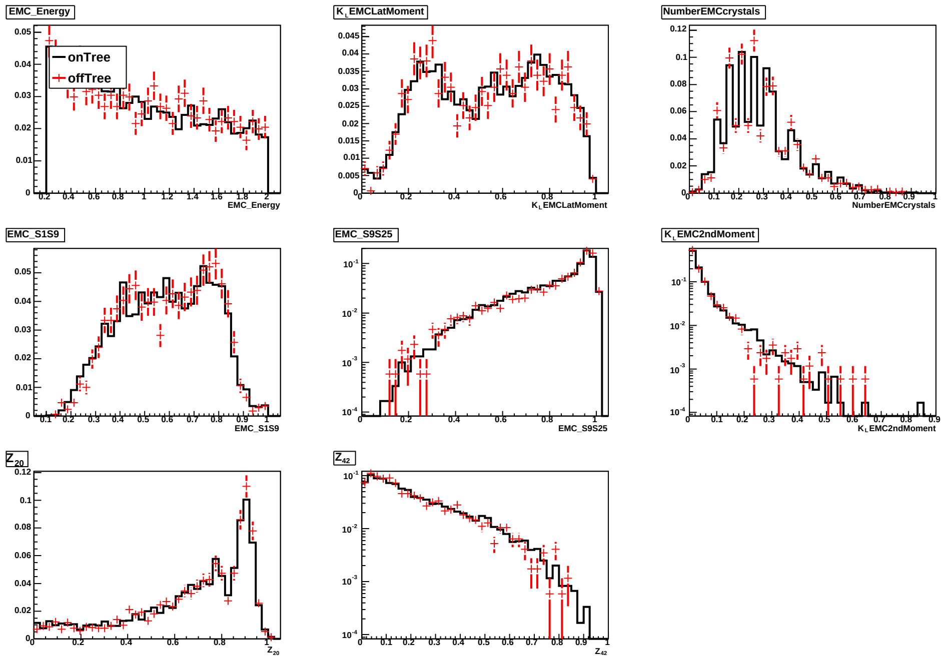

Figure 5.14: ANN input variables comparison between on-peak sideband ($0.05 < \Delta E < 0.08$ GeV) data (continuum black line) and off-peak data (red points) using $\eta'_{\eta(\gamma\gamma)\pi\pi} K^0_L$ mode.

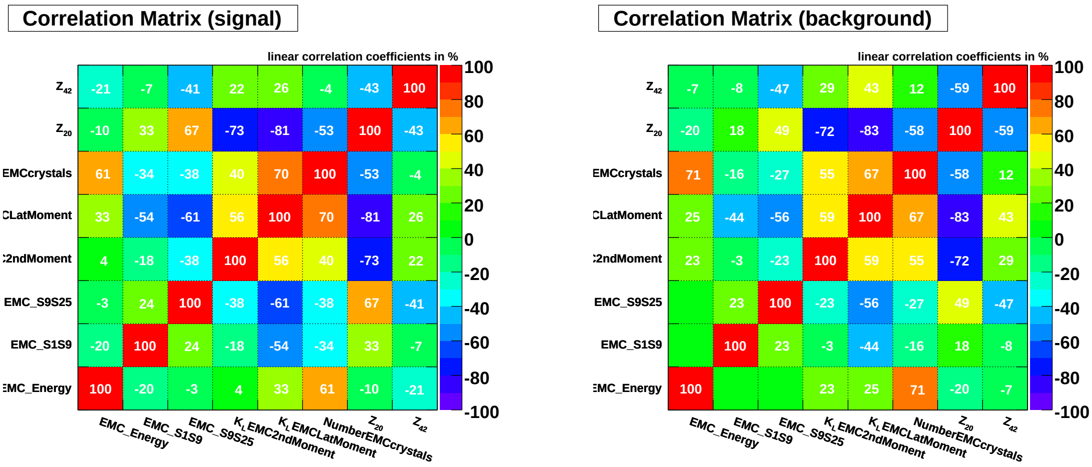

Correlation Matrix (signal)

	EMC_Energy	EMC_S1S9	EMC_S9S25	K$_L$EMC2ndMoment	K$_L$EMCLatMoment	NumberEMCcrystals	Z$_{20}$	Z$_{42}$
Z$_{42}$	-21	-7	-41	22	26	-4	-43	100
Z$_{20}$	-10	33	67	-73	-81	-53	100	-43
EMCcrystals	61	-34	-38	40	70	100	-53	-4
CLatMoment	33	-54	-61	56	100	70	-81	26
2ndMoment	4	-18	-38	100	56	40	-73	22
EMC_S9S25	-3	24	100	-38	-61	-38	67	-41
EMC_S1S9	-20	100	24	-18	-54	-34	33	-7
EMC_Energy	100	-20	-3	4	33	61	-10	-21

Correlation Matrix (background)

	EMC_Energy	EMC_S1S9	EMC_S9S25	K$_L$EMC2ndMoment	K$_L$EMCLatMoment	NumberEMCcrystals	Z$_{20}$	Z$_{42}$
Z$_{42}$	-7	-8	-47	29	43	12	-59	100
Z$_{20}$	-20	18	49	-72	-83	-58	100	-59
EMCcrystals	71	-16	-27	55	67	100	-58	12
CLatMoment	25	-44	-56	59	100	67	-83	43
2ndMoment	23	-3	-23	100	59	55	-72	29
EMC_S9S25		23	100	-23	-56	-27	49	-47
EMC_S1S9		100	23	-3	-44	-16	18	-8
EMC_Energy	100			23	25	71	-20	-7

Figure 5.15: Correlations between the EMC variables used in the ANN for signal and on-peak sideband ($0.05 < \Delta E < 0.08$ GeV) events sets.

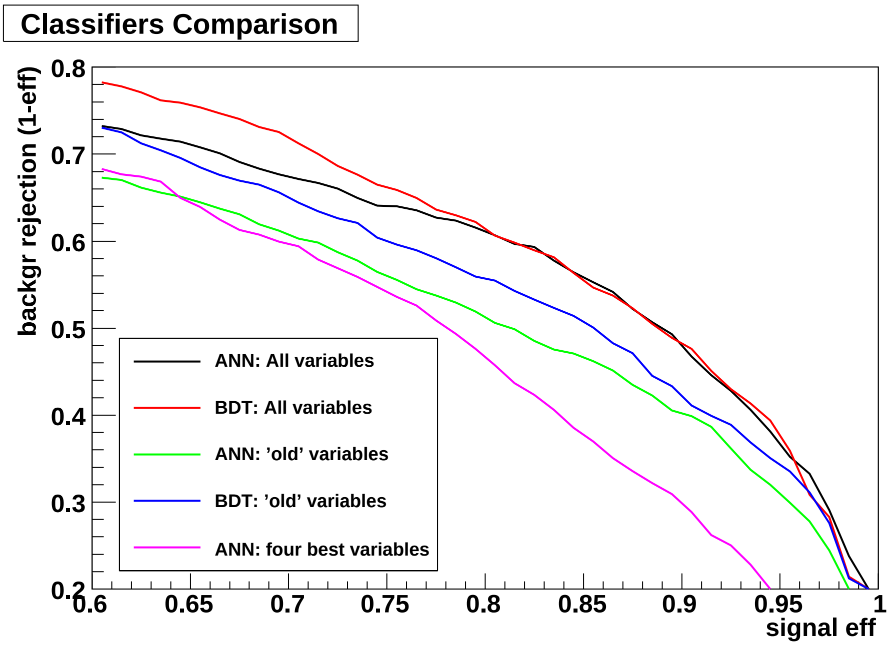

Figure 5.16: ROC curves (signal efficiency vs background rejection) for many choices of ANN and BDT input variables: ANN/BDT All variables (black/red), ANN/BDT without EMC Total Energy (green/blue), ANN four best ranked variables (violet).

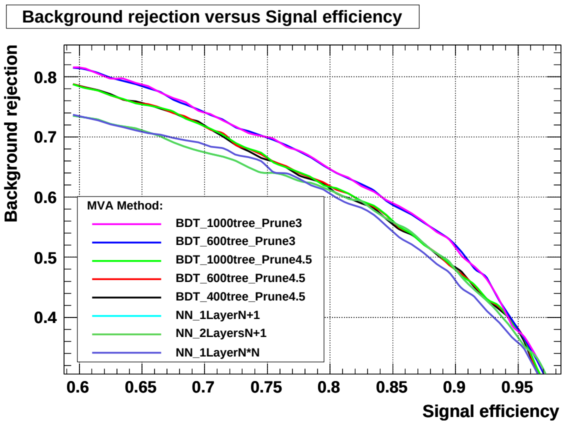

Figure 5.17: ROC curves (signal efficiency vs background rejection) for many choices of ANN and BDT architecture and training parameters using all input variables: BDT 1000 tree, prune strength 3 (violet); BDT 600 tree, prune strength 3 (blue); BDT 1000 tree, prune strength 4.5 (green) BDT 600 tree, prune strength 4.5 (red); BDT 400 tree, prune strength 4.5 (black); ANN 1 layer, N+1 neurons (azure); ANN 2 layers, N+1 neurons per layer (dark green); ANN 1 layer, N^2 neurons (dark blue).

We find that BDT with 600 trees in the forest and prune strength of 3 have some 2-3% discriminating power more than ANN with one single layer with N+1 nodes. It's important to notice that our goal is to cut on the classifiers output in order to suppress background, so our interest is focused on high signal efficiency region. In the choose of what method to use, one must consider that increasing the forest dimension and decreasing the prune strength may cause BDT overtraining, and that there is no standard and simple procedure to evaluate if a BDT is overtrained or not. Due to all these facts, we agreed that this little improvement given by BDT is not sufficient to justify a big effort in trying to estimate if BDT is overtrained.

Finally, we decided to use ANN for signal-background rejection. Our ANN has one hidden layer with 10 neurons, learning parameter is 0.05 and we have performed 500 cycles for the training. In fig. 5.19 you can see the network architecture. In fig. 5.20 we show the Neural Network errors with respect to the training epoch. The ANN is trained to return -1 for background-like events and $+1$ for signal-like ones; output of the Neural Network is shown in fig. 5.21. We apply a lower cut on the Neural Network output in order to increase the purity of the K_L^0 sample, this selection has been optimized according to the statistical significance ($S/\sqrt{S+B}$) using `StatPatternRecognition` tool [88] with 3000 $\eta'_{\eta(\gamma\gamma)\pi\pi}K_L^0$ events for both training and validating and with peel parameter 0.1. We then round the cut to the first decimal in order to increase signal efficiency. The best cut is found to be -0.20.

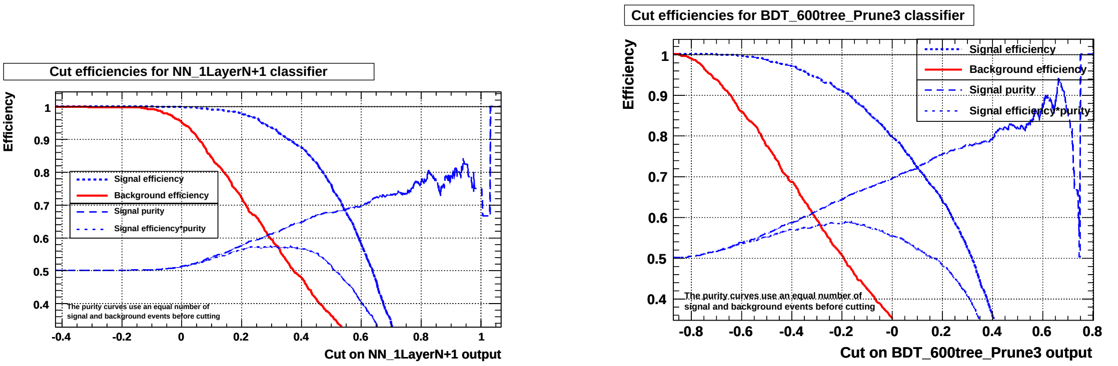

Figure 5.18: Cut efficiency for signal purity (blue dashed), signal efficiency (blue dotted) and background efficiency (red solid) for BDT and ANN with best variables (all) and architecture configuration (ANN:1 layer N+1 neurons;BDT: 600 trees, prune strength 3).

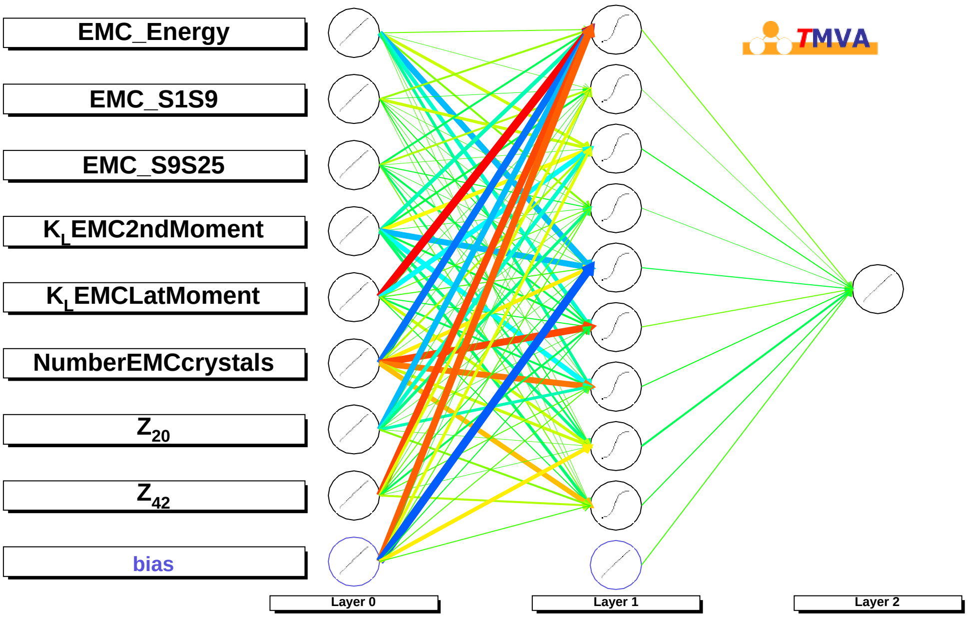

Figure 5.19: ANN Architecture

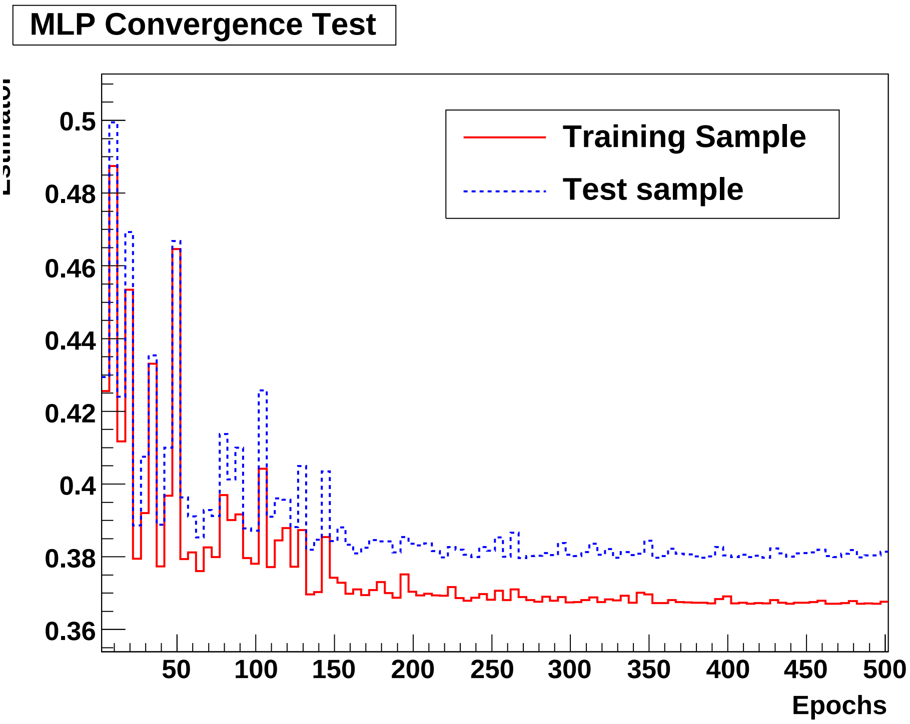

Figure 5.20: ANN Training (solid red) and testing (dashed blue) output respect to training epoch.

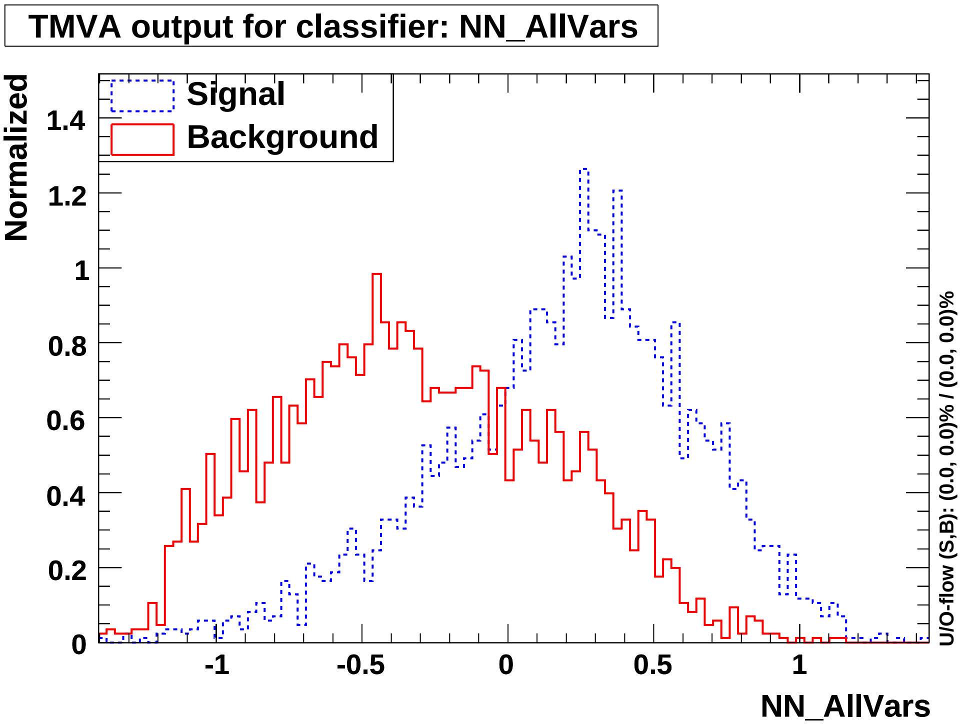

Figure 5.21: ANN output for signal (dashed blue) and background (solid red) events.

5.5.3 $B\overline{B}$ Background Suppression for $\eta_{\gamma\gamma}K^0_S$ Mode

Mode $\eta_{\gamma\gamma}K^0_S$ suffers high $B\overline{B}$ background from $B^0{\rightarrow}\pi^0K^0_S$. This is due to the fact that $B^0{\rightarrow}\pi^0K^0_S$ branching is $\sim$10 times larger than current $B^0{\rightarrow}\eta K^0_S$ upper limit, and to the fact that $\pi^0{\rightarrow}\gamma\gamma$ is $\sim$2.5 times larger than $\eta{\rightarrow}\gamma\gamma$. We optimize here the rejection technique used to suppress this background.

For each reconstructed $B^0{\rightarrow}\eta_{\gamma\gamma}K^0_S$ candidate we look for a π^0 which has a photon in common (overlaps) with the $\eta_{\gamma\gamma}$ candidate. The π^0 candidates are taken from the standard `pi0LooseMass` list, requiring their momentum in the CM frame greater than 1.9 GeV/c and the mass between 0.090 and 0.165 GeV/c^2. If there is more than one overlapping π^0, we choose the one with the most energetic second (non-overlapping) photon. We save the mass of this pion and the energy of its second photon.

As discriminant variables we use:

- the $\eta_{\gamma\gamma}$ decay angle $\mathcal{H}_\eta$, defined as the cosine of the angle between the B recoil direction and the most energetic photon, in the $\eta_{\gamma\gamma}$ rest frame.
- mass of overlapping π^0 (veto π^0 mass). This variable is flat for signal and peaks around pion nominal mass for background $B^0{\rightarrow}\pi^0K^0_S$ events.
- energy of second photon of the overlapping π^0.

In fig. 5.22 we show the distributions for these variables. We reconstruct exclusive $B^0{\rightarrow}\pi^0K^0_S$ MC events with $\eta_{\gamma\gamma}K^0_S$ reconstruction module. For these reconstructed events we fit the veto π^0 mass with a Gaussian plus a first order Chebyshev polynomial. From

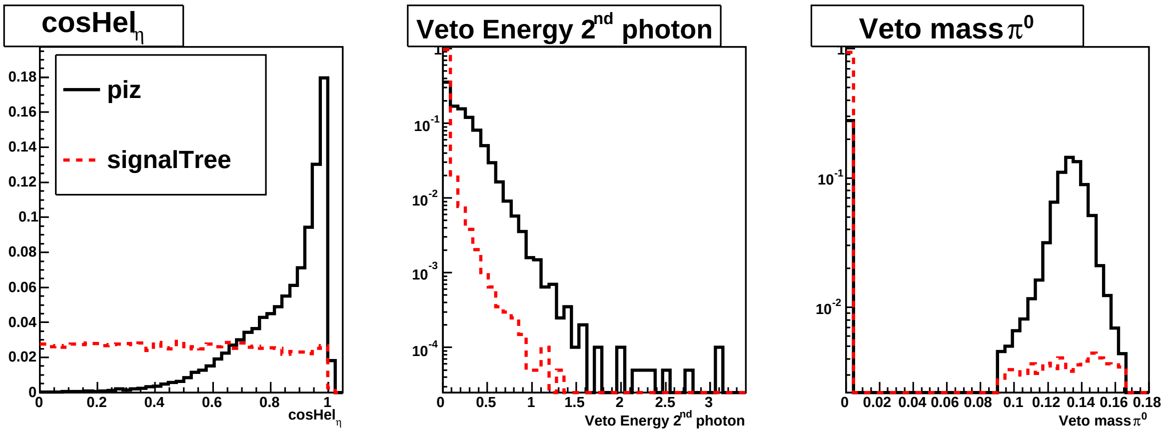

Figure 5.22: Variables of $B^0{\rightarrow}\eta_{\gamma\gamma}K^0_S$ mode used for $B^0{\rightarrow}\pi^0K^0_S$ background suppression: black solid line refers to MC $\pi^0K^0_S$ events, red dashed line to MC $\eta_{\gamma\gamma}K^0_S$ signal events. Events that peaks at zero in π^0 mass and photon energy are those where no pions overlapping with $\eta_{\gamma\gamma}$ signal candidate are found.

results of such a fit, we extract the cut to apply on the veto π^0 mass: we reject events with veto π^0 mass between 0.117 and 0.152 GeV/c^2 (two sigma cut around the mean value). Figure 5.23 shows the fit of veto π^0 mass. For cuts on η decay angle and second photon energy, we use a multidimensional cut optimization, using the Bump Hunter algorithm, implemented in `StatPatternRecognition` tool [88]. We choose to maximize the statistical significance, $SS = \frac{S}{\sqrt{S+B}}$ where S and B are the normalized number of signal and background events, respectively, in the sample used for training and validation. We use 20000 reconstructed MC $\eta_{\gamma\gamma}K^0_S$ events as signals and 20000 reconstructed MC $\pi^0K^0_S$ events as background. Independent 20000 events of the same reconstructed events are used as validation sample for both signal and background, respectively. These events are selected including the best candidate selection, choosing the candidate with highest vertex probability (see sec. 7.4.2). Best cuts were obtained with a peel parameter of 0.1. Results are shown in Table 5.3.

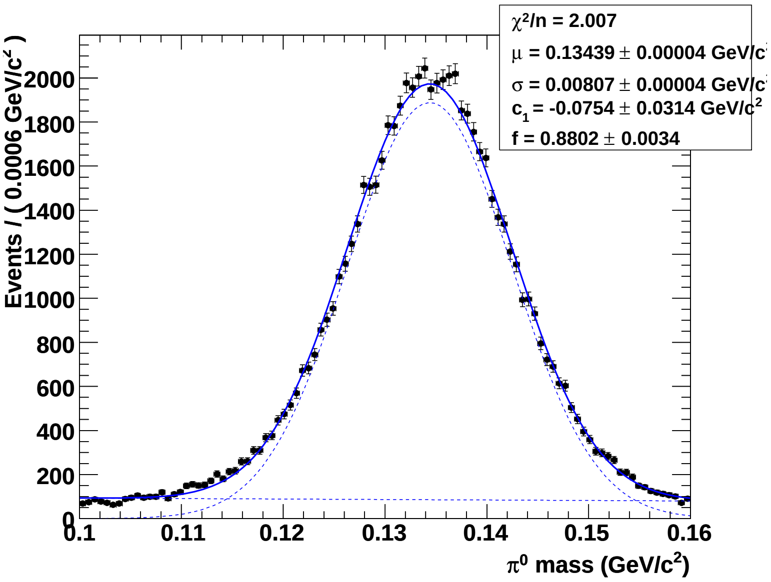

Figure 5.23: Veto π^0 mass of exclusive $B^0 \rightarrow \pi^0 K^0_S$ MC events reconstructed with $\eta_{\gamma\gamma}K^0_S$ module.. Fit function is a Gaussian plus a first order Chebyshev polynomial.

Variable	Cut
η decay angle	< 0.966
Energy of second photon	< 0.207 GeV

Table 5.3: Results of the cut optimization for $B^0 \rightarrow \pi^0 K^0_S$ background suppression in $B^0 \rightarrow \eta_{\gamma\gamma} K^0_S$ mode.

5.5.4 Summary of Selection Cuts

The reconstructed events are selected with further cuts to discriminate signal from background events. Most of these cuts are common to all analyses, like charged particles identification and daughter resonances mass cuts. However, TD $\eta' K$ analyses require further specific cuts, which are reported separately. In the following sections we will report the value of common and specific cuts for each analysis.

Common Selection Cuts

These are the common selection cuts applied to all analyses.

- **Event-wide cuts**
  - Charged tracks from $\eta_{3\pi}$, ω, $\eta'_{\eta\pi\pi}$, and $\eta'_{\rho\gamma}$ candidates satisfy electron, kaon and proton vetoes, by using `PidLHElectronSelector` (tight), `PidKaonLHSelector` (tight) and `PidProtonLHSelector` (veryTight). In $\eta' K$ analysis we use `PidKaonBDTSelector` (tight).
  - Both charged tracks from ϕ candidates satisfy electron, pion and proton vetoes, by using `PidLHElectronSelector` (tight), `PidKaonLHSelector` (notApion) and `PidProtonLHSelector` (veryTight).
  - Charged kaon in $B^+ \to \eta' K^+$ satisfies `PidKaonBDTSelector` (tight)
  - $E_\gamma > 0.030$ GeV for π^0; $E_\gamma > 0.050$ GeV for $\eta_{\gamma\gamma}$ in $\eta'_{\eta\pi\pi}$; $E_\gamma > 0.100$ GeV for primary $\eta_{\gamma\gamma}$ from B; $E_\gamma > 0.100$ GeV for the γ in $\eta_{\gamma\gamma}$ of $\eta'_{\eta(\gamma\gamma)\pi\pi}K^+$; $E_\gamma > 0.200$ GeV for $\eta'_{\rho\gamma}$. In $\eta' K$ analysis, we require $E_\gamma > 0.100$ GeV for $\eta'_{\rho\gamma}$.
- **Daughter resonances cuts**
  - M_{π^0} between 0.120 and 0.150 GeV/c^2.
  - M_η for primary η from B decay: between 0.505 and 0.585 GeV/c^2 for primary $\eta_{\gamma\gamma}$ (resolution 13 MeV/c^2) and between 0.535 and 0.555 GeV/c^2 for primary $\eta_{3\pi}$ (resolution 3 MeV/c^2).
  - M_η for η in $\eta'_{\eta\pi\pi}$: between 0.490 and 0.600 GeV/c^2 for $\eta_{\gamma\gamma}$ and between 0.520 and 0.570 GeV/c^2 for $\eta_{3\pi}$.
  - M_{ρ^0} between 0.470 and 1.000 GeV/c^2.
  - the $\mathcal{H}_\rho$, defined as the angle between the momenta of the ρ^0 daughter π^- and of the recoil η', measured in the ρ^0 rest frame, is required to be $|\mathcal{H}_\rho| < 0.9$.
  - M_ω between 0.735 and 0.825 GeV/c^2.

  - $M_{\eta'}$ between 0.930 and 0.990 GeV/c^2 for $\eta'_{\eta\pi\pi}$ and between 0.910 and 0.990 GeV/c^2 for $\eta'_{\rho\gamma}$. In $\eta' K$ analysis, we require $M_{\eta'}$ between 0.930 and 0.980 GeV/c^2 for $\eta'_{\rho\gamma}$ and between 0.945 and 0.970 GeV/c^2 for $\eta'_{\eta\pi\pi}$.
  - M_ϕ between 1.012 and 1.026 GeV/c^2 (resolution 2.2 MeV/c^2).
  - $\eta_{\gamma\gamma}$ decay angle $|\mathcal{H}_\eta| < 0.966$ for $\eta_{\gamma\gamma} K^0_S$ mode; $|\mathcal{H}_\eta| < 0.95$ for $\eta_{\gamma\gamma}\eta_{\gamma\gamma}$ and $\eta_{\gamma\gamma}\eta_{3\pi}$ modes.
  - For $K^0_S \to \pi^+\pi^-$ we consider K^0_S mass between 0.486 and 0.510 GeV/c^2, fit probability $\chi^2 > 0.001$ and flight length grater than 3 times its uncertainty. For $K^0_s \to \pi^0\pi^0$, we apply only the cut on mass between 0.468 and 0.528 GeV/c^2;
  - $\pi^0 K^0_S$ veto for $\eta_{\gamma\gamma} K^0_S$: we look for π^0 candidates which overlap with our reconstructed signal candidate. Among them we choose the π^0 with the most energetic second (non-overlapping) photon. We reject the reconstructed $\eta_{\gamma\gamma} K^0_S$ candidate if the π^0 mass is between 0.117 and 0.152 GeV/c^2 and the energy of second photon is greater than 0.207 GeV.
  - K^0_L **selection**
    - $*$ cut on transverse Missing Momentum $P^{pro}_{miss} > -0.80$ GeV/c.
    - $*$ cut on $\cos\theta_{P_{miss}}$ smaller than 0.958.
    - $*$ cut on the output of the neural network for K^0_L reconstructed in EMC Output$_{ANN} > -0.20$.

Specific Selection Cuts for $\eta' K$ Time-Dependent Analysis

Here below specific cuts that applies only for $\eta' K$ Time-Dependent analysis are listed.

- **Event-wide cuts**
  - $|\Delta t|$ (see sec. 3.3) smaller than 20 ps.
  - $\sigma_{\Delta t}$ defined as the uncertainty on Δt smaller than 2.5 ps.

Chapter 6

Measurement of Time-Dependent CP Asymmetry in $\eta' K^0$ Decay Modes

6.1 Introduction

In this chapter, we describe the measurement of the time-dependent (TD) CP violating asymmetries in the charmless B^0 meson decays to $B^0 \rightarrow \eta' K^0_S$ and $B^0 \rightarrow \eta' K^0_L$, using the total and final statistics accumulated by *BABAR* (467 million of $B\overline{B}$ pairs). We extract the parameters of CP violating asymmetry from a combined fit to the time evolution of $B^0 \rightarrow \eta' K^0_S$ and $B^0 \rightarrow \eta' K^0_L$. A detailed description of the physical interest in this measurement, and of the relation between results and CKM parameters is given in chapter 2.

6.2 Previous Results

This measurement is an update of previous ones, using the final *BABAR* statistics. For the first time we added the new submode $\eta'_{\eta(3\pi)\pi\pi} K^0_L$ to the measurement. The result of this analysis contributed to the results presented to *International Conference on High Energy Physics (ICHEP) 2008* Conference, that took place in Philadelphia. These measurements were included into a paper already submitted to *Physical Review D* [19]. The observation of CP violation in S parameter using this decay mode was first observed by *BABAR* in 2006, with a great contribution of Milan group [18]. We report in tab. 6.1 results of previous publication by *BABAR* [18, 102, 103].

Table 6.1: Results for S and C from the $B^0 \to \eta' K^0$ in the three *BABAR* already published results in 2003 [102], 2005 [103], and 2007 [18]. Subscripts for η' decay modes denote $\eta'_{\eta(\gamma\gamma)\pi\pi}$ (1), $\eta'_{\rho\gamma}$ (2), and $\eta'_{\eta(3\pi)\pi\pi}$ (3).

Mode	S	C
PRL 91, 161801 (2003)		
$\eta'_1 K^0_{\pi^+\pi^-}$	0.75 ± 0.51	-0.21 ± 0.35
$\eta'_2 K^0_{\pi^+\pi^-}$	-0.41 ± 0.42	0.24 ± 0.27
combined	$+0.02 \pm 0.34 \pm 0.03$	$0.10 \pm 0.22 \pm 0.04$
PRL 94, 191802 (2005)		
$\eta'_1 K^0_{\pi^+\pi^-}$	0.01 ± 0.28	-0.18 ± 0.18
$\eta'_2 K^0_{\pi^+\pi^-}$	0.44 ± 0.19	-0.30 ± 0.13
$\eta'_3 K^0_{\pi^+\pi^-}$	0.79 ± 0.47	0.11 ± 0.35
$\eta'_1 K^0_{\pi^0\pi^0}$	-0.04 ± 0.57	-0.65 ± 0.42
$\eta'_2 K^0_{\pi^0\pi^0}$	-0.45 ± 0.68	0.41 ± 0.40
combined	$+0.30 \pm 0.14 \pm 0.02$	$-0.21 \pm 0.10 \pm 0.02$
PRL 98, 031801 (2007)		
$\eta'_1 K^0_{\pi^+\pi^-}$	0.61 ± 0.23	-0.26 ± 0.14
$\eta'_2 K^0_{\pi^+\pi^-}$	0.56 ± 0.14	-0.24 ± 0.10
$\eta'_3 K^0_{\pi^+\pi^-}$	0.89 ± 0.35	0.14 ± 0.25
$\eta'_1 K^0_{\pi^0\pi^0}$	0.84 ± 0.42	-0.26 ± 0.36
$\eta'_2 K^0_{\pi^0\pi^0}$	0.56 ± 0.41	0.15 ± 0.27
$\eta'_1 K^0_L$	0.32 ± 0.28	0.08 ± 0.23
combined	$+0.58 \pm 0.10 \pm 0.03$	$-0.16 \pm 0.07 \pm 0.03$

6.3 Measurement of CP Asymmetries

In chapter 2 we give a detailed description of the formalism used in order to extract CP asymmetries parameters in $\eta' K^0$.

Because in the present document we fit the time dependent evolution of both $B^0 \to \eta' K^0_S$ and $B^0 \to \eta' K^0_L$, we write here explicitly the decay rate distributions in these decay modes to make clear the sign of the parameter S we are measuring.

For each $B^0 \to \eta' K^0_S$ or $B^0 \to \eta' K^0_L$ candidate (B_{CP}), we reconstruct the decay vertex of the other B meson ($B_{\rm tag}$) from the remaining charged tracks in the event and identify its flavor. The distribution of Δt is:

$$f(\Delta t) = \frac{e^{-|\Delta t|/\tau}}{4\tau} \left\{1 \mp \Delta\omega \pm (1-2\omega)\left[-\eta S \sin(\Delta m_d \Delta t) - C\cos(\Delta m_d \Delta t)\right]\right\}, \quad (6.1)$$

where the upper (lower) sign denotes a decay accompanied by a B^0 ($\overline{B}^0$) tag, τ is the mean B^0 lifetime, Δm_d is the mixing frequency, η is the CP eigenvalue of the final state ($\eta = +1$ for $B^0 \to \eta' K^0_L$, $\eta = -1$ for $B^0 \to \eta' K^0_S$) and the mistag parameters ω and $\Delta\omega$

are the average and difference, respectively, of the probabilities that a true B^0 ($\overline{B}^0$) meson is tagged as $\overline{B}^0$ (B^0). The final (observed) distribution $F(\Delta t)$ is the convolution of $f(\Delta t)$ with the signal vertex resolution function.

6.4 Data and Monte Carlo Samples

The analysis presented in this chapter is based on the full dataset accumulated by *BABAR* in the period 1999-2007 (`Run1-Run6`). In the present analysis we use the following samples:

- Data:
  - On-peak 425.7 fb^{-1}, (467.4 ± 5.1) million of $B\bar{B}$ pairs.
  - Off-peak 44.4 fb^{-1} integrated luminosity.
- generic Monte Carlo:
  - 735.9 million events for the $B^0\bar{B}^0$, corresponding to 3.1 times On-peak luminosity.
  - 731.1 million events for the B^+B^-, corresponding to 3.1 times On-peak luminosity.
- Signal Monte Carlo: Statistics used for the different modes can be seen in tab. 6.2.
- several exclusive Monte Carlo simulation for background modes, listed in sec. 6.6.

$\eta'_{\eta(\gamma\gamma)\pi\pi}K^0_{S(\pi^+\pi^-)}$	$\eta'_{\rho\gamma}K^0_{S(\pi^+\pi^-)}$	$\eta'_{\eta(3\pi)\pi\pi}K^0_S$	$\eta'_{\eta(\gamma\gamma)\pi\pi}K^0_{S(\pi^0\pi^0)}$	$\eta'_{\rho\gamma}K^0_{S(\pi^0\pi^0)}$
972K	972K	189K	195K	195K

$\eta'_{\eta(\gamma\gamma)\pi\pi}K^+$	$\eta'_{\rho\gamma}K^+$	$\eta'_{\eta(3\pi)\pi\pi}K^+$	$\eta'_{\eta(\gamma\gamma)\pi\pi}K^0_L$	$\eta'_{\eta(3\pi)\pi\pi}K^0_L$
972K	972K	195K	429K	195K

Table 6.2: Monte Carlo signal events dataset sizes

6.5 Preparation of the Input to ML Fit

The events for each mode are reconstructed and selected (see chapter 5). For each event we can have more candidates due to the possible different combinations of the reconstructed particles of the event. To prepare the samples for the input to ML fits, we have to choose one of these candidates per event, if any. In this way we obtain the final input to ML fits. In this section we report the events selection efficiencies and multiple candidates selection.

6.5.1 Selection Cut Efficiencies

We show in tab. 6.3–6.12 the selection efficiencies in the different MC and data samples: MC signal events; generic $B\overline{B}$ MC samples, where we remove our signal events, considering the cases with charm+charmless B decays (w/ charm) and only charmless B decays (w/o charm); on-peak and off-peak data. Explanation of the cuts is given in section 5.5.4. The first row gives the number of events for the samples used in the analysis (table 6.2). In the next row we give the number of events after the preliminary cuts. Then we have the efficiencies for each cut, computed after applying all the cuts in the previous rows. The last rows give: the total efficiency, calculated as ratio of the number of events surviving all cuts and the number of collected (generated) events, and the number of events as input to ML fit for data.

	MC Signal	$B^0\overline{B}^0$		B^+B^-		On-Peak	Off-Peak
		w/ charm	w/o charm	w/ charm	w/o charm		
# Events	972K	736M		731M		425.7 fb^{-1}	44.4 fb^{-1}
Preliminary	317068	259	64	287	64	8154	764
PID vetoes	98.3	66.4	75.0	64.8	79.7	76.3	75.5
η mass	96.7	82.6	83.3	83.9	94.1	84.7	84.2
η' mass	95.5	51.4	45.0	60.3	68.8	66.3	59.3
K^0_S mass	97.3	58.9	66.7	42.6	39.4	67.6	66.7
K^0_S cuts	95.7	60.5	75.0	12.5	15.4	63.0	51.6
ΔT	99.0	100.0	100.0	100.0	100.0	98.7	100.0
$\sigma_{\Delta T}$	97.5	100.0	100.0	80.0	50.0	96.7	98.0
Efficiency (%)	26.6	3.53E-06	1.22E-06	5.47E-07	1.37E-07	2.23E-05	1.60E-05
Input ML						1416	97

Table 6.3: Selection cuts and efficiency (%) for mode $\eta'_{\eta(\gamma\gamma)\pi\pi}K^0_S$ for the different MC and data samples. See the text for an explanation of different rows content.

	MC Signal	$B^0\overline{B}^0$		B^+B^-		On-Peak	Off-Peak
		w/ charm	w/o charm	w/ charm	w/o charm		
# Events	189K	736M		731M		425.7 fb $^{-1}$	44.4 fb $^{-1}$
Preliminary	48438	261	96	230	40	4070	360
PID vetoes	95.4	48.3	52.1	39.1	52.5	63.3	61.4
π^0 mass	86.3	70.6	76.0	65.6	71.4	73.9	69.7
η mass	99.4	88.8	84.2	93.2	100.0	96.4	93.5
η' mass	87.2	50.6	53.1	61.8	66.7	59.0	48.6
K_S^0 mass	97.4	67.5	76.5	44.1	50.0	68.3	61.4
K_S^0 cuts	95.9	63.0	84.6	20.0	60.0	63.9	51.2
ΔT	99.0	100.0	100.0	100.0	100.0	97.7	100.0
$\sigma_{\Delta T}$	98.1	100.0	100.0	100.0	100.0	97.6	100.0
Efficiency (%)	16.6	2.31E-06	1.49E-06	4.10E-07	4.10E-07	7.09E-06	3.62E-06
Input ML						451	22

Table 6.4: Selection cuts and efficiency (%) for mode $\eta'_{\eta(3\pi)\pi\pi}K_S^0$ for the different MC and data samples. See the text for an explanation of different rows content.

	MC Signal	$B^0\overline{B}^0$		B^+B^-		On-Peak	Off-Peak
		w/ charm	w/o charm	w/ charm	w/o charm		
# Events	972K	736M		731M		425.7 fb $^{-1}$	44.4 fb $^{-1}$
Preliminary	357361	14907	2681	17217	1558	245522	24331
PID vetoes	95.14	64.84	72.21	55.54	69.45	57.46	57.25
ρ mass	99.91	99.79	99.9	99.76	99.54	99.74	99.77
ρ Hel	98.36	84.48	87.64	85.84	88.12	89.8	90.37
η' mass	88.76	55.68	56.64	55.67	56.59	53.98	54.05
K_S^0 mass	97.26	67.25	78.85	57.26	67.04	63.16	63.34
K_S^0 cuts	95.73	52.97	74.11	34.87	58.61	49.51	48.07
ΔT	99.01	98.64	98.75	98.57	98.1	98.36	98.06
$\sigma_{\Delta T}$	98.16	97.74	97.47	98.1	98.55	97.56	97.53
Efficiency (%)	27.6	2.12E-04	7.34E-005	1.20E-04	2.79E-05	3.22E-004	3.26E-04
Input ML						20468	1977

Table 6.5: Selection cuts and efficiency (%) for mode $\eta'_{\rho\gamma}K_S^0$ for the different MC and data samples. See the text for an explanation of different rows content.

	MC Signal	$B^0\overline{B}^0$		B^+B^-		On-Peak	Off-Peak
		w/ charm	w/o charm	w/ charm	w/o charm		
# Events	195K	736M		731M		425.7 fb^{-1}	44.4 fb^{-1}
Preliminary	33749	85	25	70	9	3595	336
PID vetoes	98.2	65.9	64.0	77.1	100.0	76.2	73.2
η mass	96.6	85.7	87.5	77.8	77.8	83.1	81.7
η' mass	95.4	58.3	57.1	61.9	57.1	62.3	61.7
π^0 masses	92.2	60.7	50.0	53.8	50.0	77.9	74.2
K^0_S mass	95.2	70.6	100.0	85.7	100.0	86.2	80.4
ΔT	99.1	100.0	100.0	100.0	100.0	97.7	97.3
$\sigma_{\Delta T}$	95.2	100.0	100.0	91.7	100.0	94.2	95.8
Efficiency (%)	13.0	1.63E-06	5.44E-07	1.50E-06	2.74E-07	1.38E-05	1.14E-05
Input ML						877	69

Table 6.6: Selection cuts and efficiency (%) for mode $\eta'_{\eta(\gamma\gamma)\pi\pi} K^0_{S(\pi^0\pi^0)}$ for the different MC and data samples. See the text for an explanation of different rows content.

	MC Signal	$B^0\overline{B}^0$		B^+B^-		On-Peak	Off-Peak
		w/ charm	w/o charm	w/ charm	w/o charm		
# Events	195K	736M		731M		425.7 fb^{-1}	44.4 fb^{-1}
Preliminary	39015	4007	1003	5518	801	115224	11584
PID vetoes	94.9	56.1	55.9	53.9	71.2	60.9	60.5
ρ mass	100.0	99.6	100.0	99.8	99.5	99.7	99.7
ρ Hel	98.2	85.1	86.8	86.1	89.2	89.9	90.3
η' mass	89.4	56.6	60.0	53.7	53.2	53.3	51.7
π^0 masses	92.2	82.1	83.6	79.2	74.3	78.7	78.0
K^0_S mass	95.3	91.3	91.0	86.3	87.0	86.7	87.0
ΔT	99.1	99.0	99.5	99.0	100.0	98.5	98.2
$\sigma_{\Delta T}$	98.1	96.5	97.3	96.5	94.8	97.2	96.9
Efficiency (%)	14.2	1.05E-04	2.92E-05	1.23E-04	2.26E-05	3.44E-04	3.46E-04
Input ML						21909	2102

Table 6.7: Selection cuts and efficiency (%) for mode $\eta'_{\rho\gamma} K^0_{S(\pi^0\pi^0)}$ for the different MC and data samples. See the text for an explanation of different rows content.

	MC Signal	$B^0\overline{B}^0$		B^+B^-		On-Peak	Off-Peak
		w/ charm	w/o charm	w/ charm	w/o charm		
# Events	195K	736M		731M		425.7 fb $^{-1}$	44.4 fb $^{-1}$
Preliminary	55332	48620	3053	47198	2594	337816	31766
PID Vetoes	98.2	65.3	75.0	59.5	67.9	73.4	74.6
η mass	96.5	84.6	86.9	84.0	86.9	83.6	83.6
η' mass	93.6	51.0	63.1	49.7	63.2	56.8	57.4
Δ_T	98.9	98.0	98.4	98.1	99.3	97.6	97.5
$\sigma_{\Delta T}$	92.2	91.5	90.7	92.1	92.8	90.3	90.7
p^{Pro}_{Miss}	86.1	22.6	34.5	17.2	21.8	34.3	35.2
$\cos\theta_{Pmiss}$	98.0	96.1	96.6	95.9	95.9	91.9	91.8
ANN Cut	90.8	46.6	54.0	37.4	38.2	55.2	55.7
Efficiency (%)	17.6	1.69E-04	2.75E-05	8.96E-05	9.71E-06	5.70E-04	2.97E-04
Input ML						18036	1806

Table 6.8: Selection cuts and efficiency (%) for mode $\eta'_{\eta(\gamma\gamma)\pi\pi}K^0_L$ for the different MC and data samples. See the text for an explanation of different rows content.

	MC Signal	$B^0\overline{B}^0$		B^+B^-		On-Peak	Off-Peak
		w/ charm	w/o charm	w/ charm	w/o charm		
# Events	195K	736M		731M		425.7 fb $^{-1}$	44.4 fb $^{-1}$
Preliminary	45721	49940	2908	42534	2116	170804	15010
PID Vetoes	95.4	46.4	53.9	43.9	53.6	59.1	62.1
π^0 mass	86.7	74.5	76.7	73.4	74.5	74.8	75.0
η mass	99.3	94.8	96.3	94.5	95.0	95.6	95.6
η' mass	84.0	44.1	52.5	42.7	47.7	50.1	50.5
Δ_T	99.0	99.5	99.7	99.4	99.2	98.5	98.2
$\sigma_{\Delta T}$	97.2	98.0	97.9	97.8	97.6	96.6	96.0
p^{Pro}_{Miss}	90.4	22.2	47.4	15.9	22.9	35.4	35.9
$\cos\theta_{Pmiss}$	98.2	97.7	98.2	95.7	96.5	93.7	94.0
ANN Cut	91.0	47.1	54.7	38.3	50.0	54.4	54.2
Efficiency (%)	12.6	9.77E-05	2.05E-05	4.28E-05	5.61E-06	1.96E-04	9.59E-05
Input ML						6213	582

Table 6.9: Selection cuts and efficiency (%) for mode $\eta'_{\eta(3\pi)\pi\pi}K^0_L$ for the different MC and data samples. See the text for an explanation of different rows content.

	MC Signal	$B^0\overline{B}^0$		B^+B^-		On-Peak	Off-Peak
		w/ charm	w/o charm	w/ charm	w/o charm		
# Events	972K	736M		731M		425.7 fb^{-1}	44.4 fb^{-1}
Preliminary	355913	386	178	995	541	25069	2151
PID vetoes	98.3	65.5	70.2	72.2	86.3	77.7	75.3
PID vetoes K	90.8	26.5	22.4	35.1	37.0	40.4	33.6
η mass	96.5	77.6	75.0	86.1	86.1	85.9	84.0
η' mass	95.6	46.2	42.9	63.6	67.1	70.3	56.0
ΔT	99.1	100.0	100.0	99.3	99.0	98.8	97.3
$\sigma_{\Delta T}$	98.5	100.0	100.0	97.1	97.0	98.3	96.8
Efficiency (%)	29.4	3.26E-06	1.22E-06	1.82E-05	1.31E-05	7.24E-05	3.97E-05
Input ML						4606	241

Table 6.10: Selection cuts and efficiency (%) for mode $\eta'_{\eta(\gamma\gamma)\pi\pi}K^+$ for the different MC and data samples. See the text for an explanation of different rows content.

	MC Signal	$B^0\overline{B}^0$		B^+B^-		On-Peak	Off-Peak
		w/ charm	w/o charm	w/ charm	w/o charm		
# Events	195K	736M		731M		425.7 fb^{-1}	44.4 fb^{-1}
Preliminary	58644	490	134	1182	681	15347	1369
PID vetoes	95.4	42.7	61.2	58.5	72.2	64.2	62.1
PID vetoes K	90.9	14.8	11.0	37.6	42.9	40.4	34.8
π^0 mass	85.9	67.7	66.7	72.3	72.0	75.8	73.6
η mass	99.4	100.0	100.0	96.8	97.4	96.3	94.5
η' mass	87.6	47.6	66.7	47.3	48.0	63.0	54.9
ΔT	99.0	100.0	100.0	100.0	100.0	98.8	100.0
$\sigma_{\Delta T}$	98.6	100.0	100.0	98.8	98.6	98.5	100.0
Efficiency (%)	19.0	1.36E-06	5.44E-07	1.16E-05	9.57E-06	2.80E-05	1.86E-05
Input ML							

Table 6.11: Selection cuts and efficiency (%) for mode $\eta'_{\eta(3\pi)\pi\pi}K^+$ for the different MC and data samples. See the text for an explanation of different rows content.

	MC Signal	$B^0\overline{B}^0$		B^+B^-		On-Peak	Off-Peak
		w/ charm	w/o charm	w/ charm	w/o charm		
# Events	972K	736M		731M		425.7 fb^{-1}	44.4 fb^{-1}
Preliminary	420853	30377	11692	72540	19871	983938	99598
PID vetoes	95.1	62.0	78.2	57.6	73.8	61.9	62.1
PID vetoes K	90.6	25.8	20.6	42.0	25.4	32.8	32.3
ρ mass	99.9	99.8	99.7	99.8	99.9	99.7	99.7
ρ Hel	98.3	83.7	86.2	82.7	85.9	89.8	90.0
η' mass	88.8	55.6	54.5	56.1	56.8	54.3	53.0
ΔT	99.3	99.3	99.4	99.3	99.3	98.3	98.9
$\sigma_{\Delta T}$	98.7	98.3	98.3	98.7	98.8	97.9	98.1
Efficiency (%)	31.9	2.99E-04	1.18E-04	1.09E-03	2.43E-04	1.47E-03	1.52E-03
Input ML						93626	9225

Table 6.12: Selection cuts and efficiency (%) for mode $\eta'_{\rho\gamma}K^+$ for the different MC and data samples. See the text for an explanation of different rows content.

6.5.2 Multiple Candidate per Event

We have analyzed the problem of multiple signal candidates per event. Actually, in one single event many candidate daughter should, in principle, be combined to form a B candidate. We first make the choice of the "best" candidate and then look for events with MC truth or without MC truth[1]. In some modes with multiple particles in the final state we consider as MC truth also events where there is a permutation of the particles (PP) inside the B candidate. For example if we consider $\eta'_{\eta(3\pi)\pi\pi}K^0_S$ decay, if we exchange one of the charge pion from η with one from η', this is a PP. Events where the B candidate exchanges at least one track or neutral particle with the rest of the event are called self-cross feed (SCF) events. Efficiency of the candidate selection refers to events which have one candidate with MC truth or which have one PP event. We verified that PP events are mainly due to the permutation of pions or photons in η' daughters. These events have the same discriminating variables shapes as MC truth one. For the Time-Dependent analysis, we must be aware that the important point is o have a good vertex resolution. We checked that PP and SCF with exchange of neutral particles doesn't alter the vertex. Some worsening is observed with the SCF with exchange of more than one particle from the other B.

Concerning SCF events, the main source of SCF depend on the particular decay mode: in K^0_{S+-} modes, it is the exchange of at least one soft pion from η'; in K^0_{S00} modes, it is the exchange of at least one soft photon in K^0_S daughters; in K^0_L modes, it is the presence of a fake K^0_L. These events show wider distribution (especially for ΔE) with respect to MC truth ones, anyway we account them as signal because information about B decay vertex is only minimally altered. In some specific modes SCF component is added into the fit (see sec 6.7).

In selecting the "best" candidate we have applied an algorithm based on B vertex probability, choosing the one with the vertex probability closer to 1. Efficiency of this algorithm is in the range 95–98%. We have verified in previous analyses that this algorithm has higher efficiency than other criteria, such as the best η/η' mass.

In K^0_L modes we distinguish the candidates in two categories, depending on the subdetector where the K^0_L candidate is identified: EMC and IFR. If the direction of IFR candidate is compatible with a candidate of EMC, we consider the two candidates as the same candidate (category EMC+IFR) and we drop the IFR one, because EMC has a better spatial resolution than IFR. We use the B vertex probability to select the "best" candidate. If several candidates have the same B vertex probability, we choose the candidate with the K^0_L coming from (in order): EMC+IFR, EMC, IFR.

We summarize in Table 6.13 the number of combinations per event for data and MC

---

[1] With MC truth we denote an events which is reconstructed *exactly* as it was simulated.

signal events, the efficiency of the algorithm of selection (considering MC truth events and MC truth plus PP ones) and the MC signal composition, split into MCTruth + PP fraction and SCF fraction.

Mode	# combs/event (data)	#combs/event (MC signal)	Best Candidate Efficiency (%)		MC Signal Composition (%)	
			MCtruth	MCtruth+PP	MCtruth+PP	SCF
$\eta'_{\eta(\gamma\gamma)\pi\pi}K^0_{S(\pi^+\pi^-)}$	1.09	1.10	98.1	98.2	95.0	5.0
$\eta'_{\eta(3\pi)\pi\pi}K^0_{S(\pi^+\pi^-)}$	2.54	2.66	50.4	95.7	84.0	16.0
$\eta'_{\rho\gamma}K^0_{S(\pi^+\pi^-)}$	1.07	1.07	97.7	97.7	93.4	6.6
$\eta'_{\eta(\gamma\gamma)\pi\pi}K^0_{S(\pi^0\pi^0)}$	1.24	1.22	94.5	94.7	84.4	15.6
$\eta'_{\rho\gamma}K^0_{S(\pi^0\pi^0)}$	1.22	1.20	94.1	94.6	82.8	17.2
$\eta'_{\eta(\gamma\gamma)\pi\pi}K^0_L$	1.15	1.19	93.8	96.8	91.0	9.0
$\eta'_{\eta(3\pi)\pi\pi}K^0_L$	2.52	2.96	48.0	92.7	77.7	22.3
$\eta'_{\eta(\gamma\gamma)\pi\pi}K^+$	1.05	1.06	98.8	98.8	95.9	4.1
$\eta'_{\eta(3\pi)\pi\pi}K^+$	2.41	2.65	53.4	95.7	83.6	16.4
$\eta'_{\rho\gamma}K^+$	1.07	1.07	97.8	97.8	93.5	6.5

Table 6.13: Results of “best candidate” selection algorithm.

6.5.3 Efficiency

The MC efficiency (MC ϵ) is calculated as the ratio of the number of MC signal events which pass all cuts (i.e. as input to ML fit), independently by the MC truth matching, to the number of generated MC signal events. These values are shown in tab. 6.14. We show also the total branching fraction ($\prod \mathcal{B}_i$) of the sub-decays [98] involved for each mode, and the number of on-peak events as input to ML fit.

Mode	$\eta'_{\eta(\gamma\gamma)\pi\pi}K^0_{S(\pi^+\pi^-)}$	$\eta'_{\eta(3\pi)\pi\pi}K^0_S$	$\eta'_{\rho\gamma}K^0_{S(\pi^+\pi^-)}$	$\eta'_{\eta(\gamma\gamma)\pi\pi}K^0_{S(\pi^0\pi^0)}$	$\eta'_{\rho\gamma}K^0_{S(\pi^0\pi^0)}$
MC ϵ (%)	26.6	16.6	27.6	13.0	14.2
$\prod \mathcal{B}_i$ (%)	6.0 ± 0.2	3.5 ± 0.1	10.2 ± 0.3	2.7 ± 0.1	4.5 ± 0.1
Input to ML fit	1416	451	20468	877	21909

Mode	$\eta'_{\eta(\gamma\gamma)\pi\pi}K^+$	$\eta'_{\rho\gamma}K^+$	$\eta'_{\eta(3\pi)\pi\pi}K^+$	$\eta'_{\eta(\gamma\gamma)\pi\pi}K^0_L$	$\eta'_{\eta(3\pi)\pi\pi}K^0_L$
MC ϵ (%)	29.4	31.9	19.0	17.6	12.6
$\prod \mathcal{B}_i$ (%)	17.5 ± 0.5	29.5 ± 0.9	10.1 ± 0.4	8.8 ± 0.3	5.1 ± 0.2
Input to ML fit	4606	93626	1781	18036	6213

Table 6.14: MC efficiency, total branching fraction of the sub-decays for each mode, and number of on-peak events as input to ML fit.

6.6 $B\overline{B}$ Backgrounds

We have done a detailed analysis of $B\overline{B}$ background in all our decay modes. Our procedure is realized in three steps.

First we apply the full analysis selection to MC $B\overline{B}$ generic samples. In all samples, of course, we remove our signal MC modes. We look at all the MC events separating possible $B\overline{B}$ cross feed into charm B decays and charmless B decays. This is due to the fact that charm B decays are continuum-like in $m_{\rm ES}$ and ΔE while charmless B decays should peak, in these two variables, in the same region of the signal. In this first step we are interested in finding categories of events which could contribute to background. We show in tab. 6.15 for each decay mode and for the two samples $B^0\overline{B}^0$ and B^+B^- the total number of events passing the full selection, normalized to on-peak luminosity. Some of the modes in such generics sample are due to `JetSet` fragmentation of $b{\rightarrow}c$ modes, which are, in general, no-peaking background. We do not include this kind of backgrounds in our studies.

Mode	$B^0\overline{B}^0$ charm	$B^0\overline{B}^0$ charmless	B^+B^- charm	B^+B^- charmless
$\eta'_{\eta(\gamma\gamma)\pi\pi}K^0_{S(\pi^+\pi^-)}$	5 ± 1	3 ± 1	1 ± 1	0 ± 1
$\eta'_{\eta(3\pi)\pi\pi}K^0_{S(\pi^+\pi^-)}$	2 ± 1	3 ± 1	0 ± 1	1 ± 1
$\eta'_{\rho\gamma}K^0_{S(\pi^+\pi^-)}$	323 ± 11	171 ± 8	216 ± 9	65 ± 5
$\eta'_{\eta(\gamma\gamma)\pi\pi}K^0_{S(\pi^0\pi^0)}$	2 ± 1	1 ± 1	3 ± 1	1 ± 1
$\eta'_{\rho\gamma}K^0_{S(\pi^0\pi^0)}$	178 ± 8	68 ± 5	233 ± 5	53 ± 4
$\eta'_{\eta(\gamma\gamma)\pi\pi}K^0_L$	331 ± 11	64 ± 5	187 ± 8	23 ± 3
$\eta'_{\eta(3\pi)\pi\pi}K^0_L$	181 ± 8	48 ± 4	87±5	13 ± 2
$\eta'_{\eta(\gamma\gamma)\pi\pi}K^+$	5 ± 1	3 ± 1	12 ± 2	7 ± 2
$\eta'_{\eta(3\pi)\pi\pi}K^+$	2 ± 1	1 ± 1	5 ± 1	3 ± 1
$\eta'_{\rho\gamma}K^+$	424 ± 13	275 ± 10	1975 ± 33	569 ± 15

Table 6.15: Input to ML fit for $B\overline{B}$ generic samples for each target decay mode, normalized to the integrated on-peak luminosity.

In the second step we reconstruct large samples of MC signal events of candidate cross feed modes, which are peaking in $m_{\rm ES}$ and ΔE variables, and we evaluate reconstruction efficiency and number of expected candidates (normalized to our on-peak integrated luminosity) in ML input. In tab. 6.16–6.21 we report the results of the $B\overline{B}$ studies for each decay mode. For each decay mode we give the MC reconstruction efficiency ϵ, the branching fraction ($\mathcal{B}$), the daughter branching fraction product ($\prod\mathcal{B}_i$), the estimated background in ML input (normalized to our integrated luminosity) and the sign of the mean of the ΔE variable distribution. The branching fractions of the background $B\overline{B}$ modes studied are taken from PDG [98] and HFAG tables [48]. For modes where branching fractions aren't measured, yet, we take theoretical predicted value, taking as error the value itself. The modes $\eta'_{\eta(\gamma\gamma)\pi\pi}K^0_{S(\pi^+\pi^-)}$, $\eta'_{\eta(3\pi)\pi\pi}K^0_{S(\pi^+\pi^-)}$, $\eta'_{\eta(\gamma\gamma)\pi\pi}K^0_{S(\pi^0\pi^0)}$, and $\eta'_{\eta(3\pi)\pi\pi}K^+$ are clean (as you can see in tab. 6.15) and the remaining background is due to random combinations.

Finally, we use these MC events to fit PDFs to be introduced in the maximum likelihood fit. PDFs are fitted on a weighted average of exclusive MC background events, in order to take into account properly the different contributions. We split the background events in two categories depending if they have a positive (labeled with $+$) or negative ($-$) ΔE distribution mean (see fig. 6.1). We keep these two category separated while fitting the PDFs.

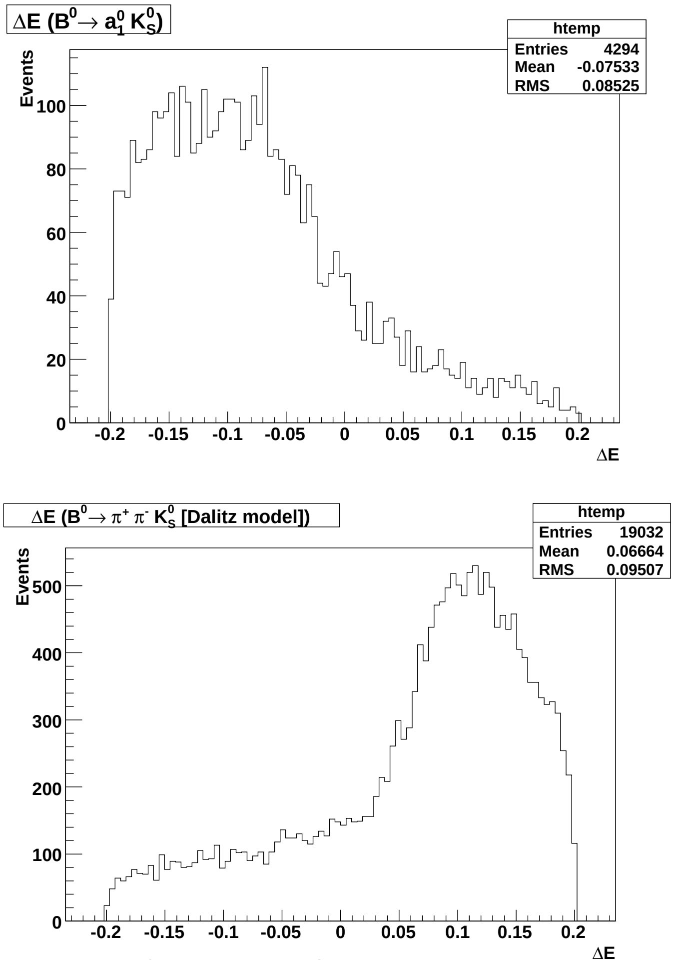

Figure 6.1: ΔE distributions for two specific B decays mode that give high background to $\eta'_{\rho\gamma}K^0_S$: $B^0 \to a^0_1 K^0_S$ (top) and $B^0 \to \pi^+\pi^- K^0_S$(Dalitz model) (bottom). The first(second) background mode has negative(positive) ΔE mean because one particle is lost(acquired) in order to form $\eta'_{\rho\gamma}K^0_S$ final state.

We perform toy-experiment studies (see sec. 6.8) where we embed these events, taken from MC samples, as expected in the ML input. In this way we see if there is a possible effect due to this kind of backgrounds on the fit results.

Our studies pointed out that $B\overline{B}$ component in the ML fit is needed for modes containing $\eta'_{\rho\gamma}$, only.

Cross Feed Channel	MC ϵ (%)	Est. $\mathcal{B}$ (10^{-6})	$\prod \mathcal{B}_i$ (%)	# evts in ML	Avg. sign
$B^0 \to \pi^+\pi^- K^0_S$ (Dalitz)	1.08 ± 0.01	44.8 ± 2.5	34.6 ± 0.1	78 ± 4	$+$
$B^+ \to a_1^+ K^0_S$	0.84 ± 0.02	34.9 ± 6.7	50	68 ± 13	$-$
$B^0 \to a^0_{1(\rho^+\pi^-)} K^0_S$	1.97 ± 0.03	15 ± 15	22.84 ± 0.03	31 ± 31	$-$
$B^+ \to \rho^+ K^0_S$	0.78 ± 0.02	8.0 ± 1.5	50	15 ± 3	$+$
$B^0 \to \phi_{3\pi} K^0_S$	5.87 ± 0.06	8.3 ± 1.1	5.29 ± 0.14	12 ± 2	$-$
$B^+ \to \rho K^*(1430)$	0.04 ± 0.01	40 ± 40	100	8 ± 8	$-$
$B^+ \to \rho^0 K^{*+}_{\pi^+ K^0_S}$ (Long.)	1.56 ± 0.02	3.6 ± 1.8	23.04 ± 0.03	6 ± 3	$-$
$B^0 \to \rho K^*(1430)$	0.05 ± 0.00	20 ± 20	100	4 ± 4	$-$
$B^0 \to \omega K^0_S$	0.55 ± 0.01	4.8 ± 0.6	30.83 ± 0.25	4 ± 0	$-$
$B^+ \to \eta'_{\rho\gamma} K^{*+}_{\pi^+ K^0_S}$	2.37 ± 0.03	4.9 ± 2.0	6.77 ± 0.21	4 ± 2	$-$
$B^+ \to f_0(980) K^{*+}_{\pi^+ K^0_S}$	0.48 ± 0.02	5.2 ± 1.3	23.04 ± 0.03	3 ± 1	$-$
$B^0 \to \eta'_{\eta_{\gamma\gamma}\pi\pi} K^0_S$	0.15 ± 0.00	65 ± 3	6.1 ± 0.2	3 ± 0	$-$
$B^+ \to a_1^0 K^{*+}_{\pi^+ K^0_S}$	0.06 ± 0.01	13.4 ± 13.4	33.3	2 ± 2	$-$
$B^+ \to \pi^+ K^{*0}_{\pi^0 K^0_S}$	0.22 ± 0.01	10 ± 1	16.7	2 ± 0	$+$
$B^+ \to b_1^+ K^0_S$	0.17 ± 0.01	9.6 ± 1.9	30.83 ± 0.25	2 ± 0	$-$
$B^+ \to \pi^+ K^0_S$	0.04 ± 0.00	23 ± 1	34.6 ± 0.1	2 ± 0	$+$
$B^0 \to \rho^- K^{*+}_{\pi^+ K^0_S}$ (Long.)	0.31 ± 0.01	2 ± 2	23.04 ± 0.03	1 ± 1	$-$
$B^0 \to K^+ K^- K^0_S$ (Dalitz)	0.04 ± 0.00	24.7 ± 2.3	34.6 ± 0.1	1 ± 0	$-$
$B^0 \to \eta'_{\omega\gamma} K^0_S$	0.44 ± 0.02	65 ± 3	0.92 ± 0.09	1 ± 0	$-$
$B^0 \to b_1^0 K^0_S$	0.11 ± 0.01	5.1 ± 1.8	30.83 ± 0.25	1 ± 1	$-$
$B^+ \to K^0_S K^{*+}_{\pi^+ K^0_S}$	0.29 ± 0.01	0.95 ± 0.95	16.6	1 ± 1	$-$
Total				97 ± 5	$+$
				152 ± 35	$-$
				249 ± 35	

Table 6.16: Potential $B\overline{B}$ background for the $\eta'_{\rho\gamma} K^0_{S(\pi^+\pi^-)}$ mode. See the text for an explanation of different columns content.

Cross Feed Channel	MC ϵ (%)	Est. $\mathcal{B}$ (10^{-6})	$\prod \mathcal{B}_i$ (%)	# evts in ML
$B^0 \to \eta'_{\eta(\gamma\gamma)\pi\pi} K^0_S$	0.39 ± 0.01	65.0 ± 3.0	6.1 ± 0.2	7 ± 0
$B^0 \to \eta'_{\eta\pi\pi} K^0_{S(\pi^0\pi^0)}$	0.45 ± 0.02	65.0 ± 3.0	2.7 ± 0.1	4 ± 0
$B^+ \to \eta' l \nu$	0.00 ± 0.00	80.0 ± 80.0	100.0	1 ± 1
$B^0 \to \omega K^0_L$	0.07 ± 0.01	4.8 ± 0.6	44.6 ± 0.4	1 ± 0
Total				13 ± 1

Table 6.17: Potential $B\overline{B}$ background for the $\eta'_{\eta(\gamma\gamma)\pi\pi} K^0_L$ mode. See the text for an explanation of different columns content.

Cross Feed Channel	MC ϵ (%)	Est. $\mathcal{B}$ (10^{-6})	$\prod \mathcal{B}_i$ (%)	# evts in ML	Avg. Sign
$B^0 \to \pi^+\pi^- K^0_{S(\pi^0\pi^0)}$	0.55 ± 0.02	44.8 ± 2.5	15.4 ± 0.1	18 ± 1	+
$B^+ \to a_1^+ K^0_S$	0.17 ± 0.01	34.9 ± 6.7	50.0	14 ± 3	–
$B^+ \to a_1^+ \pi^0$	0.05 ± 0.00	26.4 ± 6.8	100.0	6 ± 2	+
$B^+ \to \rho^+ \rho^0$ (Long.)	0.07 ± 0.00	15.2 ± 2.8	100.0	5 ± 1	+
$B^0 \to \rho^+ \rho^-$	0.03 ± 0.00	23.2 ± 3.5	100.0	4 ± 1	–
$B^+ \to \rho^+ K^0_S$	0.20 ± 0.01	8.0 ± 1.4	50.0	4 ± 1	+
$B^+ \to \eta'_{\rho\gamma} \rho^+$	0.26 ± 0.01	8.7 ± 3.3	29.4 ± 0.9	3 ± 1	–
$B^0 \to a_1^+(\rho^+\pi^0)\pi^-$	0.03 ± 0.00	31.7 ± 3.7	50.0	2 ± 0	+
$B^0 \to a^+_{1(\rho^+\pi^0)} \rho^-$ (Long.)	0.03 ± 0.00	31.4 ± 31.4	50.0	2 ± 2	–
$B^0 \to a^+_{1(\rho^0\pi^+)} \rho^-$ (Long.)	0.02 ± 0.00	31.4 ± 31.4	50.0	2 ± 2	–
$B^0 \to \pi^0\pi^0\rho^0$	0.05 ± 0.00	5.0 ± 5.0	100.0	1 ± 1	–
$B^0 \to \pi^- K^{*+}_{\pi^+ K^0_S}$	0.07 ± 0.01	9.8 ± 1.1	33.3	1 ± 0	+
$B^+ \to \pi^+\pi^0\rho^0$	0.02 ± 0.00	10.0 ± 10.0	100.0	1 ± 1	–
$B^+ \to \pi^+ K^{*0}_{\pi^0 K^0_S}$	0.07 ± 0.01	10.7 ± 0.8	16.7	1 ± 0	+
$B^0 \to \eta'_{\eta\pi\pi} K^0_{S(\pi^0\pi^0)}$	0.07 ± 0.01	65.0 ± 3.0	2.7 ± 0.1	1 ± 0	–
Total				37 ± 3	+
				28 ± 5	–
				65 ± 6	

Table 6.18: Potential $B\overline{B}$ background for the $\eta'_{\rho\gamma} K^0_{S(\pi^0\pi^0)}$ mode. See the text for an explanation of different columns content.

Cross Feed Channel	MC ϵ (%)	Est. $\mathcal{B}$ (10^{-6})	$\prod \mathcal{B}_i$ (%)	# evts in ML
$B^0 \to \eta'_{\eta(3\pi)\pi\pi} K^0_S$	0.71 ± 0.02	65.0 ± 3.0	3.5 ± 0.1	8 ± 0
$B^+ \to \eta'_{\eta(3\pi)\pi\pi} K^+$	0.02 ± 0.00	70.0 ± 2.0	10.1 ± 0.4	1 ± 0
Total				9 ± 0

Table 6.19: Potential $B\overline{B}$ background for the $\eta'_{\eta(3\pi)\pi\pi} K^0_L$ mode. See the text for an explanation of different columns content.

Cross Feed Channel	MC ϵ (%)	Est. $\mathcal{B}$ (10^{-6})	$\prod \mathcal{B}_i$ (%)	# evts in ML	Avg. Sign
$B^0 \to \eta'_{\eta(\gamma\gamma)\pi\pi} K^{*0}_{K^+\pi^-}$	2.53 ± 0.04	3.8 ± 1.2	11.7 ± 0.4	5 ± 2	–
$B^+ \to \eta'_{\eta(\gamma\gamma)\pi\pi} \pi^+$	1.22 ± 0.03	2.7 ± 0.5	17.5 ± 0.6	3 ± 1	+
$B^+ \to \omega K^+$	0.04 ± 0.00	6.7 ± 0.5	89.1 ± 0.7	1 ± 0	–
Total				3 ± 1	+
				6 ± 2	–
				9 ± 2	

Table 6.20: Potential $B\overline{B}$ background for the $\eta'_{\eta(\gamma\gamma)\pi\pi} K^+$ mode. See the text for an explanation of different columns content.

Cross Feed Channel	MC ϵ (%)	Est. $\mathcal{B}$ (10^{-6})	$\prod \mathcal{B}_i$ (%)	# evts in ML	Avg. Sign
$B^+ \to \pi^+\pi^- K^+$	1.18 ± 0.01	54.4 ± 4.7	100.0	300 ± 26	+
$B^+ \to a_1^0 K^+$	2.22 ± 0.03	9.0 ± 9.0	100.0	94 ± 94	–
$B^0 \to K^+\pi^-\pi^0$	0.55 ± 0.01	35.9 ± 2.5	100.0	92 ± 7	+
$B^0 \to \rho^- K^+$	1.54 ± 0.02	8.6 ± 1.0	100.0	62 ± 7	+
$B^0 \to a^+_{1(\rho^0\pi^+)} K^-$	2.41 ± 0.01	8.2 ± 1.9	50.0	46 ± 11	–
$B^+ \to \Phi_{3\pi} K^+$	6.70 ± 0.06	8.3 ± 0.7	15.3 ± 0.4	40 ± 3	–
$B^+ \to \rho^0 K^{*+}_{\pi^+ K^0_S}(1430)$	0.16 ± 0.00	40.0 ± 40.0	100.0	29 ± 29	–
$B^+ \to \omega K^+$	0.66 ± 0.02	6.7 ± 0.5	89.1 ± 0.7	18 ± 1	–
$B^+ \to \pi^+ K^{*0}_{2(K^+\pi^-)}(1430)$	0.89 ± 0.02	5.6 ± 1.8	66.7	16 ± 5	+
$B^0 \to \rho K^*(1430)$	0.16 ± 0.00	20.0 ± 20.0	100.0	15 ± 15	–
$B^0 \to \pi^- K^{*+}_{K^+\pi^0}(1430)$	0.19 ± 0.01	46.6 ± 6.1	33.3	13 ± 2	+
$B^+ \to \rho^0 K^{*+}_{K^+\pi^0}$ (Long.)	1.90 ± 0.02	3.6 ± 1.8	33.3	11 ± 5	–
$B^0 \to \eta'_{\rho\gamma} K^{*0}_{K^+\pi^-}$	2.87 ± 0.04	3.8 ± 1.2	19.6 ± 0.6	10 ± 3	–
$B^0 \to \rho^0 K^+\pi^-$	0.21 ± 0.01	10.0 ± 10.0	100.0	10 ± 10	–
$B^+ \to a_1^0 \pi^+$	0.11 ± 0.00	20.0 ± 20.0	100.0	10 ± 10	–
$B^+ \to \eta'_{\eta(\gamma\gamma)\pi\pi} K^+$	0.17 ± 0.00	70.0 ± 2.0	17.5 ± 0.6	10 ± 0	–
$B^+ \to \rho^0 \pi^+$	0.21 ± 0.00	8.7 ± 1.0	100.0	9 ± 1	+
$B^+ \to \eta'_{\omega\gamma} K^+$	0.99 ± 0.02	70.0 ± 2.0	2.7 ± 0.3	9 ± 1	–
$B^0 \to a^+_{1(\rho^0\pi^+)} \pi^-$	0.12 ± 0.00	31.7 ± 3.7	50.0	9 ± 1	–
$B^0 \to a^+_{1(\rho^+\pi^0)} K^-$	0.45 ± 0.02	8.2 ± 1.9	50.0	9 ± 2	–
$B^0 \to \pi^- K^+$	0.09 ± 0.00	19.4 ± 0.6	100.0	8 ± 0	+
$B^0 \to \pi^- K^{*+}_{K^+\pi^0}$	0.47 ± 0.02	10.6 ± 0.9	33.3	8 ± 1	+
$B^+ \to \eta'_{\rho\gamma} K^{*+}_{K^+\pi^0}$	3.14 ± 0.04	4.9 ± 2.0	9.8 ± 0.3	7 ± 3	–
$B^+ \to K^+K^-K^+$	0.04 ± 0.00	32.5 ± 1.5	100.0	6 ± 0	–
$B^+ \to \rho^+\rho^0$ (Long.)	0.09 ± 0.00	15.2 ± 2.8	100.0	6 ± 1	–
$B^0 \to b_1^- K^+$	0.20 ± 0.01	7.4 ± 1.4	89.1 ± 0.7	6 ± 1	–
$B^0 \to \eta\pi^+K^-(n.r.)$	0.06 ± 0.00	20.0 ± 20.0	100.0	6 ± 6	–
$B^0 \to \rho^0 K^{*0}_{K^+\pi^-}$	1.84 ± 0.02	1.0 ± 0.6	66.7	6 ± 3	–
$B^+ \to \rho^+ K^{*0}_{K^+\pi^-}$ (Long.)	0.33 ± 0.01	5.0 ± 1.3	66.7	5 ± 1	–
$B^+ \to \eta'_{\rho\gamma}\pi^+$	1.30 ± 0.03	2.7 ± 0.5	29.4 ± 0.9	5 ± 1	+
$B^+ \to b_1^0 K^+$	0.13 ± 0.01	9.1 ± 2.0	89.1 ± 0.7	5 ± 1	–
$B^+ \to \rho^+ K^+\pi^-$	0.14 ± 0.00	10.0 ± 10.0	66.7	4 ± 4	–
$B^0 \to f_0(990) K^{*0}_{K^+\pi^-}$	0.55 ± 0.02	2.0 ± 2.0	66.7	3 ± 3	–
$B^+ \to a_1^+(\rho^0\pi^+) K^{*0}_{K^+\pi^-}$ (Long.)	0.13 ± 0.01	13.9 ± 13.9	33.4	3 ± 3	–
$B^0 \to \rho^+\rho^-(Long.)$	0.02 ± 0.00	23.2 ± 3.5	100.0	2 ± 0	–
$B^+ \to K^+ K^{*0}_{K^+\pi^-}(1430)$	0.34 ± 0.01	2.2 ± 2.2	66.7	2 ± 2	–
$B^0 \to \rho^-\pi^0 K^+$	0.03 ± 0.00	10.0 ± 10.0	100.0 ± 0.0	2 ± 2	–
$B^+ \to \pi^+\pi^+\pi^-(N.R.)$	0.16 ± 0.01	3.0 ± 3.0	100.0	2 ± 2	+
$B^0 \to a_1^0 K^{*0}_{K^+\pi^-}$ (Long.)	0.10 ± 0.01	6.5 ± 6.5	66.7	2 ± 2	–
$B^+ \to \pi^0 K^+$	0.02 ± 0.00	12.9 ± 0.6	100.0	2 ± 0	–
$B^0 \to a_1^+(\rho^+\pi^0)\pi^-$	0.02 ± 0.00	31.7 ± 3.7	50.0	1 ± 0	–
$B^0 \to \rho^- K^{*+}_{K^+\pi^0}$	0.35 ± 0.01	2.0 ± 2.0	33.3	1 ± 1	–
$B^+ \to \rho^0\pi^0 K^+$	0.22 ± 0.01	1.0 ± 1.0	100.0	1 ± 1	–
$B^0 \to K^+ K^{*-}_{K^-\pi^0}$	0.25 ± 0.01	2.0 ± 2.0	33.3	1 ± 1	+
$B^0 \to \rho^0\rho^0$ (Long.)	0.25 ± 0.01	0.6 ± 0.4	100.0	1 ± 0	–
$B^0 \to \pi^+\pi^- K^{*0}_{K^+\pi^-}$	0.06 ± 0.00	5.0 ± 5.0	66.7	1 ± 1	–
Total				516 ± 28	+
				392 ± 102	–
				908 ± 106	

Table 6.21: Potential $B\overline{B}$ background for the $\eta'_{\rho\gamma}K^+$ mode. See the text for an explanation of different columns content.

6.7 Maximum Likelihood Fit

6.7.1 Overview

An unbinned multivariate maximum likelihood (ML) analysis is performed using `MiFit` [97] software. Events are selected with the cuts described in chapter 5 and choosing the best candidate as described in sec. 6.5.2.

In our sample of events we have considered five components: signal, continuum background, $B\overline{B}$ charm background, $B\overline{B}$ peaking charmless background which are peaking for positive ΔE value, $B\overline{B}$ peaking charmless background which are peaking for negative ΔE value. For each input event i, the likelihood ($\mathcal{L}_i$) is defined as:

$$\mathcal{L}_i = n_{sg}\mathcal{P}^i_{sg} + n_{q\bar{q}}\mathcal{P}^i_{q\bar{q}} + n_{bc}\mathcal{P}^i_{bc} + n_{bk+}\mathcal{P}^i_{bk+} + n_{bk-}\mathcal{P}^i_{bk-} \tag{6.2}$$

where $\mathcal{P}^i_{sg}$, $\mathcal{P}^i_{q\bar{q}}$, $\mathcal{P}^i_{bc}$, $\mathcal{P}^i_{bk+}$, and $\mathcal{P}^i_{bk-}$ are the probability for signal, continuum background, $B\overline{B}$ charm background, and $B\overline{B}$ charmless peaking background (positive and negative peaking in ΔE), evaluated with the observables of the i^{th} event as the product of the probability density functions (PDFs) for each of the observable. n_{sg} (number of signal events), $n_{q\bar{q}}$ (number of continuum events), n_{bc} (number of $B\overline{B}$ charm events), n_{bk+}, and n_{bk-} (number of $B\overline{B}$ charmless peaking events, positive and negative peaking in ΔE) are free parameters in the fit.

The $B\overline{B}$ background studies (see sec. 6.6) and MC toy-experiment studies (see sec. 6.8) suggest decay modes where it's useful to add $B\overline{B}$ charm and peaking components in the fit. From these studies it turns out that both $B\overline{B}$ peaking and charm component are needed in modes with $\eta'_{\rho\gamma}$.$B\overline{B}$ charm component is only considered in modes with K^0_S, where there are two discriminant variables, m_{ES} and ΔE, to separate it from signal one; this explain why such a component is not used in K^0_L modes. The list of components for each mode is shown in tab. 6.22. In general we consider only one signal events component, combining MC truth and SCF events to make signal component PDFs. Anyway we found (see sec. 7.6) that modes which have high SCF fraction (greater than 10%) can suffer significant biases in the signal yields in the ML fit. For these modes we found that in order to reduce the bias it's useful to split signal events component in well-reconstructed signal events component (based on MC truth and PP events, see section 6.5.2) and SCF signal events component. In this case we keep one signal yield as free parameter in the ML fit and we use the fixed fraction of SCF found in MC, to weight properly the two well-reconstructed and SCF components.

In the Time Dependent analysis the events are split in tagging categories. We use Tag04 tagger [76] as tagging algorithm. It classifies the events in 6 mutually exclusive

Decay Mode	Fit Components
$\eta'_{\eta(\gamma\gamma)\pi\pi}K^0_{S(\pi^+\pi^-)}$	*sg*, $q\bar{q}$
$\eta'_{\eta(3\pi)\pi\pi}K^0_{S(\pi^+\pi^-)}$	*sgtr*, *sgscf*, $q\bar{q}$
$\eta'_{\rho\gamma}K^0_{S(\pi^+\pi^-)}$	*sg*, $q\bar{q}$, *bc*, *bk*+, *bk*–
$\eta'_{\eta(\gamma\gamma)\pi\pi}K^0_{S(\pi^0\pi^0)}$	*sgtr*, *sgscf*, $q\bar{q}$
$\eta'_{\rho\gamma}K^0_{S(\pi^0\pi^0)}$	*sgtr*, *sgscf*, $q\bar{q}$, *bc*, *bk*+, *bk*–
$\eta'_{\eta(\gamma\gamma)\pi\pi}K^0_L$	*sg*, $q\bar{q}$
$\eta'_{\eta(3\pi)\pi\pi}K^0_L$	*sgtr*, *sgscf*, $q\bar{q}$
$\eta'_{\eta(\gamma\gamma)\pi\pi}K^+$	*sg*, $q\bar{q}$
$\eta'_{\eta(3\pi)\pi\pi}K^+$	*sgtr*, *sgscf*, $q\bar{q}$
$\eta'_{\rho\gamma}K^+$	*sg*, $q\bar{q}$, *bc*, *bk*+, *bk*–

Table 6.22: Fit components in the fit for each decay: *sg* for signal component, *sgtr* for well-reconstructed signal component (based on MC truth + PP events), *sgscf* for SCF signal component, $q\bar{q}$ for continuum background, *bc* for charm $B\overline{B}$ background, *bk*+ and *bk*– for charmless peaking $B\overline{B}$ background.

categories, plus untagged events (see sec. 3.3.1). We use the index c = (0, 1, 2, 3, 4, 5,6) to indicate that the event belongs to one specific category (0 refers to untagged events). For each input event i and category c, the likelihood is defined as:

$$\begin{aligned}\mathcal{L}_{i,c} &= n_{sg}f_{sg,c}\mathcal{P}^{i,c}_{sg} + n_{q\bar{q}}f_{q\bar{q},c}\mathcal{P}^{i}_{q\bar{q}} + f_{bc,c}n_{bc}\mathcal{P}^{i}_{bc} + \\ &\quad + f_{sg,c}(n_{bk+}\mathcal{P}^{i}_{bk+} + n_{bk-}\mathcal{P}^{i}_{bk-}) \end{aligned} \tag{6.3}$$

where $f_{sg,c}$, $f_{q\bar{q},c}$, and $f_{bc,c}$ indicate the fraction of events for each category for each specie. For $B\overline{B}$ peaking backgrounds we use fractions equal to the BReco ones, because there is not enough statistics to fit this information on MC events. The $f_{sg,c}$ values are fixed to the values obtained in BReco samples (see sec. 3.3.2), while all other parameters are free in the fits.

The extended likelihood function for all events belonging to category c is:

$$\mathcal{L}_c = \exp\left(-n_{sg}f_{sg,c} - n_{q\bar{q}}f_{q\bar{q},c} - n_{bc}f_{bc,c} - (n_{bk+} + n_{bk-})f_{sg,c}\right) \times \prod_{i}^{N_c} \mathcal{L}_{i,c} \tag{6.4}$$

where N_c is the total number of input events in category c. Finally the total likelihood function for all categories can be written as:

$$\mathcal{L} = \prod_{c=0}^{6} \mathcal{L}_c \tag{6.5}$$

To fit different sub-decay modes, the total likelihood becomes:

$$\mathcal{L} = \prod_{d} \mathcal{L}^{d} \tag{6.6}$$

where the index d runs over the fitted sub-decay modes. Our fitter minimizes the expression $-\ln \mathcal{L}$ with respect to a set of free parameters. In the final fit we have as free parameters: continuum background PDFs shape parameters, signal and backgrounds yields, S and C for both signal and $B\overline{B}$ charmed background, Δt shape parameters for continuum background, tagging category fractions of events for $B\overline{B}$ charmed and continuum background.

6.7.2 Discriminating Variables in the ML Fit

The discriminating variables used in the ML fits for each mode are: $m_{\rm ES}$, ΔE, Fisher Discriminant $\mathcal{F}$, and Δt variable. In case of modes with K^0_L we don't use the $m_{\rm ES}$.

PDFs for signal and $B\overline{B}$ background are fitted using Monte Carlo simulated events. Depending on the modes where we decide to use only one signal component, we use all signal MC events independently by the MC truth matching to make PDFs. For modes where we split the signal component in well-reconstructed signal events and SCF signal events components, we use MC truth+PP events and SCF events to make the PDFs, respectively. For $B\overline{B}$ charm PDFs we use generic MC $B\overline{B}$ charm events, and for $B\overline{B}$ peaking PDFs we use exclusive charmless decay modes (see tables in section 6.6 for a full lists), using weighted numbers of events from each background mode, where we split the events in the two components depending of the ΔE peaking region.

PDFs for continuum background were fitted using on-peak sidebands, defined as:

- *Grand Side Band* (GSB): $5.25 < m_{\rm ES} < 5.27~{\rm GeV}/c^2$
- *ΔE Side Band* (DESB): $0.1 < |\Delta E| < 0.2$ GeV for modes with K^0_S and $0.05 < \Delta E < 0.08$ GeV for modes with K^0_L

Table 6.23 reports the parametrization chosen for the different PDFs.

From previous studies reported in [104] we know that the $m_{\rm ES}$ endpoint in the Argus distribution is shifted to 5.2893 ${\rm GeV}/c^2$. We use this value in the fit.

Vertex resolution is mostly independent of the reconstructed B decay mode and small differences are reflected in the assigned Δt errors so parameters of the Δt resolution function can be taken from fit to the BReco sample. For our CP fit we use the CP model PDF of eq. 6.1 convoluted with the resolution function described in eq. 6.7. The resolution function $\mathcal{R}_{\rm sig}(\Delta t)$ is the a triple Gaussian, composed by a *core*, a *tail* and an

Fit Component	ΔE	$m_{\rm ES}$	$\mathcal{F}$	Δt
sg	CB/CR/DG	CB	AG/AG+G/DG	*CP* model
sgtr	CB/CR/DG	CB	AG+G	*CP* model
sgscf	CB/CH4/G+CH3	CB/DG	AG/AG+G	*CP* model
$q\bar{q}$	CH1/IA	A	AG+CH1	TG
bc	CH4	A/A+G	AG	*CP* model
bk+	G+CH2	A+G/CB+G	AG/AG+G	*CP* model
bk–	CH1/CH4	A/A+G	AG	*CP* model

Table 6.23: PDF parametrization used for signal, $q\bar{q}$ background and $B\overline{B}$ background (G = Gaussian, DG = double Gaussian, TG = triple Gaussian, AG = asymmetric Gaussian, CB = Crystal Ball, CR = Cruijff function, A = Argus, IA = Inverse Argus, CHn = $n^{\rm th}$ order Chebyshev polynomial).

outlier Gaussian. The mean and the with of the *core* and the *tail* Gaussian are proportional to $\sigma_{\delta t}$, while the mean and the with of the *outlier* gaussian are fixed to 0.0 and 8.0 ps, respectively. The other parameters of the triple Gaussian are fitted on the BReco sample (see sec. 3.3.2).

$$\begin{aligned}\mathcal{R}_{\rm sig}(\Delta t) &= f_{\rm core}\, G\left(\Delta t, s^{\mu}_{\rm core}\sigma_{\Delta t}, s^{\sigma}_{\rm core}\sigma_{\Delta t}\right) + \left(1 - f_{\rm core} - f_{\rm out}\right) G\left(\Delta t, s^{\mu}_{\rm tail}\sigma_{\Delta t}, s^{\sigma}_{\rm tail}\sigma_{\Delta t}\right) \\ &+ f_{\rm out}\, G\left(\Delta t, \mu_{\rm out}, \sigma_{\rm out}\right) \qquad (6.7)\end{aligned}$$

where $G(x, x_0, \sigma)$ is a Gaussian with bias x_0 and standard deviation σ. The $q\bar{q}$ background Δt distribution is modeled using on-peak sideband data. It is parametrized with a triple Gaussian where we use $\Delta t/\sigma_{\Delta t}$ as in signal Δt resolution model. For the $B\overline{B}$ background Δt distribution we use the *CP* model as in signal, we leave S and C floating for charm $B\overline{B}$ component, we fix S and C to zero for $B\overline{B}$ charmless component. We take in account a systematic effect varying these values of S and C for the $B\overline{B}$ charmless background (see sec. 6.9).

Most of the background parameters are left floating in the fit: coefficient of the Argus function for $m_{\rm ES}$ in modes with K^0_S and for ΔE in modes with K^0_L; coefficient of Chebyshev polynomial for ΔE in modes with K^0_S; mean, $\sigma_{\rm left}$ and $\sigma_{\rm right}$ of asymmetric Gaussian for $\mathcal{F}$; parameters of the triple Gaussian for Δt. Our studies (see sec. 7.6) pointed out that if the fit contains a $B\overline{B}$ charm component, the $\sigma_{\rm right}$ of the fisher and the $B\overline{B}$ yields are correlated, in this case we fix the $\sigma_{\rm right}$.

In appendix A, we show PDFs plots, correlations between input variables for all decay modes, and the values of the background parameters left floating in the final fit. The correlations are below 10% in all cases (normally 2–5%). Effects of these correlations are taken in account using Monte Carlo toy-experiments (see sec. 6.8). We deal with uncertainties in PDFs parameters in the systematic section (see sec. 6.9).

As explained in sec. 5.4.2, ΔE and $m_{\rm ES}$ have substantially a Gaussian shape for signal events. Eventually, some tails away from the core of the distribution can occur for many reasons, principally due to SCF events. If this is the case we use a different parametrization that fit better than Gaussian shape. For ΔE in K^0_S modes we use double Gaussian or Cruijff function, defined as:

$$f_{\rm cruijff}(x) \;=\; \exp\left[-\frac{(x-m)^2}{2\sigma_\pm^2+\alpha_\pm(x-m)^2}\right], \tag{6.8}$$

where the $+(-)$ corresponds to $x > 0$ or $x < 0$. This function is basically a bifurcated Gaussian with two exponential tail component. For ΔE in K^0_L modes and $m_{\rm ES}$ in K^0_S modes, we use a Crystal Ball function [105], defined as a Gaussian plus an exponential tail.

6.7.3 MC/data Matching Corrections

We have to correct the signal PDFs done using MC signal events in order to have a better matching with data.

Since we have enough signal events, we decide to use the charged mode $\eta'_{\rho\gamma}K^+$ as control sample for the neutral modes. In this way we measure the systematic difference for the variable $m_{\rm ES}$, ΔE (for K^0_S modes), and $\mathcal{F}$.

We give in tab. 6.24 these corrections applied to the signal PDFs to correct the differences between data and MC signal PDFs. We correct the signal PDFs for these values and we consider a systematic uncertainty varying these corrections of $\pm 1\sigma$ of their values, one at a time, re-running the ML fit, and taking the difference in the results as systematics (see sec. 6.9). Previous studies showed [104] that for ΔE in K^0_L modes, the main source of

	Correction
$m_{\rm ES}$ **(Crystal Ball)**	
$m_{\rm ES}$ mean bias (MeV$/c^2$)	-0.46 ± 0.07
$m_{\rm ES}$ sigma scale factor	0.955 ± 0.023
ΔE (Double Gaussian)	
ΔE means bias (MeV)	-1.5 ± 0.6
ΔE sigma scale factor	0.975 ± 0.027
$\mathcal{F}$ **(Double Gaussian)**	
$\mathcal{F}$ mean bias	-0.029 ± 0.014
$\mathcal{F}$ sigma scale factor	1.054 ± 0.025

Table 6.24: Shift and scale factor for MC/data matching to apply to the signal PDFs used to fit $m_{\rm ES}$, ΔE, and Fisher Discriminant $\mathcal{F}$.

discrepancy comes from the K_L^0 reconstruction. Since we have applied the official *BABAR* procedure to account MC/data correction for neutral particles [106], we don't apply any correction for the signal PDFs.

6.8 Verification Tests

6.8.1 TD MC Toy Experiments

We have generated 200 experiments for each decay mode in order to study any possible bias in the fit results, either yields and TD parameters. For the combined fit configuration (*i.e.*, K_S^0 submodes combined fit, K_L^0 submodes combined fit and final fit configuration,7-channels combined fit) we perform 500 toy experiments.

The events are taken from the MC for signal and $B\overline{B}$ peaking events and generated from PDFs for continuum background and $B\overline{B}$ charm events. Neutral modes MC signal events have $S = 0.703$ and $C = 0.0$. We fist perform a blind fit on the on-peak Run1–6 to extract the signal yield and embed events in each toy experiments according to the result of this fit. $B\overline{B}$ and continuum events in each experiment are as expected in data. Number of embedded $B\overline{B}$ peaking events are those shown in tab. 6.16–6.21. Number of generated $B\overline{B}$ charm events are reported in tab. 6.15. The values of the fractions for continuum and $B\overline{B}$ charm backgrounds and S and C for $B\overline{B}$ charm are as fitted on the on-peak Run1–6 sample.

Results of these toy experiments are shown in tab. 6.25 and tab. 6.26 where we consider each sub-decay. In tab. 6.27–6.28 we report results of the toys when we consider simultaneous fit on K_S^0 and K_L^0 submodes, respectively. In tab. 6.29 we give the results of the toys when we consider the simultaneous fit of all sub-decays (final fit configuration). In these tables we show results of fit of toy experiments for all the decay modes. In the second column we give the number of the embedded/generated events and the MC values of S and C parameters. In the next 2 columns we show the mean of the Gaussian distributions used to fit the distributions of fitted yield, S and C, and their fitted errors. In the last 2 columns we show the mean and sigma of the Gaussian distributions used to fit the pull distributions (the pull of x is defined as $p = \frac{x_{gen} - x_{mes}}{\sigma_x}$, where x_{gen} is the value which is generated or embedded, and x_{mes} the value measured by the fit). In fig. 6.2 we show the distribution of S, C and their error obtained performing 500 MC embedded toy experiments with the final fit configuration. Toy experiments are performed using Breco MC parameters (tab. 3.4 and 3.6). We use results of toy experiments for combined fit configuration to determine the fit bias, which is used as additive correction to the final fit value. We consider a systematic error related to the precision of this bias (see sec. 6.9). In conclusion we verified that our fit works well and origin of residual biases are understood.

Variable	Initial Value	Fitted Mean	Fitted Error	Pull Mean	Pull σ
$\eta'_{\eta(\gamma\gamma)\pi\pi}K^0_{S(\pi^+\pi^-)}$					
Sg	476	468.66 ± 0.59	23.39 ± 0.01	-0.32 ± 0.03	0.99 ± 0.02
$q\bar{q}$	940	947.35 ± 0.59	32.00 ± 0.01	0.21 ± 0.02	0.97 ± 0.01
S	0.70	0.72 ± 0.01	0.15 ± 0.00	0.05 ± 0.07	0.98 ± 0.05
C	0	-0.02 ± 0.01	0.11 ± 0.00	-0.18 ± 0.07	0.95 ± 0.05
$\eta'_{\eta(3\pi)\pi\pi}K^0_{S(\pi^+\pi^-)}$					
Sg	167	166.88 ± 0.54	13.96 ± 0.11	-0.02 ± 0.03	0.98 ± 0.02
$q\bar{q}$	284	284.16 ± 0.52	18.05 ± 0.27	0.01 ± 0.03	1.00 ± 0.02
S	0.70	0.72 ± 0.02	0.25 ± 0.00	0.02 ± 0.09	1.01 ± 0.06
C	0	0.03 ± 0.02	0.18 ± 0.00	0.06 ± 0.08	1.06 ± 0.06
$\eta'_{\rho\gamma}K^0_{S(\pi^+\pi^-)}$					
Sg	959	965.90 ± 1.67	38.86 ± 0.03	0.17 ± 0.04	0.97 ± 0.03
$q\bar{q}$	18721	18782.24 ± 5.28	151.91 ± 0.30	0.40 ± 0.03	0.99 ± 0.02
$B\overline{B}$ charm	539	574.33 ± 11.79	163.82 ± 2.40	0.21 ± 0.07	0.97 ± 0.05
$B\overline{B}$ peaking (+)	97	80.36 ± 2.95	39.92 ± 0.18	-0.45 ± 0.07	0.98 ± 0.05
$B\overline{B}$ peaking (–)	152	65.16 ± 8.66	122.14 ± 1.58	-0.75 ± 0.07	0.96 ± 0.05
S	0.70	0.70 ± 0.01	0.12 ± 0.00	-0.14 ± 0.08	1.07 ± 0.06
C	0	0.01 ± 0.01	0.09 ± 0.00	0.09 ± 0.08	0.98 ± 0.05

Table 6.25: 200 MC Toy experiments results for neutral modes. See text for details about the contents of various columns.

Variable	Initial Value	Fitted Mean	Fitted Error	Pull Mean	Pull σ
$\eta'_{\eta(\gamma\gamma)\pi\pi}K^0_{S(\pi^0\pi^0)}$					
Sg	99	97.02 ± 0.51	12.47 ± 0.07	-0.17 ± 0.04	0.95 ± 0.03
$q\bar{q}$	778	779.96 ± 0.51	28.92 ± 0.01	0.07 ± 0.02	0.97 ± 0.01
S	0.70	0.72 ± 0.03	0.39 ± 0.00	0.13 ± 0.08	1.02 ± 0.06
C	0	0.04 ± 0.02	0.27 ± 0.00	0.06 ± 0.07	1.02 ± 0.05
$\eta'_{\rho\gamma}K^0_{S(\pi^0\pi^0)}$					
Sg	164	166.28 ± 1.98	27.42 ± 0.11	0.07 ± 0.07	0.96 ± 0.05
$q\bar{q}$	21269	21269.42 ± 5.53	158.22 ± 0.17	0.00 ± 0.03	0.99 ± 0.02
$B\overline{B}$ charm	411	454.83 ± 14.10	143.53 ± 1.74	0.39 ± 0.09	1.00 ± 0.06
$B\overline{B}$ peaking (+)	37	35.32 ± 5.33	57.63 ± 0.58	-0.05 ± 0.09	1.00 ± 0.06
$B\overline{B}$ peaking (–)	28	-16.84 ± 12.79	143.26 ± 1.79	-0.38 ± 0.09	1.00 ± 0.06
S	0.70	0.71 ± 0.04	0.42 ± 0.01	0.02 ± 0.04	0.97 ± 0.04
C	0	0.04 ± 0.03	0.31 ± 0.00	0.11 ± 0.09	1.05 ± 0.07
$\eta'_{\eta(\gamma\gamma)\pi\pi}K^0_L$					
Sg	384	369.52 ± 1.65	31.00 ± 0.06	-0.48 ± 0.05	0.98 ± 0.04
$q\bar{q}$	17639	17666.56 ± 1.66	135.11 ± 0.01	0.20 ± 0.02	0.99 ± 0.01
$B\overline{B}$ peaking	13	0 (fixed)			
S	0.70	0.67 ± 0.02	0.24 ± 0.00	-0.19 ± 0.07	1.01 ± 0.05
C	0	0.03 ± 0.01	0.16 ± 0.00	0.02 ± 0.06	0.89 ± 0.04
$\eta'_{\eta(3\pi)\pi\pi}K^0_L$					
Sg	168	169.51 ± 1.15	20.51 ± 0.05	0.04 ± 0.05	0.95 ± 0.04
$q\bar{q}$	6036	6034.49 ± 1.15	79.32 ± 0.01	-0.02 ± 0.01	0.97 ± 0.01
$B\overline{B}$ peaking	9	0 (fixed)			
S	0.70	0.75 ± 0.03	0.33 ± 0.00	0.18 ± 0.10	1.06 ± 0.07
C	0	-0.05 ± 0.02	0.23 ± 0.00	-0.20 ± 0.08	1.10 ± 0.06

Table 6.26: 200 MC Toy experiments results for neutral modes. See text for details about the contents of various columns.

Variable	Initial Value	Fitted Mean	Fitted Error	Pull Mean	Pull σ
Combined Fit (K^0_S submodes)					
Sg $\eta'_{\eta(\gamma\gamma)\pi\pi}K^0_{S(\pi^+\pi^-)}$	476	467.62 ± 0.55	23.33 ± 0.01	-0.36 ± 0.02	1.01 ± 0.02
$q\bar{q}$ $\eta'_{\eta(\gamma\gamma)\pi\pi}K^0_{S(\pi^+\pi^-)}$	940	948.39 ± 0.55	31.98 ± 0.01	0.26 ± 0.02	0.99 ± 0.01
Sg $\eta'_{\eta(3\pi)\pi\pi}K^0_{S(\pi^+\pi^-)}$	167	165.93 ± 0.35	13.87 ± 0.01	-0.08 ± 0.02	1.04 ± 0.02
$q\bar{q}$ $\eta'_{\eta(3\pi)\pi\pi}K^0_{S(\pi^+\pi^-)}$	284	285.12 ± 0.35	17.62 ± 0.01	0.06 ± 0.01	1.02 ± 0.01
Sg $\eta'_{\rho\gamma}K^0_{S(\pi^+\pi^-)}$	959	971.61 ± 1.40	38.93 ± 0.02	0.34 ± 0.02	0.98 ± 0.02
$q\bar{q}$ $\eta'_{\rho\gamma}K^0_{S(\pi^+\pi^-)}$	18721	18774.03 ± 4.09	152.87 ± 0.19	0.35 ± 0.02	0.99 ± 0.02
$B\overline{B}$ charm $\eta'_{\rho\gamma}K^0_{S(\pi^+\pi^-)}$	539	574.30 ± 9.01	168.26 ± 1.19	0.21 ± 0.06	1.13 ± 0.04
$B\overline{B}$ peaking (+) $\eta'_{\rho\gamma}K^0_{S(\pi^+\pi^-)}$	97	76.96 ± 2.21	40.52 ± 0.08	-0.51 ± 0.06	1.04 ± 0.04
$B\overline{B}$ peaking (–) $\eta'_{\rho\gamma}K^0_{S(\pi^+\pi^-)}$	152	70.83 ± 6.65	123.13 ± 0.74	-0.68 ± 0.06	1.08 ± 0.04
Sg $\eta'_{\eta(\gamma\gamma)\pi\pi}K^0_{S(\pi^0\pi^0)}$	99	94.48 ± 0.41	12.15 ± 0.01	-0.38 ± 0.04	1.01 ± 0.02
$q\bar{q}$ $\eta'_{\eta(\gamma\gamma)\pi\pi}K^0_{S(\pi^0\pi^0)}$	778	782.57 ± 0.41	28.84 ± 0.01	$+0.16 \pm 0.02$	0.99 ± 0.01
Sg $\eta'_{\rho\gamma}K^0_{S(\pi^0\pi^0)}$	164	164.48 ± 1.14	25.54 ± 0.06	0.02 ± 0.05	0.96 ± 0.03
$q\bar{q}$ $\eta'_{\rho\gamma}K^0_{S(\pi^0\pi^0)}$	21269	21260.34 ± 2.78	152.76 ± 0.06	-0.06 ± 0.02	1.00 ± 0.01
$B\overline{B}$ charm $\eta'_{\rho\gamma}K^0_{S(\pi^0\pi^0)}$	411	463.85 ± 7.59	144.39 ± 0.94	0.37 ± 0.05	1.03 ± 0.04
$B\overline{B}$ peaking (+) $\eta'_{\rho\gamma}K^0_{S(\pi^0\pi^0)}$	37	34.71 ± 3.21	56.99 ± 0.38	0.05 ± 0.07	1.22 ± 0.05
$B\overline{B}$ peaking (–) $\eta'_{\rho\gamma}K^0_{S(\pi^0\pi^0)}$	28	-14.13 ± 6.80	143.11 ± 0.72	-0.29 ± 0.06	1.07 ± 0.04
S	0.703	0.715 ± 0.004	0.085 ± 0.000	$+0.15 \pm 0.04$	0.99 ± 0.05
C	0	0.013 ± 0.003	0.063 ± 0.000	$+0.21 \pm 0.04$	1.02 ± 0.05

Table 6.27: 500 MC Toy experiments results for neutral modes (K^0_S combined fit). See text for details about the contents of various columns.

Variable	Initial Value	Fitted Mean	Fitted Error	Pull Mean	Pull σ
Combined Fit (K^0_L submodes)					
Sg $\eta'_{\eta(\gamma\gamma)\pi\pi}K^0_L$	386	374.71 ± 0.92	31.08 ± 0.04	-0.38 ± 0.03	0.96 ± 0.02
$q\bar{q}$ $\eta'_{\eta(\gamma\gamma)\pi\pi}K^0_L$	17637	17657.32 ± 0.92	135.09 ± 0.01	0.15 ± 0.01	0.99 ± 0.01
$B\overline{B}$ peaking $\eta'_{\eta(\gamma\gamma)\pi\pi}K^0_L$	13	0 (fixed)			
Sg $\eta'_{\eta(3\pi)\pi\pi}K^0_L$	170	166.25 ± 0.62	20.36 ± 0.01	-0.21 ± 0.03	0.98 ± 0.02
$q\bar{q}$ $\eta'_{\eta(3\pi)\pi\pi}K^0_L$	6034	6041.76 ± 0.64	79.31 ± 0.01	0.10 ± 0.01	1.00 ± 0.01
$B\overline{B}$ peaking $\eta'_{\eta(3\pi)\pi\pi}K^0_L$	9	0 (fixed)			
S	0.703	0.681 ± 0.009	0.197 ± 0.000	-0.03 ± 0.05	1.04 ± 0.03
C	0	-0.013 ± 0.006	0.139 ± 0.000	-0.10 ± 0.05	1.04 ± 0.04

Table 6.28: 500 MC Toy experiments results for neutral modes (K^0_L combined fit). See text for details about the contents of various columns.

Variable	Initial Value	Fitted Mean	Fitted Error	Pull Mean	Pull σ
Combined Fit (All sub-modes)					
Sg $\eta'_{\eta(\gamma\gamma)\pi\pi}K^0_{S(\pi^+\pi^-)}$	476	467.52 ± 0.55	23.30 ± 0.01	-0.36 ± 0.02	1.01 ± 0.02
$q\bar{q}$ $\eta'_{\eta(\gamma\gamma)\pi\pi}K^0_{S(\pi^+\pi^-)}$	940	948.48 ± 0.55	32.02 ± 0.01	0.26 ± 0.02	0.98 ± 0.01
Sg $\eta'_{\eta(3\pi)\pi\pi}K^0_{S(\pi^+\pi^-)}$	167	164.62 ± 0.33	13.92 ± 0.01	-0.17 ± 0.02	1.04 ± 0.02
$q\bar{q}$ $\eta'_{\eta(3\pi)\pi\pi}K^0_{S(\pi^+\pi^-)}$	284	287.42 ± 0.33	17.69 ± 0.01	0.19 ± 0.01	0.99 ± 0.01
Sg $\eta'_{\rho\gamma}K^0_{S(\pi^+\pi^-)}$	959	967.01 ± 1.41	38.81 ± 0.02	0.21 ± 0.02	0.99 ± 0.01
$q\bar{q}$ $\eta'_{\rho\gamma}K^0_{S(\pi^+\pi^-)}$	18721	18780.29 ± 4.11	151.03 ± 0.17	0.39 ± 0.02	0.98 ± 0.02
$B\overline{B}$ charm $\eta'_{\rho\gamma}K^0_{S(\pi^+\pi^-)}$	539	566.29 ± 9.19	160.57 ± 1.13	0.17 ± 0.05	1.05 ± 0.04
$B\overline{B}$ peaking (+) $\eta'_{\rho\gamma}K^0_{S(\pi^+\pi^-)}$	97	76.42 ± 2.20	40.21 ± 0.10	-0.51 ± 0.05	0.97 ± 0.04
$B\overline{B}$ peaking (–) $\eta'_{\rho\gamma}K^0_{S(\pi^+\pi^-)}$	152	78.04 ± 6.67	128.31 ± 0.84	-0.58 ± 0.06	1.01 ± 0.04
Sg $\eta'_{\eta(\gamma\gamma)\pi\pi}K^0_{S(\pi^0\pi^0)}$	99	95.33 ± 0.28	12.17 ± 0.71	-0.29 ± 0.04	1.06 ± 0.02
$q\bar{q}$ $\eta'_{\eta(\gamma\gamma)\pi\pi}K^0_{S(\pi^0\pi^0)}$	778	781.67 ± 0.28	28.78 ± 0.01	0.13 ± 0.02	1.05 ± 0.01
Sg $\eta'_{\rho\gamma}K^0_{S(\pi^0\pi^0)}$	164	165.01 ± 1.02	25.28 ± 0.06	0.04 ± 0.04	1.00 ± 0.03
$q\bar{q}$ $\eta'_{\rho\gamma}K^0_{S(\pi^0\pi^0)}$	21269	21259.54 ± 3.09	152.57 ± 0.06	-0.06 ± 0.02	0.99 ± 0.01
$B\overline{B}$ charm $\eta'_{\rho\gamma}K^0_{S(\pi^0\pi^0)}$	411	460.32 ± 7.63	143.96 ± 0.95	0.33 ± 0.05	1.06 ± 0.04
$B\overline{B}$ peaking (+) $\eta'_{\rho\gamma}K^0_{S(\pi^0\pi^0)}$	37	34.11 ± 3.16	57.11 ± 0.36	-0.05 ± 0.06	1.07 ± 0.04
$B\overline{B}$ peaking (–) $\eta'_{\rho\gamma}K^0_{S(\pi^0\pi^0)}$	28	-13.99 ± 6.78	143.04 ± 0.70	-0.29 ± 0.07	1.05 ± 0.05
Sg $\eta'_{\eta(\gamma\gamma)\pi\pi}K^0_L$	384	368.73 ± 0.91	30.07 ± 0.05	-0.51 ± 0.03	0.99 ± 0.03
$q\bar{q}$ $\eta'_{\eta(\gamma\gamma)\pi\pi}K^0_L$	17639	17667.36 ± 0.93	134.97 ± 0.01	0.21 ± 0.01	1.00 ± 0.01
$B\overline{B}$ peaking $\eta'_{\eta(\gamma\gamma)\pi\pi}K^0_L$	13	0 (fixed)			
Sg $\eta'_{\eta(3\pi)\pi\pi}K^0_L$	168	165.74 ± 0.63	19.95 ± 0.01	-0.11 ± 0.01	1.00 ± 0.01
$q\bar{q}$ $\eta'_{\eta(3\pi)\pi\pi}K^0_L$	6036	6047.26 ± 0.62	79.34 ± 0.01	0.14 ± 0.01	1.02 ± 0.01
$B\overline{B}$ peaking $\eta'_{\eta(3\pi)\pi\pi}K^0_L$	9	0 (fixed)			
S	0.703	0.714 ± 0.003	0.076 ± 0.000	$+0.14 \pm 0.06$	0.98 ± 0.05
C	0	0.004 ± 0.002	0.055 ± 0.000	0.07 ± 0.06	1.01 ± 0.05

Table 6.29: 500 MC Toy experiments results for neutral modes (7-channels combined fit). See text for details about the contents of various columns.

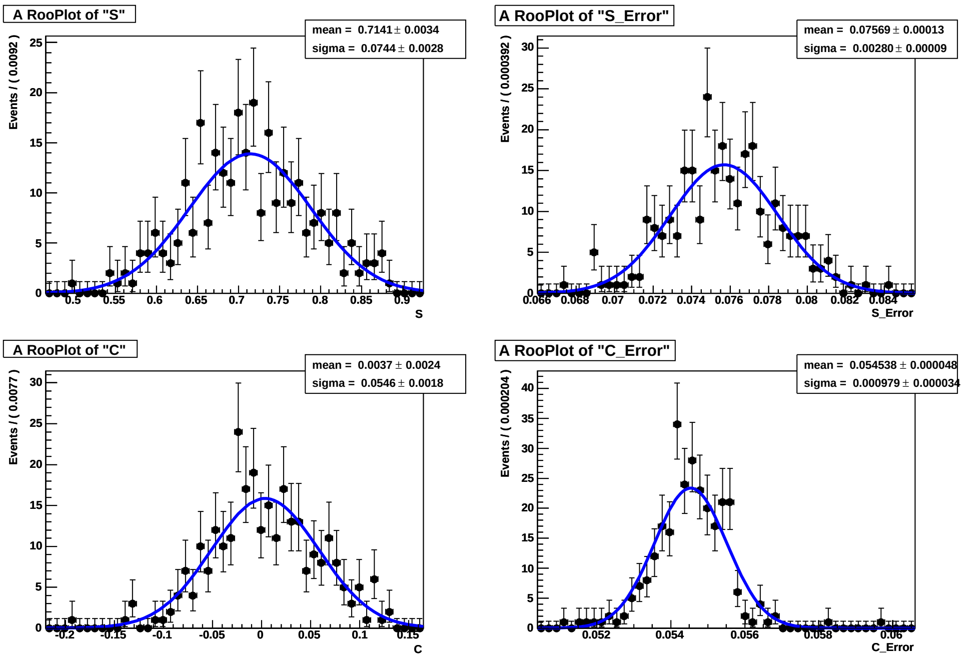

Figure 6.2: Distribution of S, C and their errors performing 500 MC embedded toy experiments with the final fit configuration.

6.8.2 TD Pure Toy Experiments

In pure toy experiments all the components are drawn from the PDFs, neglecting any correlation. Their goal is to undercover errors in the fit itself (model, PDFs shapes,...). We have generated 200 experiments for each decay mode in order to study any possible bias in the fit results, either yields and TD parameters.

The events are generated from PDFs for all components. In case of K_L^0 modes, where there is no $B\overline{B}$ peaking component, the events are taken from MC. We generated signal events with S equal to 0.70 and C equal to zero. Numbers of signal events are as fitted on the on-peak Run1–6 sample, $B\overline{B}$ and continuum in each experiment are as expected in data. Number of generated/embedded $B\overline{B}$ peaking events are those shown in tab. 6.16–6.21. Number of generated $B\overline{B}$ charm events are reported in tab. 6.15. The values of the fractions for continuum and $B\overline{B}$ charm backgrounds and S and C for $B\overline{B}$ charm are as fitted on the on-peak Run1–6 sample.

Results of these toy experiments are shown in tab. 6.30 and tab. 6.31 where we consider each sub-decay. In these tables we show results of fit of 200 toy experiments for all the decay modes. In the second column we give the number of the embedded/generated events and the MC values of S and C parameters. In the next 2 columns we show the mean of the Gaussian distributions used to fit the distributions of fitted yield, S and C, and their fitted errors. In the last 2 columns we show the mean and sigma of the Gaussian distributions used to fit the pull distributions.

Variable	Initial Value	Fitted Mean	Fitted Error	Pull Mean	Pull σ
$\eta'_{\eta(\gamma\gamma)\pi\pi}K^0_{S(\pi^+\pi^-)}$					
Sg	476	475.54 ± 1.34	23.58 ± 0.03	-0.04 ± 0.06	1.07 ± 0.04
$q\bar{q}$	940	940.47 ± 1.34	31.90 ± 0.02	$+0.01 \pm 0.04$	1.01 ± 0.03
S	0.70	0.72 ± 0.01	0.16 ± 0.00	0.13 ± 0.07	0.97 ± 0.05
C	0	-0.00 ± 0.01	0.11 ± 0.00	0.00 ± 0.07	1.05 ± 0.05
$\eta'_{\eta(3\pi)\pi\pi}K^0_{S(\pi^+\pi^-)}$					
Sg	167	167.27 ± 0.96	13.95 ± 0.14	$+0.02 \pm 0.06$	1.09 ± 0.05
$q\bar{q}$	284	283.68 ± 0.96	17.64 ± 0.11	-0.02 ± 0.05	1.07 ± 0.04
S	0.70	0.66 ± 0.02	0.26 ± 0.00	-0.06 ± 0.08	1.02 ± 0.06
C	0	0.01 ± 0.01	0.18 ± 0.00	0.03 ± 0.08	1.06 ± 0.06
$\eta'_{\rho\gamma}K^0_{S(\pi^+\pi^-)}$					
Sg	959	954.80 ± 2.81	38.89 ± 0.05	-0.13 ± 0.07	1.03 ± 0.05
$q\bar{q}$	18721	18727.93 ± 5.80	152.15 ± 0.18	0.05 ± 0.04	1.02 ± 0.03
$B\overline{B}$ charm	539	557.17 ± 11.86	166.59 ± 2.01	0.09 ± 0.07	0.97 ± 0.05
$B\overline{B}$ peaking (+)	97	87.73 ± 2.74	41.19 ± 0.15	-0.26 ± 0.07	0.92 ± 0.05
$B\overline{B}$ peaking (–)	152	140.23 ± 8.91	124.44 ± 1.33	-0.11 ± 0.07	0.97 ± 0.05
S	0.70	0.70 ± 0.01	0.12 ± 0.00	-0.02 ± 0.07	1.01 ± 0.05
C	0	-0.01 ± 0.01	0.09 ± 0.00	-0.14 ± 0.07	0.97 ± 0.05

Table 6.30: 200 Pure Toy experiments results for neutral modes. We show number of MC signal, $B\overline{B}$ peaking, continuum background and $B\overline{B}$ charm generated events, mean of the reconstructed yields and S and C parameters, mean of their errors, mean of the signal pull, σ of the signal pull.

Variable	Initial Value	Fitted Mean	Fitted Error	Pull Mean	Pull σ
$\eta'_{\eta(\gamma\gamma)\pi\pi}K^0_{S(\pi^0\pi^0)}$					
Sg	99	97.45 ± 0.90	12.41 ± 0.10	-0.19 ± 0.07	1.06 ± 0.05
$q\bar{q}$	778	779.59 ± 0.90	28.93 ± 0.02	$+0.05 \pm 0.03$	1.03 ± 0.02
S	0.70	0.68 ± 0.04	0.43 ± 0.01	-0.04 ± 0.09	1.01 ± 0.06
C	0	0.03 ± 0.02	0.28 ± 0.00	0.09 ± 0.08	1.07 ± 0.06
$\eta'_{\rho\gamma}K^0_{S(\pi^0\pi^0)}$					
Sg	164	167.57 ± 2.75	27.88 ± 0.14	0.10 ± 0.10	1.01 ± 0.07
$q\bar{q}$	21269	21244.71 ± 5.99	158.73 ± 0.61	-0.15 ± 0.04	0.98 ± 0.03
$B\overline{B}$ charm	411	473.58 ± 12.13	150.79 ± 3.54	0.46 ± 0.09	0.95 ± 0.06
$B\overline{B}$ peaking (+)	37	37.24 ± 6.84	59.43 ± 0.60	-0.03 ± 0.10	1.07 ± 0.07
$B\overline{B}$ peaking (–)	28	-15.21 ± 13.09	148.55 ± 2.89	-0.35 ± 0.10	1.07 ± 0.07
S	0.70	0.70 ± 0.05	0.46 ± 0.01	-0.02 ± 0.09	0.97 ± 0.07
C	0	0.00 ± 0.04	0.34 ± 0.01	0.03 ± 0.10	1.00 ± 0.07
$\eta'_{\eta(\gamma\gamma)\pi\pi}K^0_L$					
Sg	384	382.75 ± 2.21	31.34 ± 0.06	-0.05 ± 0.07	1.02 ± 0.05
$q\bar{q}$	17639	17653.37 ± 2.24	135.09 ± 0.01	0.10 ± 0.02	0.99 ± 0.01
$B\overline{B}$ peaking	13	0 (fixed)			
S	0.70	0.69 ± 0.02	0.25 ± 0.00	0.03 ± 0.08	1.09 ± 0.06
C	0	0.00 ± 0.01	0.17 ± 0.00	0.02 ± 0.07	0.99 ± 0.05
$\eta'_{\eta(3\pi)\pi\pi}K^0_L$					
Sg	168	169.22 ± 1.61	20.55 ± 0.07	0.01 ± 0.08	1.08 ± 0.06
$q\bar{q}$	6036	6043.79 ± 1.61	79.33 ± 0.01	0.08 ± 0.02	1.02 ± 0.01
$B\overline{B}$ peaking	9	0 (fixed)			
S	0.70	0.70 ± 0.03	0.35 ± 0.00	0.04 ± 0.08	1.01 ± 0.06
C	0	-0.01 ± 0.02	0.25 ± 0.00	-0.05 ± 0.08	1.01 ± 0.06

Table 6.31: 200 Pure Toy experiments results for neutral modes. We show number of MC signal, $B\overline{B}$ peaking, continuum background and $B\overline{B}$ charm generated events, mean of the reconstructed yields and S and C parameters, mean of their errors, mean of the signal pull, σ of the signal pull.

6.8.3 CP Fit of Charged Modes

As a check we fit on Run1–6 data for charged modes. In this case we expect either S and C consistent with zero. The results are shown in tab. 6.32. We give the number of events to fit, the MC efficiency, the signal and $B\overline{B}$ yields, the values for S and C for $B\overline{B}$ charmed events, the number of free parameters in the fit, the correlation between S and C found in the fit, and the parameters S and C. Results are consistent with zero, as expected.

Quantity	$\eta'_{\eta(\gamma\gamma)\pi\pi}K^+$	$\eta'_{\rho\gamma}K^+$	$\eta'_{\eta(3\pi)\pi\pi}K^+$
Events into fit	4606	93626	1781
MC efficiency (%)	29.4	31.9	19.0
Signal yield (expect.)	1634 ± 43 (1683)	3212 ± 75 (3079)	610 ± 27 (628)
bc yield	–	1660 ± 336	–
bk+ yield	–	446 ± 89	–
bk– yield	–	239 ± 274	–
S *bc*	–	-0.02 ± 0.12	–
C *bc*	–	-0.23 ± 0.11	–
# Free parameters	19	29	19
$S - C$ correlation (%)	-0.9	-4.8	3.4
S	-0.01 ± 0.08	-0.04 ± 0.07	-0.09 ± 0.14
C	0.07 ± 0.06	0.08 ± 0.05	-0.00 ± 0.10
TD Combined fit:			
Signal yield	1634 ± 43	3212 ± 74	610 ± 27
bc yield	–	1661 ± 335	–
bk+ yield	–	445 ± 85	–
bk– yield	–	237 ± 273	–
S *bc*	–	-0.02 ± 0.12	–
C *bc*	–	-0.22 ± 0.10	–
# Free parameters	63		
$S - C$ correlation (%)	-2.4		
S	-0.04 ± 0.05		
C	0.07 ± 0.04		

Table 6.32: Summary of ML fit results for $\eta' K^+$ decay modes.

6.9 Systematic Errors

We present here the main sources of systematic uncertainties in the measurement of time dependent CP parameters.

We consider in this section the systematic errors for S and C TD parameters in the case of all seven modes combined fit for neutral modes. Systematic contributions for K^0_S and K^0_L modes separately are shown in sec. 6.9.1–6.9.2. Contributions to the systematic uncertainties are estimated for the following:

- For PDF shapes, we estimate the errors by variation of their parameters of $\pm 1\sigma$. We also take into account the contribution from the variation of $\pm 1\sigma$ of the MC/-data corrections. In tab. 6.34, we summarize all the variations and their results. All changes are summed in quadrature for positive differences (positive error) and negative differences (negative error) to obtain an error which we round to 0.010 for S and 0.005 for C.

- Toy studies (sec. 6.8) show that there is a bias of $+0.011$ for S and of $+0.004$ for C (tab. 6.29). We correct the final fit values of S and C for these biases and we account the uncertainty of the biases as systematic. The actual amount of reconstructed signal MC allow us to perform about 200 independent final fit configuration toy experiments. So we take as systematic the uncertainty of the biases stated in tab. 6.29 multiplied for $\sqrt{500/200}$. We find 0.005 for S and 0.003 for C.

- We assign a systematics due to uncertainty of the CP content in the $B\overline{B}$ background (see sec. 6.6). Leaving float the S and C parameters for such components gives instability of the fits, so we decided to run the combined fit in several configurations, fixing each parameter to $+1$ and -1, one at a time. We sum in quadrature positive and negative changes for signal S and C with respect to the standard fit values, for the different configurations. Finally we take as systematic the largest value between positive and negative. We find 0.006 for S and 0.009 for C.

- The systematic uncertainties related to the SVT alignment and beam-spot position have been studied using the recipe suggested in [107]. Detailed results for all the SVT misalignment configurations and beam spot variation are shown in tab. 6.35 and 6.36. Nominal value is obtained with a fit on a MC sample reconstructed in refit mode. We take the maximum deviation in two main modes and then the maximum in the positive and negative deviations. We find 0.004 for S and 0.004 or C for the SVT, and 0.004 for S and 0.003 for C for the beam-spot.

- We consider effect of interference with $\overline{b}{\to}\overline{u}c\overline{d}$ amplitude in the Tag-side of the event. The B decays that are used for flavor tagging are dominated by amplitudes containing a $b \to c\overline{u}d$ transition. However, it is possible that $\overline{b} \to \overline{u}c\overline{d}$ amplitudes can also contribute to the final states used for tagging. For example, a tag B meson may be observed in the $D^+\pi^-$ mode and generate a K^- tag from the D^+. Contrary to what one may guess, the effects of the suppressed $\overline{b} \to \overline{u}c\overline{d}$ amplitude are *not* simply absorbed into the mistag fractions. This is described in detail in [79]. If the data are fitted assuming no tag-side interference ($r' = 0$), the expectation values of the fitted coefficients are [2]

$$C_{\text{fit}} = C_0 + 2\,r' \sin\gamma \sin\delta' \tag{6.9}$$

$$S_{\text{fit}} = S_0 \left[1 - 2\,r' \cos\delta' \left\{\cos 2\beta \cos(2\beta+\gamma) + \mathcal{K} \sin 2\beta \sin(2\beta+\gamma)\right\}\right] \tag{6.10}$$

where S_0 is the expected no-interference value ($\sin 2\beta$), $\mathcal{K}$ is a correction factor between 0.10 and 0.35, depending on the value of $\sin 2\beta$ ($\mathcal{K} = 0.28$ for $\sin 2\beta = 0.74$), γ and β are angles of the UT and δ' are strong phases involved in the decay. Each tagging final state, in principle, has its own r' and δ' values. If the final states do not all have the same value of δ', there will be some degree of cancellation and the deviation of the fitted coefficients from the no-tag-side-interference values will be reduced. We do not assume any cancellation in our evaluation of the systematic errors, which is the most conservative approach. We calculate $\delta C \equiv C_{\text{fit}} - C_0$ and $\delta S \equiv S_{\text{fit}} - S_0$ from a simple Bayesian toy MC that generated points from these input assumptions:

- r' uniform in [0.00,0.04]
- δ' uniform in [0,2π]
- γ uniform in [39°,80°]
- $C_0 = 0$
- $2\beta = \sin^{-1} 0.586 = 35.9°$.

At the 68% level, the non-lepton-tagged events would have at most deviations of 0.028 and 0.003 in the fitted C and S coefficients respectively. To evaluate the systematic errors for the final results, we must take into account the breakdown of semileptonic and non-semileptonic events within the tagging categories, which is given in tab. 6.33. Within a tagging category, the fitted asymmetry coefficients will be

$$S_i = S_0 + f_{\text{NSL}} \frac{D_{\text{NSL},i}}{\langle D_i \rangle} \delta S \tag{6.11}$$

$$C_i = C_0 + f_{\text{NSL}} \frac{D_{\text{NSL},i}}{\langle D_i \rangle} \delta C \tag{6.12}$$

---

[2] We use the *BABAR* sign convention for $\mathcal{C}$ here, which is opposite that of Reference [79].

	All events			SL events				non-SL events			
Category	ϵ	$\langle D \rangle$	$Q(\%)$	$\epsilon_{\rm SL}$	$D_{\rm SL}$	$Q(\%)$	$Q'(\%)$	$\epsilon_{\rm NSL}$	$D_{\rm NSL}$	$Q(\%)$	$Q'(\%)$
Lepton	0.095	0.939	8.3	0.090	0.981	8.6	7.9	0.005	0.126	0.0	0.4
Kaon1	0.104	0.878	8.1	0.027	0.970	2.6	2.1	0.077	0.845	5.5	6.0
Kaon2	0.167	0.678	7.7	0.033	0.872	2.5	1.5	0.135	0.631	5.4	6.2
KaonPion	0.137	0.488	3.3	0.023	0.733	1.2	0.5	0.114	0.439	2.2	2.7
Pion	0.145	0.309	1.4	0.021	0.506	0.6	0.2	0.124	0.274	0.9	1.2
Other	0.099	0.149	0.2	0.012	0.317	0.1	0.0	0.086	0.125	0.1	0.2
Total	0.747		28.9	0.206		15.6	12.3	0.541		14.2	16.6

Table 6.33: Breakdown of flavor tagging performance for all events and divided by whether or not the tag Bdecayed semileptonically at the truth level. The Q' values were computed using the average dilution $\langle D \rangle$ instead of $D_{\rm SL}$ or $D_{\rm NSL}$.

where δS and δC are the differences between the fitted coefficients with and without tag-side interference, $f_{{\rm NSL},i} = \epsilon_{\rm NSL,i}/\epsilon_i$, $\langle D \rangle$ is the average dilution (D_{SL} and D_{NSL} refers to dilution calculated on semileptonic and non-semileptonic events, respectively). The statistical error for tagging category i is proportional to $1/\sqrt{Q_i}$, where Q_i is the effective tagging power for the i category. So the average fitted asymmetry coefficients will be

$$\langle S_{\rm fit} \rangle = S_0 + \delta S_{\rm DCSD} = \frac{\sum_i \left(S_0 + f_{\rm NSL} \frac{D_{{\rm NSL},i}}{\langle D_i \rangle} \delta S \right) Q_i}{\sum_j Q_j} \tag{6.13}$$

$$\langle C_{\rm fit} \rangle = C_0 + \delta C_{\rm DCSD} = \frac{\sum_i \left(C_0 + f_{\rm NSL} \frac{D_{{\rm NSL},i}}{\langle D_i \rangle} \delta C \right) Q_i}{\sum_j Q_j} \tag{6.14}$$

where the Q_i values above are the ones that do not distinguish between SL and non-SL tags (column 4 of tab. 6.33). Using the values in tab. 6.33, and the 68% coverage numbers reported above, we find 0.001 for S and 0.015 for C.

- We consider a systematic for the appropriateness of using BReco parameters for the tagging performance and the Δt shape for the $B^0 \to \eta' K^0$ signal. We extract BReco parameters from MC signal events for each mode (7 set of parameters, each extracted from a different submode). Then we perform 500 final fit configuration toy experiments and we fit the same sample with either BReco parameters and with MC ones. We average the 500 biases for each of the 7 configurations of BReco parameters from MC signal events. We find 0.005 for S and 0.007 for C. We take as systematic the maximum of such averages. We also consider separately the effects of BReco tagging parameters from BReco Δt shape parameters. In order to estimate this contribution we reperformed the procedure described above extracting from our signal MC only Δt shape parameters. Differences with respect to values shown above are 0.000 for S and 0.001 for C.

We take as systematic 0.005 for S and 0.008 for C.

- The presence of SCF into our signal could introduce a systematic effect. Modes with K_L^0 or $K^0_{S(\pi^0\pi^0)}$ suffers SCF from exchange of a neutral (K_L^0 or photon) particle and this doesn't affect Δt distribution. Concerning modes with $\eta'_{\eta_{3\pi}\pi\pi}$, the effect of SCF is a worse resolution in Δt. So we should consider SCF events as signal events, but with a worse Δt resolution. In order to estimate the systematic contribution of this effect we fit the resolution function with a triple Gaussian model on MC SCF events and we use this resolution function, instead of the BReco one, in the on-peak fit. We find a systematic of 0.002 for S and 0.001 for C

Summing all systematic errors in quadrature, we find 0.015 for S and 0.021 for C as shown in tab. 6.37.

Table 6.34: Results of systematic variations. We show the nominal values, the amount that we vary these, the source of this variation amount, and the change of S and C for this amount of variation. We group similar quantities together after combining their variations in quadrature.

Quantity	Nominal	± variation	Source of variation	Change in S	Change in C
m_{ES}, ΔE, $\mathcal{F}$	PDF parameters, MC/data Corrections			$^{+0.0084}_{-0.0089}$	$^{+0.0031}_{-0.0026}$
f_{SCF}	Table 6.13	10%	–	$^{+0.0003}_{-0.0003}$	$^{+0.0001}_{-0.0001}$
Δm_d	0.507	0.005	PDG	$^{+0.0030}_{-0.0030}$	$^{+0.0014}_{-0.0014}$
τ_B	1.530	0.009	PDG	$^{+0.0006}_{-0.0006}$	$^{+0.0004}_{-0.0004}$
$\langle w \rangle$	Table 3.3	Table 3.3	Table 3.3	$^{+0.0028}_{-0.0027}$	$^{+0.0005}_{-0.0005}$
Δw	Table 3.3	Table 3.3	Table 3.3	$^{+0.0004}_{-0.0004}$	$^{+0.0042}_{-0.0042}$
μ	Table 3.3	Table 3.3	Table 3.3	$^{+0.0000}_{-0.0000}$	$^{+0.0000}_{-0.0000}$
Signal f_{cat}	Table 3.3	Table 3.3	Table 3.3	$^{+0.0003}_{-0.0003}$	$^{+0.0001}_{-0.0001}$
Signal Δt	Table 3.5	Table 3.5	Table 3.5	$^{+0.0039}_{-0.0039}$	$^{+0.0018}_{-0.0018}$
Total				$^{+0.0106}_{-0.0101}$	$^{+0.0051}_{-0.0054}$

Table 6.35: Shifts in S and C from the nominal value obtained with different SVT misalignment configurations for the main modes. The total is obtained as sum in quadrature between the largest shift found in "Time" configuration (considering positive and negative shifts separately) and the shift found in "Boost" configuration.

	$\eta'_{\eta(\gamma\gamma)\pi\pi} K^0_{S(\pi^+\pi^-)}$		$\eta'_{\rho\gamma} K^0_{S(\pi^+\pi^-)}$	
Configuration	ΔS	ΔC	ΔS	ΔC
Time 1	$+0.0003$	-0.0010	$+0.0020$	$+0.0008$
Time 2	-0.0002	$+0.0002$	$+0.0003$	$+0.0018$
Time 3	-0.0014	-0.0005	-0.0003	$+0.0008$
Time 4	-0.0007	-0.0016	-0.0021	-0.0041
Boost	-0.0033	-0.0010	-0.0005	$+0.0003$
Total	$^{+0.0033}_{-0.0036}$	$^{+0.0010}_{-0.0019}$	$^{+0.0021}_{-0.0022}$	$^{+0.0018}_{-0.0041}$

Table 6.36: Shifts in S and C from the nominal value obtained with different Beam Spot configurations for the main modes. The total is obtained as sum in quadrature between the largest shift found shifting y and the shift found in changing error.

	$\eta'_{\eta(\gamma\gamma)\pi\pi} K^0_{S(\pi^+\pi^-)}$		$\eta'_{\rho\gamma} K^0_{S(\pi^+\pi^-)}$	
Configuration	ΔS	ΔC	ΔS	ΔC
Position $y + 20\mu m$	-0.0003	-0.0007	$+0.0037$	-0.0005
Position $y - 20\mu m$	$+0.0017$	$+0.0004$	$+0.0017$	$+0.0001$
Error on y $20\mu m$	$+0.0020$	$+0.0004$	-0.0006	$+0.0024$
Total	± 0.0027	± 0.008	± 0.0037	± 0.0025

Table 6.37: Estimates of systematic errors. (U) denotes uncorrelated systematics, (C) correlated systematics.

Source of error		$\sigma(S)$	$\sigma(C)$
PDF Shapes	(C)	0.010	0.005
MC toy bias	(U)	0.005	0.003
CP content in $B\overline{B}$ Background	(U)	0.006	0.009
SCF contribution	(U)	0.002	0.001
SVT alignment	(C)	0.004	0.004
Beam position/size	(C)	0.004	0.003
Tag-side interference	(C)	0.001	0.015
BReco Δt	(C)	0.005	0.008
Total Correlated	(C)	0.013	0.018
Total Uncorrelated	(U)	0.008	0.010
Total		0.015	0.021

6.9.1 Systematic Errors for Simultaneous Fit on K_S^0 Modes Only

We consider in this section the systematic errors for S and C TD parameters in the case of combined fit for only K_S^0 sub-modes. A detailed description of various systematic contributions are reported in section 6.9. Summing all systematic errors in quadrature, we find 0.015 for S and 0.021 for C as shown in tab. 6.39. Here below we list the systematics that have a different value from the ones calculated for the all-modes fit, reported in section 6.9.

- For PDF shapes, we find 0.009 for S and 0.007 for C. Details about the source of such a systematic can be found in tab. 6.38

- Toy experiments (see tab. 6.27) show that there is a bias of $+0.012$ for S and of $+0.013$ for C. We correct the final fit values of S and C for these biases and we account the uncertainty of the biases as systematic. The actual amount of reconstructed signal MC allow us to perform about 200 independent final fit configuration toy experiments. So we take as systematic the uncertainty of the biases stated in tab. 6.27 multiplied for $\sqrt{500/200}$. We find 0.006 for S and 0.005 for C.

- We consider a systematic for the appropriateness of using BReco data for the $B^0 \rightarrow \eta' K^0$ signal. We find as systematic 0.005 for S and 0.007 for C.

- For the SCF systematic contribution we find 0.001 for both S and C.

Table 6.38: Results of systematic variations for K^0_S submodes. We show the nominal values, the amount that we vary these, the source of this variation amount, and the change of S and C for this amount of variation. We group similar quantities together after combining their variations in quadrature.

Quantity	Nominal	± variation	Source of variation	Change in S	Change in C
$m_{\rm ES}$, ΔE, $\mathcal{F}$	PDF parameters, MC/data Corrections			$^{+0.0097}_{-0.0097}$	$^{+0.0025}_{-0.0033}$
f_{SCF}	Table 6.13	10%	–	$^{+0.0003}_{-0.0003}$	$^{+0.0000}_{-0.0000}$
Δm_d	0.507	0.005	PDG	$^{+0.0029}_{-0.0029}$	$^{+0.0016}_{-0.0016}$
τ_B	1.530	0.009	PDG	$^{+0.0006}_{-0.0006}$	$^{+0.0004}_{-0.0004}$
$\langle w \rangle$	Table 3.3	Table 3.3	Table 3.3	$^{+0.0027}_{-0.0027}$	$^{+0.0006}_{-0.0006}$
Δw	Table 3.3	Table 3.3	Table 3.3	$^{+0.0005}_{-0.0005}$	$^{+0.0043}_{-0.0042}$
μ	Table 3.3	Table 3.3	Table 3.3	$^{+0.0000}_{-0.0000}$	$^{+0.0000}_{-0.0000}$
Signal $f_{\rm cat}$	Table 3.3	Table 3.3	Table 3.3	$^{+0.0003}_{-0.0003}$	$^{+0.0002}_{-0.0002}$
Signal Δt	Table 3.5	Table 3.5	Table 3.5	$^{+0.0035}_{-0.0035}$	$^{+0.0027}_{-0.0027}$
Total				$^{+0.0092}_{-0.0090}$	$^{+0.0069}_{-0.0066}$

Source of error		$\sigma(S)$	$\sigma(C)$
PDF Shapes	(C)	0.009	0.007
MC toy bias	(U)	0.006	0.005
CP content in $B\overline{B}$ Background	(U)	0.006	0.009
SCF contribution	(U)	0.001	0.001
SVT alignment	(C)	0.004	0.004
Beam position/size	(C)	0.004	0.003
Tag-side interference	(C)	0.001	0.015
BReco Δt	(C)	0.005	0.007
Total Correlated	(C)	0.012	0.019
Total Uncorrelated	(U)	0.009	0.010
Total		0.015	0.021

Table 6.39: Estimates of systematic errors for K^0_S submodes. (U) denotes uncorrelated systematics, (C) correlated systematics.

6.9.2 Systematic Errors for Simultaneous Fit on K^0_L Modes Only

We consider in this section the systematic errors for S and C TD parameters in the case of combined fit for K^0_L sub-modes. A detailed description of various systematic contributions are reported in section 6.9. Summing all systematic errors in quadrature, we find 0.018 for S and 0.021 for C as shown in tab. 6.41. Here below we list the systematics that have a different value from the ones calculated for the all-modes fit.

- For PDF shapes,we find 0.009 for S and 0.007 for C. Details about the source of such a systematic can be found in tab. 6.40
- Toy experiments (see tab. 6.28) show that there is a bias of -0.022 for S and of -0.013 for C. We correct the final fit values of S and C for these biases and we account the uncertainty of the biases as systematic. The actual amount of reconstructed signal MC allow us to perform about 200 independent final fit configuration toy experiments. So we take as systematic the uncertainty of the biases stated in tab. 6.28 multiplied for $\sqrt{500/200}$. We find 0.014 for S and 0.009 for C.
- We consider a systematic for the appropriateness of using BReco data for the $B^0 \to \eta' K^0$ signal. We find as systematic 0.004 for S and 0.008 for C.
- For the SCF systematic contribution we find 0.001 for S and 0.004 for C.

Table 6.40: Results of systematic variations for K_L^0 submodes. We show the nominal values, the amount that we vary these, the source of this variation amount, and the change of S and C for this amount of variation. We group similar quantities together after combining their variations in quadrature.

Quantity	Nominal	± variation	Source of variation	Change in S	Change in C
m_{ES}, ΔE, $\mathcal{F}$	PDF parameters, MC/data Corrections			$^{+0.0037}_{-0.0038}$	$^{+0.0044}_{-0.0040}$
f_{SCF}	Table 6.13	10%	–	$^{+0.0001}_{-0.0001}$	$^{+0.0001}_{-0.0001}$
Δm_d	0.507	0.005	PDG	$^{+0.0023}_{-0.0024}$	$^{+0.0005}_{-0.0005}$
τ_B	1.530	0.009	PDG	$^{+0.0006}_{-0.0006}$	$^{+0.0002}_{-0.0002}$
$\langle w \rangle$	Table 3.3	Table 3.3	Table 3.3	$^{+0.0034}_{-0.0035}$	$^{+0.0016}_{-0.0016}$
Δw	Table 3.3	Table 3.3	Table 3.3	$^{+0.0008}_{-0.0008}$	$^{+0.0041}_{-0.0041}$
μ	Table 3.3	Table 3.3	Table 3.3	$^{+0.0000}_{-0.0000}$	$^{+0.0000}_{-0.0000}$
Signal f_{cat}	Table 3.3	Table 3.3	Table 3.3	$^{+0.0004}_{-0.0004}$	$^{+0.0002}_{-0.0002}$
Signal Δt	Table 3.5	Table 3.5	Table 3.5	$^{+0.0070}_{-0.0072}$	$^{+0.0029}_{-0.0029}$
Total				$^{+0.0090}_{-0.0092}$	$^{+0.0069}_{-0.0066}$

Table 6.41: Estimates of systematic errors for K_L^0 submodes. (U) denotes uncorrelated systematics, (C) correlated systematics.

Source of error		$\sigma(S)$	$\sigma(C)$
PDF Shapes	(C)	0.009	0.007
MC toy bias	(U)	0.014	0.009
SCF contribution	(U)	0.001	0.004
SVT alignment	(C)	0.004	0.004
Beam position/size	(C)	0.004	0.003
Tag-side interference	(C)	0.001	0.015
BReco Δt	(C)	0.004	0.008
Total Correlated	(C)	0.011	0.019
Total Uncorrelated	(U)	0.014	0.010
Total		0.018	0.021

6.10 Results

Results of ML fits for the five $B^0 \rightarrow \eta' K^0_S$ and the two $B^0 \rightarrow \eta' K^0_L$ sub-decays are shown in tab. 6.42. We give the number of events to fit, the MC efficiency, the signal and $B\overline{B}$ yields, the values for S and C for $B\overline{B}$ charmed events, the number of free parameters in the fit, the correlation between S and C found in the fit, and the parameters S and C.

Inconsistency of our result for S with *CP* conservation ($S = 0$) has a significance of 7.2 standard deviations (only statistical error contribution). Our result for the direct-*CP* violation parameter C is 1.0 standard deviations from zero (only statistical error contribution). The statistical significance is taken as the square root of

$$-2 \ln \frac{\mathcal{L}(x=0)}{\mathcal{L}_{\max}}, \tag{6.15}$$

where x is the parameter for which we calculate the statistical significance (in our case is S or C), $\mathcal{L}(x=0)$ is the likelihood function obtained fitting with $x = 0$, and $\mathcal{L}_{\max}$ is the likelihood function obtained when x is floating in the fit.

Considering statistical and systematic errors, inconsistency of our result for S with *CP* conservation ($S = 0$) has a significance of 7.1 standard deviations. For the direct-*CP* violation parameter C is 0.9 standard deviations from zero. To include the systematics in the statistical significance calculation, we convolve the systematic error to the statistical $\mathcal{L}$, using a Gaussian approximation. In particular using the coefficient

$$f = \left(\frac{x_{\text{fitted}}}{\sigma_x^{\text{sys}}} \right)^2, \tag{6.16}$$

where x_{fitted} is the value of x obtained when it is floating in the fit and σ_x^{sys} is its systematic error, we correct the eq. 6.15 to include the systematics:

$$\frac{-2 \ln[\mathcal{L}(x=0)/\mathcal{L}_{\max}]}{-2 \ln[\mathcal{L}(x=0)/\mathcal{L}_{\max}] + f} f. \tag{6.17}$$

The statistical significance with systematics included is the root square of the eq. 6.17.

We measure a correlation of 3.6% between S and C in the fit.

Fit configuration is well-described in section 6.7. Essentially in the fit for each mode we have as free parameters: S, C for signal and $B\overline{B}$ charm, signal yield, $B\overline{B}$ background yields, 6 fractions for $B\overline{B}$ charm, continuum background yield and 6 fractions, background m_{ES}, ΔE and Δt PDF parameters. When we combine different sub-decays, we have in common S, C. So in the all sub-decays TD combined fit we have 139 free parameters: S and C for signal (2) and $B\overline{B}$ charm (4), signal yields (7), $B\overline{B}$ background yields (6) and fractions (12), continuum background yields (7) and fractions (42), background

PDF parameters (59). For all fit we run HESSE and we check that its status is OK after fitting. For the combined fit we also run MINOS.

We correct the values of S and C obtained from the simultaneous K^0_S modes, K^0_L modes and 7-channel fit for the biases observed in toy studies (sec. 6.8). Values of such biases and their contributions to systematic errors are reported in sec. 6.9. Including the bias correction, we found the following final results:

$$\begin{aligned}
S_{\eta' K^0} &= 0.586 \pm 0.078 \pm 0.015 \\
C_{\eta' K^0} &= -0.058 \pm 0.058 \pm 0.021 \\
\\
S_{\eta' K^0_S} &= 0.555 \pm 0.086 \pm 0.015 \\
C_{\eta' K^0_S} &= -0.095 \pm 0.064 \pm 0.021 \\
\\
S_{\eta' K^0_L} &= 0.818 \ {}^{+0.174}_{-0.188} \pm 0.018 \\
C_{\eta' K^0_L} &= 0.085 \ {}^{+0.134}_{-0.135} \pm 0.021
\end{aligned}$$

where the first error is statistic and the second systematic

Quantity	$\eta_1' K^0_{\pi^+\pi^-}$	$\eta_2' K^0_{\pi^+\pi^-}$	$\eta_3' K^0_{\pi^+\pi^-}$	$\eta_1' K^0_{\pi^0\pi^0}$	$\eta_2' K^0_{\pi^0\pi^0}$	$\eta_1' K^0_L$	$\eta_3' K^0_L$
Events into fit	1416	20468	451	877	21909	18036	6213
MC efficiency (%)	26.6	27.6	16.6	13.0	14.2	17.6	12.6
Signal yield	476 ± 24	960 ± 39	168 ± 14	99 ± 13	164 ± 28	386 ± 32	169 ± 21
bc yield	–	457 ± 154	–	–	233 ± 131	–	–
bk+ yield	–	64 ± 39	–	–	8 ± 56	–	–
bk– yield	–	36 ± 113	–	–	167 ± 136	–	–
S *bc*	–	0.29 ± 0.21	–	–	-0.37 ± 0.27	–	–
C *bc*	–	-0.09 ± 0.18	–	–	-0.01 ± 0.29	–	–
# Free parameters	19	29	19	19	29	18	18
$S - C$ correlation (%)	6.5	5.1	1.9	0.0	–21.8	5.0	–10.6
S	0.70 ± 0.16	0.42 ± 0.12	0.81 ± 0.23	0.39 ± 0.35	0.94 ± 0.44	0.75 ± 0.22	0.87 ± 0.30
C	-0.14 ± 0.11	-0.06 ± 0.09	0.09 ± 0.20	0.18 ± 0.31	-0.16 ± 0.32	0.02 ± 0.16	0.19 ± 0.25
TD Combined fit:							
Signal yield	476 ± 24	958 ± 39	168 ± 14	99 ± 13	169 ± 26	386 ± 32	170 ± 22
bc yield	–	450 ± 210	–	–	234 ± 134	–	–
bk+ yield	–	66 ± 40	–	–	5 ± 50	–	–
bk– yield	–	42 ± 146	–	–	165 ± 140	–	–
S *bc*	–	0.25 ± 0.22	–	–	-0.30 ± 0.27	–	–
C *bc*	–	-0.09 ± 0.17	–	–	-0.03 ± 0.27	–	–
# Free parameters	107					34	
$S - C$ correlation (%)	4.0					1.0	
S	0.567 ± 0.086					$0.796^{+0.174}_{-0.188}$	
C	-0.082 ± 0.064					$0.072^{+0.134}_{-0.135}$	
TD all modes:							
Signal yield	476 ± 24	958 ± 39	168 ± 14	99 ± 13	169 ± 26	387 ± 32	169 ± 22
bc yield	–	448 ± 224	–	–	235 ± 134	–	–
bk+ yield	–	66 ± 40	–	–	6 ± 50	–	–
bk– yield	–	43 ± 155	–	–	164 ± 141	–	–
S *bc*	–	0.23 ± 0.22	–	–	-0.31 ± 0.26	–	–
C *bc*	–	-0.10 ± 0.17	–	–	-0.04 ± 0.26	–	–
# Free parameters	139						
$S - C$ correlation (%)	3.6						
S	0.597 ± 0.078						
C	-0.054 ± 0.058						

Table 6.42: Fit results for all the neutral decay modes for Run1–6 data. Subscripts for η' decay modes denote $\eta'_{\eta(\gamma\gamma)\pi\pi}$ (1), $\eta'_{\rho\gamma}$ (2), and $\eta'_{\eta(3\pi)\pi\pi}$ (3).

6.10.1 $-\ln\mathcal{L}$ Plots

We show in fig. 6.3–6.5 the $-\ln\mathcal{L}$ for S and C in: K^0_S combined fit, K^0_L combined fit and final simultaneous fit, respectively. These figures are obtained reperforming the fit, fixing the parameter (S or C in our case) for which we do the $-2\ln\mathcal{L}$ scan.

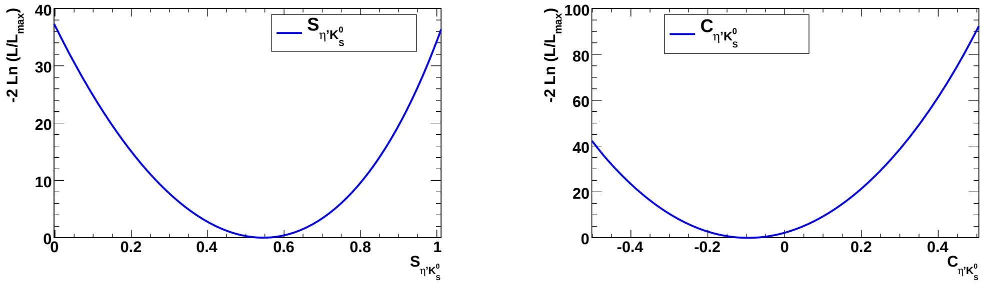

Figure 6.3: $-2\ln\mathcal{L}$ as a function of S (left) and C (right) obtained from the K^0_S modes simultaneous fit.

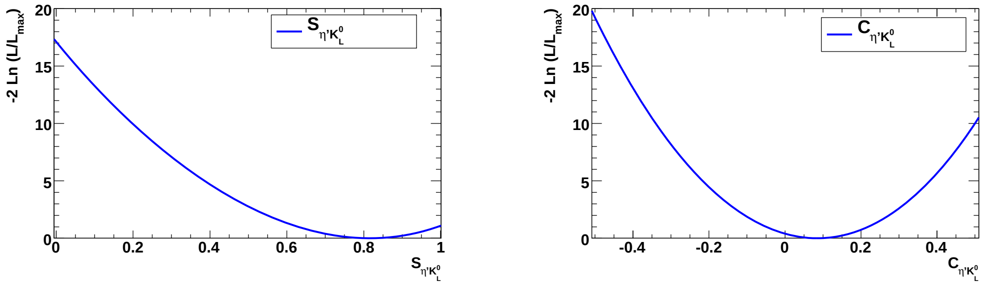

Figure 6.4: $-2\ln\mathcal{L}$ as a function of S (left) and C (right) obtained from the K^0_L modes simultaneous fit.

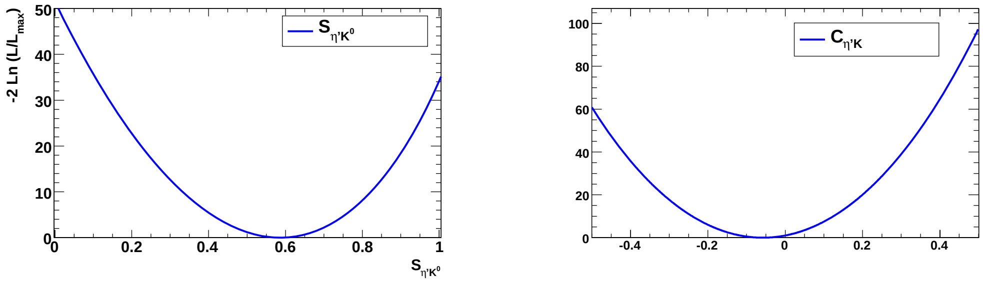

Figure 6.5: $-2\ln\mathcal{L}$ as a function of S (left) and C (right) obtained from the final simultaneous fit.

6.10.2 Projections

We draw the m_{ES}, ΔE, and Δt projection plots for our decays. To reduce the contribution of background, we optimize a cut on the quantity:

$$R = \frac{\mathcal{P}_s}{\mathcal{P}_s + \sum \mathcal{P}_b} \tag{6.18}$$

where $\mathcal{P}_s$ and $\mathcal{P}_b$ are the probability for the event to be signal or background, respectively. These probabilities are calculated from PDFs, excluding in the computation the variable being plotted. In fig. 6.6 we show the projections of m_{ES} and ΔE for neutral and charged modes, summing the submodes. In fig. 6.7 and 6.8 we show Δt projections and raw asymmetry projection for neutral and charged modes, respectively, summing the submodes. Fit curves shown are not a fit to the data in the histogram but the projection of the overall fit scaled to take into account the effect of the cut on R.

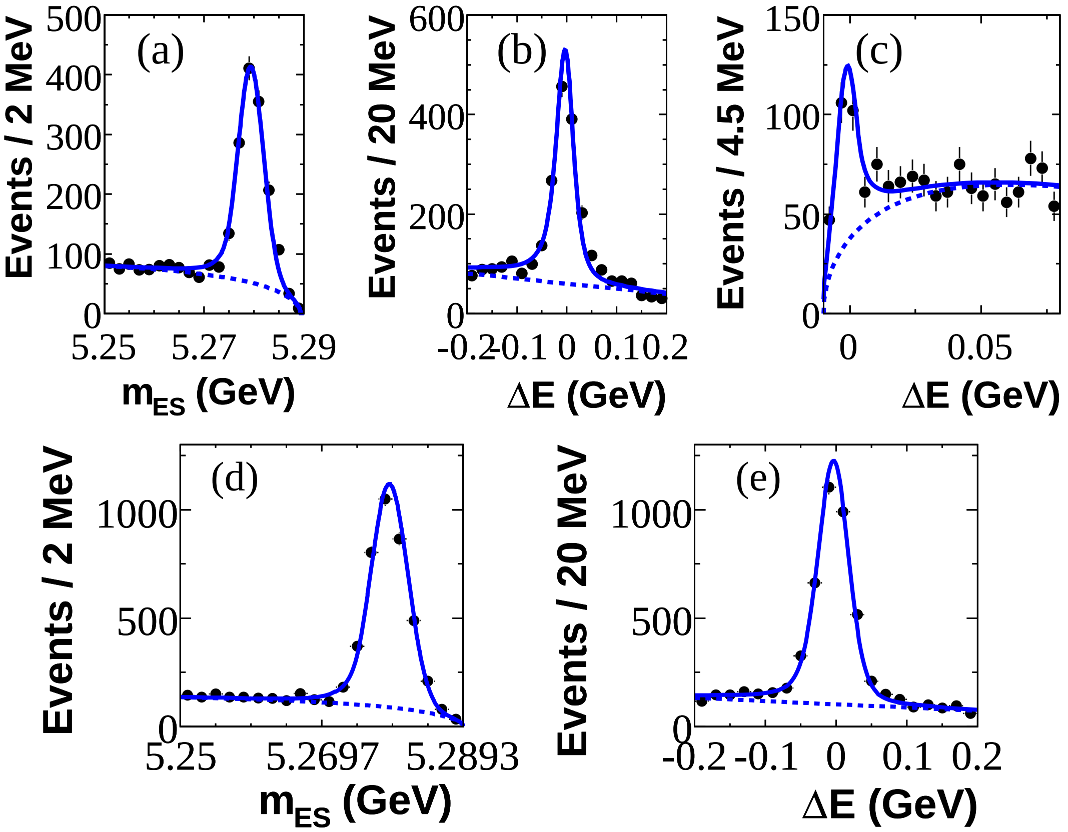

Figure 6.6: Projections of m_{ES} and ΔE for neutrals (up) and charged modes (down), summing contributions from different submodes. First row: m_{ES} for K^0_S modes (a), ΔE for K^0_S modes (b), ΔE for K^0_L modes (c). Second row: m_{ES} (d) and ΔE (e) for charged modes. See the text for details on the projection technique used.

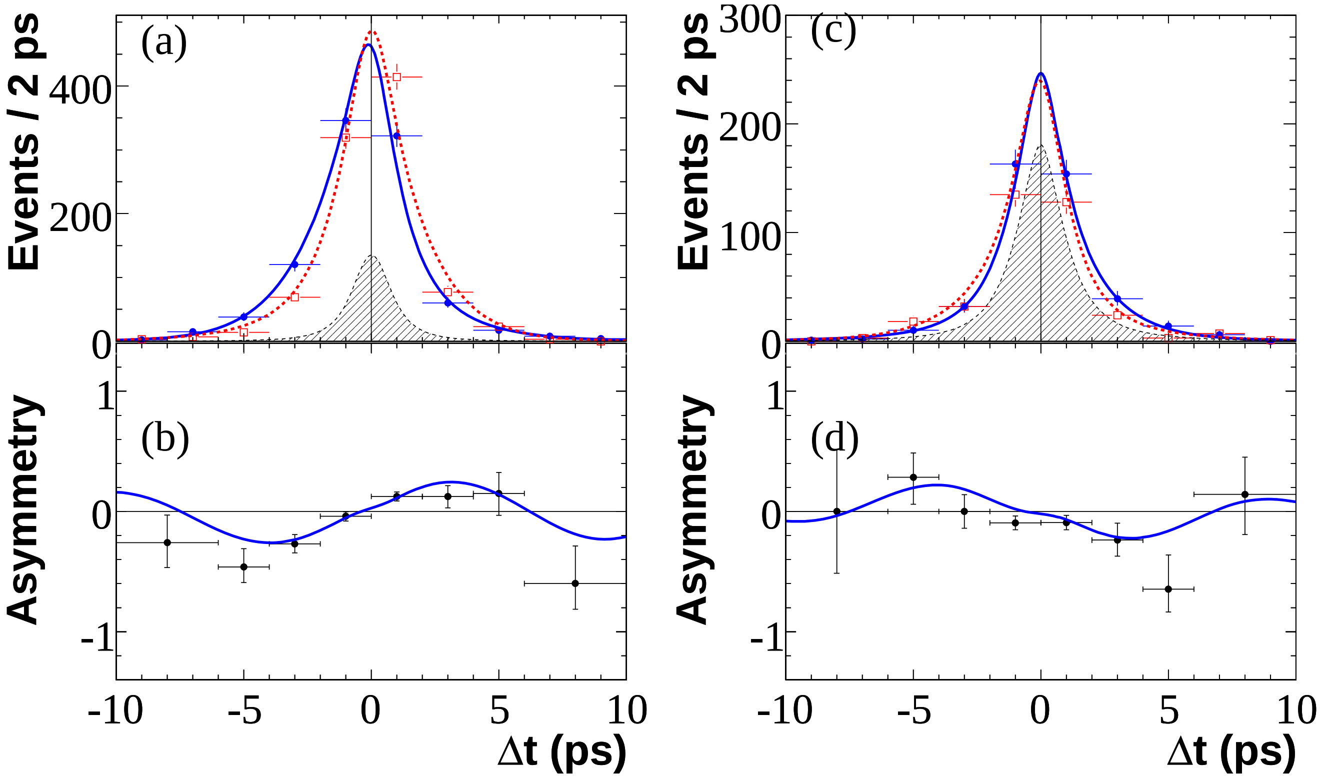

Figure 6.7: Projections onto Δt for (a) $B^0 \to \eta' K^0_S$ and (c) $B^0 \to \eta' K^0_L$ of the data (points with error bars for B^0 tags (N_{B^0}) in red empty rectangles and $\overline{B}^0$ tags ($N_{\overline{B}^0}$) in in blue solid circles), fit function (red dashed and blue solid lines for B^0 and $\overline{B}^0$ tagged events, respectively), and background function (black shaded regions). We show the raw asymmetry, $(N_{B^0} - N_{\overline{B}^0})/(N_{B^0} + N_{\overline{B}^0})$, for (b) $B^0 \to \eta' K^0_S$ and (d) $B^0 \to \eta' K^0_L$; the lines represent the fit functions. See the text for details on the projection technique used.

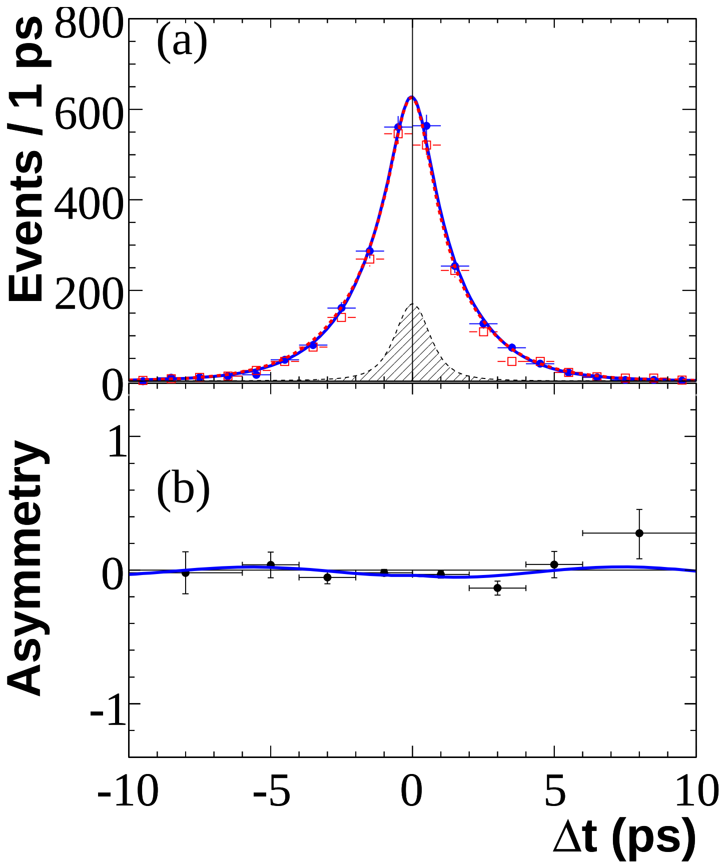

Figure 6.8: Projections onto Δt for $B^{+}\to\eta' K^{+}$ of the data (points with error bars for B^{+} tags ($N_{B^{+}}$) in red empty rectangles and B^{-} tags ($N_{B^{-}}$) in in blue solid circles), fit function (red dashed and blue solid lines for B^{0} and $\overline{B}^{0}$ tagged events, respectively), and background function (black shaded regions). We show the raw asymmetry, $(N_{B^{+}} - N_{B^{-}})/(N_{B^{+}} + N_{B^{-}})$, the lines represent the fit functions. See the text for details on the projection technique used.

6.10.3 Contour Plots

In fig. 6.9 we show the plot of the contour levels of $-2\ln\mathcal{L}$. The curves includes only statical errors and are corrected for the shift bias. We also show the most recent values of S and C measured by *BABAR* in $b \rightarrow c\bar{c}$ transitions [108]. From the plot we can see that our measurement is consisted with the value of S measured in B decays to charmonium states. It's also evident that we see a clear CP violation far from zero.

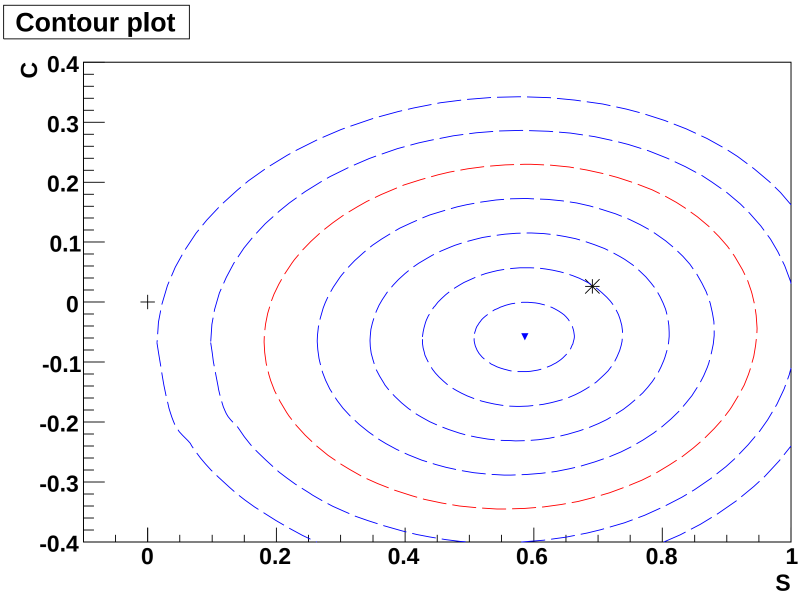

Figure 6.9: Contour levels of $-2\ln\mathcal{L}$. Blue(Red) dashed lines indicate the contour at various(five) sigma levels, the triangle represents the measured values for S and C, the star represents values for S and C measured by *BABAR* in $b \rightarrow c\bar{c}$ transitions [108], the "+" represents the parameters value in case of absence of CP violation.

6.10.4 Results for Publication

In relation to an internal agreement in *BABAR* Collaboration, results for publication [19] were provided combining results from Milan and another group in the *BABAR* Collaboration. Final result was obtained combining the $-2\ln\mathcal{L}$ curves of K^0_S submodes (provided by the other group) and K^0_L submodes (provided by Milan). K^0_S, K^0_L and combination results were in agreement between both groups.

To obtain the central value and systematic errors taking properly into account statistics and systematics effect in the two curves, the $-2\ln\mathcal{L}$ curves of the submodes are convoluted with their uncorrelated systematic errors (see sec. 6.9.1–6.9.2). Statistical error is obtained combining the unconvolved curves. Total uncorrelated systematic is obtained differing in quadrature the error obtained from convolved and unconvolved curves. Total systematic is obtained summing in quadrature the total uncorrelated systematic and the greatest correlated systematic error between K_S^0 and K_L^0 submodes.

In fig. 6.10 we show K_S^0 and K_L^0 submodes $-2\ln\mathcal{L}$ and their combination, for S and C. Results from this combination are:

$$\begin{array}{rcl} S_{\eta' K^0} & = & 0.574^{+0.076}_{-0.077}\ (\text{stat}) \pm 0.018\ (\text{syst}) \\ C_{\eta' K^0} & = & -0.076^{+0.056}_{-0.057}\ (\text{stat}) \pm 0.024\ (\text{syst}) \end{array}$$

That we round, for publication, to

$$\begin{array}{rcl} S_{\eta' K^0} & = & 0.57 \pm 0.08\ (\text{stat}) \pm 0.02\ (\text{syst}) \\ C_{\eta' K^0} & = & -0.08 \pm 0.06\ (\text{stat}) \pm 0.02\ (\text{syst}) \end{array}$$

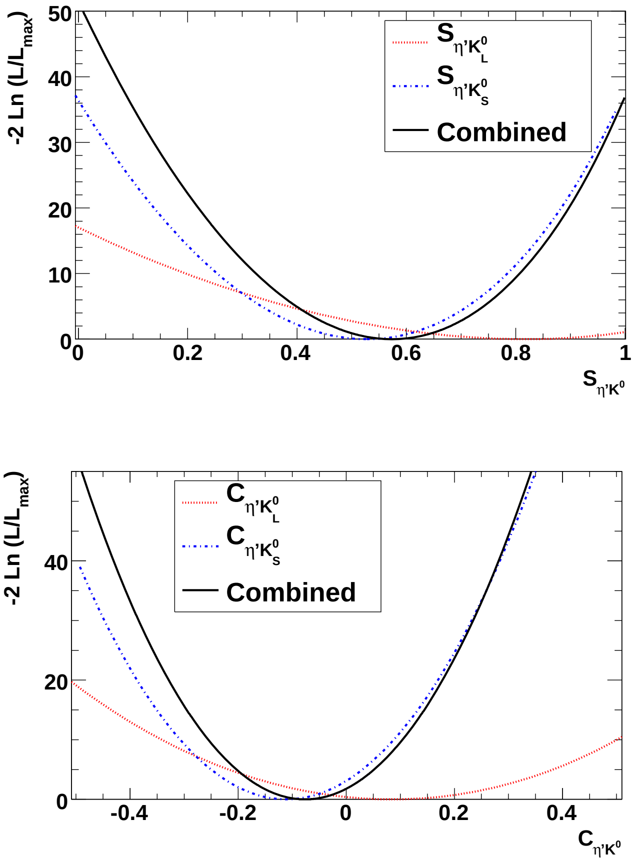

Figure 6.10: $-2\ln\mathcal{L}$ curves for S (top) and C (bottom). Red dotted curve is obtained from K_S^0 sub-modes, blue dash-point curve from K_L^0 ones, black solid curve from the combination of the two submodes curves.

6.11 Previous Results Comparison

We compare our previous published results with a statistic of 384×10^6 $B\overline{B}$ pairs, $S = 0.58 \pm 0.10$ [18] (obtained with data reconstructed with release 18, R18b) with the new one (R22d). Since in R22d a great improvement of the tracking software, `TrkFixup` (see sec: 3.4.7), was included, we expect higher efficiencies in modes with many slow charged particles.

Furthermore in the current analysis we are using some different cuts:

- the minimum number of tracks in the event is required in the `ChargedTracks` list (it was `GoodTracksVeryLoose` list);
- we use the new PID vetoes for the charged pions in the η' candidates and for the charged kaon. For the charged kaon now we use PID instead of a requirement on the pull of the Čerenkov angle for the kaon hypothesis;
- in the previous analysis we used only tagged events. In the current analysis we use all events. However for this comparison we use all events also in R18 data (except for tab. 6.47);
- we use a different definition of the Fisher discriminant (we added the absolute value of the tagging output probability), so we don't compare this variable;
- new optimization of the cuts for K^0_L selection. In particular we enlarge the upper cut on ΔE from 0.04 to 0.08 GeV.

You should also consider that now we add Run6 dataset and we include a new sub-mode, $\eta'_{\eta(3\pi)\pi\pi}K^0_L$. Concerning the ML fit, in the current analysis we added a charm component, we split the $B\overline{B}$ charmless peaking component in the two components with ΔE peaking for positive and negative values, and we split the signal component in well-reconstructed and SCF events for modes with high SCF fraction. In previous analysis there were just a $B\overline{B}$ charmless component and one signal component (no splitting in well-reconstructed and SCF events). We have also a new definition of the Fisher Discriminant and we use a different parametrization for the $B\overline{B}$ Δt PDFs.

We compare results of the reconstruction of the *BABAR* dataset, using the R18b and R22d releases. We show in tab. 6.43 the sample size used for such a comparison.

In tab. 6.44 we report, MC signal efficiency, input to ML fit, number of on-peak events per fb^{-1}, and combinations per events for each decay mode.

In tab. 6.45 we summarize the numbers of events which are reconstructed by both releases (Overlap) and the number of those reconstructed only by one of them (only), considering Run1–5 dataset. In the same table we show input to the maximum likelihood

	R18b	R22d
Signal MC	675K	972K
	Run 1	
on-peak (fb^{-1})	20.7	20.4
on-peak ($B\overline{B}$ pairs)	22.8M	22.4M
	Run 2	
on-peak (fb^{-1})	61.6	61.1
on-peak ($B\overline{B}$ pairs)	67.8M	67.4M
	Run 3	
on-peak (fb^{-1})	32.5	32.3
on-peak ($B\overline{B}$ pairs)	35.7M	35.6M
	Run 4	
on-peak (fb^{-1})	100.6	100.3
on-peak ($B\overline{B}$ pairs)	110.7M	110.4M
	Run 5	
on-peak (fb^{-1})	133.6	133.3
on-peak ($B\overline{B}$ pairs)	147.0M	147.2M
	Run 1–5	
on-peak (fb^{-1})	349.0	347.4
on-peak ($B\overline{B}$ pairs)	384M	383M
	Run 6	
on-peak (fb^{-1})	–	78.4
on-peak ($B\overline{B}$ pairs)	–	84.3M
	Run 1–6	
on-peak (fb^{-1})	349.0	425.7
on-peak ($B\overline{B}$ pairs)	384M	467M
$B^0\overline{B}^0$	472M	736M
B^+B^-	469M	731M

Table 6.43: Dataset used for validation (for all modes used). For the on-peak data we give also the information for each run period.

	R18b	R22d
$\eta'_{\eta(\gamma\gamma)\pi\pi}K^0_S$		
MC efficiency (%)	24.1	26.6
Input to ML (Run1–6)	1043	1159 (1416)
#events/fb^{-1} (Run1–6)	3.0	3.0 (3.3)
# $B^0\overline{B}^0$ events	8	8
# B^+B^- events	1	1
# MC comb. per event	1.10	1.10
# Data comb. per event	1.09	1.09
$\eta'_{\eta(3\pi)\pi\pi}K^0_{S(\pi^+\pi^-)}$		
MC efficiency (%)	11.8	16.6
Input to ML (Run1–6)	286	357 (451)
#events/fb^{-1} (Run1–6)	0.8	1.0 (1.0)
# $B^0\overline{B}^0$ events	4	5
# B^+B^- events	1	1
# MC comb. per event	1.64	2.66
# Data comb. per event	1.77	2.54
$\eta'_{\rho\gamma}K^0_S$		
MC efficiency (%)	27.8	27.6
Input to ML (Run1–6)	18839	16604 (20468)
#events/fb^{-1} (Run1–6)	54.0	47.8 (48.1)
# $B^0\overline{B}^0$ events	440	494
# B^+B^- events	234	281
# MC comb. per event	1.07	1.07
# Data comb. per event	1.08	1.07
$\eta'_{\eta(\gamma\gamma)\pi\pi}K^0_{S(\pi^0\pi^0)}$		
MC efficiency (%)	13.2	13.0
Input to ML	860	698 (877)
#events/fb^{-1} (Run1–6)	2.5	2.0 (2.1)
# $B^0\overline{B}^0$ events	1	3
# B^+B^- events	4	4
# MC comb. per event	1.23	1.22
# Data comb. per event	1.22	1.24
$\eta'_{\rho\gamma}K^0_{S(\pi^0\pi^0)}$		
MC efficiency (%)	15.8	14.2
Input to ML	24062	17560 (21909)
#events/fb^{-1} (Run1–6)	68.9	50.5 (51.5)
# $B^0\overline{B}^0$ events	157	246
# B^+B^- events	174	286
# MC comb. per event	1.22	1.20
# Data comb. per event	1.24	1.22
$\eta'_{\eta(\gamma\gamma)\pi\pi}K^0_L$		
MC efficiency (%)	15.5	17.6
Input to ML	6740	14342 (18036)
#events/fb^{-1} (Run1–6)	19.3	41.3 (42.4)
# $B^0\overline{B}^0$ events	172	395
# B^+B^- events	95	210
# MC comb. per event	1.17	1.19
# Data comb. per event	1.13	1.15

Table 6.44: MC efficiency, input to ML fit for Run1–5, # of events per fb^{-1}, and combinations per event for each decay mode. $B\overline{B}$ background generic MC events are rescaled to Run1–6 luminosity. For reference in case of R22d we give also the numbers for the full dataset Run1–6.

fit. Note that in previous analyses, in order to take into account variation in the beam energy, that affect $m_{\rm ES}$ distribution, we applied an average correction offline. In the current analysis such a correction is applied on an event by event criterion and is included in the new reconstruction software. This is particular important for the on-peak data, namely for the lower cutoff on the $m_{\rm ES}$, and it gives an higher input to the ML fit for data reconstructed in analysis-50.

Considering only events in common between the two reconstructions using Run1–5 dataset, we fit the distributions of the shift of the variables used into the fit with a Gaussian shape. The shift is computed event by event as the difference between the variable value in R18b and in R22d. In tab. 6.46 we show the mean and RMS values of these fits.

Mode	Overlap	R18b only (%)	R22d only (%)	R18b	R22d	R18b VS R22d (%)
$\eta'_{\eta(\gamma\gamma)\pi\pi}K^0_S$	779	264 (25.3)	380 (32.8)	1043	1159	$+11.1$
$\eta'_{\eta(3\pi)\pi\pi}K^0_{S(\pi^+\pi^-)}$	178	108 (37.8)	179 (50.1)	286	357	$+24.8$
$\eta'_{\rho\gamma}K^0_S$	11530	7309 (38.8)	5074 (30.6)	18839	16604	-11.9
$\eta'_{\eta(\gamma\gamma)\pi\pi}K^0_{S(\pi^0\pi^0)}$	473	387 (45.0)	225 (32.2)	860	698	-18.8
$\eta'_{\rho\gamma}K^0_{S(\pi^0\pi^0)}$	12422	11640 (48.4)	5138 (29.3)	24062	17560	-27.0
$\eta'_{\eta(\gamma\gamma)\pi\pi}K^0_L$	3385	3355 (49.8)	10957 (76.4)	6740	14342	$+212.8$

Table 6.45: R18b and R22d overlap event comparison for Run1–5 data events (left three columns). The right three columns show the number of events as input to ML fit.

		ΔE (MeV)	Δt (ps)	$\sigma_{\Delta t}$ (ps)	$m_{\rm ES}$ (MeV/c^2)
$\eta'_{\eta(\gamma\gamma)\pi\pi}K^0_S$	shift	6.362 ± 0.823	-0.035 ± 0.031	0.014 ± 0.004	-0.250 ± 0.057
	RMS	22.964	0.874	0.120	1.582
$\eta'_{\eta(3\pi)\pi\pi}K^0_{S(\pi^+\pi^-)}$	shift	10.514 ± 3.230	0.091 ± 0.059	0.007 ± 0.010	-0.418 ± 0.165
	RMS	43.095	0.783	0.138	2.199
$\eta'_{\rho\gamma}K^0_S$	shift	3.253 ± 0.209	0.008 ± 0.005	0.023 ± 0.001	-0.254 ± 0.018
	RMS	22.493	0.562	0.121	1.884
$\eta'_{\eta(\gamma\gamma)\pi\pi}K^0_{S(\pi^0\pi^0)}$	shift	13.271 ± 1.410	-0.036 ± 0.015	0.004 ± 0.004	-0.287 ± 0.089
	RMS	30.674	0.337	0.078	1.936
$\eta'_{\rho\gamma}K^0_{S(\pi^0\pi^0)}$	shift	11.758 ± 0.289	-0.007 ± 0.004	0.008 ± 0.001	-0.277 ± 0.021
	RMS	32.225	0.430	0.089	2.341
$\eta'_{\eta(\gamma\gamma)\pi\pi}K^0_L$	shift	-1.291 ± 0.233	-0.002 ± 0.026	-0.014 ± 0.007	–
	RMS	10.711	1.195	0.331	–

Table 6.46: R18b–R22d shift and RMS in the fit variable values for common events in on-peak Run1–5 events.

All differences are understood as effect of $m_{\rm ES}$ bias corrections, new tracking reconstruction (`TrkFixup`), new EMC calibrations.

As last check for the comparison we run the TD fits on the new reconstructed data (Run1–5). Results of these fits are reported in tab. 6.47.

Quantity	$\eta'_1 K^0_{\pi^+\pi^-}$	$\eta'_2 K^0_{\pi^+\pi^-}$	$\eta'_3 K^0_{\pi^+\pi^-}$	$\eta'_1 K^0_{\pi^0\pi^0}$	$\eta'_2 K^0_{\pi^0\pi^0}$	$\eta'_1 K^0_L$	$\eta'_3 K^0_L$
R18							
Signal yield	224 ± 16	566 ± 30	73 ± 9	52 ± 9	137 ± 24	206 ± 24	–
$B\overline{B}$ charmless yield	–	335 ± 39	–	–	156 ± 39	–	–
S	0.61 ± 0.23	0.56 ± 0.14	0.89 ± 0.35	0.84 ± 0.42	0.56 ± 0.41	0.32 ± 0.28	–
C	-0.26 ± 0.14	-0.24 ± 0.10	0.14 ± 0.25	-0.26 ± 0.36	0.15 ± 0.27	0.08 ± 0.23	–
TD Combined fit:							
Signal yield	224 ± 16	565 ± 30	73 ± 9	52 ± 9	132 ± 24		
$B\overline{B}$ charmless yield	–	335 ± 41	–	–	160 ± 41		
S			0.62 ± 0.11				
C			-0.18 ± 0.07				
TD all modes:							
Signal yield	224 ± 16	566 ± 30	73 ± 9	52 ± 9	133 ± 24	204 ± 24	–
$B\overline{B}$ charmless yield	–	334 ± 41	–	–	159 ± 41	–	–
S				0.58 ± 0.10			
C				-0.16 ± 0.07			
R22							
Signal yield (expect.)	373 ± 21 (407)	789 ± 35 (718)	145 ± 14 (148)	80 ± 11 (90)	147 ± 26 (163)	321 ± 29 (353)	130 ± 19 (147)
bc yield	–	426 ± 148	–	–	170 ± 127	–	–
bk+ yield	–	68 ± 36	–	–	1 ± 51	–	–
bk– yield	–	-28 ± 104	–	–	172 ± 131	–	–
S	0.48 ± 0.20	0.41 ± 0.14	1.03 ± 0.25	0.49 ± 0.38	0.86 ± 0.52	0.63 ± 0.25	0.91 ± 0.32
C	-0.27 ± 0.12	-0.05 ± 0.10	0.14 ± 0.23	-0.29 ± 0.33	-0.21 ± 0.33	0.00 ± 0.18	0.01 ± 0.27
TD Combined fit:							
Signal yield	373 ± 21	787 ± 35	142 ± 13	80 ± 11	151 ± 25	321 ± 29	129 ± 19
bc yield	–	423 ± 158	–	–	172 ± 128	–	–
bk+ yield	–	68 ± 36	–	–	-1 ± 48	–	–
bk– yield	–	-24 ± 110	–	–	169 ± 130	–	–
S			0.51 ± 0.10			0.72 ± 0.21	
C			-0.13 ± 0.07			0.01 ± 0.15	
TD all modes:							
Signal yield	373 ± 21	787 ± 35	142 ± 13	80 ± 11	151 ± 25	321 ± 29	129 ± 18
bc yield	–	423 ± 160	–	–	171 ± 128	–	–
bk+ yield	–	68 ± 36	–	–	-1 ± 48	–	–
bk– yield	–	-25 ± 111	–	–	170 ± 130	–	–
S				0.545 ± 0.088			
C				-0.103 ± 0.064			

Table 6.47: Comparison of ML fit results for all the neutral decay modes for R18 and R22 Run1–5 data. Subscripts for η' decay modes denote $\eta'_{\eta(\gamma\gamma)\pi\pi}$ (1), $\eta'_{\rho\gamma}$ (2), and $\eta'_{\eta(3\pi)\pi\pi}$ (3).

The conclusion of this comparison is that current results are compatible with previous ones [18].

6.12 Cross Checks

We report here on a number of checks we have done on the correctness and performance of the fitting procedure.

6.12.1 Likelihood Ratio

In fig. 6.11 we show the likelihood ratio $R = \frac{\mathcal{P}_s}{\mathcal{P}_s + \sum \mathcal{P}_b}$ for all neutral modes.

6.12.2 *sPlots*

In appendix C we show the $sPlots$ for each mode. We report also the yields results when we fit removing one discriminating variable at a time from the fit. The $sPlot$ technique is explained in detail in sec. 4.4.3. $sPlots$ are performed not using Δt variable and without splitting events in tagging categories.

6.12.3 Fits with $C = 0$ or $S = 0$

We perform fits to the data for full fit with the constraint of $C = 0$ or $S = 0$. Configuration and results of these fits are reported in tab. 6.12.3. Results are in agreement with those found in the nominal fits (tab. 6.42), this prove that correlations between S and C are not an issue in our measurement.

Fit Configuration	Fit Results	
	S	C
K_S^0 + K_L^0	0.600 ± 0.078	0
K_S^0 + K_L^0	0	-0.064 ± 0.059
K_S^0 submodes	0.560 ± 0.086	0
K_S^0 submodes	0	-0.090 ± 0.065
K_L^0 submodes	0.794 ± 0.183	0
K_L^0 submodes	0	0.054 ± 0.137

Table 6.48: Results of TD fits with S or C fixed to zero.

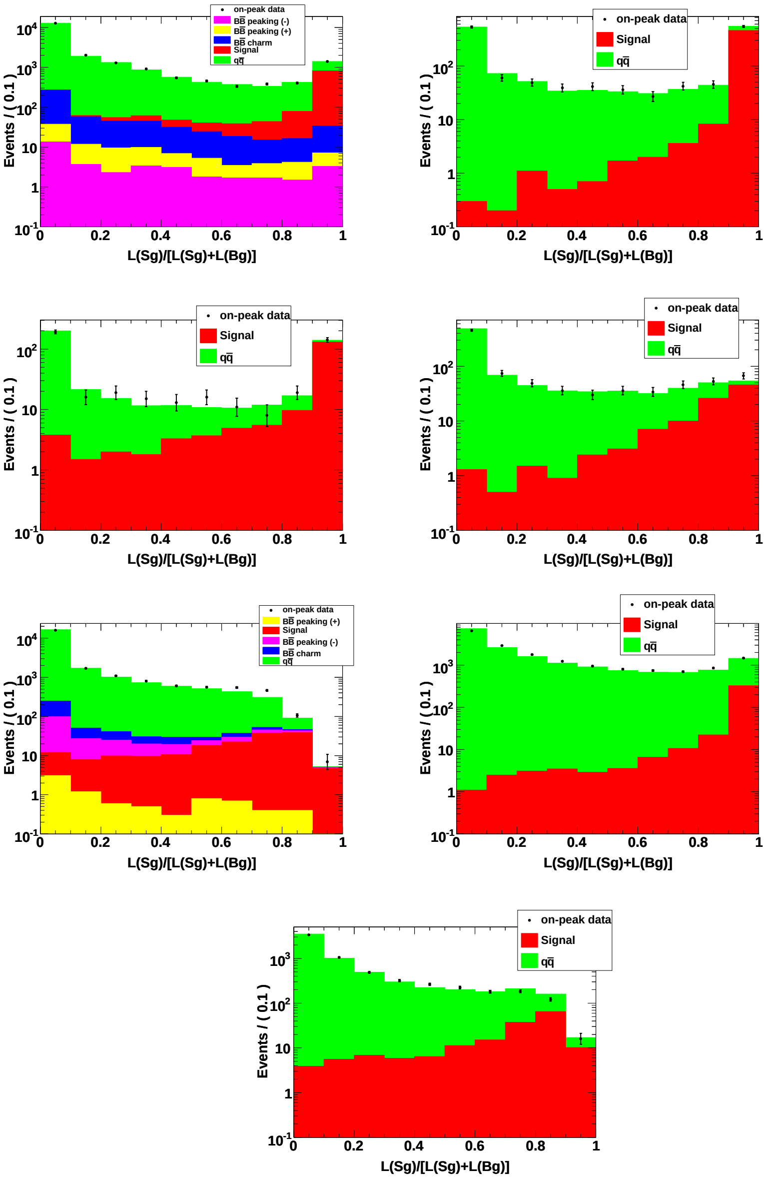

Figure 6.11: The likelihood ratio $R = \mathcal{P}_s/[\mathcal{P}_s + \sum \mathcal{P}_b]$ for the all neutral sub-decay modes: first row: $\eta'_{\rho\gamma}K^0_{S(\pi^+\pi^-)}$, $\eta'_{\eta(\gamma\gamma)\pi\pi}K^0_{S(\pi^+\pi^-)}$, $\eta'_{\eta(3\pi)\pi\pi}K^0_{S(\pi^+\pi^-)}$; second row: $\eta'_{\eta(\gamma\gamma)\pi\pi}K^0_{S(\pi^0\pi^0)}$,$\eta'_{\rho\gamma}K^0_{S(\pi^0\pi^0)}$; last row: $\eta'_{\eta(\gamma\gamma)\pi\pi}K^0_L$, $\eta'_{\eta(3\pi)\pi\pi}K^0_L$. The points represent the on-resonance data, the stacked solid histograms are from pure toy samples of events for each fit component.

6.12.4 Fits with Different S and C for Each Tagging Category

We perform fits to the data considering a different S and C for each `Tag04` tagging category. S and C for the ”Untagged” category are fixed to zero. Results are shown in tab. 6.49. The weighted average of all categories gives 0.613 ± 0.076 for S and -0.051 ± 0.057 for C. This result is consistent with the one provided by the nominal fit (tab. 6.42).

Table 6.49: Results of fits considering different S and C for each tagging category. The average values take into account proper error weighting.

Tagging category	S	C
Lepton	0.790 ± 0.128	-0.048 ± 0.099
Kaon I	0.358 ± 0.152	$+0.060 \pm 0.111$
Kaon II	0.610 ± 0.152	-0.162 ± 0.117
Kaon-Pion	0.662 ± 0.247	-0.025 ± 0.179
Pions	0.336 ± 0.379	-0.126 ± 0.273
Other	1.965 ± 0.955	-0.476 ± 0.698
Average	0.613 ± 0.076	-0.051 ± 0.057

Chapter 7

Measurement of Branching Fractions in Decays with η or η' Meson

7.1 Introduction

In this chapter, we describe results of a search for the charmless quasi-two-body B^0 meson decays to ηK^0, $\eta\eta$, $\eta'\eta'$, $\eta^{(\prime)}\phi$, and $\eta^{(\prime)}\omega$ through the dominant decay modes $\eta \to \gamma\gamma$ ($\eta_{\gamma\gamma}$), $\eta \to \pi^+\pi^-\pi^0$ ($\eta_{3\pi}$), $\eta' \to \eta\pi^+\pi^-$ (with $\eta \to \gamma\gamma$) ($\eta'_{\eta\pi\pi}$), $\eta' \to \rho^0\gamma$ ($\eta'_{\rho\gamma}$), $K^0 \to K^0_S \to \pi^+\pi^-$, $\omega \to \pi^+\pi^-\pi^0$, and $\phi \to K^+K^-$. For the $\eta'\eta'$ mode we consider only the cases $\eta'_{\eta\pi\pi}\eta'_{\eta\pi\pi}$ and $\eta'_{\eta\pi\pi}\eta'_{\rho\gamma}$. For this analysis we use a statistics of 465 million of $B\overline{B}$ pairs, accumulated by *BABAR*. A detailed description of the physical interest in this measurement, and of the relation between results and CKM parameters is given in chapter 2.

7.2 Previous Results

This measurement is an update of many previous ones, using Run1–6 *BABAR* statistics[1]. The results of this analysis were presented at *Flavor Physics and CP Violation (FPCP) 2008* Conference, that took place in Taiwan. These results will be soon included into a paper to be submitted to *Physical Review D*.

Previous *BABAR* results [109, 110, 111] and some theoretical predictions on the decays studied in this thesis work are summarized in tab. 7.1.

---

[1] The final update which will increase the dataset of abou 1% will be performed soon for the publication.

Mode	Sig. Yield	ϵ(%)	$\prod\mathcal{B}_i$(%)	Stat. Signif.	$\mathcal{B}$	90% C.L. U.L.	Th. Pred.
			288.5 fb^{-1} [111]				
$\eta_{\gamma\gamma}K^0$	19^{+10}_{-9}	28.4	13.6	2.6	$1.5^{+0.9}_{-0.8}$		
$\eta_{3\pi}K^0$	11^{+6}_{-5}	18.7	7.9	2.7	$2.4^{+1.4}_{-1.1}$		
ηK^0				3.5	$1.8^{+0.7}_{-0.6}\pm 0.1$	2.9	$1-2$
$\eta_{\gamma\gamma}\eta_{\gamma\gamma}$	17^{+10}_{-9}	22.1	15.5	1.9	$1.3^{+1.0}_{-0.9}$		
$\eta_{\gamma\gamma}\eta_{3\pi}$	10^{+7}_{-5}	19.7	17.9	2.1	$0.9^{+0.6}_{-0.5}$		
$\eta_{3\pi}\eta_{3\pi}$	2^{+3}_{-2}	12.6	5.2	1.1	$1.1^{+1.6}_{-1.0}$		
$\eta\eta$				3.0	$1.1^{+0.5}_{-0.4}\pm 0.1$	1.8	$0.06-14$
$\eta_{\gamma\gamma}\phi$	-11^{+7}_{-5}	33.7	19.4	0.0	$-0.4^{+0.3}_{-0.2}$		
$\eta_{3\pi}\phi$	6.0^{+5}_{-4}	21.9	11.2	1.5	$0.7^{+0.7}_{-0.5}$		
$\eta\phi$				0.0	$0.1^{+0.3}_{-0.2}\pm 0.1$	0.6	$0.001-0.1$
$\eta'_{\eta\pi\pi}\phi$	1^{+3}_{-2}	24.4	8.6	0.8	$0.3^{+0.5}_{-0.3}$		
$\eta'_{\rho\gamma}\phi$	-3^{+9}_{-8}	23.1	14.5	0.0	$-0.2^{+0.9}_{-0.7}$		
$\eta'\phi$				0.5	$0.2^{+0.4}_{-0.3}\pm 0.1$	1.0	$0.001-0.1$
$\eta'_{\eta\pi\pi}\eta'_{\eta\pi\pi}$	1^{+2}_{-1}	16.3	3.1	1.2	$0.8^{+1.3}_{-0.7}$		
$\eta'_{\rho\gamma}\eta'_{\eta\pi\pi}$	9^{+7}_{-5}	18.3	10.3	1.5	$1.2^{+1.1}_{-0.9}$		
$\eta'\eta'$				1.9	$1.0^{+0.8}_{-0.6}\pm 0.1$	2.4	$0.06-0.97$
			210.5 fb^{-1} [110]				
$\eta_{\gamma\gamma}\omega$	13^{+7}_{-6}	14.7	35.1	2.5	$1.1^{+0.6}_{-0.5}$		
$\eta_{3\pi}\omega$	2^{+7}_{-5}	11.9	20.2	0.6	$0.6^{+1.3}_{-1.0}$		
$\eta\omega$				2.5	$1.0\pm 0.5\pm 0.2$	1.9	$0.001-0.1$
			81.9 fb^{-1} [109]				
$\eta'_{\eta\pi\pi}\omega$	-4^{+5}_{-3}	15.2	15.6	0.0	$-1.8^{+2.5}_{-1.7}$		
$\eta'_{\rho\gamma}\omega$	1^{+6}_{-4}	14.2	26.2	0.2	$0.4^{+1.9}_{-1.3}$		
$\eta'\omega$				0.0	$-0.2^{+1.3}_{-0.9}\pm 0.4$	2.8	$0.001-0.1$

Table 7.1: Previous *BABAR* results for B decays studied in this document. We divide measurements depending by the integrated luminosity used for their analysis. Branching fractions ($\mathcal{B}$), 90% C.L. U.L. and theoretical predictions are in units of 10^{-6}. The last row for each mode gives the results combining the several sub-modes. For the ranges of theoretical predictions see refs. [112] and [113].

7.3 Data and Monte Carlo Samples

The analysis presented in this chapter is based on the data taken by *BABAR* in the period 1999-2007 (`Run1-Run6`). Results are based on the following samples:

- Data:
    - On-peak 423.5 fb^{-1}, (465.0 ± 5.0) million of $B\bar{B}$ pairs.
    - Off-peak 43.2 fb^{-1} integrated luminosity.
- generic Monte Carlo:
    - 703 million events for the $B^0\overline{B}^0$, corresponding to 3.0 times On-peak luminosity.
    - 664 million events for the B^+B^-, corresponding to 2.9 times On-peak luminosity.
- Signal Monte Carlo: Statistics used for the different modes can be seen in tab. 7.2.
- several exclusive Monte Carlo simulation for background modes, listed in sec. 7.5.

$\eta_{\gamma\gamma}K_S^0$ 165K	$\eta_{3\pi}K_S^0$ 175K	$\eta_{\gamma\gamma}\eta_{\gamma\gamma}$ 387K	$\eta_{\gamma\gamma}\eta_{3\pi}$ 387K	$\eta_{3\pi}\eta_{3\pi}$ 387K	
$\eta_{\gamma\gamma}\phi$ 195K	$\eta_{3\pi}\phi$ 195K	$\eta_{\gamma\gamma}\omega$ 387K	$\eta_{3\pi}\omega$ 387K		
$\eta'_{\eta\pi\pi}\eta'_{\eta\pi\pi}$ 195K	$\eta'_{\rho\gamma}\eta'_{\eta\pi\pi}$ 195K	$\eta'_{\eta\pi\pi}\omega$ 195K	$\eta'_{\rho\gamma}\omega$ 195K	$\eta'_{\eta\pi\pi}\phi$ 195K	$\eta'_{\rho\gamma}\phi$ 195K

Table 7.2: Number of Monte Carlo signal events for each reconstructed mode.

7.4 Preparation of the Input to ML Fit

The events for each mode are reconstructed and selected (see chapter 5). For each event we can have more candidates due to the possible different combinations of the reconstructed particles of the event. To prepare the samples for the input to ML fits, we have to choose one of these candidates per event, if any. In this way we obtain the final input to ML fits. In this sections we report the events selection efficiencies and multiple candidates selection.

7.4.1 Selection Cut Efficiencies

We show in tab. 7.3–7.17 the selection efficiencies in the different MC and data samples: MC signal events; generic $B\overline{B}$ MC samples, where we remove our signal events, considering the cases with charm+charmless B decays (w/ charm) and only charmless B decays (w/o charm); on-peak and off-peak data. Explanation of the cuts is given in section 5.5.4. The first row gives the number of events for the samples used in the analysis (table 7.2). In the next row we give the number of events after the preliminary cuts. Then we have the efficiencies for each cut, computed after applying all the cuts in the previous rows. The last rows give: the total efficiency, calculated as ratio of the number of events surviving all cuts and the number of recorded(generated) events, and the number of events as input to ML fit for data.

	MC Signal	$B^0\overline{B}^0$		B^+B^-		On-Peak	Off-Peak
		w/ charm	w/o charm	w/ charm	w/o charm		
# Events	165K	703M		664M		423.5 fb^{-1}	43.2 fb^{-1}
Preliminary	69882	1230	1085	541	362	33078	3455
γ Energy	96.5	66.2	64.2	82.1	80.4	79.0	79.0
η Mass	93.6	68.4	68.7	62.1	65.7	70.5	68.9
K^0_S Mass	96.9	64.8	67.6	64.8	71.3	61.3	59.3
K^0_S Flight Length	95.2	44.1	47.0	60.6	67.3	46.7	44.1
η Decay Angle	97.9	86.7	85.9	90.7	90.9	93.4	93.5
2^{nd} Veto γ Energy	98.8	90.7	91.1	89.1	92.8	75.2	74.2
π^0 Veto Mass	97.6	86.2	86.5	88.0	92.9	86.4	86.5
Efficiency (%)	33.3	1.5E-05	1.5E-05	1.2E-05	1.1E-05	5.1E-05	4.9E-05
Input ML						3206	295

Table 7.3: Selection cuts and efficiency (%) for $\eta_{\gamma\gamma}K^0_S$ mode for the different MC and data samples. See the text for an explanation of different rows content.

	MC Signal	$B^0\overline{B}^0$		B^+B^-		On-Peak	Off-Peak
		w/ charm	w/o charm	w/ charm	w/o charm		
# Events	175K	703M		664M		423.5 fb^{-1}	43.2 fb^{-1}
Preliminary	52745	420	190	425	89	17969	1959
PID Vetoes	97.5	61.9	70.0	52.9	70.8	66.1	68.0
π^0 Mass	87.3	68.1	73.7	68.9	73.0	70.7	69.5
η Mass	89.8	54.2	60.2	46.5	65.2	51.0	51.6
K^0_S Mass	97.2	54.2	57.6	51.4	60.0	63.7	61.7
K^0_S Flight Length	95.7	34.6	47.1	32.4	61.1	48.7	53.9
Efficiency (%)	21.4	2.56E-06	2.28E-06	1.81E-06	1.66E-06	2.10E-05	2.65E-05
Input ML						1329	159

Table 7.4: Selection cuts and efficiency (%) for $\eta_{3\pi}K^0_S$ mode for the different MC and data samples. See the text for an explanation of different rows content.

	MC Signal	$B^0\overline{B}^0$		B^+B^-		On-Peak	Off-Peak
		w/ charm	w/o charm	w/ charm	w/o charm		
# Events	387K	703M		664M		423.5 fb^{-1}	43.2 fb^{-1}
Preliminary	124355	71	45	94	56	9906	1097
γ Energy	93.0	56.3	53.3	57.4	60.7	56.6	57.98
η Mass (1)	95.3	72.5	75.0	79.6	85.3	72.6	74.53
η Mass (2)	95.4	72.4	77.8	60.5	51.7	71.1	69.41
η Decay angles	93.5	95.2	92.9	73.1	66.7	79.3	76.9
Efficiency (%)	25.4	2.85E-06	1.85E-06	2.71E-06	1.51E-06	3.63E-05	4.22E-05
Input ML						2297	253

Table 7.5: Selection cuts and efficiency (%) for $\eta_{\gamma\gamma}\eta_{\gamma\gamma}$ mode for the different MC and data samples. See the text for an explanation of different rows content.

	MC Signal	$B^0\overline{B}^0$		B^+B^-		On-Peak	Off-Peak
		w/charm	w/o charm	w/ charm	w/o charm		
# Events	387K	703M		664M		423.5 fb^{-1}	43.2 fb^{-1}
Preliminary	112336	169	111	152	81	15065	1649
γ Enrgy	96.4	77.5	73.0	82.9	75.3	74.7	75.1
PID Vetoes	97.6	49.6	45.7	49.2	55.7	71.7	72.4
π^0 Mass	87.5	64.6	59.5	74.2	76.5	71.3	70.2
$\eta_{\gamma\gamma}$ Mass	93.1	71.4	72.7	56.5	57.7	65.7	67.9
$\eta_{3\pi}$ Mass	89.1	60.0	68.8	38.5	53.3	52.9	53.7
$\eta_{\gamma\gamma}$ Decay angle	96.8	83.3	90.9	90.0	100.0	89.9	93.0
Efficiency (%)	19.2	2.1E-06	1.4E-06	1.4E-06	1.2E-06	2.8E-05	3.6E-05
Input ML						1800	214

Table 7.6: Selection cuts and efficiency (%) for $\eta_{\gamma\gamma}\eta_{3\pi}$ mode for the different MC and data samples. See the text for an explanation of different rows content.

	MC Signal	$B^0\overline{B}^0$		B^+B^-		On-Peak	Off-Peak
		w/charm	w/o charm	w/charm	w/o charm		
# Events	387K	703M		664M		423.5 fb^{-1}	43.2 fb^{-1}
Preliminary	80557	58	10	71	10	4162	405
PID Vetoes	95.1	39.7	30.0	21.1	50.0	45.9	43.5
π^0 Mass (1)	88.0	82.6	66.7	66.7	80.0	71.1	69.9
π^0 Mass (2)	86.5	73.7	50.0	40.0	50.0	69.3	67.5
η Mass (1)	89.5	78.6	100.0	50.0	0.0	54.1	53.0
η Mass (2)	88.4	27.3	100.0	50.0	0.0	51.6	56.8
Efficiency (%)	11.9	4.27E-07	1.42E-07	1.51E-07	0.00E+00	4.16E-06	4.17E-06
Input ML						263	25

Table 7.7: Selection cuts and efficiency (%) for $\eta_{3\pi}\eta_{3\pi}$ mode for the different MC and data samples. See the text for an explanation of different rows content.

	MC Signal	$B^0\overline{B}^0$		B^+B^-		On-Peak	Off-Peak
		w/ charm	w/o charm	w/ charm	w/o charm		
# Events	387K	703M		664M		423.5 fb^{-1}	43.2 fb^{-1}
Preliminary	97445	2180	1303	1763	905	47476	4927
PID Vetoes	97.7	43.2	39.8	53.1	56.2	70.1	70.1
γ Energy	96.4	77.2	70.5	78.1	71.9	73.3	71.9
π^0 Mass	94.0	84.4	84.1	86.6	85.0	85.7	85.7
η Mass	93.3	69.0	73.6	63.7	63.3	66.1	66.5
η Decay angle	96.9	87.2	85.0	86.6	84.8	89.6	89.1
ω Mass	98.9	91.3	93.8	93.1	93.4	91.6	91.0
Efficiency (%)	19.9	4.80E-05	2.56E-05	4.89E-05	2.35E-05	1.89E-03	1.92E-04
Input ML						11333	1149

Table 7.8: Selection cuts and efficiency (%) for $\eta_{\gamma\gamma}\omega$ mode for the different MC and data samples. See the text for an explanation of different rows content.

	MC Signal	$B^0\overline{B}^0$		B^+B^-		On-Peak	Off-Peak
		w/ charm	w/o charm	w/ charm	w/o charm		
# Events	387K	703M		664M		423.5 fb^{-1}	43.2 fb^{-1}
Preliminary	79534	1939	397	2303	202	66134	6845
PID Vetoes	95.1	33.5	35.0	30.1	45.0	46.9	48.7
π^0 Mass from η	87.2	70.4	80.6	69.6	73.6	70.4	69.5
π^0 Mass from ω	93.8	81.4	83.0	81.4	88.1	84.5	83.5
η Mass	88.6	48.9	69.9	42.0	47.5	51.3	52.6
ω Mass	98.8	94.5	96.9	87.3	82.1	90.9	91.5
Efficiency (%)	14.0	2.45E-05	8.96E-06	2.17E-05	3.46E-06	1.36E-04	1.55E-04
Input ML						8613	931

Table 7.9: Selection cuts and efficiency (%) for $\eta_{3\pi}\omega$ mode for the different MC and data samples. See the text for an explanation of different rows content.

	MC Signal	$B^0\overline{B}^0$		B^+B^-		On-Peak	Off-Peak
		w/ charm	w/o charm	w/ charm	w/o charm		
# Events	195K	703M		664M		423.5 fb^{-1}	43.2 fb^{-1}
Preliminary	89187	500	399	306	199	30977	3257
PID Vetoes	93.1	30.2	31.8	19.0	20.1	24.1	23.9
γ Energy	96.2	64.9	62.2	81.0	72.5	73.7	74.4
η Mass	92.8	63.3	63.3	51.1	51.7	65.8	63.1
η Decay angle	96.6	71.0	64.0	87.5	80.0	88.9	86.0
ϕ Mass	82.1	40.9	46.9	33.3	25.0	43.5	44.3
Efficiency (%)	30.2	2.56E-06	2.13E-06	1.05E-06	4.52E-07	2.21E-05	2.30E-05
Input ML						1401	138

Table 7.10: Selection cuts and efficiency (%) for $\eta_{\gamma\gamma}\phi$ mode for the different MC and data samples. See the text for an explanation of different rows content.

	MC Signal	$B^0\overline{B}^0$		B^+B^-		On-Peak	Off-Peak
		w/ charm	w/o charm	w/ charm	w/o charm		
# Events	195K	703M		664M		423.5 fb^{-1}	43.2 fb^{-1}
Preliminary	64014	296	108	319	48	16821	1728
PID Vetoes	91.0	15.5	23.1	11.9	14.6	16.8	16.3
π^0 Mass	87.2	60.9	48.0	71.1	85.7	69.7	71.9
η Mass	88.7	46.4	58.3	33.3	66.7	52.7	48.0
ϕ Mass	81.8	15.4	14.3	33.3	50.0	46.8	43.3
Efficiency (%)	18.9	2.85E-07	1.42E-07	4.52E-07	3.01E-07	7.68E-06	7.01E-06
Input ML						486	42

Table 7.11: Selection cuts and efficiency (%) for $\eta_{3\pi}\phi$ mode for the different MC and data samples. See the text for an explanation of different rows content.

	MC Signal	$B^0\overline{B}^0$		B^+B^-		On-Peak	Off-Peak
		w/charm	w/o charm	w/ charm	w/o charm		
# Events	195K	703M		664M		423.5 fb^{-1}	43.2 fb^{-1}
Preliminary	44785	21	4	11	1	510	58
PID Vetoes	98.7	61.9	100.0	45.5	100.0	63.1	60.3
η Mass (1)	96.7	69.2	100.0	60.0	100.0	85.4	88.6
η Mass (2)	96.7	66.7	75.0	100.0	100.0	84.7	90.3
η' Mass (1)	99.7	100.0	100.0	100.0	100.0	95.3	96.4
η' Mass (2)	99.7	100.0	100.0	100.0	100.0	93.7	100.0
Efficiency (%)	21.1	8.54E-07	4.27E-07	4.52E-07	1.51E-07	3.29E-06	4.51E-06
Input ML						208	27

Table 7.12: Selection cuts and efficiency (%) for $\eta'_{\eta\pi\pi}\eta'_{\eta\pi\pi}$ mode for the different MC and data samples. See the text for an explanation of different rows content.

	MC Signal	$B^0\overline{B}^0$		B^+B^-		On-Peak	Off-Peak
		w/ charm	w/o charm	w/ charm	w/o charm		
# Events	195K	703M		664M		423.5 fb^{-1}	43.2 fb^{-1}
Preliminary	52037	2935	398	3695	477	44217	4368
γ Energy	86.6	58.6	51.5	56.9	39.6	65.3	66.5
PID Vetoes	96.3	42.7	54.1	39.0	41.3	53.2	54.0
ρ Mass	99.9	100.0	100.0	99.6	100.0	99.7	99.9
η Mass	96.8	84.5	83.8	83.1	87.2	82.1	81.8
η' Mass (1)	96.7	76.5	77.4	76.9	73.5	73.7	74.1
η' Mass (2)	99.7	92.6	97.2	91.8	92.0	93.5	92.8
ρ Helicity	98.2	88.2	87.1	86.5	89.1	89.4	87.9
Efficiency (%)	20.4	5.51E-05	8.68E-06	6.23E-05	6.17E-06	1.22E-04	1.29E-04
Input ML						7746	774

Table 7.13: Selection cuts and efficiency (%) for $\eta'_{\rho\gamma}\eta'_{\eta\pi\pi}$ mode for the different MC and data samples. See the text for an explanation of different rows content.

	MC Signal	$B^0\overline{B}^0$		B^+B^-		On-Peak	Off-Peak
		w/ charm	w/o charm	w/ charm	w/o charm		
# Events	195K	703M		664M		423.5 fb^{-1}	43.2 fb^{-1}
Preliminary	42941	1299	103	1457	33	26474	2751
PID Vetoes	97.0	40.9	53.1	35.9	56.3	53.2	54.3
π^0 Mass	93.9	82.9	86.2	85.9	86.1	85.1	85.1
η Mass	96.6	83.6	85.2	83.5	87.1	82.0	81.8
ω Mass	98.8	89.1	95.7	93.6	96.3	91.5	89.8
η' Mass	99.7	91.8	87.9	91.5	84.6	93.3	92.7
Efficiency (%)	19.1	4.28E-05	4.79E-06	4.83E-05	1.72E-06	1.33E-04	1.44E-04
Input ML						8388	864

Table 7.14: Selection cuts and efficiency (%) for $\eta'_{\eta\pi\pi}\omega$ mode for the different MC and data samples. See the text for an explanation of different rows content.

	MC Signal	$B^0\overline{B}^0$		B^+B^-		On-Peak	Off-Peak
		w/ charm	w/o charm	w/ charm	w/o charm		
# Events	195K	703M		664M		423.5 fb^{-1}	43.2 fb^{-1}
Preliminary	42159	50929	2805	75231	2861	373245	35183
PID Vetoes	94.6	35.1	50.8	32.6	49.6	43.3	45.1
γ Energy	87.4	58.4	56.6	57.0	53.2	64.0	64.6
π^0 Mass	93.8	83.4	86.1	83.7	85.3	84.8	84.6
ρ Mass	99.9	99.8	99.9	99.8	99.8	99.7	99.7
ρ Helicity	98.2	87.2	89.7	87.1	88.5	89.6	90.1
ω Mass	98.7	91.1	94.4	91.0	93.3	91.3	91.9
η' Mass	96.7	74.3	74.5	74.3	72.7	73.5	73.6
Efficiency (%)	15.7	7.30E-04	6.25E-05	1.03E-03	5.79E-05	8.31E-04	8.79E-04
Input ML						52599	5268

Table 7.15: Selection cuts and efficiency (%) for $\eta'_{\rho\gamma}\omega$ mode for the different MC and data samples. See the text for an explanation of different rows content.

	MC Signal	$B^0\overline{B}^0$		B^+B^-		On-Peak	Off-Peak
		w/ charm	w/o charm	w/ charm	w/o charm		
# Events	195K	703M		664M		423.5 fb^{-1}	43.2 fb^{-1}
Preliminary	66704	167	32	145	18	6443	730
PID Vetoes	93.0	19.2	31.3	14.5	22.2	21.0	20.7
η Mass	96.4	81.3	80.0	85.7	100.0	83.3	77.5
η' Mass	99.7	84.6	100.0	77.8	75.0	94.1	91.5
ϕ Mass	82.1	45.5	50.0	42.9	33.3	42.8	43.0
Efficiency (%)	25.1	1.42E-06	5.69E-07	9.03E-07	1.51E-07	7.19E-06	7.68E-06
Input ML						455	46

Table 7.16: Selection cuts and efficiency (%) for $\eta'_{\eta\pi\pi}\phi$ mode for the different MC and data samples. See the text for an explanation of different rows content.

	MC Signal	$B^0\overline{B}^0$		B^+B^-		On-Peak	Off-Peak
		w/ charm	w/o charm	w/ charm	w/o charm		
# Events	195K	703M		664M		423.5 fb^{-1}	43.2 fb^{-1}
Preliminary	76550	9913	2313	11250	1349	216234	22017
PID Vetoes	90.8	20.0	21.6	15.0	25.3	16.4	16.1
γ Energy	86.1	52.3	46.9	54.2	56.3	65.2	64.5
ρ Mass	99.9	99.5	99.1	99.7	100.0	99.8	99.6
ρ Helicity	98.2	86.0	87.9	89.7	94.3	89.7	90.5
η' Mass	96.7	75.1	71.6	75.7	75.7	73.7	74.3
ϕ Mass	81.9	54.8	61.0	40.8	56.9	43.3	43.4
Efficiency (%)	23.9	5.21E-05	1.27E-05	3.79E-05	1.17E-05	1.05E-04	1.11E-04
Input ML						6614	664

Table 7.17: Selection cuts and efficiency (%) for $\eta'_{\rho\gamma}\phi$ mode for the different MC and data samples. See the text for an explanation of different rows content.

7.4.2 Multiple Candidate per Event

We have analyzed the problem of multiple signal candidates per event. For each event we can have more than one signal events candidates, due to different combinations of daughters resonances. We first make the choice of the “best” candidate and then look for events with MC truth or without MC truth[2], using the MC events for each mode, where we keep track of such an information. In some modes with multiple particles in the final state we consider as MC truth also events where there is a permutation of the particles (PP) inside the B candidate. For example if we consider $\eta'_{\eta\pi\pi}\omega$ decay, if we exchange one of the charge pion from η' with one from ω, this is a PP.

Events where the B candidate exchanges at least one track or neutral particle with the rest of the event are called self-cross feed (SCF) events. We calculate the efficiency of the candidate as ratio between the number of events belonging to MC truth or PP class that survive the “best” candidate selection with respect to the number of events in each class before the selection.

We verified that PP events are mainly due to the permutation of pions or photons in η' daughters. These events have the same discriminating variables shapes as MC truth one.

Concerning SCF events, the main source of SCF depends on the specific decay mode involved. These events show wider distribution (especially for ΔE) with respect to MC truth ones, anyway we account them as signal. In some specific modes SCF component is added into the fit (see sec 7.6).

In selecting the “best” candidate we have applied an algorithm based on B vertex probability, choosing the one with the highest probability. Efficiency of this algorithm is

---

[2] With MC truth we denote an events which is reconstructed *exactly* as it was simulated.

in the range 95–98%. In previous analyses it was verified that this algorithm has higher efficiency than other criteria, such as the best η/η' mass. In particular in $\eta_{\gamma\gamma}\eta_{\gamma\gamma}$ mode, where we have all neutral in the final state, we have verified that this selection algorithm has a little bit higher efficiency than the one based on the daughters mass.

We summarize in Table 7.18 the number of combinations per event for data and MC signal events, the efficiency of the algorithm of selection (considering MC truth events and MC truth plus PP ones) and the MC signal composition, splitting into MCTruth + PP fraction and SCF fraction.

Mode	# combs/event (data)	#combs/event (MC signal)	Best Candidate Efficiency (%)		MC Signal Composition	
			MCtruth	MCtruth+PP	MCtruth+PP	SCF
$\eta_{\gamma\gamma}K^0_S$	1.02	1.02	99.3	99.3	97.7	2.3
$\eta_{3\pi}K^0_S$	1.06	1.06	97.8	98.3	94.8	5.2
$\eta_{\gamma\gamma}\eta_{\gamma\gamma}$	1.04	1.04	98.6	98.6	96.1	4.0
$\eta_{\gamma\gamma}\eta_{3\pi}$	1.08	1.09	96.9	97.4	91.8	8.2
$\eta_{3\pi}\eta_{3\pi}$	1.12	1.14	95.1	96.3	88.7	11.3
$\eta_{\gamma\gamma}\phi$	1.02	1.02	99.2	99.3	97.0	2.9
$\eta_{3\pi}\phi$	1.07	1.07	97.5	97.5	94.0	6.0
$\eta_{\gamma\gamma}\omega$	1.22	1.21	93.4	94.3	85.1	14.9
$\eta_{3\pi}\omega$	1.30	1.29	91.1	92.5	81.3	18.7
$\eta'_{\eta\pi\pi}\eta'_{\eta\pi\pi}$	1.37	1.37	95.8	96.1	86.7	13.3
$\eta'_{\rho\gamma}\eta'_{\eta\pi\pi}$	1.22	1.24	95.1	95.6	86.8	13.1
$\eta'_{\eta\pi\pi}\omega$	1.43	1.41	91.3	92.4	80.3	19.7
$\eta'_{\rho\gamma}\omega$	1.28	1.26	91.5	92.7	80.9	19.1
$\eta'_{\eta\pi\pi}\phi$	1.17	1.18	97.8	97.9	93.2	6.8
$\eta'_{\rho\gamma}\phi$	1.06	1.07	96.9	96.9	92.6	7.3

Table 7.18: Results of “best candidate” selection algorithm.

7.4.3 Efficiency

The MC efficiency (MC ϵ) is calculated as the ratio of the number of MC signal events which pass all cuts (i.e. as input to ML fit), independently by the MC truth matching, to the number of generated MC signal events. These values are shown in tab. 7.19. We show also the total branching fraction ($\prod \mathcal{B}_i$) of the sub-decays [98] involved for each mode, and the number of on-peak events as input to ML fit.

The *BABAR* tracking efficiency task force [114] suggests no tracking efficiency correction for any charged track definition. Instead, the data/MC difference in track reconstruction efficiency is taken as a source of systematic uncertainty. The associated systematic error is 0.4% per track, except the tracks coming from K^0_S. For K^0_S we have followed the recipe described by the *BABAR* tracking working group and we apply a correction of -4.3% and a systematic error of 2.1%. For π^0 and η we have applied a cor-

Mode	$\eta_{\gamma\gamma}K^0_S$	$\eta_{3\pi}K^0_S$	$\eta_{\gamma\gamma}\eta_{\gamma\gamma}$	$\eta_{\gamma\gamma}\eta_{3\pi}$	$\eta_{3\pi}\eta_{3\pi}$
MC ϵ (%)	33.3	21.4	25.4	19.2	11.9
$\prod\mathcal{B}_i$ (%)	13.6 ± 0.1	7.9 ± 0.1	15.5 ± 0.1	17.9 ± 0.4	5.2 ± 0.1
Input to ML fit	3206	1329	2297	1800	263
Mode	$\eta_{\gamma\gamma}\omega$	$\eta_{3\pi}\omega$	$\eta_{\gamma\gamma}\phi$	$\eta_{3\pi}\phi$	$\eta'_{\eta\pi\pi}\eta'_{\eta\pi\pi}$
MC ϵ (%)	19.9	14.0	30.2	18.9	21.1
$\prod\mathcal{B}_i$ (%)	35.1 ± 0.4	20.2 ± 0.4	19.4 ± 0.3	11.2 ± 0.2	3.1 ± 0.1
Input to ML fit	11333	8613	1401	486	208
Mode	$\eta'_{\rho\gamma}\eta'_{\eta\pi\pi}$	$\eta'_{\eta\pi\pi}\omega$	$\eta'_{\rho\gamma}\omega$	$\eta'_{\eta\pi\pi}\phi$	$\eta'_{\rho\gamma}\phi$
MC ϵ (%)	20.4	19.1	15.7	25.1	23.9
$\prod\mathcal{B}_i$ (%)	10.3 ± 0.4	15.6 ± 0.5	26.2 ± 0.8	8.6 ± 0.3	14.5 ± 0.5
Input to ML fit	7746	8388	52599	455	6614

Table 7.19: MC efficiency, total branching fraction of the sub-decays for each mode, and number of on-peak events as input to ML fit.

rection of -3.2% and -2.9%, respectively as suggested by the BABAR neutrals working group [106, 115]. No correction is applied for photons because we use the neutral smearing procedure [106]. The corresponding systematic errors are 3% for π^0, η and 1.8% for γ.

7.5 $B\overline{B}$ Backgrounds

We have done a detailed analysis of $B\overline{B}$ background in all our decay modes. Our procedure is realized in three steps.

First we apply the full analysis selection to MC $B\overline{B}$ generic samples. In all samples, of course, we remove our signal MC modes. We look at all the MC events separating possible $B\overline{B}$ cross feed into charm B decays and charmless B decays. This is due to the fact that charm B decays are continuum-like in $m_{\rm ES}$ and ΔE while charmless B decays could peak, in these two variables, in the same region of the signal. In this first step we are interested in finding categories of events which could contribute to background. We show in tab. 7.20 for each decay mode and for the two samples $B^0\overline{B}^0$ and B^+B^- the total number of events passing the full selection, normalized to on-peak luminosity. Some of the modes present in such generics sample are due to `JetSet` fragmentation of $b \to c$ modes, which are, in general, no-peaking background. We don't consider these modes as source of specific background.

In the second step we reconstruct large samples of MC signal events of candidate cross feed modes, which are peaking in $m_{\rm ES}$ and ΔE variables, and we evaluate reconstruction efficiency and number of expected candidates (normalized to our on-peak integrated lu-

Mode	$B^0\overline{B}^0$ charm	$B^0\overline{B}^0$ charmless	B^+B^- charm	B^+B^- charmless
$\eta_{\gamma\gamma}K^0_S$	2 ± 5	34 ± 3	2 ± 4	25 ± 3
$\eta_{3\pi}K^0_S$	1 ± 2	5 ± 1	0 ± 2	4 ± 1
$\eta_{\gamma\gamma}\eta_{\gamma\gamma}$	2 ± 2	4 ± 1	3 ± 2	4 ± 1
$\eta_{\gamma\gamma}\eta_{3\pi}$	2 ± 2	3 ± 1	0 ± 1	3 ± 1
$\eta_{3\pi}\eta_{3\pi}$	1 ± 3	0 ± 3	0 ± 1	0 ± 1
$\eta_{\gamma\gamma}\omega$	50 ± 4	56 ± 4	64 ± 5	58 ± 5
$\eta_{3\pi}\omega$	34 ± 3	20 ± 2	45 ± 4	8 ± 2
$\eta_{\gamma\gamma}\phi$	1 ± 1	5 ± 1	1 ± 1	1 ± 1
$\eta_{3\pi}\phi$	0 ± 1	0 ± 1	0 ± 1	1 ± 1
$\eta'_{\eta\pi\pi}\eta'_{\eta\pi\pi}$	2 ± 1	0 ± 1	1 ± 1	0 ± 1
$\eta'_{\rho\gamma}\eta'_{\eta\pi\pi}$	108 ± 7	20 ± 3	131 ± 8	14 ± 2
$\eta'_{\eta\pi\pi}\omega$	77 ± 5	11 ± 2	103 ± 6	4 ± 1
$\eta'_{\rho\gamma}\omega$	1351 ± 20	145 ± 9	2296 ± 29	135 ± 10
$\eta'_{\eta\pi\pi}\phi$	2 ± 1	1 ± 1	2 ± 1	0 ± 1
$\eta'_{\rho\gamma}\phi$	86 ± 5	28 ± 3	64 ± 5	29 ± 3

Table 7.20: Input to ML fit for $B\overline{B}$ generic samples for each target decay mode, normalized to the integrated on-peak luminosity.

minosity) in ML input. In the Tables 7.21–7.31 we report the results of the $B\overline{B}$ studies for each decay mode. For each decay mode we give the MC reconstruction efficiency ϵ, the branching fraction ($\mathcal{B}$), the daughter branching fraction product ($\prod \mathcal{B}_i$) and the estimated background in ML input (normalized to our integrated luminosity). The branching fractions of the background $B\overline{B}$ modes studied are taken from PDG [98] and HFAG tables [48]. For modes where branching fractions aren't measured, yet, we take theoretical predicted value, taking as error the value itself.

Finally, we fit a PDF for the background and we perform toy-experiment studies (see sec. 7.7.1) where we embed these events, taken from MC samples, as expected in the ML input. In this way we see if the candidate gives any contribution as background. If this is the case, we use these MC events to fit PDFs to be introduced in the maximum likelihood fit. Otherwise, if these events are accounted in another background category when we don't use in the fit the $B\overline{B}$ component, we prefer not to introduce such a component in the ML fit. If background comes from several decay modes, the PDFs are fitted using weighted numbers of events from each decay mode, in order to weight properly the various backgrounds that contribute to maximum likelihood fit input. PDFs are fitted with all events surviving cuts and best candidate selection.

If this number is small (a few events) we prefer not to introduce a $B\overline{B}$ component in the fit but we embedded the expected number of $B\overline{B}$ cross feed in toy experiments and we consider the eventual bias introduced in signal event yield.

Cross Feed Channel	MC ϵ (%)	Est. $\mathcal{B}$ (10^{-6})	$\prod \mathcal{B}_i$ (%)	# evts in ML
$B^0 \to \pi^0 K^0_S$	0.475 ± 0.003	10.3 ± 0.7	33.79 ± 0.05	8 ± 1
$B^+ \to \eta_{\gamma\gamma} K^{*+}_{K^0_S\pi^+}$	0.841 ± 0.021	19.3 ± 1.6	8.86 ± 0.06	7 ± 1
$B^+ \to K^{*+}_{K^0_S\pi^+}\gamma$	0.121 ± 0.008	40.3 ± 2.5	22.78 ± 0.03	5 ± 1
$B^0 \to \eta_{\gamma\gamma} K^{*0}_{K^0_S\pi^0}$	1.019 ± 0.023	15.9 ± 1.0	4.43 ± 0.03	3 ± 1
$B^0 \to K^{*0}_{K^0_S\pi^0}\gamma$	0.136 ± 0.005	40.1 ± 2.0	11.25 ± 0.02	3 ± 1
$B^0 \to \eta_{\gamma\gamma} K^{*0}_{K^+\pi^0}$	0.038 ± 0.004	15.9 ± 1.0	26.27 ± 0.17	1 ± 1
Total				27 ± 2

Table 7.21: Potential $B\overline{B}$ background for the $\eta_{\gamma\gamma}K^0_S$ mode. See the text for an explanation of different columns content.

Cross Feed Channel	MC ϵ (%)	Est. $\mathcal{B}$ (10^{-6})	$\prod \mathcal{B}_i$ (%)	# evts in ML
$B^+ \to \eta_{3\pi} K^{*+}_{K^0_S\pi^+}$	0.469 ± 0.016	19.3 ± 1.6	5.17 ± 0.09	2 ± 1
$B^0 \to \eta_{3\pi} K^{*0}_{K^0_S\pi^0}$	0.594 ± 0.017	15.9 ± 1.0	2.55 ± 0.05	1 ± 1
$B^0 \to \eta'_{\eta_{\gamma\gamma}\pi\pi} K^0_S$	0.056 ± 0.002	65.0 ± 3.0	5.99 ± 0.19	1 ± 1
Total				4 ± 2

Table 7.22: Potential $B\overline{B}$ background for the $\eta_{3\pi}K^0_S$ mode. See the text for an explanation of different columns content.

Cross Feed Channel	MC ϵ (%)	Est. $\mathcal{B}$ (10^{-6})	$\prod \mathcal{B}_i$ (%)	# evts in ML
$B^0 \to \eta_{\gamma\gamma}\rho^+$	0.115 ± 0.008	5.4 ± 1.0	39.38 ± 0.26	2 ± 1
$B^0 \to \eta_{\gamma\gamma}\pi^0$	0.937 ± 0.022	1.3 ± 1.3	38.91 ± 0.26	2 ± 2
Total				4 ± 2

Table 7.23: Potential $B\overline{B}$ background for the $\eta_{\gamma\gamma}\eta_{\gamma\gamma}$ mode. See the text for an explanation of different columns content.

Cross Feed Channel	MC ϵ (%)	Est. $\mathcal{B}$ (10^{-6})	$\prod \mathcal{B}_i$ (%)	# evts in ML
$B^+ \to \eta_{3\pi}\rho^+$	0.102 ± 0.007	5.4 ± 1.2	22.70 ± 0.40	1 ± 1
$B^0 \to \eta_{3\pi}\pi^0$	0.847 ± 0.021	1.3 ± 1.3	22.43 ± 0.40	1 ± 1
Total				2 ± 2

Table 7.24: Potential $B\overline{B}$ background for the $\eta_{\gamma\gamma}\eta_{3\pi}$ mode. See the text for an explanation of different columns content.

Cross Feed Channel	MC ϵ (%)	Est. $\mathcal{B}$ (10^{-6})	$\prod \mathcal{B}_i$ (%)	# evts in ML
$B^0 \to K_1(1273)^0\gamma$	0.048 ± 0.003	60.2 ± 4.4	100.00	13 ± 1
$B^0 \to \eta_{\gamma\gamma}K^{*0}_{K^+\pi^0}$	0.496 ± 0.016	15.9 ± 1.0	26.27 ± 0.17	10 ± 1
$B^+ \to K_1(1273)^+\gamma$	0.028 ± 0.002	73.3 ± 5.5	100.00	9 ± 1
$B^0 \to \omega\pi^0$	0.865 ± 0.021	1.2 ± 1.2	88.03 ± 0.69	4 ± 4
$B^+ \to \mathcal{A}^+_\infty\pi^0$	0.023 ± 0.002	26.4 ± 6.8	98.80 ± 0.03	3 ± 1
$B^+ \to \omega\rho^+ \ Long.$	0.101 ± 0.003	4.4 ± 1.1	98.80 ± 0.03	2 ± 1
$B^+ \to \eta_{\gamma\gamma}K^{*+}_{K^0_S\pi^+}$	0.242 ± 0.011	19.3 ± 1.6	8.86 ± 0.06	2 ± 1
$B^+ \to \eta_{\gamma\gamma}K^{*+}_{K^+\pi^0}$	0.136 ± 0.008	19.3 ± 1.6	12.96 ± 0.09	2 ± 1
$B^+ \to b_1^+\pi^0$	0.069 ± 0.007	3.3 ± 3.3	98.80 ± 0.03	1 ± 1
$B^0 \to \eta_{\gamma\gamma}\eta_{3\pi}$	1.333 ± 0.019	1.8 ± 1.8	8.83 ± 0.17	1 ± 1
$B^+ \to K^{*+}_{K^0_S\pi^+}\gamma$	0.023 ± 0.003	40.3 ± 2.5	22.78 ± 0.03	1 ± 1
$B^0 \to \rho^+\rho^-$	0.006 ± 0.000	24.2 ± 3.5	97.61 ± 0.04	1 ± 1
$B^0 \to \eta_{\gamma\gamma}\rho^0$	0.238 ± 0.011	1.5 ± 1.5	39.38 ± 0.26	1 ± 1
Total				50 ± 5

Table 7.25: Potential $B\overline{B}$ background for the $\eta_{\gamma\gamma}\omega$ mode. See the text for an explanation of different columns content.

Cross Feed Channel	MC ϵ (%)	Est. $\mathcal{B}$ (10^{-6})	$\prod \mathcal{B}_i$ (%)	# evts in ML
$B^0 \to \eta_{3\pi}K^{*0}_{K^+\pi^-}$	0.44 ± 0.01	15.9 ± 1.0	15.14 ± 0.27	5 ± 1
$B^0 \to \eta_{3\pi}\eta_{3\pi}$	2.22 ± 0.02	1.8 ± 1.8	5.03 ± 0.13	1 ± 1
$B^+ \to \eta_{3\pi}\rho^+$	0.16 ± 0.01	5.4 ± 1.2	22.7 ± 0.40	1 ± 1
$B^+ \to \eta_{3\pi}K^{*+}_{K^0_S\pi^+}$	0.17 ± 0.01	19.3 ± 1.6	5.17 ± 0.09	1 ± 1
Total				8 ± 2

Table 7.26: Potential $B\overline{B}$ background for the $\eta_{3\pi}\omega$ mode. See the text for an explanation of different columns content.

Cross Feed Channel	MC ϵ (%)	Est. $\mathcal{B}$ (10^{-6})	$\prod \mathcal{B}_i$ (%)	# evts in ML
$B^0 \to \phi K^0_S (K^0_S \to \pi^0\pi^0)$	0.208 ± 0.010	8.3 ± 1.1	7.37 ± 0.09	1 ± 1
$B^0 \to \phi \pi^0$	1.389 ± 0.027	0.3 ± 0.3	48.61 ± 0.59	1 ± 1
Total				2 ± 1

Table 7.27: Potential $B\overline{B}$ background for the $\eta_{\gamma\gamma}\phi$ mode. See the text for an explanation of different columns content.

Cross Feed Channel	Mode # (%)	MC ϵ (10^{-6})	Est. $\mathcal{B}$ (%)	$\prod \mathcal{B}_i$	# evts in ML
$B^+ \to \eta'_{\eta\pi\pi}\rho^+$	0.867 ± 0.021	8.7 ± 3.3	17.31 ± 0.56	6 ± 2	
$B^0 \to \eta'_{\eta\pi\pi}\rho^0$	1.720 ± 0.030	3.7 ± 3.7	17.52 ± 0.56	5 ± 5	
$B^0 \to \eta'_{\eta\pi\pi}\omega$	0.601 ± 0.018	2.2 ± 2.2	15.43 ± 0.51	1 ± 1	
$B^0 \to \eta'_{\eta\pi\pi} f^0$	0.853 ± 0.021	1 ± 1	17.52 ± 0.56	1 ± 1	
Total				13 ± 6	

Table 7.28: Potential $B\overline{B}$ background for the $\eta'_{\rho\gamma}\eta'_{\eta\pi\pi}$ mode. See the text for an explanation of different columns content.

Cross Feed Channel	MC ϵ (%)	Est. $\mathcal{B}$ (10^{-6})	$\prod \mathcal{B}_i$ (%)	# evts in ML
$B^+ \to \eta_{3\pi}\eta'_{\eta\pi\pi}$	1.665 ± 0.029	1.7 ± 1.7	3.93 ± 0.14	1 ± 1
$B^0 \to \eta'_{\eta_{\gamma\gamma}\pi\pi} K^0_S$	0.061 ± 0.003	65.0 ± 3.0	5.99 ± 0.19	1 ± 1
$B^0 \to \eta'_{\eta\pi\pi}\rho^0$	0.308 ± 0.013	3.7 ± 3.7	17.52 ± 0.56	1 ± 1
Total				3 ± 1

Table 7.29: Potential $B\overline{B}$ background for the $\eta'_{\eta\pi\pi}\omega$ mode. See the text for an explanation of different columns content.

Cross Feed Channel	MC ϵ (%)	Est. $\mathcal{B}$ (10^{-6})	$\prod \mathcal{B}_i$ (%)	# evts in ML
$B^+ \to \omega\rho^+$ *Long.*	0.612 ± 0.008	4.4 ± 1.1	98.80 ± 0.03	12 ± 3
$B^0 \to \omega\omega$	0.729 ± 0.019	4.0 ± 4.0	77.49 ± 0.86	11 ± 11
$B^+ \to b_1^0\rho^+$	0.063 ± 0.005	35.1 ± 35.1	86.97 ± 0.68	9 ± 9
$B^+ \to a_1^+\omega(a_1^+ \to \rho^0\pi^+)$ *Long.*	0.247 ± 0.011	17.5 ± 17.5	43.14 ± 0.35	9 ± 9
$B^0 \to \omega\rho^0$ *Long.*	1.379 ± 0.028	1.5 ± 1.5	88.03 ± 0.69	8 ± 8
$B^0 \to a_1^+\rho^-(a_1^+ \to \rho^0\pi^+)$ *Long.*	0.060 ± 0.002	56.1 ± 56.1	48.41 ± 0.10	8 ± 8
$B^0 \to b_1^+\rho^-$ *Long.*	0.064 ± 0.006	18.2 ± 18.2	85.93 ± 0.68	5 ± 5
$B^0 \to b_1^0\rho^0$ *Long.*	0.238 ± 0.011	4.7 ± 4.7	88.03 ± 0.69	5 ± 5
$B^0 \to a_1^+a_1^-(a_1^\pm \to \rho^0\pi^+)$ *Long.*	0.080 ± 0.002	50.0 ± 50.0	24.01 ± 0.07	4 ± 4
$B^+ \to a_1^+\omega(a_1^+ \to \rho^0\pi^+)$ *Tran.*	0.781 ± 0.020	2.8 ± 2.8	43.14 ± 0.35	4 ± 4
$B^+ \to a_1^+\rho^0(a_1^+ \to \rho^0\pi^+)$ *Long.*	0.103 ± 0.007	18.6 ± 18.6	49.00 ± 0.10	4 ± 4
$B^+ \to a_1^0\rho^+$ *Long.*	0.035 ± 0.003	23.9 ± 23.9	100.00	4 ± 4
$B^0 \to b_1^+\pi^-$	0.075 ± 0.006	10.9 ± 1.2	86.97 ± 0.68	3 ± 0
$B^0 \to a_1^+\rho^{*-}(a_1^+ \to \rho^+\pi^0)$ *Long.*	0.025 ± 0.002	56.1 ± 56.1	49.78 ± 0.10	3 ± 3
$B^+ \to \omega\rho^+$ *Tran.*	0.712 ± 0.009	1.0 ± 0.2	98.80 ± 0.03	3 ± 1
$B^0 \to \omega K^{*0}_{K^+\pi^-}$ *Long.*	0.402 ± 0.015	2.7 ± 2.7	58.72 ± 0.46	3 ± 3
$B^+ \to a_1^+\rho^0(a_1^+ \to \rho^+\pi^0)$ *Long.*	0.057 ± 0.005	18.6 ± 18.6	49.78 ± 0.10	2 ± 2
$B^0 \to \rho^+\rho^-$	0.019 ± 0.001	24.2 ± 3.5	97.61 ± 0.04	2 ± 0
$B^+ \to b1^0\pi^+$	0.072 ± 0.006	6.7 ± 2.0	89.10 ± 0.70	2 ± 1
$B^0 \to \eta'_{\rho\gamma}K_S$	0.049 ± 0.002	65.0 ± 3.0	10.05 ± 0.31	2 ± 0
$B^+ \to b_1^+\rho^0$ *Long.*	0.243 ± 0.011	1.3 ± 1.3	86.97 ± 0.68	1 ± 1
$B^+ \to \omega K^{*+}_{\pi^+K^0_S}$	0.137 ± 0.008	3.4 ± 1.5	58.63 ± 0.46	1 ± 1
$B^0 \to a_1^0\rho^0$ *Long.*	0.142 ± 0.009	1.7 ± 1.7	100.00	1 ± 1
$B^+ \to \omega K^{*+}_{K^+\pi^0}$	0.222 ± 0.011	3.4 ± 1.5	29.31 ± 0.23	1 ± 0
$B^0 \to a_1^0K^{*0}_{K^+\pi^-}(a_1^0 \to \rho^+\pi^-)$ *Long.*	0.069 ± 0.006	6.5 ± 6.5	33.35 ± 0.01	1 ± 1
$B^+ \to b_1^0\rho^+$ *Tran.*	0.094 ± 0.007	1.5 ± 1.5	86.97 ± 0.68	1 ± 1
Total				109 ± 23

Table 7.30: Potential $B\overline{B}$ background for the $\eta'_{\rho\gamma}\omega$ mode. See the text for an explanation of different columns content.

Cross Feed Channel	MC ϵ (%)	Est. $\mathcal{B}$ (10^{-6})	$\prod \mathcal{B}_i$ (%)	# evts in ML
$B^0 \to \phi K^{*0}_{K^+\pi^-} Long.$	0.61 ± 0.01	4.6 ± 0.5	32.82 ± 0.40	4 ± 1
$B^0 \to \phi K^{*0}_{K^+\pi^-} Tran.$	0.60 ± 0.01	4.6 ± 0.5	32.82 ± 0.40	4 ± 1
$B^0 \to \phi K_2^{*0} (K_2^{*0} \to K^+\pi^-) Long.$	0.41 ± 0.01	6.7 ± 1.5	24.55 ± 0.66	3 ± 1
$B^+ \to \phi K^{*+}_{K^+\pi^0} Tran.$	0.41 ± 0.01	5.0 ± 0.8	16.19 ± 0.20	2 ± 1
$B^+ \to \phi K^{*+}_{K^+\pi^0} Long.$	0.35 ± 0.01	5.0 ± 0.8	16.19 ± 0.20	1 ± 1
$B^+ \to \phi K_2^{*+} (K_2^{*+} \to \pi^+ K_S^0) Long.$	0.44 ± 0.01	6.7 ± 1.5	8.40 ± 0.23	1 ± 1
$B^0 \to \phi \omega Long.$	0.69 ± 0.02	0.6 ± 0.6	43.84 ± 0.64	1 ± 1
$B^+ \to \phi K^{*+}_{\pi^+ K_S^0} Long.$	0.25 ± 0.01	5.0 ± 0.8	11.21 ± 0.14	1 ± 1
Total				17 ± 3

Table 7.31: Potential $B\overline{B}$ background for the $\eta'_{\rho\gamma}\phi$ mode. See the text for an explanation of different columns content.

7.6 Maximum Likelihood Fit

7.6.1 Overview

An unbinned multivariate maximum likelihood (ML) analysis is performed using `MiFit` [97] software. Events are selected with the cuts described in chapter 5 and choosing the best candidate as described in sec. 7.4.2.

In our sample of events we have considered four components: signal, continuum background, $B\overline{B}$ background generic (only charm decays), and $B\overline{B}$ peaking background (only charmless decays). For each input event i, the full likelihood ($\mathcal{L}_i$) is defined as:

$$\mathcal{L}_i = n_{sg}\mathcal{P}^i_{sg} + n_{q\bar{q}}\mathcal{P}^i_{q\bar{q}} + n_{b\bar{b}}\mathcal{P}^i_{b\bar{b}} + n_{bk}\mathcal{P}^i_{bk} \tag{7.1}$$

where $\mathcal{P}^i_{sg}$, $\mathcal{P}^i_{q\bar{q}}$, $\mathcal{P}^i_{b\bar{b}}$, and $\mathcal{P}^i_{bk}$ are the probability for signal, continuum background, $B\overline{B}$ background generic, and $B\overline{B}$ peaking background, evaluated with the observables of the i^{th} event as the product of the probability density functions (PDFs) for each of the observable. Variables used as PDFs are listed in tab. 7.33. n_{sg} (number of signal events), $n_{q\bar{q}}$ (number of continuum events), $n_{b\bar{b}}$ (number of $B\overline{B}$ generic events), and n_{bk} (number of $B\overline{B}$ peaking events) are free parameters in the fit.

For N input events, the overall likelihood is:

$$\mathcal{L} = \exp\left(-\sum_j n_j\right) \prod_i^N \mathcal{L}_i \tag{7.2}$$

where n_j is the number of events found by the fitter for j-hypothesis. Our fitter minimizes the expression $-\ln\mathcal{L}$ with respect to a set of free parameters.

The $B\overline{B}$ background studies (see sec. 7.5) and MC toy-experiment studies (see sec. 7.7) suggest decay modes where $B\overline{B}$ charm and peaking components are useful to add in the fit. The list of components for each mode is shown in tab. 7.32. In general we consider only one signal events component, combining MC truth+PP and SCF events to make signal component PDFs. Anyway in toy-experiment studies, where we embed MC signal events independently by the MC truth matching (taken in account the corresponding SCF fraction), we found significant bias for signal yield in modes which have higher SCF fraction. For these modes we found that splitting the signal events component in well-reconstructed signal events component (based on MC truth+PP events) and SCF signal events component is useful to reduce the bias. In this case we keep one signal yield as free parameter in the ML fit and we use the fixed fraction of SCF events to extract the number of well-reconstructed signal and signal SCF events. In our fits we have as free parameters the continuum background PDF shape parameters and the signal and backgrounds yields.

Decay Mode	Fit Components
$\eta_{\gamma\gamma}K^0_S$	*sg* , $q\bar{q}$, *bk*
$\eta_{3\pi}K^0_S$	*sg* , $q\bar{q}$
$\eta_{\gamma\gamma}\eta_{\gamma\gamma}$	*sg* , $q\bar{q}$
$\eta_{\gamma\gamma}\eta_{3\pi}$	*sg* , $q\bar{q}$
$\eta_{3\pi}\eta_{3\pi}$	*sg* , $q\bar{q}$
$\eta_{\gamma\gamma}\phi$	*sg* , $q\bar{q}$
$\eta_{3\pi}\phi$	*sg* , $q\bar{q}$
$\eta_{\gamma\gamma}\omega$	*sgtr* , *sgscf* , $q\bar{q}$, $b\bar{b}$, *bk*
$\eta_{3\pi}\omega$	*sg* , $q\bar{q}$, $b\bar{b}$
$\eta'_{\eta\pi\pi}\eta'_{\eta\pi\pi}$	*sg* , $q\bar{q}$
$\eta'_{\rho\gamma}\eta'_{\eta\pi\pi}$	*sg* , $q\bar{q}$, $b\bar{b}$, *bk*
$\eta'_{\eta\pi\pi}\phi$	*sg* , $q\bar{q}$
$\eta'_{\rho\gamma}\phi$	*sgtr* , *sgscf* , $q\bar{q}$, $b\bar{b}$
$\eta'_{\eta\pi\pi}\omega$	*sgtr* , *sgscf* , $q\bar{q}$, $b\bar{b}$
$\eta'_{\rho\gamma}\omega$	*sgtr* , *sgscf* , $q\bar{q}$, $b\bar{b}$, *bk*

Table 7.32: Fit components in the fit for each decay: *sg* for signal component, *sgtr* for well-reconstructed signal component (based on MC truth+PP events), *sgscf* for SCF signal component, $q\bar{q}$ for continuum background, $b\bar{b}$ for charm no-peaking $B\overline{B}$ background, *bk* for charmless peaking $B\overline{B}$ background.

Mode	PDFs
$\eta_{\gamma\gamma} K^0_S$	$m_{\rm ES}$, ΔE, $\mathcal{F}$
$\eta_{3\pi} K^0_S$	$m_{\rm ES}$, ΔE, $\mathcal{F}$
$\eta_{\gamma\gamma}\eta_{\gamma\gamma}$	$m_{\rm ES}$, ΔE, $\mathcal{F}$
$\eta_{\gamma\gamma}\eta_{3\pi}$	$m_{\rm ES}$, ΔE, $\mathcal{F}$
$\eta_{3\pi}\eta_{3\pi}$	$m_{\rm ES}$, ΔE, $\mathcal{F}$
$\eta_{\gamma\gamma}\phi$	$m_{\rm ES}$, ΔE, $\mathcal{F}$, $\mathcal{H}_\phi$
$\eta_{3\pi}\phi$	$m_{\rm ES}$, ΔE, $\mathcal{F}$, $\mathcal{H}_\phi$
$\eta_{\gamma\gamma}\omega$	$m_{\rm ES}$, ΔE, $\mathcal{F}$, ω mass, $\mathcal{H}_\omega$
$\eta_{3\pi}\omega$	$m_{\rm ES}$, ΔE, $\mathcal{F}$, ω mass, $\mathcal{H}_\omega$
$\eta'_{\eta\pi\pi}\eta'_{\eta\pi\pi}$	$m_{\rm ES}$, ΔE, $\mathcal{F}$, both η' masses
$\eta'_{\eta\pi\pi}\eta'_{\rho\gamma}$	$m_{\rm ES}$, ΔE, $\mathcal{F}$, both η' masses
$\eta'_{\eta\pi\pi}\phi$	$m_{\rm ES}$, ΔE, $\mathcal{F}$, η' mass, $\mathcal{H}_\phi$
$\eta'_{\rho\gamma}\phi$	$m_{\rm ES}$, ΔE, $\mathcal{F}$, η' mass, $\mathcal{H}_\phi$
$\eta'_{\eta\pi\pi}\omega$	$m_{\rm ES}$, ΔE, $\mathcal{F}$, η' mass, ω mass, $\mathcal{H}_\omega$
$\eta'_{\rho\gamma}\omega$	$m_{\rm ES}$, ΔE, $\mathcal{F}$, η' mass, ω mass, $\mathcal{H}_\omega$

Table 7.33: Variables used for each mode in the ML fit. The ω helicity $\mathcal{H}_\omega$ is defined as the cosine of angle between B recoil direction and the perpendicular to the plane identified by ω daughters, in ω rest frame. The ϕ helicity $\mathcal{H}_\phi$ is defined as cosine of angle between B recoil direction and a kaon direction, in ϕ rest frame.

7.6.2 Discriminating Variables in the ML Fit

The discriminating variables used in the ML fits for each B decay mode are shown in tab. 7.33.

PDFs for signal and $B\overline{B}$ background are fitted using Monte Carlo simulated events. Depending on the modes where we decide to use only one signal component, we use all signal MC events independently by the MC truth matching to make PDFs. For modes where we split the signal component in well-reconstructed signal events and SCF signal events components, we use MC truth+PP events and SCF events to make the PDFs, respectively. For $B\overline{B}$ charm PDFs we use generic MC $B\overline{B}$ charm events, and for $B\overline{B}$ peaking PDFs we use exclusive charmless decay modes (see tables in sec. 7.5 for a full lists), using weighted numbers of events from each background mode.

PDFs for continuum background have been done using on-peak sidebands, defined as:

- *Grand Side Band* (GSB): $5.25 < m_{\rm ES} < 5.27\ {\rm GeV}/c^2$
- ΔE *Side Band* (DESB): $0.1 < |\Delta E| < 0.2\ {\rm GeV}$

Table 7.34 reports the parametrization chosen for the different PDFs.

Most of the background parameters are left floating in the fit: coefficient of the Argus function for $m_{\rm ES}$; coefficient of Chebyshev polynomial for ΔE; mean, $\sigma_{\rm left}$, and

$\sigma_{\rm right}$ of asymmetric Gaussian for $\mathcal{F}$; coefficients of Chebyshev polynomial and fraction for daughter resonance masses; coefficients for Chebyshev polynomial for daughter resonance helicity. We found in blind fits on on-peak sample and in toys-experiments that there is a large correlation between the $\sigma_{\rm right}$ of the asymmetric Gaussian used for $\mathcal{F}$ and the yield of the charm $B\overline{B}$ component. For this reason we decided to keep fixed the $\sigma_{\rm right}$ for modes which have the charm $B\overline{B}$ component in the ML fit.

Appendix B reports PDFs plots, correlations between input variables for all decay modes, and the values of the background parameters left floating in the final fit. We deal with uncertainties in PDFs parameters in the systematic section.

Fit Component	ΔE	$m_{\rm ES}$	Fisher	$\eta'_{\rho\gamma}$ mass	$\eta'_{\eta\pi\pi}$ mass	ω mass	$\mathcal{H}_\phi$	$\mathcal{H}_\omega$
Signal	DG/CR	CB	DG/AG+G	DG	DG/CR	DG	P2	P2
Signal MCtruth	CR	CB	DG	DG/CR	CR	DG/CR	P2	P2
Signal SCF	CH4	CB	DG	DG/CH1	CR	G+CH2	P2	P2
$q\bar{q}$ Background	CH1	A	AG+CH1	CH1	G+CH2	G+CH1	CH2	CH4
$B\overline{B}$ Generic Background	CH2	A	DG	CH1	G+CH2	CH1	CH4	CH4
$B\overline{B}$ Peaking Background	CH4	DG	DG	CH1	G+CH2	G+CH1	CH2	CH4/G

Table 7.34: PDF parametrization used for signal, $q\bar{q}$ background and $B\overline{B}$ background (G = Gaussian, DG = double Gaussian, AG = asymmetric Gaussian, CB = Crystal Ball, CR = Cruijff function, A = Argus, CHn = $n^{\rm th}$ order Chebyshev polynomial, Pn = $n^{\rm th}$ order polynomial).

7.6.3 MC/data Matching Corrections

We have to correct the signal PDFs done using MC signal events in order to have a better matching with data.

During the reconstruction of MC samples we have applied the *BABAR* official procedure in order to properly apply MC/data correction for neutrals particles [106]. Furthermore, data and Monte Carlo control sample $B^- \to D^0\pi^-$ have been used to measure systematic difference for the variable $m_{\rm ES}$, ΔE, and the Fisher discriminant. We give in tab. 7.35 these corrections applied to the signal PDFs to correct the differences between data and signal MC. We correct the signal PDFs for these values and we consider a systematic uncertainty varying these corrections of $\pm 1\sigma$ of their values, one at a time, re-running the ML fit, and taking the difference in the results as systematics.

For signal daughter resonances mass and helicity PDFs we don't apply any correction. For the masses we consider a systematic uncertainty floating the mean of both Gaussian components (together) and the width of the core Gaussian (alone) of the double Gaussian PDFs, one at a time, re-running the ML fit, and taking the difference in the results as systematics. This procedure is performed on the on-peak data and is also applied for the coefficients of the signal helicity PDFs.

	Correction
$m_{\rm ES}$ **(Crystal Ball)**	
$m_{\rm ES}$ mean bias $({\rm MeV}/c^2)$	-0.53 ± 0.01
$m_{\rm ES}$ sigma scale factor	0.986 ± 0.004
ΔE (Double Gaussian)	
ΔE means bias $({\rm MeV})$	-2.2 ± 0.1
ΔE sigma scale factor	0.972 ± 0.005
Fisher (Double Gaussian)	
$\mathcal{F}$ mean bias (Main)	-0.029 ± 0.045
$\mathcal{F}$ sigma scale factor (Main)	0.992 ± 0.031
$\mathcal{F}$ mean bias (Minor)	0.020 ± 0.094
$\mathcal{F}$ sigma scale factor (Minor)	1.011 ± 0.051
$\mathcal{F}$ fraction scale factor	0.921 ± 0.131

Table 7.35: Shift and scale factor for MC/data matching to apply to the signal PDFs used to fit $m_{\rm ES}$, ΔE, and Fisher Discriminant.

7.7 Verification Tests

7.7.1 Yield MC Toy Experiments

We have generated 500 experiments for each decay mode in order to study any possible bias in the fit results. Events are taken from the MC for signal events and for $B\overline{B}$ peaking, independently by the MC truth matching and taking in account the correct fraction of SCF events, and drawn from PDFs for $B\overline{B}$ charm and for continuum background. Numbers of signal, $B\overline{B}$ and continuum events in each experiment are as expected in data.

The number of embedded signal events in each decay mode has been chosen using different criteria:

1. for modes where we have a significant previous measurement of the branching fractions, we embed the expected number of signal events obtained using the branching fraction or using the upper limit values (ηK^0_S and $\eta\eta$ modes);
2. no embedding signal events or embedding the expected number of signal events obtained using the upper limit values (modes not in case 1).

Number of embedded $B\overline{B}$ peaking events are those shown in tab. 7.21–7.31. Number of generated $B\overline{B}$ charm events are reported in tab. 7.20.

Results of these toy experiments are shown in tab. 7.36–7.50 for each modes. In these tables we show results of fit of 500 toy experiments for all the decay modes. In the second column we give the number of embedded events of the type specified in the first column. In the next 2 columns we show the mean of the Gaussians used to fit the distributions of fitted yield and the fitted yield errors. In the last 2 columns we show the mean and sigma of the Gaussians used to fit the pull distributions (the pull of x is defined as $p = \frac{x_{gen} - x_{mes}}{\sigma_x}$, where x_{gen} is the value which is generated or embedded, and x_{mes} the value measured by the fit). In the tables we show also the effect of embedding $B\overline{B}$ peaking background events and fitting with $B\overline{B}$ peaking component or forcing $B\overline{B}$ peaking component to zero or to the expected number of $B\overline{B}$ peaking yields. From these tables we see that the $B\overline{B}$ peaking component is useful to reduce the bias in the fit yield in the modes where we have decided to use this component.

In modes which have low statistics as input to ML fit (*e.g.* $\eta'_{\eta\pi\pi}\eta'_{\eta\pi\pi}$), we observe a negative tail that extends away from the core-Gaussian component in the distribution of the fitted signal yields, in case of no embedded signal events. For this case the distribution of the fitted signal yields is shown in fig. 7.1. This effect is mostly due to an artifact of the low signal yields and small sample sizes. This fact has been extensively studied by Milan and other groups in *BABAR* Collaboration, during previous analyses of these modes [116], and is understood. In case of negative non Gaussian tails, we fit the distributions of the toys results using a Crystall Ball function. We report the results of the mean and sigma of such fits in our toy result tables.

The $\eta'_{\rho\gamma}\omega$ mode shows a large bias for the signal yield in the configuration with 54 MC signal events embedded. We studied with more detail the source of this bias in the section 7.7.2. We found that the remaining bias is mainly due to small correlations between the input variables used in the ML fit.

We re-run all toy experiments for each mode, after the unblind, using the measured values of yields in on-peak samples, in order to reproduce the fit bias of the signal yields for each mode. We do the same procedure using pure toys, where all events are generated from PDFs. In this way we extract fit biases, from both MC toys and pure toys, for each mode. We use the difference between these biases (MC toys bias minus pure toys bias) to correct the signal yield results fitted in on-peak data [117]. We call this correction “ML fit bias”. We introduce a systematic uncertainty for the ML fit bias correction. In conclusion we verified that our fit works well and origin of residual biases are understood.

Events Type	# Events	Yield Mean	Yield Error	Pull Mean	Pull σ
$\eta_{\gamma\gamma}K_S^0$					
Signal	38	39.33 ± 0.49	11.99 ± 0.05	0.05 ± 0.04	1.05 ± 0.03
$q\bar{q}$	3168	3166.67 ± 0.49	57.20 ± 0.01	-0.02 ± 0.01	0.99 ± 0.01
$B\overline{B}$ peaking	0	0 (fixed)			
Signal	38	39.61 ± 0.50	12.37 ± 0.05	0.07 ± 0.04	1.03 ± 0.03
$q\bar{q}$	3168	3169.26 ± 1.03	59.90 ± 0.04	0.02 ± 0.02	1.00 ± 0.01
$B\overline{B}$ peaking	0	-2.88 ± 1.07	20.74 ± 0.18	-0.19 ± 0.05	1.01 ± 0.04
Signal	38	38.12 ± 0.46	12.30 ± 0.04	-0.05 ± 0.04	1.00 ± 0.03
$q\bar{q}$	3141	3140.74 ± 0.46	57.20 ± 0.01	-0.00 ± 0.01	0.99 ± 0.01
$B\overline{B}$ peaking	27	27 (fixed)			
Signal	38	37.76 ± 0.50	12.66 ± 0.05	-0.08 ± 0.04	1.02 ± 0.03
$q\bar{q}$	3141	3137.03 ± 1.04	60.27 ± 0.04	-0.06 ± 0.02	1.00 ± 0.01
$B\overline{B}$ peaking	27	31.23 ± 1.08	23.69 ± 0.14	0.09 ± 0.05	1.03 ± 0.03
Signal	61	60.63 ± 0.49	13.61 ± 0.04	-0.07 ± 0.04	0.99 ± 0.03
$q\bar{q}$	3145	3145.39 ± 0.49	57.19 ± 0.00	0.01 ± 0.01	1.00 ± 0.01
$B\overline{B}$ peaking	0	0 (fixed)			
Signal	61	62.72 ± 0.54	14.15 ± 0.04	0.08 ± 0.04	1.01 ± 0.03
$q\bar{q}$	3145	3147.61 ± 1.06	59.94 ± 0.05	0.04 ± 0.02	1.00 ± 0.01
$B\overline{B}$ peaking	0	-4.38 ± 1.12	21.08 ± 0.17	-0.28 ± 0.05	1.01 ± 0.04
Signal	61	61.18 ± 0.54	13.98 ± 0.04	-0.03 ± 0.04	1.03 ± 0.03
$q\bar{q}$	3118	3117.52 ± 0.54	57.18 ± 0.01	-0.01 ± 0.01	0.99 ± 0.01
$B\overline{B}$ peaking	27	27 (fixed)			
Signal	61	60.33 ± 0.53	14.44 ± 0.04	-0.08 ± 0.04	0.98 ± 0.03
$q\bar{q}$	3118	3117.64 ± 1.01	60.42 ± 0.04	-0.01 ± 0.02	0.99 ± 0.01
$B\overline{B}$ peaking	27	28.02 ± 1.04	24.34 ± 0.15	-0.04 ± 0.04	0.99 ± 0.03

Table 7.36: 500 MC Toy experiments results for $\eta_{\gamma\gamma}K_S^0$ modes. See text for details about the contents of various columns.

Events Type	# Events	Yield Mean	Yield Error	Pull Mean	Pull σ
$\eta_{3\pi}K_S^0$					
Signal	14	14.55 ± 0.27	7.02 ± 0.04	-0.00 ± 0.04	1.05 ± 0.03
$q\bar{q}$	1315	1314.45 ± 0.27	36.74 ± 0.00	-0.02 ± 0.01	1.00 ± 0.01
$B\overline{B}$ peaking	0	0 (fixed)			
Signal	14	13.98 ± 0.28	7.02 ± 0.04	-0.09 ± 0.04	1.06 ± 0.03
$q\bar{q}$	1311	1315.03 ± 0.28	36.75 ± 0.00	0.11 ± 0.01	1.00 ± 0.01
$B\overline{B}$ peaking	4	0 (fixed)			
Signal	23	23.29 ± 0.31	8.03 ± 0.03	-0.03 ± 0.04	1.05 ± 0.03
$q\bar{q}$	1306	1305.72 ± 0.31	36.70 ± 0.00	-0.01 ± 0.01	1.00 ± 0.01
$B\overline{B}$ peaking	0	0 (fixed)			
Signal	23	23.81 ± 0.30	8.15 ± 0.03	0.04 ± 0.04	1.05 ± 0.03
$q\bar{q}$	1302	1305.19 ± 0.30	36.72 ± 0.00	0.09 ± 0.01	1.00 ± 0.01
$B\overline{B}$ peaking	4	0 (fixed)			

Table 7.37: 500 MC Toy experiments results for $\eta_{3\pi}K_S^0$ modes. See text for details about the contents of various columns.

Events Type	# Events	Yield Mean	Yield Error	Pull Mean	Pull σ
$\eta_{\gamma\gamma}\eta_{\gamma\gamma}$					
Signal	20	21.30 ± 0.50	11.48 ± 0.06	0.03 ± 0.04	1.06 ± 0.03
$q\bar{q}$	2277	2275.74 ± 0.50	48.87 ± 0.01	-0.03 ± 0.01	1.00 ± 0.01
$B\overline{B}$ peaking	0	0 (fixed)			
Signal	20	22.30 ± 0.47	11.71 ± 0.06	0.13 ± 0.04	0.98 ± 0.03
$q\bar{q}$	2273	2274.74 ± 0.47	48.90 ± 0.01	0.04 ± 0.01	1.00 ± 0.01
$B\overline{B}$ peaking	4	0 (fixed)			
Signal	33	34.93 ± 0.52	12.90 ± 0.05	0.09 ± 0.04	1.01 ± 0.03
$q\bar{q}$	2264	2262.11 ± 0.52	48.93 ± 0.01	-0.04 ± 0.01	1.00 ± 0.01
$B\overline{B}$ peaking	0	0 (fixed)			
Signal	33	35.29 ± 0.56	13.03 ± 0.06	0.11 ± 0.04	1.08 ± 0.03
$q\bar{q}$	2260	2261.77 ± 0.56	48.96 ± 0.01	0.04 ± 0.01	1.00 ± 0.01
$B\overline{B}$ peaking	4	0 (fixed)			

Table 7.38: 500 MC Toy experiments results for $\eta_{\gamma\gamma}\eta_{\gamma\gamma}$ modes. See text for details about the contents of various columns.

Events Type	# Events	Yield Mean	Yield Error	Pull Mean	Pull σ
$\eta_{\gamma\gamma}\eta_{3\pi}$					
Signal	9	8.91 ± 0.29	6.64 ± 0.05	-0.12 ± 0.04	1.07 ± 0.03
$q\bar{q}$	1791	1791.09 ± 0.29	42.75 ± 0.01	0.00 ± 0.01	0.99 ± 0.00
$B\overline{B}$ peaking	0	0 (fixed)			
Signal	9	9.70 ± 0.28	6.78 ± 0.05	-0.02 ± 0.04	1.06 ± 0.03
$q\bar{q}$	1789	1790.29 ± 0.28	42.75 ± 0.01	0.03 ± 0.01	1.00 ± 0.00
$B\overline{B}$ peaking	2	0 (fixed)			
Signal	15	15.25 ± 0.29	7.52 ± 0.05	-0.07 ± 0.04	1.09 ± 0.03
$q\bar{q}$	1785	1784.75 ± 0.29	42.74 ± 0.00	-0.01 ± 0.01	1.00 ± 0.00
$B\overline{B}$ peaking	0	0 (fixed)			
Signal	15	15.75 ± 0.28	7.65 ± 0.04	0.01 ± 0.04	1.01 ± 0.03
$q\bar{q}$	1783	1784.25 ± 0.28	42.75 ± 0.01	0.03 ± 0.01	1.00 ± 0.00
$B\overline{B}$ peaking	2	0 (fixed)			

Table 7.39: 500 MC Toy experiments results for $\eta_{\gamma\gamma}\eta_{3\pi}$ modes. See text for details about the contents of various columns.

Events Type	# Events	Yield Mean	Yield Error	Pull Mean	Pull σ
$\eta_{3\pi}\eta_{3\pi}$					
Signal	3	2.88 ± 0.16	3.32 ± 0.03	-0.11 ± 0.04	1.09 ± 0.03
$q\bar{q}$	260	260.11 ± 0.16	16.39 ± 0.01	0.00 ± 0.01	0.99 ± 0.01
Signal	5	4.84 ± 0.15	3.66 ± 0.03	-0.16 ± 0.04	1.09 ± 0.03
$q\bar{q}$	258	258.15 ± 0.15	16.34 ± 0.01	0.01 ± 0.01	1.00 ± 0.01

Table 7.40: 500 MC Toy experiments results for $\eta_{3\pi}\eta_{3\pi}$ modes. See text for details about the contents of various columns.

Events Type	# Events	Yield Mean	Yield Error	Pull Mean	Pull σ
$\eta_{\gamma\gamma}\phi$					
Signal	0	-0.58 ± 0.19	3.95 ± 0.04	-0.15 ± 0.02	0.99 ± 0.05
$q\bar{q}$	1401	1400.83 ± 0.15	37.63 ± 0.01	-0.01 ± 0.01	0.99 ± 0.01
$B\overline{B}$ peaking	0	0 (fixed)			
Signal	0	0.40 ± 0.03	3.97 ± 0.04	0.10 ± 0.02	1.01 ± 0.05
$q\bar{q}$	1399	1400.49 ± 0.16	37.63 ± 0.01	0.04 ± 0.01	1.00 ± 0.01
$B\overline{B}$ peaking	2	0 (fixed)			
Signal	15	15.59 ± 0.22	6.34 ± 0.03	0.01 ± 0.04	1.02 ± 0.03
$q\bar{q}$	1386	1385.40 ± 0.22	37.56 ± 0.00	-0.02 ± 0.01	1.00 ± 0.00
$B\overline{B}$ peaking	0	0 (fixed)			
Signal	15	15.79 ± 0.23	6.41 ± 0.03	-0.02 ± 0.04	1.07 ± 0.03
$q\bar{q}$	1384	1385.19 ± 0.23	37.56 ± 0.00	0.03 ± 0.01	1.00 ± 0.00
$B\overline{B}$ peaking	2	0 (fixed)			

Table 7.41: 500 MC Toy experiments results for $\eta_{\gamma\gamma}\phi$ modes. See text for details about the contents of various columns.

Events Type	# Events	Yield Mean	Yield Error	Pull Mean	Pull σ
$\eta_{3\pi}\phi$					
Signal	0	-0.26 ± 0.14	2.79 ± 0.04	-0.09 ± 0.04	1.06 ± 0.03
$q\bar{q}$	486	486.26 ± 0.14	22.2 ± 0.01	0.01 ± 0.01	1.02 ± 0.01
Signal	5	5.14 ± 0.14	3.69 ± 0.03	0.04 ± 0.02	1.04 ± 0.03
$q\bar{q}$	481	480.86 ± 0.14	22.13 ± 0.00	-0.01 ± 0.01	0.99 ± 0.00

Table 7.42: 500 MC Toy experiments results for $\eta_{3\pi}\phi$ modes. See text for details about the contents of various columns.

Events Type	# Events	Yield Mean	Yield Error	Pull Mean	Pull σ
$\eta_{\gamma\gamma}\omega$					
Signal	0	-0.70 ± 0.41	8.33 ± 0.09	-0.08 ± 0.03	1.01 ± 0.04
$q\bar{q}$	11219	11220.90 ± 4.29	141.51 ± 0.10	0.02 ± 0.03	1.01 ± 0.02
$B\overline{B}$ charmed	114	114.19 ± 4.28	94.10 ± 0.17	-0.02 ± 0.05	1.02 ± 0.03
$B\overline{B}$ peaking	0	0 (fixed)			
Signal	0	-0.88 ± 0.44	9.22 ± 0.08	-0.10 ± 0.06	1.02 ± 0.02
$q\bar{q}$	11219	11224.45 ± 4.43	143.13 ± 0.11	0.04 ± 0.03	1.01 ± 0.02
$B\overline{B}$ charmed	114	109.13 ± 4.91	104.39 ± 0.18	-0.06 ± 0.05	1.05 ± 0.03
$B\overline{B}$ peaking	0	2.76 ± 3.23	69.23 ± 0.29	-0.00 ± 0.05	1.05 ± 0.03
Signal	0	-0.69 ± 0.40	8.52 ± 0.08	-0.08 ± 0.04	1.03 ± 0.04
$q\bar{q}$	11169	11158.39 ± 4.35	142.41 ± 0.10	-0.07 ± 0.03	1.00 ± 0.02
$B\overline{B}$ charmed	114	126.27 ± 4.33	95.92 ± 0.16	0.13 ± 0.04	1.01 ± 0.03
$B\overline{B}$ peaking	50	50 (fixed)			
Signal	0	-0.40 ± 0.37	9.35 ± 0.09	-0.04 ± 0.02	1.07 ± 0.04
$q\bar{q}$	11169	11168.23 ± 4.60	144.21 ± 0.11	-0.00 ± 0.03	1.02 ± 0.02
$B\overline{B}$ charmed	114	125.37 ± 4.98	106.22 ± 0.17	0.10 ± 0.05	1.05 ± 0.03
$B\overline{B}$ peaking	50	42.89 ± 3.48	72.01 ± 0.24	-0.15 ± 0.05	1.10 ± 0.04
Signal	61	62.98 ± 0.57	14.88 ± 0.05	0.09 ± 0.04	1.00 ± 0.03
$q\bar{q}$	11158	11157.50 ± 4.26	142.19 ± 0.11	-0.00 ± 0.03	1.00 ± 0.02
$B\overline{B}$ charmed	114	112.53 ± 4.20	95.00 ± 0.18	-0.03 ± 0.04	0.99 ± 0.03
$B\overline{B}$ peaking	0	0 (fixed)			
Signal	61	64.42 ± 0.62	15.86 ± 0.05	0.17 ± 0.04	1.01 ± 0.03
$q\bar{q}$	11158	11155.60 ± 4.64	143.56 ± 0.11	-0.01 ± 0.03	1.02 ± 0.02
$B\overline{B}$ charmed	114	121.36 ± 5.15	105.50 ± 0.18	0.06 ± 0.05	1.09 ± 0.03
$B\overline{B}$ peaking	0	-8.63 ± 3.41	72.39 ± 0.25	-0.16 ± 0.05	1.04 ± 0.03
Signal	61	61.52 ± 0.56	14.93 ± 0.04	-0.01 ± 0.04	0.99 ± 0.03
$q\bar{q}$	11108	11104.81 ± 4.32	142.83 ± 0.11	-0.02 ± 0.03	0.99 ± 0.02
$B\overline{B}$ charmed	114	116.85 ± 4.30	96.30 ± 0.17	0.02 ± 0.04	0.99 ± 0.03
$B\overline{B}$ peaking	50	50 (fixed)			
Signal	61	64.11 ± 0.59	15.93 ± 0.05	0.15 ± 0.04	0.98 ± 0.03
$q\bar{q}$	11108	11109.10 ± 4.57	144.62 ± 0.11	0.01 ± 0.03	1.01 ± 0.02
$B\overline{B}$ charmed	114	135.20 ± 4.83	107.26 ± 0.17	0.18 ± 0.04	1.01 ± 0.03
$B\overline{B}$ peaking	50	24.48 ± 3.31	75.19 ± 0.22	-0.38 ± 0.04	1.00 ± 0.03

Table 7.43: 500 MC Toy experiments results for $\eta_{\gamma\gamma}\omega$ modes. See text for details about the contents of various columns.

Events Type	# Events	Yield Mean	Yield Error	Pull Mean	Pull σ
$\eta_{3\pi}\omega$					
Signal	0	-0.66 ± 0.31	6.60 ± 0.06	-0.10 ± 0.02	1.03 ± 0.04
$q\bar{q}$	8534	8530.93 ± 3.34	119.90 ± 0.10	-0.03 ± 0.03	0.99 ± 0.02
$B\overline{B}$ charmed	79	84.87 ± 3.36	77.04 ± 0.16	0.06 ± 0.04	0.98 ± 0.03
$B\overline{B}$ peaking	0	0 (fixed)			
Signal	0	0.49 ± 0.27	6.54 ± 0.06	0.07 ± 0.02	1.02 ± 0.04
$q\bar{q}$	8534	8534.74 ± 3.54	120.23 ± 0.10	0.02 ± 0.03	1.02 ± 0.02
$B\overline{B}$ charmed	79	83.19 ± 3.62	78.76 ± 0.17	0.03 ± 0.05	1.03 ± 0.03
$B\overline{B}$ peaking	0	-2.55 ± 1.36	28.76 ± 0.17	-0.18 ± 0.05	1.06 ± 0.03
Signal	0	0.01 ± 0.27	6.52 ± 0.07	0.00 ± 0.01	1.03 ± 0.04
$q\bar{q}$	8526	8531.08 ± 3.51	119.64 ± 0.10	0.07 ± 0.03	1.01 ± 0.02
$B\overline{B}$ charmed	79	82.52 ± 3.61	76.90 ± 0.18	0.04 ± 0.05	1.06 ± 0.03
$B\overline{B}$ peaking	8	0 (fixed)			
Signal	0	0.05 ± 0.27	6.47 ± 0.07	0.01 ± 0.01	1.03 ± 0.04
$q\bar{q}$	8526	8531.08 ± 3.51	119.64 ± 0.10	0.07 ± 0.03	1.03 ± 0.02
$B\overline{B}$ charmed	79	74.52 ± 3.61	76.60 ± 0.18	-0.08 ± 0.05	1.06 ± 0.03
$B\overline{B}$ peaking	8	8 (fixed)			
Signal	0	-0.69 ± 0.27	6.52 ± 0.05	-0.12 ± 0.06	1.01 ± 0.05
$q\bar{q}$	8526	8526.13 ± 3.34	120.55 ± 0.10	0.00 ± 0.03	0.98 ± 0.02
$B\overline{B}$ charmed	79	79.89 ± 3.46	79.15 ± 0.17	0.01 ± 0.04	0.98 ± 0.03
$B\overline{B}$ peaking	8	8.06 ± 1.34	29.99 ± 0.15	0.00 ± 0.05	1.01 ± 0.03
Signal	24	26.88 ± 0.38	10.04 ± 0.05	0.21 ± 0.04	0.99 ± 0.03
$q\bar{q}$	8510	8506.40 ± 3.54	119.76 ± 0.10	-0.03 ± 0.03	1.01 ± 0.02
$B\overline{B}$ charmed	79	79.74 ± 3.54	76.83 ± 0.17	-0.02 ± 0.05	1.04 ± 0.03
$B\overline{B}$ peaking	0	0 (fixed)			
Signal	24	26.64 ± 0.39	10.02 ± 0.05	0.19 ± 0.04	0.99 ± 0.03
$q\bar{q}$	8510	8503.91 ± 3.39	120.25 ± 0.09	-0.05 ± 0.03	0.99 ± 0.02
$B\overline{B}$ charmed	79	81.46 ± 3.68	78.71 ± 0.17	0.00 ± 0.05	1.03 ± 0.03
$B\overline{B}$ peaking	0	0.90 ± 1.44	29.11 ± 0.17	-0.04 ± 0.05	1.09 ± 0.03
Signal	24	25.93 ± 0.38	9.92 ± 0.05	0.11 ± 0.04	1.01 ± 0.03
$q\bar{q}$	8502	8510.48 ± 3.51	120.05 ± 0.10	0.07 ± 0.03	1.00 ± 0.02
$B\overline{B}$ charmed	79	75.54 ± 3.51	77.17 ± 0.17	-0.05 ± 0.05	1.02 ± 0.03
$B\overline{B}$ peaking	8	0 (fixed)			
Signal	24	25.84 ± 0.39	9.96 ± 0.05	0.11 ± 0.04	1.02 ± 0.03
$q\bar{q}$	8502	8496.89 ± 3.25	120.13 ± 0.09	-0.04 ± 0.03	0.97 ± 0.02
$B\overline{B}$ charmed	79	81.25 ± 3.25	77.44 ± 0.16	0.02 ± 0.04	0.94 ± 0.03
$B\overline{B}$ peaking	8	8 (fixed)			
Signal	24	25.91 ± 0.38	9.93 ± 0.05	0.11 ± 0.04	1.02 ± 0.03
$q\bar{q}$	8502	8494.26 ± 3.61	120.47 ± 0.09	-0.06 ± 0.03	1.02 ± 0.02
$B\overline{B}$ charmed	79	79.65 ± 3.65	79.07 ± 0.17	-0.01 ± 0.05	1.05 ± 0.03
$B\overline{B}$ peaking	8	12.15 ± 1.36	30.24 ± 0.17	0.06 ± 0.05	1.02 ± 0.03

Table 7.44: 500 MC Toy experiments results for $\eta_{3\pi}\omega$ modes. See text for details about the contents of various columns.

Events Type	# Events	Yield Mean	Yield Error	Pull Mean	Pull σ
$\eta'_{\eta\pi\pi}\eta'_{\eta\pi\pi}$					
Signal	0	0.89 ± 0.24	2.07 ± 0.04	0.50 ± 0.08	1.00 ± 0.05
$q\bar{q}$	208	207.55 ± 0.23	15.09 ± 0.01	-0.03 ± 0.01	0.99 ± 0.01
Signal	7	7.09 ± 0.09	3.25 ± 0.02	-0.05 ± 0.03	1.08 ± 0.02
$q\bar{q}$	201	200.91 ± 0.09	14.30 ± 0.00	-0.01 ± 0.01	0.99 ± 0.01

Table 7.45: 500 MC Toy experiments results for $\eta'_{\eta\pi\pi}\eta'_{\eta\pi\pi}$ modes. See text for details about the contents of various columns.

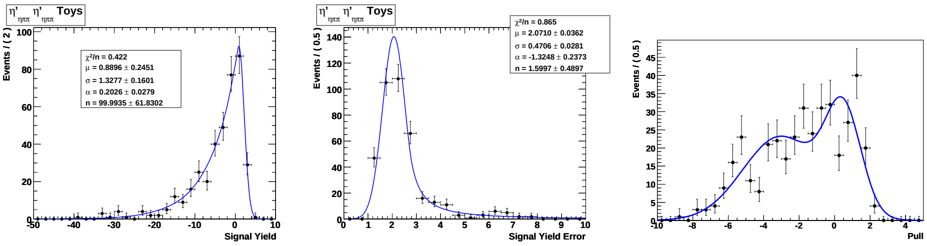

Figure 7.1: Results of 500 MC toys for $\eta'_{\eta\pi\pi}\eta'_{\eta\pi\pi}$ for fitted signal yields: distribution of the fitted yields (left), distribution of the errors of the fitted yields (center), pull distribution (right). We use a Crystal Ball function to fit the yield and error distributions (unbinned fits), and a double Gaussian for the pull distribution.

Events Type	# Events	Yield Mean	Yield Error	Pull Mean	Pull σ
$\eta'_{\rho\gamma}\eta'_{\eta\pi\pi}$					
Signal	0	-0.23 ± 0.29	6.25 ± 0.06	-0.04 ± 0.06	1.02 ± 0.04
$q\bar{q}$	7507	7507.79 ± 3.99	121.73 ± 0.10	0.01 ± 0.03	1.01 ± 0.02
$B\overline{B}$ charmed	239	240.38 ± 4.01	87.48 ± 0.15	0.01 ± 0.05	1.03 ± 0.03
$B\overline{B}$ peaking	0	0 (fixed)			
Signal	0	-0.28 ± 0.31	6.44 ± 0.07	-0.04 ± 0.02	1.02 ± 0.04
$q\bar{q}$	7507	7497.63 ± 4.04	121.83 ± 0.11	-0.07 ± 0.03	1.03 ± 0.02
$B\overline{B}$ charmed	239	248.56 ± 4.11	89.02 ± 0.17	0.09 ± 0.05	1.05 ± 0.03
$B\overline{B}$ peaking	0	0.88 ± 1.38	27.26 ± 0.18	-0.06 ± 0.05	1.03 ± 0.04
Signal	0	-0.58 ± 0.34	6.48 ± 0.07	-0.09 ± 0.02	1.02 ± 0.04
$q\bar{q}$	7494	7491.45 ± 4.06	121.91 ± 0.12	-0.01 ± 0.03	1.02 ± 0.02
$B\overline{B}$ charmed	239	242.28 ± 4.07	87.85 ± 0.17	0.02 ± 0.05	1.05 ± 0.03
$B\overline{B}$ peaking	13	13 (fixed)			
Signal	0	-0.01 ± 0.30	6.53 ± 0.07	-0.01 ± 0.01	1.03 ± 0.04
$q\bar{q}$	7494	7481.47 ± 3.93	122.19 ± 0.11	-0.03 ± 0.03	1.01 ± 0.02
$B\overline{B}$ charmed	239	242.11 ± 4.07	89.53 ± 0.16	0.02 ± 0.05	1.03 ± 0.03
$B\overline{B}$ peaking	13	16.10 ± 1.38	28.19 ± 0.16	0.04 ± 0.05	1.08 ± 0.03
Signal	12	13.38 ± 0.32	8.07 ± 0.05	0.06 ± 0.04	1.04 ± 0.03
$q\bar{q}$	7495	7500.84 ± 3.90	121.97 ± 0.12	0.05 ± 0.03	1.00 ± 0.02
$B\overline{B}$ charmed	239	231.75 ± 3.92	87.78 ± 0.17	-0.10 ± 0.04	1.01 ± 0.03
$B\overline{B}$ peaking	0	0 (fixed)			
Signal	12	13.35 ± 0.32	8.21 ± 0.05	0.07 ± 0.04	0.99 ± 0.03
$q\bar{q}$	7495	7497.93 ± 4.06	122.25 ± 0.11	0.03 ± 0.03	1.03 ± 0.02
$B\overline{B}$ charmed	239	238.66 ± 4.08	89.36 ± 0.17	-0.02 ± 0.05	1.03 ± 0.03
$B\overline{B}$ peaking	0	-3.92 ± 1.28	26.80 ± 0.19	-0.23 ± 0.05	1.07 ± 0.03
Signal	12	13.77 ± 0.33	8.16 ± 0.06	0.10 ± 0.04	1.02 ± 0.03
$q\bar{q}$	7482	7480.66 ± 4.05	122.05 ± 0.11	-0.01 ± 0.03	1.02 ± 0.02
$B\overline{B}$ charmed	239	238.48 ± 4.01	88.06 ± 0.16	-0.02 ± 0.05	1.03 ± 0.03
$B\overline{B}$ peaking	13	13 (fixed)			
Signal	12	13.70 ± 0.36	8.31 ± 0.06	0.08 ± 0.04	1.02 ± 0.03
$q\bar{q}$	7482	7491.70 ± 4.14	122.47 ± 0.11	0.08 ± 0.03	1.03 ± 0.02
$B\overline{B}$ charmed	239	229.07 ± 4.17	89.62 ± 0.17	-0.13 ± 0.05	1.05 ± 0.03
$B\overline{B}$ peaking	13	11.65 ± 1.34	28.42 ± 0.16	-0.12 ± 0.05	1.07 ± 0.03

Table 7.46: 500 MC Toy experiments results for $\eta'_{\rho\gamma}\eta'_{\eta\pi\pi}$ modes. See text for details about the contents of various columns.

Events Type	# Events	Yield Mean	Yield Error	Pull Mean	Pull σ
$\eta'_{\eta\pi\pi}\omega$					
Signal	0	-0.84 ± 0.22	4.63 ± 0.06	-0.18 ± 0.04	1.04 ± 0.04
$q\bar{q}$	8278	8279.05 ± 4.28	127.92 ± 0.13	0.01 ± 0.03	1.02 ± 0.02
$B\overline{B}$ charmed	110	110.03 ± 4.29	90.85 ± 0.19	0.01 ± 0.05	1.05 ± 0.03
$B\overline{B}$ peaking	0	0 (fixed)			
Signal	0	-0.64 ± 0.22	4.65 ± 0.06	-0.14 ± 0.06	1.02 ± 0.05
$q\bar{q}$	8275	8275.29 ± 4.11	127.32 ± 0.09	0.00 ± 0.03	1.00 ± 0.02
$B\overline{B}$ charmed	110	110.48 ± 4.06	90.85 ± 0.19	-0.00 ± 0.04	1.01 ± 0.03
$B\overline{B}$ peaking	3	0 (fixed)			
Signal	38	38.91 ± 0.33	9.77 ± 0.03	0.04 ± 0.03	0.99 ± 0.02
$q\bar{q}$	8240	8234.39 ± 4.00	128.11 ± 0.13	-0.05 ± 0.03	0.99 ± 0.02
$B\overline{B}$ charmed	110	114.76 ± 3.99	90.99 ± 0.18	0.04 ± 0.04	0.98 ± 0.03
$B\overline{B}$ peaking	0	0 (fixed)			
Signal	38	38.27 ± 0.30	9.76 ± 0.03	-0.02 ± 0.03	0.95 ± 0.02
$q\bar{q}$	8237	8241.40 ± 4.19	128.10 ± 0.13	0.03 ± 0.03	1.02 ± 0.02
$B\overline{B}$ charmed	110	108.30 ± 4.18	90.90 ± 0.18	-0.03 ± 0.05	1.04 ± 0.03
$B\overline{B}$ peaking	3	0 (fixed)			

Table 7.47: 500 MC Toy experiments results for $\eta'_{\eta\pi\pi}\omega$ modes. See text for details about the contents of various columns.

Events Type	# Events	Yield Mean	Yield Error	Pull Mean	Pull σ
$\eta'_{\rho\gamma}\omega$					
Signal	0	-0.30 ± 0.71	14.44 ± 0.14	-0.05 ± 0.05	1.02 ± 0.03
$q\bar{q}$	48952	48967.94 ± 16.42	430.35 ± 0.23	0.03 ± 0.04	0.99 ± 0.03
$B\overline{B}$ charmed	3647	3631.20 ± 16.42	373.02 ± 0.24	-0.04 ± 0.04	1.00 ± 0.03
$B\overline{B}$ peaking	0	0 (fixed)			
Signal	0	-0.48 ± 0.65	15.45 ± 0.11	-0.02 ± 0.05	1.02 ± 0.03
$q\bar{q}$	48952	48952.31 ± 18.54	471.73 ± 0.42	-0.01 ± 0.04	1.01 ± 0.03
$B\overline{B}$ charmed	3647	3647.77 ± 17.45	381.13 ± 0.32	0.01 ± 0.05	1.02 ± 0.03
$B\overline{B}$ peaking	0	2.83 ± 5.37	117.91 ± 0.29	0.01 ± 0.05	1.02 ± 0.03
Signal	0	-0.94 ± 0.69	15.21 ± 0.10	-0.10 ± 0.03	1.02 ± 0.03
$q\bar{q}$	48843	48812.10 ± 16.16	431.18 ± 0.14	-0.07 ± 0.04	0.99 ± 0.03
$B\overline{B}$ charmed	3647	3680.34 ± 16.38	374.32 ± 0.23	0.10 ± 0.04	0.99 ± 0.03
$B\overline{B}$ peaking	109	109 (fixed)			
Signal	0	-0.48 ± 0.66	15.43 ± 0.16	-0.03 ± 0.05	1.01 ± 0.04
$q\bar{q}$	48843	48866.84 ± 18.73	474.95 ± 0.37	0.04 ± 0.04	1.00 ± 0.03
$B\overline{B}$ charmed	3647	3639.45 ± 17.42	383.26 ± 0.29	-0.01 ± 0.05	1.03 ± 0.03
$B\overline{B}$ peaking	109	95.84 ± 5.47	120.38 ± 0.24	-0.13 ± 0.05	1.02 ± 0.03
Signal	10	10.58 ± 0.74	16.59 ± 0.12	0.01 ± 0.04	1.00 ± 0.03
$q\bar{q}$	48833	48840.07 ± 19.70	474.34 ± 0.40	0.01 ± 0.04	1.03 ± 0.03
$B\overline{B}$ charmed	3647	3668.15 ± 17.80	382.83 ± 0.32	0.06 ± 0.05	1.05 ± 0.03
$B\overline{B}$ peaking	109	80.44 ± 5.44	121.00 ± 0.20	-0.25 ± 0.04	1.01 ± 0.03
Signal	54	61.68 ± 0.85	19.95 ± 0.07	0.32 ± 0.04	1.03 ± 0.03
$q\bar{q}$	48898	48897.57 ± 17.37	432.45 ± 0.21	-0.01 ± 0.04	1.03 ± 0.03
$B\overline{B}$ charmed	3647	3639.62 ± 17.28	375.07 ± 0.22	-0.02 ± 0.05	1.03 ± 0.03
$B\overline{B}$ peaking	0	0 (fixed)			
Signal	54	61.96 ± 0.86	20.86 ± 0.07	0.33 ± 0.04	0.97 ± 0.03
$q\bar{q}$	48898	48910.92 ± 19.14	476.40 ± 0.32	0.02 ± 0.04	1.01 ± 0.03
$B\overline{B}$ charmed	3647	3647.05 ± 17.19	384.43 ± 0.25	0.00 ± 0.04	1.01 ± 0.03
$B\overline{B}$ peaking	0	-21.08 ± 5.52	121.08 ± 0.21	-0.19 ± 0.05	1.02 ± 0.03
Signal	54	60.42 ± 0.93	20.19 ± 0.07	0.26 ± 0.05	1.08 ± 0.03
$q\bar{q}$	48789	48735.15 ± 16.89	432.75 ± 0.20	-0.13 ± 0.04	1.01 ± 0.03
$B\overline{B}$ charmed	3647	3694.71 ± 16.87	375.37 ± 0.21	0.13 ± 0.04	1.02 ± 0.03
$B\overline{B}$ peaking	109	109 (fixed)			
Signal	54	62.32 ± 0.86	21.24 ± 0.08	0.33 ± 0.04	0.96 ± 0.03
$q\bar{q}$	48789	48790.90 ± 18.68	477.61 ± 0.35	-0.00 ± 0.04	0.99 ± 0.03
$B\overline{B}$ charmed	3647	3664.01 ± 16.82	385.24 ± 0.28	0.05 ± 0.04	0.99 ± 0.03
$B\overline{B}$ peaking	109	81.76 ± 5.66	123.41 ± 0.20	-0.24 ± 0.05	1.03 ± 0.03

Table 7.48: 500 MC Toy experiments results for $\eta'_{\rho\gamma}\omega$ modes. See text for details about the contents of various columns.

Events Type	# Events	Yield Mean	Yield Error	Pull Mean	Pull σ
$\eta'_{\eta\pi\pi}\phi$					
Signal	0	0.28 ± 0.09	2.56 ± 0.03	0.11 ± 0.01	1.18 ± 0.06
$q\bar{q}$	455	454.97 ± 0.09	21.5 ± 0.01	0.01 ± 0.01	0.94 ± 0.01
Signal	10	10.08 ± 0.14	4.24 ± 0.02	0.02 ± 0.01	1.04 ± 0.02
$q\bar{q}$	445	444.92 ± 0.14	21.28 ± 0.00	-0.01 ± 0.01	1.00 ± 0.00

Table 7.49: 500 MC Toy experiments results for $\eta'_{\eta\pi\pi}\phi$ modes. See text for details about the contents of various columns.

Events Type	# Events	Yield Mean	Yield Error	Pull Mean	Pull σ
$\eta'_{\rho\gamma}\phi$					
Signal	0	-0.22 ± 0.25	5.44 ± 0.06	-0.04 ± 0.01	1.02 ± 0.02
$q\bar{q}$	6464	6465.07 ± 2.71	98.11 ± 0.07	0.01 ± 0.02	1.01 ± 0.02
$B\overline{B}$ charmed	150	149.89 ± 2.72	58.82 ± 0.15	-0.04 ± 0.05	1.02 ± 0.03
$B\overline{B}$ peaking	0	0 (fixed)			
Signal	0	-0.20 ± 0.25	5.50 ± 0.06	-0.04 ± 0.02	1.02 ± 0.04
$q\bar{q}$	6447	6450.62 ± 2.71	98.54 ± 0.07	0.02 ± 0.03	1.02 ± 0.02
$B\overline{B}$ charmed	150	164.53 ± 2.78	59.60 ± 0.14	0.21 ± 0.05	1.02 ± 0.03
$B\overline{B}$ peaking	17	0 (fixed)			
Signal	16	16.17 ± 0.31	7.80 ± 0.05	0.01 ± 0.04	1.02 ± 0.03
$q\bar{q}$	6448	6446.51 ± 2.58	98.71 ± 0.06	-0.01 ± 0.03	1.00 ± 0.02
$B\overline{B}$ charmed	150	151.33 ± 2.60	59.13 ± 0.14	-0.01 ± 0.04	1.01 ± 0.03
$B\overline{B}$ peaking	0	0 (fixed)			
Signal	16	17.46 ± 0.31	7.97 ± 0.04	0.16 ± 0.04	1.02 ± 0.03
$q\bar{q}$	6431	6432.68 ± 2.63	99.04 ± 0.07	0.02 ± 0.03	1.01 ± 0.02
$B\overline{B}$ charmed	150	163.86 ± 2.66	59.92 ± 0.14	0.20 ± 0.04	1.02 ± 0.03
$B\overline{B}$ peaking	17	0 (fixed)			

Table 7.50: 500 MC Toy experiments results for $\eta'_{\rho\gamma}\phi$ modes. See text for details about the contents of various columns.

7.7.2 Yield Specific Toy Experiments for $\eta'_{\rho\gamma}\omega$

The $\eta'_{\rho\gamma}\omega$ mode shows a large bias for the signal yield in the configuration with 54 MC signal events embedded, as you can see in tab. 7.48. We study with more detail the source of this bias in this section.

First of all we have generated 500 experiments in order to study any possible intrinsic bias in the fit results. In this case, signal, continuum background, $B\overline{B}$ charm, and $B\overline{B}$ peaking events are generated from PDFs. We repeat here the case reported in tab. 7.48 with 54 signal events and all components in the fit. Events are generated from PDFs without correlations between the input variables, so with this check we can understand the effect of the correlations. Results of these toy experiments are shown in tab. 7.51. In this table we show results of fit of 500 toy experiments for all the decay modes. In the second column we give the number of generated events of the type specified in the first column. In the next 2 columns we show the mean of the Gaussians used to fit the distributions of fitted yields and the fitted yield errors. In the last 2 columns we show the mean and sigma of the Gaussians used to fit the pull distributions. This check clearly says that when generating events without correlations between the input variables, the bias is negligible.

Another possible source of the bias is due to SCF events. So we performed 500 toy experiments where we embed only MCtruth+PP signal events, removing the SCF component in the ML fit. The $B\overline{B}$ peaking events are taken from MC events and the continuum and $B\overline{B}$ charm backgrounds are generated from PDFs. Results of this test are shown in tab. 7.52. We see that the bias is still there also in this case. A final check to prove that the sources of the bias are the correlations between the input variables is to remove the variables that are more correlated: the ΔE and the daughter masses resonances (see appendix B.13 for the correlation tables). So we repeated the last toys removing the two daughter masses variables, the η' mass and ω mass. The results are shown in tab. 7.53. We can see that the bias now is smaller (negligible), which confirms that the source of the bias is mainly due to correlations between the input variables. We conclude that we can use our configuration of the ML fit with the daughter variables for the final fit on on-peak data, and then taking in account a correction due to the bias in the signal yield result.

Events Type	# Events	Yield Mean	Yield Error	Pull Mean	Pull σ
$\eta'_{\rho\gamma}\omega$					
Signal	54	53.89 ± 0.94	20.94 ± 0.09	-0.01 ± 0.05	1.01 ± 0.03
$q\bar{q}$	48789	48789.33 ± 18.92	478.09 ± 0.35	-0.01 ± 0.04	1.00 ± 0.03
$B\overline{B}$ charm	3647	3648.41 ± 16.93	385.29 ± 0.28	0.01 ± 0.04	1.00 ± 0.03
$B\overline{B}$ peaking	109	107.31 ± 5.64	124.49 ± 0.18	-0.03 ± 0.05	1.01 ± 0.03

Table 7.51: 500 Pure Toy experiments results. See text for details about the contents of various columns.

Events Type	# Events	Yield Mean	Yield Error	Pull Mean	Pull σ
$\eta'_{\rho\gamma}\omega$					
Signal (only MCTruth+PP)	44	50.73 ± 0.70	18.34 ± 0.06	0.37 ± 0.04	0.98 ± 0.03
$q\bar{q}$	48789	48812.12 ± 19.93	478.28 ± 0.32	0.04 ± 0.04	1.04 ± 0.03
$B\overline{B}$ charm	3647	3666.96 ± 18.01	385.68 ± 0.26	0.05 ± 0.05	1.05 ± 0.03
$B\overline{B}$ peaking	109	58.17 ± 6.00	122.59 ± 0.20	-0.43 ± 0.05	1.10 ± 0.04

Table 7.52: 500 MC Toy experiments results. These were performed embedding only Signal MCTruth+PP events and fitting only with MCTruth+PP Signal component (no SCF). See text for details about the contents of various columns.

Events Type	# Events	Yield Mean	Yield Error	Pull Mean	Pull σ
$\eta'_{\rho\gamma}\omega$					
Signal (only MCTruth+PP)	44	45.93 ± 1.18	26.25 ± 0.09	0.02 ± 0.05	1.04 ± 0.03
$q\bar{q}$	48789	48802.78 ± 19.79	498.48 ± 0.41	0.02 ± 0.04	0.98 ± 0.03
$B\overline{B}$ charm	3647	3666.03 ± 17.65	397.41 ± 0.30	0.05 ± 0.04	0.99 ± 0.03
$B\overline{B}$ peaking	109	74.34 ± 7.25	161.96 ± 0.22	-0.23 ± 0.04	1.00 ± 0.03

Table 7.53: 500 MC Toy experiments results. These were performed embedding only Signal MCTruth+PP events and fitting only with MCTruth+PP Signal component (no SCF), excluding daughters' resonances masses from fit. See text for details about the contents of various columns.

7.8 Systematic Errors

We present here the main sources of systematic uncertainties in the measurement of branching fractions.

We have to consider systematic errors coming from the fit procedure both for efficiency and yield. The systematic errors are summarized in tab. 7.54.

- *ML fit bias*: this error is related to the efficiency in the ML fit. We quote this systematic error with toy experiments, summing in quadrature half of the ML fit bias correction, the statistical uncertainty of the correction itself, and the bias due to small sample size. Toys have been performed using the final yields results extracted in the on-peak samples in order to reproduce the fit bias (see tab. 7.56–7.58). The bias due to small sample size is obtained from pure toy experiments, considering the difference between the mean of the distribution of the fitted signal yields and the mean of the Crystal Ball used to fit the distribution of the fitted yields [116].

- *MC/data corrections*: we use control samples to study how well the MC models the data in $m_{\rm ES}$ ΔE, and Fisher discriminant (see sec. 7.6.3). From these studies, we determine shifts and scale factors to apply to our signal PDFs of $m_{\rm ES}$, ΔE, and Fisher discriminant. We use the errors of these values to calculate a systematics effect due to the variation when we vary them of $\pm 1\sigma$. In this way, we apply these variations, one at a time, to our signal PDFs and re-run the ML fit. No corrections have been applied to daughter resonance masses and helicities, but we float the parameters of their signal PDFs (mean and width of Core Gaussians for masses, coefficients of the polynomials for helicities) in the on-peak fit, one at a time, and we consider the variation with respect to the nominal fit as systematic errors. The contributions are summed in quadrature.

- *Track multiplicity*: we have requested the reconstruction of at least 1 charged tracks in the rest of the event. Signal MC inefficiency for this cut is of the order of about 2%. We assign an uncertainty of 1.0%.

- *Track finding efficiency*: study of absolute tracking efficiency is performed by *BABAR* tracking working group and provides a systematic error associated with the tables for *GoodTracksLoose* tracks of 0.4% [114].

- K^0_S *finding/efficiency*: we have determined K^0_S efficiency correction and associated systematic error following the recipe suggested by the tracking working group [114]. We assign a 2.1% systematic error.

- *Single photons, $\eta_{\gamma\gamma}$, π^0 efficiency*: following the efficiency corrections procedures suggested by neutrals working group [115, 106], we assign a systematic error of 3% per π^0 (η) and 1.8% for single photons.
- *Luminosity, B counting*: the *BABAR* B counting group recommends a systematic uncertainty of 1.1% on the number or $B\overline{B}$ pairs.
- *Branching fractions of the daughters*: this value is taken using the errors of the branching fractions of the daughters from PDG [98].
- *MC statistics*: this systematic error is calculated for the specific number of MC signal events simulated for each decay.
- *Event shape cuts*: a systematic uncertainty of 1% is assigned looking at the variation of the shape of signal MC events before and after the $\cos\theta_{\mathrm{T}}$ cut.
- *PID*: we have evaluated the systematic error due to PID vetoes following the recipe by *PID working group*. This is about 1%.

Quantity	$\eta_{\gamma\gamma}K^0_S$	$\eta_{3\pi}K^0_S$	$\eta_{\gamma\gamma}\eta_{\gamma\gamma}$	$\eta_{\gamma\gamma}\eta_{3\pi}$	$\eta_{3\pi}\eta_{3\pi}$	$\eta'_{\eta\pi\pi}\eta'_{\eta\pi\pi}$	$\eta'_{\rho\gamma}\eta'_{\eta\pi\pi}$
ML Fit bias (A)	0.7	0.5	1.3	0.5	3.3	3.4	1.2
MC/data Corr. (A)	1.0	0.4	3.4	1.0	1.1	0.2	1.2
MC statistics (M)	0.4	0.5	0.3	0.4	0.5	0.5	0.5
Branching frac. (M)	0.7	1.3	0.6	2.3	2.0	3.3	3.9
Track multip. (M)	1.0	1.0	1.0	1.0	1.0	1.0	1.0
Tracking eff/qual (M)	–	0.8	–	0.8	1.6	1.6	1.6
$\pi^0/\eta_{\gamma\gamma}$ eff.(M)	3.0	3.0	6.0	6.0	6.0	6.0	3.0
γ eff.(M)	–	–	–	–	–	–	1.8
K^0_S eff. (M)	2.1	2.1	–	–	–	–	–
Number $B\overline{B}$ (M)	1.1	1.1	1.1	1.1	1.1	1.1	1.1
$\cos\theta_{\mathrm{T}}$(M)	1.0	1.0	1.0	1.0	1.0	1.0	1.0
Particle ID (M)	–	1.0	–	1.0	1.0	1.0	1.0
Total Uncorr. (events) (A)	1.2	0.6	3.6	1.1	3.6	3.4	1.7
Total Uncorr. (%) (M)	0.8	1.4	0.7	2.3	2.1	3.3	3.9
Total Corr. (%)	4.1	4.3	6.3	6.4	6.4	6.4	4.4

Quantity	$\eta_{\gamma\gamma}\phi$	$\eta_{3\pi}\phi$	$\eta_{\gamma\gamma}\omega$	$\eta_{3\pi}\omega$	$\eta'_{\eta\pi\pi}\phi$	$\eta'_{\rho\gamma}\phi$	$\eta'_{\eta\pi\pi}\omega$	$\eta'_{\rho\gamma}\omega$
ML Fit bias (A)	1.8	0.3	1.7	1.1	6.5	0.6	0.8	2.0
MC/data Corr. (A)	0.6	0.6	0.4	0.4	0.3	0.8	0.4	2.6
MC statistics (M)	0.4	0.5	0.4	0.4	0.5	0.5	0.5	0.6
Branching frac. (M)	0.3	0.2	0.4	0.4	0.3	0.5	0.5	0.8
Track multip. (M)	1.0	1.0	1.0	1.0	1.0	1.0	1.0	1.0
Tracking eff/qual (M)	0.8	1.6	0.8	1.6	1.6	1.6	1.6	1.6
$\pi^0/\eta_{\gamma\gamma}$ eff.(M)	3.0	3.0	6.0	6.0	3.0	–	3.0	3.0
γ eff.(M)	–	–	–	–	–	1.8	–	1.8
Number $B\overline{B}$ (M)	1.1	1.1	1.1	1.1	1.1	1.1	1.1	1.1
$\cos\theta_{\mathrm{T}}$(M)	1.0	1.0	1.0	1.0	1.0	1.0	1.0	1.0
Particle ID (M)	1.0	1.0	1.0	1.0	1.0	1.0	1.0	1.0
Total Uncorr. (events) (A)	1.9	0.7	1.7	1.2	6.5	1.0	0.9	3.3
Total Uncorr. (%) (M)	0.5	0.5	0.6	0.6	0.6	0.7	0.7	1.0
Total Corr. (%)	3.7	4.0	6.4	4.0	3.2	4.0	3.2	4.5

Table 7.54: Estimates of systematic errors. We divide the systematics in two parts: uncorrelated errors (first part of the table) and correlated errors (second part of the table). Uncorrelated and correlated refer to the different sub-decays of the same mode. Some of these errors are additive (A) and given in events, others are multiplicative (M) and given in %. Contributions are combined in quadrature.

7.9 Results

In this section we present results of branching fractions and upper limits on branching fractions for each mode.

Summary of all results of ML fit is shown in tab. 7.59 and 7.60. We give the number of events to fit, the signal yield, the various efficiencies and product branching fractions, the fit bias, the statistical significance, the branching fraction results, and 90% confidence level upper limit.

The ML fit bias correction is obtained performing toy-experiments. We consider 500 MC toys where for each experiment we use a sample composed by the fitted number of events found in data in order to reproduce the fit bias in the signal events. We take the signal and $B\overline{B}$ peaking events from MC samples, and we generate the continuum background and charm events from PDFs. We do the same procedure using pure toys, where all events are generated from PDFs where we have the corresponding components, otherwise they are embedded (*e.g.* the $B\overline{B}$ peaking events when we don't have the corresponding component in the ML fit). In this way we extract fit biases, from both MC toys and pure toys, for each mode. We use the difference between these biases (MC toys bias minus pure toys bias) to correct the signal yield results fitted in on-peak data [117]. Results of these toys are shown in tab. 7.56–7.58. The events are taken from MC samples (MC) or generated from PDFs (PDFs), as indicated in the second column. The results for yields and their errors are fitted with Gaussians (or Crystal Ball functions in case of negative no-Gaussian tails). Their mean is shown in the third and fourth column. In the last column we show the biases in the signal yield. We show also the bias due to small sample, obtained as difference between the mean of the distribution of the signal yields and the mean of the Crystal Ball used to fit the distribution. We use the value of the bias to correct our number of signal yields to extract the branching fraction, upper limit, and the statistical significance.

The statistical error on the number of events is taken as the change in the central value when the quantity $\chi^2 = -2\ln\mathcal{L}$ changes by one unit. The statistical significance is taken as the square root of the difference between the value of χ^2 for zero signal and the value at its minimum.

Essentially in the fit for each mode we have as free parameters: signal yield, $B\overline{B}$ background yields, continuum background yield, and background ΔE, $m_{\rm ES}$, daughter resonances mass, and Fisher discriminant PDF parameters. In Appendix B we show the values of the background PDF parameters left floating in the final fit.

Systematic errors are evaluated in section 7.8.

We combine different sub-decays for the same decay mode adding the $-2\ln\mathcal{L}$ scans for the branching fractions of the sub-decays. The $-2\ln\mathcal{L}$ scans have been obtained fixing the branching fraction for each point on the scan (in our case the signal yields used for the branching fraction, where we also consider the fit bias correction) and refitting for all other parameters. We include in these curves the uncorrelated systematic errors, using a numerical convolution of the statistical likelihood with a Gaussian with mean 0 and sigma equal to the uncorrelated systematic error.

Events Type	# Events	Yield Mean	Yield Error	Bias (Bias Small Sample)
$\eta'_{\eta\pi\pi}\eta'_{\eta\pi\pi}$				
Signal	2 (MC)	2.37 ± 0.05	2.07 ± 0.02	0.4 ± 0.1
$q\bar{q}$	206 (PDFs)	205.63 ± 0.05	14.43 ± 0.02	
Signal	2 (PDFs)	2.33 ± 0.08	2.08 ± 0.03	0.3 ± 0.1 (-3.4)
$q\bar{q}$	206 (PDFs)	205.68 ± 0.08	14.43 ± 0.01	
$\eta'_{\rho\gamma}\eta'_{\eta\pi\pi}$				
Signal	9 (MC)	11.16 ± 0.34	7.74 ± 0.06	2.2 ± 0.3
$q\bar{q}$	7519 (PDFs)	7522.45 ± 3.68	115.81 ± 0.09	
$B\overline{B}$ charm	210 (PDFs)	205.14 ± 3.77	80.10 ± 0.15	
$B\overline{B}$ peaking	8 (MC)	7.30 ± 1.26	25.85 ± 0.17	
Signal	9 (PDFs)	8.89 ± 0.36	7.67 ± 0.06	-0.1 ± 0.4 $(+0.0)$
$q\bar{q}$	7519 (PDFs)	7522.85 ± 3.57	116.00 ± 0.09	
$B\overline{B}$ charm	210 (PDFs)	209.10 ± 3.61	80.44 ± 0.15	
$B\overline{B}$ peaking	8 (PDFs)	5.19 ± 1.24	25.80 ± 0.17	

Table 7.55: 500 Toy-experiments results to extract the ML fit bias for each mode. See text for details about the contents of various columns.

Events Type	# Events	Yield Mean	Yield Error	Bias (Bias Small Sample)
$\eta_{\gamma\gamma}K_S^0$				
Signal	21 (MC)	20.01 ± 0.44	11.07 ± 0.05	-1.0 ± 0.4
$q\bar{q}$	3150 (PDFs)	3145.88 ± 1.00	60.31 ± 0.03	
$B\overline{B}$ peaking	35 (MC)	40.18 ± 1.04	24.12 ± 0.12	
Signal	21 (PDFs)	20.43 ± 0.50	11.02 ± 0.06	-0.6 ± 0.5 $(+0.0)$
$q\bar{q}$	3150 (PDFs)	3151.64 ± 1.08	60.43 ± 0.03	
$B\overline{B}$ peaking	35 (PDFs)	33.95 ± 1.13	24.23 ± 0.13	
$\eta_{3\pi}K_S^0$				
Signal	5 (MC)	5.27 ± 0.27	5.69 ± 0.05	$+0.3 \pm 0.3$
$q\bar{q}$	1320 (PDFs)	1323.71 ± 0.27	36.76 ± 0.01	
$B\overline{B}$ peaking	4 (MC)	0 (fixed)		
Signal	5 (PDFs)	4.63 ± 0.29	5.55 ± 0.05	-0.4 ± 0.3 $(+0.0)$
$q\bar{q}$	1320 (PDFs)	1324.31 ± 0.29	36.76 ± 0.01	
$B\overline{B}$ peaking	4 (MC)	0 (fixed)		
$\eta_{\gamma\gamma}\eta_{\gamma\gamma}$				
Signal	26 (MC)	28.29 ± 0.46	11.85 ± 0.05	$+2.3 \pm 0.5$
$q\bar{q}$	2267 (PDFs)	2268.72 ± 0.46	48.76 ± 0.01	
$B\overline{B}$ peaking	4 (MC)	0 (fixed)		
Signal	26 (PDFs)	26.08 ± 0.52	11.66 ± 0.06	$+0.1 \pm 0.5$ $(+0.0)$
$q\bar{q}$	2267 (PDFs)	2270.94 ± 0.52	48.76 ± 0.01	
$B\overline{B}$ peaking	4 (MC)	0 (fixed)		
$\eta_{\gamma\gamma}\eta_{3\pi}$				
Signal	9 (MC)	9.46 ± 0.30	6.74 ± 0.05	$+0.5 \pm 0.3$
$q\bar{q}$	1789 (PDFs)	1790.53 ± 0.30	42.75 ± 0.01	
$B\overline{B}$ peaking	2 (MC)	0 (fixed)		
Signal	9 (PDFs)	9.01 ± 0.32	6.72 ± 0.05	$+0.0 \pm 0.3$ $(+0.0)$
$q\bar{q}$	1789 (PDFs)	1790.98 ± 0.32	42.75 ± 0.01	
$B\overline{B}$ peaking	2 (MC)	0 (fixed)		
$\eta_{3\pi}\eta_{3\pi}$				
Signal	0 (PDFs)	0.20 ± 0.12	3.09 ± 0.03	$+0.2 \pm 0.1$ (-3.3)
$q\bar{q}$	263 (PDFs)	262.79 ± 0.12	16.41 ± 0.01	

Table 7.56: 500 Toy-experiments results to extract the ML fit bias for each mode. See text for details about the contents of various columns.

Events Type	# Events	Yield Mean	Yield Error	Bias (Bias Small Sample)
$\eta_{\gamma\gamma}\omega$				
Signal	38 (MC)	40.70 ± 0.56	14.04 ± 0.06	$+2.7 \pm 0.6$
$q\bar{q}$	11017 (PDFs)	11007.01 ± 4.40	143.64 ± 0.09	
$B\overline{B}$ charm	217 (PDFs)	250.21 ± 4.82	107.92 ± 0.15	
$B\overline{B}$ peaking	58 (MC)	32.27 ± 3.33	73.41 ± 0.22	
Signal	38 (PDFs)	37.67 ± 0.63	13.96 ± 0.06	-0.3 ± 0.6 (+0.0)
$q\bar{q}$	11017 (PDFs)	11017.99 ± 4.48	143.70 ± 0.10	
$B\overline{B}$ charm	217 (PDFs)	218.21 ± 4.86	107.37 ± 0.15	
$B\overline{B}$ peaking	58 (PDFs)	56.09 ± 3.35	74.18 ± 0.23	
$\eta_{3\pi}\omega$				
Signal	6 (MC)	5.83 ± 0.33	6.84 ± 0.07	-0.2 ± 0.3
$q\bar{q}$	8516 (PDFs)	8519.08 ± 3.18	118.10 ± 0.09	
$B\overline{B}$ charm	83 (PDFs)	88.13 ± 3.18	74.27 ± 0.17	
$B\overline{B}$ peaking	8 (MC)	0 (fixed)		
Signal	6 (PDFs)	6.45 ± 0.33	7.01 ± 0.07	$+0.5 \pm 0.3$ (-1.0)
$q\bar{q}$	8516 (PDFs)	8517.99 ± 3.36	117.82 ± 0.09	
$B\overline{B}$ charm	83 (PDFs)	88.49 ± 3.35	73.91 ± 0.16	
$B\overline{B}$ peaking	8 (MC)	0 (fixed)		
$\eta_{\gamma\gamma}\phi$				
Signal	2 (MC)	2.31 ± 0.16	4.38 ± 0.04	$+0.3 \pm 0.2$
$q\bar{q}$	1397 (PDFs)	1398.74 ± 0.18	37.59 ± 0.01	
$B\overline{B}$ peaking	2 (MC)	0 (fixed)		
Signal	2 (PDFs)	2.20 ± 0.17	4.38 ± 0.04	$+0.2 \pm 0.2$ (-1.8)
$q\bar{q}$	1397 (PDFs)	1398.85 ± 0.32	37.65 ± 0.01	
$B\overline{B}$ peaking	2 (MC)	0 (fixed)		
$\eta_{3\pi}\phi$				
Signal	5 (MC)	5.21 ± 0.13	3.55 ± 0.03	$+0.2 \pm 0.1$
$q\bar{q}$	481 (PDFs)	480.78 ± 0.14	22.10 ± 0.00	
Signal	5 (PDFs)	4.94 ± 0.19	3.50 ± 0.04	-0.1 ± 0.2 (+0.0)
$q\bar{q}$	481 (PDFs)	481.05 ± 0.19	22.11 ± 0.01	

Table 7.57: 500 Toy-experiments results to extract the ML fit bias for each mode. See text for details about the contents of various columns.

Events Type	# Events	Yield Mean	Yield Error	Bias (Bias Small Sample)
$\eta'_{\eta\pi\pi}\phi$				
Signal	0	0.51 ± 0.08	2.23 ± 0.03	$+0.5 \pm 0.1$ (-6.5)
$q\bar{q}$	455 (PDFs)	454.72 ± 2.21	21.50 ± 0.03	
$\eta'_{\rho\gamma}\phi$				
Signal	12 (MC)	12.75 ± 0.33	7.29 ± 0.05	$+0.8 \pm 0.3$
$q\bar{q}$	6399 (PDFs)	6398.68 ± 2.65	98.19 ± 0.06	
$B\overline{B}$ charm	186 (PDFs)	202.54 ± 2.69	59.18 ± 0.12	
$B\overline{B}$ peaking	17 (MC)	0 (fixed)		
Signal	12 (PDFs)	12.30 ± 0.41	7.37 ± 0.07	$+0.3 \pm 0.4$ (+0.0)
$q\bar{q}$	6399 (PDFs)	6397.97 ± 3.19	98.28 ± 0.07	
$B\overline{B}$ charm	186 (PDFs)	203.72 ± 3.21	59.37 ± 0.15	
$B\overline{B}$ peaking	17 (MC)	0 (fixed)		
$\eta'_{\eta\pi\pi}\omega$				
Signal	14 (MC)	15.16 ± 0.27	7.11 ± 0.05	$+1.2 \pm 0.3$
$q\bar{q}$	8139 (PDFs)	8137.71 ± 4.04	125.01 ± 0.10	
$B\overline{B}$ charm	236 (PDFs)	239.23 ± 4.04	87.90 ± 0.15	
$B\overline{B}$ peaking	3 (MC)	0 (fixed)		
Signal	14 (PDFs)	13.71 ± 0.32	6.97 ± 0.05	-0.3 ± 0.3 (+0.0)
$q\bar{q}$	8139 (PDFs)	8135.76 ± 3.91	124.92 ± 0.10	
$B\overline{B}$ charm	236 (PDFs)	242.57 ± 3.91	87.80 ± 0.14	
$B\overline{B}$ peaking	3 (MC)	0 (fixed)		
$\eta'_{\rho\gamma}\omega$				
Signal	15 (MC)	18.40 ± 0.74	15.71 ± 0.12	$+3.4 \pm 0.7$
$q\bar{q}$	48832 (PDFs)	48828.68 ± 16.84	414.81 ± 0.41	
$B\overline{B}$ charm	3692 (PDFs)	3717.33 ± 15.68	330.53 ± 0.35	
$B\overline{B}$ peaking	60 (MC)	34.74 ± 4.79	104.24 ± 0.24	
Signal	15 (PDFs)	14.96 ± 0.93	15.53 ± 0.15	-0.0 ± 0.9 (+0.0)
$q\bar{q}$	48832 (PDFs)	48853.86 ± 20.06	415.20 ± 0.51	
$B\overline{B}$ charm	3692 (PDFs)	3681.46 ± 18.36	330.63 ± 0.45	
$B\overline{B}$ peaking	60 (PDFs)	48.73 ± 6.25	104.93 ± 0.28	

Table 7.58: 500 Toy-experiments results to extract the ML fit bias for each mode. See text for details about the contents of various columns.

ML Fit Quantity	$\eta_{\gamma\gamma}K^0_S$	$\eta_{3\pi}K^0_S$	$\eta_{\gamma\gamma}\eta_{\gamma\gamma}$	$\eta_{\gamma\gamma}\eta_{3\pi}$	$\eta_{3\pi}\eta_{3\pi}$	$\eta'_{\eta\pi\pi}\eta'_{\eta\pi\pi}$	$\eta'_{\rho\gamma}\eta'_{\eta\pi\pi}$
Events into fit	3206	1329	2297	1800	263	208	7746
Signal yield	20^{+10}_{-9}	5^{+6}_{-4}	28^{+13}_{-12}	9^{+7}_{-6}	-5^{+4}_{-3}	2^{+2}_{-1}	11^{+9}_{-7}
$B\overline{B}$ charm yield	–	–	–	–	–	–	210 ± 83
$B\overline{B}$ peaking yield	35 ± 25	–	–	–	–	–	8 ± 22
# Data Combs/event	1.02	1.06	1.04	1.08	1.12	1.37	1.22
# MC Combs/event	1.02	1.06	1.04	1.09	1.14	1.37	1.24
SCF(%)	2.3	5.2	4.0	8.2	11.3	13.3	13.1
Fit bias (events)	-0.4 ± 0.7	$+0.7 \pm 0.4$	$+2.2 \pm 0.7$	$+0.5 \pm 0.4$	-0.2 ± 0.1	$+0.1 \pm 0.1$	$+2.3 \pm 0.5$
MC ϵ (%)	33.3	21.4	25.4	19.2	11.9	21.1	20.4
$\pi^0/\eta_{\gamma\gamma}$ corr. (%)	97.1	96.8	94.2	93.9	93.6	94.2	97.1
K^0_S corr. (%)	95.7	95.7	–	–	–	–	–
Corr. ϵ (%)	30.9	19.8	23.9	18.0	11.1	19.9	19.8
$\prod \mathcal{B}_i$ (%)	13.6	7.9	15.5	17.9	5.2	3.1	10.3
Corr. $\epsilon \times \prod \mathcal{B}_i$ (%)	4.20	1.56	3.70	3.22	0.58	0.62	2.04
Stat. sign. (σ)	2.5	1.1	2.5	1.6	0.0	2.2	1.3
$\mathcal{B}(\times 10^{-6})$	1.0 ± 0.5	$0.6^{+0.8}_{-0.6}$	$1.5^{+0.8}_{-0.7}$	$0.6^{+0.5}_{-0.4}$	$-1.8^{+1.5}_{-1.1}$	$0.7^{+0.8}_{-0.5}$	$0.9^{+0.9}_{-0.7}$
Stat. sign. with syst. (σ)	2.6		2.4			1.3	
Combined $\mathcal{B}$	$0.9^{+0.5}_{-0.4} \pm 0.1$		$0.8 \pm 0.4 \pm 0.1$			$0.9^{+0.8}_{-0.7} \pm 0.1$	
90% C.L. UL(incl. syst.)	1.6		1.4			2.1	

Table 7.59: Branching fractions results.

ML Fit Quantity	$\eta_{\gamma\gamma}\phi$	$\eta_{3\pi}\phi$	$\eta_{\gamma\gamma}\omega$	$\eta_{3\pi}\omega$	$\eta'_{\eta\pi\pi}\phi$	$\eta'_{\rho\gamma}\phi$	$\eta'_{\eta\pi\pi}\omega$	$\eta'_{\rho\gamma}\omega$
Events into fit	1401	486	11333	8613	455	6614	8388	52599
Signal yield	2^{+5}_{-4}	5^{+4}_{-3}	41^{+15}_{-13}	6^{+8}_{-7}	0^{+2}_{-1}	12^{+9}_{-8}	15^{+7}_{-6}	18^{+18}_{-16}
$B\overline{B}$ charm yield	–	–	217 ± 104	83 ± 80	–	186 ± 54	236 ± 88	3692 ± 303
$B\overline{B}$ peaking yield	–	–	58 ± 75	–	–	–	–	58 ± 108
# Data Combs/event	1.02	1.07	1.22	1.30	1.17	1.06	1.43	1.28
# MC Combs/event	1.02	1.07	1.21	1.29	1.18	1.07	1.41	1.26
SCF(%)	2.9	6.0	14.9	18.7	6.8	7.3	19.7	19.1
Fit bias (events)	$+0.1 \pm 0.2$	$+0.3 \pm 0.2$	$+3.0 \pm 0.9$	-0.7 ± 0.5	-0.5 ± 0.1	$+0.5 \pm 0.5$	$+1.5 \pm 0.4$	$+3.4 \pm 1.1$
MC ϵ (%)	30.2	18.9	19.9	14.0	25.1	23.9	19.1	15.7
$\pi^0/\eta_{\gamma\gamma}$ corr. (%)	97.1	96.8	93.9	93.6	97.1	–	93.9	96.8
Corr. ϵ (%)	29.3	18.3	18.7	13.1	24.4	23.9	17.9	15.2
$\prod \mathcal{B}_i$ (%)	19.4	11.2	35.1	20.2	8.6	14.5	15.6	26.2
Corr. $\epsilon \times \prod \mathcal{B}_i$ (%)	5.68	2.05	6.56	2.65	2.10	3.47	2.79	3.98
Stat. sign. (σ)	0.5	2.0	3.5	1.0	0.7	1.5	3.2	0.9
$\mathcal{B}(\times 10^{-6})$	$0.07^{+0.19}_{-0.15}$	$0.49^{+0.42}_{-0.31}$	$1.2^{+0.5}_{-0.4}$	0.5 ± 0.6	$0.05^{+0.21}_{-0.10}$	$0.71^{+0.56}_{-0.50}$	$1.0^{+0.5}_{-0.4}$	$0.8^{+1.0}_{-0.9}$
Stat. sign. with syst. (σ)	1.7		3.5		1.3		3.1	
Combined $\mathcal{B}$	$0.22^{+0.19}_{-0.15} \pm 0.01$		$1.0^{+0.4}_{-0.3} \pm 0.1$		$0.5 \pm 0.4 \pm 0.1$		$1.0^{+0.5}_{-0.4} \pm 0.1$	
90% C.L. UL(incl. syst.)	0.52		1.6		1.2		1.7	

Table 7.60: Branching fractions results.

7.9.1 $-\ln\mathcal{L}$ Plots

In fig. 7.2 we show the $-2\ln\mathcal{L}$ scans for the branching fractions. These figures are obtained fixing the plotted parameter (in our case the signal yields used for the branching fraction) and refitting for all other parameters. We include in these curves the uncorrelated systematic errors, using a numerical convolution of the statistical likelihood with a Gaussian with mean 0 and sigma equal to the systematic error.

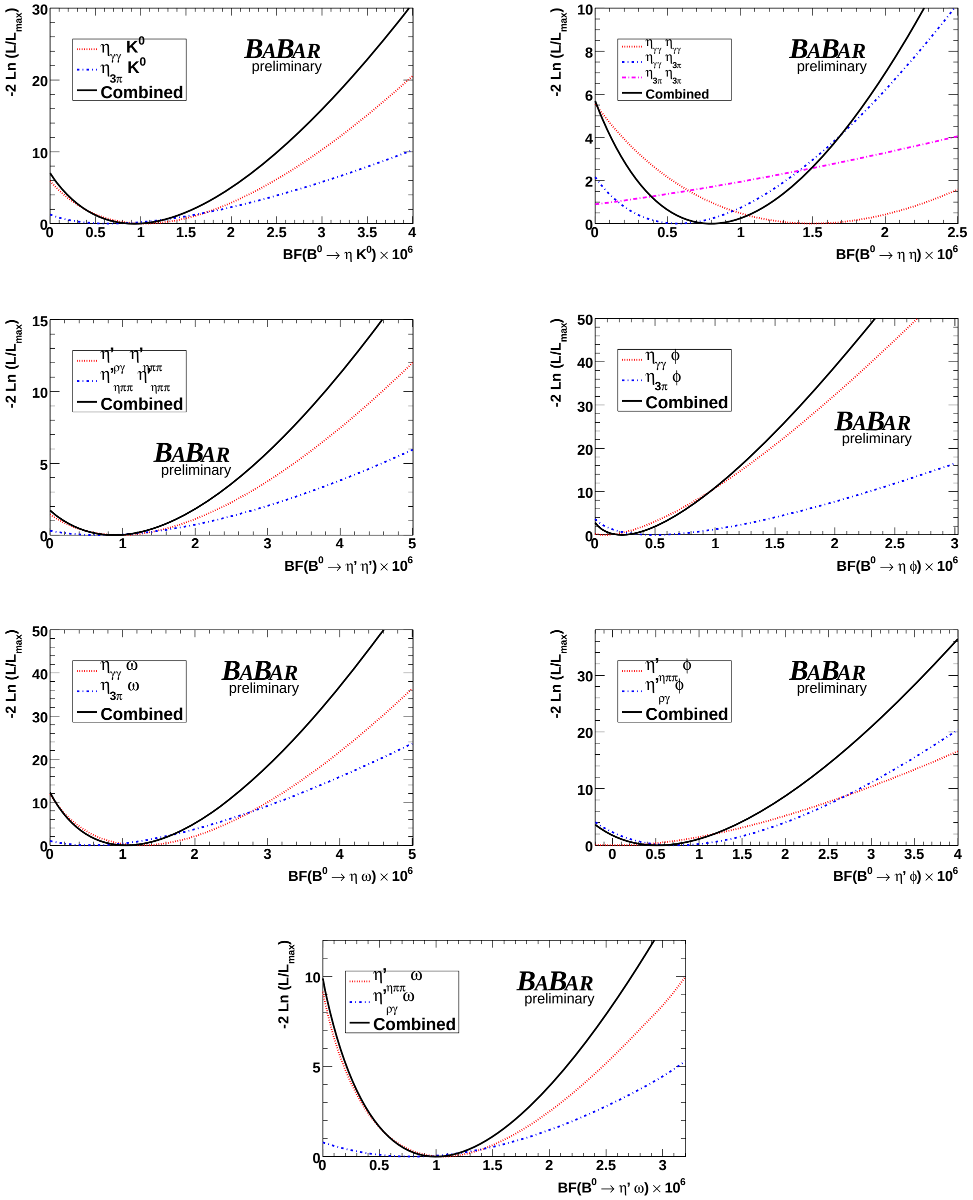

Figure 7.2: $-2\ln\mathcal{L}$ as a function of the branching fraction. Plots are for each mode. These curves include the uncorrelated systematic errors.

7.9.2 Likelihood Ratio

In fig. 7.3 and Figure 7.4 we show the likelihood ratio $R = \mathcal{P}_s/[\mathcal{P}_s + \sum \mathcal{P}_b]$ for each sub-decay mode.

7.9.3 Projections

We draw the $m_{\rm ES}$ and ΔE projection plots for our decays. To reduce the contribution of background, we optimize a cut on the quantity:

$$R = \frac{\mathcal{P}_s}{\mathcal{P}_s + \sum \mathcal{P}_b} \tag{7.3}$$

where P_s and P_b are the probability for the event to be signal or background, respectively. These probabilities are calculated from PDFs, excluding in the computation the variable being plotted. In fig. 7.5 and 7.6 we show such projections for the various modes, where we sum the submodes together. Fit curves shown are not a fit to the data in the histogram but the projection of the overall fit scaled to take into account the effect of the cut on R.

7.9.4 sPlots

In Appendix D we show the sPlots for each mode. We report also the yields results when we fit removing one discriminating variable at a time from the fit. The $sPlot$ technique is explained in detail in sec. 4.4.3.

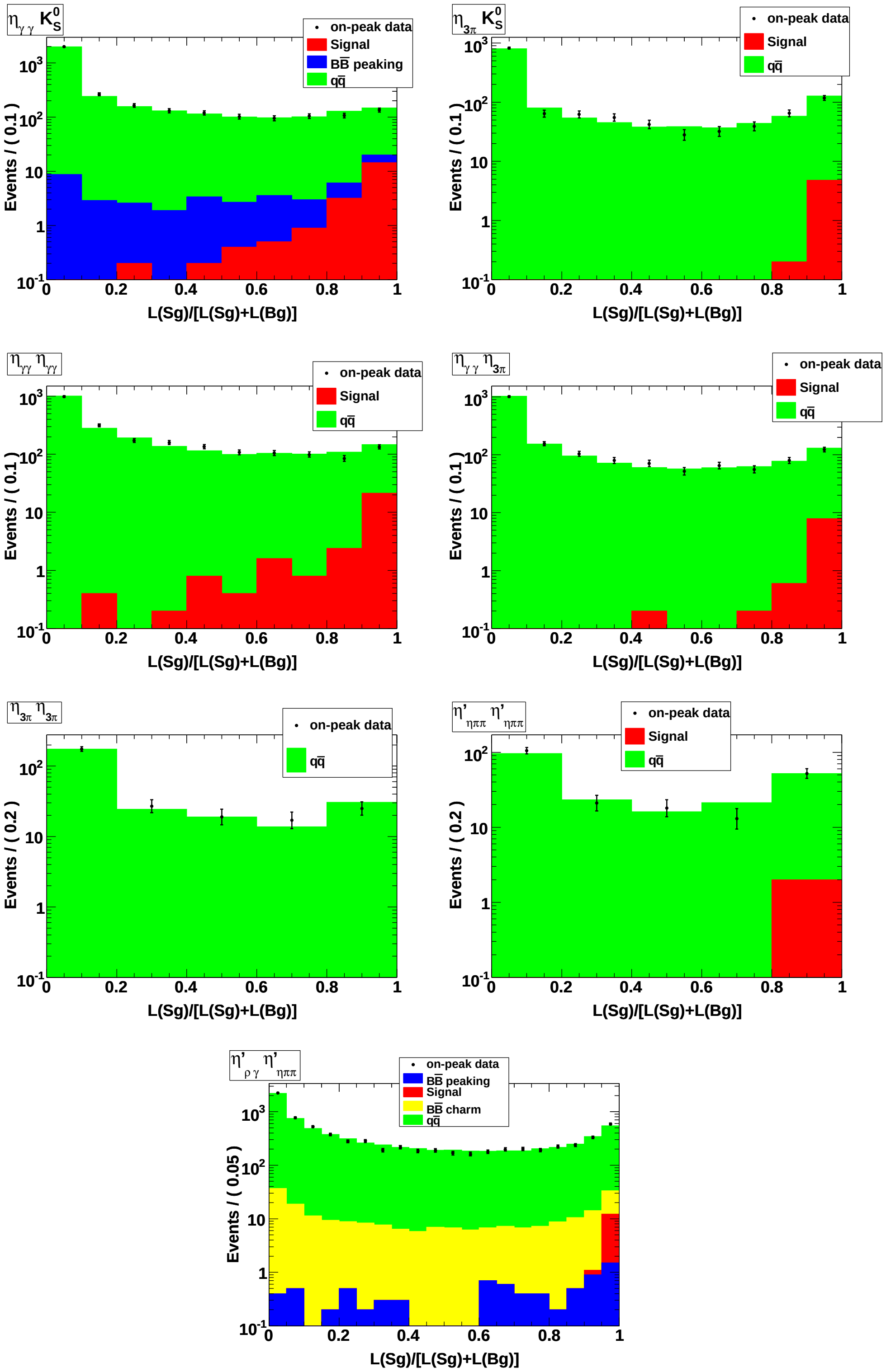

Figure 7.3: The likelihood ratio $R = \mathcal{P}_s/[\mathcal{P}_s + \sum \mathcal{P}_b]$ for each sub-decay mode. Points represent on-resonance data, stacked solid histograms are represents events belonging to to each fit component, generated from PDFs (average of 10 generations).

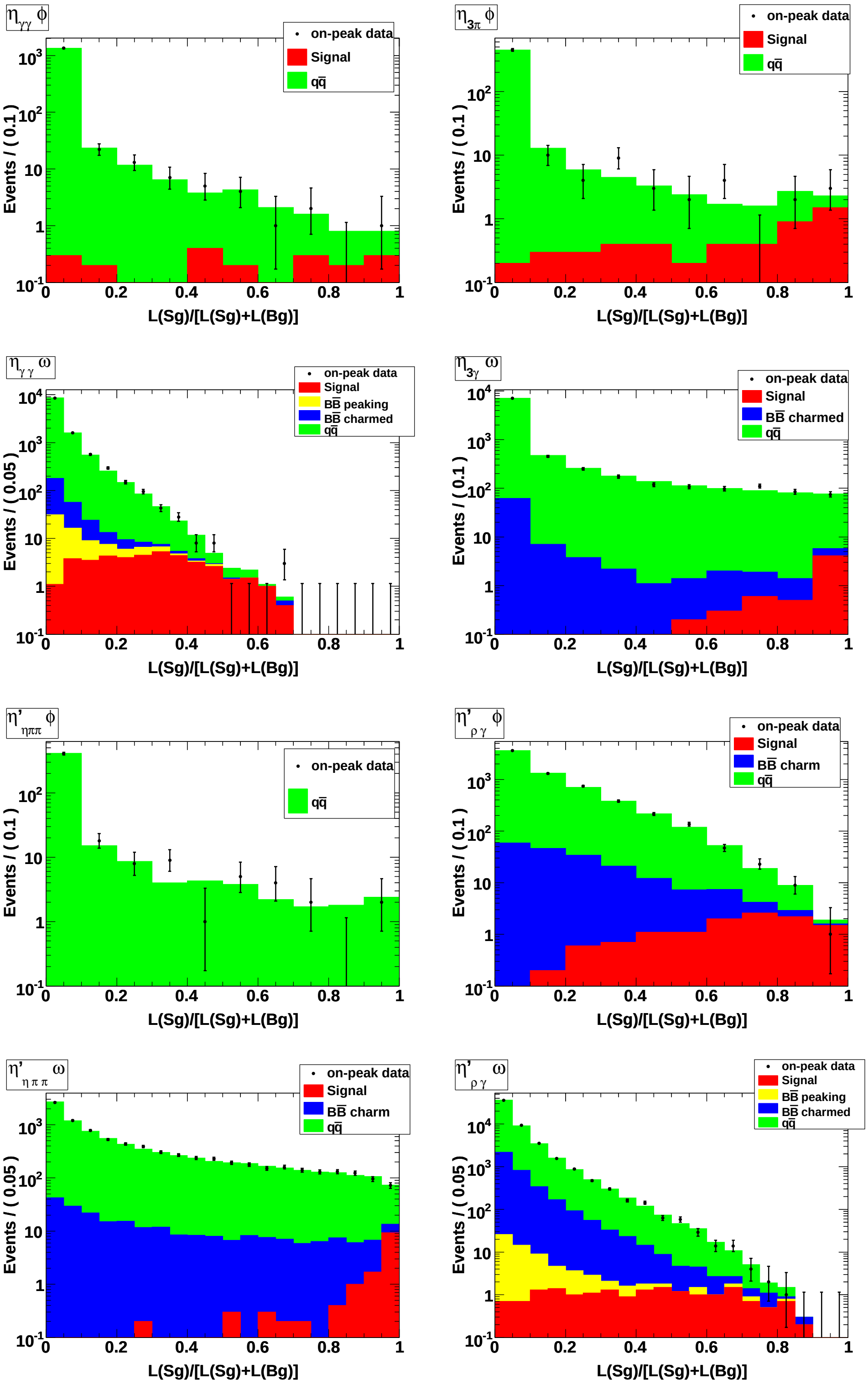

Figure 7.4: The likelihood ratio $R = \mathcal{P}_s/[\mathcal{P}_s + \sum \mathcal{P}_b]$ for each sub-decay mode. Points represent on-resonance data, stacked solid histograms are represents events belonging to to each fit component, generated from PDFs (average of 10 generations).

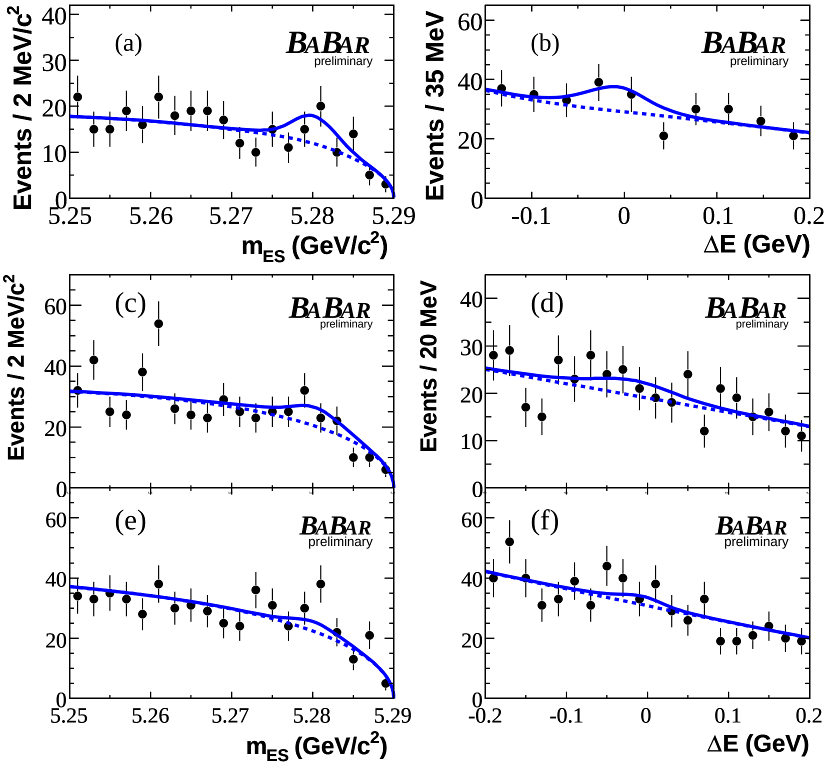

Figure 7.5: The B candidate m_{ES} and ΔE projections for ηK^0_S (a, b), $\eta\eta$ (c, d), and $\eta'\eta'$ (e, f) for the corresponding sub-decays together. Points with errors represent the data, solid curves the full fit functions, and dashed curves the background functions.

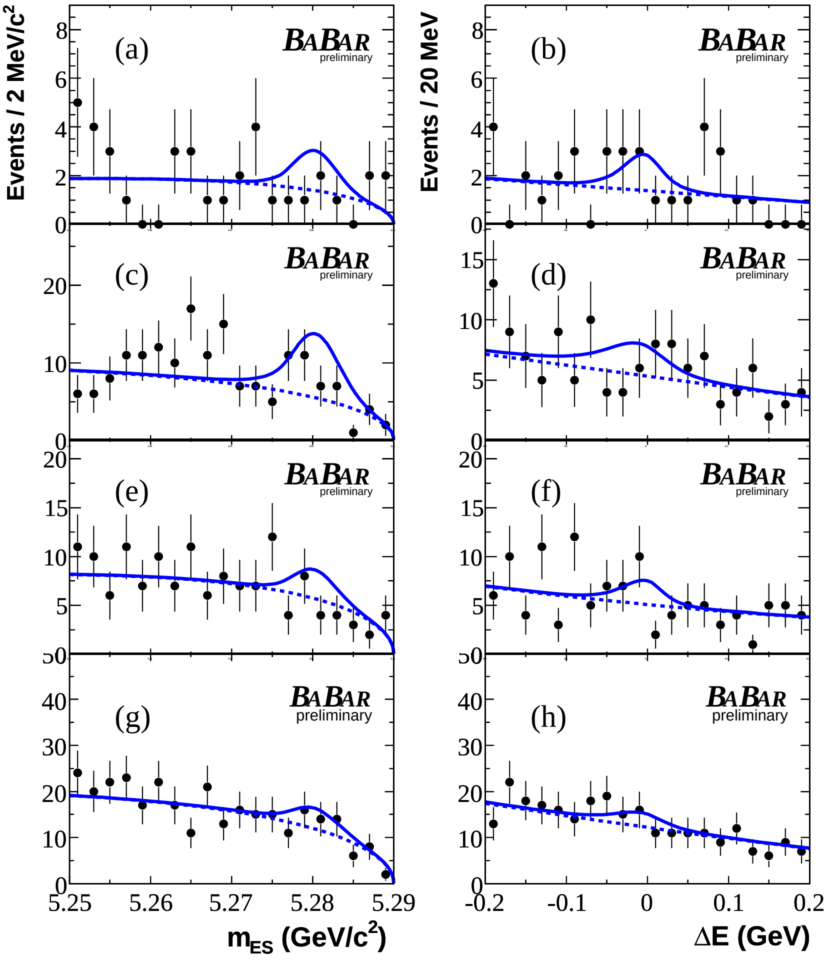

Figure 7.6: The B candidate m_{ES} and ΔE projections for $\eta\phi$ (a, b), $\eta\omega$ (c, d), $\eta'\phi$ (e, f), and $\eta'\omega$ (g, h) for the corresponding sub-decays together. Points with errors represent the data, solid curves the full fit functions, and dashed curves the background functions.

Conclusions

In this thesis work we have measured the following upper limits at 90% of confidence level, for B meson decays (in units of 10^{-6}), using a statistics of 465.0×10^6 $B\overline{B}$ pairs:

$$\begin{aligned}
\mathcal{B}(B^0 \to \eta K^0) &< 1.6 \\
\mathcal{B}(B^0 \to \eta\eta) &< 1.4 \\
\mathcal{B}(B^0 \to \eta'\eta') &< 2.1 \\
\mathcal{B}(B^0 \to \eta\phi) &< 0.52 \\
\mathcal{B}(B^0 \to \eta\omega) &< 1.6 \\
\mathcal{B}(B^0 \to \eta'\phi) &< 1.2 \\
\mathcal{B}(B^0 \to \eta'\omega) &< 1.7
\end{aligned}$$

We have no observation of any decay mode, statistical significance for our measurements is in the range 1.3–3.5 standard deviation. We have a 3.5σ evidence for $B\to\eta\omega$ and a 3.1σ evidence for $B\to\eta'\omega$. The absence of observation of the $B^0\to\eta K^0$ open an issue related to the large difference compared to the charged mode $B^+\to\eta K^+$ branching fraction, which is measured to be $3.7 \pm 0.4 \pm 0.1$ [118]. Our results represent substantial improvements of the previous ones [109, 110, 111] and are consistent with theoretical predictions. All these results were presented at *Flavor Physics and CP Violation (FPCP) 2008* Conference, that took place in Taipei, Taiwan. They will be soon included into a paper to be submitted to *Physical Review D*.

For time-dependent analysis, we have reconstructed 1820 ± 48 flavor-tagged $B^0 \to \eta' K^0$ events, using the final BABAR statistic of 467.4×10^6 $B\overline{B}$ pairs. We use these events to measure the time-dependent asymmetry parameters S and C. We find $S = 0.59 \pm 0.08 \pm 0.02$, and $C = -0.06 \pm 0.06 \pm 0.02$. A non-zero value of C would represent a directly *CP* non-conserving component in $B^0 \to \eta' K^0$, while S would be equal to $\sin 2\beta$ measured in $B^0 \to J/\psi K_S^0$ [108], a mixing-decay interference effect, provided the decay is dominated by amplitudes of a single weak phase. The new measured value of S can be considered in agreement with the expectations of the "Standard Model", inside the experimental and theoretical uncertainties. Inconsistency of our result for S with CP conservation ($S = 0$) has a significance of 7.1 standard deviations (statistical and systematics included). Our result for the direct-CP violation parameter C is 0.9 standard deviations from zero (statistical and systematics included). Our results are in agreement with the previous ones [18]. Despite the statistics is only 20% larger than the one used in previous measurement, we improved of 20% the error on S and of 14% the error on C. This error is the smaller ever achieved, by both *BABAR* and Belle, in Time-Dependent CP Violation Parameters measurement is a $b \to s$ transition. Results of this analysis contributed to the ones presented at *International Conference on High Energy Physics (ICHEP) 2008*, that took place in Philadelphia, USA. They are included into a paper already submitted to *Physical Review D* [19].

Appendix A

PDF Libraries for TD CP-Asymmetries Measurements

We show for each decay modes the signal, continuum background and $B\bar{B}$ background PDFs used in ML fits. We show also tables of the correlations between fit variables and final values of parameters which are floating in the final fit. Signal PDFs are determined from MC signal events. For background continuum PDFs we have used on-peak side-bands. For $B\bar{B}$ background PDFs we have used MC events.

A.1 $B^0 \to \eta'_{\eta(\gamma\gamma)\pi\pi} K^0_{S(\pi^+\pi^-)}$

	$m_{\rm ES}$	ΔE	Fisher	Δt	$\sigma_{\Delta t}$
$m_{\rm ES}$	$+1.000$				
ΔE	$+0.006$	$+1.000$			
$\mathcal{F}$	$+0.013$	$+0.006$	$+1.000$		
Δt	$+0.002$	$+0.006$	$+0.008$	$+1.000$	
$\sigma_{\Delta t}$	-0.015	-0.017	-0.058	-0.014	$+1.000$

Table A.1: Correlation matrix for signal MC events.

	$m_{\rm ES}$	ΔE	Fisher	Δt	$\sigma_{\Delta t}$
$m_{\rm ES}$	$+1.000$				
ΔE	-0.050	$+1.000$			
$\mathcal{F}$	$+0.025$	$+0.044$	$+1.000$		
Δt	-0.068	$+0.000$	-0.019	$+1.000$	
$\sigma_{\Delta t}$	-0.066	$+0.028$	-0.039	-0.016	$+1.000$

Table A.2: Correlation matrix in on-peak side band data.

```
mES_EppKs_xi_bg_float = -14.821 +/- 8.681 L(-50.000 - 10.000)
deltaE_EppKs_c1_bg_float = -0.376 +/- 0.055 L(-2.000 - 2.000)
fisher_EppKs_Mu1_bg_float = -1.097 +/- 0.028 L(-2.000 - 0.000)
fisher_EppKs_Sigma1_bg_float = 0.343 +/- 0.020 L(0.000 - 5.000)
fisher_EppKs_Sigma2_bg_float = 0.318 +/- 0.019 L(0.000 - 5.000)
deltaT_Mu2_bg_EppKs_float = -0.024 +/- 0.365 L(-10.000 - 10.000)
deltaT_Sigma2_bg_EppKs_float = 3.182 +/- 0.256 L(0.000 - 30.000)
deltaT_Mu1_bg_EppKs_float = 0.024 +/- 0.057 L(-10.000 - 10.000)
deltaT_Sigma1_bg_EppKs_float = 1.307 +/- 0.043 L(0.000 - 3.000)
fBg_cat1_EppKs = 0.007 +/- 0.003 L(0.000 - 0.300)
fBg_cat2_EppKs = 0.065 +/- 0.008 L(0.000 - 0.300)
fBg_cat3_EppKs = 0.152 +/- 0.012 L(0.000 - 0.300)
fBg_cat4_EppKs = 0.092 +/- 0.010 L(0.000 - 0.300)
fBg_cat5_EppKs = 0.151 +/- 0.012 L(0.000 - 0.300)
fBg_cat6_EppKs = 0.109 +/- 0.010 L(0.000 - 0.300)
```

Final values for the parameters which were allowed to float in the fit.

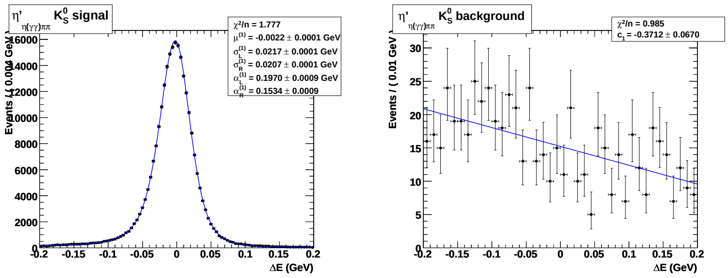

Figure A.1: ΔE PDFs: signal, Cruijff function; continuum background, Chebyshev first order polynomial.

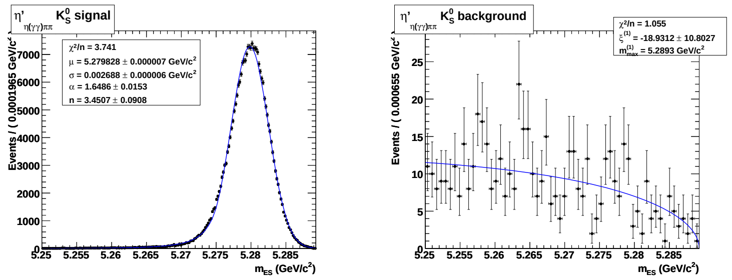

Figure A.2: m_{ES} PDFs: signal, Crystal Ball; continuum background, Argus function.

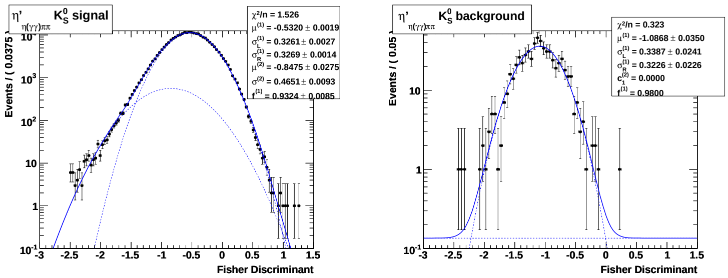

Figure A.3: Fisher PDFs: signal, asymmetric Gaussian plus Gaussian; continuum background, asymmetric Gaussian plus first order Chebyshev polynomial.

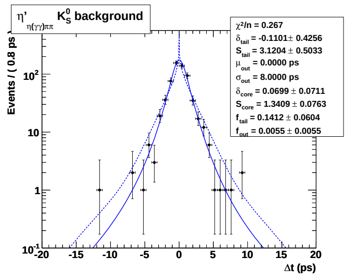

Figure A.4: Δt PDFs: continuum background, triple Gaussian where we use $\Delta t/\sigma_{\Delta t}$ as in signal Δt resolution model.

A.2 $B^0 \rightarrow \eta'_{\eta(3\pi)\pi\pi} K^0_{S(\pi^+\pi^-)}$

	$m_{\rm ES}$	ΔE	Fisher	Δt	$\sigma_{\Delta t}$
$m_{\rm ES}$	$+1.000$				
ΔE	-0.043	$+1.000$			
$\mathcal{F}$	$+0.001$	-0.002	$+1.000$		
Δt	$+0.013$	$+0.006$	$+0.021$	$+1.000$	
$\sigma_{\Delta t}$	-0.001	-0.002	-0.066	-0.021	$+1.000$

Table A.3: Correlation matrix for signal MCTruth MC events.

	$m_{\rm ES}$	ΔE	Fisher	Δt	$\sigma_{\Delta t}$
$m_{\rm ES}$	$+1.000$				
ΔE	$+0.142$	$+1.000$			
$\mathcal{F}$	$+0.015$	-0.000	$+1.000$		
Δt	-0.022	$+0.006$	$+0.023$	$+1.000$	
$\sigma_{\Delta t}$	$+0.001$	$+0.040$	-0.054	-0.063	$+1.000$

Table A.4: Correlation matrix for signal SCF MC events.

	$m_{\rm ES}$	ΔE	Fisher	Δt	$\sigma_{\Delta t}$
$m_{\rm ES}$	$+1.000$				
ΔE	$+0.048$	$+1.000$			
$\mathcal{F}$	$+0.045$	$+0.193$	$+1.000$		
Δt	-0.100	$+0.045$	-0.050	$+1.000$	
$\sigma_{\Delta t}$	$+0.095$	$+0.072$	$+0.079$	-0.078	$+1.000$

Table A.5: Correlation matrix in on-peak side band data.

```
mES_E5pKs_xi_bg_float = -12.387 +/- 14.783 L(-50.000 - 0.000)
deltaE_E5pKs_c1_bg_float = -0.480 +/- 0.102 L(-2.000 - 2.000)
fisher_E5pKs_Mu1_bg_float = -0.979 +/- 0.050 L(-2.000 - 0.000)
fisher_E5pKs_Sigma1_bg_float = 0.396 +/- 0.033 L(0.000 - 5.000)
fisher_E5pKs_Sigma2_bg_float = 0.240 +/- 0.036 L(0.000 - 5.000)
deltaT_Mu2_bg_E5pKs_float = -1.003 +/- 0.449 L(-10.000 - 10.000)
deltaT_Sigma2_bg_E5pKs_float = 2.534 +/- 0.313 L(0.000 - 30.000)
deltaT_Mu1_bg_E5pKs_float = -0.027 +/- 0.111 L(-10.000 - 10.000)
deltaT_Sigma1_bg_E5pKs_float = 1.165 +/- 0.079 L(0.000 - 3.000)
fBg_cat1_E5pKs = 0.005 +/- 0.004 L(-0.100 - 0.400)
fBg_cat2_E5pKs = 0.062 +/- 0.015 L(-0.100 - 0.400)
fBg_cat3_E5pKs = 0.147 +/- 0.022 L(-0.100 - 0.400)
fBg_cat4_E5pKs = 0.075 +/- 0.016 L(-0.100 - 0.400)
fBg_cat5_E5pKs = 0.140 +/- 0.022 L(-0.100 - 0.400)
fBg_cat6_E5pKs = 0.121 +/- 0.020 L(-0.100 - 0.400)
```

Final values for the parameters which were allowed to float in the fit.

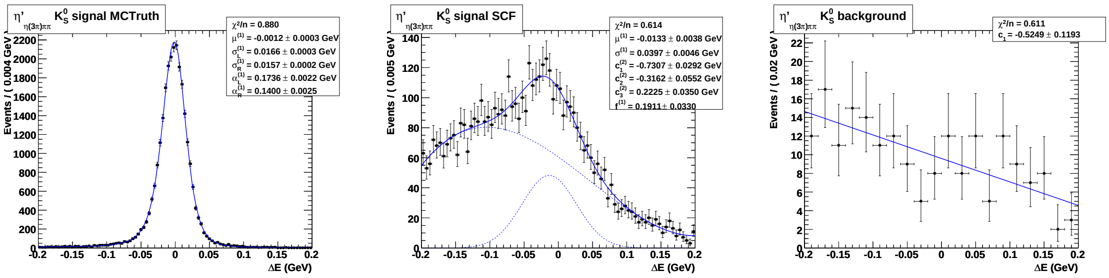

Figure A.5: ΔE PDFs: signal MCTruth, Cruijff function; signal SCF, Gaussian plus third order Chebyshev polynomial; continuum background, first order Chebyshev polynomial;

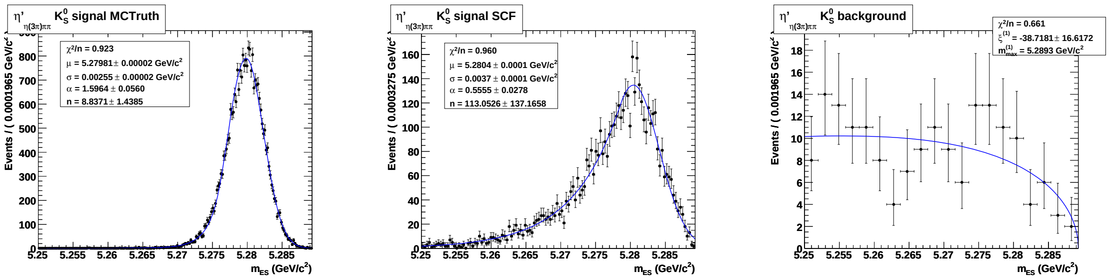

Figure A.6: m_{ES} PDFs: signal MCTruth, Crystal Ball; signal SCF, Crystal Ball continuum background, Argus function

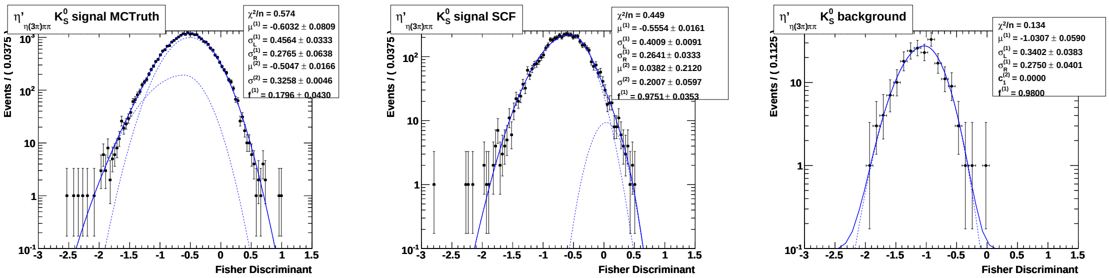

Figure A.7: Fisher PDFs: signal MCTruth, asymmetric Gaussian plus Gaussian; signal SCF, asymmetric Gaussian plus Gaussian;continuum background, asymmetric Gaussian plus first order Chebyshev polynomial.

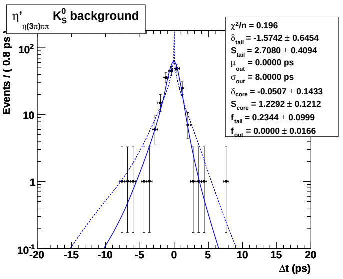

Figure A.8: Δt PDFs: continuum background, triple Gaussian where we use $\Delta t/\sigma_{\Delta t}$ as in signal Δt resolution model.

A.3 $B^0 \rightarrow \eta'_{\rho\gamma} K^0_{S(\pi^+\pi^-)}$

	$m_{\rm ES}$	ΔE	Fisher	Δt	$\sigma_{\Delta t}$
$m_{\rm ES}$	$+1.000$				
ΔE	$+0.043$	$+1.000$			
$\mathcal{F}$	$+0.033$	$+0.018$	$+1.000$		
Δt	$+0.001$	-0.004	$+0.008$	$+1.000$	
$\sigma_{\Delta t}$	-0.011	-0.012	-0.059	-0.016	$+1.000$

Table A.6: Correlation matrix for signal MC events.

	$m_{\rm ES}$	ΔE	Fisher	Δt	$\sigma_{\Delta t}$
$m_{\rm ES}$	$+1.000$				
ΔE	$+0.004$	$+1.000$			
$\mathcal{F}$	$+0.010$	$+0.030$	$+1.000$		
Δt	$+0.025$	$+0.029$	-0.029	$+1.000$	
$\sigma_{\Delta t}$	-0.003	$+0.049$	$+0.026$	$+0.044$	$+1.000$

Table A.7: Correlation matrix in on-peak side band data.

	$m_{\rm ES}$	ΔE	Fisher	Δt	$\sigma_{\Delta t}$
$m_{\rm ES}$	$+1.000$				
ΔE	$+0.228$	$+1.000$			
$\mathcal{F}$	$+0.013$	$+0.092$	$+1.000$		
Δt	-0.024	-0.005	$+0.002$	$+1.000$	
$\sigma_{\Delta t}$	-0.013	$+0.006$	-0.068	-0.018	$+1.000$

Table A.8: Correlation matrix in $B\overline{B}$ peaking events with positive ΔE mean (+).

	$m_{\rm ES}$	ΔE	Fisher	Δt	$\sigma_{\Delta t}$
$m_{\rm ES}$	$+1.000$				
ΔE	-0.044	$+1.000$			
$\mathcal{F}$	$+0.051$	-0.035	$+1.000$		
Δt	-0.000	-0.016	-0.002	$+1.000$	
$\sigma_{\Delta t}$	-0.008	$+0.022$	-0.071	-0.009	$+1.000$

Table A.9: Correlation matrix in $B\overline{B}$ peaking events with negative ΔE mean (–).

	$m_{\rm ES}$	ΔE	Fisher	Δt	$\sigma_{\Delta t}$
$m_{\rm ES}$	$+1.000$				
ΔE	$+0.026$	$+1.000$			
$\mathcal{F}$	$+0.057$	-0.006	$+1.000$		
Δt	$+0.002$	$+0.008$	-0.003	$+1.000$	
$\sigma_{\Delta t}$	$+0.019$	$+0.010$	-0.015	$+0.015$	$+1.000$

Table A.10: Correlation matrix in $B\overline{B}$ charmed events.

```
mES_ErgKs_xi_bg_float = -21.383 +/- 1.931 L(-50.000 - 0.000)
deltaE_ErgKs_c1_bg_float = -0.308 +/- 0.013 L(-2.000 - 2.000)
fisher_ErgKs_Mu1_bg_float = -1.127 +/- 0.004 L(-2.000 - 0.000)
fisher_ErgKs_Sigma1_bg_float = 0.350 +/- 0.003 L(0.000 - 5.000)
deltaT_Mu2_bg_ErgKs_float = 0.180 +/- 0.065 L(-10.000 - 10.000)
deltaT_Sigma2_bg_ErgKs_float = 2.582 +/- 0.050 L(0.000 - 30.000)
deltaT_Mu1_bg_ErgKs_float = 0.048 +/- 0.013 L(-10.000 - 10.000)
deltaT_Sigma1_bg_ErgKs_float = 1.190 +/- 0.010 L(0.000 - 3.000)
fBg_cat1_ErgKs = 0.0028 +/- 0.0005 L(-0.2000 - 0.3000)
fBg_cat2_ErgKs = 0.078 +/- 0.002 L(0.000 - 0.300)
fBg_cat3_ErgKs = 0.155 +/- 0.003 L(0.000 - 0.300)
fBg_cat4_ErgKs = 0.119 +/- 0.003 L(0.000 - 0.300)
fBg_cat5_ErgKs = 0.137 +/- 0.003 L(0.000 - 0.300)
fBg_cat6_ErgKs = 0.116 +/- 0.002 L(0.000 - 0.300)
C_Bb_ErgKs = -0.102 +/- 0.169 L(-3.000 - 3.000)
S_Bb_ErgKs = 0.278 +/- 0.213 L(-3.000 - 3.000)
fBb_cat1_ErgKs = 0.133 +/- 0.036 L(0.000 - 0.300)
fBb_cat2_ErgKs = 0.205 +/- 0.054 L(0.000 - 0.300)
fBb_cat3_ErgKs = 0.267 +/- 0.053 L(0.000 - 0.300)
fBb_cat4_ErgKs = 0.133 +/- 0.042 L(0.000 - 0.300)
fBb_cat5_ErgKs = 0.204 +/- 0.050 L(0.000 - 0.300)
fBb_cat6_ErgKs = 0.072 +/- 0.040 L(0.000 - 0.300)
```

Final values for the parameters which were allowed to float in the fit.

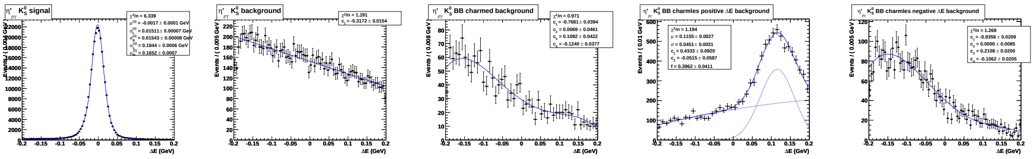

Figure A.9: ΔE PDFs: signal , Cruijff function; continuum background, Chebyshev first order polynomial, $B\overline{B}$ charmed background, Chebyshev fourth order polynomiall; $B\overline{B}$ peaking background (+), Gaussian plus Chebyshev second order polynomial; $B\overline{B}$ peaking background (-), Chebyshev fourth order polynomial.

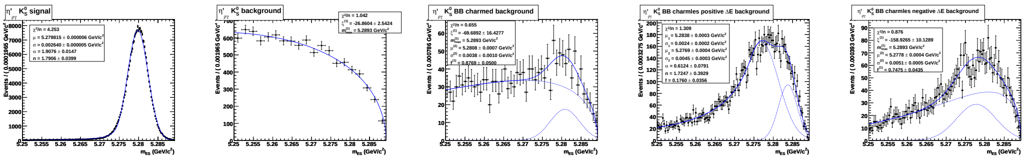

Figure A.10: m_{ES} PDFs: signal, Crystal Ball; continuum background, Argus function; $B\overline{B}$ charmed background, Gaussian plus Argus Function; $B\overline{B}$ peaking background (+), Gaussian plus Crystal Ball; $B\overline{B}$ peaking background (-), Gaussian plus Argus Function.

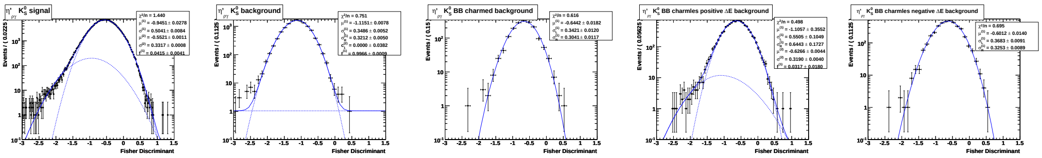

Figure A.11: Fisher PDFs: signal, Double Gaussian; continuum background, asymmetric Gaussian plus first order Chebyshev polynomial; $B\overline{B}$ charmed background, asymmetric Gaussian; $B\overline{B}$ peaking (+) background, asymmetric Gaussian plus Gaussian; $B\overline{B}$ peaking (-) background, asymmetric Gaussian.

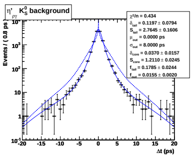

Figure A.12: Δt PDFs: continuum background, triple Gaussian where we use $\Delta t/\sigma_{\Delta t}$ as in signal Δt resolution model.

A.4 $B^0 \rightarrow \eta'_{\eta(\gamma\gamma)\pi\pi} K^0_{S(\pi^0\pi^0)}$

	m_{ES}	ΔE	Fisher	Δt	$\sigma_{\Delta t}$
m_{ES}	$+1.000$				
ΔE	$+0.034$	$+1.000$			
$\mathcal{F}$	-0.005	-0.008	$+1.000$		
Δt	$+0.000$	-0.012	$+0.010$	$+1.000$	
$\sigma_{\Delta t}$	-0.012	-0.021	-0.057	-0.021	$+1.000$

Table A.11: Correlation matrix for signal MCTruth MC events.

	m_{ES}	ΔE	Fisher	Δt	$\sigma_{\Delta t}$
m_{ES}	$+1.000$				
ΔE	$+0.034$	$+1.000$			
$\mathcal{F}$	$+0.051$	$+0.006$	$+1.000$		
Δt	-0.022	$+0.002$	$+0.001$	$+1.000$	
$\sigma_{\Delta t}$	-0.008	$+0.002$	-0.067	-0.007	$+1.000$

Table A.12: Correlation matrix for signal SCF MC events.

	m_{ES}	ΔE	Fisher	Δt	$\sigma_{\Delta t}$
m_{ES}	$+1.000$				
ΔE	$+0.006$	$+1.000$			
$\mathcal{F}$	$+0.008$	$+0.040$	$+1.000$		
Δt	$+0.014$	$+0.004$	-0.036	$+1.000$	
$\sigma_{\Delta t}$	-0.103	-0.020	-0.006	$+0.013$	$+1.000$

Table A.13: Correlation matrix in on-peak side band data.

```
mES_EppKs00_xi_bg_float = -40.427 +/- 9.098 L(-50.000 - 0.000)
deltaE_EppKs00_c1_bg_float = -0.317 +/- 0.061 L(-2.000 - 2.000)
fisher_EppKs00_Mu1_bg_float = -1.179 +/- 0.031 L(-2.000 - 0.000)
fisher_EppKs00_Sigma1_bg_float = 0.268 +/- 0.020 L(0.000 - 5.000)
fisher_EppKs00_Sigma2_bg_float = 0.330 +/- 0.021 L(0.000 - 5.000)
deltaT_Mu2_bg_EppKs00_float = 0.126 +/- 0.106 L(-10.000 - 10.000)
deltaT_Sigma2_bg_EppKs00_float = 0.992 +/- 0.068 L(0.000 - 30.000)
deltaT_Mu1_bg_EppKs00_float = -0.168 +/- 0.128 L(-10.000 - 10.000)
deltaT_Sigma1_bg_EppKs00_float = 1.953 +/- 0.091 L(0.000 - 3.000)
fBg_cat1_EppKs00 = 0.003 +/- 0.002 L(0.000 - 0.400)
fBg_cat2_EppKs00 = 0.049 +/- 0.008 L(0.000 - 0.400)
fBg_cat3_EppKs00 = 0.114 +/- 0.012 L(0.000 - 0.400)
fBg_cat4_EppKs00 = 0.113 +/- 0.012 L(0.000 - 0.400)
fBg_cat5_EppKs00 = 0.152 +/- 0.013 L(0.000 - 0.400)
fBg_cat6_EppKs00 = 0.119 +/- 0.012 L(0.000 - 0.400)
```

Final values for the parameters which were allowed to float in the fit.

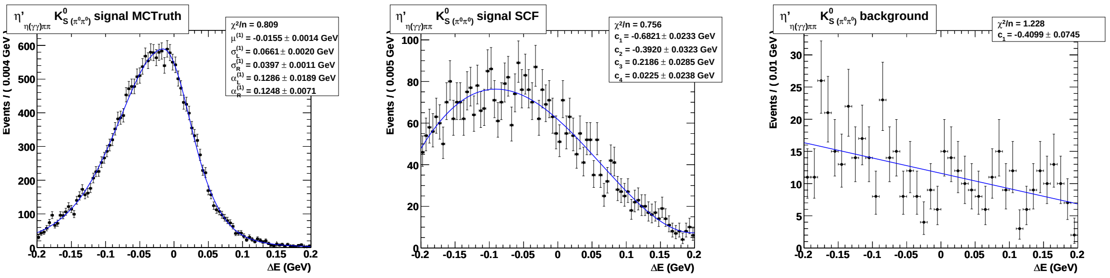

Figure A.13: ΔE PDFs: signal MCTruth, Cruijff function; signal SCF, fourth order Chebyshev polynomial; continuum background, Chebyshev first order polynomial;

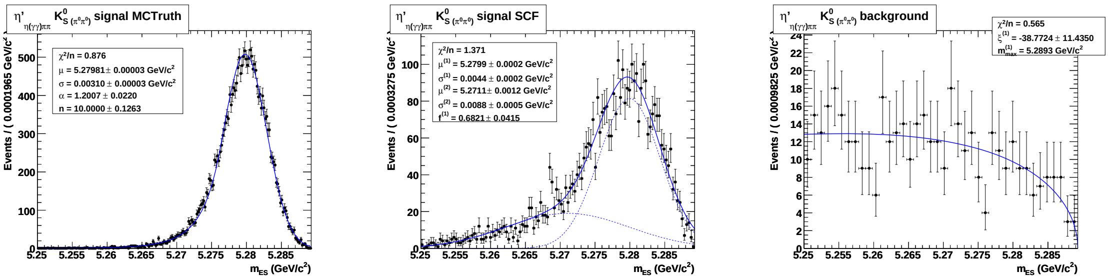

Figure A.14: $m_{\rm ES}$ PDFs: signal MCTruth, Crystal Ball; signal SCF, Double Gaussian; continuum background, Argus function

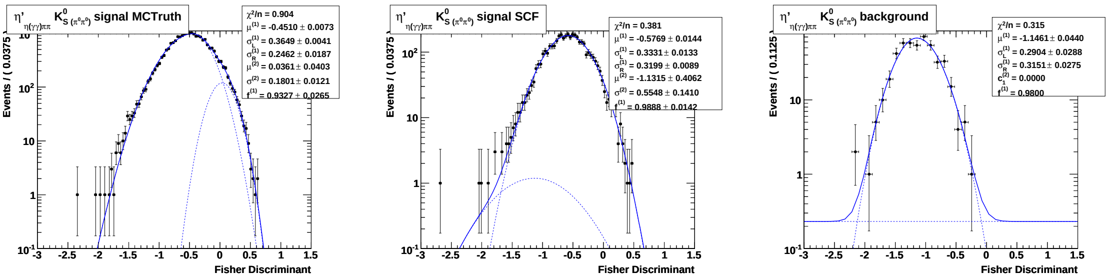

Figure A.15: Fisher PDFs: signal MCTruth, asymmetric Gaussian plus Gaussian; signal SCF, asymmetric Gaussian plus Gaussian;continuum background, asymmetric Gaussian plus first order Chebyshev polynomial.

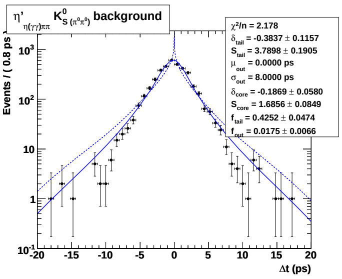

Figure A.16: Δt PDFs:continuum background, triple Gaussian where we use $\Delta t/\sigma_{\Delta t}$ as in signal Δt resolution model.

A.5 $B^0 \rightarrow \eta'_{\rho\gamma} K^0_{S(\pi^0\pi^0)}$

	$m_{\rm ES}$	ΔE	Fisher	Δt	$\sigma_{\Delta t}$
$m_{\rm ES}$	$+1.000$				
ΔE	$+0.047$	$+1.000$			
$\mathcal{F}$	-0.003	-0.010	$+1.000$		
Δt	$+0.008$	-0.019	$+0.005$	$+1.000$	
$\sigma_{\Delta t}$	$+0.006$	-0.006	-0.071	-0.003	$+1.000$

Table A.14: Correlation matrix for signal MCTruth MC events.

	$m_{\rm ES}$	ΔE	Fisher	Δt	$\sigma_{\Delta t}$
$m_{\rm ES}$	$+1.000$				
ΔE	$+0.092$	$+1.000$			
$\mathcal{F}$	$+0.057$	$+0.032$	$+1.000$		
Δt	-0.024	$+0.002$	$+0.014$	$+1.000$	
$\sigma_{\Delta t}$	-0.023	-0.007	-0.067	-0.045	$+1.000$

Table A.15: Correlation matrix for signal SCF MC events.

	$m_{\rm ES}$	ΔE	Fisher	Δt	$\sigma_{\Delta t}$
$m_{\rm ES}$	$+1.000$				
ΔE	-0.013	$+1.000$			
$\mathcal{F}$	-0.002	$+0.045$	$+1.000$		
Δt	-0.015	$+0.026$	-0.013	$+1.000$	
$\sigma_{\Delta t}$	-0.018	$+0.016$	$+0.034$	$+0.032$	$+1.000$

Table A.16: Correlation matrix in on-peak side band data.

	$m_{\rm ES}$	ΔE	Fisher	Δt	$\sigma_{\Delta t}$
$m_{\rm ES}$	$+1.000$				
ΔE	$+0.093$	$+1.000$			
$\mathcal{F}$	$+0.065$	$+0.063$	$+1.000$		
Δt	$+0.009$	$+0.015$	-0.009	$+1.000$	
$\sigma_{\Delta t}$	-0.033	$+0.030$	-0.055	-0.062	$+1.000$

Table A.17: Correlation matrix in $B\overline{B}$ peaking events with positive ΔE mean (+).

```
mES_ErgKs00_xi_bg_float = -16.496 +/- 1.784 L(-50.000 - 0.000)
deltaE_ErgKs00_c1_bg_float = -0.330 +/- 0.012 L(-2.000 - 2.000)
fisher_ErgKs00_Mu1_bg_float = -1.158 +/- 0.004 L(-2.000 - 0.000)
fisher_ErgKs00_Sigma1_bg_float = 0.330 +/- 0.003 L(0.000 - 5.000)
deltaT_Mu2_bg_ErgKs00_float = 0.426 +/- 0.080 L(-10.000 - 10.000)
```

	$m_{\rm ES}$	ΔE	Fisher	Δt	$\sigma_{\Delta t}$
$m_{\rm ES}$	$+1.000$				
ΔE	-0.081	$+1.000$			
$\mathcal{F}$	$+0.058$	-0.024	$+1.000$		
Δt	-0.077	$+0.016$	-0.007	$+1.000$	
$\sigma_{\Delta t}$	$+0.018$	-0.005	-0.006	$+0.088$	$+1.000$

Table A.18: Correlation matrix in $B\overline{B}$ peaking events with negative ΔE mean (–).

	$m_{\rm ES}$	ΔE	Fisher	Δt	$\sigma_{\Delta t}$
$m_{\rm ES}$	$+1.000$				
ΔE	-0.025	$+1.000$			
$\mathcal{F}$	$+0.005$	-0.016	$+1.000$		
Δt	-0.010	$+0.020$	-0.028	$+1.000$	
$\sigma_{\Delta t}$	-0.026	$+0.004$	-0.074	$+0.010$	$+1.000$

Table A.19: Correlation matrix in $B\overline{B}$ charmed events.

```
deltaT_Sigma2_bg_ErgKs00_float = 2.870 +/- 0.064 L(0.000 - 30.000)
deltaT_Mu1_bg_ErgKs00_float = 0.040 +/- 0.010 L(-10.000 - 10.000)
deltaT_Sigma1_bg_ErgKs00_float = 1.187 +/- 0.008 L(0.000 - 3.000)
fBg_cat1_ErgKs00 = 0.0010 +/- 0.0003 L(-0.2000 - 0.3000)
fBg_cat2_ErgKs00 = 0.042 +/- 0.002 L(0.000 - 0.300)
fBg_cat3_ErgKs00 = 0.121 +/- 0.002 L(0.000 - 0.300)
fBg_cat4_ErgKs00 = 0.111 +/- 0.002 L(0.000 - 0.300)
fBg_cat5_ErgKs00 = 0.140 +/- 0.002 L(0.000 - 0.300)
fBg_cat6_ErgKs00 = 0.134 +/- 0.002 L(0.000 - 0.300)
C_Bb_ErgKs00 = -0.020 +/- 0.278 L(-3.000 - 3.000)
S_Bb_ErgKs00 = -0.343 +/- 0.264 L(-3.000 - 3.000)
fBb_cat1_ErgKs00 = 0.097 +/- 0.039 L(0.000 - 1.000)
fBb_cat2_ErgKs00 = 0.368 +/- 0.160 L(0.000 - 1.000)
fBb_cat3_ErgKs00 = 0.172 +/- 0.078 L(0.000 - 1.000)
fBb_cat4_ErgKs00 = 0.300 +/- 0.119 L(0.000 - 1.000)
fBb_cat5_ErgKs00 = 0.143 +/- 0.071 L(0.000 - 1.000)
fBb_cat6_ErgKs00 = 0.038 +/- 0.089 L(-0.200 - 1.000)
```

Final values for the parameters which were allowed to float in the fit.

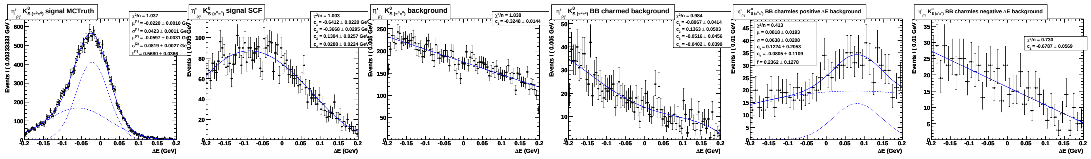

Figure A.17: ΔE PDFs: signal MCTruth, double Gaussian function; signal SCF, fourth order Chebyshev polynomial; continuum background, Chebyshev first order polynomial, $B\overline{B}$ charmed background, Chebyshev fourth order polynomiall; $B\overline{B}$ peaking background (+), Gaussian plus Chebyshev second order polynomial; $B\overline{B}$ peaking background (-), Chebyshev first order polynomial.

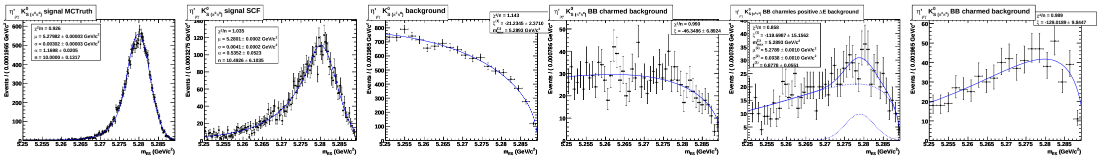

Figure A.18: $m_{\rm ES}$ PDFs: signal MCTruth, Crystal Ball; signal SCF, Crystal Ball continuum background, Argus function; $B\overline{B}$ charmed background, Argus Function; $B\overline{B}$ peaking background (+), Gaussian plus Argus Function; $B\overline{B}$ peaking background (-),Argus Function.

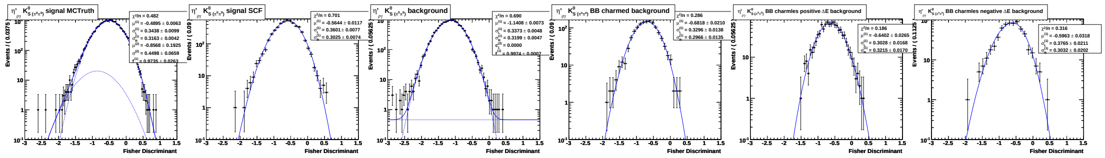

Figure A.19: Fisher PDFs: signal MCTruth, asymmetric Gaussian plus Gaussian; signal SCF,Gaussian plus Gaussian;continuum background, asymmetric Gaussian plus first order Chebyshev polynomial; $B\overline{B}$ charmed background, asymmetric Gaussian; $B\overline{B}$ peaking (+) background, asymmetric Gaussian; $B\overline{B}$ peaking (-) background, asymmetric Gaussian.

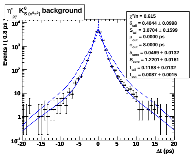

Figure A.20: Δt PDFs: continuum background, triple Gaussian where we use $\Delta t/\sigma_{\Delta t}$ as in signal Δt resolution model.

A.6 $B^0 \to \eta'_{\eta(\gamma\gamma)\pi\pi} K^0_L$

	ΔE	Fisher	Δt	$\sigma_{\Delta t}$
ΔE	$+1.000$			
$\mathcal{F}$	-0.098	$+1.000$		
Δt	$+0.000$	-0.007	$+1.000$	
$\sigma_{\Delta t}$	-0.000	-0.007	-0.000	$+1.000$

Table A.20: Correlation matrix for signal MC events.

	ΔE	Fisher	Δt	$\sigma_{\Delta t}$
ΔE	$+1.000$			
$\mathcal{F}$	-0.020	$+1.000$		
Δt	-0.000	$+0.028$	$+1.000$	
$\sigma_{\Delta t}$	$+0.000$	-0.001	$+0.035$	$+1.000$

Table A.21: Correlation matrix in off-peak band data.

```
deltaEKl_EppKl_xi_bg_float = -18.702 +/- 0.864 L(-100.000 - 10.000)
fisher_EppKl_Mu1_bg_float = -1.027 +/- 0.007 L(-2.000 - 0.000)
fisher_EppKl_Sigma1_bg_float = 0.454 +/- 0.005 L(0.000 - 5.000)
fisher_EppKl_Sigma2_bg_float = 0.302 +/- 0.005 L(0.000 - 5.000)
deltaT_Mu2_bg_EppKl_float = 0.058 +/- 0.068 L(-10.000 - 10.000)
deltaT_Sigma2_bg_EppKl_float = 3.019 +/- 0.051 L(0.000 - 30.000)
deltaT_Mu1_bg_EppKl_float = -0.021 +/- 0.014 L(-10.000 - 10.000)
deltaT_Sigma1_bg_EppKl_float = 1.252 +/- 0.011 L(0.000 - 3.000)
fBg_cat1_EppKl = 0.0056 +/- 0.0006 L(0.0000 - 0.3000)
fBg_cat2_EppKl = 0.063 +/- 0.002 L(0.000 - 0.300)
fBg_cat3_EppKl = 0.139 +/- 0.003 L(0.000 - 0.300)
fBg_cat4_EppKl = 0.125 +/- 0.003 L(0.000 - 0.300)
fBg_cat5_EppKl = 0.155 +/- 0.003 L(0.000 - 0.300)
fBg_cat6_EppKl = 0.124 +/- 0.002 L(0.000 - 0.300)
```

Final values for the parameters which were allowed to float in the fit.

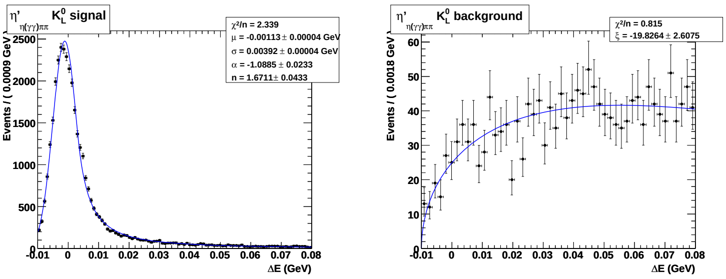

Figure A.21: ΔE PDFs: signal, Crystal Ball; continuum background, inverse Argus Function.

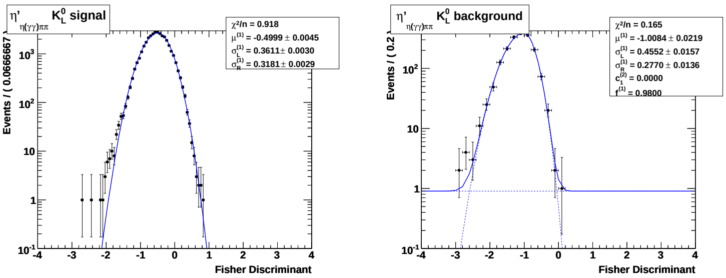

Figure A.22: Fisher PDFs: signal, asymmetric Gaussian; continuum background, asymmetric Gaussian plus first order Chebyshev polynomial.

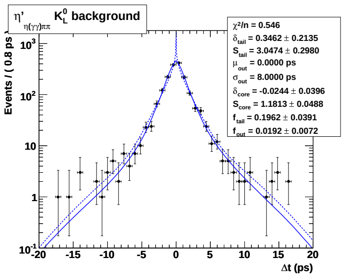

Figure A.23: Δt PDFs: continuum background, triple Gaussian where we use $\Delta t/\sigma_{\Delta t}$ as in signal Δt resolution model.

A.7 $B^0 \to \eta'_{\eta(3\pi)\pi\pi} K_L^0$

	ΔE	Fisher	Δt	$\sigma_{\Delta t}$
ΔE	$+1.000$			
$\mathcal{F}$	-0.081	$+1.000$		
Δt	-0.000	-0.006	$+1.000$	
$\sigma_{\Delta t}$	$+0.000$	-0.026	-0.008	$+1.000$

Table A.22: Correlation matrix for signal MCTruth MC events.

	ΔE	Fisher	Δt	$\sigma_{\Delta t}$
ΔE	$+1.000$			
$\mathcal{F}$	-0.107	$+1.000$		
Δt	$+0.000$	-0.012	$+1.000$	
$\sigma_{\Delta t}$	$+0.000$	$+0.011$	$+0.002$	$+1.000$

Table A.23: Correlation matrix for signal SCF MC events.

	ΔE	Fisher	Δt	$\sigma_{\Delta t}$
ΔE	$+1.000$			
$\mathcal{F}$	$+0.010$	$+1.000$		
Δt	$+0.000$	$+0.028$	$+1.000$	
$\sigma_{\Delta t}$	-0.000	-0.016	$+0.084$	$+1.000$

Table A.24: Correlation matrix in off-peak data.

```
deltaEKl_E5pKl_xi_bg_float = -17.340 +/- 1.481 L(-20.000 - 10.000)
fisher_E5pKl_Mu1_bg_float = -1.020 +/- 0.013 L(-2.000 - 0.000)
fisher_E5pKl_Sigma1_bg_float = 0.460 +/- 0.009 L(0.000 - 5.000)
fisher_E5pKl_Sigma2_bg_float = 0.307 +/- 0.008 L(0.000 - 5.000)
deltaT_Mu2_bg_E5pKl_float = 0.115 +/- 0.061 L(-10.000 - 10.000)
deltaT_Sigma2_bg_E5pKl_float = 2.434 +/- 0.045 L(0.000 - 30.000)
deltaT_Mu1_bg_E5pKl_float = 0.021 +/- 0.029 L(-10.000 - 10.000)
deltaT_Sigma1_bg_E5pKl_float = 1.081 +/- 0.022 L(0.000 - 3.000)
fBg_cat1_E5pKl = 0.007 +/- 0.001 L(0.000 - 0.300)
fBg_cat2_E5pKl = 0.064 +/- 0.003 L(0.000 - 0.300)
fBg_cat3_E5pKl = 0.140 +/- 0.005 L(0.000 - 0.300)
fBg_cat4_E5pKl = 0.124 +/- 0.004 L(0.000 - 0.300)
fBg_cat5_E5pKl = 0.151 +/- 0.005 L(0.000 - 0.300)
fBg_cat6_E5pKl = 0.122 +/- 0.004 L(0.000 - 0.300)
```

Final values for the parameters which were allowed to float in the fit.

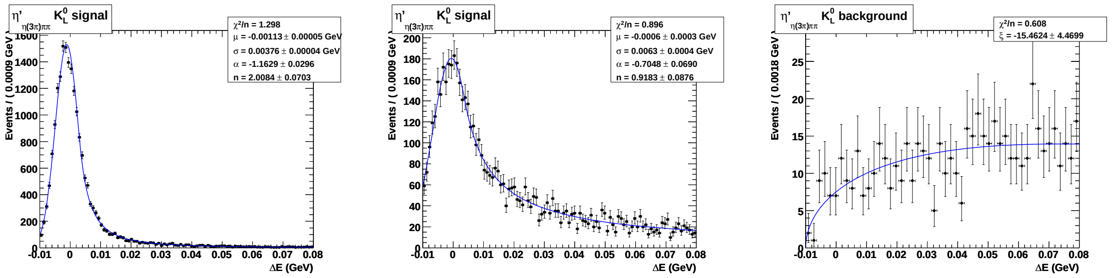

Figure A.24: ΔE PDFs: signal MCTruth, Crystal Ball; signal SCF, Crystal Ball; continuum background, inverse Argus Function.

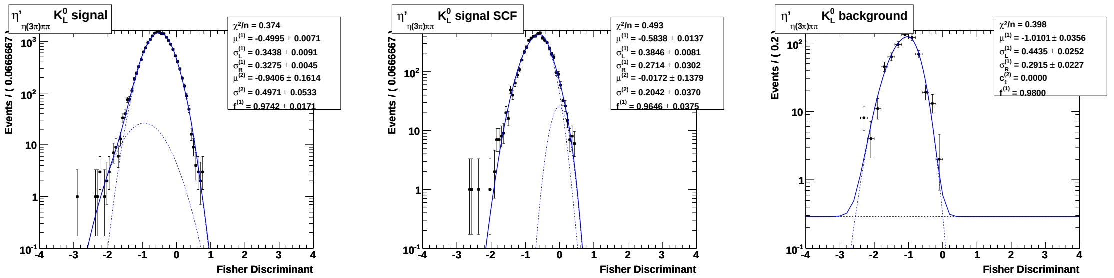

Figure A.25: Fisher PDFs: signal MCTruth, asymmetric Gaussian plus Gaussian; signal SCF, asymmetric Gaussian plus Gaussian;continuum background, asymmetric Gaussian plus first order Chebyshev polynomial.

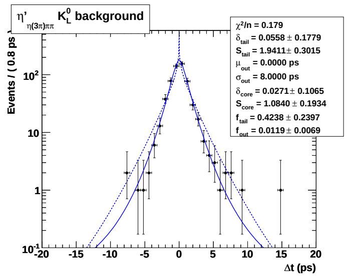

Figure A.26: Δt PDFs:continuum background, triple Gaussian where we use $\Delta t/\sigma_{\Delta t}$ as in signal Δt resolution model.

A.8 $B^+ \to \eta'_{\eta(\gamma\gamma)\pi\pi} K^+$

	$m_{\rm ES}$	ΔE	Fisher	Δt	$\sigma_{\Delta t}$
$m_{\rm ES}$	$+1.000$				
ΔE	-0.029	$+1.000$			
$\mathcal{F}$	$+0.014$	$+0.003$	$+1.000$		
Δt	$+0.003$	$+0.003$	$+0.009$	$+1.000$	
$\sigma_{\Delta t}$	-0.014	-0.006	-0.080	-0.021	$+1.000$

Table A.25: Correlation matrix for signal MC events.

	$m_{\rm ES}$	ΔE	Fisher	Δt	$\sigma_{\Delta t}$
$m_{\rm ES}$	$+1.000$				
ΔE	$+0.009$	$+1.000$			
$\mathcal{F}$	$+0.004$	$+0.018$	$+1.000$		
Δt	-0.006	$+0.070$	$+0.006$	$+1.000$	
$\sigma_{\Delta t}$	-0.028	-0.036	-0.010	-0.076	$+1.000$

Table A.26: Correlation matrix in on-peak side band data.

```
mES_EppK_xi_bg_float = -17.157 +/- 4.911 L(-50.000 - 0.000)
deltaE_EppK_c1_bg_float = -0.330 +/- 0.031 L(-2.000 - 2.000)
fisher_EppK_Mu1_bg_float = -1.084 +/- 0.016 L(-2.000 - 0.000)
fisher_EppK_Sigma1_bg_float = 0.338 +/- 0.010 L(0.000 - 5.000)
fisher_EppK_Sigma2_bg_float = 0.293 +/- 0.011 L(0.000 - 5.000)
deltaT_Mu2_bg_EppK_float = -0.388 +/- 0.273 L(-10.000 - 10.000)
deltaT_Sigma2_bg_EppK_float = 3.080 +/- 0.208 L(0.000 - 30.000)
deltaT_Mu1_bg_EppK_float = -0.012 +/- 0.030 L(-10.000 - 10.000)
deltaT_Sigma1_bg_EppK_float = 1.270 +/- 0.023 L(0.000 - 3.000)
fBg_cat1_EppK = 0.007 +/- 0.002 L(0.000 - 0.300)
fBg_cat2_EppK = 0.071 +/- 0.005 L(0.000 - 0.300)
fBg_cat3_EppK = 0.141 +/- 0.007 L(0.000 - 0.300)
fBg_cat4_EppK = 0.113 +/- 0.006 L(0.000 - 0.300)
fBg_cat5_EppK = 0.145 +/- 0.007 L(0.000 - 0.300)
fBg_cat6_EppK = 0.120 +/- 0.006 L(0.000 - 0.300)
```

Final values for the parameters which were allowed to float in the fit.

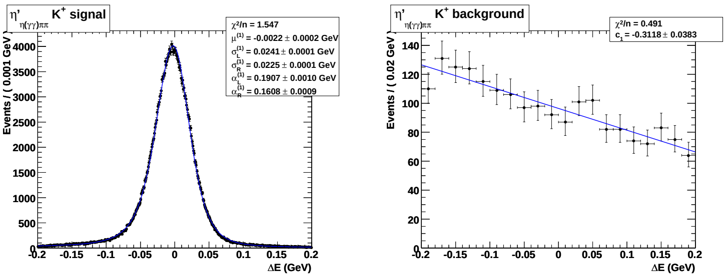

Figure A.27: ΔE PDFs: signal, Cruijff function; continuum background, Chebyshev first order polynomial.

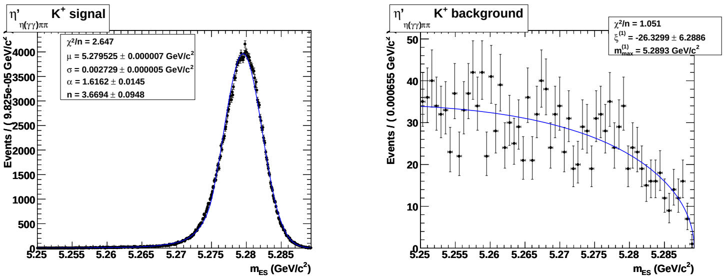

Figure A.28: m_{ES} PDFs: signal, Crystal Ball; continuum background, Argus function.

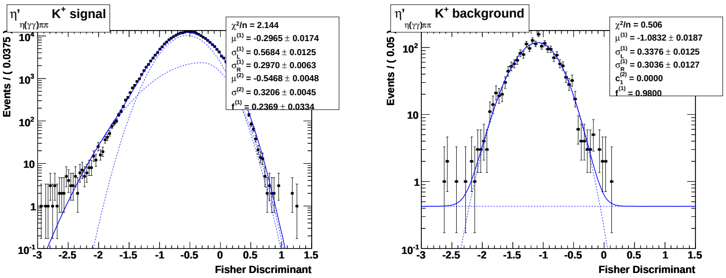

Figure A.29: Fisher PDFs: signal, asymmetric Gaussian plus Gausian; continuum background, asymmetric Gaussian plus first order Chebyshev polynomial.

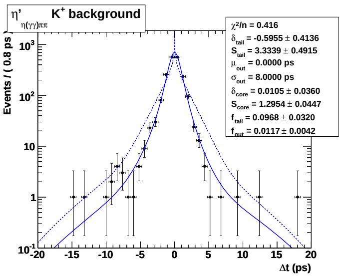

Figure A.30: Δt PDFs:continuum background, triple Gaussian where we use $\Delta t/\sigma_{\Delta t}$ as in signal Δt resolution model.

A.9 $B^+ \to \eta'_{\eta(3\pi)\pi\pi} K^+$

	$m_{\rm ES}$	ΔE	Fisher	Δt	$\sigma_{\Delta t}$
$m_{\rm ES}$	$+1.000$				
ΔE	-0.055	$+1.000$			
$\mathcal{F}$	$+0.009$	-0.008	$+1.000$		
Δt	$+0.002$	$+0.003$	$+0.002$	$+1.000$	
$\sigma_{\Delta t}$	$+0.010$	$+0.006$	-0.062	-0.008	$+1.000$

Table A.27: Correlation matrix for signal MCTruth MC events.

	$m_{\rm ES}$	ΔE	Fisher	Δt	$\sigma_{\Delta t}$
$m_{\rm ES}$	$+1.000$				
ΔE	$+0.126$	$+1.000$			
$\mathcal{F}$	$+0.048$	$+0.017$	$+1.000$		
Δt	-0.001	$+0.001$	-0.001	$+1.000$	
$\sigma_{\Delta t}$	-0.021	$+0.008$	-0.065	-0.023	$+1.000$

Table A.28: Correlation matrix for signal SCF MC events.

	$m_{\rm ES}$	ΔE	Fisher	Δt	$\sigma_{\Delta t}$
$m_{\rm ES}$	$+1.000$				
ΔE	$+0.042$	$+1.000$			
$\mathcal{F}$	-0.060	-0.057	$+1.000$		
Δt	$+0.028$	$+0.002$	-0.026	$+1.000$	
$\sigma_{\Delta t}$	-0.071	$+0.041$	$+0.102$	$+0.003$	$+1.000$

Table A.29: Correlation matrix in on-peak side band data.

```
mES_E5pK_xi_bg_float = -10.978 +/- 7.860 L(-50.000 - 0.000)
deltaE_E5pK_c1_bg_float = -0.346 +/- 0.050 L(-2.000 - 2.000)
fisher_E5pK_Mu1_bg_float = -1.096 +/- 0.025 L(-2.000 - 0.000)
fisher_E5pK_Sigma1_bg_float = 0.342 +/- 0.016 L(0.000 - 5.000)
fisher_E5pK_Sigma2_bg_float = 0.325 +/- 0.017 L(0.000 - 5.000)
deltaT_Mu2_bg_E5pK_float = -0.230 +/- 0.179 L(-10.000 - 10.000)
deltaT_Sigma2_bg_E5pK_float = 2.243 +/- 0.116 L(0.000 - 30.000)
deltaT_Mu1_bg_E5pK_float = 0.038 +/- 0.059 L(-10.000 - 10.000)
deltaT_Sigma1_bg_E5pK_float = 1.109 +/- 0.044 L(0.000 - 3.000)
fBg_cat1_E5pK = 0.004 +/- 0.002 L(0.000 - 0.300)
fBg_cat2_E5pK = 0.075 +/- 0.008 L(0.000 - 0.300)
fBg_cat3_E5pK = 0.131 +/- 0.010 L(0.000 - 0.300)
fBg_cat4_E5pK = 0.115 +/- 0.010 L(0.000 - 0.300)
fBg_cat5_E5pK = 0.149 +/- 0.011 L(0.000 - 0.300)
fBg_cat6_E5pK = 0.120 +/- 0.010 L(0.000 - 0.300)
```

Final values for the parameters which were allowed to float in the fit.

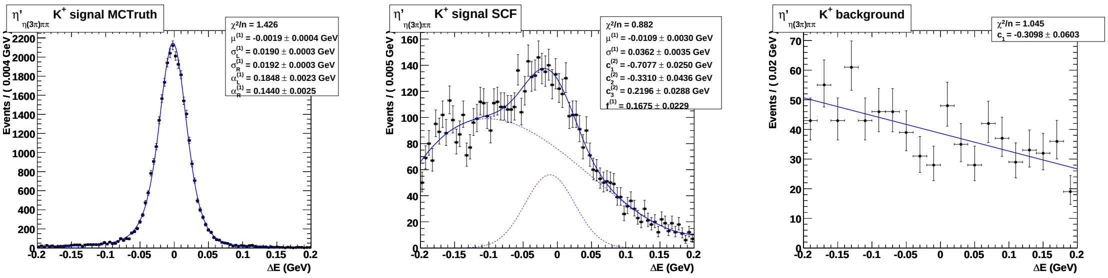

Figure A.31: ΔE PDFs: signal MCTruth, Cruijff function; signal SCF, Gaussian plus third order Chebyshev polynomial; continuum background, Chebyshev first order polynomial;

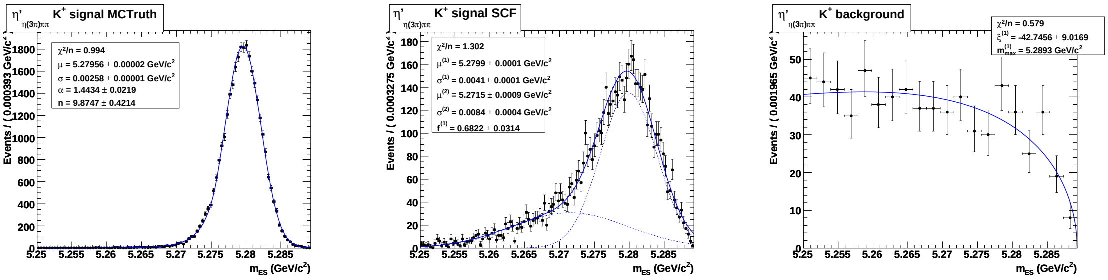

Figure A.32: m_{ES} PDFs: signal MCTruth, Crystal Ball; signal SCF, double Gaussian; continuum background, Argus function

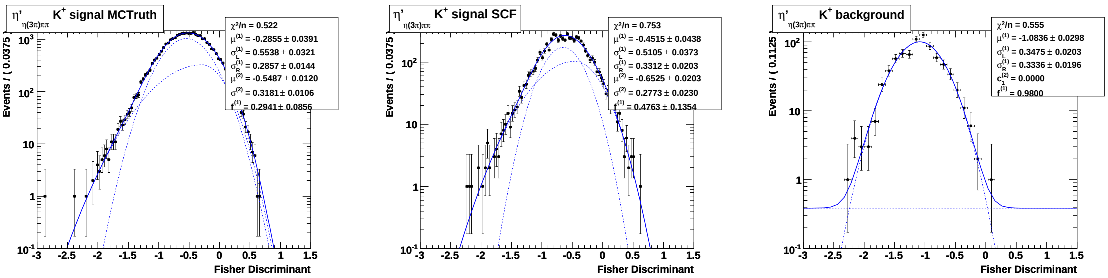

Figure A.33: Fisher PDFs: signal MCTruth, asymmetric Gaussian plus Gaussian; signal SCF, asymmetric Gaussian plus Gaussian;continuum background, asymmetric Gaussian plus first order Chebyshev polynomial.

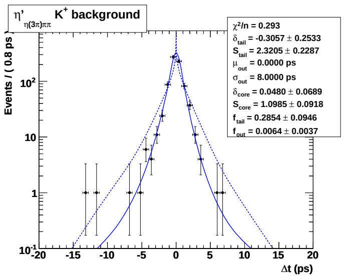

Figure A.34: Δt PDFs:continuum background, triple Gaussian where we use $\Delta t/\sigma_{\Delta t}$ as in signal Δt resolution model.

A.10 $B^+ \to \eta'_{\rho\gamma} K^+$

	$m_{\rm ES}$	ΔE	Fisher	Δt	$\sigma_{\Delta t}$
$m_{\rm ES}$	$+1.000$				
ΔE	$+0.047$	$+1.000$			
$\mathcal{F}$	$+0.030$	$+0.020$	$+1.000$		
Δt	-0.000	$+0.005$	$+0.007$	$+1.000$	
$\sigma_{\Delta t}$	-0.011	-0.014	-0.066	-0.021	$+1.000$

Table A.30: Correlation matrix for signal MC events.

	$m_{\rm ES}$	ΔE	Fisher	Δt	$\sigma_{\Delta t}$
$m_{\rm ES}$	$+1.000$				
ΔE	$+0.007$	$+1.000$			
$\mathcal{F}$	$+0.003$	$+0.026$	$+1.000$		
Δt	$+0.002$	$+0.040$	-0.009	$+1.000$	
$\sigma_{\Delta t}$	-0.018	$+0.022$	$+0.043$	-0.007	$+1.000$

Table A.31: Correlation matrix in on-peak side band data.

	$m_{\rm ES}$	ΔE	Fisher	Δt	$\sigma_{\Delta t}$
$m_{\rm ES}$	$+1.000$				
ΔE	$+0.213$	$+1.000$			
$\mathcal{F}$	$+0.033$	$+0.080$	$+1.000$		
Δt	$+0.003$	-0.001	-0.006	$+1.000$	
$\sigma_{\Delta t}$	-0.031	-0.015	-0.055	-0.014	$+1.000$

Table A.32: Correlation matrix in $B\overline{B}$ peaking events with positive ΔE mean (+).

	$m_{\rm ES}$	ΔE	Fisher	Δt	$\sigma_{\Delta t}$
$m_{\rm ES}$	$+1.000$				
ΔE	-0.067	$+1.000$			
$\mathcal{F}$	$+0.047$	-0.062	$+1.000$		
Δt	-0.009	$+0.001$	-0.001	$+1.000$	
$\sigma_{\Delta t}$	-0.019	$+0.024$	-0.055	-0.022	$+1.000$

Table A.33: Correlation matrix in $B\overline{B}$ peaking events with negative ΔE mean (–).

	$m_{\rm ES}$	ΔE	Fisher	Δt	$\sigma_{\Delta t}$
$m_{\rm ES}$	$+1.000$				
ΔE	$+0.020$	$+1.000$			
$\mathcal{F}$	$+0.044$	$+0.013$	$+1.000$		
Δt	-0.028	$+0.013$	-0.003	$+1.000$	
$\sigma_{\Delta t}$	-0.062	$+0.007$	-0.075	-0.007	$+1.000$

Table A.34: Correlation matrix in $B\overline{B}$ charmed events.

```
mES_ErgK_xi_bg_float = -21.841 +/- 0.890 L(-50.000 - -10.000)
deltaE_ErgK_c1_bg_float = -0.272 +/- 0.006 L(-2.000 - 2.000)
fisher_ErgK_Mu1_bg_float = -1.126 +/- 0.002 L(-5.000 - 5.000)
fisher_ErgK_Sigma1_bg_float = 0.344 +/- 0.002 L(0.000 - 5.000)
deltaT_Mu2_bg_ErgK_float = -0.121 +/- 0.044 L(-10.000 - 10.000)
deltaT_Sigma2_bg_ErgK_float = 3.078 +/- 0.036 L(0.000 - 30.000)
deltaT_Mu1_bg_ErgK_float = 0.002 +/- 0.005 L(-10.000 - 10.000)
deltaT_Sigma1_bg_ErgK_float = 1.225 +/- 0.004 L(0.000 - 3.000)
fBg_cat1_ErgK = 0.0027 +/- 0.0002 L(0.0000 - 0.3000)
fBg_cat2_ErgK = 0.0808 +/- 0.0010 L(0.0000 - 0.3000)
fBg_cat3_ErgK = 0.154 +/- 0.001 L(0.000 - 0.300)
fBg_cat4_ErgK = 0.115 +/- 0.001 L(0.000 - 0.300)
fBg_cat5_ErgK = 0.133 +/- 0.001 L(0.000 - 0.300)
fBg_cat6_ErgK = 0.116 +/- 0.001 L(0.000 - 0.300)
C_Bb_ErgK = -0.225 +/- 0.107 L(-3.000 - 3.000)
S_Bb_ErgK = -0.011 +/- 0.114 L(-3.000 - 3.000)
fBb_cat1_ErgK = 0.089 +/- 0.012 L(0.000 - 0.300)
fBb_cat2_ErgK = 0.210 +/- 0.029 L(0.000 - 0.300)
fBb_cat3_ErgK = 0.230 +/- 0.026 L(0.000 - 0.300)
fBb_cat4_ErgK = 0.199 +/- 0.026 L(0.000 - 0.300)
fBb_cat5_ErgK = 0.174 +/- 0.024 L(0.000 - 0.300)
fBb_cat6_ErgK = 0.074 +/- 0.020 L(0.000 - 0.300)
```

Final values for the parameters which were allowed to float in the fit.

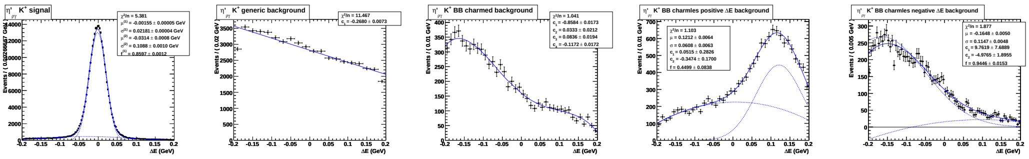

Figure A.35: ΔE PDFs: signal , Cruijff function; continuum background, Chebyshev first order polynomial, $B\overline{B}$ charmed background, Chebyshev fourth order polynomiall; $B\overline{B}$ peaking background (+), Gaussian plus Chebyshev second order polynomial; $B\overline{B}$ peaking background (-),Gaussian plus Chebyshev second order polynomial.

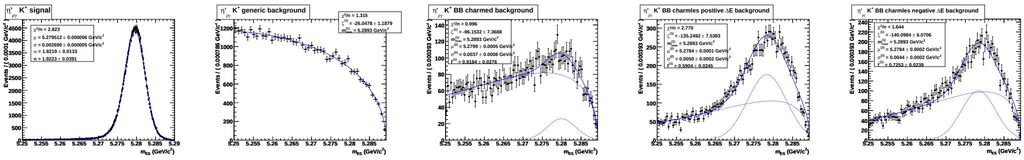

Figure A.36: m_{ES} PDFs: signal, Crystal Ball; continuum background, Argus function; $B\overline{B}$ charmed background, Gaussian plus Argus Function; $B\overline{B}$ peaking background (+), Gaussian plus Argus Function; $B\overline{B}$ peaking background (-), Gaussian plus Argus Function.

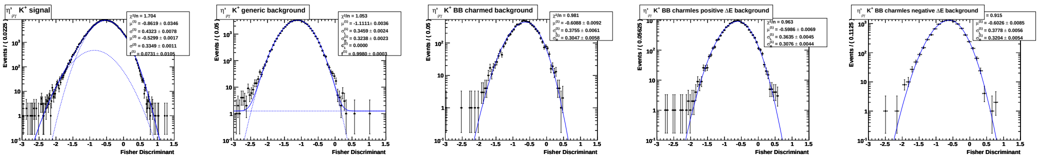

Figure A.37: Fisher PDFs: signal, double Gaussian; continuum background, asymmetric Gaussian plus first order Chebyshev polynomial; $B\overline{B}$ charmed background, asymmetric Gaussian; $B\overline{B}$ peaking (+) background, asymmetric Gaussian; $B\overline{B}$ peaking (-) background, asymmetric Gaussian.

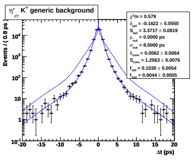

Figure A.38: Δt PDFs: continuum background, triple Gaussian where we use $\Delta t/\sigma_{\Delta t}$ as in signal Δt resolution model.

Appendix B

PDF Libraries for Branching Fraction Measurements

We show for each decay modes the signal, continuum background and $B\bar{B}$ background PDFs used in ML fits. We show also tables of the correlations between fit variables and final values of parameters which are floating in the final fit. Signal PDFs are determined from MC signal events. For background continuum PDFs we have used on-peak sidebands. For $B\bar{B}$ background PDFs we have used MC events.

B.1 $B^0 \to \eta_{\gamma\gamma} K_S^0$

	$m_{\rm ES}$	ΔE	Fisher
$m_{\rm ES}$	$+1.000$		
ΔE	-0.074	$+1.000$	
Fisher	$+0.012$	-0.012	$+1.000$

Table B.1: Correlation matrix for signal MC events.

	$m_{\rm ES}$	ΔE	Fisher
$m_{\rm ES}$	$+1.000$		
ΔE	-0.010	$+1.000$	
Fisher	$+0.023$	$+0.013$	$+1.000$

Table B.2: Correlation matrix in on-peak side band data.

	$m_{\rm ES}$	ΔE	Fisher
$m_{\rm ES}$	$+1.000$		
ΔE	-0.081	$+1.000$	
Fisher	$+0.010$	$+0.005$	$+1.000$

Table B.3: Correlation matrix in $B\overline{B}$ generics events.

```
mES_xi_bg_float = -23.288 +/- 4.580 L(-50.000 - -10.000)
deltaE_c1_bg_float = -0.169 +/- 0.032 L(-2.000 - 2.000)
fisher_Mu1_bg_float = -0.203 +/- 0.021 L(-5.000 - 5.000)
fisher_Sigma1_bg_float = 0.405 +/- 0.014 L(0.000 - 5.000)
fisher_Sigma2_bg_float = 0.455 +/- 0.016 L(0.000 - 5.000)
```

Final values for the parameters which were allowed to float in the fit.

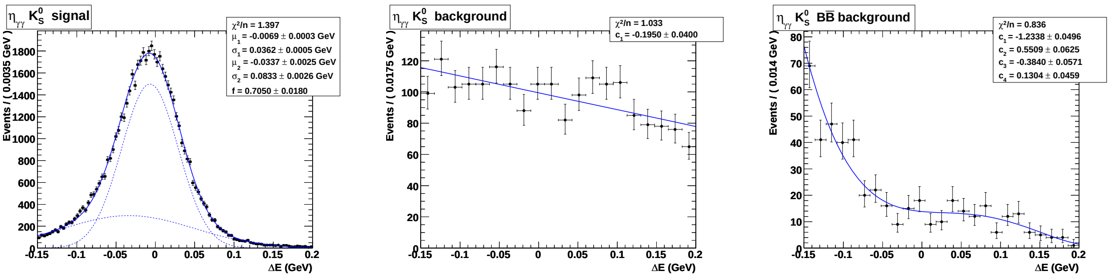

Figure B.1: ΔE PDFs: signal, double Gaussian; continuum background, Chebyshev first order polynomial, $B\overline{B}$ background, Chebyshev fourth order polynomial.

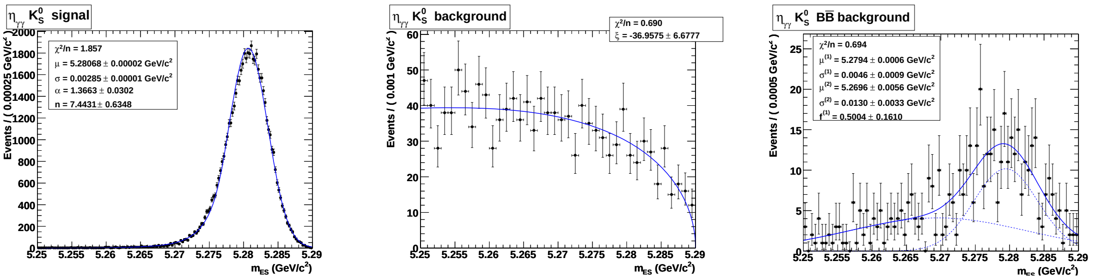

Figure B.2: m_{ES} PDFs: signal, Crystal Ball; continuum background, Argus function; $B\overline{B}$ background, double Gaussian.

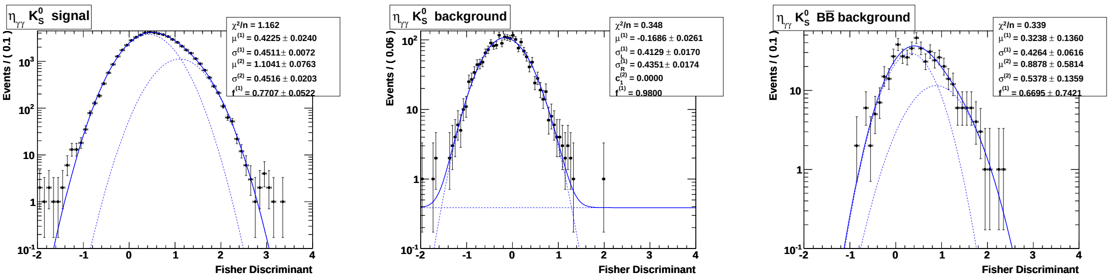

Figure B.3: Fisher PDFs: signal, double Gaussian; continuum background, asymmetric Gaussian plus first order Chebyshev polynomial; $B\overline{B}$ background, double Gaussian.

B.2 $B^0 \longrightarrow \eta_{3\pi} K_S^0$

	$m_{\rm ES}$	ΔE	Fisher
$m_{\rm ES}$	$+1.000$		
ΔE	-0.058	$+1.000$	
Fisher	$+0.000$	-0.002	$+1.000$

Table B.4: Correlation matrix for signal MC events.

	$m_{\rm ES}$	ΔE	Fisher
$m_{\rm ES}$	$+1.000$		
ΔE	$+0.017$	$+1.000$	
Fisher	-0.027	-0.004	$+1.000$

Table B.5: Correlation matrix in on-peak side band data.

```
mES_xi_bg_float = -16.586 +/- 6.920 L(-50.000 - 10.000)
deltaE_c1_bg_float = -0.262 +/- 0.045 L(-2.000 - 2.000)
fisher_Mu1_bg_float = -0.283 +/- 0.031 L(-5.000 - 5.000)
fisher_Sigma1_bg_float = 0.390 +/- 0.020 L(0.000 - 5.000)
fisher_Sigma2_bg_float = 0.521 +/- 0.022 L(0.000 - 5.000)
```

Final values for the parameters which were allowed to float in the fit.

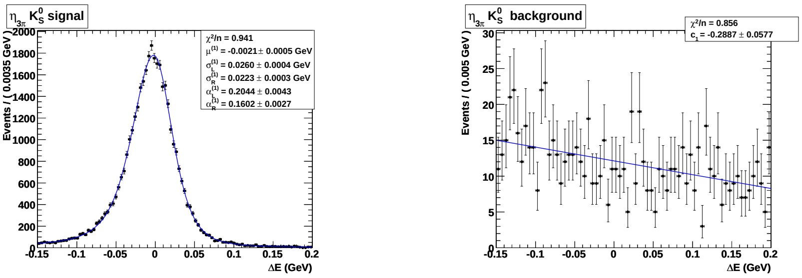

Figure B.4: ΔE PDFs: signal, Cruijff function; continuum background, first order Chebyshev polynomial.

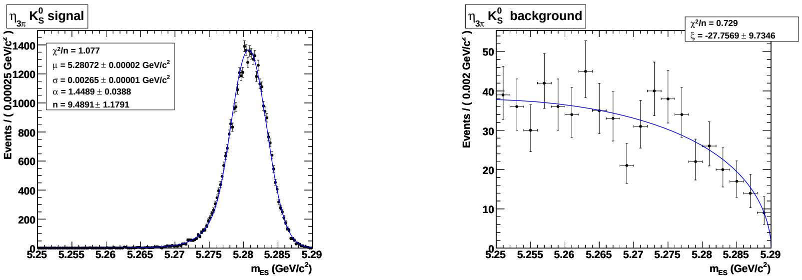

Figure B.5: m_{ES} PDFs: signal, Crystal Ball; continuum background, Argus function.

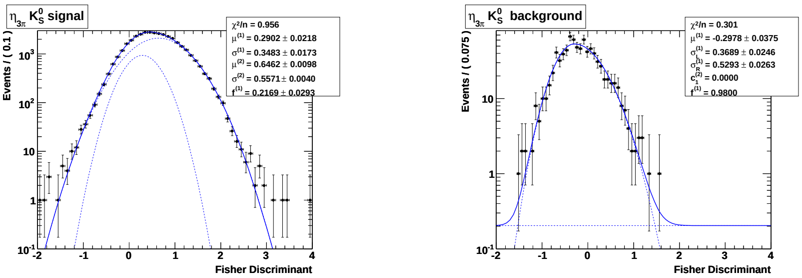

Figure B.6: Fisher PDFs: signal, double Gaussian; continuum background, asymmetric Gaussian plus first order Chebyshev polynomial.

B.3 $B^0 \to \eta_{\gamma\gamma}\eta_{\gamma\gamma}$

	$m_{\rm ES}$	ΔE	Fisher
$m_{\rm ES}$	$+1.000$		
ΔE	-0.065	$+1.000$	
Fisher	$+0.055$	-0.013	$+1.000$

Table B.6: Correlation matrix for signal MC events.

	$m_{\rm ES}$	ΔE	Fisher
$m_{\rm ES}$	$+1.000$		
ΔE	-0.003	$+1.000$	
Fisher	-0.001	$+0.014$	$+1.000$

Table B.7: Correlation matrix in on-peak side band data.

```
mES_xi_bg_float = -21.386 +/- 5.311 L(-50.000 - -10.000)
deltaE_c1_bg_float = -0.286 +/- 0.036 L(-2.000 - 2.000)
fisher_Mu1_bg_float = -0.396 +/- 0.024 L(-5.000 - 5.000)
fisher_Sigma1_bg_float = 0.343 +/- 0.015 L(0.000 - 5.000)
fisher_Sigma2_bg_float = 0.502 +/- 0.017 L(0.000 - 5.000)
```

Final values for the parameters which were allowed to float in the fit.

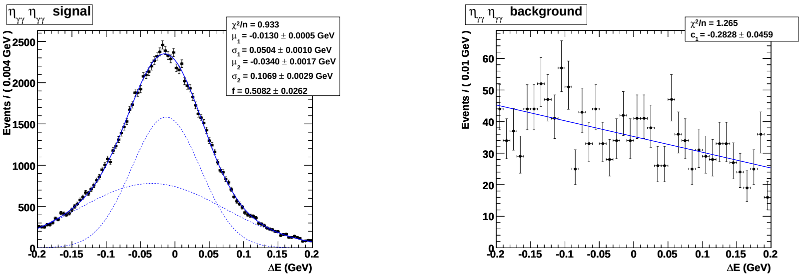

Figure B.7: ΔE PDFs: signal, double Gaussian; continuum background, Chebyshev first order polynomial.

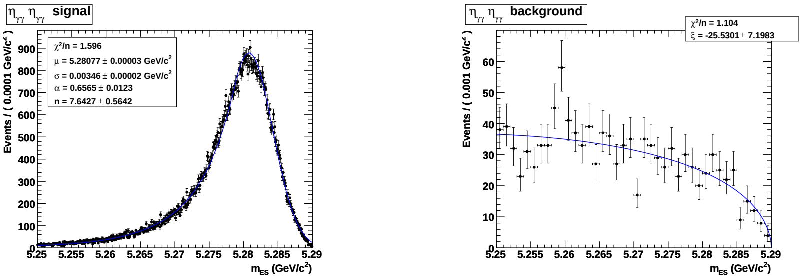

Figure B.8: $m_{\rm ES}$ PDFs: signal, Crystal Ball; continuum background, Argus function.

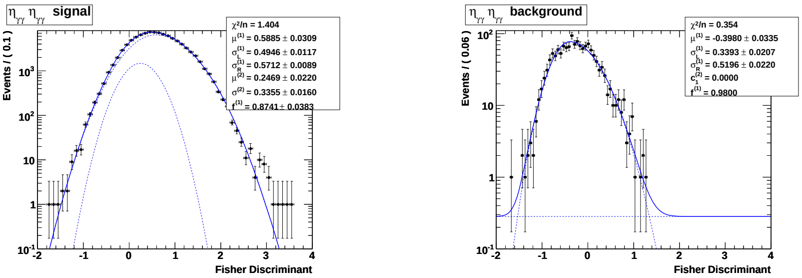

Figure B.9: Fisher PDFs: signal, asymmetric Gaussian plus Gaussian; continuum background, asymmetric Gaussian plus first order Chebyshev polynomial.

B.4 $B^0 \longrightarrow \eta_{\gamma\gamma}\eta_{3\pi}$

	$m_{\rm ES}$	ΔE	Fisher
$m_{\rm ES}$	$+1.000$		
ΔE	-0.003	$+1.000$	
Fisher	$+0.024$	-0.006	$+1.000$

Table B.8: Correlation matrix for signal MC events.

	$m_{\rm ES}$	ΔE	Fisher
$m_{\rm ES}$	$+1.000$		
ΔE	-0.011	$+1.000$	
Fisher	-0.009	$+0.038$	$+1.000$

Table B.9: Correlation matrix in on-peak side band data.

```
mES_xi_bg_float = -23.587 +/- 5.882 L(-50.000 - -10.000)
deltaE_c1_bg_float = -0.335 +/- 0.040 L(-2.000 - 2.000)
fisher_Mu1_bg_float = -0.343 +/- 0.028 L(-5.000 - 5.000)
fisher_Sigma1_bg_float = 0.387 +/- 0.018 L(0.000 - 5.000)
fisher_Sigma2_bg_float = 0.473 +/- 0.020 L(0.000 - 5.000)
```

Final values for the parameters which were allowed to float in the fit.

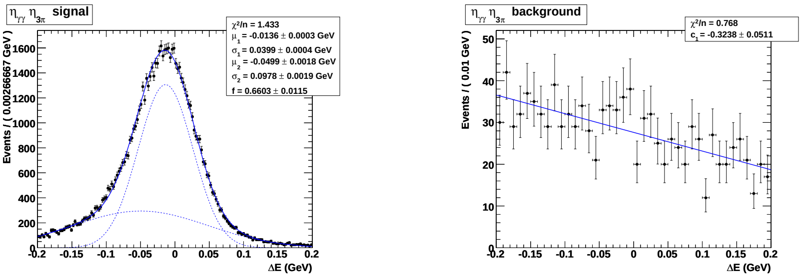

Figure B.10: ΔE PDFs: signal, double Gaussian; continuum background, Chebyshev first order polynomial.

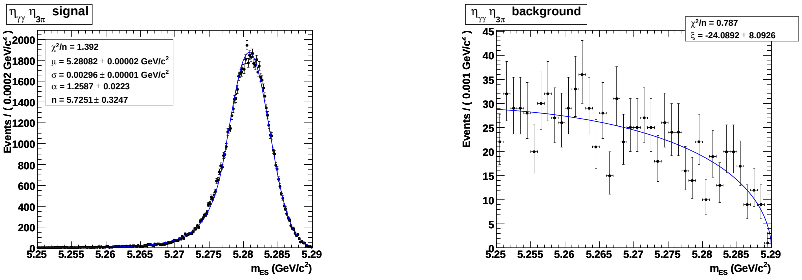

Figure B.11: m_{ES} PDFs: signal, Crystal Ball; continuum background, Argus function.

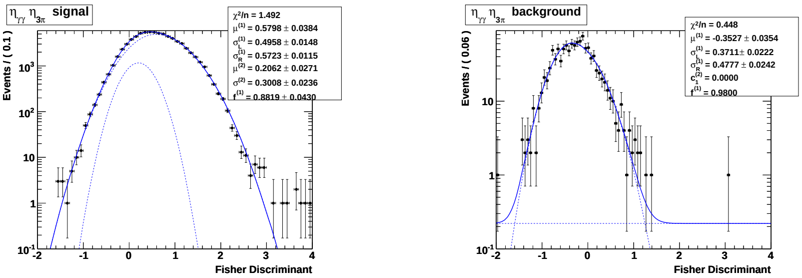

Figure B.12: Fisher PDFs: signal, asymmetric Gaussian plus Gaussian; continuum background, asymmetric Gaussian plus first order Chebyshev polynomial.

B.5 $B^0 \longrightarrow \eta_{3\pi}\eta_{3\pi}$

	$m_{\rm ES}$	ΔE	Fisher
$m_{\rm ES}$	$+1.000$		
ΔE	$+0.031$	$+1.000$	
Fisher	$+0.019$	$+0.010$	$+1.000$

Table B.10: Correlation matrix for signal MC events.

	$m_{\rm ES}$	ΔE	Fisher
$m_{\rm ES}$	$+1.000$		
ΔE	-0.092	$+1.000$	
Fisher	$+0.019$	-0.062	$+1.000$

Table B.11: Correlation matrix in on-peak side band data.

```
mES_xi_bg_float = -21.839 +/- 15.632 L(-100.000 - 15.000)
deltaE_c1_bg_float = -0.407 +/- 0.100 L(-2.000 - 2.000)
fisher_Mu1_bg_float = -0.620 +/- 0.071 L(-5.000 - 5.000)
fisher_Sigma1_bg_float = 0.201 +/- 0.046 L(0.000 - 5.000)
fisher_Sigma2_bg_float = 0.668 +/- 0.053 L(0.000 - 5.000)
```

Final values for the parameters which were allowed to float in the fit.

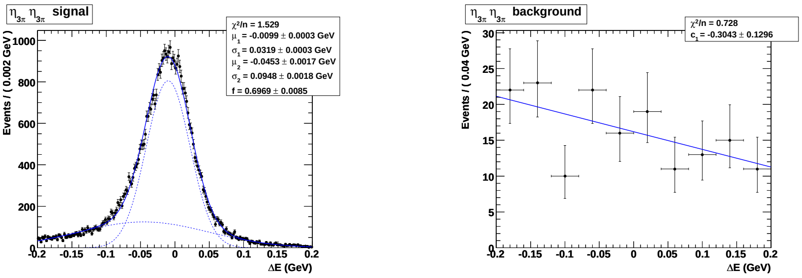

Figure B.13: ΔE PDFs: signal, double Gaussian; continuum background, Chebyshev first order polynomial.

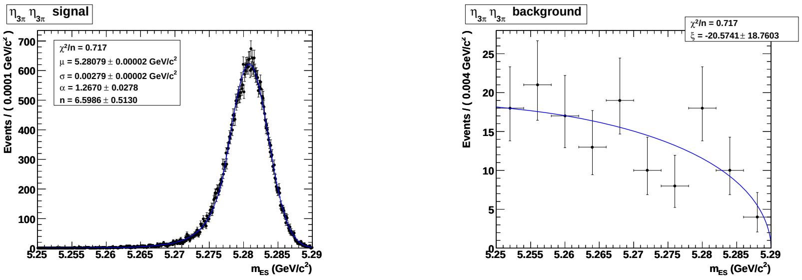

Figure B.14: m_{ES} PDFs: signal, Crystal Ball; continuum background, Argus function.

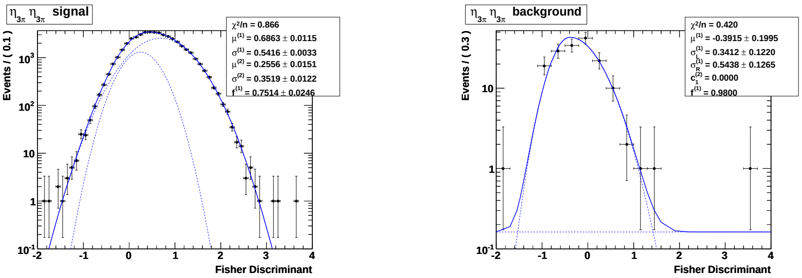

Figure B.15: Fisher PDFs: signal, double Gaussian; continuum background, asyimmetric Gaussian plus first order Chebyshev polynomial.

B.6 $B^0 \longrightarrow \eta_{\gamma\gamma}\omega$

	$m_{\rm ES}$	ΔE	ω Helicity	ω Mass	Fisher
$m_{\rm ES}$	$+1.000$				
ΔE	-0.031	$+1.000$			
ω Helicity	-0.002	$+0.004$	$+1.000$		
ω mass	$+0.006$	$+0.052$	$+0.007$	$+1.000$	
Fisher	$+0.010$	-0.011	-0.004	$+0.000$	$+1.000$

Table B.12: Correlation matrix for signal MCTruth MC events.

	$m_{\rm ES}$	ΔE	ω Helicity	ω Mass	Fisher
$m_{\rm ES}$	$+1.000$				
ΔE	$+0.064$	$+1.000$			
ω Helicity	$+0.006$	-0.000	$+1.000$		
ω mass	-0.016	$+0.063$	-0.004	$+1.000$	
Fisher	$+0.040$	-0.022	-0.003	-0.011	$+1.000$

Table B.13: Correlation matrix for signal SCF MC events.

	$m_{\rm ES}$	ΔE	ω Helicity	ω Mass	Fisher
$m_{\rm ES}$	$+1.000$				
ΔE	$+0.009$	$+1.000$			
ω Helicity	$+0.016$	-0.001	$+1.000$		
ω mass	-0.003	$+0.013$	-0.004	$+1.000$	
Fisher	-0.004	-0.022	$+0.014$	-0.006	$+1.000$

Table B.14: Correlation matrix in on-peak side band data.

	$m_{\rm ES}$	ΔE	ω Helicity	ω Mass	Fisher
$m_{\rm ES}$	$+1.000$				
ΔE	$+0.059$	$+1.000$			
ω Helicity	-0.005	$+0.023$	$+1.000$		
ω mass	-0.031	-0.015	-0.012	$+1.000$	
Fisher	$+0.050$	$+0.033$	-0.009	$+0.010$	$+1.000$

Table B.15: Correlation matrix in $B\overline{B}$ peaking events.

	$m_{\rm ES}$	ΔE	ω Helicity	ω Mass	Fisher
$m_{\rm ES}$	$+1.000$				
ΔE	$+0.071$	$+1.000$			
ω Helicity	-0.034	$+0.106$	$+1.000$		
ω mass	-0.010	$+0.061$	-0.050	$+1.000$	
Fisher	$+0.035$	-0.005	-0.066	$+0.115$	$+1.000$

Table B.16: Correlation matrix in $B\overline{B}$ charmed events.

```
deltaE_c1_bg_float = -0.300 +/- 0.017 L(-2.000 - 2.000)
mES_xi_bg_float = -19.345 +/- 2.568 L(-200.000 - 100.000)
omegaMass_Frac1_bg_float = 0.105 +/- 0.008 L(0.000 - 1.000)
omegaMass_c1_bg_float = 0.203 +/- 0.018 L(-2.000 - 2.000)
helicityOmega_c1_bg_float = -0.008 +/- 0.016 L(-2.000 - 2.000)
helicityOmega_c2_bg_float = -0.375 +/- 0.022 L(-5.000 - 5.000 )
fisher_Mu1_bg_float = -0.140 +/- 0.008 L(-5.000 - 5.000)
fisher_Sigma1_bg_float = 0.284 +/- 0.005 L(0.000 - 5.000)
```

Final values for the parameters which were allowed to float in the fit.

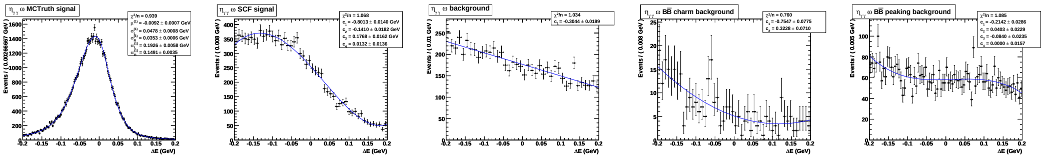

Figure B.16: ΔE PDFs: signal MCTruth, Cruijff function; signal SCF, fourth order Chebyshev polynomial; continuum background, Chebyshev first order polynomial; $B\overline{B}$ charmed background, Chebyshev second order polynomiall; $B\overline{B}$ peaking background, Chebyshev fourth order polynomial.

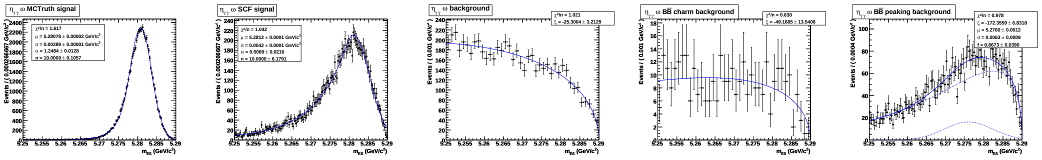

Figure B.17: m_{ES} PDFs: signal MCTruth, Crystal Ball; signal SCF, Crystal Ball continuum background, Argus function; $B\overline{B}$ charmed background, Argus Function; $B\overline{B}$ peaking background, Gaussian plus Argus Function.

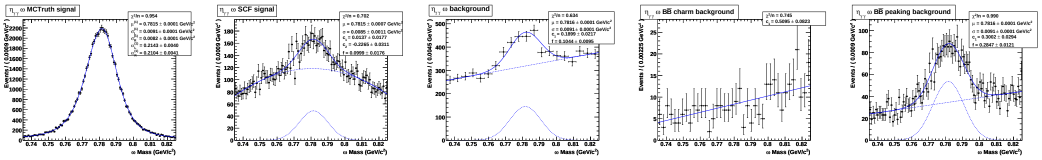

Figure B.18: ω mass PDFs: signal MCTruth, Cruijff function; signal SCF, Gaussian plus second order Chebyshev polynomial; continuum background, MC Gaussian plus first order Chebyshev polynomial; $B\overline{B}$ charmed background, first order Chebyshev polynomial; $B\overline{B}$ peaking background, MC Gaussian plus first order Chebyshev polynomial.

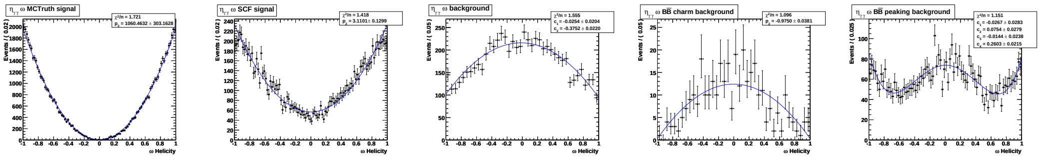

Figure B.19: ω helicity PDFs: signal MCTruth, second order polynomial; signal SCF, second order polynomial; continuum background, second order Chebyshev polynomial; $B\overline{B}$ charmed background, second order Chebyshev polynomial; $B\overline{B}$ peaking background, fourth order Chebyshev polynomial.

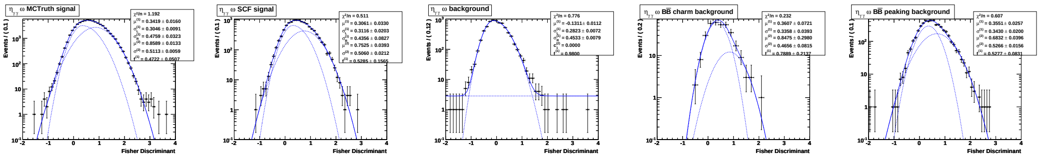

Figure B.20: Fisher PDFs: signal MCTruth, asymmetric Gaussian plus Gaussian; signal SCF, asymmetric Gaussian plus Gaussian;continuum background, asymmetric Gaussian plus first order Chebyshev polynomial; $B\overline{B}$ charmed background, double Gaussian; $B\overline{B}$ peaking background, double Gaussian.

B.7 $B^0 \rightarrow \eta_{3\pi}\omega$

	$m_{\rm ES}$	ΔE	ω Helicity	ω Mass	Fisher
$m_{\rm ES}$	$+1.000$				
ΔE	$+0.090$	$+1.000$			
ω Helicity	-0.001	$+0.001$	$+1.000$		
ω mass	-0.009	$+0.073$	-0.001	$+1.000$	
Fisher	$+0.039$	$+0.022$	-0.001	-0.001	$+1.000$

Table B.17: Correlation matrix for signal MC events.

	$m_{\rm ES}$	ΔE	ω Helicity	ω Mass	Fisher
$m_{\rm ES}$	$+1.000$				
ΔE	-0.016	$+1.000$			
ω Helicity	$+0.002$	-0.006	$+1.000$		
ω mass	-0.003	$+0.000$	-0.004	$+1.000$	
Fisher	$+0.003$	$+0.013$	-0.015	-0.015	$+1.000$

Table B.18: Correlation matrix in on-peak side band data.

	$m_{\rm ES}$	ΔE	ω Helicity	ω Mass	Fisher
$m_{\rm ES}$	$+1.000$				
ΔE	$+0.034$	$+1.000$			
ω Helicity	$+0.027$	-0.010	$+1.000$		
ω mass	-0.023	-0.024	-0.047	$+1.000$	
Fisher	$+0.071$	$+0.048$	-0.003	-0.056	$+1.000$

Table B.19: Correlation matrix in $B\overline{B}$ peaking events.

	$m_{\rm ES}$	ΔE	ω Helicity	ω Mass	Fisher
$m_{\rm ES}$	$+1.000$				
ΔE	$+0.072$	$+1.000$			
ω Helicity	-0.039	-0.055	$+1.000$		
ω mass	-0.062	-0.058	-0.076	$+1.000$	
Fisher	-0.011	-0.092	-0.046	$+0.057$	$+1.000$

Table B.20: Correlation matrix in $B\overline{B}$ charmed events.

```
deltaE_c1_bg_float = -0.331 +/- 0.018 L(-2.000 - 2.000)
mES_xi_bg_float = -14.973 +/- 2.747 L(-200.000 - 100.000)
omegaMass_Frac1_bg_float = 0.107 +/- 0.009 L(0.000 - 1.000)
omegaMass_c1_bg_float = 0.206 +/- 0.020 L(-2.000 - 2.000)
helicityOmega_c1_bg_float = -0.001 +/- 0.021 L(-2.000 - 2.000)
helicityOmega_c2_bg_float = -0.263 +/- 0.023 L(-20.000 - 20.000)
helicityOmega_c3_bg_float = 0.017 +/- 0.018 L(-200.000 - 200.000)
helicityOmega_c4_bg_float = 0.121 +/- 0.018 L(-200.000 - 200.000)
fisher_Mu1_bg_float = -0.376 +/- 0.010 L(-5.000 - 5.000)
fisher_Sigma1_bg_float = 0.378 +/- 0.007 L(0.000 - 5.000)
```

Final values for the parameters which were allowed to float in the fit.

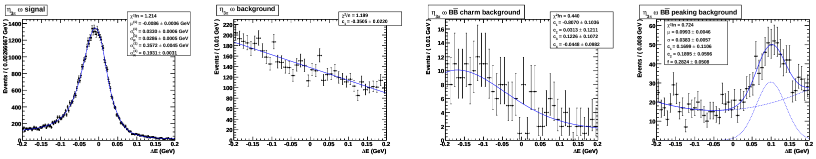

Figure B.21: ΔE PDFs: signal, Cruijff function; continuum background, Chebyshev first order polynomial; $B\overline{B}$ charmed background, Chebyshev fourth order polynomiall; $B\overline{B}$ peaking background, Gaussian plus Chebyshev second order polynomial.

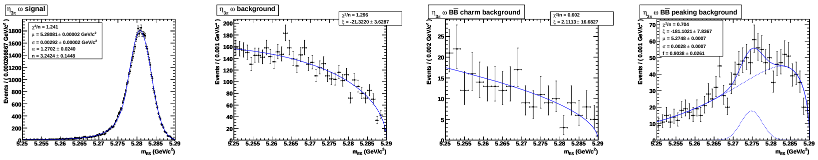

Figure B.22: $m_{\rm ES}$ PDFs: signal, Crystal Ball; continuum background, Argus function; $B\overline{B}$ charmed background, Argus Function; $B\overline{B}$ peaking background, Gauusian plus Argus Function.

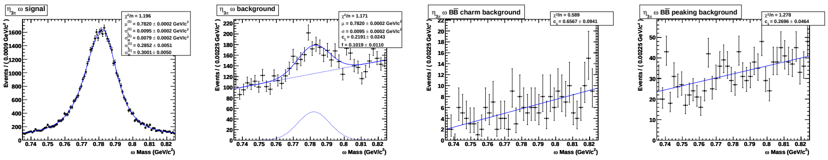

Figure B.23: ω mass PDFs: signal, Cruijff function; continuum background, MC Gaussian plus first order Chebyshev polynomial; $B\overline{B}$ charmed background, first order Chebyshev polynomial; $B\overline{B}$ peaking background, first order Chebyshev polynomial.

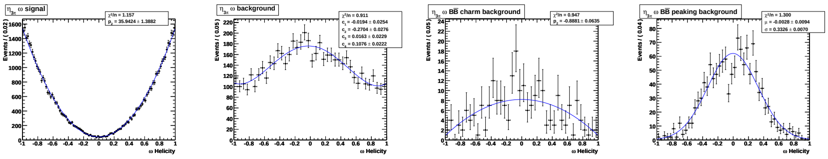

Figure B.24: ϕ helicity PDFs: signal, second order polynomial; continuum background, fourth order Chebyshev polynomial; $B\overline{B}$ charmed background, second order polynomial; $B\overline{B}$ peaking background, Gaussian.

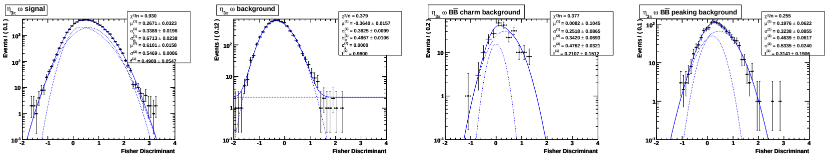

Figure B.25: Fisher PDFs: signal, asymmetric Gaussian plus Gaussian; continuum background, asymmetric Gaussian plus first order Chebyshev polynomial; $B\overline{B}$ charmed background, double Gaussian; $B\overline{B}$ peaking background, double Gaussian.

B.8 $B^0 \to \eta_{\gamma\gamma}\phi$

	$m_{\rm ES}$	ΔE	$\mathcal{H}_\phi$	Fisher
$m_{\rm ES}$	$+1.000$			
ΔE	-0.009	$+1.000$		
$\mathcal{H}_\phi$	-0.001	-0.002	$+1.000$	
Fisher	$+0.008$	-0.009	$+0.002$	$+1.000$

Table B.21: Correlation matrix for signal MC events.

	$m_{\rm ES}$	ΔE	$\mathcal{H}_\phi$	Fisher
$m_{\rm ES}$	$+1.000$			
ΔE	$+0.034$	$+1.000$		
$\mathcal{H}_\phi$	$+0.029$	-0.080	$+1.000$	
Fisher	-0.049	-0.027	-0.009	$+1.000$

Table B.22: Correlation matrix in on-peak side band data.

```
mES_xi_bg_float = -39.622 +/- 6.676 L(-100.000 - 10.000)
deltaE_c1_bg_float = -0.326 +/- 0.045 L(-2.000 - 2.000)
fisher_Mu1_bg_float = -0.365 +/- 0.032 L(-5.000 - 5.000)
fisher_Sigma1_bg_float = 0.356 +/- 0.021 L(0.000 - 5.000)
fisher_Sigma2_bg_float = 0.517 +/- 0.022 L(0.000 - 5.000)
helicityPhi_c0_bg_float = -0.053 +/- 0.045 L(-10.000 - 100.000)
```

Final values for the parameters which were allowed to float in the fit.

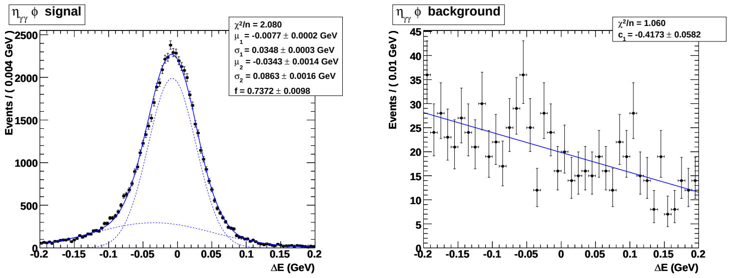

Figure B.26: ΔE PDFs: signal, double Gaussian; continuum background, Chebyshev first order polynomial.

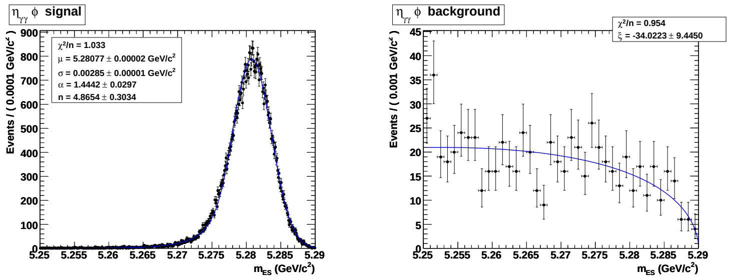

Figure B.27: m_{ES} PDFs: signal, Crystal Ball; continuum background, Argus function.

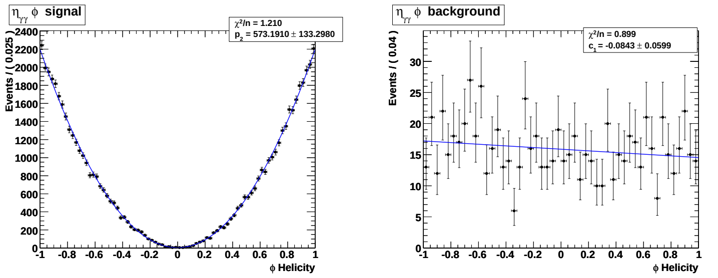

Figure B.28: ϕ helicity PDFs: signal, second order polynomial; background, first order Chebyshev polynomial.

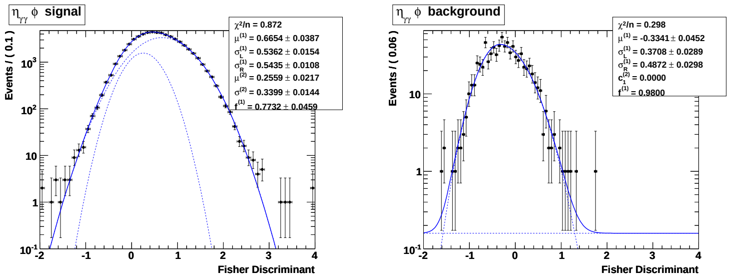

Figure B.29: Fisher PDFs: signal, double Gaussian; continuum background, asymmetric Gaussian plus first order Chebyshev polynomial.

B.9 $B^0 \longrightarrow \eta_{3\pi}\phi$

	$m_{\rm ES}$	ΔE	$\mathcal{H}_\phi$	Fisher
$m_{\rm ES}$	$+1.000$			
ΔE	$+0.008$	$+1.000$		
$\mathcal{H}_\phi$	$+0.007$	$+0.000$	$+1.000$	
Fisher	$+0.014$	$+0.011$	$+0.006$	$+1.000$

Table B.23: Correlation matrix for signal MC events.

	$m_{\rm ES}$	ΔE	$\mathcal{H}_\phi$	Fisher
$m_{\rm ES}$	$+1.000$			
ΔE	-0.021	$+1.000$		
$\mathcal{H}_\phi$	$+0.001$	-0.047	$+1.000$	
Fisher	$+0.037$	-0.057	$+0.072$	$+1.000$

Table B.24: Correlation matrix in on-peak side band data.

```
mES_xi_bg_float = -28.869 +/- 11.379 L(-100.000 - 10.000)
deltaE_c1_bg_float = -0.373 +/- 0.075 L(-2.000 - 2.000)
fisher_Mu1_bg_float = -0.341 +/- 0.050 L(-5.000 - 5.000)
fisher_Sigma1_bg_float = 0.366 +/- 0.033 L(0.000 - 5.000)
fisher_Sigma2_bg_float = 0.509 +/- 0.035 L(0.000 - 5.000)
helicityPhi_c0_bg_float = 0.038 +/- 0.075 L(-10.000 - 100.000)
```

Final values for the parameters which were allowed to float in the fit.

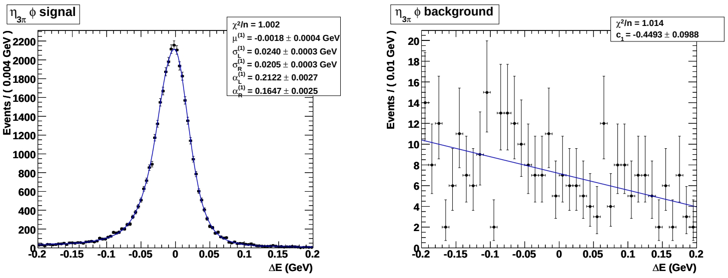

Figure B.30: ΔE PDFs: signal, Cruijff function; continuum background, Chebyshev first order polynomial.

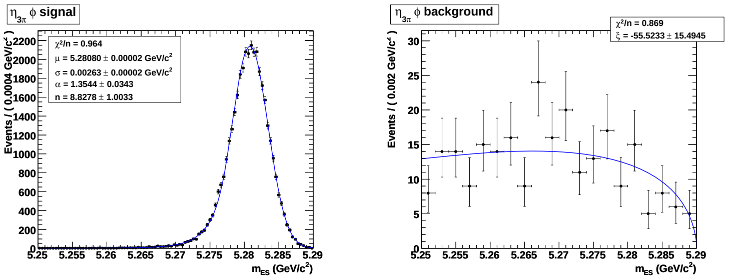

Figure B.31: m_{ES} PDFs: signal, Crystal Ball; continuum background, Argus function.

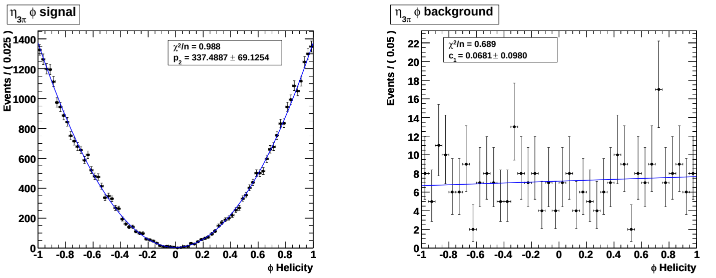

Figure B.32: ϕ helicity PDFs: signal, second order polynomial; background, first order Chebyshev polynomial.

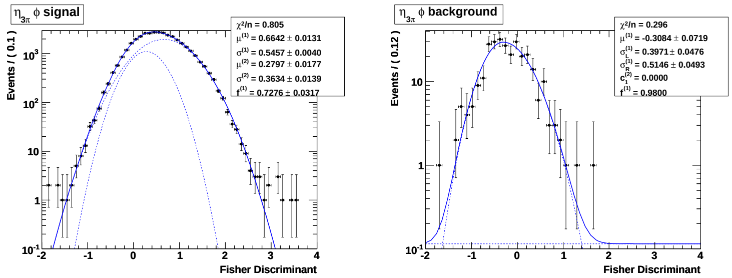

Figure B.33: Fisher PDFs: signal, double Gaussian; continuum background, asymmetric Gaussian plus first order Chebyshev polynomial.

B.10 $B^0 \rightarrow \eta'_{\eta\pi\pi}\eta'_{\eta\pi\pi}$

	$m_{\rm ES}$	ΔE	Fisher	$\eta'_{\eta\pi\pi}$ Mass (1)	$\eta'_{\eta\pi\pi}$ Mass (2)
$m_{\rm ES}$	$+1.000$				
ΔE	$+0.068$	$+1.000$			
Fisher	$+0.028$	$+0.003$	$+1.000$		
$\eta'_{\eta\pi\pi}$ Mass (1)	-0.017	-0.018	-0.002	$+1.000$	
$\eta'_{\eta\pi\pi}$ Mass (2)	-0.004	-0.007	-0.011	$+0.004$	$+1.000$

Table B.25: Correlation matrix for signal MC events.

	$m_{\rm ES}$	ΔE	Fisher	$\eta'_{\eta\pi\pi}$ Mass (1)	$\eta'_{\eta\pi\pi}$ Mass (2)
$m_{\rm ES}$	$+1.000$				
ΔE	$+0.141$	$+1.000$			
Fisher	-0.013	-0.070	$+1.000$		
$\eta'_{\eta\pi\pi}$ Mass (1)	-0.014	-0.121	-0.003	$+1.000$	
$\eta'_{\eta\pi\pi}$ Mass (2)	-0.073	-0.086	$+0.039$	$+0.018$	$+1.000$

Table B.26: Correlation matrix in on-peak side band data.

```
mES_xi_bg_float = -0.076 +/- 17.708 L(-200.000 - 100.000)
deltaE_c1_bg_float = -0.399 +/- 0.107 L(-2.000 - 2.000)
fisher_Mu1_bg_float = -0.454 +/- 0.058 L(-5.000 - 5.000)
fisher_Sigma1_bg_float = 0.290 +/- 0.039 L(0.000 - 5.000)
fisher_Sigma2_bg_float = 0.511 +/- 0.043 L(0.000 - 5.000)
etapMassEPP1_Mu_bg_float = 0.9597 +/- 0.0010 L(0.9400 - 0.9700)
etapMassEPP1_Sigma_bg_float = 0.0133 +/- 0.0009 L(0.0000 - 1.0000)
etapMassEPP2_Mu_bg_float = 0.9591 +/- 0.0009 L(0.9400 - 0.9700)
etapMassEPP2_Sigma_bg_float = 0.0127 +/- 0.0008 L(0.0000 - 1.0000)
```

Final values for the parameters which were allowed to float in the fit.

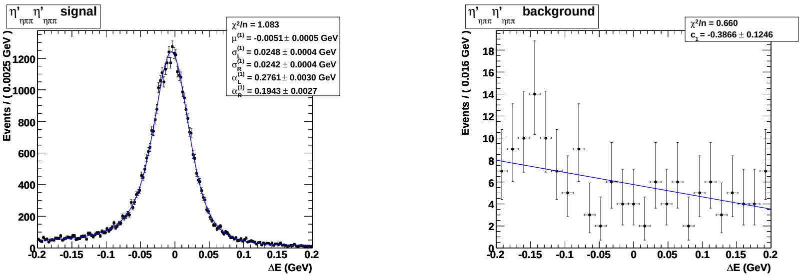

Figure B.34: ΔE PDFs: signal, Cruijff function; continuum background, Chebyshev first order polynomial.

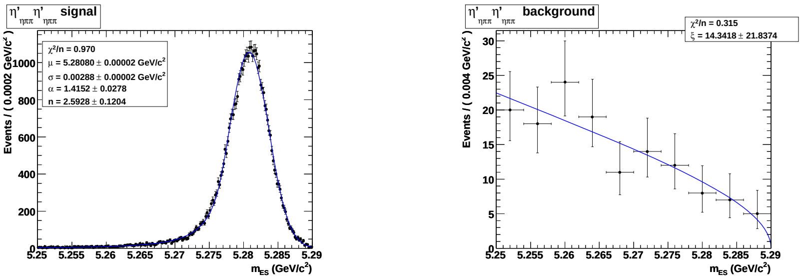

Figure B.35: m_{ES} PDFs: signal, Crystal Ball; continuum background, Argus function.

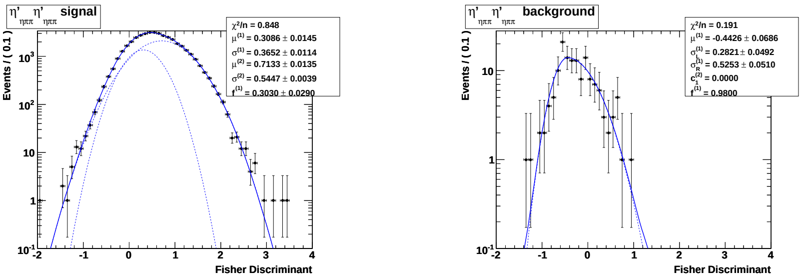

Figure B.36: Fisher PDFs: signal, double Gaussian; continuum background, asymmetric Gaussian plus first order Chebyshev polynomial.

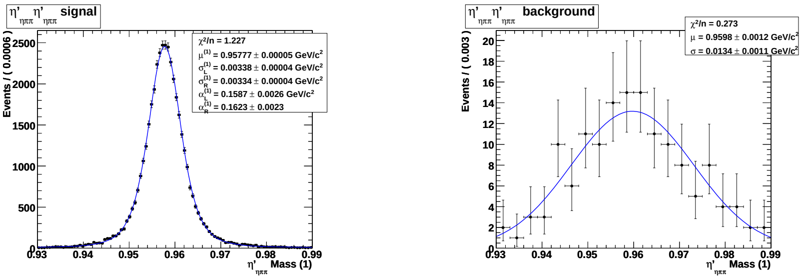

Figure B.37: $\eta'_{\eta\pi\pi}$ mass (1) PDFs: signal, Cruijff function; continuum background, Gaussian.

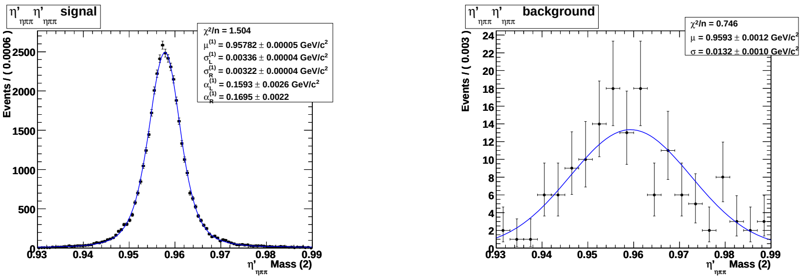

Figure B.38: $\eta'_{\eta\pi\pi}$ mass (2) PDFs: signal,Cruijff function; continuum background, Gaussian.

B.11 $B^0 \to \eta'_{\rho\gamma}\eta'_{\eta\pi\pi}$

	$m_{\rm ES}$	ΔE	Fisher	$\eta'_{\rho\gamma}$ Mass	$\eta'_{\eta\pi\pi}$ Mass
$m_{\rm ES}$	$+1.000$				
ΔE	$+0.023$	$+1.000$			
Fisher	$+0.030$	-0.003	$+1.000$		
$\eta'_{\rho\gamma}$ Mass	$+0.023$	$+0.080$	-0.006	$+1.000$	
$\eta'_{\eta\pi\pi}$ Mass	-0.005	-0.005	-0.004	$+0.003$	$+1.000$

Table B.27: Correlation matrix for signal MC events.

	$m_{\rm ES}$	ΔE	Fisher	$\eta'_{\rho\gamma}$ Mass	$\eta'_{\eta\pi\pi}$ Mass
$m_{\rm ES}$	$+1.000$				
ΔE	$+0.011$	$+1.000$			
Fisher	-0.040	-0.022	$+1.000$		
$\eta'_{\rho\gamma}$ Mass	-0.003	$+0.019$	-0.004	$+1.000$	
$\eta'_{\eta\pi\pi}$ Mass	-0.002	-0.009	-0.021	-0.010	$+1.000$

Table B.28: Correlation matrix in on-peak side band data.

	$m_{\rm ES}$	ΔE	Fisher	$\eta'_{\rho\gamma}$ Mass	$\eta'_{\eta\pi\pi}$ Mass
$m_{\rm ES}$	$+1.000$				
ΔE	$+0.185$	$+1.000$			
Fisher	$+0.019$	$+0.065$	$+1.000$		
$\eta'_{\rho\gamma}$ Mass	-0.014	$+0.054$	$+0.032$	$+1.000$	
$\eta'_{\eta\pi\pi}$ Mass	-0.029	-0.046	-0.013	-0.030	$+1.000$

Table B.29: Correlation matrix in $B\overline{B}$ peaking events.

	$m_{\rm ES}$	ΔE	Fisher	$\eta'_{\rho\gamma}$ Mass	$\eta'_{\eta\pi\pi}$ Mass
$m_{\rm ES}$	$+1.000$				
ΔE	-0.017	$+1.000$			
Fisher	$+0.013$	-0.082	$+1.000$		
$\eta'_{\rho\gamma}$ Mass	-0.061	-0.064	-0.011	$+1.000$	
$\eta'_{\eta\pi\pi}$ Mass	$+0.010$	-0.071	-0.005	-0.056	$+1.000$

Table B.30: Correlation matrix in $B\overline{B}$ charmed events.

```
mES_xi_bg_float = -20.683 +/- 2.963 L(-50.000 - -10.000)
deltaE_c1_bg_float = -0.338 +/- 0.020 L(-2.000 - 2.000)
fisher_Mu1_bg_float = -0.401 +/- 0.011 L(-5.000 - 5.000)
fisher_Sigma1_bg_float = 0.354 +/- 0.007 L(0.000 - 5.000)
etapMassRG1_c1_bg_float = 0.091 +/- 0.020 L(-100.000 - 100.000)
etapMassEPP2_Mu1_bg_float = 0.9582 +/- 0.0003 L(0.9400 - 0.9700)
etapMassEPP2_Sigma1_bg_float = 0.0049 +/- 0.0005 L(0.0000 - 1.0000)
etapMassEPP2_Frac_bg_float = 0.218 +/- 0.021 L(0.000 - 1.000)
etapMassEPP2_c1_bg_float = 0.104 +/- 0.022 L(-100.000 - 100.000)
etapMassEPP2_c2_bg_float = -0.630 +/- 0.035 L(-100.000 - 100.000)
```

Final values for the parameters which were allowed to float in the fit.

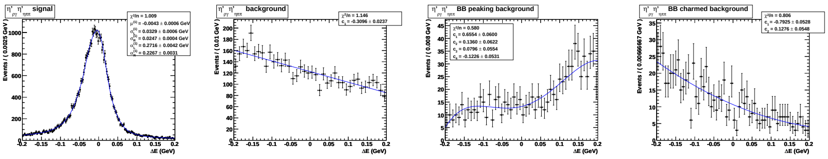

Figure B.39: ΔE PDFs: signal, Cruijff function; continuum background, Chebyshev first order polynomial; peaking $B\overline{B}$, fourth order Chebyshev polynomial; charmed $B\overline{B}$, second order Chebyshev polynomial.

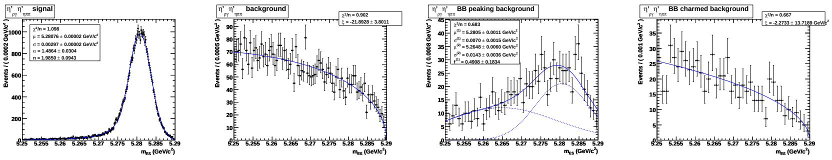

Figure B.40: m_{ES} PDFs: signal, Crystal Ball; continuum background, Argus function; peaking $B\overline{B}$, double Gaussian; charmed $B\overline{B}$, Argus function.

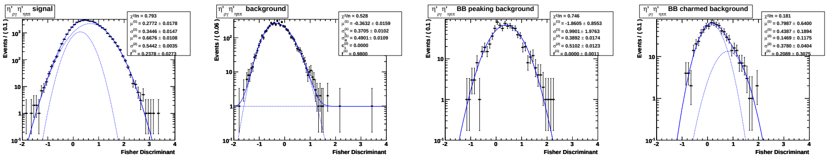

Figure B.41: Fisher PDFs: signal, double Gaussian; continuum background, asymmetric Gaussian plus first order Chebyshev polynomial; peaking $B\overline{B}$, double Gaussian; charmed $B\overline{B}$, double Gaussian.

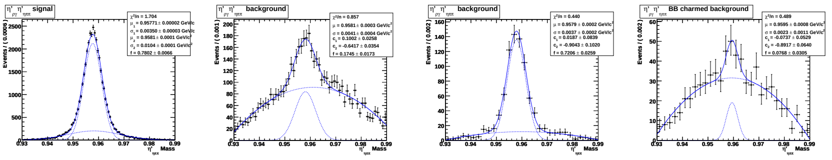

Figure B.42: $\eta'_{\eta\pi\pi}$ mass PDFs: signal, double Gaussian; continuum background, Gaussian plus second order Chebyshev polynomial; peaking $B\overline{B}$, Gaussian plus second order Chebyshev polynomial; charmed $B\overline{B}$, Gaussian plus second order Chebyshev polynomial.

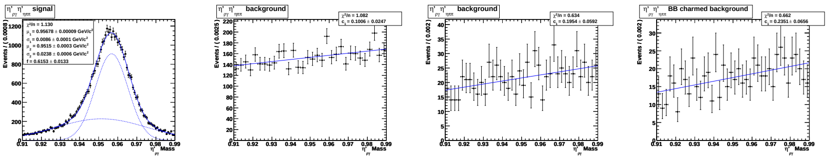

Figure B.43: $\eta'_{\rho\gamma}$ mass PDFs: signal, double Gaussian; continuum background, first order Chebyshev polynomial; peaking $B\overline{B}$, first order Chebyshev polynomial; charmed $B\overline{B}$, first order Chebyshev polynomial.

B.12 $B^0 \longrightarrow \eta'_{\eta\pi\pi}\omega$

	m_{ES}	ΔE	η' Mass	ω Helicity	ω Mass	Fisher
m_{ES}	$+1.000$					
ΔE	-0.039	$+1.000$				
η' Mass	-0.000	$+0.004$	$+1.000$			
ω Helicity	-0.002	-0.002	-0.011	$+1.000$		
ω Mass	$+0.011$	$+0.114$	$+0.005$	$+0.006$	$+1.000$	
Fisher	$+0.001$	-0.017	-0.007	$+0.011$	-0.011	$+1.000$

Table B.31: Correlation matrix for signal MCtruth MC events.

	m_{ES}	ΔE	η' Mass	ω Helicity	ω Mass	Fisher
m_{ES}	$+1.000$					
ΔE	$+0.089$	$+1.000$				
η' Mass	-0.005	-0.039	$+1.000$			
ω Helicity	$+0.001$	$+0.003$	-0.001	$+1.000$		
ω Mass	-0.017	$+0.052$	-0.009	-0.003	$+1.000$	
Fisher	$+0.036$	$+0.004$	-0.000	$+0.002$	-0.029	$+1.000$

Table B.32: Correlation matrix for signal SCF MC events.

	m_{ES}	ΔE	η' Mass	ω Helicity	ω Mass	Fisher
m_{ES}	$+1.000$					
ΔE	$+0.008$	$+1.000$				
η' Mass	-0.002	-0.028	$+1.000$			
ω Helicity	$+0.005$	-0.014	-0.015	$+1.000$		
ω Mass	-0.008	-0.021	-0.001	$+0.003$	$+1.000$	
Fisher	-0.006	$+0.016$	-0.005	$+0.007$	$+0.009$	$+1.000$

Table B.33: Correlation matrix in on-peak side band data.

	m_{ES}	ΔE	η' Mass	ω Helicity	ω Mass	Fisher
m_{ES}	$+1.000$					
ΔE	$+0.040$	$+1.000$				
η' Mass	$+0.029$	$+0.010$	$+1.000$			
ω Helicity	-0.018	-0.000	-0.074	$+1.000$		
ω Mass	$+0.036$	$+0.065$	$+0.022$	-0.082	$+1.000$	
Fisher	$+0.052$	$+0.109$	$+0.020$	-0.005	$+0.024$	$+1.000$

Table B.34: Correlation matrix in $B\overline{B}$ peaking events.

	m_{ES}	ΔE	η' Mass	ω Helicity	ω Mass	Fisher
m_{ES}	$+1.000$					
ΔE	-0.004	$+1.000$				
η' Mass	$+0.023$	-0.017	$+1.000$			
ω Helicity	-0.007	$+0.027$	-0.020	$+1.000$		
ω Mass	$+0.004$	$+0.075$	$+0.007$	-0.016	$+1.000$	
Fisher	-0.089	-0.100	-0.055	$+0.018$	-0.044	$+1.000$

Table B.35: Correlation matrix in $B\overline{B}$ charmed events.

```
deltaE_c1_bg_float = -0.388 +/- 0.019 L(-2.000 - 2.000)
mES_xi_bg_float = -16.276 +/- 2.826 L(-200.000 - 100.000)
etapMassEPP_Frac1_bg_float = 0.157 +/- 0.008 L(0.000 - 1.000)
etapMassEPP_c1_bg_float = 0.110 +/- 0.019 L(-2.000 - 2.000)
etapMassEPP_c2_bg_float = -0.733 +/- 0.023 L(-2.000 - 2.000)
omegaMass_Frac_bg_float = 0.089 +/- 0.009 L(0.000 - 1.000)
omegaMass_c1_bg_float = 0.192 +/- 0.020 L(-2.000 - 2.000)
helicityOmega_c1_bg_float = 0.000 +/- 0.021 L(-2.000 - 2.000)
helicityOmega_c2_bg_float = -0.293 +/- 0.023 L(-20.000 - 20.000)
helicityOmega_c3_bg_float = -0.005 +/- 0.019 L(-200.000 - 200.000)
helicityOmega_c4_bg_float = 0.096 +/- 0.019 L(-200.000 - 200.000)
fisher_Mu1_bg_float = -0.416 +/- 0.011 L(-5.000 - 5.000)
fisher_Sigma1_bg_float = 0.351 +/- 0.007 L(0.000 - 5.000)
```

Final values for the parameters which were allowed to float in the fit.

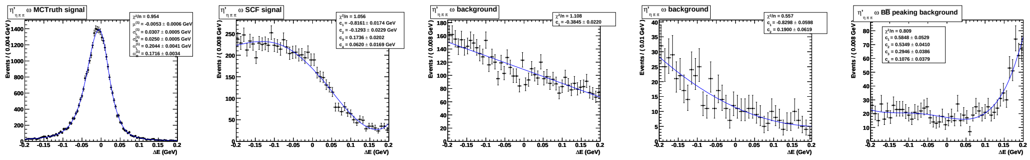

Figure B.44: ΔE PDFs: signal MCTruth, Cruijff function; signal SCF, fourth order Chebyshev polynomial; continuum background, Chebyshev first order polynomial, $B\overline{B}$ charmed background, Chebyshev second order polynomial; $B\overline{B}$ charmless background, Chebyshev fourth order polynomial.

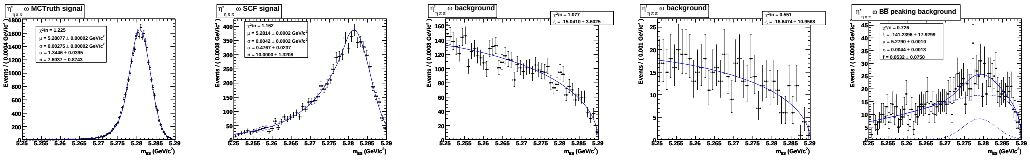

Figure B.45: m_{ES} PDFs: signal MCTruth, Crystal Ball; signal SCF, Crystal Ball; continuum background, Argus function; $B\overline{B}$ charmed background, Argus function; $B\overline{B}$ peaking background, Gaussian plus Argus function.

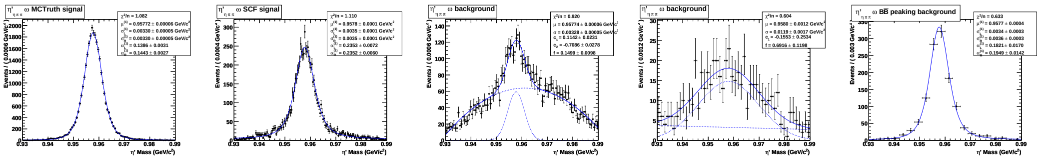

Figure B.46: η' mass PDFs: signal MCTruth, Cruijff function; signal SCF, Cruijff function; continuum background, MC Gaussian plus Chebyshev second order polynomial; $B\overline{B}$ charmed background, Gaussian plus first order Chebyshev polynomial; $B\overline{B}$ peaking background, Cruijff function.

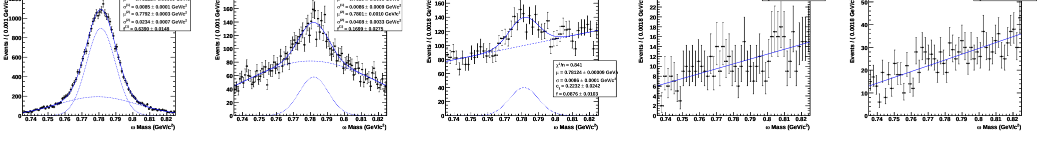

Figure B.47: ω mass PDFs: signal MCTruth, double Gaussian; signal SCF, double Gaussian; continuum background, MC Gaussian plus Chebyshev first order polynomial; $B\overline{B}$ charmed background, first order Chebyshev polynomial;$B\overline{B}$ peaking background, first order Chebyshev polynomial.

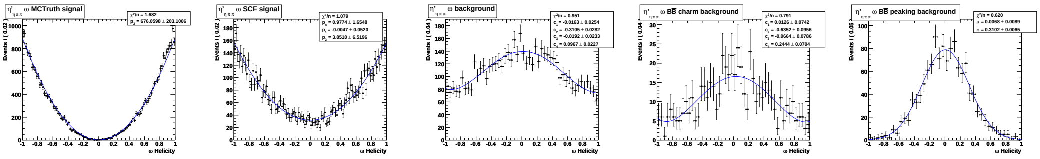

Figure B.48: ω helicity PDFs: signal MCTruth, second order polynomial; signal SCF, second order polynomial; continuum background, fourth order Chebyshev polynomial; $B\overline{B}$ charmed background, fourth order Chebyshev polynomial; $B\overline{B}$ peaking background, Gaussian.

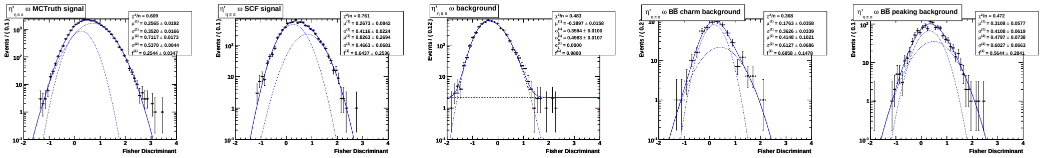

Figure B.49: Fisher PDFs: signal MCTruth, double Gaussian; signal SCF, double Gaussian;continuum background, asymmetric Gaussian plus first order Chebyshev polynomial; $B\overline{B}$ charmed background, double Gaussian; $B\overline{B}$ peaking background, double Gaussian.

B.13 $B^0 \to \eta'_{\rho\gamma}\omega$

	$m_{\rm ES}$	ΔE	η' Mass	ω Helicity	ω Mass	Fisher
$m_{\rm ES}$	$+1.000$					
ΔE	-0.060	$+1.000$				
η' Mass	$+0.004$	$+0.097$	$+1.000$			
ω Helicity	-0.004	$+0.002$	$+0.000$	$+1.000$		
ω Mass	$+0.012$	$+0.275$	-0.012	-0.011		
Fisher	$+0.004$	-0.011	-0.004	$+0.001$	$+0.007$	$+1.000$

Table B.36: Correlation matrix for signal MCTruth events.

	$m_{\rm ES}$	ΔE	η' Mass	ω Helicity	ω Mass	Fisher
$m_{\rm ES}$	$+1.000$					
ΔE	$+0.024$	$+1.000$				
η' Mass	$+0.009$	$+0.014$	$+1.000$			
ω Helicity	-0.004	-0.023	-0.002	$+1.000$		
ω Mass	-0.031	$+0.042$	-0.014	-0.026		
Fisher	$+0.041$	-0.013	$+0.009$	-0.013	-0.006	$+1.000$

Table B.37: Correlation matrix for signal SCF events.

	$m_{\rm ES}$	ΔE	η' Mass	ω Helicity	ω Mass	Fisher
$m_{\rm ES}$	$+1.000$					
ΔE	-0.005	$+1.000$				
η' Mass	$+0.007$	-0.001	$+1.000$			
ω Helicity	$+0.001$	-0.001	$+0.001$	$+1.000$		
ω Mass	-0.002	$+0.002$	-0.001	$+0.001$	$+1.000$	
Fisher	$+0.000$	-0.040	$+0.005$	$+0.005$	$+0.021$	$+1.000$

Table B.38: Correlation matrix in on-peak side band data.

	$m_{\rm ES}$	ΔE	η' Mass	ω Helicity	ω Mass	Fisher
$m_{\rm ES}$	$+1.000$					
ΔE	$+0.096$	$+1.000$				
η' Mass	-0.005	$+0.004$	$+1.000$			
ω Helicity	$+0.015$	$+0.011$	$+0.003$	$+1.000$		
ω Mass	-0.002	$+0.032$	$+0.014$	$+0.011$	$+1.000$	
Fisher	$+0.031$	$+0.005$	$+0.004$	-0.006	$+0.009$	$+1.000$

Table B.39: Correlation matrix in $B\overline{B}$ peaking events.

	m_{ES}	ΔE	η' Mass	ω Helicity	ω Mass	Fisher
m_{ES}	$+1.000$					
ΔE	$+0.003$	$+1.000$				
η' Mass	$+0.004$	-0.001	$+1.000$			
ω Helicity	$+0.005$	$+0.006$	-0.013	$+1.000$		
ω Mass	$+0.011$	$+0.016$	$+0.009$	$+0.009$	$+1.000$	
Fisher	$+0.001$	-0.045	-0.013	-0.011	$+0.016$	$+1.000$

Table B.40: Correlation matrix in $B\overline{B}$ charmed events.

```
mES_xi_bg_float = -19.903 +/- 1.200 L(-200.000 - 100.000)
deltaE_c1_bg_float = -0.336 +/- 0.009 L(-5.000 - 5.000)
etapMassRG_c1_bg_float = 0.086 +/- 0.008 L(-2.000 - 2.000)
omegaMass_c1_bg_float = 0.213 +/- 0.008 L(-2.000 - 2.000)
omegaMass_Frac_bg_float = 0.087 +/- 0.004 (0.000 - 1.000)
helicityOmega_c1_bg_float = 0.010 +/- 0.008 L(-2.000 - 2.000)
helicityOmega_c2_bg_float = -0.349 +/- 0.011 L(-2.000 - 2.000)
helicityOmega_c3_bg_float = 0.010 +/- 0.008 L(-200.000 - 200.000)
helicityOmega_c4_bg_float = 0.102 +/- 0.009 L(-2.000 - 2.000)
fisher_Mu1_bg_float = 0.130 +/- 0.010 L(-5.000 - 5.000)
fisher_Mu2_bg_float = -0.080 +/- 0.003 L(-5.000 - 5.000)
```

Final values for the parameters which were allowed to float in the fit.

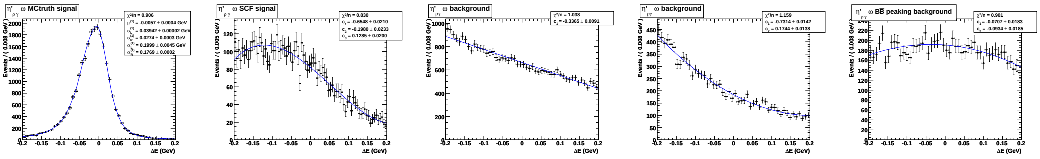

Figure B.50: ΔE PDFs: signal MCTruth, Cruijff function; signal SCF, third order Chebyshev polynomial; continuum background, Chebyshev first order polynomial; $B\overline{B}$ charmed background, Chebyshev second order polynomial; $B\overline{B}$ peaking background, Chebyshev second order polynomial.

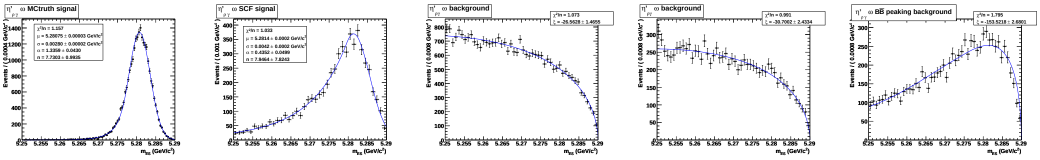

Figure B.51: m_{ES} PDFs: signal MCTruth, Crystal Ball;signal SCF, Crystal Ball; continuum background, Argus function; $B\overline{B}$ charmed background, Argus function; $B\overline{B}$ peaking background, Argus function.

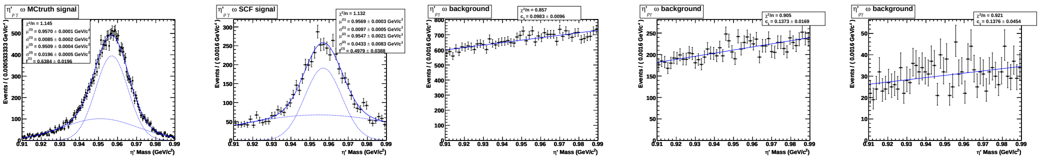

Figure B.52: η' mass PDFs: signal MCTruth, double Gaussian; signal SCF, double Gaussian; continuum background, first order polynomial; $B\overline{B}$ charmed background, first order Chebyshev polynomial; $B\overline{B}$ peaking background, first order Chebyshev polynomial.

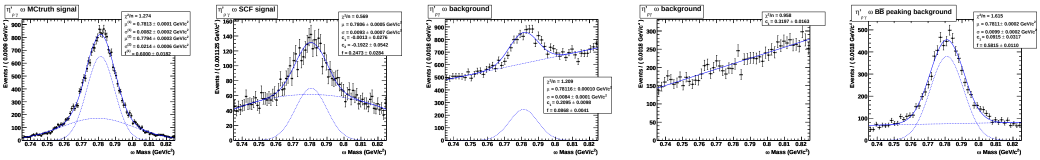

Figure B.53: ω mass PDFs: signal MCTruth, double Gaussian; signal SCF, Gaussian plus second order Chebyshev polynomial; continuum background, MC Gaussian plus Chebyshev first order polynomial; $B\overline{B}$ charmed background, first order Chebyshev polynomial; $B\overline{B}$ background, Gaussian plus first order Chebyshev polynomial.

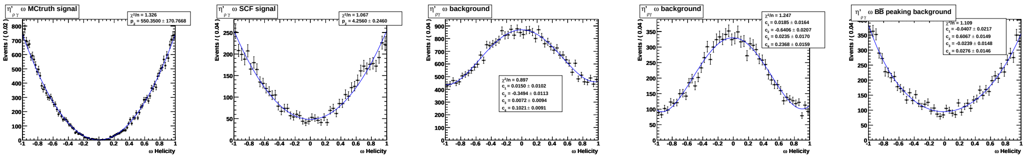

Figure B.54: ω helicity PDFs: signal MCTruth, second order polynomial; signal SCF, second order polynomial; continuum background, Chebyshev fourth order polynomial; $B\overline{B}$ charmed background, fourth order Chebyshev polynomial; $B\overline{B}$ peaking background, fourth order Chebyshev polynomial.

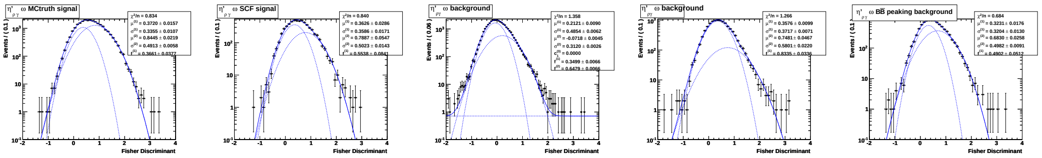

Figure B.55: Fisher PDFs: signal MCTruth, double Gaussian; signal SCF, double Gaussian; continuum background, double Gaussian plus first order Chebyshev polynomial; $B\overline{B}$ charmed background, double Gaussian; $B\overline{B}$ peaking background, double Gaussian.

B.14 $B^0 \rightarrow \eta'_{\eta\pi\pi}\phi$

	$m_{\rm ES}$	ΔE	η' Mass	ϕ Helicity	Fisher
$m_{\rm ES}$	$+1.000$				
ΔE	$+0.048$	$+1.000$			
η' Mass	-0.023	-0.024	$+1.000$		
ϕ Helicity	-0.001	$+0.007$	-0.001	$+1.000$	
Fisher	$+0.027$	$+0.008$	-0.003	-0.002	$+1.000$

Table B.41: Correlation matrix for signal MC events.

	$m_{\rm ES}$	ΔE	η' Mass	ϕ Helicity	Fisher
$m_{\rm ES}$	$+1.000$				
ΔE	$+0.092$	$+1.000$			
η' Mass	-0.022	$+0.008$	$+1.000$		
ϕ Helicity	$+0.061$	-0.043	$+0.005$	$+1.000$	
Fisher	$+0.123$	-0.033	$+0.077$	$+0.011$	$+1.000$

Table B.42: Correlation matrix in on-peak side band data.

```
mES_xi_bg_float = -15.297 +/- 11.806 L(-200.000 - 100.000)
deltaE_c1_bg_float = -0.342 +/- 0.079 L(-2.000 - 2.000)
fisher_Mu1_bg_float = -0.290 +/- 0.051 L(-5.000 - 5.000)
fisher_Sigma1_bg_float = 0.364 +/- 0.032 L(0.000 - 5.000)
fisher_Sigma2_bg_float = 0.464 +/- 0.034 L(0.000 - 5.000)
helicityPhi_c1_bg_float = 0.037 +/- 0.077 L(-2.000 - 2.000)
etapMassEPP_Frac1_bg_float = 0.213 +/- 0.035 L(0.000 - 1.000)
etapMassEPP_c1_bg_float = 0.205 +/- 0.085 L(-2.000 - 2.000)
etapMassEPP_c2_bg_float = -0.568 +/- 0.099 L(-2.000 - 2.000)
```

Final values for the parameters which were allowed to float in the fit.

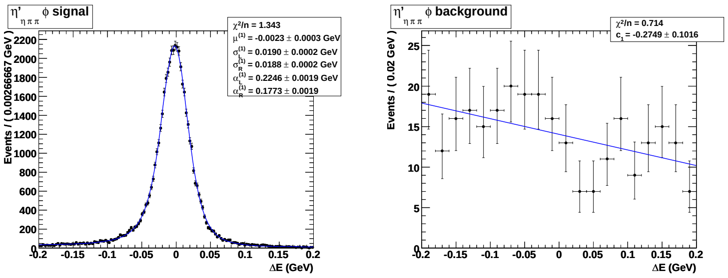

Figure B.56: ΔE PDFs: signal, Cruijff function; continuum background, Chebyshev first order polynomial.

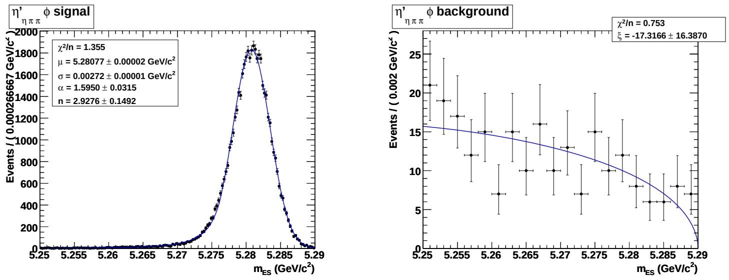

Figure B.57: m_{ES} PDFs: signal, Crystal Ball; continuum background, Argus function.

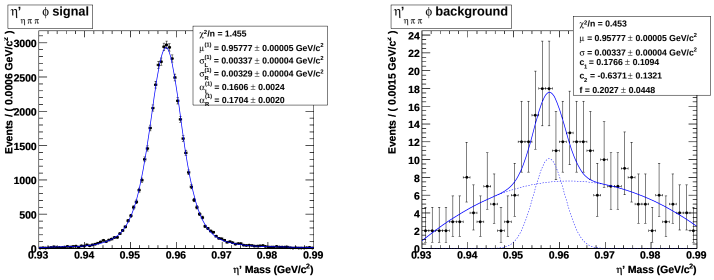

Figure B.58: η' mass PDFs: signal, Cruijff function; continuum background, MC Gaussian plus second order Chebyshev polynomial.

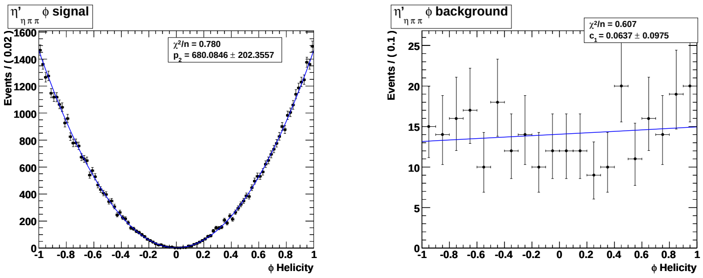

Figure B.59: ϕ helicity PDFs: signal, second order polynomial; continuum background, first order Chebyshev polynomial.

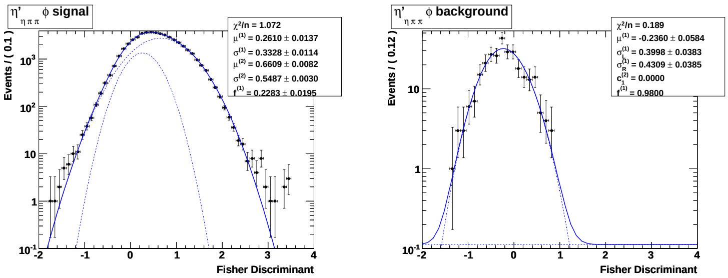

Figure B.60: Fisher PDFs: signal, double Gaussian; continuum background, asymmetric Gaussian plus first order Chebyshev polynomial.

B.15 $B^0 \to \eta'_{\rho\gamma}\phi$

	$m_{\rm ES}$	ΔE	η' Mass	ϕ Helicity	Fisher
$m_{\rm ES}$	$+1.000$				
ΔE	-0.061	$+1.000$			
η' mass	$+0.031$	$+0.140$	$+1.000$		
ϕ Helicity	-0.001	$+0.007$	$+0.005$	$+1.000$	
Fisher	$+0.001$	-0.004	$+0.000$	-0.004	$+1.000$

Table B.43: Correlation matrix for signal MCTruth MC events.

	$m_{\rm ES}$	ΔE	η' Mass	ϕ Helicity	Fisher
$m_{\rm ES}$	$+1.000$				
ΔE	$+0.051$	$+1.000$			
η' mass	-0.023	$+0.003$	$+1.000$		
ϕ Helicity	$+0.010$	-0.013	-0.010	$+1.000$	
Fisher	$+0.014$	-0.006	$+0.023$	-0.004	$+1.000$

Table B.44: Correlation matrix for signal SCF MC events.

	$m_{\rm ES}$	ΔE	η' Mass	ϕ Helicity	Fisher
$m_{\rm ES}$	$+1.000$				
ΔE	-0.014	$+1.000$			
η' mass	-0.022	$+0.031$	$+1.000$		
ϕ Helicity	$+0.021$	-0.004	$+0.008$	$+1.000$	
Fisher	-0.035	$+0.009$	$+0.001$	-0.014	$+1.000$

Table B.45: Correlation matrix in on-peak side band data.

	$m_{\rm ES}$	ΔE	η' Mass	ϕ Helicity	Fisher
$m_{\rm ES}$	$+1.000$				
ΔE	$+0.049$	$+1.000$			
η' mass	$+0.013$	-0.015	$+1.000$		
ϕ Helicity	-0.010	-0.001	$+0.011$	$+1.000$	
Fisher	$+0.048$	$+0.025$	$+0.025$	$+0.019$	$+1.000$

Table B.46: Correlation matrix in $B\overline{B}$ peaking events.

	m_{ES}	ΔE	η' Mass	ϕ Helicity	Fisher
m_{ES}	$+1.000$				
ΔE	-0.029	$+1.000$			
η' mass	-0.026	$+0.054$	$+1.000$		
ϕ Helicity	$+0.036$	$+0.018$	-0.039	$+1.000$	
Fisher	$+0.118$	-0.032	-0.003	-0.056	$+1.000$

Table B.47: Correlation matrix in $B\overline{B}$ charmed events.

```
deltaE_c1_bg_float = -0.227 +/- 0.022 L(-2.000 - 2.000)
mES_xi_bg_float = -31.321 +/- 3.180 L(-200.000 - 100.000)
etapMassRG_c1_bg_float = 0.040 +/- 0.022 L(-2.000 - 2.000)
helicityPhi_c1_bg_float = -0.031 +/- 0.027 L (-2.000 - 2.000)
helicityPhi_c2_bg_float = 0.131 +/- 0.025 L (-2.000 - 2.000)
fisher_Mu1_bg_float = -0.333 +/- 0.010 L(-5.000 - 5.000)
fisher_Sigma1_bg_float = 0.387 +/- 0.008 L(0.000 - 5.000)
```

Final values for the parameters which were allowed to float in the fit.

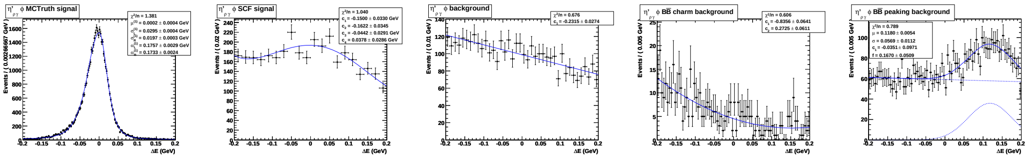

Figure B.61: ΔE PDFs: signal MCTruth, Cruijff function; signal SCF, fourth order Chebyshev polynomial; continuum background, Chebyshev first order polynomial; $B\overline{B}$ charmed background, Chebyshev second order polynomiall; $B\overline{B}$ peaking background, Gaussian plus Chebyshev first order polynomial.

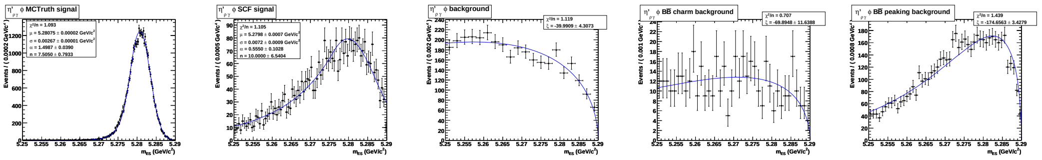

Figure B.62: m_{ES} PDFs: signal MCTruth, Crystal Ball; signal SCF, Crystal Ball; continuum background, Argus function; $B\overline{B}$ charmed background, Argus Function; $B\overline{B}$ peaking background, Argus Function.

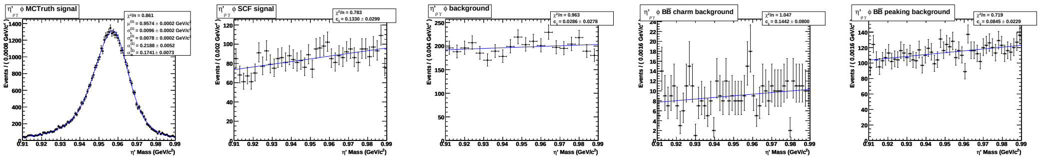

Figure B.63: η' mass PDFs: signal MCTruth, Cruijff function; signal SCF, first order Chebyshev polynomial; continuum background, first order Chebyshev polynomial; $B\overline{B}$ charmed background, first order Chebyshev polynomial; $B\overline{B}$ peaking background, first order Chebyshev polynomial.

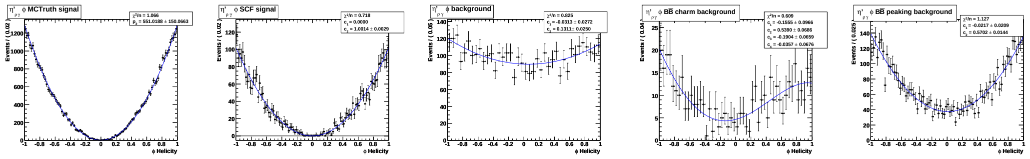

Figure B.64: ϕ helicity PDFs: signal MCTruth, second order polynomial; signal SCF, second order Chebyshev polynomial; continuum background, second order Chebyshev polynomial; $B\overline{B}$ charmed background, fourth order Chebyshev polynomial; $B\overline{B}$ peaking background, second order Chebyshev polynomial.

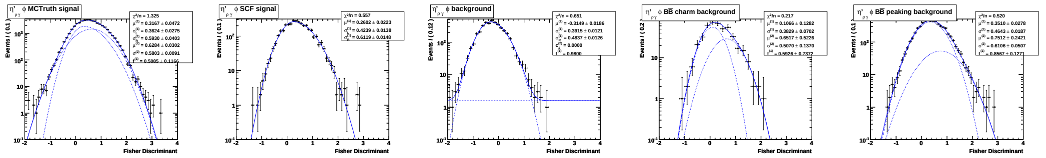

Figure B.65: Fisher PDFs: signal MCTruth, asymmetric Gaussian plus Gaussian; signal SCF, asymmetric Gaussian; continuum background, asymmetric Gaussian plus first order Chebyshev polynomial; $B\overline{B}$ charmed background, double Gaussian; $B\overline{B}$ peaking background, double Gaussian.

Appendix C

$sPlots$ Libraries for TD CP-Asymmetries Measurements

We show for each decay modes $sPlots$ (see sec. 4.4.3) for signal, continuum background and $B\bar{B}$. We perform this plots only for those variables that are included into the fit.

C.1 $B^0 \to \eta'_{\eta(\gamma\gamma)\pi\pi} K^0_{S(\pi^+\pi^-)}$

sPlot for	Signal yield	$q\bar{q}$ yield
ΔE	484 ± 25	932 ± 33
$m_{\rm ES}$	476 ± 26	940 ± 34
Fisher	483 ± 25	932 ± 33

Table C.1: Fit yields for signal and $q\bar{q}$ background observed while making sPlots, effectively removing one discriminating variable at a time from the fit.

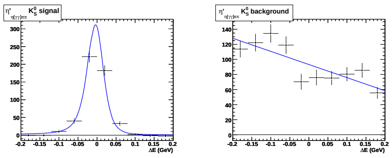

Figure C.1: sPlots for ΔE, in order: signal, continuum background.

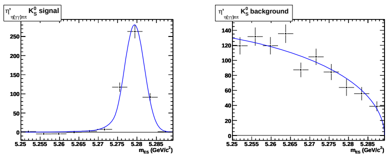

Figure C.2: sPlots for $m_{\rm ES}$: in order: signal, continuum background.

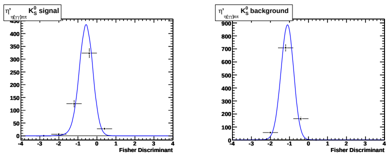

Figure C.3: sPlots for $\mathcal{F}$: in order: signal, continuum background.

C.2 $B^0 \to \eta'_{\eta(3\pi)\pi\pi} K^0_{S(\pi^+\pi^-)}$

sPlot for	Signal yield	$q\bar{q}$ yield
ΔE	176 ± 15	275 ± 18
$m_{\rm ES}$	170 ± 15	281 ± 19
Fisher	166 ± 15	286 ± 18

Table C.2: Fit yields for signal and $q\bar{q}$ background observed while making sPlots, effectively removing one discriminating variable at a time from the fit.

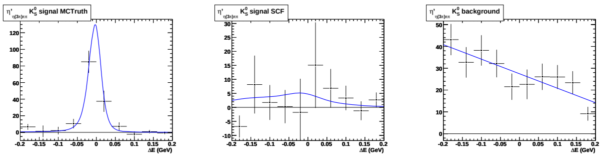

Figure C.4: sPlots for ΔE, in order: signal MC truth, signal SCF, continuum background.

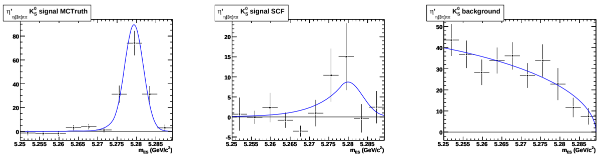

Figure C.5: sPlots for $m_{\rm ES}$: in order: signal MC Truth, signal SCF, continuum background.

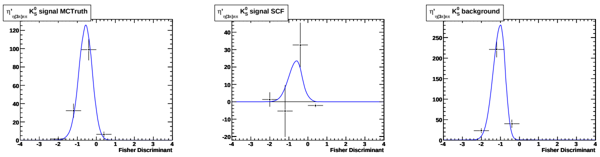

Figure C.6: sPlots for $\mathcal{F}$: in order: signal MC Truth, signal SCF, continuum background.

C.3 $B^0 \rightarrow \eta'_{\rho\gamma} K^0_{S(\pi^+\pi^-)}$

sPlot for	Signal yield	$q\bar{q}$ yield	$B\overline{B}$ charmed yield	$B\overline{B}$ ch/less (+) yield	$B\overline{B}$ ch/less (–) yield
ΔE	959 ± 72	19356 ± 160	-444 ± 209	581 ± 276	11 ± 243
m_{ES}	949 ± 49	19394 ± 167	-686 ± 376	146 ± 65	659 ± 283
Fisher	972 ± 47	18496 ± 537	978 ± 1016	298 ± 108	-282 ± 563

Table C.3: Fit yields for signal,$q\bar{q}$ background and different kind of $B\overline{B}$ background observed while making sPlots, effectively removing one discriminating variable at a time from the fit.

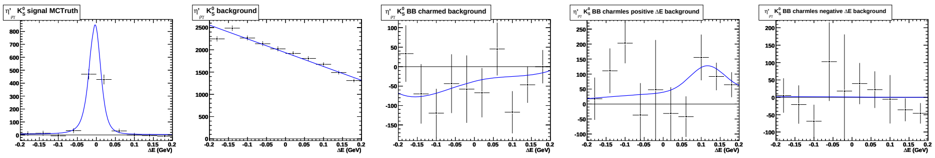

Figure C.7: sPlots for ΔE, in order: signal, continuum background, $B\overline{B}$ charm background, $B\overline{B}$ peaking background (positive ΔE mean), $B\overline{B}$ peaking background (negative ΔE mean).

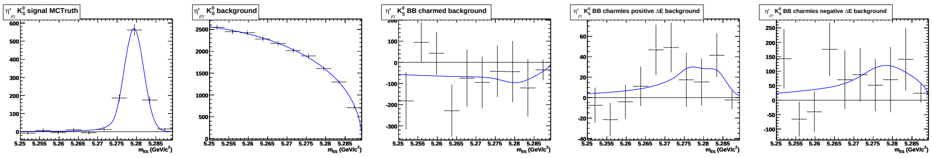

Figure C.8: sPlots for m_{ES}: in order: signal, continuum background, $B\overline{B}$ charm background, $B\overline{B}$ peaking background (positive ΔE mean), $B\overline{B}$ peaking background (negative ΔE mean).

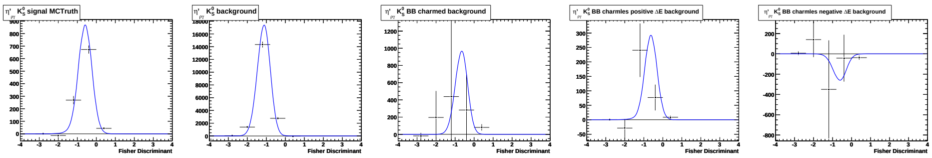

Figure C.9: sPlots for $\mathcal{F}$: in order: signal, continuum background, $B\overline{B}$ charm background, $B\overline{B}$ peaking background (positive ΔE mean), $B\overline{B}$ peaking background (negative ΔE mean).

C.4 $B^0 \longrightarrow \eta'_{\eta(\gamma\gamma)\pi\pi} K^0_{S(\pi^0\pi^0)}$

sPlot for	Signal yield	$q\bar{q}$ yield
ΔE	104 ± 14	778 ± 29
m_{ES}	107 ± 15	775 ± 30
Fisher	112 ± 18	771 ± 31

Table C.4: Fit yields for signal and $q\bar{q}$ background observed while making sPlots, effectively removing one discriminating variable at a time from the fit.

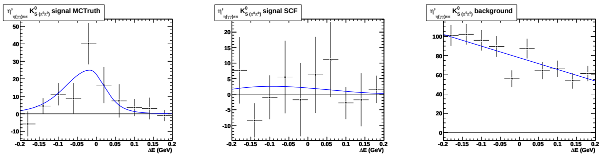

Figure C.10: sPlots for ΔE, in order: signal MC Truth, signal SCF, continuum background.

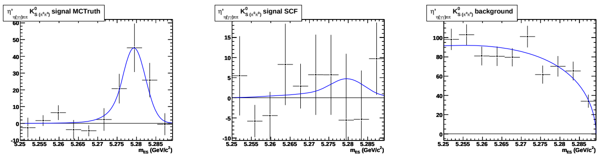

Figure C.11: sPlots for m_{ES}: in order: signal MC Truth, signal SCF, continuum background.

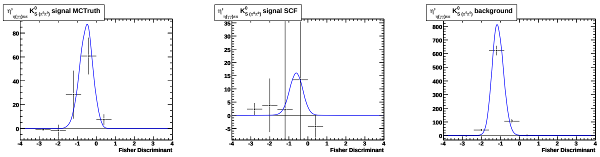

Figure C.12: sPlots for $\mathcal{F}$: in order: signal MC Truth, signal SCF, continuum background.

C.5 $B^0 \to \eta'_{\rho\gamma} K^0_{S(\pi^0\pi^0)}$

sPlot for	Signal yield	$q\bar{q}$ yield	$B\overline{B}$ charmed yield	$B\overline{B}$ ch/less (+) yield	$B\overline{B}$ ch/less (–) yield
ΔE	63 ± 37	21631 ± 176	-392 ± 268	1046 ± 577	-447 ± 394
m_{ES}	111 ± 64	21704 ± 175	-941 ± 356	-66 ± 105	1091 ± 387
Fisher	262 ± 77	21986 ± 721	-573 ± 943	-64 ± 365	289 ± 669

Table C.5: Fit yields for signal,$q\bar{q}$ background and different kind of $B\overline{B}$ background observed while making sPlots, effectively removing one discriminating variable at a time from the fit.

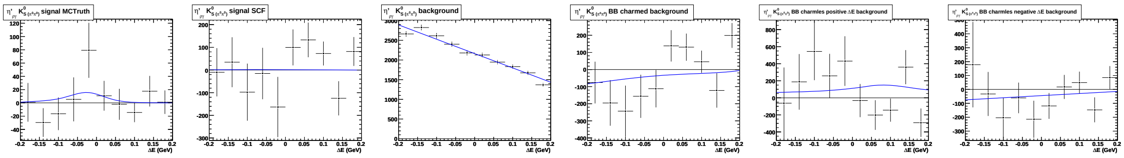

Figure C.13: sPlots for ΔE, in order: signal MC Truth, signal SCF, continuum background, $B\overline{B}$ charm background, $B\overline{B}$ peaking background (positive ΔE mean), $B\overline{B}$ peaking background (negative ΔE mean).

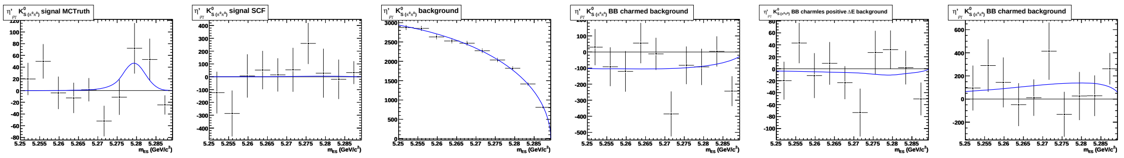

Figure C.14: sPlots for m_{ES}: in order: signal MC Truth, signal SCF, continuum background, $B\overline{B}$ charm background, $B\overline{B}$ peaking background (positive ΔE mean), $B\overline{B}$ peaking background (negative ΔE mean).

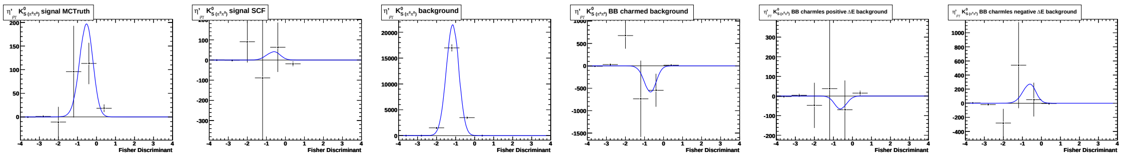

Figure C.15: sPlots for $\mathcal{F}$: in order: signal MC Truth, signal SCF, continuum background, $B\overline{B}$ charm background, $B\overline{B}$ peaking background (positive ΔE mean), $B\overline{B}$ peaking background (negative ΔE mean).

C.6 $B^0 \to \eta'_{\eta(\gamma\gamma)\pi\pi} K^0_L$

sPlot for	Signal yield	$q\bar{q}$ yield
ΔE	428 ± 56	17610 ± 142
Fisher	395 ± 61	17642 ± 145

Table C.6: Fit yields for signal and $q\bar{q}$ background observed while making sPlots, effectively removing one discriminating variable at a time from the fit.

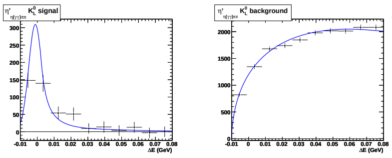

Figure C.16: sPlots for ΔE, in order: signal, continuum background.

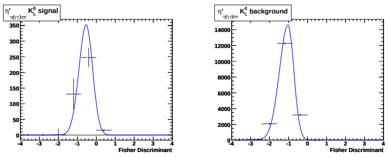

Figure C.17: sPlots for $\mathcal{F}$: in order: signal, continuum background.

C.7 $B^0 \to \eta'_{\eta(3\pi)\pi\pi} K^0_L$

sPlot for	Signal yield	$q\bar{q}$ yield
ΔE	210 ± 37	6008 ± 85
Fisher	167 ± 37	6051 ± 85

Table C.7: Fit yields for signal and $q\bar{q}$ background observed while making sPlots, effectively removing one discriminating variable at a time from the fit.

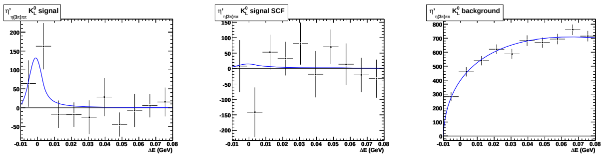

Figure C.18: sPlots for ΔE, in order: signal MC truth, signal SCF, continuum background.

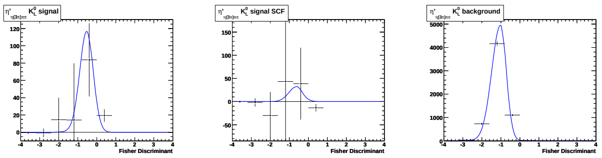

Figure C.19: sPlots for $\mathcal{F}$: in order: signal MC Truth, signal SCF, continuum background.

C.8 $B^0 \to \eta'_{\eta(\gamma\gamma)\pi\pi}K^+$

sPlot for	Signal yield	$q\bar{q}$ yield
ΔE	1655 ± 46	2948 ± 58
$m_{\rm ES}$	1670 ± 48	2933 ± 60
Fisher	1631 ± 46	2972 ± 59

Table C.8: Fit yields for signal and $q\bar{q}$ background observed while making sPlots, effectively removing one discriminating variable at a time from the fit.

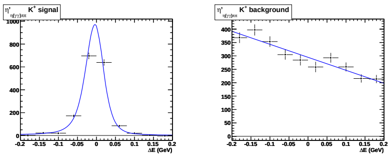

Figure C.20: sPlots for ΔE, in order: signal, continuum background.

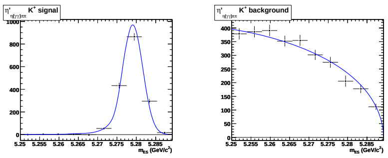

Figure C.21: sPlots for $m_{\rm ES}$: in order: signal, continuum background.

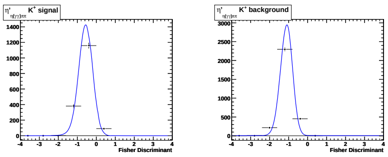

Figure C.22: sPlots for $\mathcal{F}$: in order: signal, continuum background.

C.9 $B^0 \rightarrow \eta'_{\eta(3\pi)\pi\pi} K^+$

sPlot for	Signal yield	$q\bar{q}$ yield
ΔE	611 ± 29	1171 ± 37
m_{ES}	602 ± 31	1179 ± 39
Fisher	590 ± 29	1191 ± 38

Table C.9: Fit yields for signal and $q\bar{q}$ background observed while making sPlots, effectively removing one discriminating variable at a time from the fit.

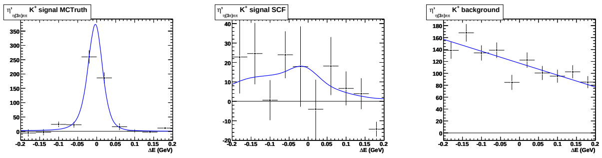

Figure C.23: sPlots for ΔE, in order: signal MC truth, signal SCF, continuum background.

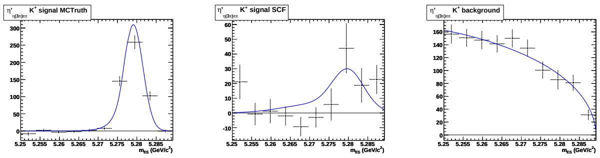

Figure C.24: sPlots for m_{ES}: in order: signal MC Truth, signal SCF, continuum background.

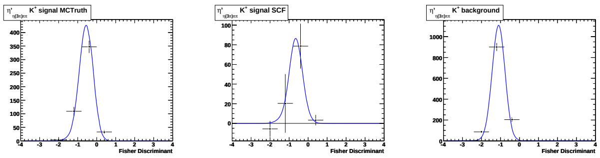

Figure C.25: sPlots for $\mathcal{F}$: in order: signal MC Truth, signal SCF, continuum background.

C.10 $B^0 \to \eta'_{\rho\gamma} K^+$

sPlot for	Signal yield	$q\bar{q}$ yield	$B\overline{B}$ charmed yield	$B\overline{B}$ ch/less (+) yield	$B\overline{B}$ ch/less (–) yield
ΔE	3239 ± 154	89368 ± 338	-3702 ± 834	-4786 ± 1858	8867 ± 2433
m_{ES}	3209 ± 102	89370 ± 346	-6542 ± 1568	1446 ± 231	6102 ± 1300
Fisher	3360 ± 104	89746 ± 1082	-3760 ± 2236	689 ± 271	3546 ± 1358

Table C.10: Fit yields for signal,$q\bar{q}$ background and different kind of $B\overline{B}$ background observed while making sPlots, effectively removing one discriminating variable at a time from the fit.

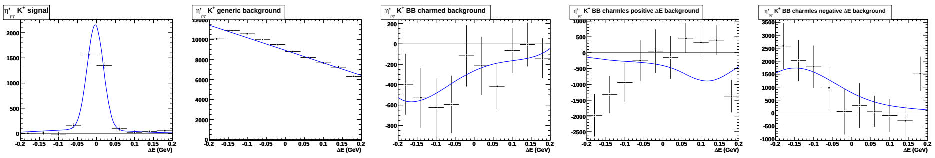

Figure C.26: sPlots for ΔE, in order: signal, continuum background, $B\overline{B}$ charm background, $B\overline{B}$ peaking background (positive ΔE mean), $B\overline{B}$ peaking background (negative ΔE mean).

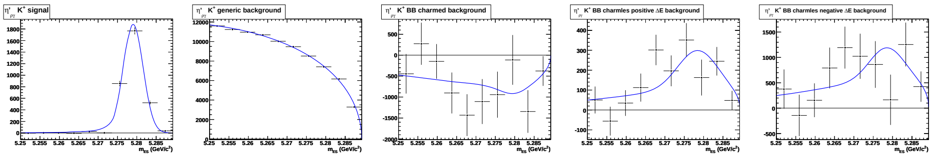

Figure C.27: sPlots for m_{ES}: in order: signal, continuum background, $B\overline{B}$ charm background, $B\overline{B}$ peaking background (positive ΔE mean), $B\overline{B}$ peaking background (negative ΔE mean).

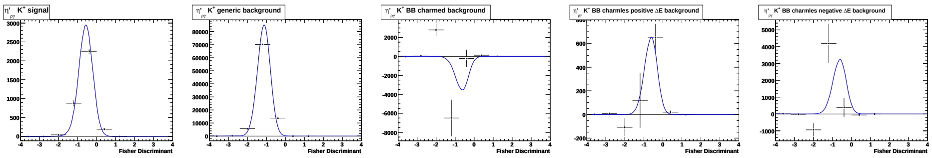

Figure C.28: sPlots for $\mathcal{F}$: in order: signal, continuum background, $B\overline{B}$ charm background, $B\overline{B}$ peaking background (positive ΔE mean), $B\overline{B}$ peaking background (negative ΔE mean).

Appendix D

$sPlots$ Libraries for Branching Fraction Measurements

We show for each decay modes $sPlots$ (see sec. 4.4.3) for signal, continuum background and $B\bar{B}$. We perform this plots only for those variables that are included into the fit.

D.1 $B^0 \to \eta_{\gamma\gamma} K^0_S$

sPlot for	Signal yield	$q\bar{q}$ yield	$B\overline{B}$ peaking yield
ΔE	8 ± 19	3134 ± 61	63 ± 38
m_{ES}	52 ± 20	3145 ± 60	8 ± 25
Fisher	-16 ± 20	3201 ± 74	22 ± 49

Table D.1: Fit yields for signal, $q\bar{q}$ and $B\overline{B}$ peaking background observed while making sPlots, effectively removing one discriminating variable at a time from the fit.

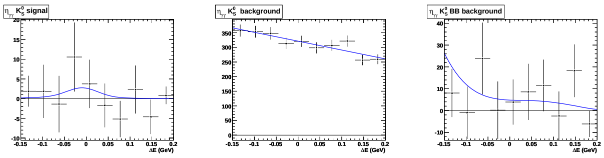

Figure D.1: sPlots for ΔE, in order: signal, continuum background, $B\overline{B}$ peaking background.

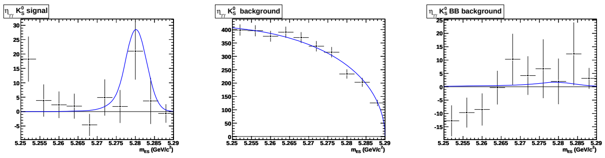

Figure D.2: sPlots for m_{ES}: in order: signal, continuum background, $B\overline{B}$ peaking background.

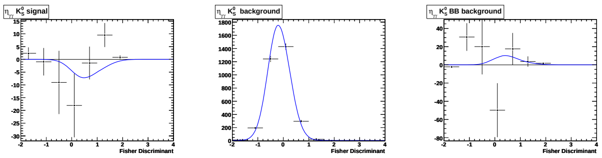

Figure D.3: sPlots for $\mathcal{F}$: in order: signal, continuum background, $B\overline{B}$ peaking background.

D.2 $B^0 \longrightarrow \eta_{3\pi} K^0_S$

sPlot for	Signal yield	$q\bar{q}$ yield
ΔE	6 ± 8	1323 ± 37
m_{ES}	-4 ± 7	1333 ± 37
Fisher	15 ± 11	1315 ± 38

Table D.2: Fit yields for signal and $q\bar{q}$ background observed while making sPlots, effectively removing one discriminating variable at a time from the fit.

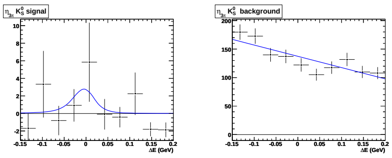

Figure D.4: sPlots for ΔE, in order: signal, continuum background.

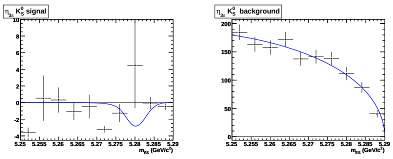

Figure D.5: sPlots for m_{ES}: in order: signal, continuum background.

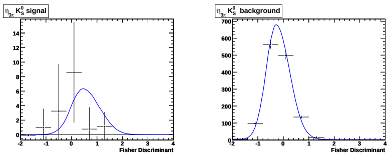

Figure D.6: sPlots for $\mathcal{F}$: in order: signal, continuum background.

D.3 $B^0 \to \eta_{\gamma\gamma}\eta_{\gamma\gamma}$

sPlot for	Signal yield	$q\bar{q}$ yield
ΔE	29 ± 12	2268 ± 49
$m_{\rm ES}$	28 ± 16	2269 ± 50
Fisher	20 ± 27	2277 ± 55

Table D.3: Fit yields for signal and $q\bar{q}$ background observed while making sPlots, effectively removing one discriminating variable at a time from the fit.

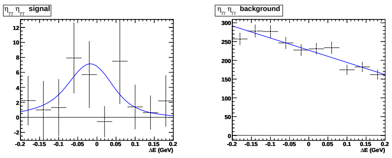

Figure D.7: sPlots for ΔE, in order: signal, continuum background.

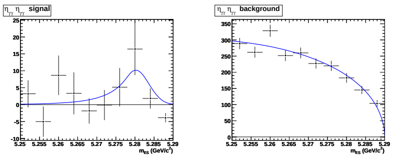

Figure D.8: sPlots for $m_{\rm ES}$: in order: signal, continuum background.

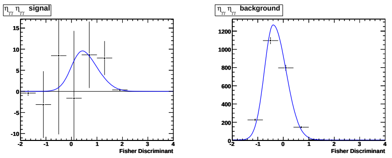

Figure D.9: sPlots for $\mathcal{F}$: in order: signal, continuum background.

D.4 $B^0 \rightarrow \eta_{\gamma\gamma}\eta_{3\pi}$

sPlot for	Signal yield	$q\bar{q}$ yield
ΔE	6 ± 7	1794 ± 43
$m_{\rm ES}$	9 ± 10	1792 ± 43
Fisher	17 ± 17	1783 ± 45

Table D.4: Fit yields for signal and $q\bar{q}$ background observed while making sPlots, effectively removing one discriminating variable at a time from the fit.

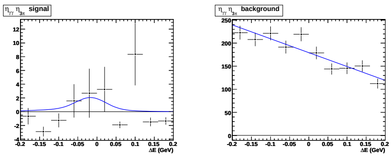

Figure D.10: sPlots for ΔE, in order: signal, continuum background.

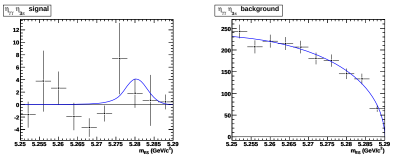

Figure D.11: sPlots for $m_{\rm ES}$: in order: signal, continuum background.

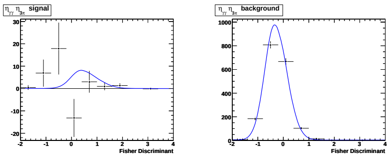

Figure D.12: sPlots for $\mathcal{F}$: in order: signal, continuum background.

D.5 $B^0 \longrightarrow \eta_{3\pi}\eta_{3\pi}$

sPlot for	Signal yield	$q\bar{q}$ yield
ΔE	-3 ± 3	266 ± 17
$m_{\rm ES}$	-12 ± 8	275 ± 18
Fisher	-12 ± 10	275 ± 17

Table D.5: Fit yields for signal and $q\bar{q}$ background observed while making sPlots, effectively removing one discriminating variable at a time from the fit.

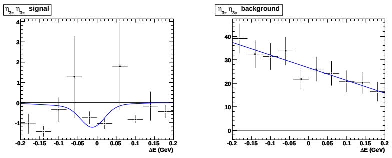

Figure D.13: sPlots for ΔE, in order: signal, continuum background.

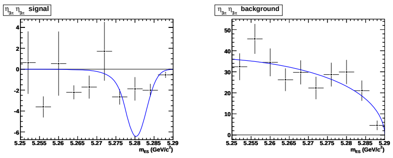

Figure D.14: sPlots for $m_{\rm ES}$: in order: signal, continuum background.

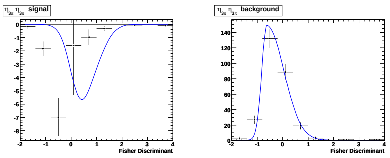

Figure D.15: sPlots for $\mathcal{F}$: in order: signal, continuum background.

D.6 $B^0 \to \eta_{\gamma\gamma}\omega$

sPlot for	Signal yield	$q\bar{q}$ yield	$B\overline{B}$ charmed yield	$B\overline{B}$ peaking yield
ΔE	47 ± 19	11038 ± 126	178 ± 104	70 ± 89
$m_{\rm ES}$	40 ± 23	11003 ± 126	193 ± 94	97 ± 95
Fisher	48 ± 23	10656 ± 265	267 ± 199	362 ± 142
ω Mass	34 ± 16	11014 ± 125	211 ± 91	74 ± 74
ω Helicity	50 ± 18	11020 ± 125	257 ± 97	7 ± 76

Table D.6: Fit yields for signal, $q\bar{q}$, $B\overline{B}$ charm, and $B\overline{B}$ peaking background observed while making sPlots, effectively removing one discriminating variable at a time from the fit.

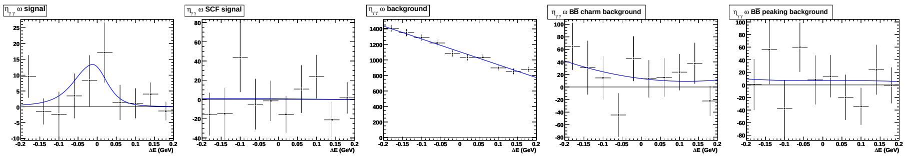

Figure D.16: sPlots for ΔE, in order: signal MC Truth, signal SCF continuum background, $B\overline{B}$ charm background, $B\overline{B}$ peaking background.

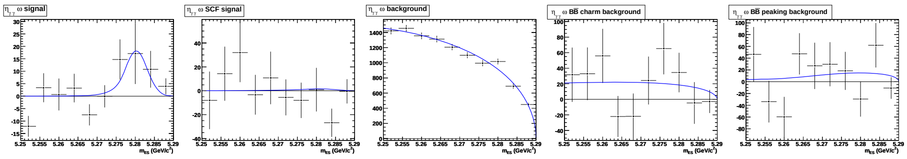

Figure D.17: sPlots for $m_{\rm ES}$: in order: signal MC Truth, signal SCF , continuum background, $B\overline{B}$ charm background, $B\overline{B}$ peaking background.

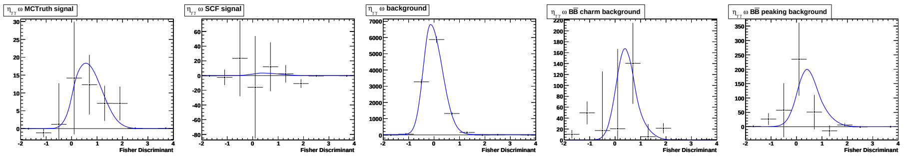

Figure D.18: sPlots for $\mathcal{F}$: in order: signal MC Truth, signal SCF , continuum background, $B\overline{B}$ charm background, $B\overline{B}$ peaking background.

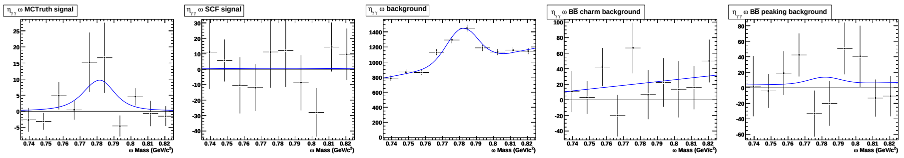

Figure D.19: sPlots for ω mass: in order: signal MC Truth, signal SCF , continuum background, $B\overline{B}$ charm background, $B\overline{B}$ peaking background.

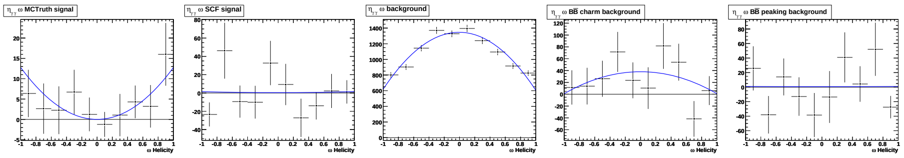

Figure D.20: sPlots for $\mathcal{H}_{\omega}$: in order: signal MC Truth, signal SCF , continuum background, $B\overline{B}$ charm background, $B\overline{B}$ peaking background.

D.7 $B^0 \longrightarrow \eta_{3\pi}\omega$

sPlot for	Signal yield	$q\bar{q}$ yield	$B\overline{B}$ charmed yield
ΔE	13 ± 10	8506 ± 108	94 ± 57
m_{ES}	-3 ± 12	8527 ± 106	89 ± 55
Fisher	15 ± 18	8431 ± 201	167 ± 176
ω Mass	3 ± 8	8502 ± 107	108 ± 56
ω Helicity	-10 ± 10	8526 ± 107	96 ± 57

Table D.7: Fit yields for signal, $q\bar{q}$ and $B\overline{B}$ charm background observed while making sPlots, effectively removing one discriminating variable at a time from the fit.

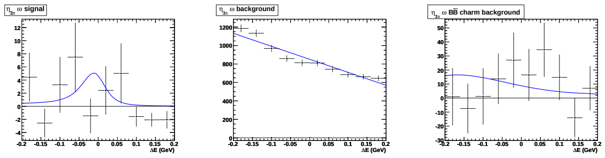

Figure D.21: sPlots for ΔE, in order: signal, continuum background, $B\overline{B}$ charm background

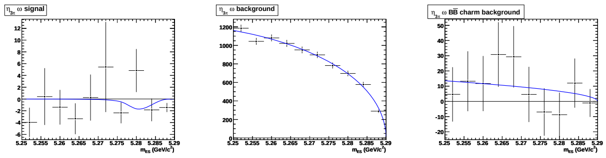

Figure D.22: sPlots for $m_{\rm ES}$: in order: signal, continuum background, $B\overline{B}$ charm background

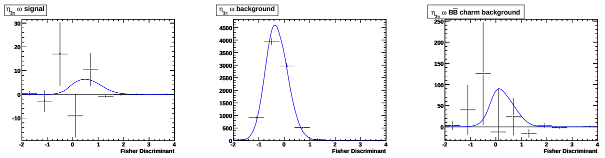

Figure D.23: sPlots for $\mathcal{F}$: in order: signal, continuum background, $B\overline{B}$ charm background

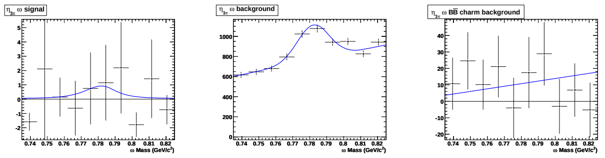

Figure D.24: sPlots for ω mass: in order: signal, continuum background, $B\overline{B}$ charm background

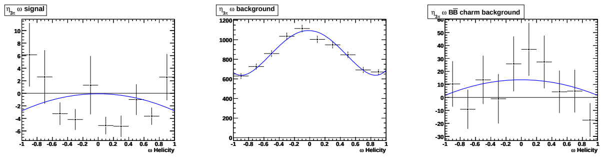

Figure D.25: sPlots for $\mathcal{H}_\omega$: in order: signal, continuum background, $B\overline{B}$ charm background

D.8 $B^0 \longrightarrow \eta_{\gamma\gamma}\phi$

sPlot for	Signal yield	$q\bar{q}$ yield
ΔE	10 ± 8	1391 ± 38
m_{ES}	6 ± 8	1395 ± 38
Fisher	5 ± 10	1396 ± 38
ϕ Helicity	-1 ± 4	1402 ± 38

Table D.8: Fit yields for signal and $q\bar{q}$ background observed while making sPlots, effectively removing one discriminating variable at a time from the fit.

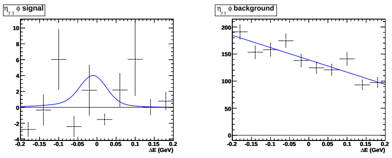

Figure D.26: sPlots for ΔE, in order: signal, continuum background.

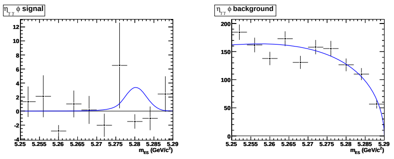

Figure D.27: sPlots for m_{ES}: in order: signal, continuum background.

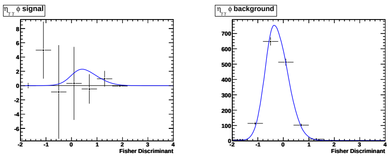

Figure D.28: sPlots for $\mathcal{F}$: in order: signal, continuum background.

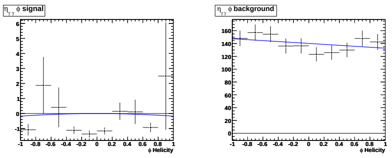

Figure D.29: sPlots for $\mathcal{H}_{\phi}$: in order: signal, continuum background.

D.9 $B^0 \longrightarrow \eta_{3\pi}\phi$

sPlot for	Signal yield	$q\bar{q}$ yield
ΔE	6 ± 4	480 ± 22
$m_{\rm ES}$	9 ± 6	477 ± 22
Fisher	8 ± 5	478 ± 22
ϕ Helicity	4 ± 3	482 ± 22

Table D.9: Fit yields for signal and $q\bar{q}$ background observed while making sPlots, effectively removing one discriminating variable at a time from the fit.

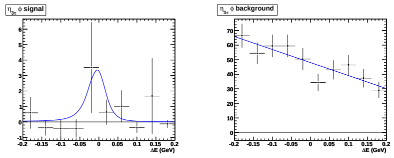

Figure D.30: sPlots for ΔE, in order: signal, continuum background.

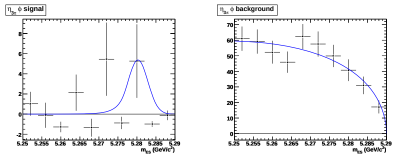

Figure D.31: sPlots for $m_{\rm ES}$: in order: signal, continuum background.

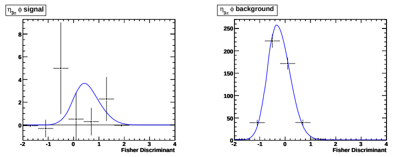

Figure D.32: sPlots for $\mathcal{F}$: in order: signal, continuum background.

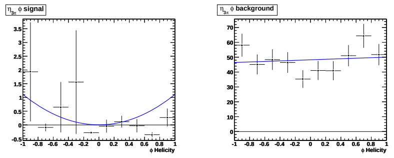

Figure D.33: sPlots for $\mathcal{H}_\phi$: in order: signal, continuum background.

D.10 $B^0 \to \eta'_{\eta\pi\pi}\eta'_{\eta\pi\pi}$

sPlot for	Signal yield	$q\bar{q}$ yield
ΔE	2 ± 2	207 ± 15
$m_{\rm ES}$	3 ± 2	206 ± 15
Fisher	4 ± 3	206 ± 15
η' Mass (1)	3 ± 2	206 ± 15
η' Mass (2)	2 ± 2	207 ± 14

Table D.10: Fit yields for signal and $q\bar{q}$ background observed while making sPlots, effectively removing one discriminating variable at a time from the fit.

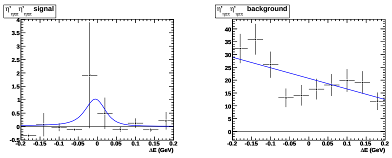

Figure D.34: sPlots for ΔE, in order: signal, continuum background.

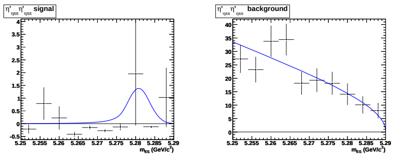

Figure D.35: sPlots for m_{ES}: in order: signal, continuum background.

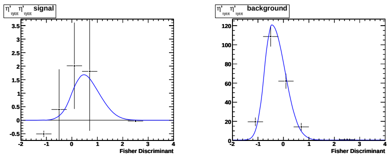

Figure D.36: sPlots for $\mathcal{F}$: in order: signal, continuum background.

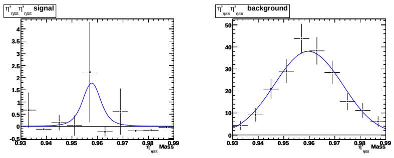

Figure D.37: sPlots for η' mass (1): in order: signal, continuum background.

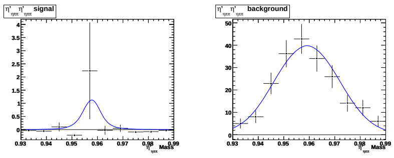

Figure D.38: sPlots for η' mass (2): in order: signal, continuum background.

D.11 $B^0 \to \eta'_{\rho\gamma}\eta'_{\eta\pi\pi}$

sPlot for	Signal yield	$q\bar{q}$ yield	$B\overline{B}$ peaking yield	$B\overline{B}$ charmed yield
ΔE	-1 ± 11	7547 ± 103	56 ± 41	144 ± 67
m_{ES}	15 ± 12	7526 ± 102	33 ± 30	171 ± 61
Fisher	41 ± 19	7158 ± 317	49 ± 69	498 ± 270
$\eta'_{\rho\gamma}$ Mass	10 ± 8	7515 ± 102	7 ± 21	215 ± 58
$\eta'_{\eta\pi\pi}$ Mass	11 ± 9	7513 ± 102	-40 ± 41	262 ± 58

Table D.11: Fit yields for signal, $q\bar{q}$, $B\overline{B}$ peaking, and $B\overline{B}$ charmed background observed while making sPlots, effectively removing one discriminating variable at a time from the fit.

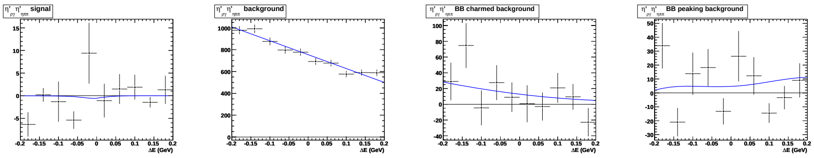

Figure D.39: sPlots for ΔE, in order: signal, continuum background, $B\overline{B}$ charm background, $B\overline{B}$ peaking background.

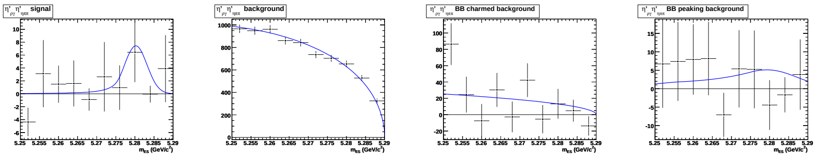

Figure D.40: sPlots for m_{ES}: in order: signal, continuum background, $B\overline{B}$ charm background, $B\overline{B}$ peaking background.

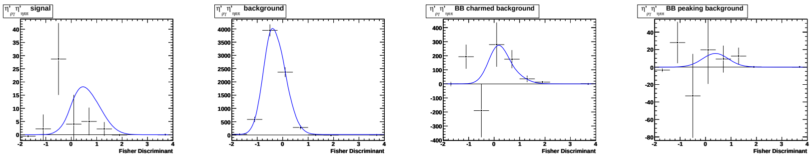

Figure D.41: sPlots for $\mathcal{F}$: in order: signal, continuum background, $B\overline{B}$ charm background, $B\overline{B}$ peaking background.

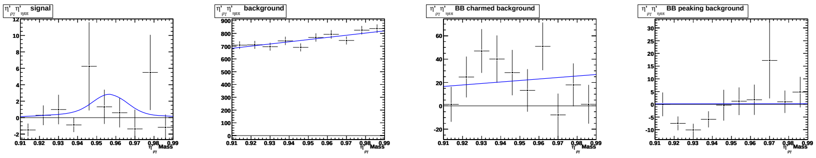

Figure D.42: sPlots for $\eta'_{\rho\gamma}$: in order: signal, continuum background, $B\overline{B}$ charm background, $B\overline{B}$ peaking background.

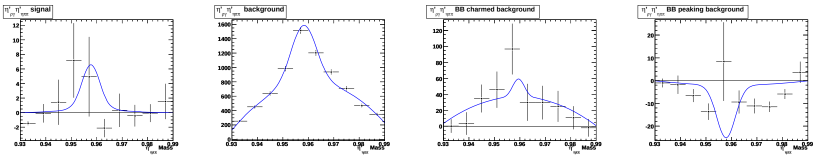

Figure D.43: sPlots for $\eta'_{\eta\pi\pi}$: in order: signal, continuum background, $B\overline{B}$ charm background, $B\overline{B}$ peaking background.

D.12 $B^0 \rightarrow \eta'_{\eta\pi\pi}\omega$

sPlot for	Signal yield	$q\bar{q}$ yield	$B\overline{B}$ charmed yield
ΔE	16 ± 8	8151 ± 108	221 ± 62
$m_{\rm ES}$	9 ± 7	8140 ± 106	239 ± 59
Fisher	37 ± 14	7792 ± 205	558 ± 185
η' Mass	18 ± 8	8116 ± 107	254 ± 60
ω Mass	12 ± 6	8132 ± 107	243 ± 60
ω Helicity	19 ± 9	8161 ± 107	207 ± 59

Table D.12: Fit yields for signal, $q\bar{q}$, $B\overline{B}$ charm, and $B\overline{B}$ peaking background observed while making sPlots, effectively removing one discriminating variable at a time from the fit.

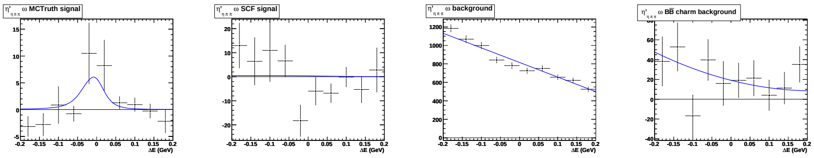

Figure D.44: sPlots for ΔE, in order: signal MC Truth, signal SCF, continuum background, $B\overline{B}$ charm background, $B\overline{B}$ peaking background.

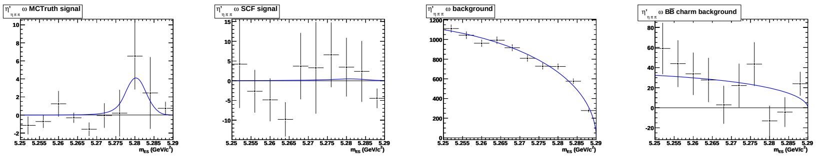

Figure D.45: sPlots for $m_{\rm ES}$: in order: signal MC Truth, signal SCF, continuum background, $B\overline{B}$ charm background, $B\overline{B}$ peaking background.

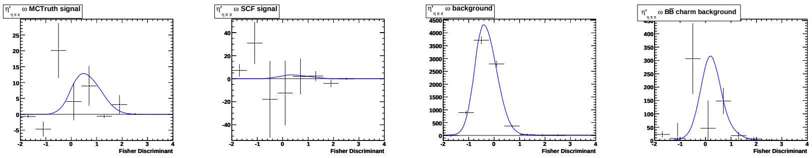

Figure D.46: sPlots for $\mathcal{F}$: in order: signal MC Truth, signal SCF, continuum background, $B\overline{B}$ charm background, $B\overline{B}$ peaking background.

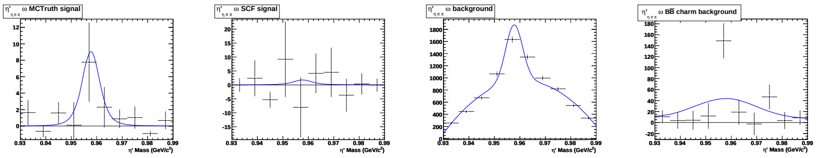

Figure D.47: sPlots for η' mass: in order: signal MC Truth, signal SCF, continuum background, $B\overline{B}$ charm background plus $B\overline{B}$ peaking background.

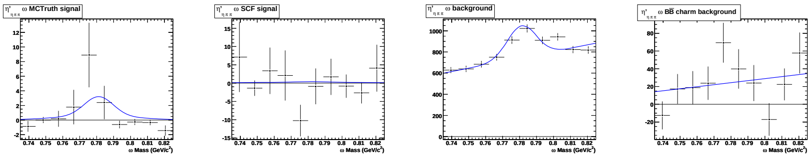

Figure D.48: sPlots for ω mass: in order: signal MC Truth, signal SCF, continuum background, $B\overline{B}$ charm background plus $B\overline{B}$ peaking background.

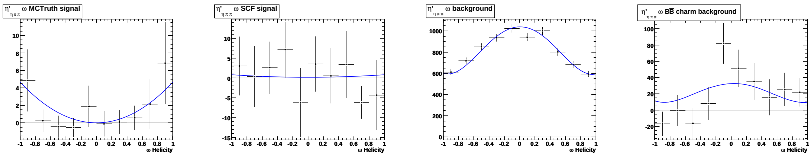

Figure D.49: sPlots for $\mathcal{H}_\omega$: in order: signal MC Truth, signal SCF, continuum background, $B\overline{B}$ charm background plus $B\overline{B}$ peaking background.

D.13 $B^0 \rightarrow \eta'_{\rho\gamma}\omega$

sPlot for	Signal yield	$q\bar{q}$ yield	$B\overline{B}$ charmed yield	$B\overline{B}$ peaking yield
ΔE	0 ± 23	49030 ± 289	3327 ± 211	242 ± 111
$m_{\rm ES}$	-37 ± 33	48774 ± 285	3637 ± 202	225 ± 124
Fisher	-10 ± 30	47124 ± 836	3966 ± 702	1518 ± 212
η' Mass	28 ± 23	48841 ± 284	3693 ± 199	37 ± 105
ω Mass	-2 ± 13	48844 ± 284	3755 ± 189	
ω Helicity	29 ± 22	48874 ± 286	3696 ± 193	

Table D.13: Fit yields for signal, $q\bar{q}$, $B\overline{B}$ charm, and $B\overline{B}$ peaking background observed while making sPlots, effectively removing one discriminating variable at a time from the fit.

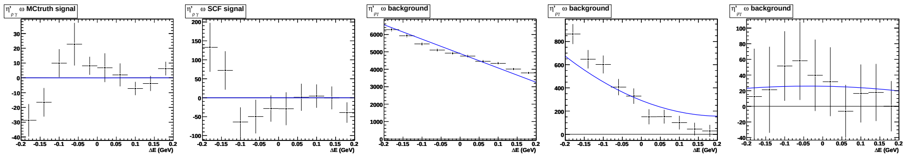

Figure D.50: sPlots for ΔE, in order: signal MC Truth, signal SCF, continuum background, $B\overline{B}$ charm background, $B\overline{B}$ peaking background.

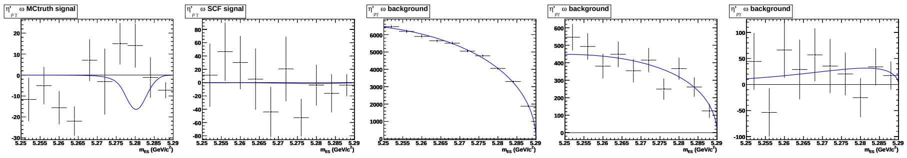

Figure D.51: sPlots for m_{ES}: in order: signal MC Truth, signal SCF, continuum background, $B\overline{B}$ charm background, $B\overline{B}$ peaking background.

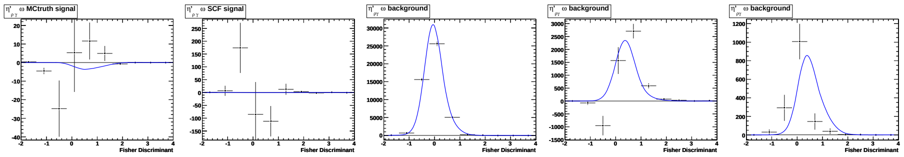

Figure D.52: sPlots for $\mathcal{F}$: in order: signal MC Truth, signal SCF, continuum background, $B\overline{B}$ charm background, $B\overline{B}$ peaking background.

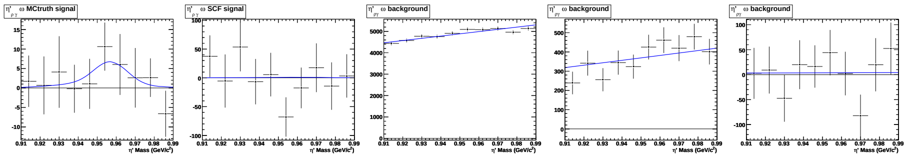

Figure D.53: sPlots for η' mass: in order: signal MC Truth, signal SCF, continuum background, $B\overline{B}$ charm background, $B\overline{B}$ peaking background.

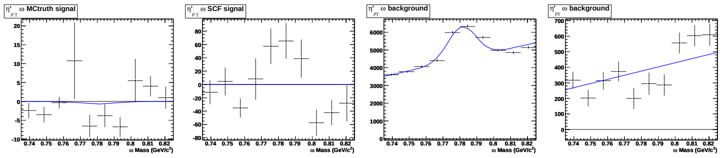

Figure D.54: sPlots for ω mass: in order: signal MC Truth, signal SCF, continuum background, $B\overline{B}$ charm background plus $B\overline{B}$ peaking background.

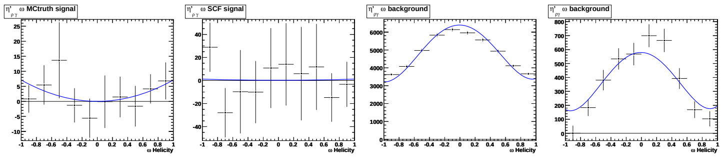

Figure D.55: sPlots for $\mathcal{H}_{\omega}$: in order: signal MC Truth, signal SCF, continuum background, $B\overline{B}$ charm background plus $B\overline{B}$ peaking background.

D.14 $B^0 \rightarrow \eta'_{\eta\pi\pi}\phi$

sPlot for	Signal yield	$q\bar{q}$ yield
ΔE	0 ± 2	456 ± 11
m_{ES}	4 ± 4	451 ± 21
Fisher	-3 ± 3	458 ± 22
η' Mass	-1 ± 2	456 ± 21
ϕ Helicity	0 ± 2	455 ± 21

Table D.14: Fit yields for signal and $q\bar{q}$ background observed while making sPlots, effectively removing one discriminating variable at a time from the fit.

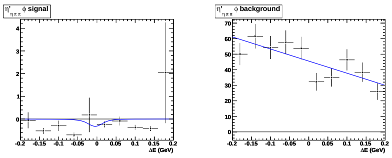

Figure D.56: sPlots for ΔE, in order: signal, continuum background.

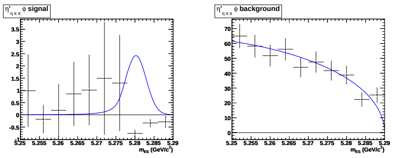

Figure D.57: sPlots for m_{ES}: in order: signal, continuum background.

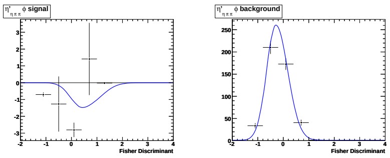

Figure D.58: sPlots for $\mathcal{F}$: in order: signal, continuum background.

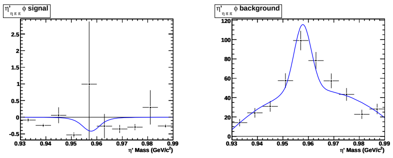

Figure D.59: sPlots for η': in order: signal, continuum background.

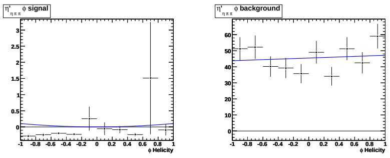

Figure D.60: sPlots for $\mathcal{H}_{\phi}$: in order: signal, continuum background.

D.15 $B^0 \rightarrow \eta'_{\rho\gamma}\phi$

sPlot for	Signal yield	$q\bar{q}$ yield	$B\overline{B}$ charmed yield
ΔE	23 ± 13	6442 ± 93	149 ± 51
m_{ES}	19 ± 14	6417 ± 90	178 ± 45
Fisher	38 ± 16	6484 ± 157	92 ± 135
η' Mass	7 ± 11	6416 ± 90	190 ± 45
ϕ Helicity	6 ± 10	6448 ± 91	160 ± 46

Table D.15: Fit yields for signal, $q\bar{q}$ and $B\overline{B}$ charm, background observed while making sPlots, effectively removing one discriminating variable at a time from the fit.

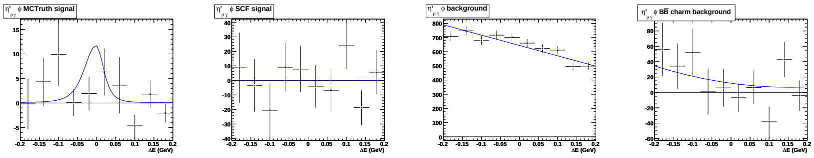

Figure D.61: sPlots for ΔE, in order: signal MC Truth, signal SCF, continuum background, $B\overline{B}$ charm background.

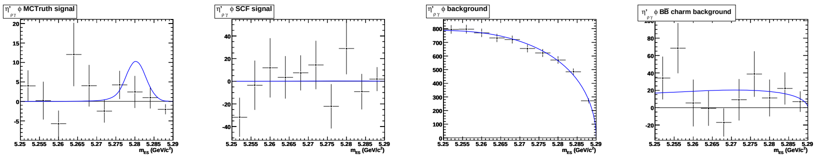

Figure D.62: sPlots for $m_{\rm ES}$: in order: signal MC Truth, signal SCF, continuum background, $B\overline{B}$ charm background.

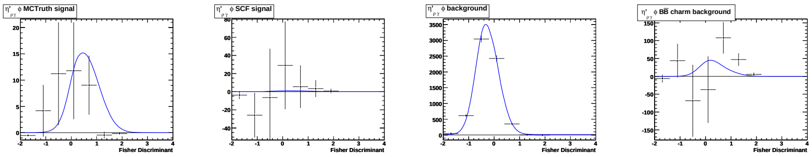

Figure D.63: sPlots for $\mathcal{F}$: in order: signal MC Truth, signal SCF, continuum background, $B\overline{B}$ charm background.

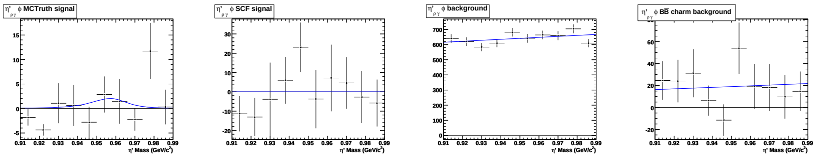

Figure D.64: sPlots for η' mass: in order: signal MC Truth, signal SCF, continuum background, $B\overline{B}$ charm background.

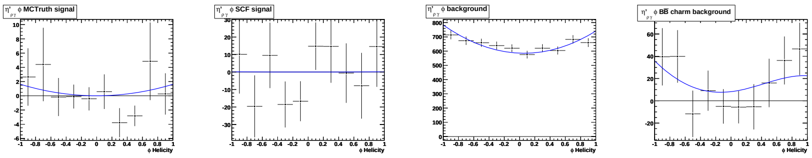

Figure D.65: sPlots for $\mathcal{H}_{\phi}$: in order: signal MC Truth, signal SCF, continuum background, $B\overline{B}$ charm background.

Appendix E

Misura della Violazione di CP Dipendente dal Tempo nel Decadimento del Mesone B in $\eta' K^0$ e delle Frazioni di Decadimento dei Canali SU(3)-Collegati con l'Esperimento *BABAR* a SLAC.

E.1 Introduzione

Il presente lavoro di tesi è stato realizzato nell'ambito dell'esperimento *BABAR* che ha operato dal 1999 al 2008 alla b-factory PEP-II presso Stanford Linear Accelerator Center (SLAC), CA, USA.

Il principale scopo dell'esperimento *BABAR* è stato lo studio della violazione di CP nel sistema dei mesoni B. La violazione di CP ha avuto un ruolo centrale nella fisica delle particelle elementari fin dalla sua scoperta nel 1964 [5] e tuttora è una delle tematiche di maggior interesse. Precedentemente alla sua scoperta, l'osservazione dell'enigma $\theta - \tau$ agli inizi degli anni 50 del secolo scorso segnò il principio della scoperta delle proprietà di violazione delle simmetrie discrete[1] nelle interazioni deboli, simmetrie che fino ad allora erano alla base della conoscenza di tutte le interazioni fondamentali. Due particelle a spin zero della stessa massa e vita media (adesso note come kaoni) decadevano in differenti stati finali di opposta parità, una in due pioni e l'altra in tre, apparentemente violando la conservazione di parità. Nel 1956, Lee e Yang mostrarono che la conservazione della parità non era sufficientemente verificata sperimentalmente nelle

---

[1] inversione temporale (T), coniugazione di carica (C) e inversione spaziale o parità (P).

interazioni deboli, mentre lo era per quelle forti ed elettromagnetiche, e proposero una serie di test sperimentali [1]. Subito dopo, C. S. Wu e collaboratori eseguirono uno di questi esperimenti e mostrarono che la parità non era conservata nel decadimento nucleare β [2], dimostrando quindi l'unicità dell'interazione debole tra le forze. Comunque, la trasformazione combinata CP era ancora assunta essere una simmetria della natura poiché l'interazione debole era difficile da spiegare senza di essa. La scoperta otto anni dopo del decadimento del kaone neutro a vita media lunga (K^0_L) in due pioni [5] mostrò che anche la CP non era conservata. Quasi dieci anni dopo (1973), Kobayashi e Maskawa proposero, generalizzando l'ipotesi di Cabibbo della matrice di mescolamento tra quark [6], che la violazione di CP nel sistema dei kaoni neutri poteva essere spiegata in un modello con tre famiglie di quark [7]. Questo avveniva quando ancora non si aveva nessuna evidenza per la terza famiglia e un anno prima che il quark charm fosse scoperto. I quark della terza famiglia, adesso indicati con b per bottom e t per top, sono stati in seguito scoperti rispettivamente nel 1977 [9] e nel 1994 [10].

Più di trent'anni di ricerche sperimentali nel settore dei kaoni hanno portato solo recentemente all'osservazione della violazione di CP diretta [11]. Tutte le misure sono consistenti con la descrizione della violazione di CP di Cabibbo, Kobayashi e Maskawa (CKM). Comunque, il piccolo effetto della violazione di CP nel sistema dei kaoni rende difficile di progredire ulteriormente in questo settore. Il presente e il futuro per verificare la descrizione offerta dalla CKM e per mostrare evidenza per Nuova Fisica (NP) oltre il Modello Standard (MS) sono adesso rappresentati dai decadimenti di adroni contenenti quark b. Un mesone contenente un quark $\bar{b}$ e un quark u o d è indicato come mesone B, allo stesso modo del mesone K che contiene un quark $\bar{s}$[2]. I suoi decadimenti, come mostrato negli ultimi anni da *BABAR* e da Belle[3], manifestano una significante violazione di CP, prevista dal Modello Standard. Molte ragionevoli estensioni teoriche del MS portano a differenti previsioni per la violazione di CP, quindi una misura precisa di tale fenomenologia potrebbe confermare o smentire questi scenari di NP. Inoltre il piccolo valore della violazione di CP previsto dal MS, non riesce a spiegare la manifesta asimmetria barionica dell'universo. Tutto ciò rende lo studio della violazione CP un argomento di frontiera nell'attuale ricerca nella fisica delle alte energie.

I canali di decadimento del mesone B utili per lo studio della violazione di CP hanno frazioni di decadimento molto piccole, dell'ordine di 10^{-4} o inferiori, con una sezione d'urto di produzione della risonanza $\Upsilon(4S)$[4] di 1.2 nb. Per osservare la violazione di CP

---

[2] Per mesoni contenenti il quark b e s e' utilizzata la notazione B_s

[3] L'analogo esperimento in corso di svolgimento a KEK-B, Tsukuba (Giappone).

[4] $\Upsilon(4S)$ è una risonanza composta da una coppia di quark $b\bar{b}$, che ha massa di circa 10.58 GeV e che decade in una coppia di mesoni $B\overline{B}$ ($\sim 50\%$ $B\overline{B}$ neutri e $\sim 50\%$ $B\overline{B}$ carichi). I numeri quantici di questa risonanza sono $J^{CP} = 1^{--}$.

è necessario perciò un collisionatore ad elevata luminosità (una cosiddetta B-*factory* [5]). La misura delle asimmetrie dipendenti dal tempo dipende dalla possibilità di misurare i vertici di decadimento dei due mesoni B provenienti dal decadimento del mesone $\Upsilon(4S)$. Nell'esperimento *BABAR* la misura di questi vertici è resa possibile dall'asimmetria del collisionatore (e^- di 9 GeV ed e^+ di 3.1 GeV) nel quale vengono prodotti mesoni Υ in moto nel sistema di riferimento del laboratorio. Il *boost* dei due B fa sì che le distanze percorse nel decadimento siano misurabili.

Il gruppo di Milano partecipa al gruppo di analisi dei decadimenti adronici senza *charm* del mesone B. A causa dell'assenza della transizione favorita $b{\rightarrow}c$, questi processi sono manifestazioni di diagrammi a loop (pinguino) o ad albero soppressi, con ampiezze proporzionali ai piccoli coefficienti di accoppiamento tra quark della matrice CKM. La presenza di nuove particelle nel loop potrebbe risultare in una variazione del valore di violazione si CP, rendendo, quindi, queste transizione uno dei fenomeni in cui la NP potrebbe manifestarsi in modo evidente.

In questo lavoro di tesi è descritto lo studio dei decadimenti del mesone B in $\eta' K$. L'analisi è stata eseguita su un campione di dati raccolti sulla risonanza $\Upsilon(4S)$ pari a 467.4×10^6 coppie $B\overline{B}$. La tecnica di analisi finale utilizzata per la selezione degli eventi di segnale e la misura dei parametri dell'asimmetria CP è quella della massima verosimiglianza estesa multivariata. I risultati di questa analisi sono stati presentati all' *International Conference on High Energy Physics 2008* (ICHEP08), svoltasi a Philadelphia, USA e hanno, inoltre, contribuito ai risultati presenti in un articolo sottomesso a *Physical Review D* [19]. La presenza di ampiezze dovute a diagrammi di SM soppressi, porta al sorgere di discrepanze del valore dei parametri della asimmetria CP misurato in $\eta' K$ da quanto previsto per una transizione pura $b{\rightarrow}s$. Diversi metodi consentono di stimare l'entità di tale scostamento, a partire dalle misure delle ampiezze di decadimento dei canali collegati a $\eta' K$. Uno di tali metodi, ad esempio, è quello basato su considerazioni relative alla simmetria (approssimata) SU(3) [20, 21, 68]. Inoltre diverse ipotesi sono state proposte per giustificare la differenza tra le frazioni di decadimento $B{\rightarrow}\eta K$ e $B{\rightarrow}\eta' K$ [25, 70, 72, 67, 22]. Al fine di fornire dati per calcolare il succitato scostamento e validare le differenti ipotesi il candidato ha inoltre investigato i decadimenti del mesone B in differenti stati finali contenenti i mesoni η ed η'. I risultati saranno inclusi in un articolo che verrà presto sottomesso a *Physical Review D* e sono stati presentati alla *Flavour Physics and CP Violation Conference 2008* (FPCP08), svoltasi a Taipei, Taiwan.
Il candidato ha difeso la validità scientifica dei risultati di entrambe le analisi durante due distinti *BABAR Collaboration Wide Talks*.

---

[5] B-*factory* è un'espressione comunemente usata per descrivere un acceleratore che in grado di produrre una gran numero di mesoni B ($\geq 10^7$ B per anno).

Dopo una presentazione della violazione CP dell'apparato sperimentale utilizzato, passeremo a descrivere il metodo di analisi e più specificatamente dapprima la misura della violazione di CP in $B\rightarrow\eta' K$ quindi la ricerca dei decadimenti rari del mesone B in coppie di mesoni isoscalari.

E.2 Fenomenologia e Origine della Violazione di CP

E.2.1 Introduzione

Il Modello Standard descrive la violazione di CP con il meccanismo di Kobayashi e Maskawa [7]. Più specificatamente, la sorgente della violazione di CP è una singola fase nella matrice di mixing dei quark, detta anche matrice Cabibbo-Kobayashi-Maskawa (CKM). Gli elementi di tale matrice rientrano nella descrizione delle correnti cariche delle interazioni deboli tra quark. La violazione di CP è stata osservata nei decadimenti del mesone K [5] e anche del mesone B [12, 13, 18], ma non è ancora stabilito se la sorgente di violazione di CP predetta dal Modello Standard sia l'unica presente in natura. Misure indipendenti dei parametri della violazione CP in diversi canali, permettono di imporre un numero ridondante di condizioni sui parametri del Modello Standard. L'eventuale scoperta della non unicità nella scelta di tali parametri, in modo che siano consistenti con tutte le misure, sarebbe una chiara evidenza di fisica oltre il Modello Standard.

E.2.2 Mixing dei Mesoni B Neutri

Ci sono due sistemi fondamentali di mesoni neutri che interessano i quark b: i mesoni ${B^0}_d$ (${\overline{B}^0}_d$), costituiti da un quark $\bar{b}$ (b) e da uno d ($\bar{d}$), e i mesoni ${B^0}_s$ (${\overline{B}^0}_s$), formati da un $\bar{b}$ (b) ed un s ($\bar{s}$). Queste due coppie di mesoni neutri coniugati, che decadono debolmente, possono mescolarsi con le loro rispettive antiparticelle secondo i due diagrammi a box:

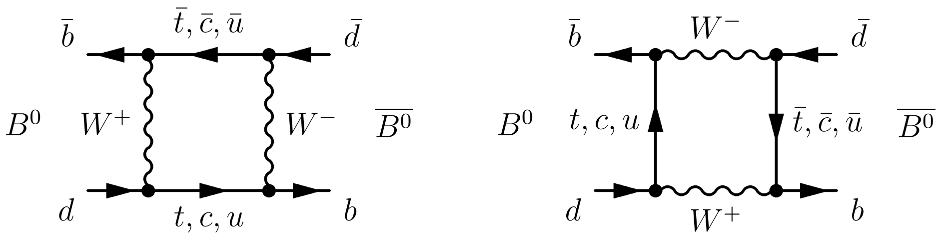

Figure E.1: Diagrammi di Feynman responsabili del mixing $B^0 - \overline{B}^0$.

Nella trattazione del sistema dei mesoni B neutri esistono diversi autostati importanti utilizzati a seconda del contesto:

- autostati di sapore, con un ben preciso contenuto di quark, utili per trattare i processi di produzione e di decadimento;
- autostati (dell'hamiltoniana) di massa e vita media definite, utili per trattare la propagazione.
- autostati di CP;

La capacità di mescolamento implica che gli autostati di sapore potrebbero non essere equivalenti agli autostati di massa; dalla presenza osservata di mescolamento (nei decadimenti di sapore specifico coniugati) si conclude che gli autostati di massa e sapore sono di fatto differenti. Se CP fosse conservata, gli autostati di massa e di CP coinciderebbero. La violazione di tale simmetria implica, quindi, che anche il terzo insieme di autostati non coincide con quelli di massa.

E.2.3 I Tre Tipi di Violazione di CP

Le manifestazioni della violazione di CP che potenzialmente possono essere osservate in una B-*factory* si possono classificare, indipendentemente dal modello, in tre tipologie:

1. violazione di CP nel decadimento (spesso indicata come violazione di CP diretta): avviene quando più ampiezze con differenti fasi deboli e differenti fasi forti contribuiscono ad un dato stato finale. Essa può manifestarsi sia per i decadimenti dei mesoni carichi sia per quelli dei neutri, ed è misurabile come differenza tra il modulo dell'ampiezza del decadimento e quella del suo CP coniugato;

2. violazione di CP nel mixing: compare quando gli autostati di massa di un mesone neutro sono differenti dagli autostati di CP;

3. violazione di CP nell'interferenza tra decadimenti con e senza mixing: si verifica nei decadimenti in stati finali comuni ad un mesone neutro e alla sua antiparticella.

Poiché in questa tesi studieremo il processo $B \rightarrow \eta' K$, ove si manifesta il terzo tipo di violazione, trattiamo di seguito gli aspetti legati a tale fenomenologia.

Stati finali che possono essere raggiunti sia da decadimenti del B^0 o del $\overline{B}^0$ possono esibire violazione di CP, risultante dell'interferenza tra l'ampiezza del decadimento nello stato finale di mesoni che abbiano o non abbiano subito il mixing. Questi stati finali sono gli autostati di CP, che indichiamo con f_{CP}. Possiamo quindi definire λ

$$\lambda_{f_{CP}} \equiv \frac{q}{p}\frac{\bar{A}_{f_{CP}}}{A_{f_{CP}}} = \eta_{f_{CP}}\frac{q}{p}\frac{\bar{A}_{\bar{f}_{CP}}}{A_{f_{CP}}}, \tag{E.1}$$

ove $A_{f_{CP}}$ e $\bar{A}_{\bar{f}_{CP}}$ sono le ampiezze di decadimento, $\eta_{f_{CP}}$ è l'autovalore dello stato f_{CP} per la trasformazione di CP e la seconda forma deriva dalla relazione

$$\bar{A}_{f_{CP}} = \eta_{f_{CP}} \bar{A}_{\bar{f}_{CP}}, \tag{E.2}$$

Le ampiezze $A_{f_{CP}}$ e $\bar{A}_{f_{CP}}$ sono legate dalla trasformazione di CP e differiscono solo per il segno della fase debole di ciascun termine, mentre $\eta_{f_{CP}} = \pm 1$. In questo caso è $\lambda_{f_{CP}}$, che è indipendente dalle convenzioni, ad essere fisicamente significativa. Quando CP si conserva, $|q/p| = 1$, $|\bar{A}_{\bar{f}_{CP}}/A_{f_{CP}}| = 1$, e inoltre la fase relativa tra (q/p) e $(A_{\bar{f}_{CP}}/A_{f_{CP}})$ svanisce. Dunque l'equazione (E.1) implica:

$$\lambda_{f_{CP}} \neq \pm 1 \quad \Rightarrow \quad \text{violazione di } CP \tag{E.3}$$

Tuttavia è possibile che si verifichi $|q/p| = 1$ e $|\bar{A}/A| = 1$. In tal caso si ha $|\lambda_{f_{CP}}| = 1$, ma se $\mathrm{Im}\,\lambda_{f_{CP}} \neq 0$ si osserva comunque violazione di CP. Questa situazione di violazione è detta *violazione di CP nell'interferenza tra decadimenti con e senza mixing*. Detto ${B^0}_{phys}(t)(\overline{B}^0{}_{phys}(t))$ l'evoluto temporale al tempo t dello stato che al tempo t_0 era un $B^0(\overline{B}^0)$, l'asimmetria dipendente dal tempo può essere scritta come:

$$a_{f_{CP}}(t) = \frac{\Gamma({B^0}_{phys}(t) \rightarrow f_{CP}) - \Gamma(\overline{B}^0{}_{phys}(t) \rightarrow f_{CP})}{\Gamma({B^0}_{phys}(t) \rightarrow f_{CP}) + \Gamma(\overline{B}^0{}_{phys}(t) \rightarrow f_{CP})}. \tag{E.4}$$

Questa asimmetria può essere scritta come

$$a_{f_{CP}}(t) = \frac{1 - |\lambda_{f_{CP}}|^2}{1 + |\lambda_{f_{CP}}|^2} \cos(\Delta m_B t) - \frac{2\,\mathrm{Im}\,\lambda_{f_{CP}}}{1 + |\lambda_{f_{CP}}|^2} \sin(\Delta m_B t), \tag{E.5}$$

che scritta in modo più sintetico diventa

$$a_{f_{CP}}(t) = C \cos(\Delta m_B t) - S \sin(\Delta m_B t), \tag{E.6}$$

dove,

$$C = \frac{1 - |\lambda_{f_{CP}}|^2}{1 + |\lambda_{f_{CP}}|^2}, \tag{E.7}$$

$$S = \frac{2\,\mathrm{Im}\,\lambda_{f_{CP}}}{1 + |\lambda_{f_{CP}}|^2}. \tag{E.8}$$

Questa asimmetria non si annulla se almeno uno dei tre tipi di violazione di CP è presente (in assenza di violazione, S e C devono entrambi andare a zero). C è diverso da zero solo quando il rapporto delle norme delle ampiezze differisce dall'unità, in caso cioè di violazione di CP diretta. Nei decadimenti con $|\lambda_{f_{CP}}| = 1$, $\mathrm{Im}\,\lambda_{f_{CP}} \neq 0$ la (E.5) si semplifica ulteriormente in

$$a_{f_{CP}}(t) = -\operatorname{Im}\lambda_{f_{CP}} \sin \Delta m_B t. \tag{E.9}$$

In quest'ultimo caso, quindi, un valore di S diverso da zero è evidenza di violazione di CP nell'interferenza tra decadimenti con e senza mixing, che può avvenire anche in assenza di violazione di CP puramente dovuta al decadimento o al mixing. Dalla (E.1), scritta come

$$\lambda_{f_{CP}} = \eta_{f_{CP}} |\lambda_{f_{CP}}| e^{-2i(\phi_B+\phi_f)}, \tag{E.10}$$

dove $2\phi_B$ è la fase di p/q e $2\phi_f$ è la fase del decadimento, ricaviamo l'espressione di $\operatorname{Im}\lambda_{f_{CP}}$ quando $|\lambda_{f_{CP}}| = 1$:

$$\operatorname{Im}\lambda_{f_{CP}} = -\eta_{f_{CP}} \sin[2(\phi_B + \phi_f)]. \tag{E.11}$$

La violazione di CP nell'interferenza dei decadimenti con e senza mixing è stata osservata per il sistema dei B neutri. L'abbondanza di autostati di CP nei decadimenti e le alte luminosità integrate raggiunte dalle B-*factories* ha reso possibile, negli ultimi anni, la misura di tali asimmetrie in diversi canali. Ulteriori decadimenti diventerebbero accessibili con un ulteriore aumento del dataset disponibile, presso una B-*factory* di nuova generazione.

E.3 L'Apparato Sperimentale

Esplorare la violazione di CP nel sistema dei B per il suo potenziale impatto sul Modello Standard e sulla cosmologia, richiede copiose produzioni di mesoni B, accurate misure dei tempi di volo e del sapore del B e ragionevolmente basso fondo per la ricostruzione. Queste richieste sono in buona misura soddisfatte dalle B-*factory* e^+e^- simmetriche e asimmetriche all'energia di produzione della $\Upsilon(4S)$.

La risonanza $\Upsilon(4S)$ fornisce un ambiente molto pulito per la ricostruzione dei B. Fasci e^+e^- asimmetrici forniscono un *boost* alla coppia dei mesoni B prodotti, permettendo la ricostruzione dei B di sapore come funzione del tempo di volo che intercorre nella separazione dei vertici dei B nel sistema del laboratorio, Δz. Limitazioni statistiche, per le quali la luminosità è il fattore critico, sono la dominante sorgente di errori per la asimmetria di CP dipendente dal tempo.

Due *b-factory* asimmetriche sono state costruite: PEP-II /BABAR, che ha cessato le sue operazioni nel 2008, e KEK-B/Belle, attualmente in presa dati. Precedentemente, la B-*factory* simmetrica CLEO (nell'anello CESR a Cornell) era stata in grado di produrre buoni risultati per la fisica del B, ma la sua simmetria non permetteva misure di violazione di CP dipendenti dal tempo. I dati usati in questa tesi sono stati collezionati ad un'energia del centro di massa pari a $\sqrt{s} = 10.58$ GeV, corrispondente alla massa della risonanza $\Upsilon(4S)$. L'asimmetria della macchina risulta in un boost tra il sistema di riferimento del laboratorio (LAB) e quello del centro di massa (CM) pari a $\beta\gamma \approx 0.56$. Nel corso delle sue operazioni PEP-II ha integrato 432.89 fb^{-1} alla risonanza $\Upsilon(4S)$; KEK-B ha integrato ad oggi più di 857.0 fb^{-1}alla risonanza $\Upsilon(4S)$[6].

Il detector *BABAR* [80] e i suoi sottosistemi sono stati progettati per soddisfare i requisiti cruciali per la misura di asimmetrie di CP dipendenti dal tempo. Attorno al punto di interazione è situato un detector di vertice composto da cinque piani di rivelatori a silicio (SVT), ciascuno dei quali compie una misura (sia nel senso longitudinale z, che in quello radiale ϕ) del punto di collisione. Lo scopo principale dell'SVT è la misura di precisione del vertice di decadimento dei mesoni B. L'SVT è circondato da una camera a deriva (DCH) ed entrambi sono immersi in un campo magnetico di 1.5 T, generato da un magnete superconduttore. Questi due sottosistemi forniscono una misura del parametro di impatto e del momento delle particelle cariche. L'identificazione delle particelle cariche è realizzata attraverso la misura della perdita di energia nell'SVT e nella DCH, coadiuvata da un rivelatore di luce Čerenkov a riflessione interna (DIRC), che misura l'angolo Čerenkov associato alle tracce cariche. Un calorimetro elettromagnetico (EMC) composto da cristalli di CsI(Tl) assicura la misura dei fotoni, dell'energia delle particelle cariche, l'identificazione di elettroni e dei mesoni K_L^0. Infine, rivelatori inseriti nel ferro di ritorno del magnete (IFR) permettono la rivelazione dei muoni e dei mesoni K_L^0. Per i primi 214fb^{-1} collezionati, l' IFR era composto da *resistive plate chambers* (RPC), per i 212fb^{-1} più recenti, una parte dell'RPC è stata sostituita da tubi a *stramer* (LST).

Le varie tecniche strumentali sono state scelte sulla base delle loro prestazioni e della loro affidabilità e robustezza.

E.4 Ricostruzione degli Eventi

La ricostruzione degli eventi è stata effettuata utilizzando il software del framework di *BABAR*. Per ogni evento, le particelle neutre e cariche, identificate nel detector, vengono combinate, mediante il software di *BABAR* a formare le liste dei candidati.

---

[6] Entrambe le macchine hanno collezionato dati anche alle risonanze $\Upsilon(2S)$ e $\Upsilon(3S)$ (KEK anche alla $\Upsilon(5S)$). Il dataset collezionato da PEP-II a tali risonanze è circa dieci volte maggiore dei precedenti dataset a tali energie.

– $\boldsymbol{\pi^0}$: I due fotoni con energia superiore a 30 MeV sono combinati per formare un candidato π^0 con massa compresa tra 0.110 e 0.160 GeV/c^2.

– $\boldsymbol{\rho^0}$: I mesoni ρ^0 sono stati ricostruiti combinando due particelle cariche con l'ipotesi di massa pioni. La massa dei candidati ρ^0 è stata tagliata tra 0.496 e 1.000 GeV/c^2.

– $\boldsymbol{\omega}$: Due tracce cariche della lista con l'ipotesi di pioni sono state combinate con un candidato π^0 per formare una ω. La massa dei candidati ω è stata tagliata 0.050 GeV/c^2 attorno alla massa nominale [98].

– $\boldsymbol{\eta_{\gamma\gamma}}$: I mesoni η che decadono nel canale $\eta \to \gamma\gamma$ sono ricostruiti combinando due fotoni di energia minima pari a 50 MeV. Viene effettuato un taglio sulla massa tra 0.470 e 0.620 GeV/c^2.

– $\boldsymbol{\eta_{3\pi}}$: Due tracce cariche con l'ipotesi di massa di pioni sono state combinate con un candidato π^0 per formare una η. Il taglio sulla massa è tra 0.510 e 0.575 GeV/c^2.

– $\boldsymbol{\eta'_{\rho\gamma}}$: I mesoni η' in $\eta' \to \rho^0\gamma$ sono ottenuti combinando un fotone di energia minima 100 MeV con un candidato ρ^0. Il candidato $\eta'_{\rho\gamma}$ è accettato se la massa è compresa nell'intervallo 0.900–1.010 GeV/c^2.

– $\boldsymbol{\eta'_{\eta\pi\pi}}$: I mesoni η' sono stati ricostruiti nei canali $\eta' \to \eta\pi^+\pi^-$ con $\eta \to \gamma\gamma$ o $\eta \to \pi^+\pi^-\pi^0$ combinando due particelle cariche con l'ipotesi di massa di pioni con un candidato η. I candidati hanno un taglio sulla massa nell'intervallo 0.900–1.010 GeV/c^2.

– $\boldsymbol{\phi}$: Due particelle cariche con l'ipotesi di massa di kaoni sono state combinate a formare un candidato ϕ. I candidati hanno un taglio sulla massa a 0.030 GeV/c^2 attorno al valore nominale [98]

– $\boldsymbol{K^0_S \to \pi^+\pi^-}$: Due tracce cariche con l'ipotesi di massa di pioni sono combinate a formare i candidati $K^0_S \to \pi^+\pi^-$. Il punto di produzione del mesone K^0_S è assunto essere nelle regione di interazione (IP); i canditati sono selezionati nella regione di massa 0.450–0.550 GeV/c^2.

– $\boldsymbol{K^0_S \to \pi^0\pi^0}$: Per $K^0_S \to \pi^0\pi^0$ inizialmente il punto di decadimento è scelto nell'origine, per cui gli angoli tra i fotoni sono sottostimati. Dopo aver determinato la direzione del momento della K^0_S, l'evento viene rifittato muovendo il punto di decadimento, in tal modo si perviene a un fit cinematico migliore, ove gli angoli tra i fotoni e la massa della K^0_S sono correttamente stimati. Sulla massa è stato effettuato un taglio 0.340 – 0.610 GeV/c^2.

- **$\boldsymbol{K^0_L}$**: I candidati K^0_L cono ricostruiti nell'EMC o nell'IFR. In entrambi i casi è nota la direzione e non il modulo del loro momento. Il modulo del momento e' determinato da un fit in cui la massa dei mesoni η' e B sono costretti al loro valore nominale [98].

E.4.1 Individuazione del Sapore del Mesone B (Tagging)

Un punto cruciale nell'analisi dipendenti dal tempo è la conoscenza del sapore del mesone B al momento del decadimento. Al momento della ricostruzione un algoritmo specifico (`Tag04`) [76], costituito da un insieme di reti neurali detti *sub-tagger*, determina il sapore del B, a partire dai parametri dell'oscillazione e dal sapore del B decaduto nel resto dell'evento ($B_{\rm tag}$). Il sapore di $B_{\rm tag}$ e' determinato a partire dal fatto che diversi decadimenti (soprattutto semileptonici e con kaoni veloci dal B o da prodotti charmati del suo decadimento) sono accessibili solo al B^0 (o al $\overline{B}^0$). A seconda dell'output dell'algoritmo di tagging l'evento viene taggato con un dato sapore e inserito in una di sette categorie, mutuamente esclusive, che mantengono traccia del metodo di determinazione del sapore (es. presenza di un leptone veloce, di un kaone, etc.).

E.5 Variabili Discriminanti

Ci sono due tipi di fondo che assumono particolare rilievo nell'ambito della nostra analisi: il fondo continuo $e^+e^-\to q\bar{q}$ $(q = u, d, s, c)$ e gli eventi $e^+e^-\to\Upsilon(4S)\to B\overline{B}$ con stati finali differenti da quelli da noi studiati, con o senza charm (che chiameremo rispettivamente $B\overline{B}$ con charm e $B\overline{B}$ senza charm (*charmless*)).

Il fondo $q\bar{q}$ puó essere studiato utilizzando i dati raccolti al di sotto della risonanza (dati *off-peak*). Gli eventi $B\overline{B}$ generici e senza charm sono stati studiati nel corso dell'analisi con eventi Monte Carlo. Questo tipo di fondo si è dimostrato piuttosto problematico poiché le forme delle variabili sia topologiche che cinematiche sono molto simili a quelle attese per gli eventi di segnale.

Dallo studio cinematico della reazione $e^+e^-\to q\bar{q}$ si deduce che gli eventi di fondo continuo e quelli $B\overline{B}$ hanno una diversa geometria. Poiché l'energia del fascio nel centro di massa è pari a 10.580 GeV, l'energia cinetica a disposizione delle coppie di quark $c\bar{c}$, e a maggior ragione per le coppie $u\bar{u}$, $d\bar{d}$, $s\bar{s}$ (*uds*), risulta essere molto elevata; i due jet dell'evento saranno quindi quasi antiparalleli tra loro. Nel caso di un processo del tipo $e^+e^-\to\Upsilon(4S)\to B\overline{B}$ l'energia cinetica a disposizione dei mesoni B sarà piuttosto bassa, di conseguenza l'evento risulterà maggiormente isotropo.

Per questo motivo distinguiamo due tipi di variabili discriminanti: variabili di tipo cinematico e variabili di tipo topologico. Come variabili cinematiche consideriamo :

- $\Delta E = E^*_B - \frac{1}{2}\sqrt{s}$: la differenza tra l'energia del candidato B e l'energia del fascio nel centro di massa.
- $m_{\text{ES}} = \sqrt{\frac{s}{4} - p^{*2}_B}$: la massa del B ricostruita sostituendo all'energia del B metà dell'energia del fascio, nel sistema di riferimento del centro di massa.

Tra le variabili topologiche troviamo:

- $\cos\theta_T$:il coseno dell'angolo di thrust, ovvero l'angolo compreso tra l'asse di thrust del candidato B definito come

  $$\mathrm{T} = max_{|\vec{n}|=1}\frac{\sum_i |\vec{n}\vec{p_i}|}{\sum_i |\vec{p_i}|}.$$

  e l'asse di thrust del resto dell'evento, calcolato nel centro di massa.
- $\mathcal{F}$: il discriminante di Fisher, un test statistico funzione di alcune variabili topologiche dell'evento, da noi ottimizzato appositamente sui canali studiati. Il discriminante di Fisher è dato dalla combinazione lineare delle seguenti variabili discriminanti: L_0 e L_2 definiti come $L_n = \sum_{i\in ROE} p_i \times |\cos(\theta_i)|^n$, dove la somma si estende sulle tracce non provenienti dal B, p_i rappresenta il momento della traccia e θ_i il suo angolo rispetto il thrust del candidato B; il valore assoluto del coseno dell'angolo compreso tra la direzione del B e l'asse del fascio; il valore assoluto del coseno dell'angolo tra la direzione del thrust del B e l'asse del fascio; il valore assoluto dell'output dell'algoritmo di tagging.

E.6 Selezione degli Eventi

Riassumiamo ora i tagli per la preparazione del campione di dati per il fit:

E.6.1 Tagli Comuni

- $5.25 < m_{\text{ES}} < 5.29\ \text{GeV}/c^2$ (Questo taglio non si applica nei modi con K^0_L).
- $|\Delta E < 0.2|$ GeV, $-0.15 < \Delta E < 0.15$ GeV per il decadimento $B{\rightarrow}\eta K^0_S$ (il taglio negativo asimmetrico sopprime gran parte del fondo $B\overline{B}$), $-0.01 < \Delta E < 0.08$ GeV per i decadimenti con K^0_L.
- un numero minimo di tracce cariche nell'evento maggiore di $\max[3, n_{tracce\ nel\ decadimento\ del\ B} + 1]$. Per sopprimere il fondo $e^+e^-{\rightarrow}\tau^+\tau^-$.
- $|\cos\theta_T| < 0.9$ ($|\cos\theta_T| < 0.8$ in $\eta_{\gamma\gamma}\omega$ e $\eta'_{\rho\gamma}\omega$).

- la probabilità di fit del vertice del B maggiore di zero.
- Le tracce cariche dai candidati $\eta_{3\pi}$, ω, $\eta'_{\eta\pi\pi}$, e $\eta'_{\rho\gamma}$ non devono essere consistenti con le ipotesi di kaoni, elettroni e protoni.
- Entrambe le tracce cariche dai candidati ϕ non devono essere consistenti con le ipotesi di pioni, elettroni e protoni
- I kaoni in $\eta' K^+$ soddisfano l'ipotesi di kaoni.
- $E_\gamma > 0.030$ GeV per π^0; $E_\gamma > 0.050$ GeV per $\eta_{\gamma\gamma}$ in $\eta'_{\eta\pi\pi}$; $E_\gamma > 0.100$ GeV per $\eta_{\gamma\gamma}$ primarie dal B, per γ in $\eta_{\gamma\gamma}$ di $\eta'_{\eta(\gamma\gamma)\pi\pi}K^+$ e per γ in $\eta'_{\rho\gamma}K$; $E_\gamma > 0.200$ GeV per $\eta'_{\rho\gamma}$ in $B{\rightarrow}\eta'_{\rho\gamma}\left(\eta'_{\eta\pi\pi}, \omega, \phi\right)$.
- M_{π^0} tra 0.120 e 0.150 GeV/c^2.
- M_η per η primaria dal B: tra 0.505 e 0.585 GeV/c^2 per $\eta_{\gamma\gamma}$ e tra 0.535 e 0.555 GeV/c^2 per $\eta_{3\pi}$.
- M_η per η in $\eta'_{\eta\pi\pi}$: tra 0.490 e 0.600 GeV/c^2 per $\eta_{\gamma\gamma}$ e tra 0.520 e 0.570 GeV/c^2 per $\eta_{3\pi}$.
- M_{ρ^0} tra 0.470 e 1.000 GeV/c^2.
- $\mathcal{H}_\rho$, definita come l'angolo tra il momento nel π^-, generato dal decadimento della ρ, e il momento di η' nel sistema di riferimento della ρ, è richiesta essere $|\mathcal{H}_\rho| < 0.9$.
- M_ω tra 0.735 e 0.825 GeV/c^2.
- $M_{\eta'}$ tra 0.930 e 0.990 GeV/c^2 per $\eta'_{\eta\pi\pi}$ e tra 0.910 e 0.990 GeV/c^2 per $\eta'_{\rho\gamma}$. $M_{\eta'}$ tra 0.930 e 0.980 GeV/c^2 per $\eta'_{\rho\gamma}$ in $B{\rightarrow}\eta' K$.
- M_ϕ tra 1.012 e 1.026 GeV/c^2.
- angolo di decadimento $\eta_{\gamma\gamma}$, $|\mathcal{H}_\eta| < 0.966$ per $\eta_{\gamma\gamma}K^0_S$; $|\mathcal{H}_\eta| < 0.95$ per $\eta_{\gamma\gamma}\eta_{\gamma\gamma}$ e $\eta_{\gamma\gamma}\eta_{3\pi}$.
- Per $K^0_S \rightarrow \pi^+\pi^-$ richiediamo la massa di K^0_S tra 0.486 e 0.510 GeV/c^2, la probabilità del fit $\chi^2 > 0.001$ e la lunghezza di volo maggiore di tre volte la sua incertezza . Per $K^0_s \rightarrow \pi^0\pi^0$, applichiamo solo il taglio sulla massa tra 0.468 e 0.528 GeV/c^2;
- $\pi^0 K^0_S$ veto per $\eta_{\gamma\gamma}K^0_S$: cerchiamo candidati π^0 che abbiano un fotone in comune con il nostro evento candidato. Tra questi scegliamo il π^0 con il secondo (non in comune) fotone più energetico. Rigettiamo il candidato $\eta_{\gamma\gamma}K^0_S$ se la massa del π^0 è tra 0.117 e 0.152 GeV/c^2 e l'energia del secondo fotone è più grande di 0.207 GeV.

- Taglio sul momento mancante trasverso della K_L^0, calcolato sottraendo il momento trasverso della K_L^0 dalla somma dei momenti trasversi, rispetto alla direzione di volo della K_L^0, delle altre particelle, neutre e cariche, dell'evento, $P_{miss}^{pro} > -0.80\,\mathrm{GeV}/c$;

- Taglio sul coseno del momento mancante, definito come il coseno dell'angolo polare del momento mancante, rispetto alla direzione del fascio nel sistema di riferimento del LAB, $\cos\theta_{P_{miss}} < 0.958$;

- Taglio su una rete neurale da noi costruita e ottimizzata per il rigetto di false K_L^0 ricostruite nell'EMC, $\mathrm{Output}_{ANN} > -0.20$.

E.6.2 Tagli Specifici per l'Analisi della Violazione di CP Dipendente dal Tempo

- $|\Delta t| < 20$ ps.

- $\sigma_{\Delta t} < 2.5$ ps.

E.7 Campione di Dati

Le analisi presentate in questa tesi sono basate sul campione di dati raccolto da *BABAR* nel periodo 1999-2007 (il campione è diviso in runs da 1 a 6, corrispondenti a diversi periodi di presa dati). Per l'analisi dell'asimmetria CP dipendente dal tempo utilizziamo il dataset finale di *BABAR* pari a , corrispondente a una luminosità integrata di 425.7 fb^{-1} di dati sulla risonanza (*on-peak*), per un totale di 467.4 ± 5.1 milioni di coppie $B\overline{B}$. Per l'analisi relativa ai decadimenti in stati finali formati da coppie di mesoni isoscalari utilizziamo una luminosità integrata di 423.5 fb^{-1} di dati sulla risonanza, per un totale di 465.0 ± 5.0 milioni di coppie $B\overline{B}$[7]. Sono inoltre usati dati presi 40 MeV al di sotto della risonanza (*off-peak*) pari a circa il 10% dei dati *on-peak*, per lo studio del fondo continuo. Per quanto riguarda gli eventi Monte Carlo, sono stati usati diversi milioni di eventi generici $B^0\overline{B}^0$ e B^+B^- simulati e diverse migliaia di decadimenti simulati nei canali da noi studiati.

---

[7] l'aggiornamento di quest'ultima analisi al dataset finale (circa 1% in più di dati) è prevista per la pubblicazione)

E.8 Misura dell'Asimmetria di CP Dipendente dal Tempo in $B\to\eta' K^0$

E.8.1 Interesse dei Canali Analizzati

I decadimenti adronici del mesone B in stati finali di particelle senza la presenza di charm, dei quali fanno parte quelli con mesoni η o η', sono di notevole importanza per la comprensione della violazione di CP. In essi un mesone B nello stato iniziale decade in due mesoni leggeri nello stato finale; tale decadimento implica l'emissione di un bosone vettore W carico, alla cui interazione sono associati gli elementi della matrice CKM. In particolare i canali da noi studiati procedono attraverso un diagramma a loop (pinguino), che risulta essere uno dei luoghi ove cercare Nuova Fisica, grazie alla possibilità delle presenza di nuove particelle pesanti nel loop. Il valore di S misurato in questo canale è atteso essere uguale a $\sin 2\beta$ misurato nei decadimenti $b\to c\bar{c}q$, a meno di piccole deviazioni dell'ordine di $\Delta S \approx 0.05$ [22, 64, 69, 65]. Nel presente lavoro di tesi il decadimento $B^0\to\eta' K^0$ è stato studiato nei sottodecadimenti $\eta'_{\eta(\gamma\gamma)\pi\pi}K^0_{S(\pi^+\pi^-)}$, $\eta'_{\rho\gamma}K^0_{S(\pi^+\pi^-)}$, $\eta'_{\eta(3\pi)\pi\pi}K^0_S$, $\eta'_{\eta(\gamma\gamma)\pi\pi}K^0_{S(\pi^0\pi^0)}$, $\eta'_{\rho\gamma}K^0_{S(\pi^0\pi^0)}$, $\eta'_{\eta(\gamma\gamma)\pi\pi}K^0_L$, $\eta'_{\eta(3\pi)\pi\pi}K^0_L$. Sono stati inoltre studiati i decadimenti carichi $B^+\to\eta' K^+$, come campione di controllo, nei sottodecadimenti $\eta'_{\eta(\gamma\gamma)\pi\pi}K^+$, $\eta'_{\rho\gamma}K^+$, $\eta'_{\eta(3\pi)\pi\pi}K^+$.

E.8.2 Fit a Massima Verosimiglianza

Gli eventi sono selezionati come descritto in sezione E.6. In caso di candidati multipli viene scelto quello con la più alta probabilità del fit del vertice del B, la scelta del candidato ha una efficienza (numero di volte in cui l'algoritmo sceglie un candidato ben ricostruito quando esso è presente) nel range 95–98%.

Nel fit abbiamo considerato cinque componenti: segnale, fondo continuo, fondo $B\overline{B}$ con charm, fondo $B\overline{B}$ senza charm con ΔE peaking per valori positivi, fondo $B\overline{B}$ senza charm con ΔE peaking per valori negativi. Le variabili utilizzate sono $m_{\rm ES}$ (solo nei canali con K^0_S), ΔEe $\mathcal{F}$. Per ciascun evento i, la likelihood ($\mathcal{L}_i$) è definita come:

$$\mathcal{L}_i = n_{sg}\mathcal{P}^i_{sg} + n_{q\bar{q}}\mathcal{P}^i_{q\bar{q}} + n_{bc}\mathcal{P}^i_{bc} + n_{bk+}\mathcal{P}^i_{bk+} + n_{bk-}\mathcal{P}^i_{bk-} \tag{E.12}$$

dove $\mathcal{P}^i_{sg}$, $\mathcal{P}^i_{q\bar{q}}$, $\mathcal{P}^i_{bc}$, $\mathcal{P}^i_{bk+}$, e $\mathcal{P}^i_{bk-}$ sono le probabilità per le componenti sopra elencate, valutate con le osservabili dell'i-esimo evento, come prodotto delle densità di probabilità (PDF) per ogni osservabile. n_{sg}, $n_{q\bar{q}}$, n_{bc}, n_{bk+} e n_{bk-} sono i numeri di segnali di eventi di segnale, fondo continuo, fondo $B\overline{B}$ con charm, fondo $B\overline{B}$ senza charm peaking positivo e fondo $B\overline{B}$ senza charm peaking negativo, rispettivamente. Tali parametri sono liberi nel fit. Studi sulle sorgenti di fondo ed esperimenti simulati (*toy experiments*) mostrano che le componenti di fondo $B\overline{B}$ sono utili solo nei canali con $\eta'_{\rho\gamma}$. La lista delle componenti di ciascun modo è mostrata in tab. E.1. Gli eventi che da studi sui Monte Carlo (MC) di segnale, risultano avere una o più particelle dell'evento di segnale ricostruito provenienti dal resto dell'evento sono detti self-cross-feed (SCF). Se la frazione di SCF, cioè il numero di eventi ricostruiti che presenta SCF rispetto al numero di eventi ricostruiti totali nel MC di segnale, in un dato canale è maggiore del 10%, il segnale è diviso in due componenti: ben ricostruita e SCF. In tal caso consideriamo un solo numero di eventi di segnale come parametro libero del fit e fissiamo il peso relativo delle due componenti in accordo a quanto trovato nel MC di segnale.

Decadimento	Componenti del fit
$\eta'_{\eta(\gamma\gamma)\pi\pi} K^0_{S(\pi^+\pi^-)}$	*sg*, $q\bar{q}$
$\eta'_{\eta(3\pi)\pi\pi} K^0_{S(\pi^+\pi^-)}$	*sgtr*, *sgscf*, $q\bar{q}$
$\eta'_{\rho\gamma} K^0_{S(\pi^+\pi^-)}$	*sg*, $q\bar{q}$, *bc*, *bk+*, *bk–*
$\eta'_{\eta(\gamma\gamma)\pi\pi} K^0_{S(\pi^0\pi^0)}$	*sgtr*, *sgscf*, $q\bar{q}$
$\eta'_{\rho\gamma} K^0_{S(\pi^0\pi^0)}$	*sgtr*, *sgscf*, $q\bar{q}$, *bc*, *bk+*, *bk–*
$\eta'_{\eta(\gamma\gamma)\pi\pi} K^0_L$	*sg*, $q\bar{q}$
$\eta'_{\eta(3\pi)\pi\pi} K^0_L$	*sgtr*, *sgscf*, $q\bar{q}$
$\eta'_{\eta(\gamma\gamma)\pi\pi} K^+$	*sg*, $q\bar{q}$
$\eta'_{\eta(3\pi)\pi\pi} K^+$	*sgtr*, *sgscf*, $q\bar{q}$
$\eta'_{\rho\gamma} K^+$	*sg*, $q\bar{q}$, *bc*, *bk+*, *bk–*

Table E.1: Componenti del fit per ciascun decadimento: *sg* segnale, *sgtr* segnale ben ricostruito, *sgscf* segnale SCF, $q\bar{q}$ fondo continuo, *bc* fondo $B\overline{B}$ con charm, *bk+* e *bk–* fondo $B\overline{B}$ senza charm.

Nell'analisi di violazione CP dipendente dal tempo, gli eventi sono divisi in categorie in accordo con le categorie dell'algoritmo di tagging. Per ciascun evento appartenente alla categoria c, la likelihood è definita come:

$$\begin{aligned} \mathcal{L}_{i,c} &= n_{sg} f_{sg,c} \mathcal{P}^{i,c}_{sg} + n_{q\bar{q}} f_{q\bar{q},c} \mathcal{P}^{i}_{q\bar{q}} + f_{bc,c} n_{bc} \mathcal{P}^{i}_{bc} + \\ & \quad + f_{sg,c} (n_{bk+} \mathcal{P}^{i}_{bk+} + n_{bk-} \mathcal{P}^{i}_{bk-}) \end{aligned} \tag{E.13}$$

dove $f_{sg,c}$, $f_{q\bar{q},c}$, e $f_{bc,c}$ indicano le frazioni di eventi di ciascuna categoria per ciascuna specie (le frazioni delle componenti di fondo $B\overline{B}$ senza charm sono assunte essere uguali a quelle del segnale). I valori di $f_{sg,c}$ sono fissati ai valori ottenuti dai fit di “BReco” sui canali ad alta statistica $B \to D^{(*)-} \left(\pi^+, \rho^+, a_1^+\right)$, mentre gli altri parametri sono lasciati liberi nel fit.

La likelihood estesa per tutti gli eventi appartenenti alla categoria c è data da:

$$\mathcal{L}_c = \exp\left(-n_{sg}f_{sg,c} - n_{q\bar{q}}f_{q\bar{q},c} - n_{bc}f_{bc,c} - (n_{bk+} + n_{bk-})f_{sg,c}\right) \times \prod_i^{N_c} \mathcal{L}_{i,c} \tag{E.14}$$

dove N_c è il numero totale di eventi in input, relativamente alla categoria c. La likelihood totale per tutte le categorie può essere scritta come:

$$\mathcal{L} = \prod_{c=0}^{6} \mathcal{L}_c \tag{E.15}$$

Per il fit combinato dei diversi sotto-decadimenti la likelihood diventa:

$$\mathcal{L} = \prod_d \mathcal{L}^d \tag{E.16}$$

dove l'indice d varia sull'insieme dei sottodecadimenti fittati. La likelihod utilizzata assume che le variabili discriminanti siano completamente scorrelate. Tali variabili presentano difatti solo piccole correlazioni residue, il cui effetto sul risultato finale è stimato usando toy experiments.
Il nostro fitter [97] minimizza l'espressione $-\ln\mathcal{L}$, in relazione a un dato set di parametri liberi.

E.8.3 Variabili Discriminanti e Loro PDF

Le variabili discriminanti usate nei fit a massima verosimiglianza sono: m_{ES}, ΔE, $\mathcal{F}$. Verranno ora descritte le PDF delle variabili discriminanti per le varie componenti. Le PDF per il segnale, il "self cross feed" e il fondo $B\overline{B}$ sono state fittate usando eventi simulati Monte Carlo mentre per il fondo continuo gli eventi nell'*on-peak sideband*, definito come:

- *Grand Side Band* (GSB): $5.25 < m_{\mathrm{ES}} < 5.27\ \mathrm{GeV}/c^2$
- ΔE *Side Band* (DESB): $0.1 < |\Delta E| < 0.2\ \mathrm{GeV}$ ($0.05 < \Delta E < 0.08\ \mathrm{GeV}$ per i modi con K_L^0)

I valori dei parametri delle PDF del fondo continuo in questi fit sono usati come valori iniziali nei fit a massima verosimiglianza dove vengono lasciati liberi. In caso di presenza di fondo $B\overline{B}$ con charm i nostri studi hanno mostrato una forte correlazione tra alcuni di questi parametri e gli yield. Si è quindi reso necessario bloccare il valore di tali parametri a quello fittato sulle *sideband*. La tabella E.2 riporta la parametrizzazione scelta per le differenti PDF. Dagli studi sul canale $\eta'_{\rho\gamma}K^+$, usato come campione di controllo, ricaviamo le seguenti correzioni tra i dati reali e i Monte Carlo per i parametri delle PDF di segnale:

- $m_{\rm ES}$ (Crystal Ball [105]): shift della media $-0.46 \pm 0.07\,{\rm MeV}/c^2$, fattore correttivo della sigma 0.955 ± 0.023.

- ΔE (Doppia Gaussiana): shift della media $-1.5 \pm 0.6\,{\rm MeV}$, fattore correttivo della sigma 0.975 ± 0.027.

- $\mathcal{F}$ (Doppia Gaussiana): shift della media -0.029 ± 0.014, fattore correttivo della sigma 1.054 ± 0.025.

Tali correzioni consentono di tenere conto delle piccole differenze tra dati reali e simulati e sono applicate durante i fit sui dati reali.

Componente	ΔE	$m_{\rm ES}$	$\mathcal{F}$	Δt
sg	CB/CR/DG	CB	AG/AG+G/DG	*CP* model
sgtr	CB/CR/DG	CB	AG+G	*CP* model
sgscf	CB/CH4/G+CH3	CB/DG	AG/AG+G	*CP* model
$q\bar{q}$	CH1/IA	A	AG+CH1	TG
bc	CH4	A/A+G	AG	*CP* model
bk+	G+CH2	A+G/CB+G	AG/AG+G	*CP* model
bk–	CH1/CH4	A/A+G	AG	*CP* model

Table E.2: Parametrizzazione delle PDF usate per segnale, fondo continuo e fondo $B\overline{B}$. (G = Gaussiana, DG = doppia Gaussiana, TG = tripla Gaussiana, AG = Gaussiana asimmetrica, CB = Crystal Ball [105], CR = funzione di Cruijff, A = Argus [101], IA = Argus [101] inversa, CHn = polinomio di Chebyshev di grado n.)

E.8.4 Fit sulla Violazione di *CP* Dipendente dal Tempo

Introduzione

Definendo $\Delta t = t_{CP} - t_{\rm tag}$, dove t_{CP} e $t_{\rm tag}$ sono i tempi propri di decadimento dei due B, rispettivamente B_{CP} e $B_{\rm tag}$, la distribuzione del tasso di decadimento f_+ (f_-) per $B_{CP}\to f$ quando $B_{\rm tag}$ è un B^0 $(\overline{B}^0)$ è dato da

$$f_\pm(\Delta t) = \frac{e^{-|\Delta t|/\tau}}{4\tau}\left[1 \pm S_f \sin(\Delta m_d \Delta t) \mp C_f \cos(\Delta m_d \Delta t)\right], \qquad \text{(E.17)}$$

dove le varie quantità sono state definite in precedenza.

Nel caso di "tagging" imperfetto, l'eq. E.17 deve essere modificata e includere la probabilità di "mistag":

$$\begin{aligned} f_{B^0\,\mathrm{tag}} &= (1-w_{B^0})f_+ + w_{\bar{B}^0}f_-, \\ f_{\overline{B}^0\,\mathrm{tag}} &= (1-w_{\bar{B}^0})f_- + w_{B^0}f_+, \end{aligned} \tag{E.18}$$

dove w_{B^0} ($w_{\bar{B}^0}$) è la probabilità che un vero mesone B^0 ($\overline{B}^0$) sia taggato come $\overline{B}^0$ (B^0). Definendo il "mistag" medio $\langle w\rangle$, e la differenza di "mistag" Δw,

$$\begin{aligned} \langle w\rangle &= \frac{w_{B^0}+w_{\bar{B}^0}}{2}, \\ \Delta w &= w_{B^0}-w_{\bar{B}^0}, \end{aligned} \tag{E.19}$$

le distribuzioni del tasso di decadimento, assumendo una perfetta risoluzione del vertice, sono allora

$$\begin{aligned} f_{B^0\,\mathrm{tag}} &= \frac{e^{-|\Delta t|/\tau}}{4\tau}\left[1-\Delta w+(1-2\langle w\rangle)\left(S_f\sin(\Delta m_d\Delta t)-C_f\cos(\Delta m_d\Delta t)\right)\right], \\ f_{\overline{B}^0\,\mathrm{tag}} &= \frac{e^{-|\Delta t|/\tau}}{4\tau}\left[1+\Delta w-(1-2\langle w\rangle)\left(S_f\sin(\Delta m_d\Delta t)-C_f\cos(\Delta m_d\Delta t)\right)\right] \end{aligned} \tag{E.20}$$

La distribuzione finale (osservata) $F(\Delta t)$ è la convoluzione di $f(\Delta t)$ con la funzione della risoluzione del vertice sul segnale $\mathcal{R}_{\mathrm{sig}}(\Delta t)$

$$\begin{aligned} F_{B^0\,\mathrm{tag}} &= f_{B^0\,\mathrm{tag}}\otimes\mathcal{R}_{\mathrm{sig}}, \\ F_{\overline{B}^0\,\mathrm{tag}} &= f_{\overline{B}^0\,\mathrm{tag}}\otimes\mathcal{R}_{\mathrm{sig}}. \end{aligned} \tag{E.21}$$

Nei nostri fit fissiamo il valore di Δm_d e delle vite del B ai valori nominali [98]: $\Delta m_d = 0.507\pm0.005$ ps^{-1}, $\tau_{B^\pm} = 1.638\pm0.011$ ps, e $\tau_{B^0} = 1.530\pm0.009$ ps.

Parametrizzazione del Δt

L'intervallo di tempo Δt tra il decadimento del B_{tag} e del B_{CP} è calcolato a partire della separazione misurata Δz tra i vertici di decadimento dei due mesoni B lungo la direzione (z) dell'asse del fascio. Nella ricostruzione del vertice di B_{CP}, usiamo tutte le tracce cariche provenienti dal B. Il vertice di decadimento del B_{tag} è determinato a partire da tutte le tracce cariche eccetto quelle provenienti da B_{CP}.

La risoluzione del vertice è indipendente dal modo di decadimento del B ricostruito così i parametri per la funzione di risoluzione del Δt sono determinati dal fit sul campione BReco.

Per gli eventi di segnale, la funzione di risoluzione $\mathcal{R}_{\mathrm{sig}}(t)$ è modellata con una tripla gaussiana. Due gaussiane, dette principale (*core*) e coda (*tail*), hanno la larghezza proporzionale all'errore σ_t e la terza, detta esterna (*outlier*), ha la larghezza fissata a 8 ps. La media della gaussiana *outlier* è fissata a 0, mentre quelle della gaussiane *core* e *tail* sono moltiplicate per σ_t.

$$\begin{aligned}\mathcal{R}_{\rm sig}(t) &= (1 - f_{\rm tail} - f_{\rm out})\, G\left(t, s^{\mu}_{\rm core}\sigma_t, s^{\sigma}_{\rm core}\sigma_t\right) + f_{\rm tail} G\left(t, s^{\mu}_{\rm tail}\sigma_t, s^{\sigma}_{\rm tail}\sigma_t\right) \\ &+ f_{\rm out} G\left(t, \mu_{\rm out}, \sigma_{\rm out}\right) \qquad \text{(E.22)}\end{aligned}$$

dove $G(x, x_0, \sigma)$ è una gaussiana con media x_0 e deviazione standard σ.

La distribuzione Δt del fondo $q\bar{q}$ è modellata usando dati dell'*on-peak sideband*, mentre per il segnale e il fondo $B\overline{B}$ si utilizzano i parametri estratti dal fit sul BReco.

E.9 Sorgenti di Fondo

La principale sorgente di fondo nelle nostre analisi è il processo $e^+e^-\!\rightarrow\! q\bar{q}$, che presenta comunque caratteristiche ben distinte dal segnale. I canali con $\eta'\!\rightarrow\!\rho\gamma$ e quelli con K^0_L, soffrono inoltre di fondo da decadimenti del B diversi da quelli da noi studiati, sia con la presenza che con l'assenza del quark charm nello stato finale. La procedura seguita nell'analisi di tali fondi consiste nell'individuazione, mediante studi MC, dei canali che contribuiscono ad essi e nell'introduzione di opportune PDFs nel fit, per tenerne conto in modo corretto. I nostri studi mostrano che solo i canali con $\eta'_{\rho\gamma}$ necessitano l'introduzione di tale componente nel fit.

E.10 Errori Sistematici

Sono stati considerati i possibili contributi all'errore sistematico della misura. Sono qui presentati tali contributi nel caso del fit combinato a 7 canali.

- L'errore sulla forma delle PDFs è stimato variando i parametri del fit di $\pm 1\sigma$. Le variazioni dello stesso segno sono sommate in quadratura e il massimo delle due somme è considerato come sistematico. Troviamo 0.010 per S e 0.005 per C.
- Il bias trovato nei *toy experiments*, utilizzati per studiare l'effetto delle correlazioni tra le variabili usate nel fit e i possibili bias da esse derivanti, ha un'incertezza di 0.005 per S e 0.003 per C.
- Cambiando i valori di S e C per il fondo $B\overline{B}$ senza charm (fissati a zero nel fit nominale), otteniamo un contributo sistematico, relativo all'incertezza del contenuto di CP nel fondo, di 0.006 per S e 0.009 per C.

- Le incertezze dovute all'allineamento dell'SVT e alla posizione del beam-spot sono state stimate in accordo a quanto suggerito in [107]. Troviamo 0.004 per S e 0.004 per C per l'SVT, e 0.004 per S e 0.003 per C per il beam-spot.
- Il contributo di interferenza da transizioni Doppio Cabibbo Soppresse $\overline{b} \to \overline{u} c \overline{d}$ [79] nella parte di tag dell'evento sono state stimate in 0.005 per S e 0.008 per C.
- L'errore dovuto alla appropriatezza dell'utilizzo dei parametri del BReco è stato stimato ripetendo i fit con parametri estratti dai Monte Carlo di segnale. Consideriamo come sistematico il contributo maggiore tra i vari set di parametri. Troviamo 0.005 per S e 0.008 per C.
- L'errore dovuto alla presenza di SCF nel nostro segnale è stato stimato sostituendo la distribuzione Δt del BRreco con una fittata sugli eventi di SCF, per i canali con $\eta'_{\eta(3\pi)\pi\pi}$. Troviamo 0.002 per S e 0.001 per C.

Sommando tutti i sistematici in quadratura troviamo 0.015 per S e 0.021 per C.

E.11 Risultati

I risultati dei fit sono mostrati in tab. E.3, ove sono riportati il numero di eventi nel fit, le efficienze MC, il numero di eventi di segnale e fondo $B\overline{B}$, i valori di S e C per gli eventi $B\overline{B}$ con charm, il numero di parametri liberi nel fit, la correlazione tra S e C e i valori misurati di S e C per il segnale. I nostri risultati hanno una significanza statistica di 7.1 deviazioni standard per S e 0.9 deviazioni standard per C (includendo l'errore sistematico), rispetto all'ipotesi di assenza di violazione di CP.

I valori trovati nel fit (tab. E.3)sono corretti per il bias determinato nei *toy experiments*, i risultati finali sono

$$\begin{aligned}
S_{\eta' K^0} &= 0.586 \pm 0.078 \ \text{(stat)} \pm 0.015 \ \text{(syst)} \\
C_{\eta' K^0} &= -0.058 \pm 0.058 \ \text{(stat)} \pm 0.021 \ \text{(syst)} \\
\\
S_{\eta' K^0_S} &= 0.555 \pm 0.086 \ \text{(stat)} \pm 0.015 \ \text{(syst)} \\
C_{\eta' K^0_S} &= -0.095 \pm 0.064 \ \text{(stat)} \pm 0.021 \ \text{(syst)} \\
\\
S_{\eta' K^0_L} &= 0.818 \ ^{+0.174}_{-0.188} \ \text{(stat)} \pm 0.018 \ \text{(syst)} \\
C_{\eta' K^0_L} &= 0.085 \ ^{+0.134}_{-0.135} \ \text{(stat)} \pm 0.021 \ \text{(syst)}
\end{aligned}$$

Dove le prime due righe si riferiscono al fit combinato su tutti i sottodecadimenti, le successive due al fit combinato sui modi con K^0_S e le ultime a quello sui modi con K^0_L.

Quantità	$\eta'_1 K^0_{\pi^+\pi^-}$	$\eta'_2 K^0_{\pi^+\pi^-}$	$\eta'_3 K^0_{\pi^+\pi^-}$	$\eta'_1 K^0_{\pi^0\pi^0}$	$\eta'_2 K^0_{\pi^0\pi^0}$	$\eta'_1 K^0_L$	$\eta'_3 K^0_L$
Eventi in input	1416	20468	451	877	21909	18036	6213
Efficienza MC (%)	26.6	27.6	16.6	13.0	14.2	17.6	12.6
Eventi di segnale	476 ± 24	960 ± 39	168 ± 14	99 ± 13	164 ± 28	386 ± 32	169 ± 21
Eventi *bc*	–	457 ± 154	–	–	233 ± 131	–	–
Eventi *bk*	–	64 ± 39	–	–	8 ± 56	–	–
Eventi *bk*–	–	36 ± 113	–	–	167 ± 136	–	–
S *bc*	–	0.29 ± 0.21	–	–	-0.37 ± 0.27	–	–
C *bc*	–	-0.09 ± 0.18	–	–	-0.01 ± 0.29	–	–
# Parametri liberi	19	29	19	19	29	18	18
Correlazione $S-C$ (%)	6.5	5.1	1.9	0.0	–21.8	5.0	–10.6
S	0.70 ± 0.16	0.42 ± 0.12	0.81 ± 0.23	0.39 ± 0.35	0.94 ± 0.44	0.75 ± 0.22	0.87 ± 0.30
C	-0.14 ± 0.11	-0.06 ± 0.09	0.09 ± 0.20	0.18 ± 0.31	-0.16 ± 0.32	0.02 ± 0.16	0.19 ± 0.25
Fit TD Combinato:							
Eventi di segnale	476 ± 24	958 ± 39	168 ± 14	99 ± 13	169 ± 26	386 ± 32	170 ± 22
Eventi *bc*	–	450 ± 210	–	–	234 ± 134	–	–
Eventi *bk*+	–	66 ± 40	–	–	5 ± 50	–	–
Eventi *bk*–	–	42 ± 146	–	–	165 ± 140	–	–
S *bc*	–	0.25 ± 0.22	–	–	-0.30 ± 0.27	–	–
C *bc*	–	-0.09 ± 0.17	–	–	-0.03 ± 0.27	–	–
# Parametri liberi	107					34	
Correlazione $S-C$ (%)	4.0					1.0	
S	0.567 ± 0.086					$0.796^{+0.174}_{-0.188}$	
C	-0.082 ± 0.064					$0.072^{+0.134}_{-0.135}$	
TD all modes:							
Eventi di Segnale	476 ± 24	958 ± 39	168 ± 14	99 ± 13	169 ± 26	387 ± 32	169 ± 22
Eventi *bc*	–	448 ± 224	–	–	235 ± 134	–	–
Eventi *bk*+	–	66 ± 40	–	–	6 ± 50	–	–
Eventi *bk*–	–	43 ± 155	–	–	164±141	–	–
S *bc*	–	0.23 ± 0.22	–	–	-0.31 ± 0.26	–	–
C *bc*	–	-0.10 ± 0.17	–	–	-0.04 ± 0.26	–	–
# Parametri liberi	139						
Correlazione $S-C$ (%)	3.6						
S	0.597 ± 0.078						
C	-0.054 ± 0.058						

Table E.3: Risultati del fit per i modi neutri. I pedici per i modi di decadimento di η' denotano $\eta'_{\eta(\gamma\gamma)\pi\pi}$ (1), $\eta'_{\rho\gamma}$ (2) e $\eta'_{\eta(3\pi)\pi\pi}$ (3).

E.11.1 Proiezioni

Abbiamo effettuato le proiezioni di $m_{\rm ES}$, ΔE, e Δt per i nostri modi di decadimento. Il segnale è stato esaltato applicando un taglio su $R = \frac{\mathcal{P}_s}{\mathcal{P}_s+\sum\mathcal{P}_b}$, ove P_s e P_b sono le probabilità di un evento di essere segnale o fondo, rispettivamente. In fig. E.2 sono mostrate le proiezioni di $m_{\rm ES}$ e ΔE per i modi carichi e neutri. In fig. E.3 sono mostrate le proiezioni di Δt e le proiezioni delle asimmetrie per i modi neutri.

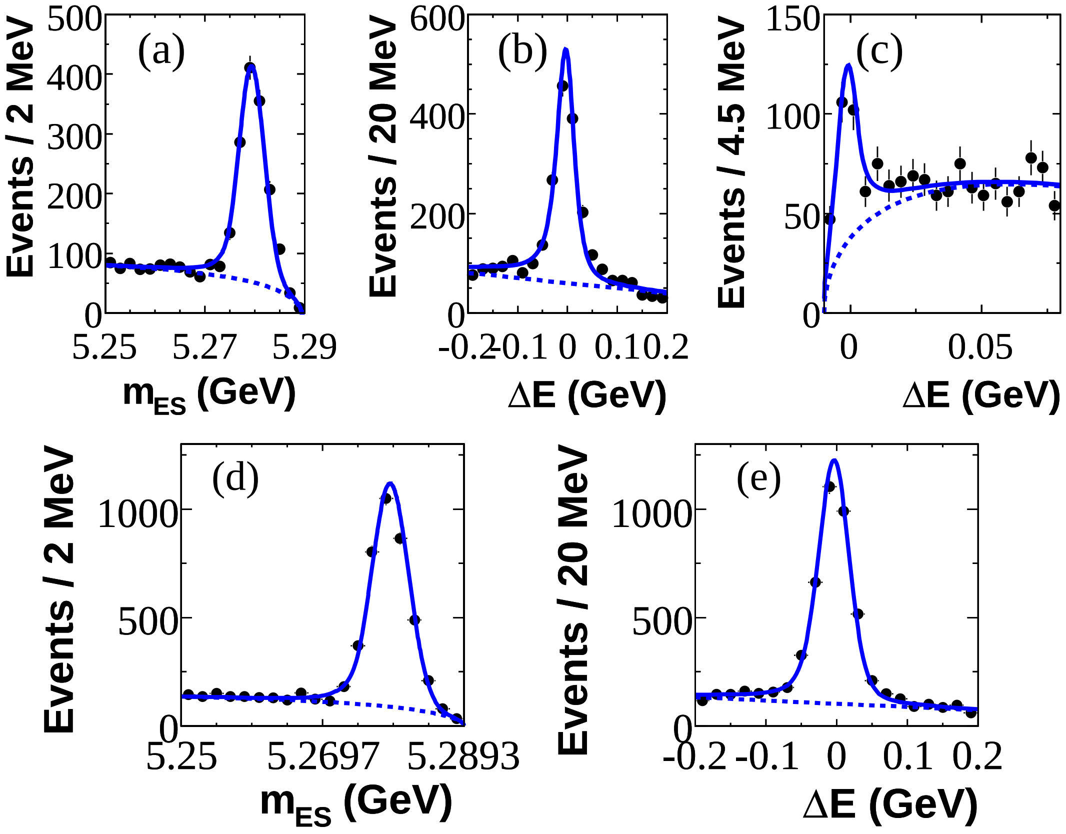

Figure E.2: Proiezioni di $m_{\rm ES}$ e ΔE per i canali neutri (in alto) e quelli carichi (in basso). Prima riga: $m_{\rm ES}$ per i modi con K^0_S (a), ΔE per i modi con K^0_S (b), ΔE per i modi con K^0_L (c). Seconda riga: $m_{\rm ES}$ (d) e ΔE (e) per i canali carichi.

E.11.2 Risultati per la Pubblicazione

A seguito di un accordo interno alla Collaborazione *BABAR*, i risultati per la pubblicazione [19] sono stati ottenuti combinando le curve delle likelihood fornite dal gruppo di Milano e da un altro gruppo della Collaborazione. I risultati di tale combinazione, ottenuta utilizzano la curva di Milano per i canali con K^0_L, e quella dell'altro gruppo per i

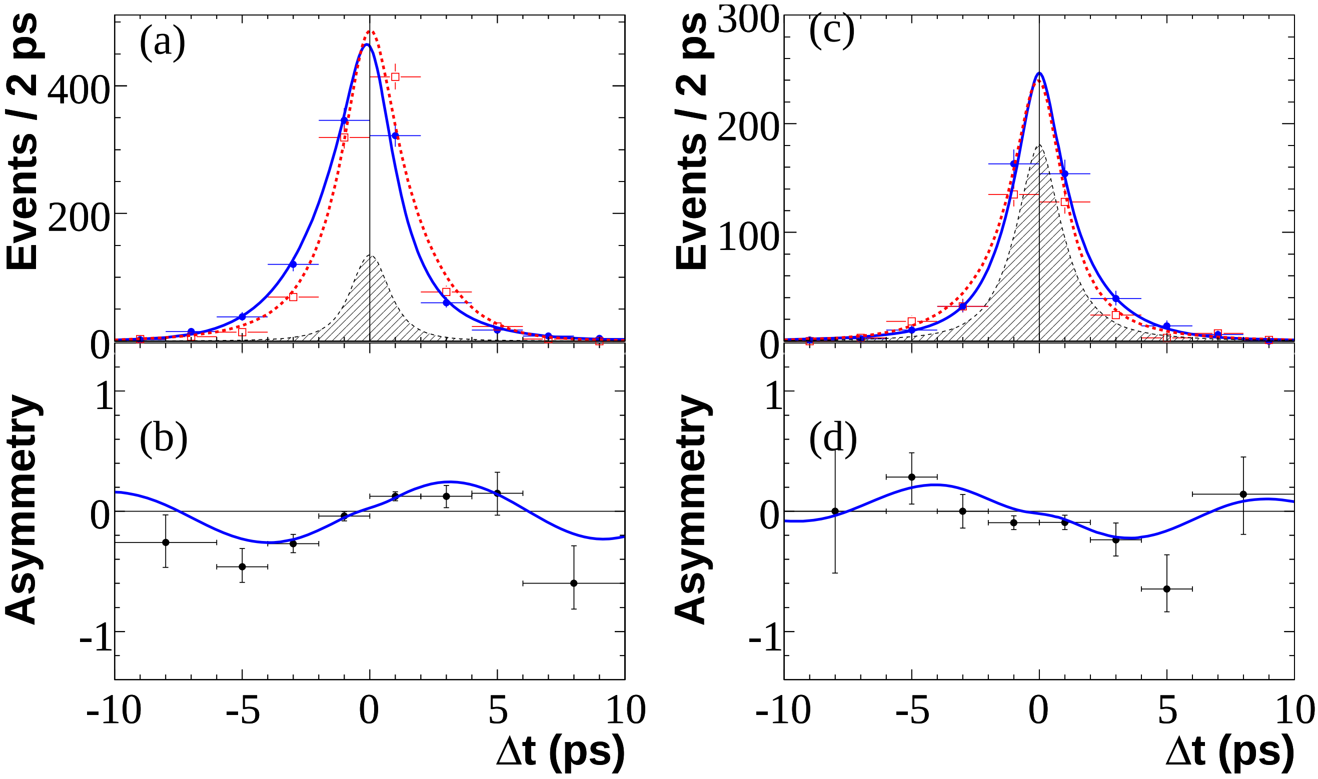

Figure E.3: Proiezioni su Δt per (a) $B^0 \to \eta' K_S^0$ e (c) $B^0 \to \eta' K_L^0$ dei dati (punti con bande di errore, per eventi taggati B^0 (N_{B^0}) in rettangoli rossi e taggati $\overline{B}^0$ ($N_{\overline{B}^0}$) in cerchi blu), funzioni di fit (tratteggiata rossa e continua blu per eventi taggati B^0 e $\overline{B}^0$ rispettivamente) e funzione di fit del fondo (regione nera). Mostriamo l'asimmetria $(N_{B^0} - N_{\overline{B}^0})/(N_{B^0} + N_{\overline{B}^0})$, per (b) $B^0 \to \eta' K_S^0$ e (d) $B^0 \to \eta' K_L^0$; le linee rappresentano le funzioni di fit.

canali con K_S^0, sono:

$$\begin{aligned} S_{\eta' K^0} &= 0.57 \pm 0.08 \ \ (\mathrm{stat}) \pm 0.02 \ \ (\mathrm{syst}) \\ C_{\eta' K^0} &= -0.08 \pm 0.06 \ \ (\mathrm{stat}) \pm 0.02 \ \ (\mathrm{syst}) \end{aligned}$$

E.12 Misure di Frazioni di Decadimento del Mesone B in Stati Finali Contenenti η o η'

E.12.1 Interesse dei Canali Analizzati

I canali da noi studiati sono legati alla determinazione della deviazione di S da $\sin 2\beta$ nei decadimenti $B\to\eta' K$ e $B\to\phi K$ [21, 20, 68]. Inoltre, la misura della frazione di decadimento di $B\to\eta K$ aiuterebbe la comprensione del motivo per cui il canale $B\to\eta' K$ è favorito mentre $B\to\eta K$ è soppresso [25, 70, 72, 67, 22]. La misura di tali canali sarebbe anche utile per confermare o confutare i modelli teorici [67, 22] che producono previsioni su di essi. Nel presente lavoro di tesi sono stati studiati i decadimenti del mesone B negli stati finali ηK^0_S, $\eta\eta$, $\eta'\eta'$, $\eta^{(\prime)}\omega$ ed $\eta^{(\prime)}\phi$, considerando i sottodecadimenti $\eta\to\gamma\gamma$, $\eta\to\pi^+\pi^-\pi^0$, $K^0_S\to\pi^+\pi^-$, $\eta'\to\eta_{\gamma\gamma}\pi^+\pi^-$, $\eta'\to\rho\gamma$, $\omega\to\pi^+\pi^-\pi^0$ e $\phi\to K^+K^-$. Non e' stato considerato il canale η' η' con entrambe le η' nel canale $\eta'\to\rho\gamma$ a causa della presenza di fondi molto alti.

E.12.2 Fit a Massima Verosimiglianza

Gli eventi sono selezionati come descritto in sezione E.6. In caso di candidati multipli viene scelto quello con la più alta probabilità del fit del vertice del B. La forma della likelihood usata è uguale a quella mostrata in eq. E.12, dove è considerato una unica componente di fondo $B\overline{B}$ senza charm, senza distinzioni basate sul segno della media della distribuzione del ΔE. Le variabili discriminanti usate nei fit a massima verosimiglianza per i vari canali sono elencate in tab. E.5. La lista delle componenti di ciascun modo e' mostrata in tab. E.4. La trattazione del SCF è uguale a quella esposta in sezione E.8.2.

E.12.3 Variabili Discriminanti e Loro PDF

La procedura utilizzata per fittare le PDFs delle variabili discriminanti è descritta in sezione E.8.3. I valori dei parametri delle PDF del fondo in questi fit sono usati come valori iniziali nei fit a massima verosimiglianza dove vengono lasciati liberi. In caso di presenza di fondo $B\overline{B}$ con charm i nostri studi hanno mostrato una forte correlazione tra alcuni di questi parametri ed il numero di eventi delle varie componenti, si è quindi reso necessario bloccare il valore di tali parametri a quello fittato sulle *sidebands*. La tabella E.6 riporta la parametrizzazione scelta per le differenti PDF. Dagli studi sul canale $B^-\to D^0\pi^-$, usato come campione di controllo, ricaviamo le seguenti correzioni tra i dati reali e i Monte Carlo per i parametri delle PDF di segnale:

Decadimento	Componenti nel Fit
$\eta_{\gamma\gamma}K^0_S$	*sg* , $q\bar{q}$, *bk*
$\eta_{3\pi}K^0_S$	*sg* , $q\bar{q}$
$\eta_{\gamma\gamma}\eta_{\gamma\gamma}$	*sg* , $q\bar{q}$
$\eta_{\gamma\gamma}\eta_{3\pi}$	*sg* , $q\bar{q}$
$\eta_{3\pi}\eta_{3\pi}$	*sg* , $q\bar{q}$
$\eta_{\gamma\gamma}\phi$	*sg* , $q\bar{q}$
$\eta_{3\pi}\phi$	*sg* , $q\bar{q}$
$\eta_{\gamma\gamma}\omega$	*sgtr* , *sgscf* , $q\bar{q}$, *bc* , *bk*
$\eta_{3\pi}\omega$	*sg* , $q\bar{q}$, *bc*
$\eta'_{\eta\pi\pi}\eta'_{\eta\pi\pi}$	*sg* , $q\bar{q}$
$\eta'_{\rho\gamma}\eta'_{\eta\pi\pi}$	*sg* , $q\bar{q}$, *bc* , *bk*
$\eta'_{\eta\pi\pi}\phi$	*sg* , $q\bar{q}$
$\eta'_{\rho\gamma}\phi$	*sgtr* , *sgscf* , $q\bar{q}$, *bc*
$\eta'_{\eta\pi\pi}\omega$	*sgtr* , *sgscf* , $q\bar{q}$, *bc*
$\eta'_{\rho\gamma}\omega$	*sgtr* , *sgscf* , $q\bar{q}$, *bc* , *bk*

Table E.4: Componenti del fit per ciascun decadimento: *sg* segnale, *sgtr* segnale ben ricostruito, *sgscf* segnale SCF, $q\bar{q}$ fondo continuo, *bc* fondo $B\overline{B}$ con charm, *bk* fondo $B\overline{B}$ senza charm.

Decadimento	Variabili
$\eta_{\gamma\gamma}K^0_S$	$m_{\rm ES}$, ΔE, $\mathcal{F}$
$\eta_{3\pi}K^0_S$	$m_{\rm ES}$, ΔE, $\mathcal{F}$
$\eta_{\gamma\gamma}\eta_{\gamma\gamma}$	$m_{\rm ES}$, ΔE, $\mathcal{F}$
$\eta_{\gamma\gamma}\eta_{3\pi}$	$m_{\rm ES}$, ΔE, $\mathcal{F}$
$\eta_{3\pi}\eta_{3\pi}$	$m_{\rm ES}$, ΔE, $\mathcal{F}$
$\eta_{\gamma\gamma}\phi$	$m_{\rm ES}$, ΔE, $\mathcal{F}$, $\mathcal{H}_\phi$
$\eta_{3\pi}\phi$	$m_{\rm ES}$, ΔE, $\mathcal{F}$, $\mathcal{H}_\phi$
$\eta_{\gamma\gamma}\omega$	$m_{\rm ES}$, ΔE, $\mathcal{F}$, M_ω , $\mathcal{H}_\omega$
$\eta_{3\pi}\omega$	$m_{\rm ES}$, ΔE, $\mathcal{F}$, M_ω , $\mathcal{H}_\omega$
$\eta'_{\eta\pi\pi}\eta'_{\eta\pi\pi}$	$m_{\rm ES}$, ΔE, $\mathcal{F}$, M'_η (entrambe)
$\eta'_{\eta\pi\pi}\eta'_{\rho\gamma}$	$m_{\rm ES}$, ΔE, $\mathcal{F}$, M'_η (entrambe)
$\eta'_{\eta\pi\pi}\phi$	$m_{\rm ES}$, ΔE, $\mathcal{F}$, M'_η, $\mathcal{H}_\phi$
$\eta'_{\rho\gamma}\phi$	$m_{\rm ES}$, ΔE, $\mathcal{F}$, M'_η, $\mathcal{H}_\phi$
$\eta'_{\eta\pi\pi}\omega$	$m_{\rm ES}$, ΔE, $\mathcal{F}$, M'_η, M_ω, $\mathcal{H}_\omega$
$\eta'_{\rho\gamma}\omega$	$m_{\rm ES}$, ΔE, $\mathcal{F}$, M'_η, M_ω, $\mathcal{H}_\omega$

Table E.5: Variabili usate nei fit, divise per canale di decadimento. L'elicità della ω, $\mathcal{H}_\omega$, è definita come il coseno dell'angolo tra la direzione di rinculo del B e la perpendicolare al piano identificato dai prodotti di decadimento della ω, nel sistema di riferimento della ω. L'elicità della ϕ, $\mathcal{H}_\phi$, è definita come il coseno dell'angolo tra la direzione di rinculo del B e la direzione del kaone più energetico, nel sistema di riferimento della ϕ.

- $m_{\rm ES}$ (Crystal Ball): shift della media $-0.53 \pm 0.01\ {\rm MeV}/c^2$, fattore correttivo della sigma 0.986 ± 0.004.

- ΔE (Doppia Gaussiana): shift della media $-2.2 \pm 0.1\ {\rm MeV}$, fattore correttivo della sigma 0.972 ± 0.005.

- $\mathcal{F}$ (Doppia Gaussiana): shift della media principale -0.029 ± 0.045, fattore correttivo della sigma principale 0.992 ± 0.005, shift della media secondaria 0.020 ± 0.094, fattore correttivo della sigma secondaria 1.011 ± 0.051 .

Tali correzioni sono applicate nel fit sui dati reali.

Componente	ΔE	$m_{\rm ES}$	$\mathcal{F}$	Massa $\eta'_{\rho\gamma}$	Massa $\eta'_{\eta\pi\pi}$	Massa ω	$\mathcal{H}_\phi$	$\mathcal{H}_\omega$
Segnale	DG/CR	CB	DG/AG+G	DG	DG/CR	DG	P2	P2
Segnale MCTruth	CR	CB	DG	DG/CR	CR	DG/CR	P2	P2
Segnale SCF	CH4	CB	DG	DG/CH1	CR	G+CH2	P2	P2
Fondo $q\bar{q}$	CH1	A	AG+CH1	CH1	G+CH2	G+CH1	CH2	CH4
Fondo $B\overline{B}$ con charm	CH2	A	DG	CH1	G+CH2	CH1	CH4	CH4
Fondo $B\overline{B}$ senza charm	CH4	DG	DG	CH1	G+CH2	G+CH1	CH2	CH4/G

Table E.6: Parametrizzazione delle PDF usate per segnale, fondo continuo e fondo $B\overline{B}$. (G = Gaussiana, DG = doppia Gaussiana, AG = Gaussiana asimmetrica, CB = Crystal Ball [105], CR = funzione di Cruijff, A = Argus [101], CHn = polinomio di Chebyshev di grado n.)

E.13 Sorgenti di Fondo

L'origine e la trattazione del fondo nella nostra analisi è uguale a quella esposta in sezione E.9. Le componenti di fondo utilizzate (quando necessario) in ciascun canale sono riportate in tab. E.5.

E.14 Errori Sistematici sulle Frazioni di Decadimento

Sono stati considerati i possibili contributi all'errore sistematico della misura delle frazioni di decadimento. Sono qui presentati tali contributi che sono poi riassunti in tab. E.7.

- *Errore sulla forma delle PDFs*: è stimato variando i parametri del fit di $\pm 1\sigma$. Le variazioni dello stesso segno sono sommate in quadratura e il massimo delle due somme è considerato come sistematico.

- *Errore sistematico dato dal bias*: è pari all'errore statistico del bias stesso (ricavato dai *toy experiments*), sommato in quadratura con metà del bias e con un contributo che tiene conto della presenza di code negative nel numero di eventi fittati nei canali a bassa statistica.
- *Molteplicità delle tracce*: errore sistematico associato alla richiesta di un minimo di tracce cariche nell'evento, stimato in 1%.
- *Efficienza di Track finding* : il *BABAR tracking working group* suggerisce un errore di 0.4% per tracia carica.
- *Efficienza di Track finding per* K_S^0: seguendo quanto prescritto dal *BABAR tracking working group* abbiamo un errore del 2.1%.
- *Efficienza per fotoni,* $\eta_{\gamma\gamma}$, π^0: seguendo quanto suggerito dal *BABAR neutrals working group*, troviamo un errore del 3% per π^0 (η) e dell'1.8% per fotoni isolati.
- *Luminosità,* B *counting*: Il *BABAR* B *counting group* suggerisce un errore dell'1.1% sul numero delle coppie $B\overline{B}$.
- *Frazioni di decadimento dei prodotti del* B: Tratti dai risultati esistenti [98].
- *Statistica MC* : l'errore sull'efficienza è calcolato per ciascun modo a partire dal numero di eventi di segnale simulati.
- *Forma dell'evento*: un errore sistematico dell'1% è assegnato a causa della variazione della forma delle variabili dopo il taglio su $\cos\theta_{\mathrm{T}}$.
- *PID*: Seguendo quanto indicato dal *BABAR PID working group* abbiamo stimato l'errore del PID in circa 1%.

Errore	$\eta_{\gamma\gamma}K^0_S$	$\eta_{3\pi}K^0_S$	$\eta_{\gamma\gamma}\eta_{\gamma\gamma}$	$\eta_{\gamma\gamma}\eta_{3\pi}$	$\eta_{3\pi}\eta_{3\pi}$	$\eta'_{\eta\pi\pi}\eta'_{\eta\pi\pi}$	$\eta'_{\rho\gamma}\eta'_{\eta\pi\pi}$
ML Fit bias (A)	0.7	0.5	1.3	0.5	3.3	3.4	1.2
MC/data Corr. (A)	1.0	0.4	3.4	1.0	1.1	0.2	1.2
Statistica MC (M)	0.4	0.5	0.3	0.4	0.5	0.5	0.5
Branching Frac. (M)	0.7	1.3	0.6	2.3	2.0	3.3	3.9
Moltiplic. Tracce (M)	1.0	1.0	1.0	1.0	1.0	1.0	1.0
Eff. Tracking (M)	–	0.8	–	0.8	1.6	1.6	1.6
Eff.π^0/$\eta_{\gamma\gamma}$ (M)	3.0	3.0	6.0	6.0	6.0	6.0	3.0
Eff. γ(M)	–	–	–	–	–	–	1.8
Eff. K^0_S (M)	2.1	2.1	–	–	–	–	–
B Counting (M)	1.1	1.1	1.1	1.1	1.1	1.1	1.1
$\cos\theta_{\mathrm{T}}$(M)	1.0	1.0	1.0	1.0	1.0	1.0	1.0
PID (M)	–	1.0	–	1.0	1.0	1.0	1.0
Totale Scorr. (eventi) (A)	1.2	0.6	3.6	1.1	3.6	3.4	1.7
Totale Scorr. (%) (M)	0.8	1.4	0.7	2.3	2.1	3.3	3.9
Totale Corr. (%)	4.1	4.3	6.3	6.4	6.4	6.4	4.4

Errore	$\eta_{\gamma\gamma}\phi$	$\eta_{3\pi}\phi$	$\eta_{\gamma\gamma}\omega$	$\eta_{3\pi}\omega$	$\eta'_{\eta\pi\pi}\phi$	$\eta'_{\rho\gamma}\phi$	$\eta'_{\eta\pi\pi}\omega$	$\eta'_{\rho\gamma}\omega$
ML Fit bias (A)	1.8	0.3	1.7	1.1	6.5	0.6	0.8	2.0
MC/data Corr. (A)	0.6	0.6	0.4	0.4	0.3	0.8	0.4	2.6
Statistica MC (M)	0.4	0.5	0.4	0.4	0.5	0.5	0.5	0.6
Branching Frac. (M)	0.3	0.2	0.4	0.4	0.3	0.5	0.5	0.8
Molteplic. Tracce (M)	1.0	1.0	1.0	1.0	1.0	1.0	1.0	1.0
Eff. Tracking (M)	0.8	1.6	0.8	1.6	1.6	1.6	1.6	1.6
Eff. π^0/$\eta_{\gamma\gamma}$(M)	3.0	3.0	6.0	6.0	3.0	–	3.0	3.0
Eff.γ(M)	–	–	–	–	–	1.8	–	1.8
B Counting (M)	1.1	1.1	1.1	1.1	1.1	1.1	1.1	1.1
$\cos\theta_{\mathrm{T}}$(M)	1.0	1.0	1.0	1.0	1.0	1.0	1.0	1.0
PID (M)	1.0	1.0	1.0	1.0	1.0	1.0	1.0	1.0
Totale Scorr. (eventi) (A)	1.9	0.7	1.7	1.2	6.5	1.0	0.9	3.3
Totale Scorr. (%) (M)	0.5	0.5	0.6	0.6	0.6	0.7	0.7	1.0
Totale Corr. (%)	3.7	4.0	6.4	4.0	3.2	4.0	3.2	4.5

Table E.7: Stima degli errori sistematici. Dividiamo gli errori sistematici in: errori scorrelati (prima parte delle tabelle) e correlati (seconda parte). I termini correlati e scorrelati sono in rapporto a diversi sottodecadimenti dello stesso canale. Alcuni di questi errori sono additivi (A) e sono dati in numero di eventi, altri sono moltiplicativi (M) e sono dati in percentuale. I vari contributi sono sommati in quadratura.

E.15 Risultati

I risultati sono mostrati in tab. E.8 and E.9. Riportiamo il numero di eventi nel fit, il numero di eventi di segnale, le efficienze e le produttorie dei Branching Fractions dei sottodecadimenti, il bias del fit, la significanza statistica, il valore della frazione di decadimento e il suo limite superiore ad un livello di confidenza del 90%. I differenti sottodecadimenti sono combinati attraverso la somma delle curve delle loro likelihood, tenendo opportunamente conto del bias del fit e degli errori sistematici. Tali errori sono inclusi nei risultati delle nostre misure convolvendo le curve delle likelihood con una gaussiana di media zero e larghezza pari all'errore sistematico scorrelato. Il limite superiore al livello di confidenza del 90% per la frazione di decadimento di ciascun canale è calcolato integrando numericamente la likelihood ottenuta combinando i sottodecadimenti.

E.15.1 Proiezioni

Abbiamo effettuato le proiezioni di $m_{\rm ES}$ e ΔE per i nostri modi di decadimento, utilizzando la tecnica esposta in sezione E.11.1. In fig. E.4 e E.5 mostriamo tali proiezioni.

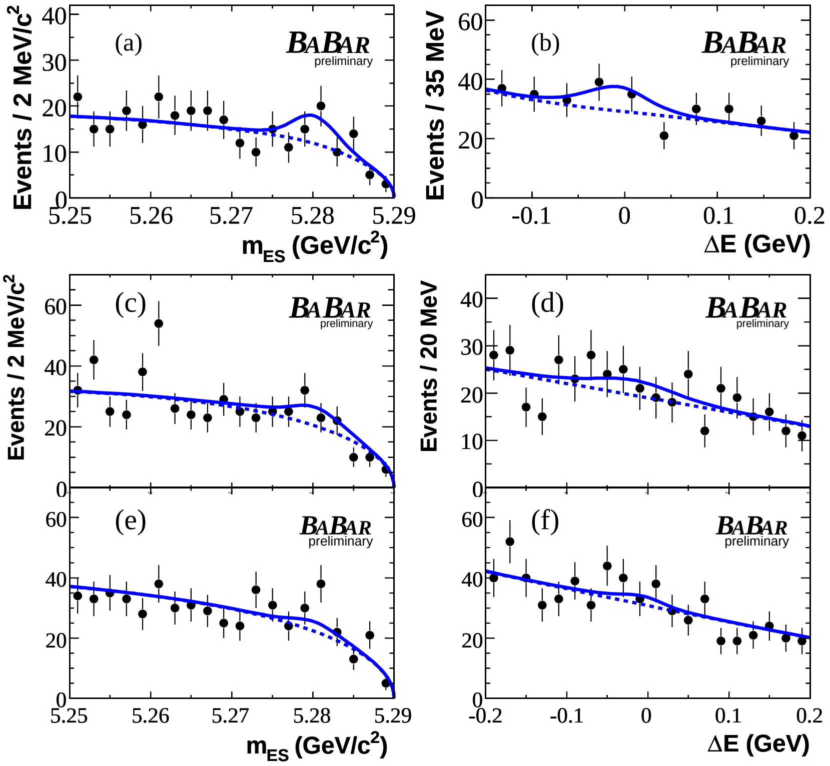

Figure E.4: Proiezioni di m_{ES} e ΔE per ηK^0_S (a, b), $\eta\eta$ (c, d) e $\eta'\eta'$ (e, f), considerando la somma dei sottodecadimenti. I punti con gli errori rappresentano i dati, le curve continue sono le funzioni di fit, le curve tratteggiate quelle del fondo.

Risultati del fit	$\eta_{\gamma\gamma}K^0_S$	$\eta_{3\pi}K^0_S$	$\eta_{\gamma\gamma}\eta_{\gamma\gamma}$	$\eta_{\gamma\gamma}\eta_{3\pi}$	$\eta_{3\pi}\eta_{3\pi}$	$\eta'_{\eta\pi\pi}\eta'_{\eta\pi\pi}$	$\eta'_{\rho\gamma}\eta'_{\eta\pi\pi}$
Eventi in input	3206	1329	2297	1800	263	208	7746
Eventi di Segnale	20^{+10}_{-9}	5^{+6}_{-4}	28^{+13}_{-12}	9^{+7}_{-6}	-5^{+4}_{-3}	2^{+2}_{-1}	11^{+9}_{-7}
Eventi $B\overline{B}$ charm	–	–	–	–	–	–	210 ± 83
Eventi $B\overline{B}$ peaking	35 ± 25	–	–	–	–	–	8 ± 22
# Combs/evento Dati	1.02	1.06	1.04	1.08	1.12	1.37	1.22
# Combs/evento MC	1.02	1.06	1.04	1.09	1.14	1.37	1.24
SCF(%)	2.3	5.2	4.0	8.2	11.3	13.3	13.1
Fit bias (eventi)	-0.4 ± 0.7	$+0.7 \pm 0.4$	$+2.2 \pm 0.7$	$+0.5 \pm 0.4$	-0.2 ± 0.1	$+0.1 \pm 0.1$	$+2.3 \pm 0.5$
MC ϵ (%)	33.3	21.4	25.4	19.2	11.9	21.1	20.4
Corr. $\pi^0/\eta_{\gamma\gamma}$ (%)	97.1	96.8	94.2	93.9	93.6	94.2	97.1
Corr. K^0_S (%)	95.7	95.7	–	–	–	–	–
ϵ corr. (%)	30.9	19.8	23.9	18.0	11.1	19.9	19.8
$\prod \mathcal{B}_i$ (%)	13.6	7.9	15.5	17.9	5.2	3.1	10.3
Corr. $\epsilon \times \prod \mathcal{B}_i$ (%)	4.20	1.56	3.70	3.22	0.58	0.62	2.04
Sign. Stat. (σ)	2.5	1.1	2.5	1.6	0.0	2.2	1.3
$\mathcal{B}(\times 10^{-6})$	1.0 ± 0.5	$0.6^{+0.8}_{-0.6}$	$1.5^{+0.8}_{-0.7}$	$0.6^{+0.5}_{-0.4}$	$-1.8^{+1.5}_{-1.1}$	$0.7^{+0.8}_{-0.5}$	$0.9^{+0.9}_{-0.7}$
Sign. Stat. con sist. (σ)	2.6		2.4			1.3	
$\mathcal{B}$ Combinato	$0.9^{+0.5}_{-0.4} \pm 0.1$		$0.8 \pm 0.4 \pm 0.1$			$0.9^{+0.8}_{-0.7} \pm 0.1$	
90% C.L. UL(sist. incl.)	1.6		1.4			2.1	

Table E.8: Risultati della misura delle frazioni di decadimento.

Risultati del fit ML Fit Quantity	$\eta_{\gamma\gamma}\phi$	$\eta_{3\pi}\phi$	$\eta_{\gamma\gamma}\omega$	$\eta_{3\pi}\omega$	$\eta'_{\eta\pi\pi}\phi$	$\eta'_{\rho\gamma}\phi$	$\eta'_{\eta\pi\pi}\omega$	$\eta'_{\rho\gamma}\omega$
Eventi in input	1401	486	11333	8613	455	6614	8388	52599
Eventi di Segnale	2^{+5}_{-4}	5^{+4}_{-3}	41^{+15}_{-13}	6^{+8}_{-7}	0^{+2}_{-1}	12^{+9}_{-8}	15^{+7}_{-6}	18^{+18}_{-16}
Eventi $B\overline{B}$ charm	$-$	$-$	217 ± 104	83 ± 80	$-$	186 ± 54	236 ± 88	3692 ± 303
Eventi $B\overline{B}$ peaking	$-$	$-$	58 ± 75	$-$	$-$	$-$	$-$	58 ± 108
# Combs/evento Dati	1.02	1.07	1.22	1.30	1.17	1.06	1.43	1.28
# Combs/evento MC	1.02	1.07	1.21	1.29	1.18	1.07	1.41	1.26
SCF(%)	2.9	6.0	14.9	18.7	6.8	7.3	19.7	19.1
Fit bias (eventi)	$+0.1 \pm 0.2$	$+0.3 \pm 0.2$	$+3.0 \pm 0.9$	-0.7 ± 0.5	-0.5 ± 0.1	$+0.5 \pm 0.5$	$+1.5 \pm 0.4$	$+3.4 \pm 1.1$
MC ϵ (%)	30.2	18.9	19.9	14.0	25.1	23.9	19.1	15.7
Corr. $\pi^0/\eta_{\gamma\gamma}$ (%)	97.1	96.8	93.9	93.6	97.1	$-$	93.9	96.8
ϵ corr. (%)	29.3	18.3	18.7	13.1	24.4	23.9	17.9	15.2
$\prod \mathcal{B}_i$ (%)	19.4	11.2	35.1	20.2	8.6	14.5	15.6	26.2
Corr. $\epsilon \times \prod \mathcal{B}_i$ (%)	5.68	2.05	6.56	2.65	2.10	3.47	2.79	3.98
Sign. Stat. (σ)	0.5	2.0	3.5	1.0	0.7	1.5	3.2	0.9
$\mathcal{B}(\times 10^{-6})$	$0.07^{+0.19}_{-0.15}$	$0.49^{+0.42}_{-0.31}$	$1.2^{+0.5}_{-0.4}$	0.5 ± 0.6	$0.05^{+0.21}_{-0.10}$	$0.71^{+0.56}_{-0.50}$	$1.0^{+0.5}_{-0.4}$	$0.8^{+1.0}_{-0.9}$
Sign. Stat. con sist. (σ)	1.7		3.5		1.3		3.1	
$\mathcal{B}$ Combinato	$0.22^{+0.19}_{-0.15} \pm 0.01$		$1.0^{+0.4}_{-0.3} \pm 0.1$		$0.5 \pm 0.4 \pm 0.1$		$1.0^{+0.5}_{-0.4} \pm 0.1$	
90% C.L. UL(sist. incl.)	0.52		1.6		1.2		1.7	

Table E.9: Risultati della misura delle frazioni di decadimento.

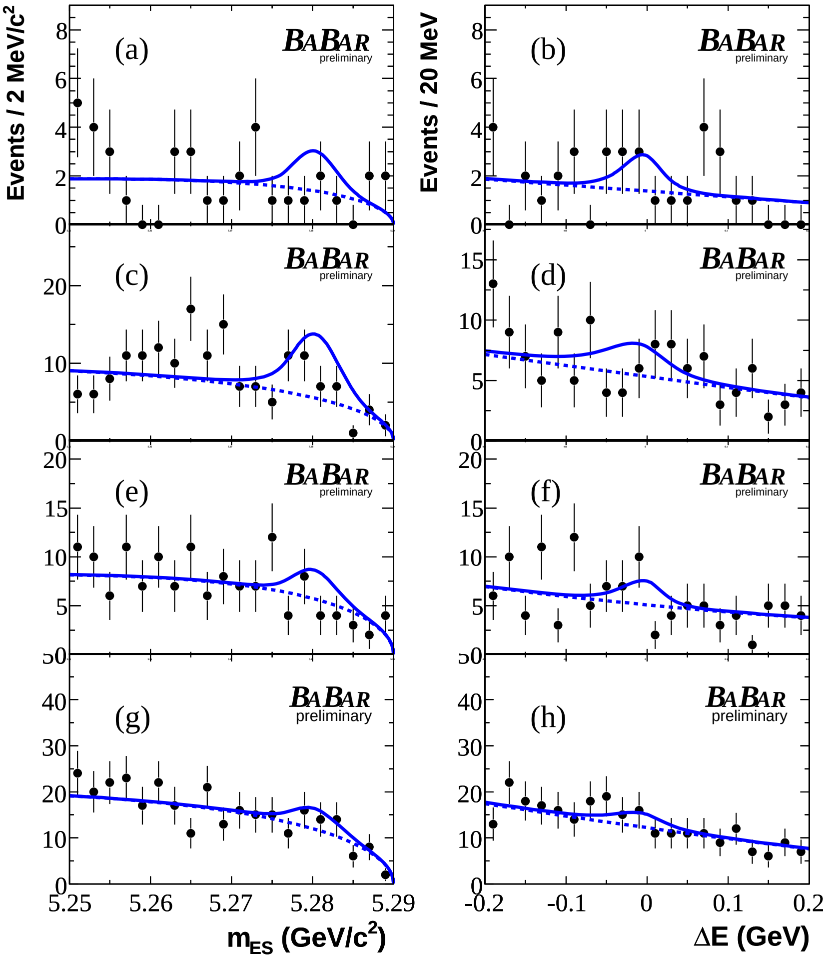

Figure E.5: Proiezioni di m_{ES} e ΔE per $\eta\phi$ (a, b), $\eta\omega$ (c, d), $\eta'\phi$ (e, f) e $\eta'\omega$ (g, h), considerando la somma dei sottodecadimenti. I punti con gli errori rappresentano i dati, le curve continue sono le funzioni di fit, le curve tratteggiate quelle del fondo.

E.16 Conclusioni

In questo lavoro di tesi abbiamo misurato i seguenti limiti superiori, con un livello di confidenza del 90%, delle frazioni di decadimento del mesone B (in unità di 10^{-6}), usando una statistica pari a 465.0×10^6 coppie $B\overline{B}$

$$\begin{aligned}
\mathcal{B}(B^0 \to \eta K^0) &< 1.6 \\
\mathcal{B}(B^0 \to \eta\eta) &< 1.4 \\
\mathcal{B}(B^0 \to \eta'\eta') &< 2.1 \\
\mathcal{B}(B^0 \to \eta\phi) &< 0.52 \\
\mathcal{B}(B^0 \to \eta\omega) &< 1.6 \\
\mathcal{B}(B^0 \to \eta'\phi) &< 1.2 \\
\mathcal{B}(B^0 \to \eta'\omega) &< 1.7
\end{aligned}$$

Non abbiamo avuto osservazioni di alcun modo. La significanza statistica per le nostre misure è nel range 1.3–3.5σ. È stata trovata un'evidenza a 3.5σ per il decadimento $B\to\eta\omega$ ed a 3.1σ per il decadimento $B\to\eta'\omega$. L'assenza dell'osservazione del decadimento $B^0\to\eta K^0$ apre degli interrogativi legati alla grande differenza con il decadimento del modo carico $B^+\to\eta K^+$, la cui frazione di decadimento è misurata essere $3.7 \pm 0.4 \pm 0.1$ [118]. I nostri risultati rappresentano sostanziali miglioramenti rispetto ai precedenti [109, 110, 111] e sono consistenti con le previsioni teoriche. Questi risultati saranno inclusi in un articolo che verrà presto sottomesso a *Physical Review D* e sono stati presentati alla Conferenza *Flavor Physics and CP Violation (FPCP) 2008*, svoltasi a Taipei, Taiwan.

Riguardo l'analisi della simmetria di CP dipendente dal tempo, abbiamo ricostruito 1820 ± 48 eventi $B^0 \to \eta' K^0$ utili per la misura dei parametri di asimmetria, usando il dataset completo di *BABAR*, con una statistica di 467.4×10^6 coppie $B\overline{B}$. Usiamo questi eventi per misurare i parametri di asimmetria CP dipendente dal tempo S e C. Troviamo $S = 0.59 \pm 0.08 \pm 0.02$ e $C = -0.06 \pm 0.06 \pm 0.02$. Un valore di C diverso da zero indicherebbe una violazione di CP diretta in $B^0 \to \eta' K^0$, mentre S è atteso essere uguale a $\sin 2\beta$ misurato in $B^0 \to J/\psi K^0_S$ [108]. Il nuovo valore misurato di S è in accordo con le previsioni del Modello Standard entro gli errori teorici e sperimentali. L'inconsistenza del nostro risultato per S rispetto all'ipotesi di conservazione della simmetria CP ($S = 0$) è pari a 7.1σ (includendo gli errori sistematici). La misura del parametro di violazione di CP diretta C si discosta di 0.9σ da zero (includendo gli errori sistematici). I nostri risultati sono in accordo con le precedenti misure [18]. Nonostante la statistica usata sia solo 20% più grande di quella usata nella precedente misura, otteniamo un miglioramento del 20% sull'errore di S e del 14% su quello di C Questo errore è il più piccolo mai raggiunto, sia da *BABAR* che da Belle, nella misura dei parametri della violazione CP dipendente dal tempo in una transizione $b{\rightarrow}s$. I risultati di questa analisi hanno contribuito ai risultati presentati alla *International Conference on High Energy Physics (ICHEP) 2008*, che ha avuto luogo in Philadelphia, USA, e sono inclusi in un articolo già sottomesso a *Physical Review D* [19].

Bibliography

[1] T. D. Lee and C. N. Yang, Phys. Rev. **104**, 254 (1956).

[2] C. S. Wu *et al.*, Phys. Rev. **105**, 1413 (1957).

[3] G. D. Rochester *et al.* Nature **4077**, 855 (1947).

[4] R. H. Dalitz, Proc. Third Int'l Conf. Cosmic Rays, Bagneres-de-Bigorre, France, pp. 236-239 (1953).

[5] J.H. Christensen *et al.*, Phys. Rev. Lett.**13** (1964) 138.

[6] N. Cabibbo, Phys. Rev. Lett.**10**, 531 (1963).

[7] M. Kobayashi and T. Maskawa, Prog. Theor. Phys. **49**, 652 (1973).

[8] J. E. Augustin *et al.* , Phys. Rev. Lett. **33**, 1406 (1974) ; J. J. Aubert *et al.* , Phys. Rev. Lett.**33**, 1404 (1974)

[9] S. W. Herb *et al.*, Fermilab E288 Collaboration, Phys. Rev. Lett. **39**, 252 (1977); W. R. Innes *et al.*, Phys. Rev. Lett. **39**, 1240 (1977).

[10] F. Abe *et al.*, CDF Collaboration, Phys. Rev. D **50**, 2966 (1994); **51**, 4623 (1994); **52**, 2605 (1995); Phys. Rev. Lett. **73**, 225 (1994); **74**, 2626 (1995); S. Abachi *et al.* ,D0 Collaboration, Phys. Rev. Lett. **72**, 2138 (1994); **74**, 2422 (1995); **74**, 2632 (1995); Phys. Rev. D **52**, 4877 (1995).

[11] V. Fanti *et al.*, NA48 Collaboration, Phys. Lett. B **465**, 335 (1999); A. Alavi-Harati *et al.*, KTEV Collaboration, Phys. Rev. Lett. **83**, 22, (1999).

[12] B. Aubert *et al.*, *BABAR* Collaboration, Phys. Rev. Lett. **89**, 201802 (2002); K. Abe *et al.*, Belle Collaboration, Phys. Rev. D **66**, 071102(R) (2002).

[13] B. Aubert *et al.*, *BABAR* Collaboration, Phys. Rev. Lett. **93**, 131801 (2004); Y. Chao *et al.*, Belle Collaboration, Phys. Rev. Lett. **93**, 191802 (2004).

[14] B. Aubert *et al.*, *BABAR* Collaboration, Phys. Rev. Lett.98, 211802 (2007); M. Staric *et al.*, Belle Collaboration, Phys. Rev. Lett.98, 211903 (2007).

[15] S.-K. Choi *et al.*, Belle Collaboration, Phys. Rev. Lett.100, 142001 (2008);

[16] B. Aubert *et al.*, *BABAR* Collaboration, hep-ex/0807.1086v3, (2008). To appear on *Physical Review Letters*.

[17] Y. Grossman and M. P. Worah, Phys. Lett. B **395**, 241 (1997); D. Atwood and A. Soni, Phys. Lett. B **405**, 150 (1997); M. Ciuchini *et al.*, Phys. Rev. Lett. **79**, 978 (1997).

[18] B. Aubert *et al.*, *BABAR* Collaboration, Phys. Rev. Lett.**98**, 031801 (2007).

[19] B. Aubert *et al.*, *BABAR* Collaboration, hep-ex/0809.1174

[20] Y. Grossman *et al.*, Phys. Rev. D **68**, 015004 (2003).

[21] C.-W. Chiang *et al.*, Phys. Rev. D **68**, 074012 (2003); M. Gronau *et al.*, Phys. Lett. B **596**, 107 (2004).

[22] M. Beneke and M. Neubert, Nucl. Phys. B **675**, 333 (2003).

[23] D. London and A. Soni, Phys. Lett. B **407**, 61 (1997).

[24] CLEO Collaboration, B. Behrens *et al.*, Phys. Rev. Lett. **80**, 3710 (1998).

[25] H. J. Lipkin, Phys. Lett. B **254**, 247 (1991).

[26] A. D. Sakharov, Sov. Phys Jour. Exp. Theor. Phys. (JEPT) **5**, 24 (1967)

[27] S. Weinberg, Phys. Rev. Lett. **19**, 1264 (1967).

[28] A. Salam, *Elementary Particle Physics*, Almquist and Wiksells, Stockhol (1968).

[29] S. Weinberg, Phys. Rev. Lett. **37**, 657 (1976).

[30] M. E. Peskin and D. V. Shroeder, *An Introduction to Quantum Field Theory*, Addison-Wesley, New York (1995).

[31] I. I. Bigi and A. I. Sanda, *CP Violation*, Cambridge University Press (2000).

[32] M. Gell-Mann and A. Pais, Phys. Rev. **97**, 1387 (1955).

[33] C. Albajar *et al.*, UA1 Collaboration, Phys. Lett. B **186**, 247 (1987).

[34] H. Albrecht *et al.*, ARGUS Collaboration, Phys. Lett. B **192**, 245 (1987).

[35] S. N. Ahmed *et al.*, SNO Collaboration, Phys. Rev. Lett. **92**, 181301 (2004). Y. Ashie *et al.*, Super-Kamiokande Collaboration, Phys. Rev. Lett. **93**, 101801 (2004).

[36] S. L. Glashow *et al.*, Phys. Rev. D **2**, 1285 (1970).

[37] L. L. Chau and W. Y. Keung, Phys. Rev. Lett. **53**, 1802 (1984).

[38] L. Wolfenstein, Phys. Rev. Lett. **51**, 1945 (1983).

[39] A. J. Buras *et al.*, Phys. Rev. D **50**, 3433 (1994).

[40] G. Buchalla *et al.*, Rev. Mod. Phys. **68**, 1125 (1996).

[41] N. Isgur and M.B. Wise, Phys. Lett. B **237**, 527 (1990); Phys. Lett. B **232**, 113 (1989).

[42] A.V. Manohar and M.B. Wise, Camb. Monogr. Part. Phys. Nucl. Phys. Cosmol. **10**, 1 (2000).

[43] H. Georgi, Phys. Lett. B **240**, 447 (1990).

[44] J.D. Bjorken, Nucl. Phys. Proc. Suppl. **11**, 325 (1989).

[45] M.J. Dugan and B. Grinstein, Phys. Lett. B **255**, 583 (1991).

[46] C.W. Bauer *et al.*, Phys. Rev. D **63**, 014006 (2001); C.W. Bauer *et al.*, Phys. Rev. D **63**, 114020 (2001); C.W. Bauer and I.W. Stewart, Phys. Lett. B **516**, 134 (2001); C.W. Bauer *et al.*, Phys. Rev. D **65**, 054022 (2002).

[47] C.Amsler *et al.*, Phys. Lett. B **667**, 1 (2008).

[48] `http://www.slac.stanford.edu/xorg/hfag/`

[49] CKMfitter Group (J. Charles *et al.*), Results as of Summer 2008 (ICHEP08), URL:`http://www.slac.stanford.edu/xorg/ckmfitter/`.

[50] A. Abulencia *et al.*, CDF Collaboration, Phys. Rev. Lett. **97**, 242003 (2006).

[51] M. Beneke *et al.*, Phys. Lett. B **576**, 173 (2003);
M. Ciuchini *et al.*, JHEP **0308**, 031 (2003)

[52] B. Aubert *et al.*, *BABAR* Collaboration, Phys. Rev. Lett. **99**, 171803 (2007); R. Itoh *et al.*, Belle Collaboration, Phys. Rev. Lett. **95**, 091601 (2005).

[53] Belle Collaboration, P. Krokovny *et al.*, Phys. Rev. Lett. **97**, 081801 (2006).

[54] M. Gronau and D. London, Phys. Rev. Lett. **65**, 3381 (1990).

[55] H.R. Quinn and A.E. Snyder, Phys. Rev. D **48**, 2139 (1993).

[56] B. Aubert *et al.*, *BABAR* Collaboration, Phys. Rev. Lett. **97**, 051802 (2006)

[57] M. Gronau and J. Zupan, Phys. Rev. D **73** 057502 (2006).

[58] Unitarity Triangle fit Group (M. Bona *et al.*), ICHEP'08 update, URL:`http://www.utfit.org`.

[59] M. Gronau and D. London, Phys. Lett. B **253**, 483 (1991); M. Gronau and D. Wyler, Phys. Lett. B **265**, 172 (1991).

[60] D. Atwood *et al.*, Phys. Rev. Lett. **78**, 3257 (1997); Phys. Rev. D **63**, 036005 (2001).

[61] A. Giri *et al.*, Phys. Rev. D **68**, 054018 (2003); Belle Collaboration (A. Poluektov *et al.*), Phys. Rev. D **70**, 072003 (2004).

[62] *BABAR* Collaboration, B. Aubert *et al.*, Phys. Rev. D **71**, 112003 (2005); Belle Collaboration, K. Abe *et al.*, Phys. Rev. Lett. **93**, 031802 (2004) [Erratumibid. **93**, 059901 (2004)]; Belle Collaboration, T. Gershon *et al.*, Phys. Lett. B **624**, 11 (2005).

[63] G. Buchalla *et al.*, JHEP **0509**, 074 (2005).

[64] M. Beneke, Phys. Lett. B **620**, 143 (2005).

[65] A. R. Williamson and J. Zupan, Phys. Rev. D **74**, 014003 (2006).

[66] M. Gronau *et al.*, Phys. Rev. D **74**, 093003 (2006)

[67] A. Ali *et al.*, Phys. Rev. D **58**, 094009 (1998); Y. H. Chen *et al.*, Phys. Rev. D **60**, 094014 (1999).

[68] G. Engelhard *et al.*, Phys. Rev. D **72**, 075013 (2005).

[69] H. Y. Cheng *et al.*, Phys. Rev. D **71**, 014030 (2005), Phys. Rev. D **72**, 014006 (2005); S. Fajfer *et al.*, Phys. Rev. D **72**, 114001 (2005).

[70] M. Gronau and J. L. Rosner, Phys. Rev. D **53**, 2516 (1996); A. S. Dighe *et al.*, Phys. Rev. Lett. **79**, 4333 (1997);

[71] M. R. Ahmady *et al.*, Phys. Rev. D **58**, 014015 (1998); D. Du *et al.*, Phys. Lett. **B426**, 133 (1998).

[72] I. Halperin and A. Zhitnitsky, Phys. Rev. D **56**, 7247 (1997); E. V. Shuryak and A. Zhitnitsky, *ibid.* **57**, 2001 (1998).

[73] P. Oddone, in *Procedings of the UCLA Workshop: Linear Collider* $B\overline{B}$ *Factory Conceptual Design*, edited by D. Stork (World Scientific), 243 (1987).

[74] PEP-II, *An Asymmetric B-Factory: Conceptual Design Report*, SLAC-PUB-418 (1993).

[75] S. Kurokawa and E. Kikutani, Nucl. Instrum. Methods Phys. Res., Sect. A **499**, 1 (2003).

[76] M. Bruinsma *et al.*, *BABAR Analysis Document #1025. (internal)*

[77] C. M. Bishop, *"Neural Networks for Pattern Recognition"*, Oxford University Press.

[78] M.P. Perrone and L.N. Cooper, in *Artificial Neural Networks for Speech and Vision, pp 126-142*, Chapman & Hall. (1993).

[79] O. Long, M. Baak, R. N. Cahn, D. Kirkby, Phys. Rev. D **68**, 034010 (2003).

[80] B. Aubert *et al.*,*BABAR* Collaboration, Nucl. Instrum. Methods Phys. Res., Sect. A **479**, 1 (2002).

[81] S. Patton, *Object Oriented Programming (For a novice, by a novice)*, CSN 95-341 C3S 95-003 (1995).

[82] For a C++ language description see B. Stroustrup, *The C++ Programming Language (Third Edition)*, Addison-Wesley, Reading, Massachussetts (1997).

[83] S. Agostinelli *et al.*, Nucl. Instrum. Methods Phys. Res., Sect. A **506**, 250 (2003).

[84] ROOT project web site:
`URL:http://root.cern.ch`.

[85] G. Cowan, *Statistical Data Analysis*, Clarendon Press, Oxford (1998).

[86] J. Friedman *et al.* , *The Elements of Statistical Learning*, Springer, New York (2001).

[87] S. Brandt, *Datenanalyse*, BI-Wissenshaftsverlag, Mannehim (1992); S. Brandt, *Statistical and Computational Methods in Data Analysis*, Springer, New York (1997).

[88] For a description of StatPatternRecognition package please refer to `URL:https://sourceforge.net/projects/statpatrec`.

[89] R. A. Fisher, Ann. Eugen. **7**, 179 (1936)

[90] For a description of TMVA package please refer to `URL:http://tmva.sourceforge.net/`.

[91] Y. Freund *et al.* , F. of Computer and System Science **55**, 119 (1997)

[92] M. Pivk and F. R. Le Diberder, Nucl. Instrum. Methods Phys. Res., Sect. A **555**, 356 (2005).

[93] See the web page the PAW project:
`URL:http://wwwasd.web.cern.ch/wwwasd/paw`.

[94] See the web page of the CINT project:
`URL:http://root.cern.ch/root/Cint.html`.

[95] See the web page of the RooFit project:
`URL:http://roofit.sourceforge.net/`.

[96] F. James, *MINUIT - function minimization and error analysis*, CERN Program Library Long Writeup D506.

[97] See the web page of the `MiFit` project:
`URL:http://lxmi.mi.infn.it/~lazzaro/MiFit/index.html`.

[98] W.-M. Yao *et al.*, J. Phys. G **33**, 1 (2006).

[99] B. Aubert *et al.*, *BABAR* Collaboration,Phys. Rev. Lett.94, 161803 (2005)

[100] B. Aubert *et al.*, *BABAR* Collaboration, Phys. Rev. D **66**, 032003 (2002).

[101] H. Albrecht *et al.*, ARGUS Collaboration, Phys. Lett. B **241**, 278 (1990); **254**, 288 (1991).

[102] B. Aubert *et al.*, *BABAR* Collaboration, Phys. Rev. Lett.91, 161801 (2003).

[103] B. Aubert *et al.*, *BABAR* Collaboration, Phys. Rev. Lett.94, 191802 (2005).

[104] A. Lazzaro *et al.*, *BABAR Analysis Document #1507 (internal)* (2006).

[105] J.E. Gaiser, Appendix-F, *Charmonium Spectroscopy from Radiative Decays of the J/ψ and ψ'*, Ph.D. thesis, SLAC-R-255 (1982).

[106] `http://www.slac.stanford.edu/BFROOT/www/Physics/ Analysis/AWG/Neutrals/validation/recipie22.html`

[107] `http://www.slac.stanford.edu/BFROOT/www/Detector/SVT/LocalAlignment/systematics-14/`

[108] B. Aubert *et al.*, *BABAR* Collaboration, hep-ex/0808.1903v1, (2008).

[109] B. Aubert *et al.*, *BABAR* Collaboration, Phys. Rev. Lett. **93**, 181806 (2004).

[110] B. Aubert *et al.*, *BABAR* Collaboration, Phys. Rev. Lett. **95**, 131803 (2005).

[111] B. Aubert *et al.*, *BABAR* Collaboration, Phys. Rev. D **74**, 051106 (2006).

[112] K. Lingel , *et al.Ann. Rev. Nucl. Part. Sci.* **48**, 253 (1998)

[113] Y. H. Chen *et al.*, Phys. Rev. D **60**, 094014 (1999)

[114] `http://www.slac.stanford.edu/BFROOT/www/Physics/TrackEfficTaskForce/TrackingTaskForce-2007-R22.html`

[115] M. Allen *et al.*, *BABAR Analysis Document #870 (internal)* (2004).

[116] A. Lazzaro *et al.*, *BABAR Analysis Document #705 (internal)* (2004). F. Blanc *et al.*, *BABAR Analysis Document #744 (internal)* (2004).

[117] E. Antillon *et al.*, *BABAR Analysis Document #1244 (internal)* (2006).

[118] B. Aubert *et al.*, *BABAR* Collaboration, Phys. Rev. Lett. **97**, 201802 (2006)

Acknowledgments

First of all, I would like to thank Professor Fernando Palombo for his help in my thesis work and Doctor Alfio Lazzaro for his constant work of teaching me data analysis and advanced programming. Many thanks also to Dr. Vincenzo Lombardo, for his interest in my thesis work and for many important suggestions. I'd also like to thank Dr. Simone Stracka, Dr. Alessandro Berra, Dr. Paolo Gandini and all other members of Milan *BABAR* group for their help in different situation and the time we spent together during my thesis work. Finally I thank all *BABAR* AWG conveners, AWG members, RC members, CWR readers and FN readers involved into the review process of these analyses.

Ringraziamenti

Vorrei ringraziare innanzitutto il Professor Fernando Palombo, per avermi seguito nella mie analisi e per il molto sostegno, pratico e morale, nei giorni della *Battaglia Finale*. Un grandissimo grazie ad Alfio, che mi ha iniziato, giorno per giorno, all'arte dell'analisi e della programmazione. Come suprema forma di riconoscenza per essere riuscito in quest'opera pur essendo fisicamente in (nell'ordine) California, Bologna, Australia, Ginevra, ecco per lui un piccolo poema epico:

```
TPostDoc *alfio = new TPostDoc("Milano");
TCompCenter *cineca = new TCompCenter("Cineca","Bologna");
alfio->GoTo(cineca);
TProgram *xfit = new TProgram("fitter");
alfio->Run(xfit,cineca,"ncpus=40");
alfio->Dream("Run(xfit,cineca,"ncpus=500")");
```

Grazie anche a `“DiFineDiMondo”` Vincenzo, moderno scinziato diviso tra la fisica e le neuroscienze, sempre pronto a cogliere lo stato della mia analisi in 3 minuti e a dare preziosi consigli. Grazie a Simone che, sotto una scorza di fisico integerrimo e severo nasconde tanta gentilezza e disponibilita'. Come dimenticare poi Ale, con i molti discorsi sui *La-Li-Lu-Le-Lo*, e Paolo, che mi ha reso edotto sul processo di fermentazione carbonica della birra e su come arrivare vittoriosi al *bloody river*. Un grazie anche a Gino e Mario (al secolo Francesco e Vittorio) per la compagnia nell'ultimo periodo. Un sentito ringraziamento va al Professor Francesco Ragusa, per il molto tempo dedicatomi in questi anni per aiutarmi a scegliere che strada intraprendere nel mio corso di studi.

Un grazie davvero grande a mia mamma Piera, che mi ha trasmesso fin da bambino la passione per la fisica, a mio papà Carlo, che mi ha sempre sostenuto in tutte le mie scelte, e a mio fratello Enrico, che ha capito presto quando era il momento di lasciarmi in pace a studiare e quando quello di giocare insieme alla `Play`.

Un grande grazie agli amici che mi sono stati vicini in quest'ultimo periodo, la Cicci, fantastica giramondo, Angelo (Bell'Uomo) e Simona. Impossibile poi trascurare chi mi è stato accanto per tanti anni, anche se ultimamente li vedo sempre meno: Nando, Matteo

“Zio”, Yuri, Cisco, Chiara, Daniela, Massimo, Marco “DePo”, Simo, la Lele, il Lele “Verga” e Valentina “Raffi”, grazie per tutti i momenti belli passati insieme.

I compagni dell’università sono tanti e, vista la mia scarsa memoria, qualcuno sfuggirà di certo: Serena, Diana, Marco, Roberto “Nico”, il chiarissimo Simone, la dottoressa Giulia, il gaio Michele, Elia “Zari”, Andrea F., Pietro, Fede, Margherita.

Un grazie a due amici del liceo che vedo molto poco ma a cui sono estremamente legato: Elena e Gigi.

Dulcis in fundo grazie a Valentina, la persona che mi è stata vicina più di tutte, che mi ha sostenuto nei momenti tristi, ha gioito con me in quelli felici e ha fatto in modo che cambiassi per essere una persona migliore: grazie amore, di tutto.